The Molecular Enzymology of Cytochromes P450

of Biotechnological and Medical Interest

Thesis submitted for the degree of

Doctor of Philosophy

at the University of Leicester

by

Ashley James Warman BSc (Hons) (Liverpool)

Department of Biochemistry

University of Leicester

January 2007

UMI Number: U222873

UMI

Dissertation Publishing

ProQuest

Acknowledgements

Firstly, I would like to express my gratitude towards Professor Andrew Munro for allowing me the opportunity study in his research group, which was a thoroughly gratifying experience. Furthermore, I thank him for the generous donation of his time and expertise during the supervision of this thesis, as well as his encouragement, inspiration, and support. Secondly, I would like to thank my committee members Professor Nigel Scrutton and Professor Michael Sutcliffe for their helpful discussions and guidance during this research project. I must also acknowledge the invaluable assistance and advice provided by Dr. Ker Marshall throughout the molecular biology aspects of this work, and by Dr. Kirsty McLean with respect to the spectroscopic studies. A number of collaborators, without whom parts of this thesis would not have been possible, also merit acknowledgement: I thank Dr. Miles Cheesman and Dr. Harriet Seward for their assistance with, and explanations of, EPR and MCD studies, as well as Dr. John Clarkson and Dr. Rachael Littleford at the University of Strathclyde for running resonance Raman investigations. Additionally, I thank Andrew Lawrence at Queen Mary, University of London, for his assistance with LCMS studies, and also Professor Nigel Brown, University of Birmingham, for providing the genetic material essential for the CYP116B1 characterization. I express my appreciation to all members, past and present, of the Munro and Scrutton research groups who assisted, discussed, guided, and above all made my time at Leicester enjoyable. I also thank the B.B.S.R.C. for funding this work. Finally, I must thank Rachel and all the members of my family, whose support and encouragement throughout the course of my research has been immeasurable.

Table of contents

Abstract

The cytochromes P450 are a diverse superfamily of heme *b*-containing monooxygenase enzymes found in all kingdoms of life. Their roles range from the synthesis of antibiotics and microbial cell wall components to xenobiotic detoxification and drug metabolism; and hence these enzymes are of interest to both the medical and biotechnological sectors. This thesis reports the characterization of two members of this superfamily of enzymes, namely CYP51 from the human pathogen *Mycobacterium tuberculosis* and CYP116B1 from the soil bacterium *Ralstonia metallidurans*. CYP51 is one of twenty P450s encoded in the *M. tuberculosis* genome and has been demonstrated to demethylate sterol compounds. In this study, the spectroscopic and biophysical properties of CYP51 are extensively characterized, focussing on the unusual collapse of its carbon monoxy-ferrous form to a novel, protonated species, and interactions with a proposed physiological redox partner: a ferredoxin protein found adjacent to CYP51 in the *M. tuberculosis* genome. Additionally, the plausibility of this enzyme as a target for novel anti-tubercular agents, particularly azole-antifungal derivatives, is assessed. The study of CYP116B1 describes initial characterization of a novel fusion of a cytochrome P450 to its flavin mononucleotide- and iron sulphur cluster-containing redox partner protein, which is of potential biotechnological interest due to its proposed role in thiocarbamate herbicide degradation. Assessment of the spectroscopic properties of this enzyme are reported, including electron paramagnetic resonance and resonance Raman investigations of the heme macrocycle, in addition to kinetic studies of the electron transfer capabilities of the reductase component. Furthermore, the search for a substrate for this P450 and subsequent LCMS product analysis assays with the thiocarbamates EPTC and vernolate are detailed. The dissection of CYP116B1 into its constituent domains, in order to facilitate studies of the P450 and reductase components in isolation and further resolve structural, spectroscopic, and thermodynamic properties of this enzyme is also reported.

Abbreviations

Commonly used abbreviations in this report:

2Fe-2S	Iron-sulphur cluster consisting of 2 iron and 2 sulphur atoms
CD	Circular dichroism
CIP	Calf intestinal phosphatase
CPR	Cytochrome P450 reductase
Da	Daltons
DCPIP	Dichlorophenolindophenol
ddH20	Distilled, deionised water
DMSO	Dimethyl sulfoxide
dNTPs	Deoxynucleotide triphosphates
DTT	Dithiothreitol
EDTA	Ethylenediaminetetraacetic acid
EPR	Electron paramagnetic resonance
EPTC	S-ethyl dipropylthiocarbamate
FAD	Flavin adenine dinucleotide
FMN	Flavin mononucleotide
GdmCl	Guanidinium chloride
HCl	Hydrochloric acid
HPLC	High-pressure liquid chromatography
IPTG	Isopropyl-β-D-thiogalactoside
kb	Kilobases
kbp	Kilobase pairs
kDa	Kilodaltons
KPi	Potassium phosphate
LCMS	Liquid chromatography mass spectroscopy
Mbp	Megabase pairs
MS	Mass spectroscopy
MS^2	Tandem mass spectroscopy
Mtb	*Mycobacterium tuberculosis*
NADH	β-Nicotinamide-adenine-dinucleotide (reduced form)
NADPH	β-Nicotinamide-adenine-dinucleotide-phoshate (reduced form)
NAD(P)H	Either of the above
nm	Nanometers
O.D.	Optical density
PCR	Polymerase chain reaction
PFOR	Phthalate-family oxygenase reductase
Pfu	*Pyrococcus furiosus* DNA polymerase
PMSF	Phenylmethylsulfonyl fluoride
PNACL	Protein and Nucleic Acid Laboratory (University of Leicester)
SDS	Sodium dodecyl sulfate
TAE	Tris acetate buffer
TBE	Tris borate buffer
Tm	Melting temperature
UV	Ultra-violet
X-gal	5-bromo-4-chloro-3-indolyl β-D-galactopyranoside

Chapter 1

Introduction

1.1 General information

This project investigates a number of cytochromes P450 of potential interest in either a medical or biotechnological context. In order to do this, the project will focus on two distinct cytochromes P450. One of these is a novel P450/redox partner fusion enzyme derived from a species of soil bacteria, namely *Ralstonia metallidurans*, which is capable of existing in the presence of heavy metals (1). The other is a 14α-sterol demethylase found in the mycobacterial species *Mycobacterium tuberculosis* (Mtb). The study hopes to encompass the characterization of these P450s using a multitude of spectroscopic, thermodynamic, and kinetic techniques, more of which will be described in Chapter 3. Ahead of the presentation of the results of these characterizations, this chapter serves as a general introduction to the cytochromes P450 and the current understanding of these proteins, before moving on to discuss both of the studied enzymes and the organisms to which they pertain. Hence, this chapter begins with a description of the position the cytochromes P450 within enzyme hierarchy, followed by an account of how the P450s perform their physiological roles in both prokaryotes and eukaryotes.

1.2 Enzymes: Biological catalysts

Enzymes are distinguished from other proteins, such as collagen, insulin, and albumin, by their ability to catalyse biologically-relevant chemical reactions. They do this by lowering the activation energy required for the reaction to occur, and frequently increase the rate of reaction to a level of use to the cells in which they are contained (Figure 1). Significantly, enzymes, which are either tethered to a membrane or free-floating within the cytosol, are not permanently altered during reaction catalysis and can perform the same reaction many thousands of times if required to do so (2,3). In order to catalyse a reaction, the enzyme must form a complex with a substrate molecule within its active site, be it e.g. a xenobiotic compound, a molecule of DNA, or a nucleotide triphosphate. Importantly, the shape and size of this active site, and the positions and types of amino acids therein, define the substrate(s) of all enzymes, allowing certain molecules to enter and bind in productive modes, whilst others are excluded. The enzyme:substrate interactions, which occur by random molecular collisions, result in structural/conformational changes of the enzyme and/or substrate

that put strain on chemical bonds within the substrate, thus lowering the activation energy of the reaction and facilitating catalysis (2). Catalysis is often further aided by the incorporation of a cofactor, for example a transition metal such as zinc, iron or copper bound within the protein structure on the boundary of the active site, whose electronic flexibility is utilised during the reaction. Other cofactors include flavin adenine dinucleotide (FAD), flavin mononucleotide (FMN) and iron-sulphur clusters (e.g. 2Fe-2S or 3Fe-4S), which act to transport electrons required for catalytic activity (3-6), and will be detailed further in Chapter 1.8. Other enzymes may require coenzymes (such as NADPH and NADH), which are reversibly bound to the enzymes and are regenerated by other enzyme systems in the cell following their reactions with the relevant enzyme.
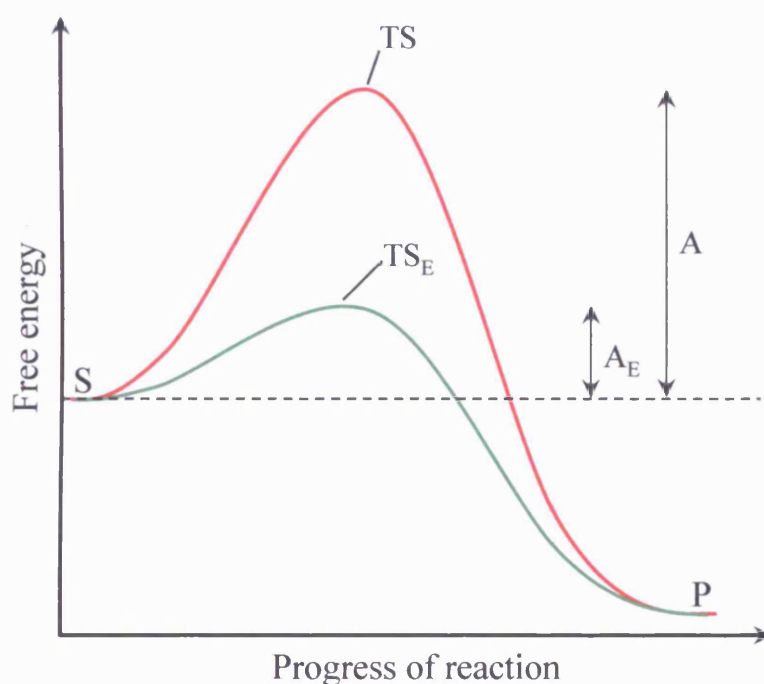
Figure 1 In all chemical reactions an unstable, high-energy species (transition state, TS) must be achieved before products (P) can be formed from the substrates/reagents (S). In the case of an enzyme-free reaction (red), the energy required to achieve this state (i.e. the activation energy, A) can be substantial, and thus rate-limiting (or prohibitive) for product formation. In an enzyme-catalysed reaction (green), the energies of the reactants and products are unaltered, however the enzyme reduces the activation energy (A_E) required to achieve the transition state (TS_E), thus allowing the reaction to proceed more rapidly than the equivalent enzyme-free reaction. Enzymes are not consumed in the reactions that they catalyse and do not increase the yield of a reaction *per se*, however by increasing the reaction rate more product may be obtained than for an enzyme-free reaction over the same time course (2,7).

Enzymes, which are found in organisms from all domains of life, perform a multitude of physiological roles ranging from involvement in cell replication and protein degradation to metabolic pathways and xenobiotic elimination. Whilst it is not possible to list all of the roles that enzymes play, a number of examples are given here in order to give a sense of the scope of their physiological importance, and a summary of the major enzyme classes is given in Table 1. For example, DNA unwinding prior to its replication is facilitated by enzymes named helicases, whilst DNA polymerases are required for the polymerization of dioxyribonucleotides during this same replication process (8,9). Enzymes can also perform anabolic (synthetic) roles, such as in the biosynthesis of the amino acid glutamine from glutamic acid by glutamine synthase, or catabolic (degradative) roles, such as the breakdown of proteins by serine proteases (10,11). Additionally, enzymes can mediate other chemical modifications of their substrates. Examples of such enzymes are isomerases, which can interconvert *cis* and *trans* forms of chemicals, and aromatases, which catalyse the conversion of cyclic hydrocarbons to aromatic rings structures (12,13). Further examples of the physiological roles of enzymes include the hydrolysis of ATP by myosin ATPase, integral to the cross-bridging of actin and myosin filaments that leads to muscle movement, as well as the breakdown of starch to maltose by the enzyme amylase found in human saliva (14,15).

Class	Type of reaction catalysed	Example
1 – Oxidoreductases	Transfer of electrons	Alcohol dehydrogenase
2 – Transferases	Transfer of functional groups	Hexokinase
3 – Hydrolases	Hydrolysis reactions	Trypsin
4 – Lyases	Bond cleavage	Pyruvate decarboxylase
5 – Isomerases	Transfer of groups within a molecule	Maleate isomerase
6 – Ligases/Synthases	Bond formation coupled to ATP hydrolysis	Pyruvate carboxylase

Table 1 The major enzyme classes, as determined by the internationally recognized enzyme nomenclature system. All enzymes are assigned to a particular class depending on the type of reaction that they catalyse, and are subsequently uniquely classified by the specific reaction that they facilitate. For example, the cytochromes P450 are oxidoreductases and are thus members of Class 1. However, they are differentiated from non-heme oxidoreductases such as alcohol dehydrogenases and cytochrome P450 reductase, and are thus members of different sub-classes to these zinc- and flavin-containing oxidoreductases (7,16,17).

A significant group of enzymes are the oxidoreductases, of which the enzymes studied in Chapter 3, 4 and 5 are members. These enzymes catalyse electron transfer reactions. Examples of these redox enzymes include alcohol dehydrogenases which facilitate the conversion of ethanol to acetylaldehyde, the important first step in alcohol detoxification in mammals, as well as monoamine oxidase, which catalyses the breakdown of neurotransmitters by oxidative deamination of monoamines to aldehyde compounds (16,18). As previously mentioned, this group of enzymes also includes the cytochromes P450, as well as the flavin- and iron-sulphur-containing proteins that serve these monooxygenases. These proteins have been shown to be involved in the xenobiotic detoxification reactions within the human liver, as well as energy-generating pathways in bacteria (i.e. catabolism of molecules such as camphor and terpenes), and cell wall-component synthesis (sterols) in fungi (3,19,20), and will be dealt with in more depth in the next section. Whilst the oxidoreductases themselves demonstrate a large range of activities, they are bound together by the fact that they all catalyze the transfer of electrons from one molecule to another in order to catalyze physiologically significant reactions (21). Although the nature of the proteins and the catalytic roles in individual systems involving oxidoreductases vary, their overall purpose remains constant; the oxidation of an electron donating species in order to derive electrons with which to reduce the next part of the redox system, be it another protein or the substrate of the terminal protein (3). As members of the oxidoreductases, cytochromes P450 are no exception to this general rule, generally receiving their electrons from iron-sulphur- and flavin-containing proteins that ultimately derive electrons (again almost invariably) from reductants such as β-Nicotinamide-Adenine-Dinucleotide-Phoshate (NADPH) or β-Nicotinamide-Adenine-Dinucleotide (NADH). In the ensuing sections a description of the reactions catalysed by the cytochromes P450 is given, detailing how they execute chemical modifications (i.e. oxygenations of substrates) with the aid of their associated redox proteins.

1.3 General physiology of the cytochromes P450

The term "cytochrome P450" (P450) covers a vast number of enzymes that form a superfamily (i.e. a hierarchically organised collection of families that are grouped according to amino acid sequence identity and (usually) substrate preference) related by a key structural feature, namely their cysteinate-ligated heme-based active centre (3).

The P450s bind a *b*-type heme and the conserved cysteinate ligates the heme iron. They are found throughout nature, having been identified in mammals, plants, lower eukaryotes and bacteria (3,22-24). Their functions are numerous and wide-ranging, and these enzymes perform many cell-essential catalysis reactions. They have been shown to be involved in drug metabolism, activation, and detoxification in mammals; antibiotic synthesis in fungi, herbicide resistance in plants; as well as in multiple biosynthetic and metabolic pathways in bacterial species (25), roles that will be discussed further in Chapter 1.6. It is the broad and varied roles of this family of enzymes that has led them to be widely investigated, typically utilising studies such as ligand binding, characterization of the incorporated heme macrocycle and its spin-state modulation, kinetic studies of substrate turnover and electron transfer between members of P450 redox systems, product analysis, mutational engineering of substrate selectivity, as well as the determination of intermediates of the P450 catalytic cycle, and structural studies, in order to better understand their functions and mechanisms (21,26-30). A number of P450 structures have now been resolved (~160 including mutant forms), including those of the well-characterized P450cam from *Ps. putida*, P450 BM3 from *B. megaterium*, and *M. tuberculosis* CYP51 (31-36). These studies have enhanced the understanding of interactions between substrates and inhibitors and the P450, identifying key active site residues and catalytically important electron transfer pathways within the proteins, as well as identifying novel heme ligations that occur during P450 catalysis (37-40). Furthermore, investigations in the areas of bioremediation, environmental monitoring, biotechnology, and medicine are frequently performed in order that man may utilise and manipulate cytochromes P450 for its own benefit. For example, biotechnological applications of the cytochromes P450 include the bioremediation of herbicide-contaminated soils, as well as the catalysis of various chemical reactions/biotransformations that are otherwise expensive or unattainable by laboratory methods. For example, enantiopure arene *cis*-diols, which are used in the synthesis of prostaglandins and polyethylene, can be generated only by P450-mediated reactions (22,41,42). The P450s also have many medical applications, including the generation of the anticancer agents tamoxifen and epothilone, in addition to the synthesis of steroids (e.g. progesterone and hydrocortisone), vitamin D precursors, antibiotics (e.g. erythromycin A), and the antimitotic taxol (22,41,43-46).

The term cytochrome P450 stems from a characteristic of these enzymes to absorb light at a wavelength of approximately 450 nm when in the reduced, carbon monoxide-

bound form. The major absorbance band of cytochromes P450, also named the Soret band, occurs at approximately 418 nm when a P450 is oxidised (ferric) and in the low-spin heme iron configuration, shifting to the characteristic 450 nm when carbon monoxide ligates to the reduced heme iron. This feature was first discovered through studies of pigmented extracts of mammalian liver (47,48) towards the end of the 1950s. In the ensuing years the pigment was characterized to be a heme-containing protein with catalytic activity. Over time, a multitude of related P450 enzymes have been characterized, sometimes with a specific substrate, but often having a wide range of substrates, depending on the role of the particular P450 (3,49,50). Subsequent work identified these enzymes in a wide range of organisms from yeast and fungi, bacteria, and many eukaryotes, including plants and mammals (3,22-25), showing them to be almost ubiquitous in biology. However, P450s are absent from the genome of *Escherichia coli*.

In addition to possessing a heme macrocycle, structural studies have demonstrated that the cytochromes P450 demonstrate strong structural similarity, with all members of this superfamily of enzymes being predominantly composed of α-helices (51,52). Of the crystal structures solved to date, the majority identify that the typical shape of the cytochromes P450 is a triangular pyramid, as is demonstrated in Figure 2, and that these enzymes possess an active site that usually descends deeply within the protein structure from one or more openings at the protein surface. This active site, which is defined largely by amino acid side chains deriving from α-helical sections of the protein, is key to the activity of the P450s, as it facilitates selective binding of substrate molecules in the proximity of the heme macrocycle in a position suitable for their oxygenation. This has been shown recently for a number of substrate-bound P450 crystal structures and one of the key structural elements that helps to define the active site channel (and also provides key residues involved in proton delivery and oxygen association) is the long I helix that extends across one side of the protein and across the face of the heme (52). Crystal structures of the P450s have shown the volume of their active sites to vary considerably, from 1350 Å^3 in CYP121 from *M. tuberculosis* to 645 Å^3 in human CYP2C5 (40,53), thus demonstrating the variation in active site cavities in the P450s and likely highlighting their ability to catalyse oxygenation of molecules of widely differing sizes (and chemical character). Additionally, the amino acids that comprise the surfaces of the active site cavity select for particular structural components of the relevant substrate(s), favouring interactions with the desired substrates by hydrogen

bonding and other interactions, enabling their binding in catalytically productive modes. For example, residues such as leucine, valine, arginine, tyrosine, and phenylalanine are frequently observed in the active sites of cytochromes P450, forming various electrostatic, hydrogen bonding and hydrophobic interactions with substrates that aid their positioning with respect to the heme and so enable productive catalysis (Figure 3) (25,35,52,54).

Having identified the basic features of the cytochromes P450, the next sections look in more depth at the heme macrocycle that is fundamental for the catalytic activity of these monooxygenases, before moving on to the reactions mediated by these proteins.
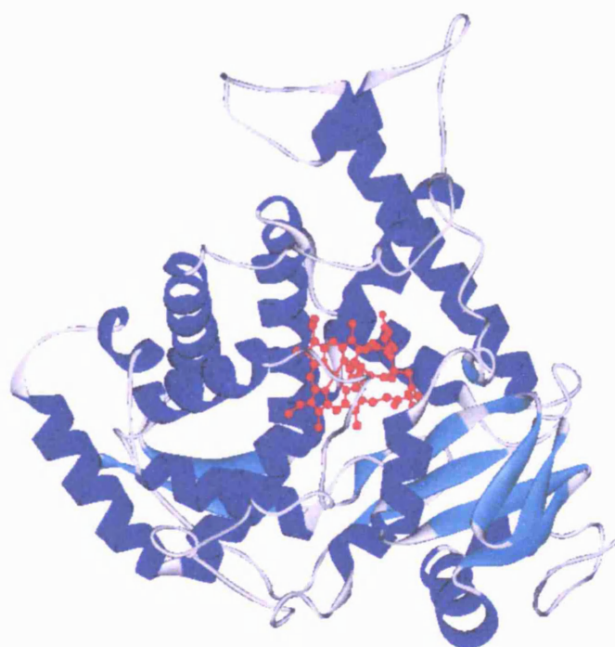
Figure 2 The structure of cytochrome P450 CYP51 from *Mycobacterium tuberculosis* as solved by Podust *et al.* (PDB no. 1EA1, (51)). Structure solved by X-ray diffraction of CYP51 crystals and resolved to 2.21Å. α-helices identified in blue, β-sheets in cyan, linker regions in grey, and heme macrocycle in red. The structure identifies that the protein folds into a triangular pyramid, and that the heme is deeply buried at the bottom of a large active site defined mainly by residues in α-helical sections surrounding the heme. The image was created using Weblab ViewerPro (Molecular Simulations Inc.).
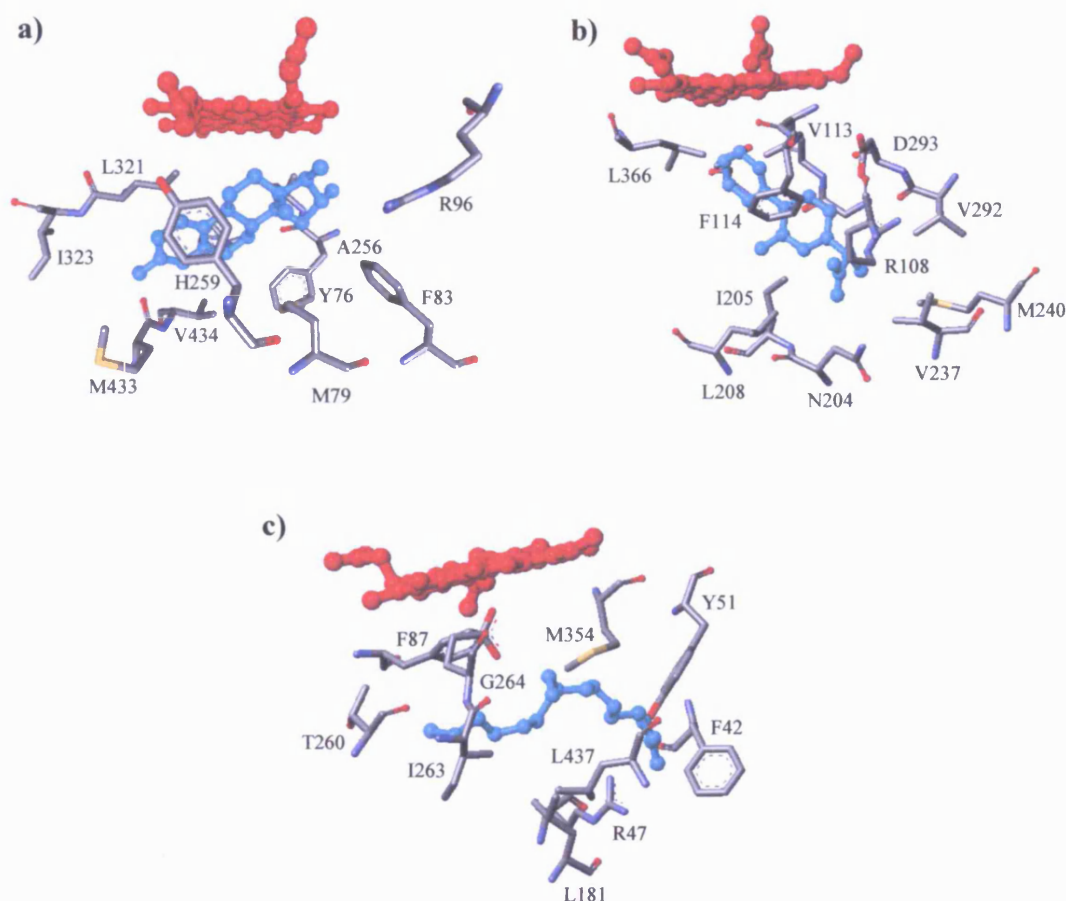
Figure 3 The active sites of **a)** estriol-bound Mtb CYP51 (PDB no. 1X8V, (35)), **b)** flurbiprofen-bound human CYP2C9 (1R90, (55)) and **c)** palmitoleic acid-bound P450 BM3 from *B. megaterium* (1SMJ, (34)), as determined by crystallographic studies. For each P450, amino acid residues identified as significant for the binding of these substrates/substrate-like molecules are displayed, whilst the heme macrocycle and ligands are shown in red and cyan, respectively. The images demonstrate how the residues comprising the active sites of cytochromes P450 define the different substrate specificities of these enzymes. In the case of CYP51, Y76, F83, V113, and H259 are particularly important for the positioning of sterol/steroid compounds in the active site, being conserved in all isoforms of this sterol demethylase. For flurbiprofen binding to CYP2C9, residues R108, F114, and D293 form salt bridges and hydrogen bonds with the substrate in order to correctly position this molecule for catalysis. In P450 BM3, R47 and Y51 stabilise the carboxyl group of palmitoleic acid, whilst F87 is implicated in the regiospecificity of substrate oxidation. The image was created using Weblab ViewerPro (Molecular Simulations Inc.).

1.4 The heme macrocycle of the cytochromes P450

The heme at the heart of all cytochromes P450 is the molecule from which these monooxygenases derive both their activity and name. It is this molecule which, when bound to carbon monoxide produces a characteristic Soret peak at 450nm, and which causes the red pigmentation of the proteins to which it is incorporated. While several proteins bind heme and interact with oxygen (e.g. hemoglobin), the P450s go on to reduce and activate the bound dioxygen, leading to its scission and the incorporation of a single atom of oxygen into the substrate (48-50). Heme itself consists of a porphyrin molecule; four pyrrole molecules linked together by one-carbon bridges, with an atom of iron that coordinates to four centrally orientated nitrogen atoms. In heme-binding proteins, the iron is also coordinated to amino acid residues, frequently cysteine or histidine (3,56). The nature of the heme coordination (and whether the ligands are displaceable) is pivotal to the reactivity and cellular function of the hemoprotein.

There are a number of different hemes (structures shown in Figure 4), all with the same basic structure, but decorated with different side-chains. The side-chains vary in size and type but are significant to the differing properties of the hemes, some allowing alternative interactions (sometimes covalent) with amino acid side chains in the protein environment. For example the c-type heme of horse heart cytochrome c (and other forms of cytochrome c) is covalently attached to the protein backbone via linkages between cysteine side chains and heme vinyl groups (57). In addition, recent studies of eukaryotic family IV (fatty acid hydroxylases) have shown that catalysis dependent covalent attachment of a heme methyl group to a protein glutamate residue occurs (38,39). Such covalent binding of heme is also observed in other hemoproteins (e.g. peroxidases) and may be used to alter e.g. stability of heme binding and thermodynamic properties of the heme (58).
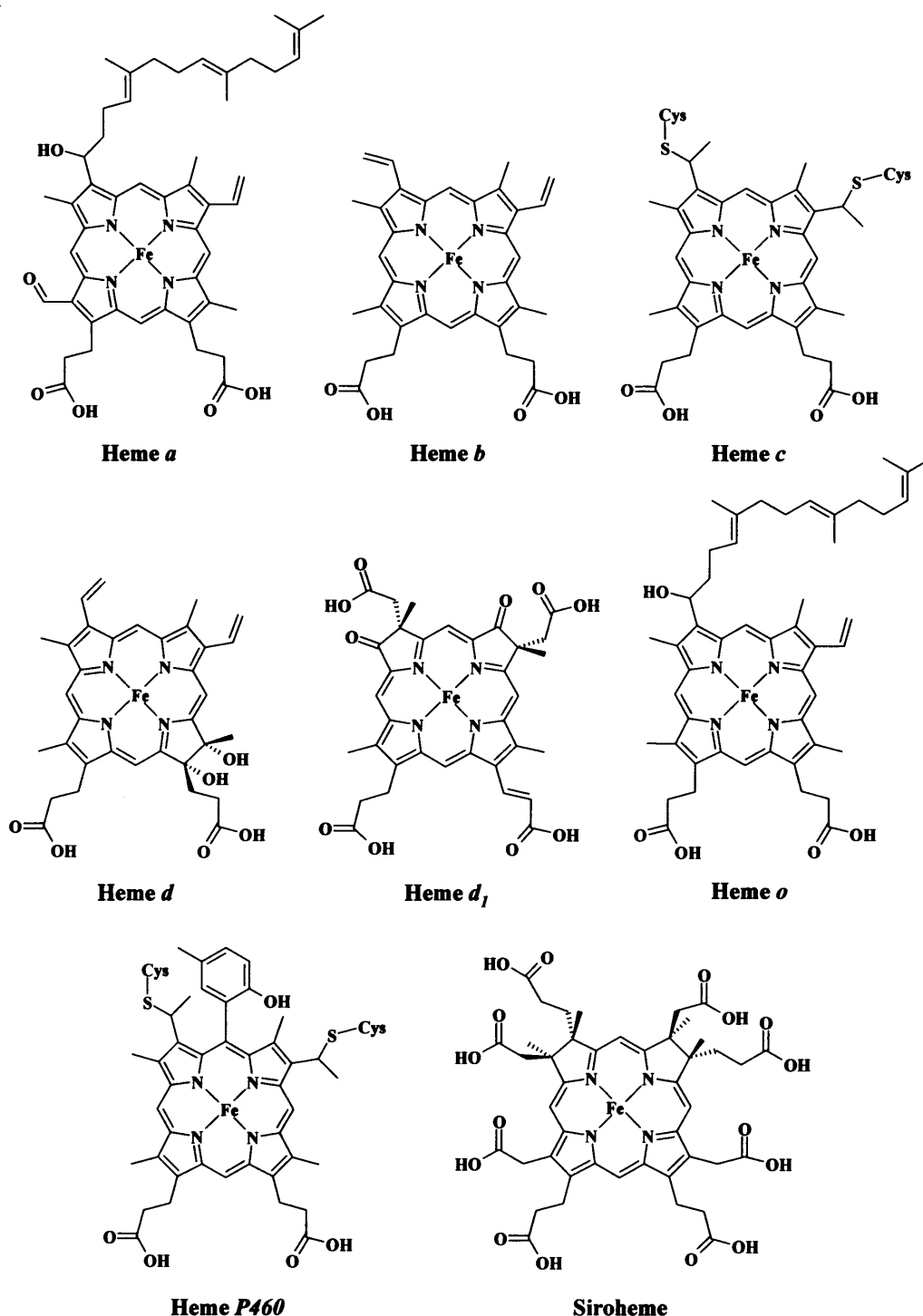
Figure 4 The chemical structures of the main forms of the heme macrocycle found in nature. The diagrams demonstrate variations in side-chain composition, as well as the non-iron ligations to the protein backbone that occur with heme *c* and heme P460. Heme *a* is found in cytochrome *c* oxidase, whilst heme *b* is found in nitric oxide synthase, hemoglobin, and the cytochromes P450 (3,59-61). Heme *c* is found in proteins shown to be involved in the conversion of ammonia to nitrite and is also present in respiratory cytochromes *c*, whilst heme *d* and siroheme are present in nitrite reductases (57,62,63). Hydroxylamine oxidoreductase from *Nitrosomonas europaea* contains heme P460 and heme *o* is present in the quinol oxidase of *E. coli* (64,65).

Cytochromes P450 incorporate a *b*-type heme that is adorned with two propionate groups, four methyl groups, and two vinyl groups that extend from the edge of the ring structure. The heme iron is held equatorially by four in-plane bonds to the four pyrrole nitrogens, whilst also forming a fifth-coordinate ligand with a cysteine residue of the host protein, and a sixth-coordinate ligand with (in most cases) a molecule of water when in the ferric resting state. The heme *b*, as seen in the P450s, is frequently observed in nature. Among the best known heme *b*-containing proteins are nitric oxide synthase (NOS), hemoglobin, and various peroxidases. The axial amino acid ligands vary in these proteins, from cysteinate and water in NOS to histidine in haemoglobin and the peroxidases (3,59,60,66). Heme *a*, which possesses a long, unsaturated and branched alkyl chain is found axially coordinated via histidine residues, in cytochrome *c* oxidase (61). Similarly, enzymes that have been shown to oxidise hydroxylamine to nitrite (hydroxylamine oxidoreductase from *Nitrosomonas europaea*) incorporate heme *c* axially coordinate via a histidine residue. However, as previously mentioned the hemes in these proteins (cytochrome *c* and hydroxylamine oxidoreductase) may also be covalently linked to other regions of the protein via cysteinate side chains (57,67). The *d*-type hemes, which are histidine coordinated, and siroheme-containing proteins, which are cysteinate coordinated and possesses multiple acidic groups, catalyse reduction of nitrites and sulphites in nature, whereas heme P460 is found in hydroxylamine oxidoreductase and is histidine ligated (62-64,67).

These heme molecules are synthesised in the mitochondria and cytosol of cells in which they are contained via a pathway (Figure 5) that begins with the universal heme precursor δ-aminolevulinic acid, which itself is synthesised from either glutamate, or glycine and succinyl CoA. The actions of δ-aminolevulinic acid dehydratase, porphobilinogen deaminase, and uroporhyrinogen III synthase convert this precursor molecule into uroporhyrinogen III, the final universal precursor of all tetrapyrroles. An additional three reactions, mediated by uroporhyrinogen decarboxylase, coporphyrinogen oxidase, and protporphyrinogen oxidase, generate protoporphyrin IX. Finally, ferrochelatase catalyses the insertion of the iron atom at the centre of the heme. Whilst this pathway is conserved in all organisms possessing heme-containing enzymes, the subsequent adornments, mentioned above, that distinguish the various heme types shown in Figure 4 are the result of the actions of non-conserved enzymes (68).
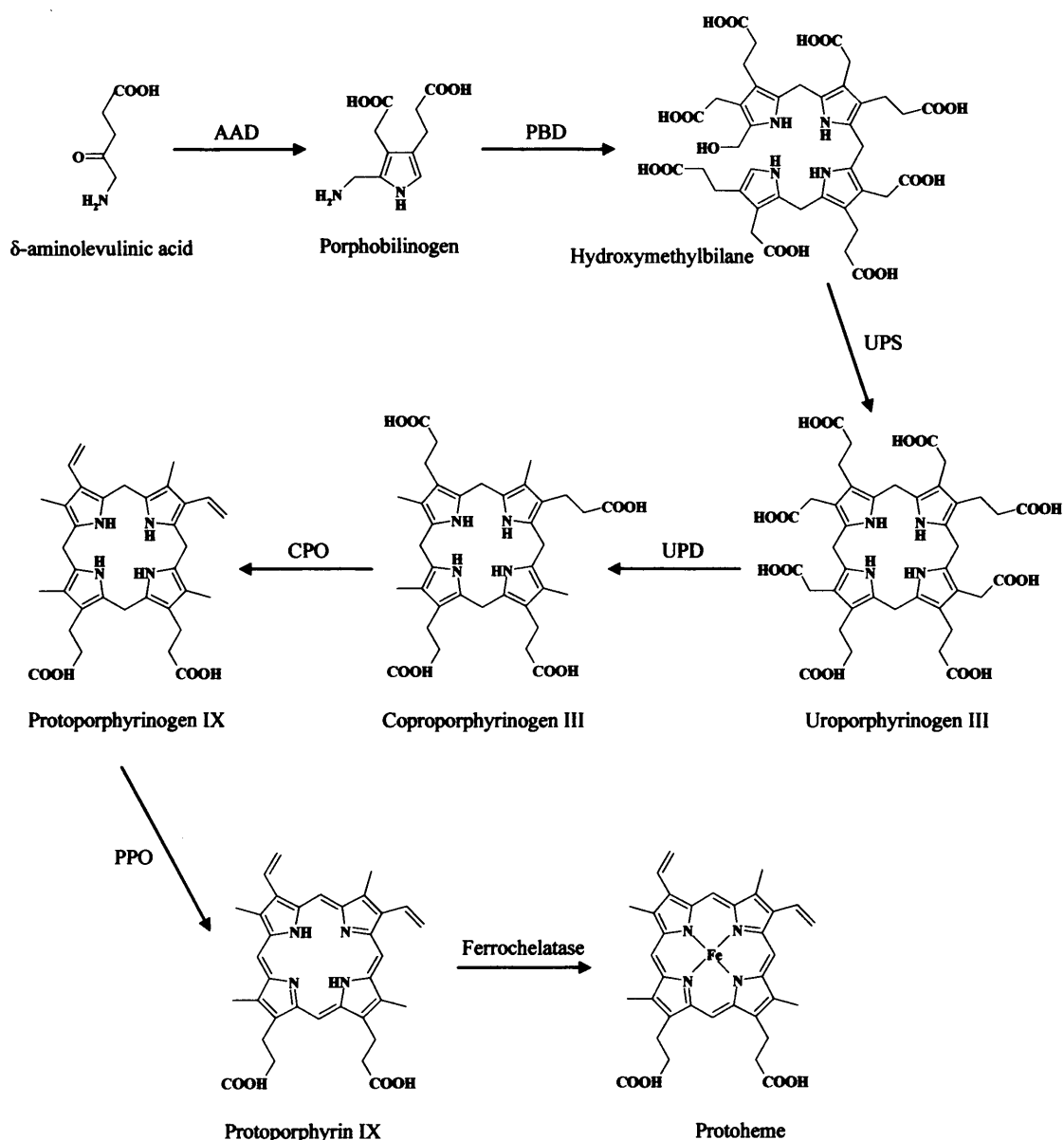
Figure 5 The heme biosynthetic pathway from δ-aminolevulinic acid to protoheme, identifying the enzymes responsible for the creation of this tetrapyrrole compound. Protoheme is the ubiquitous precursor to the various heme macrocycles (Figure 4) incorporated into proteins such as cytochrome c, nitric oxide synthase, and the cytochromes P450, whilst δ-aminolevulinic acid is itself derived from glutamate, or glycine and succinyl CoA (68). The abbreviated enzymes denoted in the figure are δ-aminolevulinic acid dehydratase (ALAD), porphobilinogen deaminase (PBGD), uroporphyrinogen synthase (UPS), uroporphyrinogen decarboxylase (UPD), coproporphyrinogen oxidase (CPO), and protoporphyrinogen oxidase (PPO). This pathway is conserved in all hemoprotein-containing organisms, however the enzymes that facilitate the addition of the side chains that distinguish the different heme types (e.g. heme a, heme b, etc) are not conserved.

An intrinsic property of heme molecules is the variable spin state of their core iron atom. Each electron orbiting an atom possesses a spin value (S) of $+\frac{1}{2}$ or $-\frac{1}{2}$, dependent on the direction of the rotation (spin) about its axis. In the most energetically favourable state electrons preferentially pair with electrons of opposing spin, with the net spins of $+\frac{1}{2}$ and $-\frac{1}{2}$ cancelling each other out. In higher energy configurations, or where an odd number of electrons are present, unpaired electrons (whose spins are not cancelled by a counterpart with opposing spin) are present and hence the iron atom has a spin value that reflects the number of these non-coupled electrons (69). For example, when in the ferric resting state, axially coordinated by a water molecule and a cysteinate, the P450 heme iron is found in the low-spin state with a spin value of $S = \frac{1}{2}$. This relates to the configuration of the five d-orbital electrons of the ferric (Fe^{3+}) iron, which can be distributed between five pairing possibilities (see Figure 6). In the case of ferric low-spin heme, which is the most energetically favourable configuration, this consists of four of the five electrons being paired, thus cancelling out each other's spin, and leaving one remaining electron unpaired. When substrate binds in the active site of model P450s (e.g. the P450cam and P450 BM3 enzymes) the bound water molecule is displaced and a spin-state change occurs. The electrons of the d-orbital rearrange so that none are paired, and hence there is no cancellation of the spins of the electrons, thus creating a spin value of $S = \frac{5}{2}$ (Figure 6). These changes in spin-state are detected by UV/Visible spectroscopy as changes in the P450 Soret peak position, as they produce changes in UV-visible absorbance features of the heme. In the case of substrate binding, a Type I Soret peak shift to shorter wavelengths (~390 nm) is observed due to the conversion from low-spin to high-spin ferric heme iron. However a Type II shift of the Soret to longer wavelengths (typically to ~422 – 450 nm) is seen with binding of certain types of inhibitor to P450s. Such inhibitors usually coordinate the heme iron in the distal position (i.e. that position previously occupied by a water molecule). Typical of this type of interaction is the binding of imidazoles and triazoles to ferric P450 heme iron, where interaction between these molecules and the heme iron occurs through lone electron pairs on nitrogen atoms in the former. This type of Soret shift is associated with the reinforcement of the low-spin state and with inhibition of P450 activity (69,70). However, certain P450 substrates are also known to induce a shift in heme iron spin-state equilibrium from high-spin towards low-spin (reverse type I binding), and inhibitors may also induce type I spectral changes (71,72). Thus the

heme spectrum can be used, via UV/visible spectroscopy, as a sensitive technique for analysing binding of substrates from inhibitors, and for defining binding constants (K_d values) from optical titrations. Spin-states can also be detected using techniques such as electron paramagnetic resonance, which identify unpaired electrons of oxidised heme, and can hence differentiate between low and high spin forms (28,37,69). Such methods will be discussed in future chapters with regards to the characterization of the featured cytochromes P450.

Ferric (Fe^{3+})   **Ferrous (Fe^{2+})**
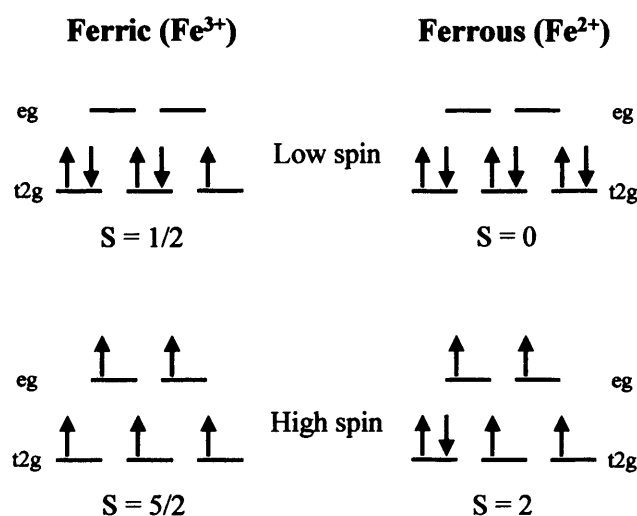
Figure 6 The distribution of the P450 heme iron d-orbital electrons between the t2g (lower energy) and eg (higher energy) levels for the ferric and ferrous, low-spin and high-spin configurations. In the low-spin, ferrous form, electrons adopt a low energy configuration where all six electrons pair up in the low energy t2g level. The resultant spin value of this form is S = 0 as the spins of each electron pair cancel each other out. Similarly, in the ferric, low-spin form, all electrons are found in the t2g level, however S = 1/2 for this form as ferric iron has one fewer electron, which cannot be paired. In the high-spin forms of both ferric and ferrous iron (frequently induced by substrate binding to the P450), electrons from the t2g level are elevated to the higher energy eg level, resulting in multiple unpaired electrons, and thus S = 5/2 and S = 2 values, respectively. These transitions from the low-spin to the high spin-states are detectable by UV-Visible and EPR spectroscopy as they perturb the absorption properties of the atoms to which they pertain (28,37,69,70).

1.5 The cytochrome P450 catalytic cycle

As previously mentioned, the predominant reaction of the cytochromes P450 is the monooxygenation of a substrate compound to produce, most frequently, a hydroxylated chemical species of physiological significance, or for detoxification purposes. This reaction, which usually requires the supply of electrons from the coenzymes NADPH or NADH, is summarised in Figure 7.

17

$$RH + O_2 + 2e^- + 2H^+ \rightarrow ROH + H_2O$$

Figure 7 The general hydroxylation reaction catalysed by cytochromes P450 showing the conversion of substrate (RH) to hydroxylated product (ROH), and the simultaneous formation of a molecule of water. The electrons required for heme reduction in this process are typically derived from the concomitant oxidation of NAD(P)H to NAD(P)$^+$ (not shown) (73-75).

The catalytic activity of all cytochromes P450 stems from a universally conserved cysteine residue that binds, via its sulphur atom, to the iron centre of a protoporphyrin IX molecule as the 5th ligand (27). The iron acts as the catalytic centre and relies upon being reduced from Fe^{3+} to Fe^{2+} (and subsequently to an active ferryl intermediate responsible for oxygen cleavage) by two subsequent single electrons being transferred from NAD(P)H, via the redox partners of the enzyme. The only known exceptions to this rule are P450nor (where NADH reduces the heme directly) and P450BSβ (where peroxide provides the reducing equivalents) enzyme types. Substrate binding typically elicits a spin state shift in the P450 heme iron equilibrium from low- to high-spin (See Chapter 1.4 for more information), following which the first reduction occurs. The reduction converts ferric heme to the ferrous state, to which molecular oxygen then ligates as the 6th ligand. A second electron is then transferred, along with two protons from the surrounding solvent, ultimately causing oxygen scission to occur. These protonation steps lead to the formation of water via peroxo-iron and hydroperoxo-iron species, which have been spectroscopically studied, but which are transient and generally require low temperature analysis for convincing identification (3,25,52,76). The subsequently formed oxo-ferryl-iron intermediate mono-oxygenates the substrate, which is then released from the active site whilst the heme macrocycle returns to the resting, water-bound, ferric state. A schematic diagram of the catalytic cycle is shown in Figure 8 (52,73,74,77).
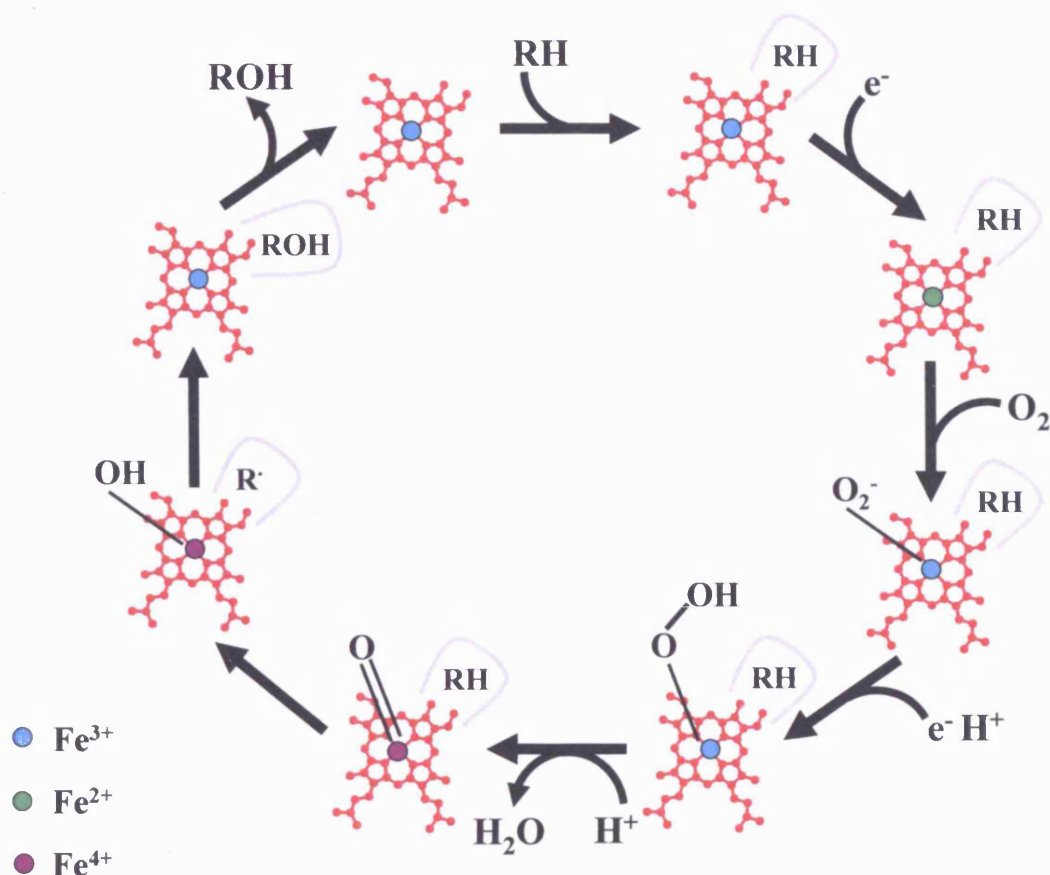
Figure 8 The catalytic cycle of cytochromes P450 demonstrating the change in oxidation state of the reactive iron at the centre of the heme from Fe^{3+}, to Fe^{2+}, and returning to Fe^{3+} via Fe^{4+}. Upon binding of substrate the ferric heme shifts from the low- to high-spin state, returning to the resting low-spin form at the end of the cycle. Following substrate binding, an electron delivered (usually) from NAD(P)H via redox partner proteins (Chapter 1.8) reduces the heme iron, thus permitting the binding of molecular oxygen to this atom. Subsequently, the transfer of a second electron and two solvent-derived protons causes the scission of the oxygen molecule at the heme iron, resulting in the formation of a molecule of water. Monooxygenation of the substrate then proceeds via an oxo-ferryl iron intermediate, hydrogen abstraction from the substrate, and oxygen 'rebound', with the resultant hydroxylated organic product being released from the active site and the heme returning to the low-spin, ferric form in readiness for subsequent rounds of catalysis (52,73,74,77). RH represents the substrate, whilst the product molecule is represented by ROH.

Whilst this catalytic cycle is widely accepted as the route by which P450s perform their physiological roles, a few members of this monooxygenase superfamily have been shown to utilise alternative mechanisms. These enzymes, which include P450$_{BS\beta}$ (CYP152A1) from *Bacillus subtilis* and P450$_{SP\alpha}$ and P450$_{SP\beta}$ (CYP152B1 and CYP152A1) from *Sphingomonas paucimobilis*, utilise a "peroxide shunt" to catalyse the insertion of oxygen into a substrate molecule. This mechanism requires no electron-

transferring proteins, with the reducing equivalents, protons and the oxygen being supplied by a peroxide species, such as hydrogen peroxide. Peroxide interacts with the resting heme iron and converts it directly to the ferric hydroperoxy intermediate. However, although this mechanism has been shown to support catalytic activity of these P450s, it is thought that the "peroxide shunt" is unlikely to be a physiological process in other types of P450, as most P450s interact with peroxide inefficiently and since non-specific oxidative destruction of the heme macrocycle leads to inactivation of the P450 in parallel with any productive interactions. In addition, for many cytochromes P450 and peroxidases, the peroxide shunt turnover rate is orders of magnitude slower than that supported by physiological redox partners (74,78-80). In addition, the *F. oxysporum* P450nor enzyme catalyses the reduction of two molecule of nitric oxide (NO) leading to the production of a molecule of dinitrogen oxide (N_2O). This is achieved by the direct reaction of NAD(P)H with the P450 and does not involve electron transfer through redox partners (81-83). In the next section, a summary of the reactions mediated by P450s utilising the orthodox catalytic cycle are described, illustrating their wide range of physiological applications.

1.6 Cytochrome P450-catalysed reactions

The major reactions catalysed by cytochromes P450 are oxygenations leading to hydroxylation. For instance, as is observed with the fatty acid-oxidising human P450 CYP4A enzymes (84), ω-oxygenation at the terminal methyl carbon is the most common reaction. Various other oxygenation reactions have been identified for the cytochromes P450, including N-oxidation, sulphoxidation, epoxidation, N-, S-, and O-dealkylation and deamination (23,85), and these are summarised in Table 2. The majority of these P450-mediated reactions are either involved in biosynthetic pathways, or in the activation of a compound for further reactions (86). The main purpose of these reactions is either to produce compounds of physiological importance to the organism from other endogenous compounds, or to inactivate exogenous compounds from the environment, which have the potential for accumulation in or toxicity towards the organism (23,77).

Reaction catalysed	Example
Hydrocarbon hydroxylation	CYP102A1 (33)
Alkene epoxidation	CYP102A1 (87)
Alkyne oxygenation	CYP2B4 (88)
Arene epoxidation	CYP1A1 (89)
Aromatic hydroxylation	CYP3A4 (90)
N-dealkylation	CYP1A2 (90)
S-dealkylation	CYP3A4 (91)
O-dealkylation	CYP2A6 (92)
N-hydroxylation	CYP79D1 (93)
N-oxidation	CYP2C8 (44)
S-oxidation	CYP3A4 (94)
Oxidative deamination	CYP2C19 (95)
Oxidative dehalogenation	CYP1A2 (96)
Alcohol and aldehyde oxidations	CYP2C9 (97)
Dehydrogenation	CYP2D6 (98)
Dehydration	CYP3A4 (99)
Reductive dehalogenation	CYP101 (100)
N-oxide reduction	CYP2A6 (44)
Reductive β-scission	CYP2E1 (101)
NO reduction	CYP55A1 (81)
Isomerizations	CYP1B1 (46)
Oxidative C-C bond cleavage	CYP17 (102)

Table 2 A list of the numerous types of reaction reported to be catalysed the cytochromes P450 with examples of the members of this superfamily of heme-containing enzymes identified as performing these chemical transformations.

Examples of biosynthetic reactions in which compounds of importance, such as reproductive hormones, are created include the conversion of testosterone to estradiol by CYP19 in man (12). In plants, such as Cassava, CYP79D1 and D2 are utilised in the initial steps of the biosynthesis of cyanogenic glucosides linamarin and lotaustralin, compounds that defend the plant against herbivores, including insects (93) (Figure 9). In bacteria, the cytochromes P450 have been shown to be involved in the initial steps of metabolic fuel production. Noteworthy examples of this role include the hydroxylation of monoterpene d-camphor by P450cam from *Ps. putida* (103,104) and the hydroxylation of α-terpeneol by P450terp from a *Pseudomonas* species (105). Fungal P450s are numerous with wide ranging functions that include the biosynthesis of the membrane integrity-maintaining compound ergosterol (CYP51) (106,107). The inhibition of these enzymes, which results in cell wall disruption, in organisms such as *C. albicans* and *S. apiospermum*, is a key route to the treatment of these human fungal infections (108), and is detailed further in Chapter 1.9.

A bacterial P450 of interest, due to its role in antibiotic production, is P450eryF (CYP107) from the organism *Saccharopolyspora erythraea*. This P450 converts 6-deoxyerythronolide to erythronolide B, a precursor to the antibiotic erythromycin A, via a hydroxylation reaction (45). In fungi, the P450s have also been shown to be involved in nitric oxide reduction. For example, P450nor (CYP55A1) from *Fusarium oxysporum* converts nitric oxide (NO) to nitrous oxide (N_2O) under anaerobic conditions as the second step of a process that detoxifies nitrite within the host organism (81-83,109). Vitamin biosynthesis is another cellular function in which the bacterial P450s are involved, with CYP105A2 from *Amycolata autotrophica* facilitating the conversion of vitamin D3 to the biologically active compound 1, 25-dihydroxyvitamin D3 (110). As well as biosynthetic reactions, the bacterial cytochromes P450 also catalyse degradation of toxic compounds. An illustration of this comes from *Sphingomonas* sp. strain AO1, in which bisphenol A, a compound that is widespread in soils and watercourses, and which is immunotoxic to mammals, is broken down to the less toxic compounds 1,2-bis(4-hydroxyphenyl)-2-propanol and 2,2-bis(4-hydroxyphenyl)-1-propanol (111).

The cytochromes P450 catalyse numerous reactions which have medical significance, resulting in compounds that are used in the treatments of various human disease states. An illustration of this is the production of an antimitotic agent by cytochromes P450 from plants of the *Taxus* species (112). The compound that results from the catalytic activity of this P450 (CYP725), taxol, is utilised in the treatment of carcinomas and melanomas. Further examples of the utilisation of plant P450s for the benefit of humans include the production of terpenoid indole alkaloids, such as the antihypertensive reserpine and the antineoplastic agent vincristine (22).

In addition to involvement in biosynthetic pathways, such as the aforementioned synthesis of estradiol, other mammalian P450s are predominantly involved in the functionalisation of xenobiotic compounds in order to facilitate their excretion. The Phase I P450-mediated reactions, which include hydroxylation, deamination, and dealkylation, result in substrates that can be conjugated, by Phase II enzymes such as UDP-glucuronyl transferase, to compounds that further increase their solubility, and hence promote excretion in urine or bile (113). An example of this is the conversion of the local anaesthetic compound lignocaine to monoethylglycinexylidide and 3-hydroxylignocaine. These N-dealkylation and aromatic hydroxylation reactions, which prepare the parent compounds for Phase II metabolism, are catalysed by the mammalian liver P450s CYP1A2 and CYP3A4, respectively (90). As well as degrading drug

compounds to inactive forms, the activity of mammalian P450s also result in the activation of some compounds. For example, the opioid analgesic codeine is inactive when ingested, but when metabolised by a hepatic cytochrome P450 (i.e. CYP2D6) is converted to the potent pain-suppressing compound morphine (114). Whilst these reactions benefit the host organism, others are less favourable, resulting in cytotoxic products. Halothane, a general anaesthetic, is metabolised by CYP2E1 to the non-toxic metabolite trifluoroacetic acid. However, during this process an unstable intermediate is formed which, in approximately 1 in 35000 human cases, can acetylate liver proteins. This acetylation generates an antigen against which the human immune system responds, resulting in severe hepatic necrosis, and, in 75 % of cases, death (115).

These are just a few of the reactions mediated by prokaryotic and eukaryotic cytochromes P450, demonstrating that this class of enzyme catalyse a diverse range of chemical transformations, which can be significant to the survival of the host organism, and also to man by e.g. the employment of their products in the treatment of human disease states or their application in biotechnological processes.
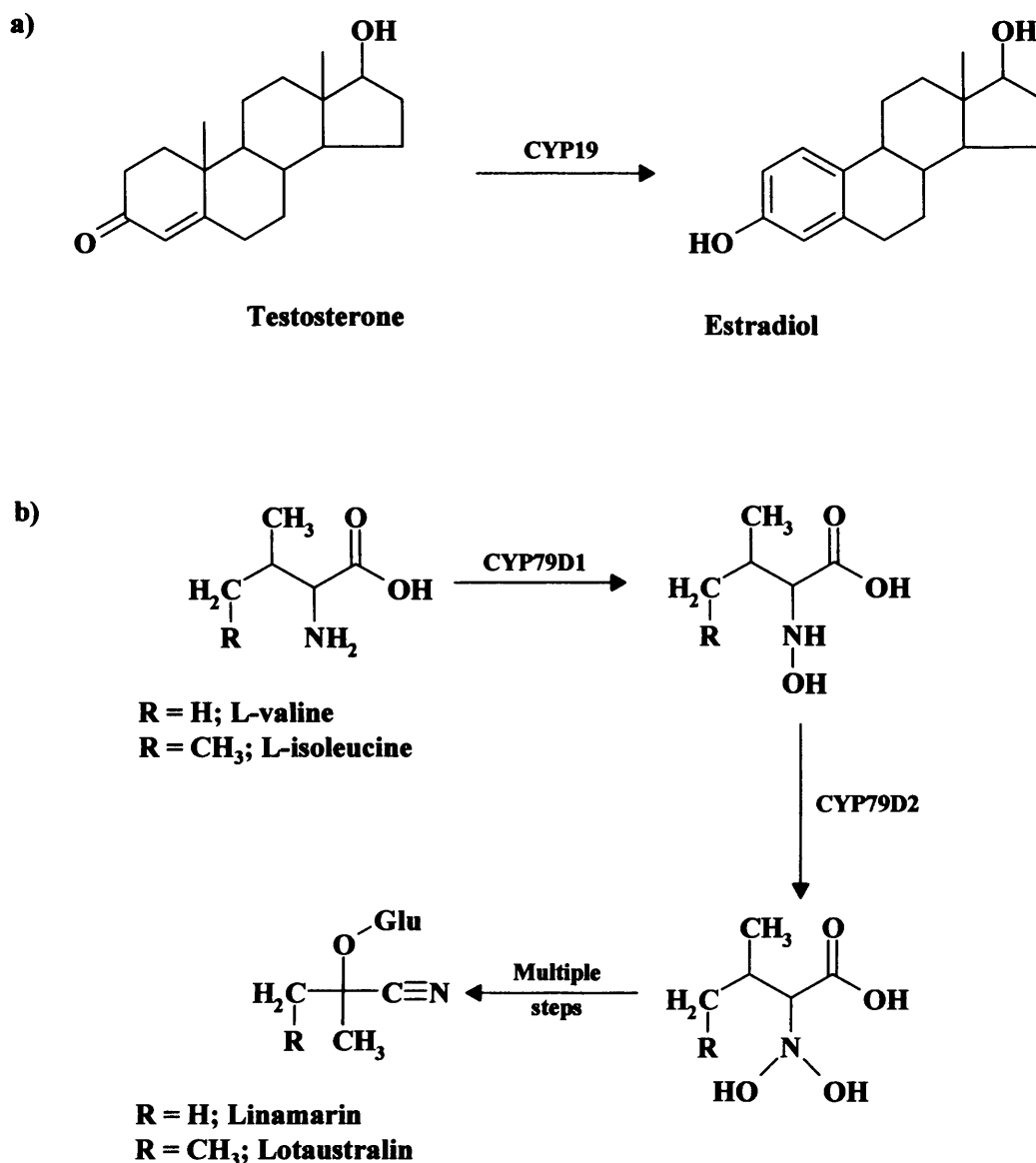
Figure 9 Two examples of reactions catalysed by cytochromes P450 from different kingdoms. **a)** The CYP19-mediated conversion of testosterone to estradiol that occurs in mammalian ovary cells (12). In this reaction, which is essential in the generation of estrogenic reproductive hormones, a hydrocarbon ring is aromatised by the action of the P450 in question. **b)** The principal steps in the conversions of L-valine and L-isoleucine to the cyanogenic glucosides linamarin and lotaustralin catalysed by CYP79D1 and D2 in Cassava plants (93). These cytochromes P450 facilitate two successive hydroxylations at the amine groups of the substrates as part of a pathway that generates compounds that defend the host plants against insects.

1.7 Classification of the cytochromes P450

The superfamily of cytochromes P450 has expanded greatly since its inception following the early studies by Omura and Sato, Klingenberg, and Estabrook and co-workers (48-50,116). It now stands as a superfamily divided into familial groups based upon sequence homology. This classification pertains to the degree of conserved amino acid residues in the protein, including those of the active site of the enzyme (3,24,25,27,117-119)(see Figure 2 for typical P450 structure). In nomenclature devised by Nelson (118) the cytochromes P450 are divided into families and sub-families, denoted by the cytochrome P450 (CYP) number. According to this nomenclature, P450s of greater than 40 % identity are defined as being in the same family, whilst those with identities greater than 55 % are classified as being in the same sub-family. However, it should be noted that even those cytochromes in the same sub-families may differ in endogenous function. For example, human CYP2C9 metabolises non-steroidal anti-inflammatory drugs such as ibuprofen and diclofenac, whilst human CYP2C19 mediates demethylation of diazepam and other anxiolytic compounds (20). Such differences in the substrate specificity of the cytochromes P450 have been extensively researched by Gotoh (120), revealing that there are six structural recognition sequences that are conserved in all the cytochromes P450. These sequences, found in regions of the B', F, G, and I helices, and the β3 and β5 structures, constitute approximately 16 % of the total residues of a P450, and many mutations that alter substrate specificity can be mapped to these areas of the protein. Hence, these regions are identified as significant for substrate coordination with the heme iron, and it is evident that the differences in substrate specificity of members of the same P450 sub-family correspond to amino acid changes in these structural recognition sequences.

The P450s are also further divided into classes dependent upon certain characteristics unrelated to the primary protein structure. These divisions are based upon the localisation of the P450 within the host cell, as well as their associated redox partners, without which P450 catalysis reactions cannot occur (see Chapter 1.8). For example, Class II P450s are exemplified by the membrane-bound microsomal P450s of eukaryotic organisms (3,121), such as the hepatic Phase I P450s in man. A major role of such P450s is in xenobiotic functionalisation leading directly to product excretion or to product recognition by Phase II enzymes such as UDP-glucuronyl transferase (113). These P450s are driven by electrons supplied by the diflavin (FAD- and FMN-

containing) protein NADPH-cytochrome P450 reductase, which is also anchored to microsomal membranes by a N-terminal anchor peptide region (17,122). Class I P450s are typically found in prokaryotes, usually unassociated with a membrane, and located in the cytosol of the cell (123). An example of this class is P450cam, a P450 shown to catalyse the hydroxylation of the monoterpene D-camphor, the initial step in a pathway that derives metabolic fuel for the organism from camphor (3,25). Class I P450s were considered (as with P450cam) to be driven by a NADH-dependent FAD-containing reductase and an iron-sulphur protein (ferredoxin), both of which are soluble (103).

Up until recent years, these two classes were used to categorise the P450 superfamily into more workable groups, and were even considered to reflect the entire diversity of the P450 superfamily redox systems. Latterly, discoveries arising from studies of P450 function, structure, and redox partners (i.e. the proteins that supply electrons, the driving force for catalysis) have further dissected the P450s into additional classes, including Class III and Class IV (124,125). A schematic representation of the P450 classes can be seen in Figure 10, demonstrating the currently identified arrangements of the cytochromes P450 and their associated redox partner proteins, and hence the diversity of routes of electron supply that exist for this superfamily of monooxygenases. With the advent of these novel classes, we are beginning to see even greater diversity in these proteins from their structure and function through to their catalytic mechanistics. The classes are expanding rapidly, with the boundaries between them becoming increasingly blurred as investigation reveals that numerous combinations of flavin-, iron-sulphur- and heme-containing proteins are capable of creating redox systems. As well as the extensively studied P450 BM3 from *B. megaterium*, studies in recent years have identified a number of novel P450 systems. These include P450nor from the fungal species *Fusarium oxysporum* that detoxifies cellular NO by reduction to the less cytotoxic compound N_2O. This system, which can turn over at rates exceeding 500 s^{-1} (81), requires no redox partner proteins and directly binds NADH, possibly via a positively charged region on the distal side of the heme (109), to obtain the necessary electrons for catalysis (82,83). Another system of interest is CYP51FX from *Methylococcus capsulatus* which consists of a P450 fused to a 3Fe-4S cluster-containing ferredoxin. This system operates similarly to other CYP51 P450s, as a sterol 14α-demethylase, but with the additional benefit of interaction with its ferredoxin not being dependent upon random collisions in solution (126). Another "non-standard"

26

system is $P450_{BS\beta}$ (CYP152A1) from *Bacillus subtilis*, a cytochrome P450 that utilises hydrogen peroxide to hydroxylate fatty acids (66,79,80). The capacity of P450s to be driven (inefficiently) by the "peroxide shunt" pathway has long been recognised (74,79,80,127). However, finding a bacterial P450 that exploits this mechanism naturally was a revelation (128). As part of this project it is intended to characterize one of these novel systems, and this will be discussed in greater detail in later sections.
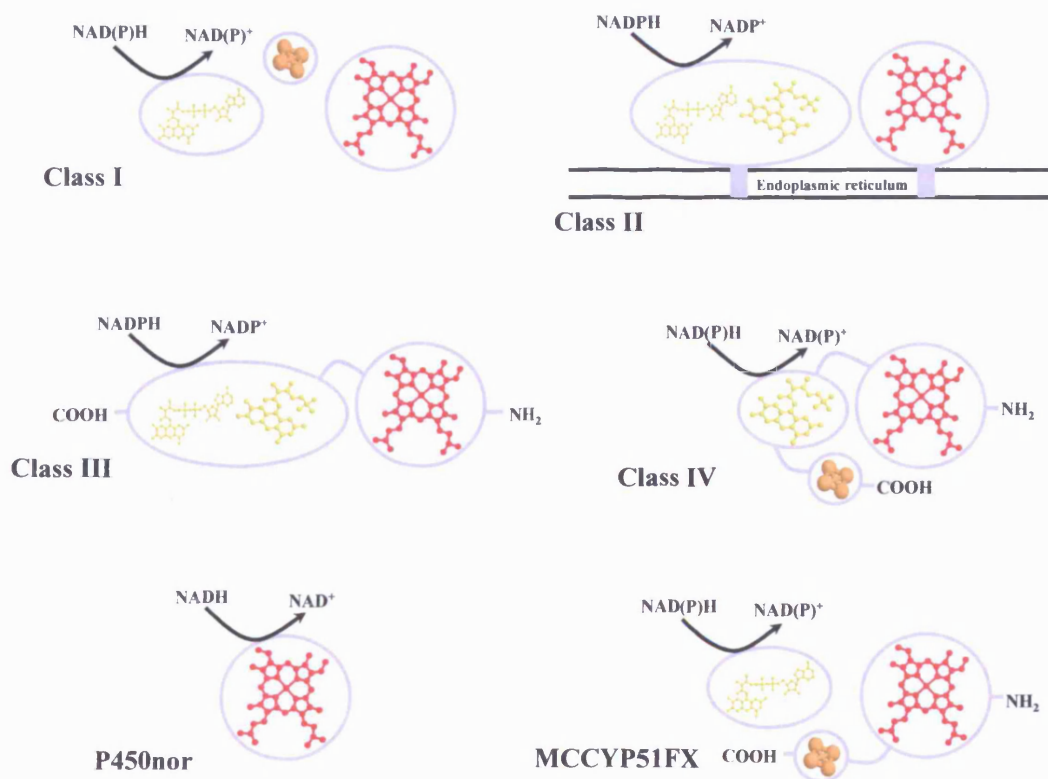
Figure 10 A schematic diagram of a number of classes of cytochromes P450, showing the combinations of P450 and associated flavin and/or iron-sulphur containing redox-partners. FAD and FMN are shown in yellow, iron-sulphur clusters in orange, and heme in red in order to indicate redox-active cofactors in the systems. Bacterial systems such as P450cam from *Pseudomonas putida* are typical of Class I cytochromes P450 (103). Class II cytochromes P450 are typified by the microsomal membrane-bound P450 (e.g. human CYP19) (12,122) that interact with a co-localised membrane-bound P450 reductase (CPR). The Class III system is a soluble fusion of bacterial P450 and mammalian-like CPR, exemplified by the fatty acid hydroxylase flavocytochrome P450 BM3 from *Bacillus megaterium* (129). Cytochromes P450 of Class IV are soluble P450/redox partner fusions typified by the systems from *R. metallidurans* (CYP116B1) and *Rhodococcus* sp. NCIMB 9784 (CYP116B2) in which the redox partner is a phthalate dioxygenase reductase (130). P450nor from *Fusarium oxysporum* represents a class of P450 that requires no peripheral redox partners but instead binds NADH directly (82). The MCCYP51FX diagram indicates the arrangement of redox active cofactors in the *M. capsulatus* CYP51/ferredoxin fusion protein CYP51FX (126).

1.8 Cytochrome P450 redox partner proteins

As previously discussed, electrons are supplied to the P450 heme from the redox partners of the enzyme and, although all redox partners effectively perform the same role of electron supply/reduction of the P450, they differ between classes of cytochrome P450. Bacterial P450 redox partners are most frequently identified as flavin adenine dinucleotide-containing reductases (FAD), which derive electrons from the oxidation of β-Nicotinamide-Adenine-Dinucleotide-Phoshate (NADPH) or β-Nicotinamide-Adenine-Dinucleotide (NADH), and a ferredoxin which consists of a protein incorporating an iron-sulphur cluster, the composition of which can vary (i.e. 2Fe-2S, 3Fe-4S or 4Fe-4S) (131-133). The structures of FAD, FMN, and a 2Fe-2S cluster are shown in Figure 11, and demonstrate the points on these molecules that are reduced as they perform their physiological functions. Examples of the bacterial system include adrenodoxin reductase homologue FprA and ferredoxin proteins from *Mycobacterium tuberculosis* (134), as well as putidaredoxin and its associated putidaredoxin reductase from *Pseudomonas putida* (103). Areas of current investigation using the bacterial three-component system include the use of ferredoxin reductases that derive electrons from coenzymes other than NAD(P)H. An example of this is the use of 2-oxoacid ferredoxin oxidoreductase from *Sulfolobus tokodaii* that can utilise pyruvate, in the presence of CoA, to derive electrons for catalysis. This may be a significant development for the biotechnology industry as pyruvate and CoA are a cost effective alternative to the costly and unstable pyridine nucleotide coenzymes currently used to drive P450-catalysed reactions (135,136).

Like the P450 they serve, the redox partners of eukaryotic P450s are typically membrane bound and consist of an FAD- and FMN-containing reductase. The protein that supports most eukaryotic P450s, known as NADPH-cytochrome P450 reductase (CPR), oxidises NADPH to supply electrons to the associated P450 for use in its catalytic cycle. This organisation of the reductase co-factors is such that FAD (located in a domain that also binds the NADPH cofactor) accepts electrons from NADPH and shuttles these through FMN, contained in a separate flavodoxin-like domain of the enzyme, and onto the heme iron (17,122). Thus, the FMN domain of the enzyme acts as the key mediator of electron transport between the FAD domain and the P450, and is likely mobile, with structural reorganization mediated by a linker domain that joins the FAD and FMN domains of CPR (137). A large amount of work has been done on

structural and catalytic properties of CPR, including expression of the respective FAD and FMN domains and detailed analysis of electron transfer reactions (122,129,137-139). In contrast to these multi-component systems are those systems, such as the previously mentioned P450nor (82,83), where reduction of the P450 is achieved directly through electron transfer from the coenzyme to the P450.

Other reductase systems exist in the form of fusions of a P450 to their redox partners. One such example is the well-characterized P450 BM3 (CYP102A1) from *Bacillus megaterium*, a P450 with a very high catalytic rate, which is a fatty acid hydroxylase P450 fused to a soluble Class II redox partner akin to the CPR from eukaryotes (140). This fusion has subsequently been classified separately as a Class III P450, as it is not typical of either the standard Class I or Class II P450s (124). The BM3 system has served as a model for the microsomal P450s (due to its soluble nature, single component arrangement and use of a CPR redox partner) and has also been used as a basis on which to create artificial fusion proteins between P450 and CPR proteins. The awareness that the BM3 system displays an extremely rapid substrate turnover rate has led to studies into the creation of more catalytically active systems through artificially engineered P450/CPR fusions, and other types of P450-redox partner fusions (25,29). Some of these fusions have shown moderately increased substrate turnover compared to their respective non-fused systems (141,142). However, many of these fusions show little or no improvement upon the reconstituted multi-component systems (143,144), and thus are, in general, of limited use to the biotechnology industry. However, optimised fusion proteins clearly have potential as single component P450 systems, and would obviate requirement for additions of multiple redox partner proteins.

Recent discoveries in the area of natural fused P450 redox systems have included a novel class (Class IV) of cytochromes P450 in various bacterial species (including *Rhodococcus* sp. NCIMB 9784 and *Ralstonia metallidurans*). In these systems the P450 is fused to an FMN- and iron-sulphur-containing reductase protein that resembles the enzyme phthalate dioxygenase reductase from *Burkholderia cepacia* by sequence homology comparisons (3,25,124,125). Phthalate dioxygenase reductase from *B. cepacia* is itself a fusion formed from ancestral genes encoding a 2Fe-2S-containing domain and an FMN containing domain, and has been identified as interacting with an iron-containing enzyme, namely phthalate dioxygenase, in a pathway that degrades phthalate to provide metabolic fuel (145-147). The reductase has a requirement for NADH, from which electrons for catalysis are derived, and has been shown to reduce

the dioxygenase at a rate exceeding 5000 min^{-1} (145). This rate of reduction also suggests that fusion systems incorporating this reductase may be highly efficient in the transfer of electrons for catalysis.

These fusion P450s are of great interest at present due to their self-sufficiency. That is, the lack of necessity for the P450 to interact randomly with the appropriate redox partners in the cytosol in order for catalysis to occur. These systems are hence of interest to the biotechnology sector due to their potential for e.g. engineering desired oxidative activity into a system with high turnover and good catalytic efficiency. Thus, part of this PhD project will focus on a novel fusion from one of the bacterial species mentioned (*R. metallidurans*) (25,124,125). Furthermore, these fusion P450s are of interest for advancing the understanding of P450 redox systems and their biological roles, as well as determining exactly how such fusions facilitate more catalytically efficient P450 systems and electron transfer reactions, and why the host organism requires them. Studies of these fusions may elucidate better the mechanisms of P450 redox systems, as well as identifying new catalytic and structural phenomena, opening avenues for further research.
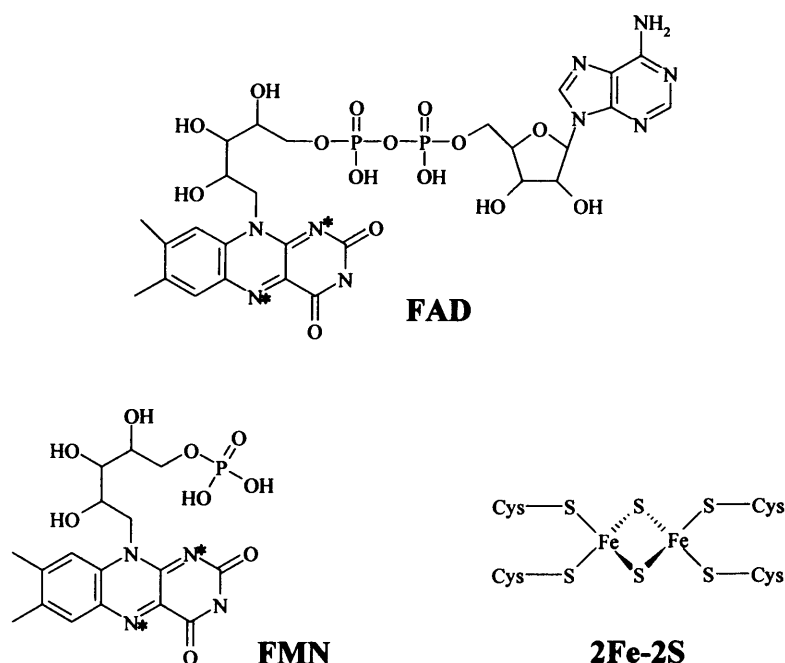
Figure 11 The structures of Flavin adenine dinucleotide (FAD), Flavin mononucleotide (FMN), and a 2Fe-2S cysteine-ligated iron sulphur cluster. In the FAD and FMN structures, nitrogen centres to which electrons are preferentially donated (N5 and N10) in order to produce the one electron- (semiquinone) and two electron-reduced (hydroquinone) forms are denoted with an asterisk.

1.9 *Mycobacterium tuberculosis*

Mycobacterium tuberculosis is a gram-positive bacterium with a thick waxy envelope, and that is the organism responsible for the disease that manifests as tuberculosis in humans (148,149). This contagious disease is spread by airborne particles from the coughs, sneezes, and speech of infected individuals, who may be responsible for infecting an estimated 10-15 million people each year if untreated (150). In a climate of escalating long-distance air travel, there is the potential for the organism to be spread very rapidly across large areas, thus giving the disease a high priority for treatment and containment. The World Health Organisation (WHO) pronounced tuberculosis to be a global emergency almost ten years ago, and the disease currently kills approximately 2 – 3 million people each year; a figure that is rising annually, and which the WHO regards as its priority to reduce (150). Projected figures suggest that, without improvement in treatment programmes, 1000 million individuals will become infected with TB between 2002 and 2020, 150 million of these will become sick from the disease, and as a result 36 million people will die. Whilst the biggest burden of TB cases stems from South East Asia and Africa, after forty years of decline the disease is currently on the increase in Europe, with London currently possessing the largest population of TB-infected individuals of any west-European city (150).

Much of the increase in TB incidence (especially in Africa) has occurred alongside the increase in HIV cases, as the two diseases act synergistically, each speeding up the other's progress in the host. In individuals suffering from tuberculosis, the pathogen is usually "walled in" by the immune system, preventing the disease's progression, and thus reducing the life-threatening nature of the disease. However, when HIV compromises the individual's immune system, the disease progresses rapidly unless treated, as the sufferer's body can no longer contain the disease as efficiently (148,149). Current treatments, such as isoniazid, rifampicin, and ethambutol, costing around $10 for a six-month course, cure up to 96% of cases at the first attempt if administered correctly. However, this is often not the case (148,150). Patient compliance in the Third World is low and poorly managed treatment programs are leading to incomplete courses of drugs being administered. In recent years drug resistant and multi-drug resistant strains (defined by resistance to at least two of the commonly used drugs, namely rifampicin and isoniazid) have been identified, especially in regions such as the former Soviet Union. This is often due to the spread of the disease from individuals in

whom the bacteria developed drug resistance following incomplete treatment. This necessitates the production of novel drug therapies for the multi-drug resistant strains in order to halt their further spread and to minimise unnecessary deaths (150).

It has been shown that the genome of *M. tuberculosis* (Mtb) contains approximately 20 genes that encode P450 monooxygenase enzymes, and further genes for their redox partners (151,152). Such a large number of cytochromes P450 is rare in a bacterium. For example, the genome of *E. coli* (which is of a similar size to that of Mtb) encodes no P450s, and this fact is thus indicative that many of these P450 enzymes may be essential to either cell viability or pathogenesis of *M. tuberculosis* (152).

Mycolic acids (60-90 Carbon atoms) (10 nm)

Arabinogalactan

Peptidoglycan

Lipid bilayer (5 nm)
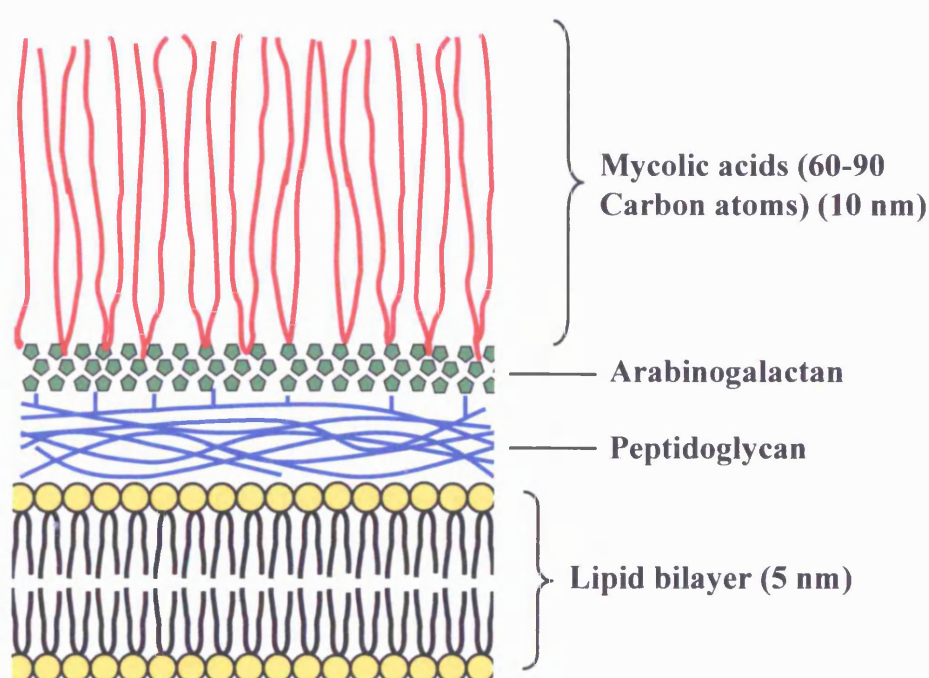
Figure 12 A schematic representation of the waxy cell envelope of *Mycobacterium tuberculosis*. The image identifies the major components of the waxy envelope and their arrangement in relation to the cell membrane. The complex of these lipids and glycolipids is synthesised within *M. tuberculosis* by a set of convergent, partially-defined pathways. Mycolic acid is synthesised from acetyl CoA, while peptidoglycan and arabinogalactan are derived from uridine diphosphate N-acetylglucosamine, pyruvate and glyceraldehyde-3-phosphate, with the three components being joined by an as-of-yet unidentified enzyme system. This envelope likely protects *M. tuberculosis* against immune responses of the host organism, and may be a key factor in the virulence of this pathogen, thus indicating that inhibition of its synthesis is a potential route for novel Mtb treatments (152-154).

The waxy envelope is one way in which the mycobacterium protects itself from anti-microbial agents, as well as desiccation. This envelope has been investigated thoroughly and has been shown to consist of a complex arrangement of compounds,

synthesised within the organism. These include mycolic acids and an arabinogalactan-peptidoglycan complex, all contained beneath a polysaccharide capsule (152) (Figure 12). Many P450s have been demonstrated to have substrate specificity for long-chain fatty acids and polyketides, as well as for sterols, and thus it is speculated that some of the P450s in *M. tuberculosis* may have roles in the biosynthesis of components of the waxy envelope. Work on two Mtb P450s: CYP51, a sterol demethylase of which more will be mentioned later, and a putative polyketide-synthesising P450 (CYP121) has shown these P450s to be strongly inhibited by various azole anti-fungal drugs (e.g. clotrimazole, econazole, and miconazole, Figure 13) which act against fungi by binding to the active site of their sterol demethylase P450 (CYP51) and preventing the conversion of lanosterol to the membrane integrity-maintaining compound ergosterol (155). This inhibition suggests a route by which azole anti-fungal drugs may be of potential as anti-Mtb agents; possibly by attacking the pathways of envelope synthesis of *M. tuberculosis*, thus increasing its permeability to these drugs and other anti-microbial agents to give more effective treatment. However, it could also be possible that inhibition of some of the P450s may be cell-fatal *per se* in any case (156). Preliminary studies of the action of azoles against *Mycobacterium smegmatis* and related actinobacteria (*Streptomyces* strains, which also contain multiple P450s) demonstrate that azole antifungals have potent antibacterial effects. These effects are not manifest on the P450-free *E. coli*, indicating that they are P450-specific (157). Although it does not appear that *M. tuberculosis* has a sterol synthesis pathway, interference with the pathway of synthesis of, for example, mycolic acids would likely have a similar effect on cell wall integrity as that mediated by the azole drugs on fungal membranes. Furthermore, with so many P450s in *M. tuberculosis* (and assuming that many of the P450s play important roles in lipid transformations in Mtb), this may give multiple targets for an azole anti-fungal or other P450-inhibiting drug to act upon. The presence of multiple targets would undoubtedly reduce the likelihood of drug resistance occurring with any newly developed treatments targeting the P450s, particularly if several of the 20 P450s prove essential for viability or infectivity of Mtb.

Econazole

Ketoconazole

Clotrimazole

Miconazole

Fluconazole

Voriconazole
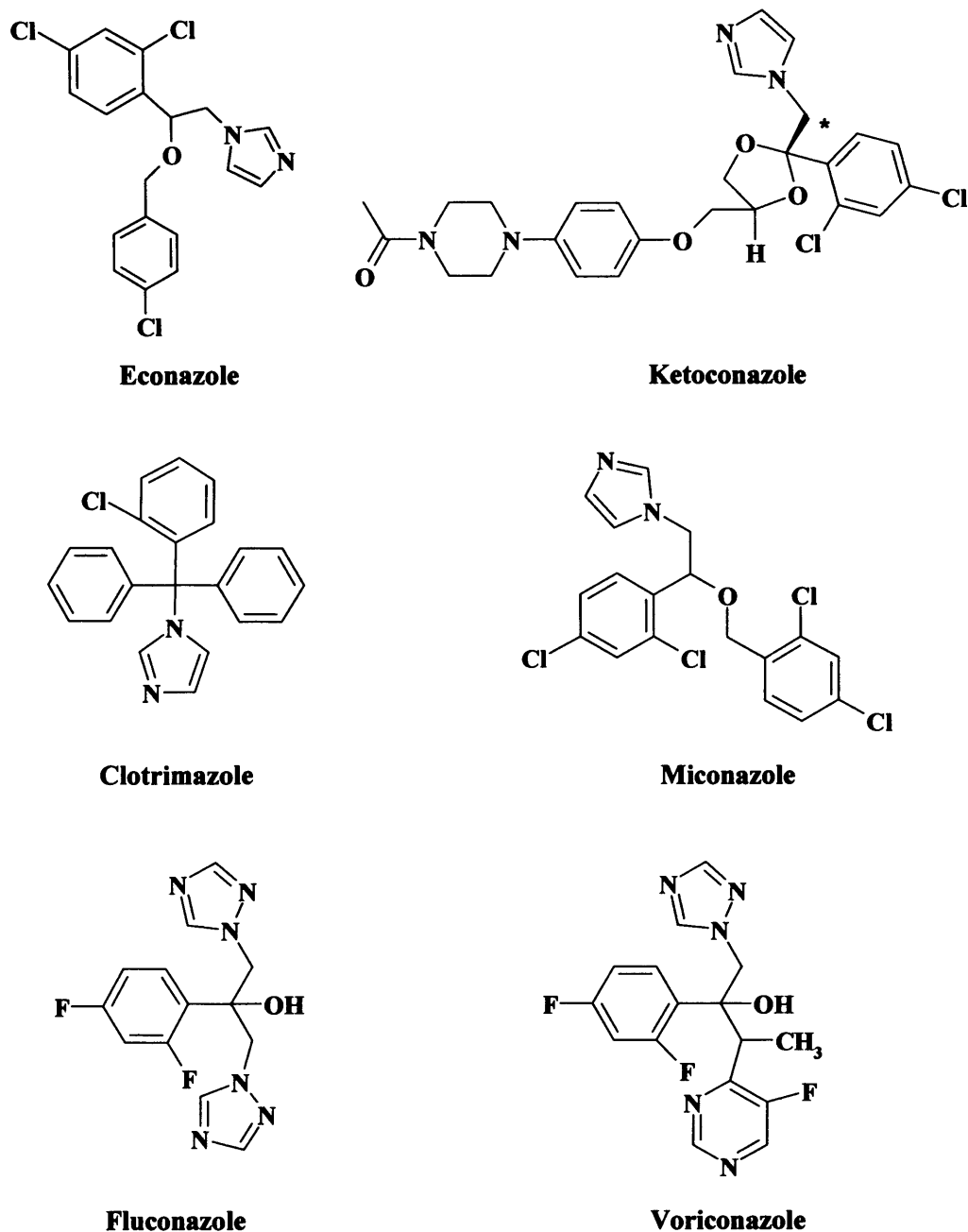
Figure 13 The chemical structures of six common azole compounds shown to possess anti-fungal activity. Each of these molecules is known to bind tightly to the *M. tuberculosis* P450s CYP51 and CYP121 (158,159). In each case the compounds bind to cytochromes P450 by coordination via the lone pair electrons of the nitrogen of an imidazole or triazole ring to the heme iron. This action displaces the bound water molecule and forms a tight and stable complex between drug and P450, thus preventing the binding and activation of molecular oxygen and enzyme catalysis. The chiral centre in ketoconazole is denoted by an asterisk*.

There have been a number of studies into determining the genes essential for the growth, virulence, and pathogenicity of a number of mycobacterial species, including *M. tuberculosis*, *M. bovis*, and *M. smegmatis*, as well as analyses of essential genes for viability of the related actinobacterium *Streptomyces coelicolor* (157,160-165). These studies have involved various techniques, embracing transposon mutagenesis, selective gene knockouts, and microarray methods. These and other methods have allowed identification of genes indispensable for viability and growth, as well as those required under certain growth conditions, including states of infection. Studies by Sassetti and co-workers (161) used a transposon mutation method to make random genomic insertion libraries for *M. tuberculosis* and *M. bovis*. In these studies, unsustainable mutations were considered to identify essential genes. In *M. tuberculosis* they identified 21 genes that were essential to the organism. These included 10 genes involved in biosynthetic pathways such as amino acid synthesis, and 2 from heptose and fatty acid metabolic pathways. However, nine of the genes identified could not be assigned a function at the time of the study. In a similar investigation using mouse spleen cells infected with the *M. tuberculosis* strain H37Rv, a number of genes involved with amino acid and lipid metabolism or cell wall synthesis were determined as essential. This further highlights the significance of the waxy, lipid-rich envelope of *M. tuberculosis* in virulence, pathogenicity and survival in the infective state (160). Research has also determined that in isoniazid-resistant strains of *M. tuberculosis*, where the antioxidant protection provided by a catalase–peroxidase (KatG) is suppressed, there is increased expression of genes (*AphC* and *AphD*) encoding antioxidant peroxiredoxins (163). A further study into the essential genes in *M. tuberculosis* has identified a larger number of genes that are required for growth. As well as the various genes encoding amino acid biosynthesis and metabolic pathway components, two sets of genes of particular interest were identified. These were genes pertaining to heme and flavin synthesis pathways and thus suggest that the roles of proteins incorporating these cofactors, such as cytochromes P450 and their associated flavoproteins, may be important for mycobacterial growth and pathogenicity, and indeed an Mtb ferredoxin (FdxA) has been shown to be induced by various stresses, including those experienced by *M. tuberculosis* in host cells. Furthermore, microarray studies have identified that one Mtb P450 (CYP128) is essential for growth, whilst another (CYP125) is important for infectivity of this human pathogen (164,166-168). Further research implicating the role of cytochromes P450 in mycobacterial species is

35

seen in a study using *M. tuberculosis* and *M. smegmatis* (162). Here a gene, *Rv1395*, is identified as being a transcriptional regulator for the adjacent gene, *Rv1394c*, which by sequence homology is a member of the CYP132 family. The same results are seen in both mycobacteria, suggesting a possible physiological role for CYP132 in these organisms. Although cytochromes P450 may be required by mycobacterial species under certain conditions, it appears likely that some are non-essential under laboratory growth conditions. For instance, two studies have been done using *S. coelicolor* as a model for the mycobacteria, due to the similarly high number of P450s encoded in its genome and the evolutionary relationships between these bacteria. In both studies the sterol 14α-demethylase CYP51 was knocked out, but growth was not attenuated in these knockouts when compared to wild-type (157,165). A second P450, which showed some homology to *M. tuberculosis* CYP121 (but was not from the same CYP family), was also knocked out in *S. coelicolor*, and also found to be non-essential, suggesting that this cytochrome P450 may not be required for normal growth (157). However, the level of identity between Mtb CYP121 and the *S. coelicolor* P450 was rather low (28 % identical at amino acid level) suggesting that their roles are distinct. However, it is important to recognise that these data do not rule out the importance of either Mtb P450 in pathogenicity or virulence of the mycobacteria, but merely indicates that CYP51 (and possibly CYP121) may not be essential for growth of Mtb in rich growth media. Clearly further studies are required for these and other Mtb P450s to establish in detail their physiological function.

A cytochrome P450 of interest from *M. tuberculosis* will be studied in this project. The product of gene *Rv0764c* from *M. tuberculosis* was shown to possess between 29 and 30 % sequence identity to a sterol 14α-demethylase cytochrome P450 (CYP51) found in a number of animals, fungi, and plants (169). In such organisms the enzyme is known to be involved in a sterol biosynthetic pathway that provides sterol compounds that are important for cell membrane integrity and fluidity. In plants the enzyme catalyses the conversion of obtusifoliol to phytosterol; in fungi and yeast lanosterol is demethylated as part of the pathway to produce ergosterol, and in mammals 24,25-dihydrolanosterol is converted to cholesterol (170).

Although CYP51 (the structure of which is shown in Figure 2 for the Mtb isoform) has been shown to be a sterol demethylase in other organisms, there is little evidence that a sterol pathway exists in the majority of prokaryotes, and there has been no

evidence supporting the presence of sterols in Mtb. This suggests that sterols may not be the true substrate for CYP51 in *M. tuberculosis*, although it has been shown that Mtb CYP51 can, albeit with low efficiency, demethylate sterol compounds, (169). The results in this study showed that rather small amounts of demethylated products were obtained in turnover of lanosterol, dihydrolanosterol and obtusifoliol, with the plant sterol obtusifoliol being the substrate yielding the most product. It is possible that Mtb CYP51 has a role in a sterol pathway that has yet to be identified in *M. tuberculosis*, or that the enzyme is a vestigial P450 that once acted as a sterol demethylase, but no longer has this function. Alternatively, Mtb CYP51 could have evolved to utilise a substrate other than a sterol under physiological conditions, but happens to have retained activity with sterols when studied in non-physiological conditions. In the latter case, it is known that several bacteria contain sterol-like molecules, known as hopanoids (171), and hence this activity could be a relic of a function performed by a common ancestor of the CYP51 proteins. A further possibility is that Mtb CYP51 has some role in the infective state, and that it binds host sterols. An interesting observation here is that cholesterol is required for Mtb to infect human cells (172).

In other organisms (e.g. fungi and yeast), CYP51 has been implicated as a target for the inhibitory effects of azole compounds (Figure 13). For instance, the anti-fungal actions of fluconazole and itraconazole, which are prescribed for the treatment of infections with the pathogenic fungus *Candida albicans*, are considered to be mediated by their inactivation of CYP51 function (108,173). Several studies into the effects of azoles on eukaryotic P450s have been performed, and these are consistent with CYP51 as the major azole target in fungi. Several antifungal azoles have been demonstrated to bind very tightly to the fungal CYP51s (although there is also some levels of cross-reactivity with other fungal P450s) (155). Studies have identified that tight binding of azoles to CYP51 in fungi translates to the *M. tuberculosis*, *M. smegmatis*, and *Streptomyces coelicolor* CYP51 isoforms (106,157,174,175), and azole anti-fungals are shown to be very potent inhibitors of mycobacterial and streptomycetes growth (157). However, as previously mentioned, CYP51 knockouts of *S. coelicolor* showed that CYP51 deletion was not lethal and also did not affect sensitivity to azole drugs (157,165). Thus, the azoles may act upon other P450 enzymes to inhibit cell proliferation. Further evidence that azole compounds inhibit CYP51 comes from the crystallisation of Mtb CYP51 with the azole compound fluconazole bound its active site (51). In this structure, fluconazole clearly coordinates the heme iron of the P450.

Many of the results indicate azoles to be potent inhibitors of Mtb CYP51 (and at least one other Mtb P450) and also suggest that the design of novel azole compounds for the treatment of tuberculosis is a viable proposition. A problem with the azoles, however, is that they can have adverse effects upon the patient, caused by inhibition of the human form of CYP51 and other P450s. Thus, it would be necessary to carefully consider this problem when designing and testing novel azole anti-P450 compounds (106). In addition, relatively few azole drugs are systemically tolerated and the majority are for topical use only. A study has been performed using non-azole compounds (based on a benzopyran ring structure with a long alkyl side chain) to inhibit CYP51 in *C. albicans*. These compounds were shown to be potent in their inhibition of the sterol 14α-demethylase of the fungi. With potentially less toxicity than the azoles, they may suggest an alternative strategy for the design of tuberculosis treatments, although there may be little bearing between the actions on a fungal CYP51 and the Mtb CYP51 (176).

1.10 *Ralstonia metallidurans*

The monooxygenase CYP116B1, a fusion of a cytochrome P450 and a phthalate dioxygenase reductase homologue (125), is found in the gram-negative bacterium *Ralstonia metallidurans* CH34 (previously *Alcaligenes eutrophus*). This bacterium was first isolated in 1976 from a wastewater tank at a zinc factory in Belgium that was highly polluted by heavy metals, including zinc (1). Latterly the bacteria has been found in both soils and sediments and has been verified in various studies as possessing genes enabling the organism to flourish in the presence of millimolar concentrations of metals such as Cd, Zn, Pb, Co, Hg, Ni, and Cr, the resistance to which resides on two megaplasmids found within the organism (177-181).

Novel fusion P450s of the type found in *R. metallidurans* were first identified during speculative Blast searches seeking proteins similar to the herbicide metabolising-monooxygenase ThcB from *Rhodococcus erythropolis* (125,182). These studies identified a number of these fusions, including the *R. metallidurans* example studied here and another in the soil bacterium *Rhodococcus sp.* NCIMB 9784. Following further investigation, these P450s were found to be unusual fusions of a P450 monooxygenase with its redox partner proteins. Alignment of the of *R. metallidurans* protein with the sequence of the fused P450 from *Rhodococcus* sp. NCIMB 9784 yields an identity of 66 %, whilst alignment with ThcB (CYP116) from *Rhodococcus*

erythropolis gives an identity of 52 %. This level of identity is sufficient to include this new *R. metallidurans* P450 in the CYP116 family (125,183). This high level of identity may well give an indication of the substrate of the fused CYP116 enzyme, since this level of similarity (assuming the encoded *R. metallidurans* protein forms a functional P450) is rare amongst P450s that have widely differing substrate selectivity. The first characterised CYP116 enzyme, CYP116A1 from *R. erythropolis*, has been identified as catalysing oxygenation reactions with thiocarbamate herbicides (182), and thus it may be true that the *R. metallidurans* homologue performs a similar role. Blast searches with the fused redox partner region of the *R. metallidurans* P450 were also done, and it was found that there was ~40 % identity with a phthalate-family dioxygenase reductase (PFOR) found in certain bacterial genomes (see Figure 14 for its structure). The lack of homology with the redox partners of previously identified classes of P450 (i.e. human CPR, prokaryotic systems, and P450 BM3 from *B. megaterium*) has led to these PFOR-fused enzymes being classified as a novel class of P450 – Class IV (125). The PFOR domain, as previously mentioned, has been characterized previously as a single polypeptide chain consisting of an amino terminal FMN-containing domain linked to the carboxyl terminal 2Fe-2S ferredoxin domain, which together act to mediate electron transfer from NADH to the enzyme it serves – phthalate dioxygenase (125,136,145-147). In the *R. metallidurans* and *Rhodococcus* sp. NCIMB 9784 fusions, the P450 heme domain forms the amino terminal part of the protein, joined by a short polypeptide linker region, highlighted in the amino acid alignment shown in Figure 99, Chapter 5.2, to the FMN-binding domain of a PFOR-like reductase. It is speculated that the fusion of a P450 with this atypical P450 redox partner may give rise to a P450 enzyme with greater catalytic efficiency than for an enzyme driven by distinct and more conventional partners, such as CPR or a flavin-containing reductase and a ferredoxin (125). This would give an explanation for the reason why this fusion has evolved and persists in nature, as evolution generally disfavours those changes that are negative or detrimental to the host organism. This fusion may well be self-sufficient and not necessitate interactions with other exogenous proteins to facilitate catalysis. Such an enzyme may thus be of benefit to the organism as a more efficient P450, assuming a role that requires fast turnover of a key substrate. Another point to consider is that fusion enzymes of this type may have developed in order to coordinate expression of both redox components of a P450 system at once, whereas if the genes are chromosomally distinct such regulation might be more problematic to achieve.

39
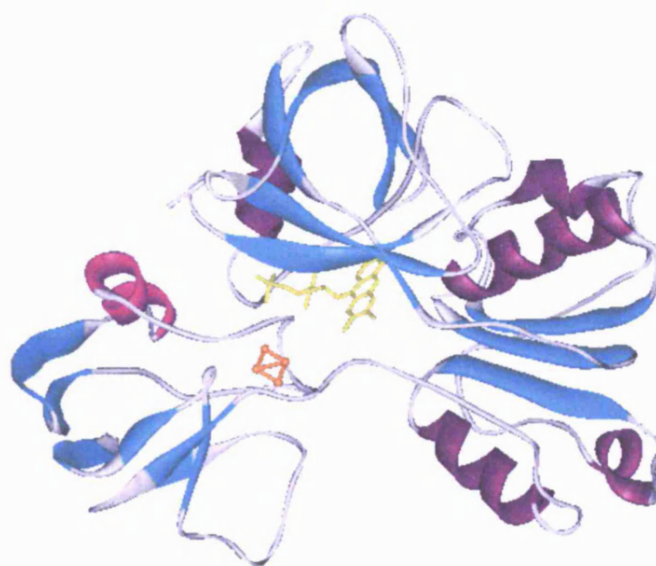
Figure 14 Structure of the phthalate oxygenase reductase (PFOR) from *Pseudomonas cepacia* (6) solved by X-ray crystallography to a resolution of 2.0 Å (PDB no. 2PIA). The iron-sulphur (2Fe-2S) cluster is shown in orange and the FMN molecule is shown in yellow. The α-helices are identified in purple, β-sheets in cyan, linker regions in grey. The image was created using the Weblab ViewerPro program (Molecular Simulations Inc.).

As mentioned in Chapter 1.8, P450-redox partner fusions have been artificially engineered previously, although these incorporated more conventional redox partners (e.g. CPR) and not the PFOR-type partner identified in *R. metallidurans* and *Rhodococcus* sp. NCIMB 9784. With some notable exceptions, engineered fusions have been generally unsuccessful in achieving substantially greater efficiency and electron transfer rates when contrasted with their natural two or three-component counterparts (or with P450 BM3) (25,125). As the use of P450s for biotechnologically relevant chemical transformations has the drawbacks of requirements for costly and unstable co-enzymes and multi-component redox partner systems, it is clear that a single polypeptide fusion with efficient internal electron transport has great potential for exploitation in biotechnology. By fusing PFOR to P450s that currently catalyse reactions at inefficient rates, it may be possible to improve their turnover numbers and to produce oxy-compounds of special interest to the drug and biotechnology industries (124).

Another aspect of interest with the CYP116B1 P450 from *R. metallidurans* is that it may have a role in the degradation of thiocarbamate herbicides in soils (124,125), as

does the homologous Class I P450 CYP116A1 from *R. erythropolis*. If this is the case, incorporation of the fusion into a soil bacterium may allow the removal of such herbicides from the soil in a biosafening/bioremediation role. Ultimately, this may protect crops by means of these bacteria accumulating and functioning in the rhizosphere of the plants. It may also be possible to integrate such fused P450 systems, capable of herbicide degradation, directly into the genomes of plants. Here they could function to protect plants grown on soils containing higher herbicide concentrations, in order to reduce incidences of competitive plants threatening crops and damaging profit and productivity. Plants clearly possess the systems required for generation of NAD(P)H coenzyme needed to drive P450. However, there are some ethical aspects to be considered in such procedures, especially as some P450s are known to produce carcinogens from organic substrates (25,184). Moreover, there are clearly issues with the marketing and general customer desire for genetically modified plant products.

The work on CYP116B1 will also yield results that can be compared to those from the study of the homologous enzyme CYP116B2 from *Rhodococcus* sp. NCIMB 9784 (124,185). The data produced in this study suggest that CYP116B2 is a fully functional fusion of P450 and reductase components with the potential for highly efficient electron transfer from the FMN co-factor to the heme via the iron-sulphur centre. It also showed that the reductase favoured electron donation from NADPH, which differs from the specificity of the homologous phthalate dioxygenase reductase enzyme (6,145). O-dealkylation of 7-ethoxycoumarin was catalysed by CYP116B2, although this is not the physiological reaction and proceeds at a very slow rate. It will be interesting to compare and contrast the data obtained with CYP116B1 with those from the preceding study of the CYP116B2 enzyme, in order to compare and contrast their catalytic properties. Such studies have the potential to identify the reasons underlying the evolution of these systems, to determine the roles of these systems in the host organisms, and to establish thermodynamic, kinetics and other biophysical properties of the enzymes. In the next section, the aims of studies to be performed with this novel *R. metallidurans* cytochrome P450, as well as with CYP51 from *M. tuberculosis* are discussed in more depth.

1.11 Research aims

As has been identified in Chapters 1.9 and 1.10, the *M. tuberculosis* and *R. metallidurans* P450s to be studied here likely perform two diverse physiological roles, with a uniting feature being that both derive from the same superfamily of monooxygenase enzymes. Whilst the former has a potential role in the treatment of the human pathogen *M. tuberculosis* (as its inhibition may lead to a reduction in the viability of the organism that it serves), the latter has a potential role in the bioremediation of herbicide-contaminated soils. Studies of the CYP116B1 enzyme will clearly enable a better understanding of the diverse mechanisms by which cytochromes P450 obtain electrons in order to drive catalysis, and why redox partner fused P450 systems occur in nature. Thus, having established the reasons for the studies of these cytochromes P450s, this section identifies the approaches that will be taken in order to characterise the *M. tuberculosis* and *R. metallidurans* monooxygenases.

The first part of the project focuses upon the further characterisation of Mtb CYP51, starting with basic studies of ligand binding before moving on to a thorough characterisation of the interaction of this P450 with the well-documented CYP51-inhibiting compounds, the azole anti-fungals. These studies will hopefully help with the elucidation of the biological role, and enable structure/function relationships of this P450 to be established. Spectroscopic techniques, including electron paramagnetic resonance, resonance Raman, and circular dichroism, are used in order to investigate the oxidation and spin-states of the heme iron at the heart of this enzyme, as well as structural aspects of the protein. An aspect of Mtb CYP51 which has not been investigated significantly in other studies is its interaction with the protein expressed from gene *Rv0763c* in the *M. tuberculosis* genome. This gene, which is adjacent to *CYP51* on the Mtb genome, has been shown to encode a ferredoxin protein that, due to its genomic location, is proposed as a redox partner of the monooxygenase (134,159). It has been seen that reconstitution of a redox system involving a ferredoxin reductase, the ferredoxin (*Rv0763c* product), and CYP51 facilitates the transformation (demethylation) of lanosterol and other sterols, albeit at very low rates (169). However, as no kinetic data regarding the electron transfer between these potential redox-partner proteins have been published, this study aims to characterise the interactions of these two proteins by a combination of kinetic and spectroscopic techniques. Stopped-flow kinetic methods are used to measure the transfer of electrons between these proteins, and to confirm that

they are able to form a functional redox system. CYP51:ferredoxin interactions are analysed by techniques such as UV-visible absorption and circular dichroism in order to determine affinity and electronic effects. A further facet of the *M. tuberculosis* protein studied is its midpoint reduction potential in substrate-free and ligand-bound forms, as this biophysical parameter is an important determinant of electron transfer in P450 systems and, in part, controls the inter-protein electron transfer rates.

From these findings progress will be made in understanding the medical relevance of the *M. tuberculosis* P450, since more detailed knowledge will be obtained that relates to the affinity of Mtb CYP51 for azole drugs. Ultimately, these drugs may prove useful in treatment of sufferers from this serious human pathogen. Furthermore, these studies have a broader aim of expanding the database on the cytochromes P450, increasing our understanding of their roles in cellular functions, as well as identifying key similarities and differences between important members of this superfamily of monooxygenases.

The study of newly-identified CYP116B1 from *R. metallidurans* is the second major theme of this thesis, and involves the first systematic investigation and characterisation of this novel redox partner-fused monooxygenase. The generation of novel data on its structure and function will enable important comparisons of this protein to be made with enzymes homologous to both of the CYP116B1 domains. Following cloning of the CYP116B1 gene and expression of the encoded protein, UV-visible spectroscopy and allied techniques are used to determine that the enzyme produced is a true cytochrome P450, containing the proposed heme, FMN, and iron-sulphur co-factors. As with Mtb CYP51, further detailed spectroscopic studies are performed in order to characterise the overall structural properties and active site characteristics of this P450. Work is presented to identify a substrate for the enzyme, whilst further important properties of CYP116B1 and its heme cofactor are established by other spectroscopic methods such as circular dichroism, electron paramagnetic resonance (EPR), and resonance Raman. The system is also investigated by stopped-flow and steady-state kinetic assays in order to determine that the reductase is functional and capable of reduction of its heme, to define rates of electron transfer through the system, and to establish if there is strong preference for pyridine nucleotide cofactors (NAD(P)H). Elucidating the mechanistics of the CYP116B1 fusion will be very useful in understanding this novel class of cytochromes P450, and to this end the determination of the redox potentials of the redox components of the fusion protein is presented, with clear demonstration that the binding of substrate-like molecule should provide a thermodynamic or structural trigger that

accelerates electron transfer to the heme centre. The identification of a substrate for CYP116B1 is made, opening up further avenues of investigation including analysis of the products of CYP116B1-mediated reactions, and steady-state kinetic investigations. A longer term aim of the research on the CYP116B1 project is the determination of its atomic structure. Ultimately, the structure of a complex multi-domain P450 redox partner fusion enzyme will provide important information on the nature of the interactions between the redox partners. However, as the crystallisation of such large, multi-domain enzymes is very challenging, preliminary steps to resolving structural properties of CYP116B1 are made through the cloning, expression and characterization of the individual P450 and reductase domains of R. metallidurans CYP116B1. These domains will provide smaller and simpler entities for structural characterization, and ultimately the data collected will be of enormous use in determining the structure of an intact CYP116B1 enzyme. These domain proteins are analysed by kinetic and other methods in order to confirm their cofactor content and functionality, and to ensure that the properties of the individual domains are consistent with those observe in the full-length enzyme.

The findings reported for the R. metallidurans system enable a better overall understanding of this class of redox-partner-fused P450 enzyme system, which exists in other bacterial organisms. The findings reported in this thesis may potentially be utilised to aid and develop the biotechnology industries in both the aspects of herbicide bioremediation and improved catalytic efficiency and cost effectiveness of engineered P450 systems. The study of the R. metallidurans protein reported here also impacts in the general understanding of the function of P450-reductase fusion systems, and the reasons for their evolution in their host organisms.

Collectively, these studies on two diverse P450 redox system provides extensive details on many aspects of catalytic, thermodynamic, kinetic, substrate-preference and structural properties of Mtb CYP51 and R. metallidurans CYP116B1. In Chapter 2, the methods utilised throughout these P450 studies are detailed. Chapters 3 and 4, respectively, describe the results of the characterizations of CYP51 from Mycobacterium tuberculosis and CYP116B1 from Ralstonia metallidurans, whilst Chapter 5 describes the characterization of the heme and reductase domains of CYP116B1.

Chapter 2

Methods and Materials

2.1 General information

This chapter gives details of the techniques employed during the characterizations of Mtb CYP51 and the *R. metallidurans* proteins. Unless indicated otherwise, reagents detailed were obtained from Sigma-Aldrich (Poole, UK) and molecular biology methods adhere to those reported by Sambrook *et al.* (186).

2.2 Template DNA

Cosmid DNA produced from *Mycobacterium tuberculosis* was supplied by Professor S. Cole at the Institut Pasteur for use in the cloning of the CYP51 gene. The soil bacterium *Ralstonia metallidurans* was obtained from Professor N. Brown's Laboratory, University of Birmingham. Heating single colonies of *R. metallidurans* from an agar plate to 99 °C for 9 minutes in 50 µl ddH2O produced template DNA for the cloning of the *R. metallidurans* P450s. In subsequent PCR reactions 2 µl of this template DNA-containing solution was required to produce sufficient quantities of cloned fragment for ligation into the pGEM-T vector (Novagen, Nottingham, UK).

2.3 PCR

All PCR reaction were carried out in a 50 µl volume containing 200 nmol of each primer, along with 0.2 mM dNTPs (New England BioLabs, Hitchin, UK), appropriate quantities of the DNA to be cloned (typically 10 ng), 2 units Pfu Turbo DNA polymerase and 5 µl of its associated x10 buffer containing the necessary magnesium salts for polymerisation (both Stratagene Ltd, Cambridge, UK). Any shortfall in reaction volume was made up by the addition of sterile ddH₂O. The DNA was first denatured at 94 °C for 45 seconds, followed by primer annealing, and polymerisation at 72 °C in a cycle which was repeated between 30 – 35 times (performed in a Techne Genius PCR machine). The annealing temperature was set at a temperature 5 °C less than the lowest Tm (melting temperature) of the pair of primers used, in order to promote annealing to the template DNA, whilst the polymerisation time used was calculated as approximately two minutes per kb of DNA to be replicated. The PCR was then loaded to a 1 % agarose gel (Melford Laboratories, Ipswich, UK) containing ethidium bromide (1.3 µl of a 10 mg/ml stock per 50 ml gel) and run alongside 1 kb DNA Ladder (NEB) to confirm the size of the cloned fragments matched the calculated

size. If this was the case, the fragment was excised from the gel and purified using a Qiagen PCR purification kit (Qiagen, Hilden, Germany) in order to remove contaminants that may hinder later stages of the cloning processes.

2.4 A-tailing of PCR fragments

PCR products was A-tailed (the addition of dATP to either end of the fragment) in order to produce cohesive ends for the insertion of the fragment into the pGEM-T cloning vector (Novagen). The reaction, containing 7 μl PCR product (~50 ng), 1 μl of 2mM dATP, 5 units *Taq* polymerase, and 1 μl x10 *Taq* polymerase buffer (all New England BioLabs), was incubated at 70 °C for 30 minutes, which would allow the A-tailing to occur and produce substrate for the next step involving PCR product ligation into the required vector.

2.5 Ligation reactions

A-tailed fragments were ligated into pGEM-T using 400 units T4 DNA ligase (New England BioLabs) and its x10 buffer (1 μl) with both vector and insert being present at 50 ng. All ligations were carried out in a 10 μl reaction volume with any shortfall in volume being made up with ddH$_2$O. Following overnight incubation at 4 °C the ligation reactions were transformed into JM109 competent cells. It should be noted that ligation reactions not involving A-tailed fragments or pGEM-T vector were performed in the same way.

2.6 Oligonucleotide primers

Pairs of oligonucleotide primers for PCR reactions were designed, based upon published DNA sequence of the gene, to be complementary to the DNA of the gene to be replicated, with one primer designed to bind the sense strand and another for antisense strand. The primers were produced to be of between 18 and 30 nucleotides in length with similar G+C contents, in order to achieve good annealing of the primers to their complementary sequences. Where appropriate, transcriptional termination codons and restriction sites were added to allow straightforward cloning of the PCR fragment as a functional gene. The primers were also designed to incorporate, where necessary, the ATG initiation codon, so that the gene could be replicated by the host organism under the control of a plasmid promoter system.

Primers for sequencing were designed to be complementary to the sequence of interest and of 18 to 30 nucleotides in length to allow good annealing to the target gene. With larger fragments (1 – 2.5 kb), a series of primers were designed to span the length of the gene in order that the whole of the gene could be sequenced in steps. Primers for mutagenesis were designed with the same considerations as above, as well as incorporating the appropriate mutation. All primers were designed to avoid or minimise primer-dimer occurrences and the replication of other fragments of DNA from the genome. All oligonucleotides were synthesised at PNACL, University of Leicester.

2.7 DNA sequencing

Once a clone had been confirmed as correct by restriction digest analysis, the plasmid DNA was prepared and sent to PNACL at University of Leicester for nucleotide sequencing. DNA was supplied at between 0.2 – 0.5 µg along with the appropriately designed primers (100 pM) to sequence the region of interest. Subsequent sequencing data returned were compared to the published nucleotide sequence of the cloned gene to determine correct cloning and/or identify the presence or absence of mutations in the clone. Further cloning or protein expression was carried out dependent upon these sequencing results being in agreement with those expected i.e. the clone contained the correct nucleotide sequence. DNA sequencing was done by standard fluorescence-based dideoxy chain termination methods (186).

2.8 Mutagenic reactions

Mutagenesis reactions were carried out using the QuikChange Site-Directed Mutagenesis kit (Stratagene). Forward and reverse primers were designed to rectify or generate the mutation in the plasmid DNA and were diluted to provide 125 ng of each. A PCR was carried out using 50 ng template DNA, 125 ng of each primer, 2 units Pfu polymerase, 5 µl x10 Pfu polymerase buffer, and 0.2 mM dNTPs. The reaction was performed in a 50 µl volume with shortfalls in volume made up with sterile ddH$_2$O. The PCR was cycled 18 times with a denaturation phase of 95 °C for 30 seconds, an annealing phase set at 5 °C less than the lowest Tm of the primer pair for 1 minute, and an extension phase at 68 °C for a period of time equating to 2 minutes per kb of plasmid. Following the completion of the PCR, 20 units of *Dpn*I restriction enzyme was added to the reaction and the mixture incubated at 37 °C for 1 hour in order to

completely digest the methylated template DNA. The reaction was then run on a 1 % agarose gel to confirm the replication of the correctly sized plasmid. The DNA was then sequenced (as described above) to confirm successful mutagenesis.

2.9 DNA transformations into JM109 competent cells

A standard volume (50 µl) of JM109 *E. coli* competent cells (New England BioLabs) were transformed with recombinant plasmid DNA (5 µl) by firstly co-incubating on ice for 10 minutes followed by heat shock at 42 °C for 45 seconds, before being returned to ice for 2 minutes. 450 µl of pre-warmed LB medium were added to the cells, which were then incubated at 37 °C in a shaking incubator for 1 hour. 100 – 200 µl of the cells were then plated to agar plates containing appropriate antibiotics to sustain plasmid transformant growth, and incubated overnight at 37 °C. The following day, colonies were picked from the plates and grown in 5 ml LB media containing appropriate concentrations of antibiotic. These cultures could then be used for making glycerol stocks of the plasmid-containing cells and for larger scale plasmid preparations. When transforming pGEM-T vectors, 20 µl of 0.125 M X-gal and 100 µl of 0.1 M IPTG were added to the cells before plating in order to blue/white screen colonies for successfully ligated plasmid. Recombinant plasmid-containing cells appear white due to the disruption of the *lacZ* gene.

2.10 Calcium chloride competent cells

In order to express protein, competent cells were required to incorporate and replicate the plasmid containing the gene to be expressed. Competent HMS174 (DE3), Rosetta (DE3), Origami (DE3), and Rosetta-gami (DE3) were produced by the calcium chloride method. This involved the overnight culture of the cells in LB media enriched with the appropriate antibiotics required by the cells. An aliquot (300 µl) of the overnight culture was used to inoculate 30 ml of antibiotic-enriched LB media, which was incubated at 37 °C until the culture reached an $O.D._{600} = 0.4 - 0.6$. The cells were then divided into two aliquots of 15 ml, before being centrifuged (6000 rpm) for 10 minutes at 4 °C. The cells were resuspended in 7.5 ml ice-cold 50 mM calcium chloride and kept on ice for 15 minutes with occasional mixing. The cells were then centrifuged as before, resuspended in 1.5 ml of ice-cold calcium chloride solution with the addition

of 10 % glycerol. The cells were then aliquoted (300 μl) into cold Eppendorf tubes and stored at −80 °C until required.

2.11 DNA transformations into calcium chloride competent cell strains

Although JM109 cells were well suited to receive newly cloned plasmid and for the production of larger quantities of recombinant DNA, they were generally not suitable for protein expression. Hence it was necessary to transform the recombinant plasmid into cell strains including HMS174 (DE3), Origami (DE3), Rosetta (DE3), and Rosetta-gami (DE3) (Novagen), in order that the desired gene could be expressed from a powerful T7 RNA polymerase/promoter system for protein production. These transformations involved the addition of 1 − 10 ng plasmid DNA to 300 μl competent cells. The cells were then incubated on ice for 30 minutes, heat shocked for 2 minutes at 42 °C, returned to ice for a further 5 minutes, before 500 μl cold LB media were added and the cells were shaken for 1 hour at 37 °C. The cells were then plated neat and also from 1/10 and 1/100 dilutions (100 − 200 μl added to each agar plate containing the appropriate antibiotic), and incubated overnight at 37 °C. Again colonies were picked and cultured in LB media for use as glycerol stocks, and as inoculants for subsequent protein production.

2.12 Glycerol stocks

Glycerol stocks were produced from 5 ml cultures of transformed *E. coli* cells grown for 6 − 8 hours at 37 °C until mid-late exponential phase. 500 μl of culture and 100 μl glycerol were mixed and added to sterile Eppendorf tubes, and the tubes stored at −80 °C until required.

2.13 Mini/Midi preps of plasmid DNA

Plasmid DNA was prepared on two scales (mini and midi) dependent upon required concentration or quantity of DNA. Minipreps were produced from a 5 ml culture of cells transformed with recombinant plasmid, whilst Midipreps were produced from 50 ml cultures. In both cases the plasmid DNA was prepared from overnight cultures using Qiagen's Miniprep Kit and stored at −20 °C until required. Concentrations of the DNA prepared were estimated by gel electrophoresis and ethidium bromide staining or spectrophotometrically.

2.14 Restriction digests

Restriction digests were either carried out in order to diagnose that a successful recombinant plasmid had been produced, or for the excision of fragments and the cutting of plasmid backbones in further rounds of cloning. In all cases the reaction was performed in a 30 μl volume containing up to 1 μg plasmid DNA, 2 μl of each restriction endonuclease used (typically 10 – 20 units), 3 μl of the appropriate buffer for optimal performance of the endonuclease(s) and Bovine Serum Albumin (100 μg/ml) if required (all New England BioLabs). Shortfalls in volume were made up with sterile ddH$_2$O. The reactions were incubated at 37 °C and allowed to run for no longer than 4 hours to avoid star ('*') activity (excessive DNA digestion due to recognition of secondary sites by the endonuclease). Conditions were varied in some cases if the endonuclease required a lower incubation temperature or a longer incubation period to completely digest the target DNA.

2.15 Gel purification of restriction digests

Following digestion, reactions were heated for twenty minutes at 65 °C to inactivate the restriction endonucleases, and were then run alongside 1 kb DNA ladder (New England BioLabs) on 1 % agarose gels containing ethidium bromide (1.3 μl of a 10 mg/ml stock) and viewed under UV light in order to identify the correctly sized fragments of plasmid DNA. If fragments were to be used for further cloning, then those of the correct size were cut from the gel and purified further using a Qiagen Gel Purification Kit in order to remove contaminants (e.g. restriction enzymes). The concentrations of these fragments were calculated spectrophotometrically on a Cary UV-50 UV-visible spectrophotometer (assuming A$_{260}$ = 1 = 50 μg/ml DNA), or by examining relative intensities on an agarose gel against a known amount of 1 kb DNA ladder, after which the fragments could be used for cloning.

2.16 LB media

All growth of transformed cells was carried out in sterilised LB media that consisted of 10 g/L NaCl, 10 g/L tryptone, and 5 g/L yeast extract (All Melford Laboratories) solubilised in ddH$_2$O.

2.17 Agar plate media

Sterile agar plates were prepared using LB media produced in the ratios described in Chapter 2.16 and enriched with 12.5 g/L of bacteriological agar (Melford Laboratories). Required antibiotics were added to the agar/LB solution when the media had cooled below 50 °C, but prior to setting.

2.18 Antibiotic concentrations in LB media and agar plates

Stock solutions of antibiotics were prepared in ddH$_2$O with the exception of tetracycline and chloramphenicol, which were dissolved in ethanol. In Table 3 the concentrations of antibiotics added to liquid and agar media are described. The antibiotic enrichment of media served to facilitate selective growth of certain E. coli cell strains (e.g. Origami (DE3), Rosetta (DE3), and Rosetta-gami (DE3) cells), whilst also selecting for those cells that had successfully incorporated ampicillin resistance-conferring plasmids.

Antibiotic	LB media	Agar plate media
Ampicillin	50 µg/ml	50 µg/ml
Carbenicillin	50 µg/ml	50 µg/ml
Tetracycline	12.5 µg/ml	12.5 µg/ml
Kanamycin	30 µg/ml	15 µg/ml
Chloramphenicol	34 µg/ml	34 µg/ml

Table 3 The concentrations of antibiotic compounds utilised in liquid culture and agar plates during the cloning and expression of Mtb CYP51 and the R. metallidurans proteins. Apart from tetracycline and chloramphenicol, which were solubilised in ethanol, all compounds were prepared in ddH$_2$O. The concentrations listed are the final solution concentrations in the respective media.

2.19 Protein expression

Once recombinant plasmid had been transformed into expression strains (HMS174 (DE3), Rosetta (DE3), Origami (DE3), and Rosetta-gami (DE3)), small-scale trials to determine the optimum conditions for expression of the encoded protein could be carried out. To perform small-scale trials, 10 – 50 ml volumes of transformant culture were grown in the presence of the appropriate antibiotics for the selection of plasmid. Determination of optimal expression was achieved by analysing the effects of varying the cell strain from which the protein was expressed, as well as the effects of differing concentrations of IPTG on protein expression, via its action as an inducer of expression

of the T7 RNA polymerase encoded on the chromosome (leading to expression of the target gene on the plasmid). Protein expression levels were determined by SDS-PAGE analysis of samples taken from the relevant *E. coli* cultures at different times before and after induction. By running samples derived from intact expression cells and their soluble and insoluble fractions (generated using Bugbuster™ – see Chapter 2.21), the relative proportions of target protein in the soluble and insoluble (or membrane-associated) fractions could be determined. Systematic analysis of protein expression from different cell strains and under different growth and induction conditions enabled identification of growth conditions where expression of the target protein was optimal, and for which the protein was produced predominantly as a soluble entity. Culture growths of 500 ml LB media (Chapter 2.16) in 2 L flasks were then used to produce the protein on a large scale (typically 6-10 litres total) in order to generate sufficient protein for biophysical and kinetic studies. In further studies to optimise expression systems, the effects of growth temperature (18 – 37 °C) and overall culture growth time post-induction were routinely evaluated in order to optimise the production of protein from the large scale cultures.

2.20 Agarose gels for electrophoresis

All agarose gels were used at 1 % and contained 1.3 µl ethidium bromide (10 mg/ml) per 50 ml gel. For fragment purification, agarose gels were made using Tris acetate buffer (TAE), due to the potential for ligation inhibition when using Tris borate buffer (TBE) and the greater resolution achieved with TAE. Gels for diagnostic restriction digests generally did not require greater resolution; the fragments were not required for subsequent reactions and were hence produced using TBE buffer. The compositions of the two buffers are shown in Table 4.

10x TAE buffer	10x TBE buffer
48.46 g/l Tris base (0.4 M)	107.82 g/l Tris base (0.89 M)
11.4 ml/l Glacial acetic acid	55.03 g/l Boric acid (0.89 M)
2.92 g/l EDTA (0.01 M)	5.84 g/l EDTA (0.04 M)

Table 4 The compositions of TAE and TBE buffers utilised in the preparation of (1 %) agarose gels for subsequent DNA electrophoresis. Visualisation of diagnostic restriction digests was performed on TBE-containing gels, whilst purification of DNA fragments was performed from TAE-containing gels in order to avoid TBE-mediated inhibition of later ligation reactions.

2.21 SDS-PAGE analysis of protein expression

Expression of soluble protein from *E. coli* transformants was determined using SDS-PAGE analysis of cell cultures under varying conditions. The total protein sample was prepared by centrifuging 500 µl of culture (13000 g for 1 minute) and resuspending the pellet in 50 µl of buffer A. The soluble and insoluble fractions were produced by centrifuging 1 ml of the same culture (13000 g for 1 minute), and resuspending the pellet in 200 µl of Bugbuster (Novagen) solution. The cells were shaken at room temperature for 20 minutes before being centrifuged at 13000 g for 20 minutes at 4 °C. The supernatant was retained as the soluble protein sample whilst the pellet was resuspended in 150 µl buffer A to give the insoluble protein sample. 10 µl aliquots of each sample, mixed with 20 µl of SDS running buffer containing 10 % DTT (both New England BioLabs), were incubated at 95 °C for 5 minutes to denature the protein in the sample. Samples were run on a 10 % acrylamide gel consisting of a stacking gel (containing 2 % SDS) layered on top of a resolving gel (1 % SDS). The full details of the two gels are shown in Table 5.

Stacking gel	Resolving gel
2.1 ml H₂O	4 ml H₂O
380 µl 1.5 M Tris pH 6.8	2.5 ml 1.5 M Tris pH 8.8
500 µl 30 % acrylamide mix	3.3 ml 30 % acrylamide mix
30 µl 10 % SDS	100 µl 10 % SDS
30 µl 20 % ammonium persulphate	100 µl 20 % ammonium persulphate
6 µl TEMED	10 µl TEMED

Table 5 The constituents of the two parts of the SDS-PAGE gels utilised for the analysis of protein expression from *E. coli* cell strains. The upper layer (stacking gel) serves to condense the protein sample to a tight band before it enters the resolving gel, in order to improve resolution of expressed proteins.

Electrophoresis of samples was performed at a constant 150 V in a buffer composed of 25 mM Tris, 250 mM glycine, and 0.1 % SDS in ddH₂O. Run alongside the samples in each gel were a Broad Range Protein Marker (New England BioLabs) and a total protein sample from untransformed cells of the same strain as that used for the expression of the protein. These were used in order that it was clear that the size of the target protein was correct and that it was being overexpressed in the *E. coli* cells. Once run, the protein was visualized by staining gels for 10 – 15 minutes with Coomassie blue stain (0.25 g per 90 ml methanol:H₂O (1:1 v/v)) before destaining with a solution

of 90 % H₂O, 10 % methanol, and 5 % acetic acid. When thoroughly de-stained, the gels were photographed and used to analyse the extent of protein expression, or to determine the purity of protein following various stages of fractionation.

2.22 Cell harvesting

The cells from the large-scale growths were harvested by centrifugation at 5000 g for 20 – 30 minutes using a Beckman Avanti J-20 XP centrifuge. Following supernatant removal, the cell pellets were resuspended in 50 – 100 ml of ice-cold Buffer A and centrifuged at 5000 g for 20 – 30 minutes. The supernatant was removed and the subsequent pellet stored at –20 °C until required for protein extraction.

2.23 Protein purification

The cell pellet was firstly resuspended in ~50 ml ice cold buffer A and homogenised using a Bandelin Sonoplus GM2600 sonicator. The suspension was subjected to six sonications at 75 % full power, each lasting twenty seconds. Between each pulse 2 minutes rest was allowed to prevent overheating of the protein sample. Benzamidine hydrochloride and phenylmethylsulfonyl fluoride (both at 1 mM) were added to the resuspended pellet prior to homogenisation, in order to retard the activity of proteases that may have acted upon the protein once the cells were disrupted. The sonicated material was then passed through a French press twice at 950 lb/in² in order to complete cell breakage and to free further proteins contained within cells that remained intact after sonication. The resulting cellular material was centrifuged at 18000 g for 40 minutes. The supernatant was retained and subjected to a second centrifugation under the same conditions. The crude cellular extract was then dialysed for 4 – 6 hours in buffer A (Chapter 2.24) containing the aforementioned protease inhibitors, before being subjected to column chromatography. The exact details of the column chromatography steps utilised for the M. tuberculosis and R. metallidurans proteins are described in Chapters 3.3, 4.7, and 5.3. CYP51 was purified by successive chromatography steps on DEAE Sepharose, hydroxyapatite and Q-Sepharose columns, whilst CYP116 B1 (intact) was purified by DEAE Sepharose, phenyl Sepharose and Q-Sepharose columns. DEAE Sepharose, hydroxyapatite and Q-Sepharose resins were employed to purify the heme domain of CYP116B1, whilst DEAE Sepharose and Q-Sepharose were used for reductase domain purification. For each chromatography step the cell extracts were

55

loaded onto a column equilibrated in at least 2 column volumes of buffer matching the composition as that previously used for dialysis. Once loaded, the column was washed thoroughly with buffer (1 – 2 column volumes) before the protein was eluted using a linear gradients of either buffer A and buffer B, or buffer C and buffer D, depending on the column used (see Chapter 2.24 below for composition of buffers A – D). Fractions from the column were collected and those exhibiting the greatest proportions of viable P450 (as determined by spectral analysis) were retained and pooled. The protein was then dialysed into buffer appropriate for the next column to be used and the process repeated until an acceptable degree of purity (identified by the ratio of heme-specific absorbance at ~418 nm to general protein-specific absorption at ~280 nm) was achieved. The fractions from the final column were pooled and concentrated by ultrafiltration using Centriprep tubes (Millipore, Watford, UK) before the addition of sterile glycerol (to a final concentration of 50 % v/v) and storage at –80 °C. Throughout the purification steps, the presence of protease inhibitors and glycerol (10 %) was maintained in order to prevent the degradation and aggregation of the protein before it could be used experimentally.

2.24 Buffers

Various buffers were used throughout this work for dialysis, cell pellet resuspension and for use with ion-exchange columns and other protein purification resins. The compositions of the most commonly used buffers are listed in Table 6. Other buffers reported in this and other chapters were prepared according to the recipes reported in Table 6, but were adjusted to the appropriate pH as required.

Buffer	Composition
A	50 mM Trizma base and 1 mM EDTA dissolved in ddH$_2$O and adjusted to pH 7.2 using HCl
B	Buffer A additionally containing 500 mM KCl
C	25 mM KH$_2$PO$_4$ (dibasic) added to 25 mM K$_2$HPO$_4$ (monobasic) until pH 6.5
D	500 mM KH$_2$PO$_4$ (dibasic) added to 500 mM K$_2$HPO$_4$ (monobasic) until pH 6.5

Table 6 The composition of the four main buffers utilised during expression and purification of the *M. tuberculosis* and *R. metallidurans* proteins, as well as for protein suspension for spectroscopic assays performed with these enzymes. EDTA (Ethylenediaminetetraacetic acid, 1 mM) was added in order to chelate metal ions that may otherwise be used by metalloproteases. Both dibasic and monobasic potassium phosphate buffers were prepared in ddH$_2$O.

2.25 Spectroscopic characterization

Initial UV-visible spectroscopic analysis of freshly prepared and purified protein was carried out on a Cary UV-50 UV-Visible spectrophotometer (Varian, Crawley, UK) and was performed with enzyme suspended in Buffer A (Chapter 2.24). Spectra over a wavelength range of 250 – 800 nm were recorded for the oxidised proteins alone, as well as in the presence of the reductants sodium dithionite, NADH and NADPH to observe reduced forms of the enzymes studied. Spectral shifts due to the addition of the gaseous ligands carbon monoxide and nitric oxide were also recorded, and in the case of the binding of carbon monoxide the enzymes were firstly reduced with an excess of solid sodium dithionite. Typically, 5 – 6 bubbles of the gaseous compound nitric oxide were introduced gently to the cuvette containing the enzyme sample in order to produce the nitrosyl complex and so as to avoid sample acidification that would occur on excessive bubbling of this gas. Carbon monoxide was generally bubbled very slowly (to prevent protein agitation and foaming, and solution turbidity) for approximately one minute into solutions of reduced P450. NADH and NADPH were added from 20 mM stock solutions to typical final concentrations of 200 μM in order to determine, where appropriate, the presence of flavin (by reduction of this centre and perturbation of its UV-visible spectrum). In order to determine their spectral influences on coordinating heme iron, sodium cyanide and imidazole were added to P450 enzyme samples from stock solutions of 500 and 200 mM, respectively, in buffer A.

2.26 Hemochromagen assay

The determinations of the extinction coefficients of the cytochromes P450 studied in Chapters 3.6, 4.10, and 5.5 were carried out using the hemochromagen assay reported by Berry and Trumpower (187). An aliquot of enzyme was diluted to a final concentration of 2 – 4 μM in 50 mM Tris.HCl (pH 7.2). 500 μl of this protein solution was placed in a 1 cm pathlength quartz cuvette, to which was added 500 μl of a solution of 200 mM sodium hydroxide, 40 % pyridine (by volume), and 0.6 mM $K_3Fe(CN)_6$. Following thorough agitation of the cuvette contents, a UV/Visible absorption spectrum was recorded between 250 and 800 nm using a Cary UV-50 UV-Visible spectrophotometer (Varian). The sample was then reduced by the addition of 2 – 5 mg solid sodium dithionite, following which a second spectrum was recorded. A second addition of sodium dithionite and re-recording of the UV/Visible spectrum was

subsequently performed in order to confirm complete sample reduction (i.e. lack of further spectral change). A difference spectrum was generated by subtracting the oxidised spectrum from the reduced spectrum, and from this spectrum the difference between absorbance at 557 and 540 nm was calculated. Subsequently, using an extinction coefficient ($\Delta \varepsilon_{r-o\ 557-540}$) of 22.1 mM^{-1} cm^{-1} and the Beer-Lambert Law (Equation 1) the concentration of the heme pyridine adduct was calculated. As the adduct concentration relates directly to the amount of heme in the sample, this concentration and the absorbance of the oxidised sample at 419 nm were subsequently employed to calculate the ε_{419} for the studied P450, again using the Beer-Lambert Law.

$$A = \varepsilon \times c \times l$$

Equation 1 The Beer-Lambert Law that describes the relationship between the absorbance and concentration of an absorbing species. In this equation "A" is the absorbance of the sample (no units), "ε" is the extinction coefficient (M^{-1} cm^{-1}), "c" is the concentration of the sample (M), and "l" is the pathlength of the cuvette containing the sample (cm). This equation was employed in order to calculate the concentrations of Mtb CYP51 and *R. metallidurans* CYP116B1 following the formation of their pyridine adducts, as described above.

2.27 Binding titrations

Titrations of various compounds (substrates and ligands) against the studied enzymes were performed, and data collected using a Cary UV-50 UV-visible spectrophotometer (Varian) to determine the extent of binding of the compound to the enzyme and in attempts to define dissociation constants (K_d values) for the interactions. Small volumes, typically 0.2 – 2.0 µl, of a solution of known concentration of compound (typically 0.5 – 2.0 mg/ml) were added to the enzyme and following each addition an absorbance spectrum was recorded. Additions were made until no further spectral change was observed. Data analysis was performed by firstly generating difference spectra from the recorded UV-Visible data. This involved the subtraction of the starting (substrate/ligand-free) spectrum from those recorded following each successive ligand addition. Subsequently, the dissociation constant for the compound was calculated by plotting the difference between peak and trough of the difference spectra (at wavelengths reflecting the maximal overall absorbance change and using the same wavelength pair for the difference spectrum for each titration point) and fitting the

resultant data with an appropriate binding equation (typically a rectangular hyperbola, Equation 2, Chapter 3.7) using Origin software (Microcal). Compounds used in these studies included the azoles clotrimazole, fluconazole, miconazole, ketoconazole, econazole, and voriconazole (all 0.5 - 1 mg/ml stocks in DMSO), as well as sodium cyanide (500 mM in ddH$_2$O) and imidazole (500 and 200 mM stocks in ddH$_2$O). The same protein preparations were used for each series of titrations in order to maintain consistency of results.

2.28 Guanidinium chloride protein denaturation

Denaturation of CYP51 by the chaotrope guanidinium chloride (GdmCl) was studied by observing the absorbance spectra of CYP51 (diluted in buffer A at various GdmCl concentrations) using a Cary UV-50 UV-visible spectrophotometer scanning between 250 and 800 nm. Aliquots of enzyme at a final concentration of 3.7 μM were incubated at room temperature in solutions of GdmCl ranging in concentration from 0.1 to 8 M for 10 minutes, before an absorbance spectrum was recorded for the sample. The experiment was repeated across the same range of GdmCl concentrations on a Cary Eclipse fluorescence spectrophotometer using the same enzyme preparation (3.7 μM final concentration) and GdmCl stock solution. Aromatic amino acid residue fluorescence was recorded by excitation of the pre-incubated sample at 290 nm, with the subsequent emission spectra collected between 300 – 500 nm with slit widths for both emission and excitation set at 5 nm on the Cary instrument. All data were recorded at 30 °C to ensure consistency between samples and the two different experiments. Data were collected and analysed to determine the effects of increasing guanidine concentrations upon the stability of the heme cofactor and the tertiary structure of the protein. UV-visible and fluorescence spectral changes at wavelengths of major signal change were plotted *versus* [GdmCl] and data fitted (where appropriate) to a sigmoidal function (see Chapter 3.15) to estimate the midpoint value of chaotrope required to effect heme dissociation or loss of protein tertiary structure

2.29 Flavin determination assays

Flavin determination was carried out using a Cary Eclipse fluorescence spectrometer using a 2 ml fluorescence cuvette. FAD and FMN (10 μM stocks) were dissolved in 100 mM KPi pH 7.7, as was 3 μM CYP116B1. A fluorescence spectrum of a 2 ml

sample of co-factor was measured by excitation of the sample at 450 nm, whilst emission data were collected between 500 and 600 nm. An aliquot (20 µl) of concentrated perchloric acid was then added to the sample and the spectrum re-recorded. The change in fluorescence at 530 nm was calculated from the two spectra and the assay repeated at various FAD and FMN concentrations from 10 nM to 10 µM. From these data, plots of FAD and FMN concentrations versus acid-induced change in fluorescence were created, giving standard curves for the effects of concentrated perchloric acid (i.e. pH decrease) on the flavins FAD and FMN. Aliquots (2.5 ml) of CYP116B1 at a number of concentrations (3 µM to 150 nM) were heated to 95 °C for three minutes to denature the protein and release the flavin. The aliquots were then centrifuged at 14000 g for 10 minutes at 4 °C and the supernatant recovered. Using the same technique as with the free flavins, fluorescence spectra pre- and post-acid addition were recorded and the difference plotted against initial protein concentrations of the samples. Thus the results for the fluorescence changes of flavin released from CYP116B1 could be contrasted with those of FMN and FAD to determine which of the two flavins was present in CYP116B1. The basis of the assay is that free FMN is substantially more fluorescent than is FAD, but that acidification (to ~pH 2) leads to hydrolysis of FAD to FMN and an increase in its fluorescence (188-191). Comparison of the behaviour of the CYP116B1 flavin with those of free FAD and FMN should enable its assignment as one or other of these flavins.

2.30 Circular dichroism

Far-UV, near-UV and visible CD spectra of CYP51 and CYP116B1 were recorded on a JASCO J715 spectropolarimeter baselined with 50 mM KPi pH 7.4. Far-UV spectra were measured between 190 – 260nm using protein diluted to 2 µM in a cell of pathlength 0.2 cm and with a scan rate of 10 nm/minute. Near-UV and visible spectra were recorded between 260 – 600 nm using protein diluted to 10 µM in a cell of pathlength 0.5 cm and at a scan rate of 20 nm/minute. For both wavelength ranges, 5 accumulations of CYP51 and CYP116B1 data were made and averaged to generate the final baseline-corrected spectra. All data were recorded at 25 °C in order to maintain data consistency.

Circular dichroism was also utilised to investigate the interactions of Mtb CYP51 and a ferredoxin protein from the same organism. The Near-UV/Visible CD spectrum

of a protein sample containing 20 μM Mtb CYP51 and 285 μM Mtb ferredoxin (donated by Dr. K.J. McLean, University of Manchester) was recorded under the same conditions as described above. Additional spectra of the individual proteins at the aforementioned concentrations were also recorded in order to comprehensively compare their secondary structures to those of the protein complex and to discern any CD spectral perturbations induced by complexation.

2.31 Electron Paramagnetic Resonance

The EPR spectra of CYP51 were collected at the University of East Anglia by Dr. M. Cheesman and Dr. H. Seward. The EPR was performed using a Bruker ER-300D series electromagnet and microwave source interfaced to a Bruker EMX control unit (Bruker, Coventry, UK) and fitted with an ESR-9 liquid Helium flow cryostat (Oxford Instruments, Oxford, UK), and using a dual mode microwave cavity from Bruker (ER-4116DM). Spectra were recorded at 10 K with 2 mW microwave power and modulation amplitude of 10 G. Typically, spectra were recorded using protein diluted to 200 μM in 50 mM KPi pH 7.4.

2.32 Resonance Raman spectroscopy

The resonance Raman spectra of *M. tuberculosis* CYP51 was obtained by excitation of an enzyme sample at 406.7 nm using a 15 mW Coherent Innova 300 krypton ion laser at a scan rate of 12 x 15 s. Data acquisition between 250 and 2000 cm^{-1} was performed using a Renishaw micro-Raman system 1000 spectrometer (Renishaw, New Mills, UK). Protein samples were diluted to 50 μM in 50 mM Tris.HCl, 1 mM EDTA pH 7.2. Peaks of interest with respect to the oxidation state, spin state, and symmetry of the heme are identified by their v numbers, and the significance of data collected are described in Chapters 3.11 and 4.16. Spectroscopy was performed by Dr. J. Clarkson and Dr. R. Littleford, Department of Chemistry, University of Strathclyde.

2.33 Magnetic circular dichroism

Magnetic circular dichroism studies of ligand-free and fluconazole-bound Mtb CYP51 were performed at the University of East Anglia by Dr. H. Seward using a Jasco J-500D to collect UV-Visible data between 280 – 1000 nm, and a Jasco J-730 for

obtaining near-infrared data between 800 and 2000 nm. Samples of protein were diluted to a final concentration of 150 – 200 μM in deuterated 50 mM HEPES (adjusted to pH 7.5 with concentrated potassium hydroxide), and were subsequently mounted on a SM-1, 6 Tesla superconducting solenoid (Oxford Instruments) with an ambient-temperature bore for measurements at room temperature. A ligand-bound sample of CYP51 was prepared by the addition of solid fluconazole until no further UV-visible absorption spectral changes were observed, thus indicating saturation of the protein sample.

2.34 Steady-state kinetic assays

Studies of the steady-state kinetics of the CYP116B1 enzyme in the presence of potassium ferricyanide (10 mM stock solution in assay buffer (50 mM Tris.HCl, 1 mM EDTA pH 7.2)) and cytochrome c (2 mM stock solution in assay buffer) were performed on a Cary UV-50 UV-visible spectrophotometer. Reduction of the artificial electron acceptors were measured over the time course of 1 minute at 420 nm for potassium ferricyanide ($\Delta\varepsilon_{420}$ = 1.02 mM^{-1} cm^{-1}) and 550 nm for cytochrome c ($\Delta\varepsilon_{550}$ = 22.64 mM^{-1} cm^{-1}) using NADH and NADPH (both 20 mM stocks in assay buffer) as the reducing agents for the enzyme. Concentrations of ferricyanide or cytochrome c were firstly varied with NAD(P)H concentrations remaining constant (400 μM) in order to determine saturating levels of the electron acceptors and to define the k_{cat} and K_m parameters from plots of the observed reduction rate *versus* substrate concentration. The concentrations of the electron acceptors were then kept constant at saturating levels (typically 1 mM) whilst the reductant concentration was varied in order to determine apparent K_m values for the reductants. Throughout the kinetic study the same enzyme preparation was used to avoid the possibility of differences in protein behaviour between batches.

All the assays were performed using a dual-beam spectrophotometer (Jasco V550 UV/Visible spectrophotometer) in order to compensate for the non-specific reduction of the artificial electron acceptors by NAD(P)H, that can make K_m and k_{cat} values difficult to determine accurately. The dual-beam arrangement utilises a reference cuvette and a reaction cuvette in which reactions are started at the same time by the addition of NAD(P)H. Reaction components are added to both cuvettes to give the same final concentrations but enzyme is not added to the reference cuvette. The spectrophotometer

automatically subtracts the absorbance recorded in the reference cuvette from the reaction cuvette to give corrected absorbance changes over the time course studied, and thus negates the non-specific reduction of the artificial electron acceptors.

Steady-state kinetic studies of the activity of CYP116B1 in the presence of the herbicides vernolate and EPTC were performed using a Cary UV-50 UV-visible spectrophotometer, as non-specific reduction of these compounds by NAD(P)H was not observed in these assays. The assays were performed similarly to those reported by Ost *et al.* (192), and monitored the oxidation of NADH and NADPH at 340 nm. Each reaction contained 75 – 100 nM enzyme diluted in 50 mM Tris.HCl, 1 mM EDTA pH 7.2 and 200 µM NAD(P)H, and these mixtures were incubated at 30 °C using a Peltier system to maintain temperature in the cuvette. The reactions were started by the addition of aliquots of EPTC or vernolate (diluted in ethanol) at final concentrations ranging between 0 and 2 mM, and were monitored for 1 minute. The rates of coenzyme oxidation over this minute were calculated from the resultant absorption changes using an extinction coefficient of $\Delta\varepsilon_{340} = 6.21$ mM^{-1} cm^{-1} for NADH and NADPH (27,193). All data points were duplicated or triplicated and the same enzyme preparation was used throughout in order to ensure data consistency and to avoid batch to batch activity variations and anomalous data points. The resultant rate data were plotted against the concentrations of vernolate and EPTC, and were subsequently fitted with a hyperbolic function (Equation 8, Chapter 4.19) in order to determine maximal reaction rates (k_{cat}) and K_m values.

2.35 Stopped-flow kinetic assays

Stopped-flow kinetic analysis of the interaction between CYP51 and Mtb ferredoxin was done under anaerobic conditions in a Belle Technology glove-box. Absorbance spectral data were collected across a range of wavelengths from 250 to 800 nm using a photodiode array attachment and were analysed using the Applied Photophysics ProKin software. The ferredoxin (~20 µM) was pre-reduced with excess sodium dithionite and both the ferredoxin and CYP51 were passed through a BioRad Econo-Pac 10DG desalting column to remove salts and excess dithionite. CYP51 was diluted to 5 µM in 10 mM KPi pH 7.4 (degassed by bubbling with argon) and then bubbled with carbon monoxide for 10 minutes to saturate the solution. The CO-saturated CYP51 was firstly mixed with 10 mM KPi in the stopped-flow to obtain an absorption spectrum in the

absence of ferredoxin. The CO-saturated CYP51 was then mixed with various concentrations of pre-reduced ferredoxin (between 250 µM and 12.5 µM) using the stopped-flow apparatus, with the subsequent CO complex formation and collapse being recorded until the spectrum resembled that of the starting material. From the data obtained, rates for the formation and collapse of the CO complex in the presence of the ferredoxin were calculated. The experiment was repeated in the presence of sodium dithionite (absence of ferredoxin) and in the presence of lanosterol and cholesterol solutions, with data being collected and analysed in the same manner. In this way, the influence of the nature of the reductant and the presence of putative substrates on the rate of formation and decay of the Fe^{2+}-CO complex could be determined.

Stopped-flow studies of coenzyme preference of CYP116B1 were performed using the aforementioned stopped-flow apparatus. Studies were performed at a single wavelength (465 nm) using 6.6 µM CYP116B1 in KPi buffer (50 mM, pH 7.4). Changes in absorbance following rapid mixing with NAD(P)H were recorded over 0.5 s, at 25 °C. Data points were the mean of at least three transients fitted to a single exponential decay curve. Data sets were recorded using coenzyme concentrations that varied from stoichiometric levels to several-fold excess over enzyme (400 – 500 µM) with the results plotted as observed reduction rate *versus* co-enzyme concentration, and fitted as appropriate (either a linear or hyperbolic dependence, see Chapter 4.18) to determine limiting enzyme reduction rates (k_{red}) and co-enzyme preference/affinity (K_d). In these assays all protein and co-enzyme solutions were prepared under anaerobic conditions in argon-degassed buffers to eliminate the influences of oxygen.

2.36 Redox potentiometry

The redox potential of CYP51 was determined in the anaerobic conditions of a Belle Technology glove-box, where virtually all oxygen had been displaced by oxygen-free nitrogen (oxygen maintained at < 2 ppm). Enzyme was diluted in 100 mM KPi pH 7.0 with the addition of 5 µM hydroxynaphthoquinone, 2 µM phenazine methosulphate, 0.5 µM methyl viologen, and 1 µM benzyl viologen to act as mediators. The enzyme was titrated at 25 °C with small volumes (typically 0.5 – 1.0 µl) of a sodium dithionite solution (typically 10 mM) in order to progressively reduce the enzyme to completion, followed by a reverse titration with potassium ferricyanide (also 10 mM) to return it to the oxidised form. Between each addition of reductant/oxidant, absorbance spectra

were recorded using a Cary UV-50 UV-visible spectrophotometer, and the potential of the solution recorded from a calibrated Pt/Calomel electrode (Thermo Russell Ltd.) linked to a pH meter set to read in mV. Data were analysed and corrected by +244 mV to give results relative to a standard hydrogen electrode. Plots of data at wavelengths reflecting best the change between oxidised and reduced forms of the enzyme versus the applied potential were created. The data were fitted to a single electron Nernst function (Equation 6, Chapter 3.17) using Origin software to define the midpoint reduction potential for the Fe^{3+}/Fe^{2+} transition of the CYP51 heme iron.

Redox potential determinations were also performed for CYP51 in the presence of estriol and 2-phenylimidazole. Both compounds were added at near-saturating concentrations from stock solutions prepared anaerobically in DMSO and 1:1 (v/v) H_2O:ethanol, respectively, to avoid the introduction of oxygen. Estriol was added to a final concentration of 90 μM, whilst 2-phenylimidazole was added to a final concentration of 7.5 mM. The titrations were otherwise performed and analysed as reported above.

2.37 Product analysis

In order to identify the products of vernolate and EPTC metabolism by *R. metallidurans* CYP116B1, a series of reactions were performed based on the methods reported by Lawson *et al.* (194) for the study of P450 BioI from *B. subtilis*. The 10 ml reactions contained CYP116B1 at a final concentration of 6 μM, 1 mM NADPH, 20 mM glucose, 8.25 units of glucose dehydrogenase, and 0.33 mM of either vernolate or EPTC. The reaction constituents were all solubilised in assay buffer (50 mM Tris.HCl, 1 mM EDTA pH 7.2), with the exception of vernolate and EPTC, which were solubilised in ethanol. 30 ml glass vials that had been wrapped in foil to exclude light and washed with methanol, dichloromethane and ddH$_2$O to remove potential contaminants, were used to contain the reactions. Control reactions lacking either enzyme or substrate were also performed to ensure observed results derived solely from CYP116B1-mediated activity, with shortfalls in volume compensated for by additions of assay buffer. The glucose dehydrogenase, and its substrate glucose, were utilised in order to regenerate NADPH during the course of the reaction. The reaction mixtures were incubated at room temperature and stirred continuously for 16 hours before they were terminated by the addition of 0.5 ml of 1.0 M HCl. Subsequently, solvent

extraction of the reaction products was performed by adding 3 ml of HPLC grade dichloromethane to each reaction. The resultant organic phases were retained whilst the aqueous phases were subjected to a second treatment with dichloromethane in order to maximise product extraction from the samples. The two organic phases from each reaction were recombined and any residual aqueous phase removed by the addition of anhydrous magnesium sulphate. The samples were then filtered to remove any particulates arising from the drying process, before being evaporated to dryness under vacuum. The resultant pellets were resuspended in a minimal volume of HPLC grade methanol (typically 50 µl) and maintained at 2 – 6 °C until LCMS could be performed.

The LCMS analysis of the CYP116B1 reactions was carried out by Andrew Lawrence at Queen Mary, University of London using an Agilent 1100 series HPLC-MSD (Agilent Technologies, Waldbronn, Germany). The material extracted from the reaction mixtures was resolved using a Vydac C_8 column (21 x 150 mm) run at a flow rate of 1 ml min^{-1} and maintained at 30 °C. Following sample loading, an isocratic gradient of the mobile phase, which was composed of 66 % solvent A (100 % HPLC grade acetonitrile) and 34 % solvent B (0.2 % acetic acid in ddH$_2$O), was run for 28 minutes. Subsequently the concentration of solvent B was raised to 100 % and the column run for an additional 32 minutes. Detection of the presence of reaction products from the column-resolved samples was performed using the ion trap mass spectrometer in the positive electrospray mode, with resultant m/z ratio peaks being assigned to molecules corresponding to plausible CYP116B1-mediated metabolites of EPTC and vernolate.

Chapter 3

Characterization of CYP51; a 14α-sterol demethylase

from *Mycobacterium tuberculosis*

3.1 General information

This chapter presents the results obtained from the characterization of *M. tuberculosis* 14α-sterol demethylase (CYP51). The purpose of this study was to serve as a thorough characterization of an enzyme that is widely thought of as one of the ancestral cytochromes P450 (24,195), and also to provide a benchmark with which other P450s studied in this thesis can be contrasted and compared.

As previously mentioned in Chapter 1.9, 20 cytochromes P450s were identified contained within the genome of *Mycobacterium tuberculosis* H37Rv strain by Cole and co-workers (151,156). Of the 20 putative P450s, one gene, *Rv0764c*, was identified as a putative 14α-sterol demethylase and was shown to encode a protein with the properties of a cytochrome P450 (196). Following that work, a number of studies have been done to identify the gene product as a 14α-sterol demethylase with many similarities to CYP51s from other organisms (19,126,165,197,198). Other studies (51,169) have identified unique properties of Mtb CYP51 such as its ability to demethylate the sterol obtusifoliol, which is not present in *M. tuberculosis*, as well as its unusually large access channel to the active site. There are now at least four high-resolution crystal structures of Mtb CYP51 encompassing inhibitor-bound, substrate-free, and mutant forms of CYP51 (35,51). This characterization of the Mtb enzyme expands on the current catalytic and spectroscopic data gathered for CYP51, and enhances our general understanding of both one of the most ancient of P450s and cytochromes P450.

3.2 The genomics of *Mycobacterium tuberculosis* CYP51

The *Mycobacterium tuberculosis* genome encodes approximately 4000 genes contained within 4,411,529 base pairs (151,156). The *Rv0764c* gene, which encodes CYP51, is found between 856682 and 858037 base pairs in a region of the genome where a number of other redox active enzymes are also encoded. These include another cytochrome P450 (CYP123) as well as an oxidoreductase (*Rv0765c*), two alcohol dehydrogenases (*aldA* and *aldB*), and a ferredoxin (*Rv0763c*) which lies adjacent to CYP51 (Figure 15). This ferredoxin (and the oxidoreductase) is postulated to be a redox partner of CYP51 and this is another aspect explored in this chapter.
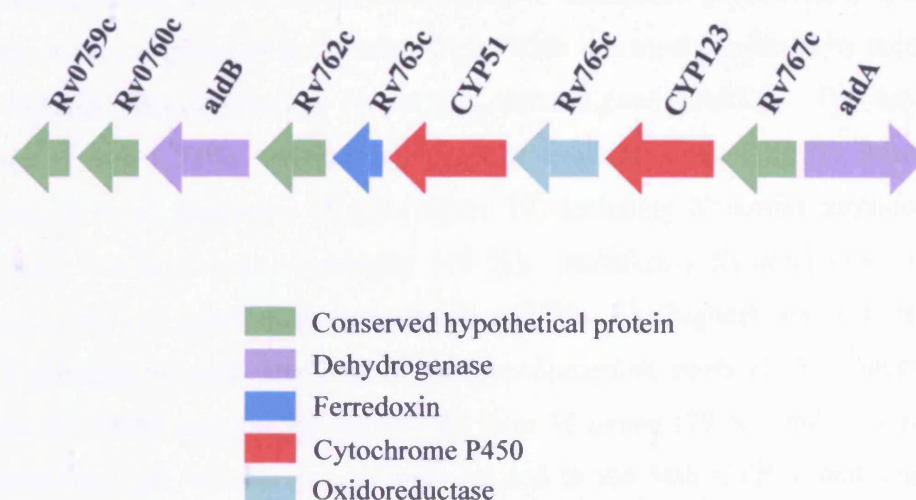
Figure 15 The position of the CYP51 gene (*Rv0764c*) in the context of the *M. tuberculosis* genome (www.genolist.pasteur.fr/TubercuList). This cytochrome P450-encoding gene is found adjacent to genes encoding an oxidoreductase and a ferredoxin, both of which are postulated to be the redox partners of CYP51.

The *Rv0764c* gene is 1356 base pairs in length and encodes a protein of 451 amino acids that has been (perhaps arbitrarily) classified as being involved in intermediary metabolism (151). The utilisation of a bioinformatic program (Protparam, www.expasy.org) predicts a molecular weight of the encoded protein as 50.877 kDa, with a pI of 5.54. The amino acid sequence contains four cysteine residues, three of which have been shown to be important in structural integrity (173). Further bioinformatics tools (ScanProsite, www.expasy.org) identify the sequence as possessing a motif that is common to all cytochromes P450 (see Figure 16). The motif identified for Mtb CYP51 is FGAGRHRCVG and contains the fourth cysteine (Cys 394) that is known to ligate to the iron at the centre of the heme (173).

[FW]-[SGNH]-X-[GD]-X-[RHPT]-X-C-[LIVMFAP]-[GAD]

Figure 16 The motif utilised by the ScanProsite (www.expasy.org) program that identifies the CYP51 protein as possessing residues pertaining to the heme-binding site typical of cytochromes P450. Residues at each position can be selected from any of those identified within the square brackets. Residue X can be any amino acid residue, whilst the cysteine is obligatory for heme ligation.

As well as being able to identify the *Rv0764c* translation product as a cytochrome P450, the amino acid sequence reveals which P450s it is most similar to by using amino acid similarity (Blast) searches (www.ncbi.nhm.nih.gov/BLAST/). The amino acid sequence of Mtb CYP51 has varying levels of similarity with CYP51s from various organisms from all kingdoms of life (Figure 17) including *Nocardia farcinica* (77 % homology), *Methylococcus capsulatus* (49 %), *Arabidopsis thaliana* (38 %), *Homo sapiens* (33 %), and *Saccharomyces cerevisiae* (28%). The highest similarity is with the CYP51 encoded by gene *Mb0787c* from *Mycobacterium bovis* (100 % identity). In addition, the P450s encoded by *MAP0598c* from *M. avium* (79 %), and by a gene from *M. vanbaalenii* (80 %) are also strongly related to the Mtb CYP51 and suggests an ancestry of CYP51 amongst mycobacterial species.

```
Myctb    DFVPARYEQPRQED---------------LLNRWTWIPFGAGRHRCVGAAFAIMQIKAIFSVLLREY    415
Mycbo    DFVPARYEQPRQED---------------LLNRWTWIPFGAGRHRCVGAAFAIMQIKAIFSVLLREY    415
Mycav    AFKPDRYNKPEQAD---------------IVNRWTWIPFGAGRHRCVGAAFAQMQIKAIFSVLLREY    416
Mycvn    DFDPDRYEKPRQED---------------LINRWTWIPFGAGKHRCVGAAFAQMQIKAIFSVLLREY    415
Nocfa    TFDPGRYIDPNQED---------------LVNRWTWIPFGAGRHRCVGAAFALMQLKAIFSILLRDW    415
Metca    LFDPDRYT-PERAE---------------DKDLYGWQAFGGG-HKCSGNAFAMFQIKAIVCVLLRNY    414
Arath    TYDPERFSPGREEDK-------------AAGAFSYIAFGGGRHGCLGEPFAYLQIKAIWSHLLRNF    453
Strpu    EFNPDRFLDESKSN---------------SEKFSYVPFGAGRHRCIGENFAYVQIKTIWSVMLRIF    461
Human    DFNPDRYLQDNPAS---------------GEKFAYVPFGAGRHRCIGENFAYVQIKTIWSTMLRLY    470
Yeast    QFNIHRWNKDSASSYSVGEEVDYGFGAISKGVSSPYLPFGGGRHRCIGEHFAYCQLGVLMSIFIRTL    491
         :    *:        .                :  .**.* * *    **   *:  .:  . ::*
```

Figure 17 Multiple amino acid alignment of CYP51 sequences from various organisms. The region shown is taken from full-length sequence alignments and shows the stretch containing the heme-binding motif. The motif is highlighted in blue whilst the conserved cysteine residue is shown in red. The organisms included in the alignment are *M. tuberculosis* (Myctb), *M. bovis* (Mycbo), *M. avium* (Mycav), *M. vanbaalenii* (Mycvn), *N. farcinica* (Nocfa), *Methylococcus capsulatus* (Metca), *A. thaliana* (Arath), *Strongylocentrotus purpuratus* (Strpu), *H. sapiens* (Human), and *S. cerevisiae* (Yeast). The alignment was carried out using ClustalW software (www.ebi.ac.uk/clustalw)

3.3 Molecular biology, expression, and purification of Mtb CYP51

The gene encoding *Mycobacterium tuberculosis* cytochrome P450 CYP51 was previously cloned into the expression vector pET20b by Dr. K. McLean, following PCR amplification from cosmid DNA donated by Professor S. Cole at the Institut Pasteur. Further information about oligonucleotide primers, amplification conditions, and sub-cloning steps are found our 2006 publication on the CYP51 enzyme (159).

The optimised growth conditions had been previously determined and were used to overexpress the encoded protein from the plasmid, which was transformed into HMS174 (DE3) *E. coli* cells (159). These cells were made competent using the calcium

chloride technique as described in Sambrook *et al.* (186). A flask containing 30 ml of sterile, antibiotic-enriched LB media was inoculated with a 300 μl aliquot of an overnight culture of *E. coli* cells (e.g. HMS174 (DE3)). The cells were incubated at 37 °C until the culture reached an $O.D._{600}$ of 0.4 – 0.6, at which point the culture was centrifuged at 6000 rpm for 10 minutes at 4 °C. The resultant cell pellet was resuspended in 7.5 ml ice-cold 50 mM calcium chloride and maintained on ice for 15 minutes. Subsequently, the cell solution was centrifuged as previously described and resuspended in 3 ml of ice-cold calcium chloride containing 10 % glycerol. The cells were then aliquoted (300 μl) into cold, sterile Eppendorf tubes and stored at −80 °C until required. Transformation of the CYP51 pET-20b construct was performed using the technique of Sambrook *et al.* in which 300 μl of competent cells and 1 – 10 ng plasmid DNA are co-incubated on ice for 30 minutes. The solution is then heat shocked for 2 minutes at 42 °C before being returned to ice for 30 minutes. Following the addition of 500 μl of LB media and incubation at 37 °C in a shaking incubator at 220 rpm for one hour, 100 – 200 μl aliquots of the cells are plated on antibiotic-enriched agar plates and grown overnight at 37 °C. Resultant colonies are then replated and subsequently utilised as inoculants for bacterial cultures.

Large-scale cultures (typically 6 litres) were grown initially at 37 °C in a shaking incubator (220 rpm) until a spectrophotometrically determined optical density at 600 nm $(O.D._{600})$ of 0.6 was reached, at which point the incubation temperature was reduced to 26 °C. As the gene expression was under the control of a T7 RNA polymerase promoter, induction with 100 μM IPTG was performed when the $O.D._{600} = 0.8$ and cells were then incubated for a further 14-16 hours. Cells were harvested by centrifugation at 5000 g for 20 minutes at 4 °C and then resuspended in buffer A (50 mM Tris.HCl, 1 mM EDTA, pH 7.2), pooled and re-centrifuged using the same conditions as previously. The pellet was resuspended in a minimal volume of ice-cold buffer A and, to avoid protein degradation, the protease inhibitors benzamidine hydrochloride and phenylmethylsulfonyl fluoride (PMSF) were added to final concentrations of 1 mM. Cells were broken by sonication using a Bandelin Sonopuls instrument (6 x 20 second bursts at 45 % full power with 5 minutes cooling time between pulses) followed by two passes through a French press at 950 lb/in^2. Before beginning column chromatography, the broken cells were then centrifuged for 40 minutes at 18000 g, 4 °C, to remove cellular debris. The resultant cell extract was loaded onto a DEAE ion-exchange column pre-equilibrated in buffer A. The column was washed with 1 – 2 column

volumes buffer A to remove unbound extract before elution of protein using a linear gradient of buffer B (buffer A containing 500 mM KCl). Fractions were collected and the reddest of these were pooled and dialysed into buffer A to remove salt. The extract was loaded to a Q-Sepharose anion-exchange column (equilibrated in buffer A) and eluted as for DEAE. The reddest fractions were again pooled and dialysed, this time into buffer C (25 mM potassium phosphate (KPi), pH 6.5). The extract was then loaded to a hydroxyapatite column pre-equilibrated in buffer C, before elution with a linear gradient of 500 mM KPi pH 6.5 (buffer D). A summary of the efficiency and yields of the aforementioned purification steps is detailed in Table 7, indicating that approximately 28 mg of Mtb CYP51 was obtained per cell culture. Spectrophotometric analysis was used to confirm purity and this was achieved when the ratio of absorbance at 419 nm was greater than the absorbance peak at 280 nm relating to aromatic amino acid residues present in the sample, and specifically when an A_{419}/A_{280} ratio (or R_z value) of ~1.4 was obtained (Figure 18). Homogeneity was also confirmed by 10 % SDS-PAGE gel analysis (Figure 19). The purified protein was pooled, concentrated, dialysed into 10 mM Tris.HCl pH 7.5, and stored at –80 °C.

Purification step	Concentration (mg/ml)	Volume (ml)	Total protein (mg)	R_z value (419 nm/280 nm)	Yield (%)
Crude extract	5.1	60.0	306	0.04	100
DEAE	5.6	27.5	154.0	0.24	50.3
Hydroxyapatite	17.4	3.5	60.9	0.66	19.9
Q-Sepharose	43.3	0.65	28.1	1.39	9.2

Table 7 Table for the purification of *M. tuberculosis* CYP51 from *E. coli* cell strain HMS174 (DE3). As described in Chapter 3.3, following breaking of pelleted cells by French press and sonication Mtb CYP51 was purified using three successive column chromatography steps (DEAE-Sephacel, Hydroxyapatite, and Q-Sepharose). Typically, 6 L of cell culture yielded approximately 28 mg (~9 %) of cytochrome P450 with a relative purity (R_z value) of 1.39, indicating that the three-step purification process resulted in homogenous Mtb CYP51. Data were calculated from UV-Visible spectra recorded following each step of the purification process, as exemplified in Figure 18.
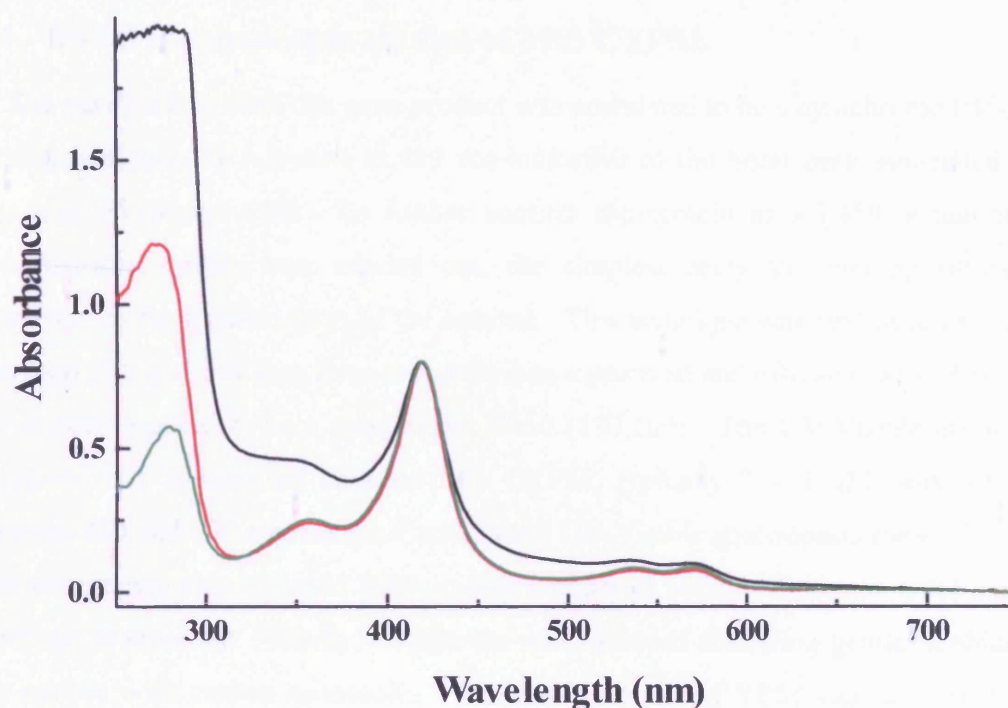
Figure 18 The absorbance spectra of CYP51 collected after each step of purification. The spectra show how the purity of the protein increases from the rather crude post-DEAE sample (black) with a very large feature at 280 nm, to the post-Q Sepharose sample (red) where the 280 nm band is only slightly greater than the Soret band, and finally to the post-Hydroxyapatite sample (green) where the Soret band predominates over the 280 nm band. For comparison, the intensity of the Soret band is equalised in all spectra.
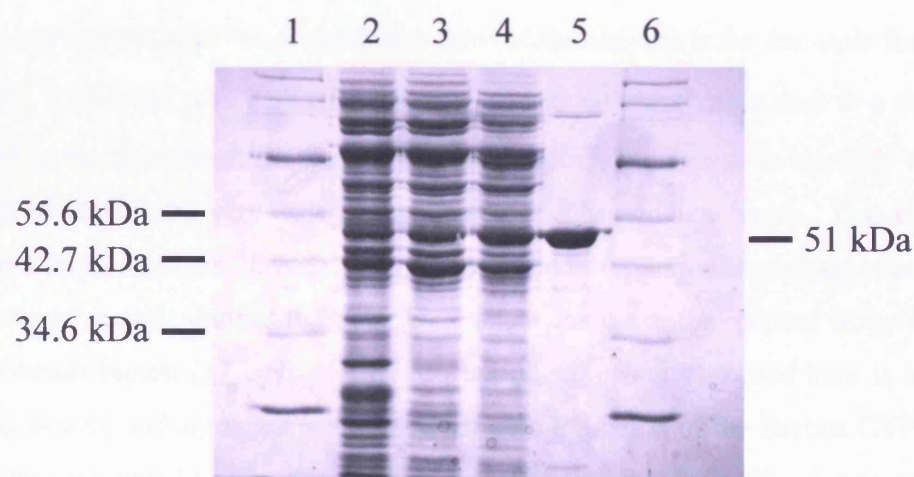

Figure 19 SDS-PAGE analysis of the purification of Mtb CYP51 showing the progress of the purification steps from crude cell extract to purified enzyme. Lane 1: Broad range protein marker (New England BioLabs), Lane 2: Pre-DEAE, Lane 3: Post-DEAE, Lane 4: Post-Q Sepharose, Lane 5: Post-Hydroxyapatite, Lane 6: Broad range protein Marker.

3.4 Initial spectroscopic studies of Mtb CYP51

The purified Mtb *Rv0764c* gene product was postulated to be a cytochrome P450 and indeed demonstrated a feature at 419 nm indicative of the Soret peak associated with this type of enzyme (50). To further confirm the protein as a P450, a number of spectroscopic studies were carried out, the simplest being the binding of carbon monoxide to the reduced form of the enzyme. This technique was first used by Omura and Sato (50) and has long been recognised as a practical and effective way of proving the enzyme studied to be a cytochrome P450 (130,169). The UV-Visible absorption spectrum of a solution of oxidised Mtb CYP51, typically 2 – 4 μM, was recorded between 250 and 800 nm using a Cary UV-50 UV-Visible spectrophotometer (Varian). The sample was then reduced with a small amount of sodium dithionite solid and the spectrum re-recorded. Finally, a spectrum was recorded following gentle bubbling of the sample with carbon monoxide. The result for Mtb CYP51 can be seen below (Figure 20) and shows that in the oxidised form the enzyme has a Soret band at 419 nm, and at longer wavelengths, alpha and beta (or Q) bands at 571 nm and 537 nm, all of which are typical of a cytochrome P450. For example, the Soret bands of P450 BM3 and P450cam are found at 419 nm and 418 nm respectively whilst the Q-bands are at 568 and 534 nm and 570 and 535 nm, respectively (37,199). There is no significant absorption feature at ~390 nm implying that there is minimal high-spin (S = $\frac{5}{2}$) ferric heme iron content and that the predominant form of the enzyme is the low-spin form (S = $\frac{1}{2}$) (69). Reduction with sodium dithionite induces no perceivable shift to a shorter wavelength in the Soret band (blue-shift) although there is a decrease in intensity of the Soret band. There is also very little alteration in the alpha and beta bands. This lack of change for a P450 might be considered unusual, as P450 reduction frequently results in a shift to shorter wavelengths at the Soret band and a change in the spectral shape in the visible (Q-band) region (37,199). However, the phenomenon observed here is by no means uncommon, and is related to the fact that auto-oxidation of the ferrous CYP51 is relatively fast compared to the rate of chemical reduction by dithionite. Upon carbon monoxide bubbling the Soret band is seen to shift from 419 to 448.5 nm and the visible bands fuse together to form a broad peak centred at 554 nm, thus identifying the displacement of a distally bound water molecule and the formation of the ferrous carbon-monoxy complex (37,199). This confirms that carbon monoxide has ligated to the iron at the centre of the heme and that the Mtb CYP51 is indeed a cytochrome P450.

Carbon monoxide binding "traps" the ferrous enzyme as a "dead-end" species, and pulls the equilibrium over almost completely to the ferrous form in the presence of dithionite. Further confirmation that CYP51 from Mtb is a P450 can be seen in later sections (Chapters 3.5, 3.11, 3.11, and 3.14). It should be noted that conversion from the reduced enzyme to the ferrous carbon-monoxy complex appears not to be complete, with a small amount (5 – 10 %) of non-complexed enzyme remaining at the end of the experiment. Over time the band at 448.5 nm collapses with a concomitant increase in absorption at 420 nm. This phenomenon is relatively rare, but is not unique to Mtb CYP51, and is subsequently investigated further in Chapters 3.18, 3.19, 3.20, and 3.21. The formation of the P420 form is typically considered to reflect inactivation of a P450 enzyme.
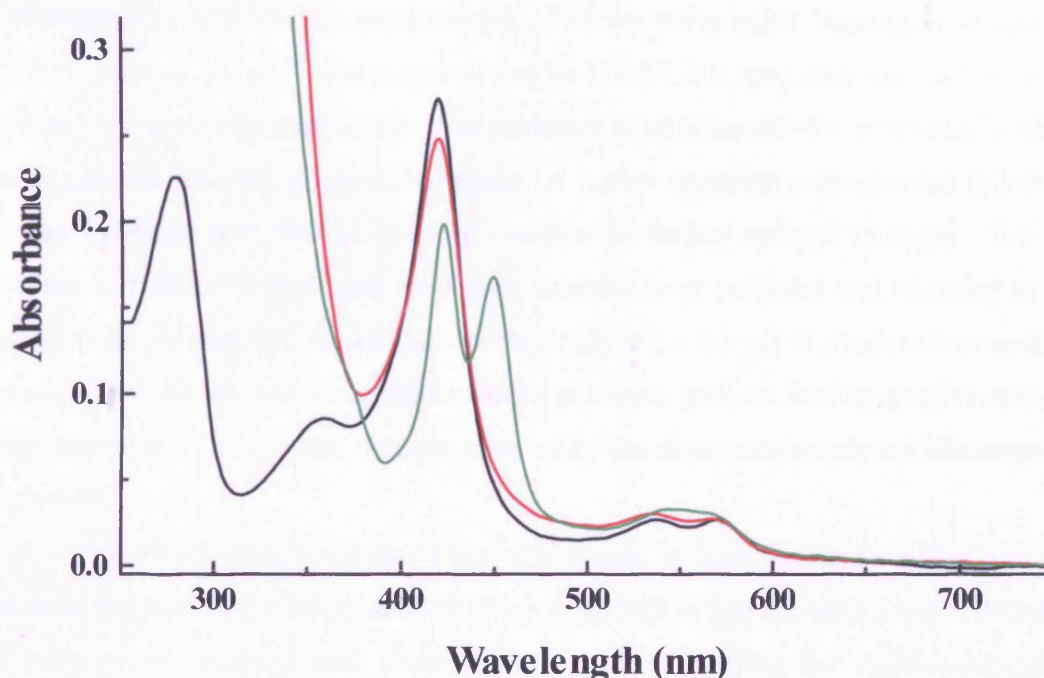

Figure 20 The oxidised (black), sodium dithionite-reduced (red), and ferrous carbon-monoxy complex (green) forms of Mtb CYP51. The oxidised form of the enzyme shows a Soret peak at 419 nm, as well as alpha and beta bands at 571 and 537 nm respectively, all of which are the typical spectral properties of a cytochrome P450. The dithionite-reduced form shows no obvious shift to shorter wavelengths in the Soret band region, as is seen with other P450s (e.g. BM3, P450cam (37,199)), although there is a slight decrease in intensity of the band. The ferrous carbon-monoxy complex shows the typical P450 feature at 448.5 nm, as well as a peak at 554 nm resulting from the apparent spectral "fusion" of the visible bands. A considerable amount of the P420 form of CYP51 (with spectral maximum at ~420 nm) is also present. Enzyme concentration is approximately 2.1 μM.

3.5 Further spectroscopic studies of Mtb CYP51

The formation of the ferrous carbon-monoxy complex is a robust and frequently used technique to establish a protein as a cytochrome P450. It is also common practice to bind other small molecules to the enzyme in order to attest that the enzyme possesses a heme molecule and as a simple comparison of the binding and spectral properties of the P450s (33,199). Typical molecules used in such analyses are nitric oxide, sodium cyanide, and imidazole, which all ligate to the heme iron either via a nitrogen atom or (in the case of cyanide) via carbon. As well as ligating to the heme, these molecules vary somewhat in size and chemical character and act as good reporters on the active site of the enzyme (33,199).

The binding of Mtb CYP51 to nitric oxide, sodium cyanide, and imidazole was investigated by UV-Visible spectroscopy. For the nitric oxide binding, a sample of CYP51 (approx. 1.5 μM) was prepared and its UV-Visible spectrum recorded between 250 and 800 nm. The sample was then subjected to addition of ~5 – 6 bubbles of nitric oxide gas and the spectrum recorded again. A further spectrum was recorded following further bubbling with NO in order to confirm no further spectral changes. For the binding of sodium cyanide and imidazole, samples were prepared and recorded as for the nitric oxide binding. Small aliquots (typically 0.2 – 0.5 μl) of imidazole or sodium cyanide were added from concentrated stock solutions until no further spectral changes were observed. The spectral changes induced by the three compounds are illustrated in Figure 21.

The UV-Visible data show that when nitric oxide is presented to the Mtb CYP51 it causes a red shift in the Soret band of 15 nm from 419 to 434 nm with a slight decrease in intensity of the band also observed. As well as shifting the visible absorption features from 571 to 573 nm, and from 537 nm to 542 nm, binding of nitric oxide also causes both bands to become more pronounced, especially the shorter wavelength band. Imidazole interacts with CYP51 causing the Soret band to decrease more significantly than is seen with NO. A shift to a longer wavelength (424 nm) is witnessed, as is a fusing of the Q bands. Sodium cyanide also binds to Mtb CYP51 and causes the 419 nm peak to shift to 435.5 nm. There is an even greater decrease in the intensity of the Soret peak and a more substantial fusing of the Q bands than seen with imidazole, resulting in a peak at 556 nm. These shifts are all typical of compounds that ligate in the distal position to the heme iron of cytochromes P450 and add further evidence that a

P450 (CYP51) is encoded by *Rv0764c* from the *M. tuberculosis* genome. Similar shifts are observed for P450 BM3 from *B. megaterium* and P450cam from *Ps. putida* (33,199), although the changes in intensity of the Soret are not always as pronounced. This may relate to the fact that the extinction coefficients of the Mtb CYP51 vary considerably according to the nature of the distal ligand, and that imidazole, cyanide and nitric oxide adducts have Soret coefficients substantially lower than those of the aqua-coordinated oxidised form.
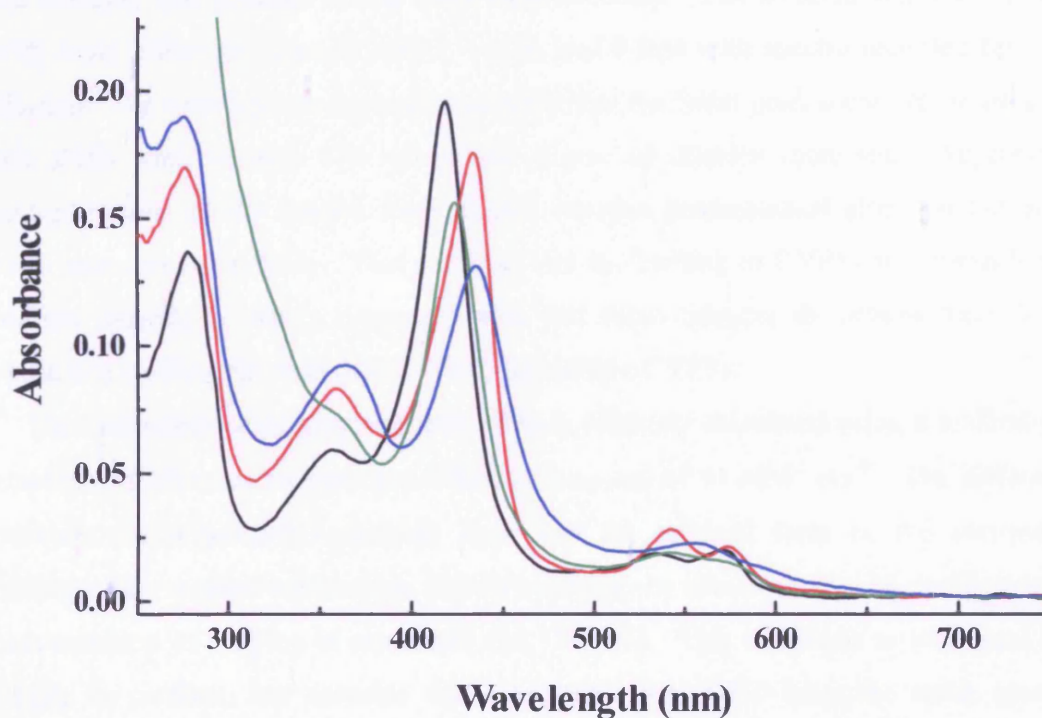

Figure 21 The absorption spectra of Mtb CYP51 bound to nitric oxide (red), imidazole (green), and sodium cyanide (blue). The oxidised spectrum of CYP51 (black) is shown for comparison. All samples were prepared at an enzyme concentration of 1.5 μM and ligands added until no further spectral changes were observed. All three compounds induced type II Soret band shifts to longer wavelength, indicating that the compounds are inhibitory in nature and push the heme iron further towards the low spin form. The Soret band is shifted from 419 nm (oxidised, ligand-free CYP51) to maxima at 434 nm (nitric oxide), 424 nm (imidazole), and 435.5 nm (sodium cyanide). In all cases, the intensity of the Soret band is decreased in the inhibitor-bound forms.

3.6 Hemochromagen assay of Mtb CYP51

The low intensities of the imidazole and sodium cyanide adducts were investigated to ensure that they were reversible and thus attributable to altered (lower) extinction coefficients for the adducted forms of CYP51 by comparison with the resting (aqua-coordinated) form. To confirm reversibility, samples were prepared using $2 - 4$ μM enzyme in assay buffer with the addition of either sodium cyanide or imidazole at their apparent K_d concentrations (Chapter 3.7). The UV-Visible spectrum was recorded and the intensity and position of the Soret band recorded. The solution was then diluted with assay buffer (no ligand) 2-fold, 4-fold, and 8-fold with spectra recorded for each dilution. For both ligands the results identify that the Soret peak increases in intensity and shifts back towards 419 nm as the degree of dilution increases. Appropriate multiplications of the spectra from diluted samples demonstrated also that the Soret band increases in intensity. This confirms that the binding of CYP51 to imidazole and sodium cyanide is freely reversible and that these adducts do indeed have lower extinction coefficients than the oxidised, ligand-free CYP51.

The concentration of a cytochrome P450 is routinely calculated using a method that employs a difference extinction coefficient $\Delta\varepsilon_{450-490}$ of 91 mM^{-1}.cm^{-1}. The difference between the reduced/CO-adducted form and the reduced form of the enzyme is calculated by spectral subtraction, and by applying the above-mentioned coefficient the concentration of enzyme is calculated (50,158,194). This technique is well used and simple to perform, but assumes that all cytochromes P450 have the same spectral properties and that all possess an extinction coefficient of 91 mM^{-1}.cm^{-1} for the wavelength couple stated, which may not be the case. Omura and Sato determined the aforementioned extinction coefficient ($\Delta\varepsilon_{450-490}$) for the cytochromes P450 based on the protoheme content of their P450 samples (itself determined by the application of a hemochromagen assay akin to that described herein). However, the assay was performed on semi-purified rabbit liver microsome extracts, likely containing a whole host of cytochrome P450 isoforms, and possibly other heme-containing proteins. Hence, the value of 91 mM^{-1}.cm^{-1} describes the aggregate $\Delta\varepsilon_{450-490}$ of a mixture of cytochromes P450 rather than a single isoform, and hence may not be applicable to highly purified individual P450s. Furthermore, it relies on complete formation of the ferrous-CO adduct if it is to be an accurate measurement of the enzyme concentration. In the case of Mtb CYP51, where the carbon monoxy-ferrous adduct is unstable and

there may be alterations in the nature of the proximal ligand (see Chapter 3.18), this technique is not useful. A technique that has been cited regularly for calculating heme concentration is the pyridine hemochromagen technique (187). The pyridine adduct of the heme is created by preparing a sample of enzyme (2 - 4 μM) and mixing this with a solution containing 200 mM NaOH, 40 % pyridine (by volume), and 0.6 mM $K_3Fe(CN)_6$. The oxidized UV-visible spectrum of Mtb CYP51 thus treated was recorded and the sample reduced with 2 - 5 mg solid sodium dithionite. These spectra were used to calculate the difference between the absorbance at 557 and 540 nm, having ensured that reduction was complete and that no further spectral changes occurred. The absorbance change was then utilized to calculate the extinction coefficient for CYP51 and resulted in a value of $\varepsilon_{419} = 134$ mM^{-1}.cm^{-1} for the oxidized species. The value is considerably larger than that reported by Omura and Sato for rat liver cytochrome P450 (91 mM^{-1}.cm^{-1}, (50)); a value which is used in the majority of cytochrome P450 studies (158,194). However, several replicates of the experiment gave identical results and thus this value was assigned as the extinction coefficient of Mtb CYP51. From this value the coefficients for the imidazole, sodium cyanide and nitric oxide adducts were calculated as $\varepsilon_{424} = 107$ mM^{-1}.cm^{-1}, $\varepsilon_{435.5} = 90$ mM^{-1}.cm^{-1}, and $\varepsilon_{434} = 120$ mM^{-1}.cm^{-1} respectively, thus providing quantitative data for the extinction coefficients of these adducts. The relatively high value obtained for the extinction coefficient of oxidised CYP51 using the hemochromagen method has actually been noted for other P450s including CYP176A (P450cin) from *Citrobacter braakii*, which has been shown to degrade cineole. This P450 has a coefficient (ε_{419}) of 150 mM^{-1}.cm^{-1} (200), suggesting that the standard value of 91 mM^{-1}.cm^{-1} is an outmoded value that may apply accurately to only a few P450s. Furthermore, it identifies the fact that variation in the properties of cytochromes P450 is greater than previously thought and that these differences will become more frequent as greater numbers of these enzymes are studied.

3.7 Determination of Mtb CYP51 ligand binding constants

Having established that the three compounds above (nitric oxide, cyanide and imidazole) bound to CYP51, the binding constants for sodium cyanide and imidazole were determined by performing binding titrations with these compounds. This allowed the first direct contrast with other cytochromes P450, although it was not readily

possible to determine a binding constant for nitric oxide using the same procedure, due to its gaseous nature (and due to rapid "scavenging" of any oxygen in the solution by NO to form nitrite). Binding titrations were performed as reported in McLean *et al.* (157). A solution of oxidised enzyme was prepared (typically 2 – 4 μM) and the UV-Visible spectrum recorded. Stock solutions of imidazole or sodium cyanide were prepared from solid compound dissolved in solvent (1 mM in water) and added in aliquots (0.2 – 1 μl). The UV-Visible spectrum was recorded following each subsequent addition of compound until no further optical changes were perceived. The absorbance spectra were baseline corrected and the initial spectrum subtracted from all subsequent spectra to produce difference spectra. The difference between the peak and trough of the spectra (at wavelengths reflecting the maximal overall absorbance change) were calculated and plotted *versus* concentration of imidazole or sodium cyanide. From the resultant curve, K_d values for each compound were calculated by fitting the curve with a rectangular hyperbola (Equation 2). All data fitting was performed using Origin software (Microcal).

$$A_{obs} = A_{max} \times S/(K_d + S)$$

Equation 2 Rectangular hyperbola function used for fitting plots of absorbance change *versus* concentration of bound compound in order to determine K_d values. A_{obs} is the observed absorbance change induced by addition of ligand at concentration S. A_{max} is the maximal absorbance change induced at ligand saturation, and K_d is the equilibrium binding constant for ligand binding to the P450.

The results of the binding titrations for imidazole are shown in Figure 22. The raw data (not shown) identifies that the Soret band shifts from 419 nm to longer wavelengths (approx. 424 nm), suggesting a type II binding mode that identifies imidazole as a typical P450 inhibitor (28,69). Sodium cyanide also binds to the P450 in an inhibitory manner and the Soret band exhibits a shift to longer wavelengths (434 nm). The binding constant (K_d) for imidazole was determined as 11.7 ± 0.9 mM, whilst the K_d for sodium cyanide was 18.8 ± 3.1 mM. These values show that both compounds bind weakly to CYP51 due to the polar nature of these compounds, and this is most evident when compared with e.g. the binding of hydrophobic compounds such as arachidonate and laurate to P450 BM3 from *B. megaterium* (K_d = 3.6 μM and 241 μM respectively) (192). Being small molecules, imidazole and sodium cyanide can readily diffuse into the active site of the CYP51, which has an unusually wide and open access

channel (51). However, the active site of cytochromes P450 are generally hydrophobic in nature (51) and do not promote tight binding of these relatively hydrophilic compounds, which also presumably have few direct stabilizing interactions with active site amino acids. This results in the weak binding constants observed for these compounds. Imidazole appears to bind slightly more tightly than sodium cyanide, which may relate to its slightly less polar nature as it possesses a hydrophobic azole ring structure. In the next sections (Chapter 3.8, 3.9, and 3.10), the binding of a range of molecules that are less polar and less hydrophilic than sodium cyanide and imidazole is investigated in order to probe the active site of Mtb CYP51 with a view to identifying potent inhibitors of this cytochrome P450, as well as potential substrate molecules.
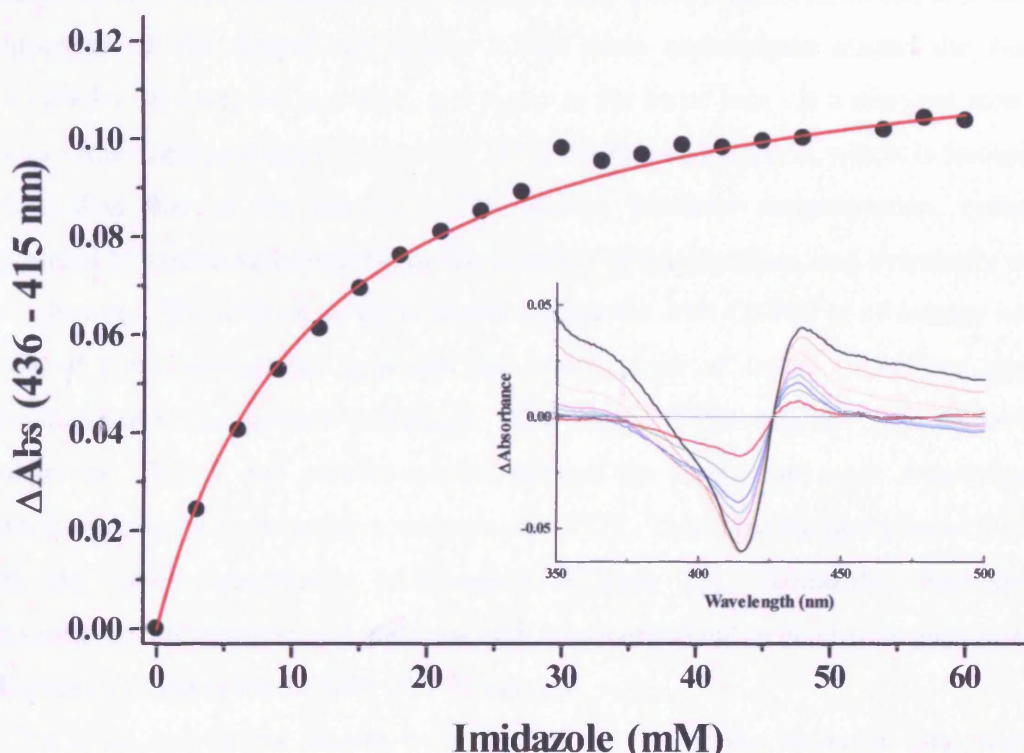

Figure 22 The binding titration curve for the interaction of imidazole with Mtb CYP51. The change in absorbance of the Soret band of CYP51 induced by imidazole was shown to be type II in nature and thus the compound was determined as an inhibitor of Mtb CYP51. The K_d for imidazole was calculated as 11.1 ± 0.9 mM. The difference spectra for the titration are shown inset and were created by subtracting the initial UV-Visible spectrum for ligand-free CYP51 from all subsequently recorded spectra in the presence of imidazole. The titration curve was produced by calculating the difference between the peak (436 nm) and the trough (415 nm) of the difference spectra and plotting these data against the concentration of imidazole at which each spectrum was recorded. The curve was then fitted with a rectangular hyperbola (Equation 2) to calculate the binding constant and associated error.

3.8 Mtb CYP51 azole binding studies

Having identified that Mtb CYP51 showed inhibitory (type II) shifts when presented with imidazole and sodium cyanide, further binding studies were carried out. Among the numerous compounds that inhibit cytochromes P450, the azole family of compounds are amongst the most potent (158,169). They are often referred to as the azole anti-fungals and are the most commonly used agent in the treatment of fungal and yeast infections (e.g. *Candida albicans*) due to their potency against, and reasonable specificity for, the infection-causing organisms (108). The metabolism of lanosterol, catalysed by cytochromes P450 (CYP51 isoforms), in fungi and yeast is essential to cell membrane integrity and to the organisms' survival within their hosts (108,201). The product of the CYP51 reaction is the demethylated sterol ergosterol, which is a crucial component of the fungal membrane. The azole anti-fungals mimic the bulky, hydrophobic structure of lanosterol and ligate to the heme iron via a nitrogen atom on one or more azole or triazole rings (51). This binding of the azole, which is frequently tighter than that of the substrate (28), inhibits substrate demethylation, reducing ergosterol formation and diminishing the viability of the organism, and eventually ousts the infection. The activity of these azoles against the Mtb CYP51 is of interest as the study of these interactions may aid the development of future treatments against *Mycobacterium tuberculosis* infections. The Mtb CYP51 was the first discovered prokaryotic CYP51, and parallel studies showed the potency of azole drugs against related mycobacteria and other actinomycetes (157). Thus binding titrations of CYP51 with six azole compounds (clotrimazole (Figure 23), econazole, fluconazole, ketoconazole, miconazole, and voriconazole) were carried out to determine their relative affinities (K_d values) for the Mtb CYP51 enzyme.

The azole anti-fungal studies were carried out as for the imidazole and sodium cyanide titrations. Enzyme was prepared at 2 – 4 μM in assay buffer, whilst the azoles were prepared as 0.5 or 1.0 mg/ml stock solutions solubilised in DMSO. The UV-Visible spectra were recorded and analysed as previously described for imidazole and sodium cyanide except that, where applicable, the rectangular hyperbola was not used. In its place a quadratic function (Equation 3) was applied to data that indicated very tight binding. This function takes into consideration enzyme concentration and is more accurate for K_d determination when tight-binding is in evidence. Specifically, this

equation is more appropriate on occasions when K_d values are not >10-fold that of the enzyme concentration required for the optical titration.

$$A_{obs} = (A_{max}/2 \times ET) \times (X + ET + K_d) - \left(\left((X + ET + K_d)^2 - (4 \times X \times ET)\right)^{0.5}\right)$$

Equation 3 The quadratic equation used to determine K_d values for azole ligand binding to Mtb CYP51 (159). This quadratic function was applied to data that showed tight-binding of the ligand. A_{obs} is the absorption change determined at ligand concentration X. A_{max} is the maximal absorption change induced at saturating ligand concentration. ET is the enzyme concentration used and K_d is the dissociation constant for the ligand.

The UV-Visible absorption spectra, difference spectra, and binding curve in Figure 23 represent the titration of clotrimazole with Mtb CYP51, but are typical of the results for all of the six azole anti-fungals studied. In all cases there is a shift to longer wavelengths in the Soret band from 419 nm to approximately 424 nm, and the azoles also induce a partial apparent spectral "merging" of the alpha and beta bands to form a broad band centred at 542 nm. As with CYP51s from different organisms and other P450s (197,198,202), the six compounds produce typical Type II absolute spectral shifts when the data are analysed. These data attest to the displacement of a weakly bound distal water molecule by the ligand, which itself then ligates directly to the ferric heme iron. This suggests that the azole anti-fungals are inhibitors of Mtb CYP51 and may (assuming that the Mtb CYP51 is a viable target, as are its fungal counterparts) be effective for treating infections by *Mycobacterium tuberculosis*. This is further backed by the dissociation constants (K_d values) calculated from the binding titration curves (Table 8). The data demonstrate that the six azole compounds all bind very tightly in the active site of CYP51 with the K_d values calculated showing an order of tightness of clotrimazole>miconazole>econazole>voriconazole>ketoconazole>fluconazole, with an approximate thirty-fold difference between the tightest and the weakest binding.
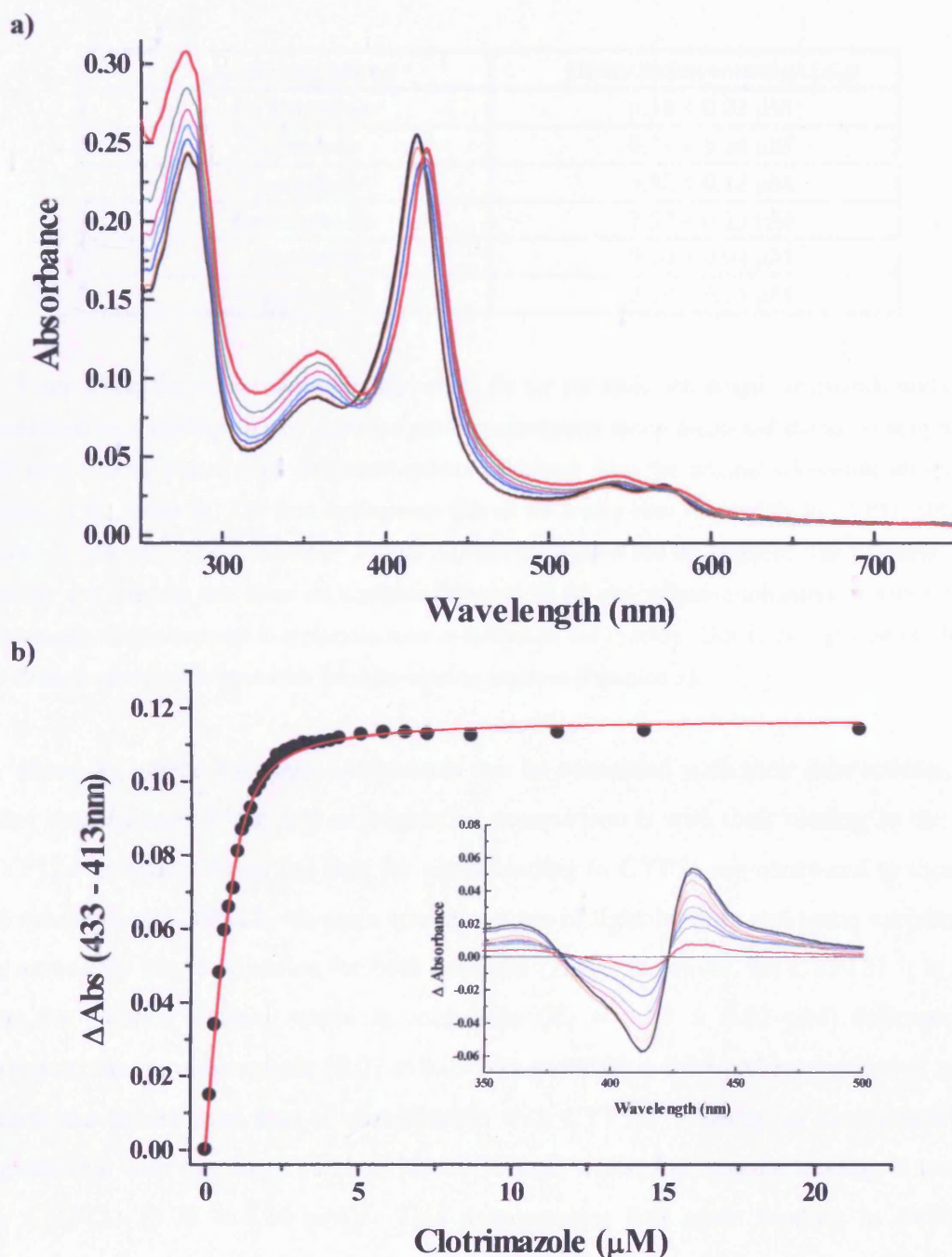
a)

b)

Figure 23 a) Selected UV-Visible spectra recorded during the titration of clotrimazole (0.5 mg/ml stock solution) with Mtb CYP51 (2 μM). The spectra identify clotrimazole as an inhibitor of the P450 as it induces a type II (inhibitory) shift of the Soret band from 419 nm to 424 nm. The spectra also show evidence of spectral shifts and partial fusion of the Q bands, with a peak at 542 nm. The initial and final spectra are shown as thick black and red lines, respectively. **b)** The binding titration curve and selected difference spectra (inset) created from the UV-visible data. The titration curve was calculated from the difference spectra by subtraction of the absorbance values of each spectrum at the wavelength at which the trough was maximal from the values corresponding to the wavelength at which the peak was maximal (413 nm and 433 nm, respectively). Titration data were fitted with the tight-binding function (Equation 3) and produced a K_d of 0.18 ± 0.02 μM that suggests clotrimazole to bind very tightly to the P450.

Azole compound	Dissociation constant (K_d)
Clotrimazole	0.18 ± 0.02 µM
Econazole	0.31 ± 0.04 µM
Fluconazole	5.82 ± 0.12 µM
Ketoconazole	3.57 ± 0.25 µM
Miconazole	0.20 ± 0.04 µM
Voriconazole	2.19 ± 0.15 µM

Table 8 The dissociation constants (K_d values) for the six azole anti-fungal compounds studied, as determined from binding titration curves of azole concentration *versus* associated change in absorbance. The curves were created from difference spectra calculated from the original UV-visible absorbance spectra of the titrations. The data demonstrate that all the azoles bind very tightly to CYP51, although there is a difference of approximately 30-fold between the tightest and the weakest. The tightness of the binding also suggests that these six compounds would all be very effective inhibitors of Mtb CYP51, particularly when compared to molecules such as imidazole and cyanide. Due to the tightness of binding all titration curves were fitted with the tight-binding equation (Equation 3).

These K_d values for these compounds can be compared with their interactions with other cytochromes P450, and an interesting comparison is with their binding to the Mtb CYP121 enzyme. When the data for azole binding to CYP51 are compared to those of *M. tuberculosis* CYP121, we see a similar degree of tight-binding and some variation of K_d across the range of azoles for both isoforms (158). However, for CYP121 it is seen that the tightest binding azole is econazole (K_d = 0.03 ± 0.02 µM) followed by clotrimazole and miconazole (0.07 ± 0.03 µM and 0.09 ± 0.05 µM respectively), all of which are tighter than that of clotrimazole with CYP51. Binding of ketoconazole is comparable with that for CYP51 (3.30 ± 0.30 µM) whilst fluconazole binding is weaker for CYP121 (9.70 ± 0.60 µM). This demonstrates that azole binding to P450s is strongly isoform dependent, and this clearly relates to active site structure and chemical character. This suggests that although there is a common mechanism for binding of these compounds (specifically the coordination of the heme iron by the basic nitrogen of the drug) there are factors, such as the binding site environment and active site residues, which lead to the different affinities of the azoles to the cytochromes P450 (36).

These data demonstrate that certain azole compounds that bind tighter to CYP51 should act as more potent inhibitors of the enzyme than those with weaker binding. This may relate in turn to the interaction of active site residues with the functional groups of the azoles, or of the hydrophobicity of the azole, which must enter the

hydrophobic active site of the enzyme (36). Indeed, fluconazole is a much more hydrophilic compound than clotrimazole, and thus some of the differences in binding (i.e. the weaker binding of fluconazole) may be attributed to this general difference. These data identify that the Mtb CYP51's activity would be significantly inhibited by the presence of azole compounds akin to those utilised here, due to inactivation of its oxygenase function. If the enzyme was of significance to the survival of Mtb or involved in biochemical/biological pathways leading to the production of components of the waxy envelope, then the use of the azoles or similar compounds that inactivate heme redox function would be a viable option as an antibiotic therapy against Mtb.

3.9 Further Mtb CYP51 drug binding studies

Binding titrations were also performed with three non-azole compounds (dithiocarbamate derivatives) of unknown structure, believed to be effective anti-tuberculosis agents (supplied by Dr. U. Möllman, Jena, Germany). No absorbance spectra records were made for these titrations, as no significant shift in the CYP51 Soret absorbance peak at 419 nm was observed at high concentrations of these substances. The only observed effect of the addition of these compounds was the very rapid precipitation and aggregation of the protein in each case. This was at least in part due to the high concentrations of solvent required for delivery of the compounds. Due to the protein precipitation, no binding of the compounds could be discerned in the accessible concentration range and thus no K_d values were determinable.

It has been reported in previous studies that Mtb CYP51 is a 14α-sterol demethylase with the capability of utilising lanosterol as a substrate (169). In order to verify this information and determine K_d values, binding titrations were carried out with lanosterol, as well as a number of other sterol and steroid compounds. These titrations were performed in the same manner as were the azole titrations (see Chapter 3.8) and analysed similarly with the appropriate curve fitting function (rectangular hyperbola or quadratic tight-binding equation). The lanosterol titration with Mtb CYP51 was found to be inconclusive due to the insoluble nature of lanosterol in the assay buffer. The compound was solubilised in various polar and non-polar solvents, including DMSO, but in all cases very large degrees of precipitation of the enzyme and the compound occurred to the extent that no binding constant could be obtained. This also meant that the rather minor optical shift of the Soret band to shorter wavelengths (type I) seen in

the work of Bellamine *et al.* (169), which is typically induced by P450 substrates (69,192), could not be detected. Other steroids and sterols tested for inducement of Soret band shifts were androstenedione, estriol, progesterone, and testosterone. These compounds all caused the Soret band of Mtb CYP51 to shift to shorter wavelengths, although the degree of shift varied considerably. As with lanosterol, androstenedione was subject to insolubility issues that made the determination of a K_d value unfeasible, although it was possible to observe that the compound caused a minimal shift of the Soret band to shorter wavelengths (by approximately 1 nm). Studies with testosterone and progesterone were more promising, with both compounds inducing convincing shifts from 419 nm to 417 and 416 nm, respectively. The titrations of these compounds were sufficiently clear that a K_d value for progesterone was calculated as 54.3 ± 4.3 µM, whilst it was found that testosterone bound less tightly with a K_d of 100.0 ± 16.8 µM.

The most significant shift in the Soret band towards shorter wavelengths was induced by estriol, thus confirming the findings of Podust and co-workers that demonstrated this sterol compound induced a type I shift of the Soret band of Mtb CYP51 (35). Addition of this compound caused the 419 nm peak to decrease in intensity with a concomitant increase in absorbance at 392 nm (Figure 24a). This is typically seen when a substrate causes a shift in equilibrium from the ferric low-spin P450 to the ferric high-spin form of the enzyme (28,69) and has previously been described for, among other systems, the binding of arachidonate to P450 BM3 (192). As well as modulation of Q bands, the development of a broad peak at 650 nm is observed during the titration. This has been observed in a number of cytochromes P450 (203,204) and is utilised as a further indication of substrate binding, and thought to be a charge transfer band associated with substrate binding in the vicinity of the heme iron.

The titration data were analysed (Figure 24b) and a K_d value of 21.68 ± 0.78 µM calculated, which suggests that the binding of estriol is between 2- and 5-fold tighter than that of progesterone and testosterone, but is weaker than that of the azole anti-fungals. The fact that a substrate-like compound binds more weakly than an inhibitor is to be expected, as it is important that a substrate binds tightly enough to interact with the enzyme but weakly enough that, once catalysis has occurred, the product(s) can leave the active site in order to allow for further reactions to occur. In addition, the substrate-like molecules lack the imidazole/triazole functional groups that coordinate the heme iron and further stabilise binding of the inhibitors.
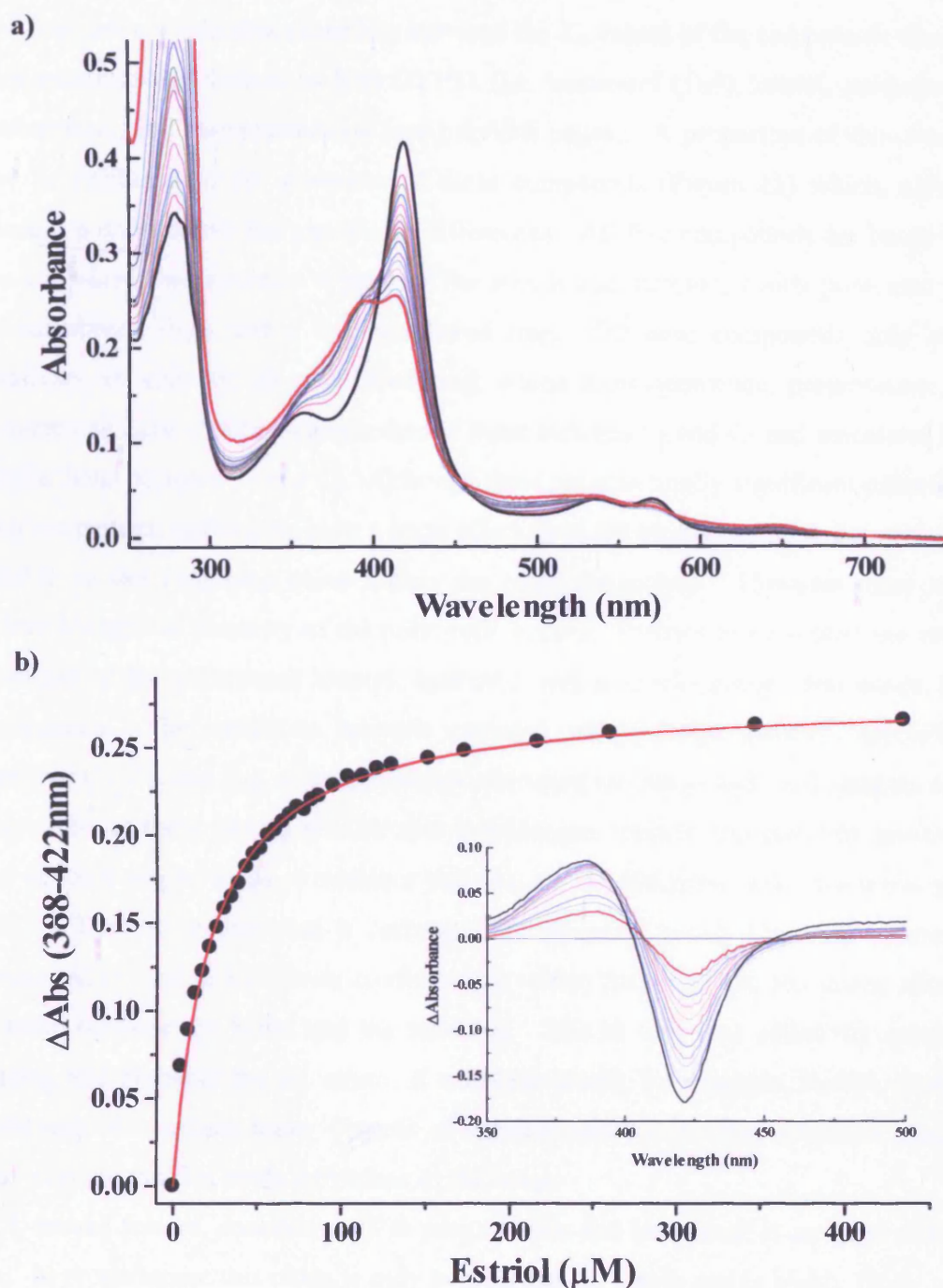
a)

b)

Figure 24 a) Selected UV-Visible spectra for the titration of estriol with Mtb CYP51 (~3.0 μM). The starting and final spectra are denoted in thick black and red lines respectively. The spectra identify estriol as inducing a substrate-like shift to shorter wavelengths (392 nm) of the Soret band. The presence of estriol also causes the Q bands to fuse and a peak to develop at 650 nm, typically seen only when a cytochrome P450 is bound to a substrate. **b)** The binding titration curve and difference spectra (inset) for the titration of estriol with CYP51. The difference spectra show evidence of a type I Soret band shift that indicates the binding of a substrate in the active site of the enzyme and a conversion of the heme from the low- to high-spin state. When fitted with the appropriate function, a K_d of 21.68 ± 0.78 μM was determined, which shows estriol to bind moderately tightly to CYP51.

There are considerable variations between the K_d values of the compounds that bind in a substrate-like fashion to Mtb CYP51 (i.e. lanosterol (169), estriol, progesterone, testosterone, and androstenedione (see previous pages). A proportion of this diversity can be attributed to the structures of these compounds (Figure 25) which, although similar, possess subtle but significant differences. All five compounds are based upon the conjoined ring structure typical of the sterols and steroids, which possesses three six-membered rings and a five-membered ring. Of these compounds only estriol possesses an aromatic six-membered ring, whilst androstenedione, progesterone, and testosterone have a carbon-carbon double bond between C_4 and C_5 and lanosterol has a similar bond between C_8 and C_9. Although these are structurally significant differences, they are perhaps unlikely to have a large affect upon the binding of these compounds to CYP51 as the variations occur within the rings themselves. However, they might induce changes in planarity of the polycyclic system. Perhaps more significant are the positions of the substituent methyl, hydroxyl, and carbonyl groups that adorn these compounds. The variations between carbonyl and hydroxyl groups, especially at positions C_3, C_{16} and C_{17}, affect interactions between the compounds and residues of the active site, as these groups will be able to hydrogen bond to appropriately positioned and charged amino acids or residues that can act as hydrogen bond donor/acceptors (173). The switch between a carbonyl and hydroxyl group thus may cause the compound to bind in a different conformation within the active site and hence alter the distance between the heme and the substrate. This in turn may affect the nature of binding and probably the K_d value. A substrate bound, for example, further from the heme may also induce lesser degrees of spectral perturbation (i.e. spin-state change) than a compound that binds very close to the heme.

A second feature, common only to progesterone and lanosterol, is an alkyl chain at C_{17}. In progesterone this chain is only two carbons in length and is highly likely to be the cause for the difference between the K_d values of progesterone and testosterone, probably by increasing points of contact within the active site and/or by increasing the compound's solubility in assay buffer, which thus aids in its delivery to the site. The group at C_{17} of lanosterol has a total of eight carbons (including substituent methyl groups) and it is most likely that this side-chain further increases the hydrophobicity of the compound, making it more difficult to solubilise and for the molecule to reach the point of binding within the enzyme. The increased bulk of this molecule compared with the other four compounds may also be a hindrance to entry into, and positioning within,

the active site of CYP51, and thus cause the difficulties experienced here in determining the dissociation constant for this sterol.
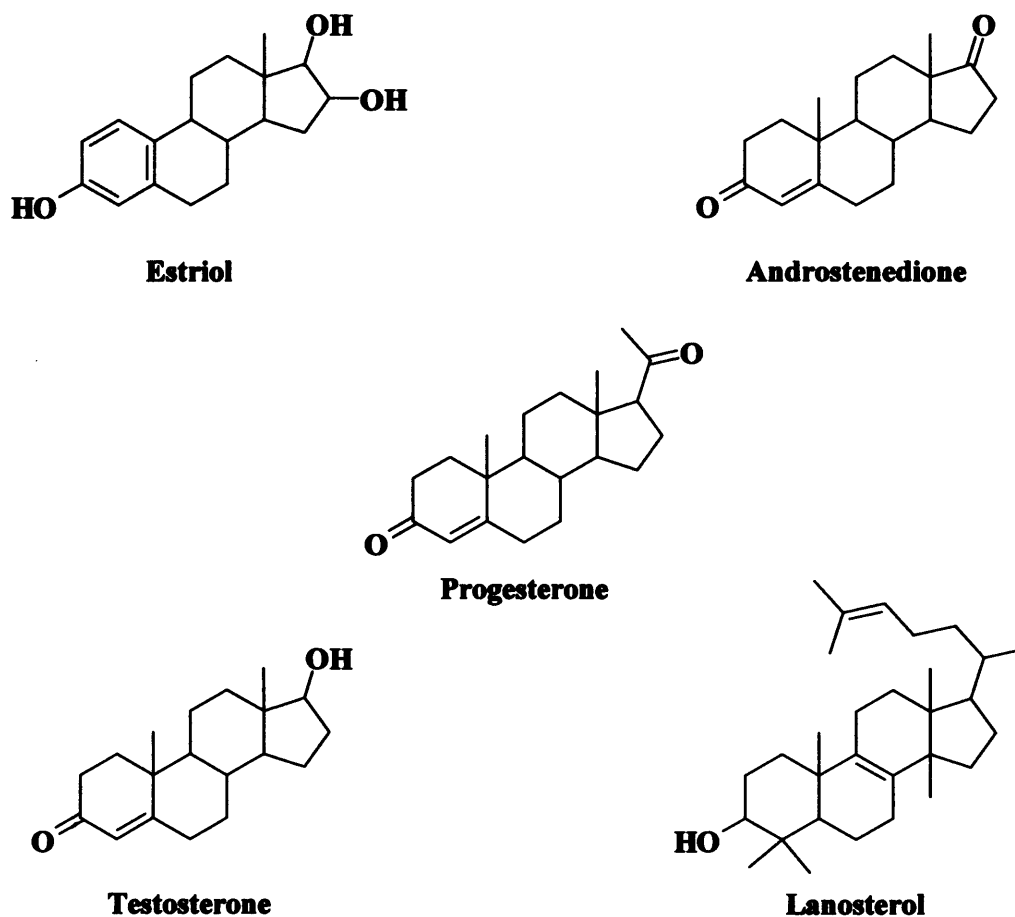

Estriol

Androstenedione

Progesterone

Testosterone

Lanosterol

Figure 25 The structures of the four sterol (estriol) and steroid compounds (androstenedione, progesterone, and testosterone) shown to induce substrate-like spectral shifts of the Mtb CYP51 Soret band. These compounds all cause the 419 nm band to shift towards 390 nm, although the extent of shift varies considerably. Estriol induces the greatest degree of shift followed by progesterone, testosterone, and then androstenedione. The chemical structure of lanosterol, which has been identified as an Mtb CYP51 substrate in other studies (169), is also shown. In this study spectral shifts induced by lanosterol were poorly defined due to insolubility of the sterol and to precipitation of the protein due to high solvent concentrations required for sterol delivery, which meant that a K_d value could not be determined with any accuracy.

Another aspect of the sterol/steroid structure that affects their binding to Mtb CYP51 is the positioning of the methyl groups that adorn all of these compounds. A methyl group at C_{13} is ubiquitous to all five compounds and may well be significant for location in the active site, as well as adding to the hydrophobic nature of the compounds. All the compounds, except for estriol, also possess a methyl group at the C_{10} position that may have similar roles and purpose to the group at C_{13}. Lanosterol has two additional methyl groups at C_4 and a further two attached to the alkyl chain that extends from C_{17}. These four methyl groups vastly increase the hydrophobicity of lanosterol and most likely are the cause for its insolubility in the assay buffer, thus making a K_d determination extremely difficult. Furthermore, these methyl groups contribute additional bulk to lanosterol that may act to diminish the compound's ability to enter the active site of CYP51 and to hinder the close interactions with the heme required to induce large spin state shifts. In previous work (169), it has been shown that Mtb CYP51 demethylates lanosterol, and other sterols, at the C_{14} position. However, although lanosterol possesses a C_{14} methyl group, the other compounds, which induce greater spectral shifts and bind more tightly than lanosterol, do not have this catalytically essential methyl group. This significant difference in compound structure could indicate that testosterone, progesterone, androstenedione, and estriol are not substrates for Mtb CYP51, but happen to bind in a way that induces spectral shifts consistent with substrate binding. Alternatively, demethylation of lanosterol may be an artefact of an ancient function of the CYP51 enzyme family and the role that it plays in Mtb physiology could have evolved to be distinct from the 14α demethylation of sterols. Until the physiological role of Mtb CYP51 has been conclusively determined, this unusual difference between binding of the various sterol/steroid ligands will remain unexplained. The phenomenon is not rare, and the physiological basis underlying oxidation of favoured substrates remains unclear for several prokaryotic cytochromes P450 characterized to date (170,173,204).

3.10 Binding of substituted imidazoles to Mtb CYP51

In Chapter 3.9 it is seen that the binding of certain compounds (i.e. estriol, progesterone, and testosterone) effects type I Soret band shifts to shorter wavelengths, indicative of their being substrate-like compounds. Further binding studies using substituted imidazole compounds showed that 2-phenylimidazole also provoked this shift of the Soret band towards 390 nm. However, the structurally similar compounds 1-phenylimidazole and 4-phenylimidazole did not: instead producing the expected type II optical transitions consistent with the coordination of the heme iron by the imidazole group. All titrations were performed and recorded identically to those previously described, with enzyme prepared in buffer A at 2.3 μM and the substituted imidazoles solubilised at appropriate concentrations in a 1:1 mix of water and ethanol. The obtained spectra, of which a composite can be seen in Figure 26, were analyzed using suitable curve-fitting functions to produce the apparent dissociation constant (K_d) values.
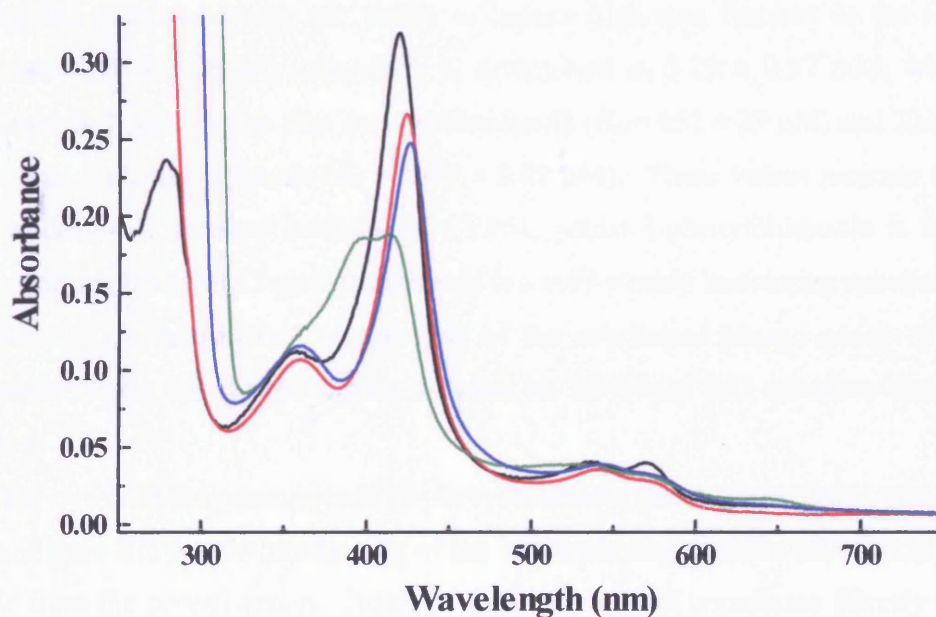

Figure 26 The spectra of CYP51 in complex with 1-phenylimidazole (red), 2-phenylimidazole (green), and 4-phenylimidazole (blue) recorded at near-saturating concentrations of the substituted imidazoles (3.2 μM, 7.5 mM, and 1.2 mM respectively). Ligand-free CYP51 at a final concentration of 2.3 μM is shown for contrast (black). Type II inhibitory Soret band shifts are identified for 1-phenylimidazole and 4-phenylimidazole with maxima found at 424 and 425 nm, respectively. The 2-phenylimidazole spectrum shows the compound to induce a type I substrate-like shift to shorter wavelengths, with maxima at 414 and 395 nm, and is symptomatic of a heme iron transition to the high-spin state.

The addition of 1-phenylimidazole and 4-phenylimidazole to samples of CYP51 cause the Soret band to shift to 424 and 425 nm respectively, as well as causing a decrease of approximately 25 % in the intensity of the band. These shifts in wavelength and intensity are very similar to those produced by imidazole (Figure 21) and suggest that these substituted imidazoles interact with the active site of Mtb CYP51 in an inhibitory manner. In contrast, the binding of 2-phenylimidazole, whose only structural difference is the position of the phenyl group on the imidazole (Figure 27), causes the Soret band to decrease in intensity and shift towards shorter wavelengths. The spectra show that binding of 2-phenylimidazole induces a shift of the heme iron in CYP51 towards the high-spin form, with peaks observed at 395 and 414 nm for the ligand-saturated sample. The shift induced by 2-phenylimidazole, typical of a type I Soret shift, is in agreement with other studies of the interaction between Mtb CYP51 and 2-phenylimidazole (202). Similarly to the data presented here, the work of Matsuura *et al.* identified that 2-phenylimidazole caused a Soret band shift to 396 nm with simultaneous decreases in intensity of the band, suggesting that 2-phenylimidazole is a substrate-like compound with the ability to induce high-spin features in the CYP51 heme iron. The K_d for this interaction is determined as 3.19 ± 0.37 mM, which is approximately 7-fold weaker than 4-phenylimidazole (K_d = 452 ± 27 μM) and 7000-fold weaker than 1-phenylimidazole (K_d = 0.44 ± 0.07 μM). These values indicate that 1-phenylimidazole is a potent inhibitor of CYP51, whilst 4-phenylimidazole is far less potent as an inhibitor, and 2-phenylimidazole is a very weakly interacting substrate-like compound. This implies that the position of the substituted phenyl group of these compounds effects the differentiation between an inhibitory and substrate-like Soret band shift.

For the two inhibitory compounds (1-phenylimidazole and 4-phenylimidazole) it can be seen (Figure 27) that the positioning of the imidazole ring places a nitrogen as far as possible from the phenyl group. As these compounds must coordinate directly to the heme iron in order to act as inhibitors of the P450, it is suggested that it is these nitrogens which coordinate to the heme iron and cause increased low-spin state stability. For 2-phenylimidazole the imidazole ring is positioned such that the two nitrogen molecules are nearer to the phenyl group than for the two inhibitors. This implies that the orientation of the imidazole ring is critical and that the conformation found in 2-phenylimidazole is not conducive with direct coordination of imidazole nitrogen to the heme iron. Instead, the compound binds in the active site of CYP51 displacing the

heme-ligated water molecule and effecting a shift to the high-spin form of the heme by inducing the reorganization of electrons in the d-orbitals of the heme iron in the 5-coordinated form. This shift to the high-spin state form infers that 2-phenylimdazole is a substrate-like compound (69), unlike the subtly differently structured compounds 1-phenylimidazole and 4-phenylimidazole, and features of this interaction will be investigated further in Chapter 3.12 and 3.13.
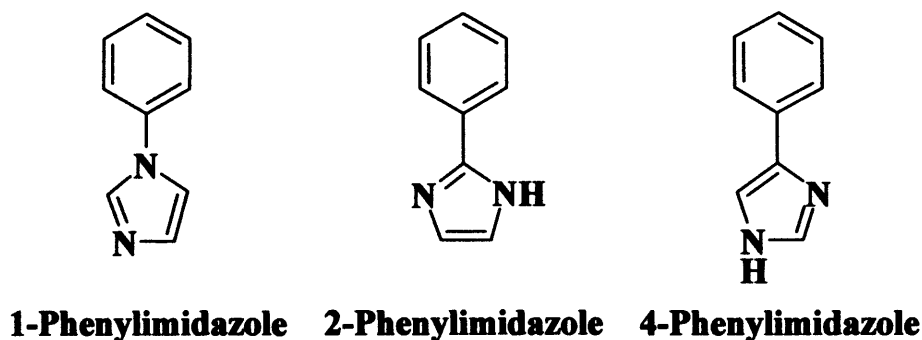

1-Phenylimidazole   2-Phenylimidazole   4-Phenylimidazole

Figure 27 The chemical structures of 1-phenylimidazole, 2-phenylimidazole, and 4-phenylimidazole. The structures identify the differences in position of the imidazole ring and its associated nitrogen atoms that relate to their tightness of binding and abilities of these compounds to act as cytochrome P450 substrate-like molecules (2-phenylimidazole) and inhibitors (1-phenylimidazole and 4-phenylimidazole).

3.11 Resonance Raman spectroscopy of Mtb CYP51

Apart from UV-Visible spectroscopy, there are a number of other spectroscopic techniques that are used for the characterization of cytochromes P450. One such technique is resonance Raman spectroscopy, which is frequently used to look at the properties of the heme of the P450s (194,205,206). Resonance Raman reports on vibrations and movements of molecules, and parts of molecules, by detecting the scattered photons that are emitted from samples excited by a monochromatic light source, frequently delivered from a laser (207,208). Resonance Raman differs from Raman spectroscopy in that the wavelength of irradiation is resonant with a particular chromophore in the sample (the heme in the case of P450s) and provides specific information on the chromophore without (in the case of P450s) interference from the protein itself. The spectrum created from the detection of the scattered photons features a number of peaks that can be assigned v values, corresponding to the wavenumber at which they are found. In the case of cytochromes P450s the v values can report on the

94

spin state and oxidation state of the heme, as well as identifying, for example, bending and stretching of the bonds in the plane of the heme and the orientation of substituent groups such as vinyls and propionates. For example, a study of Mtb CYP121 by McLean *et al.* identifies, by the positions of the v_2, v_3, v_4, and v_{10} peaks, the heme iron of this P450 to be in the ferric, low-spin form, whilst the v_{11} and v_{37} peaks identified in studies of P450 BM3 from *B. megaterium* identify a non-planar heme with asymmetrical vinyl groups (205).

Resonance Raman spectroscopy was carried out using an aliquot of oxidised, ligand-free Mtb CYP51 at a concentration of 50 μM. The spectrum was obtained at room temperature using a 15 mW a Coherent Innova 300 krypton ion laser with an excitation wavelength of 406.7 nm (close to the Soret maximum) and data acquisition was performed using a Renishaw micro-Raman system 1000 spectrophotometer. The sample was held in a capillary under the microscope and submitted to an extended scan of 12 x 15 second bursts of excitation with data collected between 250 and 2000 cm^{-1}. A spectrum (Figure 28) was produced and v values, relating to vibrational bond bending and stretching in the plane of the heme of CYP51, were assigned to the major peaks of the spectrum, according to the formal nomenclature developed by Hildebrandt and co-workers (209,210).

The peak of greatest amplitude at 1372 cm^{-1} was assigned as v_4. This peak identifies a 'breathing' of the porphyrin ring whose main contribution comes from the stretches of C-N bonds within the ring (205,211,212). The peak is an indication of the oxidation state of the heme and here identifies the iron at its centre as being in the Fe^{3+} oxidised state, as was expected. This is complemented by a previous study in which ferric low-spin CYP121 (from *M. tuberculosis*) was shown to have a v_4 peak at the same frequency (158) and hence further suggests that CYP51 is purified predominantly in the ferric, low-spin form, as is usual for P450s – due to the relatively rapid reaction of the ferrous heme iron with dioxygen. Further confirmation of the oxidation state of Mtb CYP51 was sought using other spectroscopic techniques (i.e. EPR and MCD) and is discussed in Chapters 3.12 and 3.13.
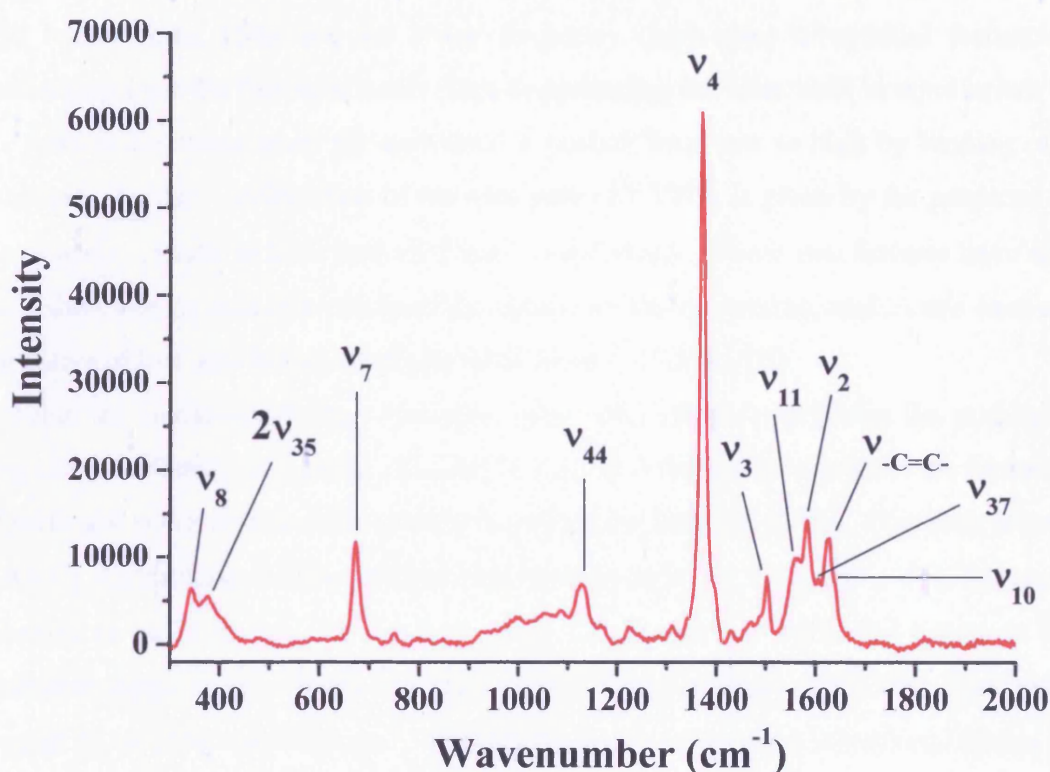
Figure 28 The resonance Raman spectrum of *M. tuberculosis* CYP51 obtained by excitation of 50 μM enzyme at 406.7 nm with a 15 mW Coherent Innova 300 krypton ion laser at a scan rate of 12 x 15 s. Data acquisition between 250 and 2000 cm^{-1} was performed using a Renishaw micro-Raman system 1000 spectrometer. Peaks of interest with respect to the oxidation state, spin state, and symmetry of the heme are identified by their ν numbers and their significance described below. Spectroscopy performed by Dr. J. Clarkson, Department of Chemistry, University of Strathclyde. Band nomenclature is according to Hildebrandt *et al.* (209,210).

The other peaks in the spectrum were also assigned ν numbers and from these further information concerning the oxidation state and the nature of the porphyrin ring in the environment of the CYP51 protein was obtained. The peak at 1502 cm^{-1} was assigned as ν_3, which has been identified as a spin-state marker for predominantly low-spin iron in the heme macrocycle. The CYP51 sample was shown to possess only a very small high-spin component, as the ν_3 peak showed only a very small shoulder at 1487 cm^{-1}, which is indicative of high-spin heme. This concurs with the study of Mtb CYP121 by McLean *et al.* (158) where it is similarly noted that the ν_3 spin-state marker is dominated by a peak at 1500 cm^{-1} with only a very small feature at 1487 cm^{-1}, again confirming the purified enzyme to be mostly in the low-spin, ferric form. A contrasting

study of P450 BioI from *Bacillus subtilis* (194), which is purified in the high-spin, fatty acid bound form, identifies the lower frequency (high-spin) vibrational feature as dominating over the low-spin band. This demonstrates the clear shift in equilibrium of the peak components when the spin state is pushed from low to high by binding of a substrate. Further confirmation of the spin state of CYP51 is given by the positions of the v_2 and v_{10} peaks at 1583 and 1637 cm^{-1}, respectively. These two features have also been shown to be spin-state markers for heme-containing systems, and in this case are indicative of low spin hexa-coordinate ferric heme (157,194,205).

From the resonance Raman spectrum, other information concerning the porphyrin ring can be collated. A number of peaks at various wavenumbers indicate the presence of particular bond stretches and vibrations induced by laser excitation. One such feature is the C_β -C_β stretches which are identified by the peak v_{11} at 1558 cm^{-1}. This feature is sensitive to the heme type (in this case *b*-type heme) and is a signal that relates to the electronic conjugation of heme and vinyl groups in the porphyrin ring (205). The peaks v_{11} and v_{44} at 1558 and 1130 cm^{-1}, respectively, are indications of vibrational modes of the heme that occur when the heme is non-planar, and suggest that some disruption to the plane of the heme may occur in CYP51. The v_{37} peak at 1600 cm^{-1} insinuates further asymmetry of the heme, possibly indicating that the macrocycle of CYP51 is domed like that of P450 BM3, whose resonance Raman spectrum also demonstrates similarly positioned v_{11}, v_{44}, and v_{37} peaks (205). This peak identifies that the vinyl groups, which protrude from the heme macrocycle, are asymmetrical, and is a mode that should not exist in planar heme (205,209,210).

In summary, this resonance Raman study identifies that Mtb CYP51 is typical of the cytochromes P450, being purified with a low-spin, ferric heme iron, whilst also demonstrating that the heme macrocycle, like that of P450 BM3 from *B. megaterium* (205), is non-planar with asymmetrical vinyl groups. In the following section electron paramagnetic resonance, which reports on paramagnetic species such as oxidised heme iron, is utilised to corroborate the findings of this study, whilst also investigating the effects of ligands, such as 2-phenylimidazole and fluconazole, on the oxidation, spin, and ligation states of the CYP51 heme iron.

3.12 Mtb CYP51 electron paramagnetic resonance

Electron paramagnetic resonance (EPR) is a spectroscopic technique that is often utilised as a method for reporting on the oxidation state, spin-state, and ligation state of heme macrocycles (37,158,213). This makes it a good source for information concerning the heme of cytochromes P450, and produces data that clearly distinguish differences and similarities between the P450s. The technique is based upon the absorbance of microwave energy of paramagnetic species, such as iron (Fe(III)), nickel (Ni(III)), cobalt (Co(II)), and copper (Cu(II)), within a sample under the influence of a magnetic field. At a particular magnetic field strength the paramagnetic species, which contains an unpaired electron, will resonate and subsequently absorbs microwave energy as the field perturbs the magnetic spin of the electron. By recording microwave absorbance whilst varying the magnetic field strength, a spectrum of the paramagnetic species is obtained. The first derivative of the microwave absorption data results in a spectrum whose features, each of which is assigned a g-value, identify the spin-state, oxidation state, and (often) ligation state of the sample by their position and shape. The g-values, which are a function of the magnetic field strength at which paramagnetic resonance occurs and the frequency of the microwave source, provide a suitable numerical indicator with which to compare samples of similar type, e.g. the heme b-containing cytochromes P450 (214,215). The cytochromes P450 make very good samples for EPR, as in the oxidised state the ferric iron of the heme has an unpaired electron in its d-orbitals and thus the oxidised enzyme is easily detected. In the oxidised, low-spin state the P450s exhibit g-values typically at around $g_x = 2.42$, $g_y = 2.25$, and $g_z = 1.92$ (37,158,194,213). The low spin-form of a P450 is distinguishable from the high-spin form as the change from S = $\frac{1}{2}$ to S = $\frac{5}{2}$ when the electrons reconfigure in the d-orbitals (often due to substrate binding) causes a broadening of the spectrum as there are more paramagnetic species (unpaired electrons) in the sample, and subsequently increases the g-values associated with the sample. For example, when P450 BM3 binds arachidonic acid $g_x = 2.42$, $g_y = 2.26$, and $g_z = 1.92$ shift to $g_x = 8.18$, $g_y = 3.44$, and $g_z = 1.66$, indicating that this substrate has pushed the heme iron from the low-spin form to the high-spin form (37). Hence, as well as identifying the oxidation, ligation, and spin states of a ligand-free cytochrome P450, this technique is very useful for identifying whether a compound bound in the active site of a P450 ligates directly to the heme iron or displaces a bound water molecule in order to induce a shift of the heme

iron to the high-spin form. Thus, this technique will be utilised to support UV-Visible and resonance Raman studies of Mtb CYP51, in addition to verifying the nature of the spectral shifts observed for the binding of 2- and 4-phenylimidazole, fluconazole, and testosterone.

The EPR data presented here (Figure 29 and Figure 30) were recorded using a Bruker ER-300D series electromagnet and microwave source interfaced to a Bruker EMX control unit and fitted with an ESR-9 liquid helium flow cryostat (Oxford Instruments), and a dual mode microwave cavity from Bruker (ER-4116DM). All spectra were recorded at 10 K using a 2.08 mW microwave source and a modulation amplitude of 10 G. Samples of CYP51 were prepared at 200 μM in 50 mM KPi pH 7.4 and spectra recorded in either the presence or absence of ligand compounds that were selected due to their effects on the UV-Visible spectrum of CYP51. The ligands 2-phenylimidazole, 4-phenylimidazole, and testosterone were added at near-saturating concentrations, as determined in UV-Visible binding titrations (see Chapters 3.9 and 3.10). Fluconazole was added to the CYP51 sample as a solid and was allowed to equilibrate until no further spectral changes were observed.

The spectrum of CYP51 (Figure 29) is typically rhombic in shape with no visible high-spin component and gives g-values of $g_z = 2.44$, $g_y = 2.25$, and $g_x = 1.91$. These values are comparable to those obtained for Mtb CYP51 in a previous study by Matsuura et al. (2.42, 2.26, and 1.91, (202)) and also Mtb CYP121 (2.47, 2.25, 1.90 (158)), which is the only other Mtb P450 that has been characterized to date. Homologous enzymes from *Methylococcus capsulatus* and *Saccharomyces cerevisiae* also give very similar g-values (2.43, 2.26, 1.91, and 2.45, 2.27, 1.92 respectively, (126,216)) to those obtained for Mtb CYP51, and suggest that the Mtb P450 is typical of the CYP51 family. The g_z-value falls within the typical range (2.48 – 2.40) of cytochromes P450 with a cysteinate/water ligation and these data confirm the presence of a cysteine-ligated, low-spin, 6-coordinate ferric P450 heme iron in the oxidised sample of Mtb CYP51. The results of the EPR, which agree with the resonance Raman data (Chapter 3.11), further attest to the heme of Mtb CYP51 as having no significant structural or electronic "abnormalities" and serves both as a characterization of the heme, as well as adding certainty to the analysis of the other spectroscopic data for this P450.
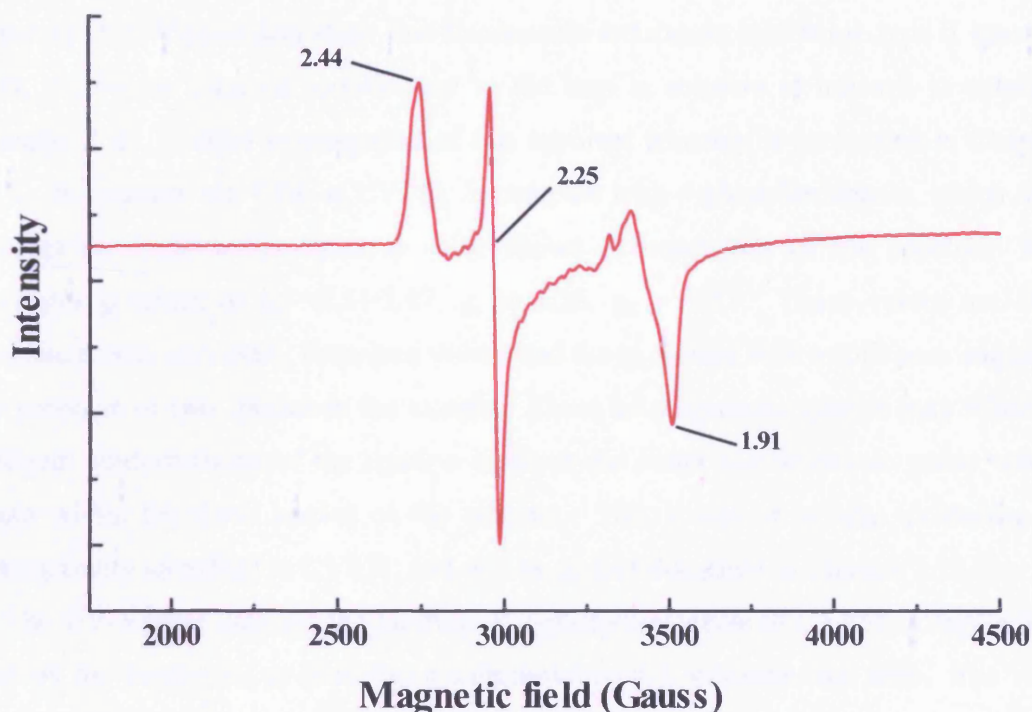
Figure 29 The EPR spectrum of ligand-free, oxidised *M. tuberculosis* CYP51 collected at UEA by Dr. Myles Cheesman. The EPR was performed using a Bruker ER-300D series electromagnet and microwave source interfaced to a Bruker EMX control unit and fitted with a liquid helium flow-cryostat (ESR-9, Oxford Instruments) and a dual mode microwave cavity from Bruker (ER-4116DM). Spectra were recorded at 10 K with 2.08 mW microwave power and modulation amplitude of 10 G. CYP51 was used at 200 µM in 50 mM KPi pH 7.5. The spectrum identifies g-values of g_z = 2.44, g_y = 2.25, and g_x = 1.91 and shows that the heme of CYP51 possesses a typical cysteine-ligated, hexa-coordinated, low-spin ferric iron molecule.

The EPR spectra of CYP51 in complex with the ligands 2-phenylimidazole, 4-phenylimidazole, testosterone, and fluconazole are shown in Figure 30 and demonstrate a number of interesting phenomena.

The EPR of CYP51 in complex with fluconazole produces g-values of 2.45, 2.26, and 1.90 and thus shows no significant variation from the ligand-free form of the enzyme. These g-values are consistent with data published by Matsuura *et al.* and imply that fluconazole does not coordinate directly to the heme of CYP51, contrary to structural data (51,202). Since atomic structural data demonstrate that the azole does coordinate directly to the CYP51 heme iron (51), an alternative explanation might be that the g-values for the complex are indistinguishable between the aqua- and azole-ligated forms, or that (in solution) azole coordination to the heme iron might occur predominantly via a bridging water molecule. A similar phenomenon has recently been observed with the atomic structure of the CYP121-fluconazole complex (Seward *et al.*,

100

in press). UV-Visible data show that fluconazole induces an inhibitory, type II spectral shift, thus some form of coordination to the iron in solution is inferred in solution (Chapter 3.8). Further investigation of this apparent anomaly is performed in Chapter 3.13. In contrast, the EPR of CYP51 in complex with 4-phenylimidazole, which also induces an inhibitor-like spectral shift, shows a broadening of the spectrum and generates g-values of g_z =2.53/2.47, g_y = 2.26, g_x = 1.87. These values are also consistent with previously described values and the g_z feature with a split peak suggests the presence of two species in the sample. These heterogeneous species may relate to different conformations of the ligation between the heme and imidazole group which occur within the distal pocket of the enzyme. This is one of several incidences of heterogeneity identified in CYP51, and will be further discussed in Chapter 3.13.

The UV-Visible data for the binding of 2-phenylimidazole to CYP51 (Chapter 3.1) identify the compound as inducing a substantial type I, substrate-like shift. The EPR data for this complex are typical of a low-spin, ferric heme and produce g-values of 2.42, 2.26 and 1.92. The enzyme also demonstrates minor components at g_z = 2.47 and g_x = 1.90 but there is no evidence for any high-spin heme in the sample (which would produce a different set of g-values). The thawed sample displayed the same high-spin UV-visible spectrum as it had prior to running the EPR spectrum, and thus the EPR spectrum was also recorded at a lower temperature and higher power. This again showed no evidence of high-spin features and suggests that a thermal equilibrium may exist between the high-spin and low-spin species. At room temperature or when the sample is thawed, the 2-phenylimidazole-bound enzyme lies predominantly in the high-spin form, but reducing the temperature to 10 K shifts the equilibrium towards the low-spin form with a negligible high-spin component. The existence of a thermal equilibrium is backed by resonance Raman studies by Matsuura et al. (202) that were performed at room-temperature. The data show that the binding of 2-phenylimidazole to Mtb CYP51 induces a peak at 1488 cm^{-1} in the spectrum, a feature that is typical of a five-coordinate high-spin heme. This agrees with UV-Visible spectra recorded at room temperature for the interaction between CYP51 and 2-phenylimidazole, and as there is an absence of a high-spin signal in the EPR spectrum for this interaction, the existence of a thermal equilibrium between the spin-states seems apparent. A further investigation of this phenomenon is made in Chapter 3.22.

As reported in Chapter 3.9, the binding of testosterone to CYP51 induces a minimal type I substrate shift of the Soret band from 419 nm to 417 nm. The binding of

testosterone to CYP51 was also investigated by EPR and produced g-values of $g_z =$ 2.47/2.40, $g_y = 2.25$, and $g_x = 1.93$. These values are typical of a cysteine- and water-ligated heme and are very similar to those of the ligand-free form of the enzyme, suggesting that, as with 2-phenylimidazole, the sample has no high-spin content. Although there is only a small amount of high-spin heme in the sample prior to EPR, it would be expected that this extremely sensitive technique would pick out the features of any high-spin heme in the sample. This again proposes the existence of a thermal equilibrium in which the high-spin component is inconsequential at the extremely low temperatures at which EPR is carried out and, as previously mentioned, this facet will be addressed in later sections.
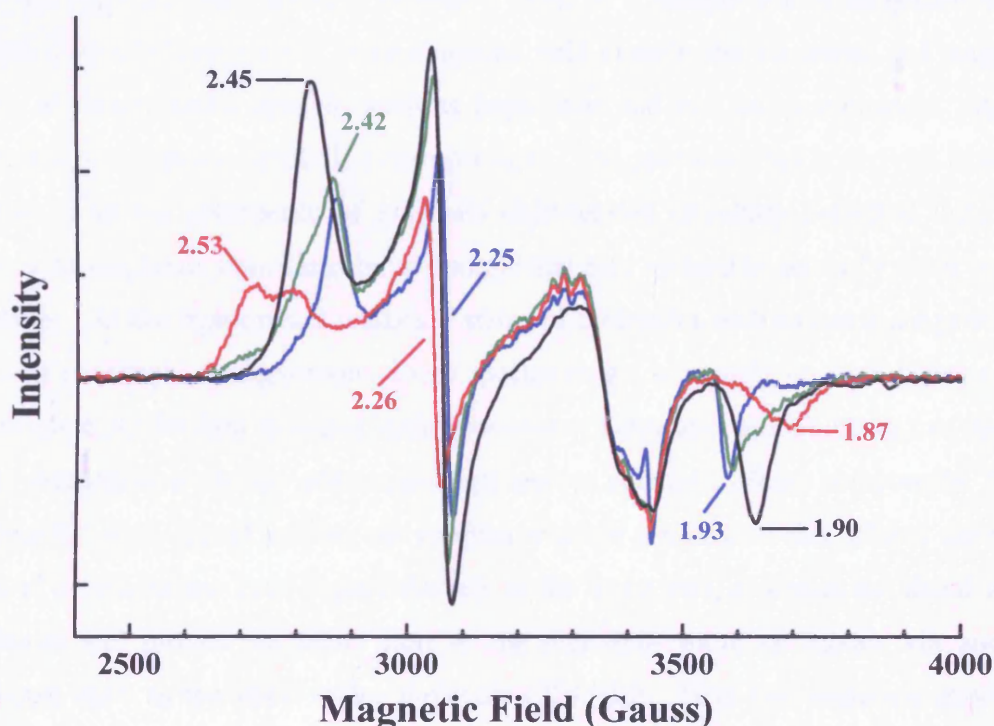

Figure 30 The EPR spectra of Mtb CYP51 in complex with the ligands fluconazole (black), 4-phenylimidazole (red), 2-phenylimidazole (green), and testosterone (blue), with significant g-values identified correspondingly. The spectra indicate that fluconazole shows no evidence of coordination with the heme of CYP51, contrary to structural data (51). Similarly the 2-phenylimidazole data does not substantiate the presence of a high-spin component that is observed using UV-Visible spectroscopy and suggests the presence of a thermal equilibrium between the high-spin and low-spin entities. The features of the 4-phenylimidazole spectrum identify that the ligand coordinates to the heme of CYP51 and that this ligation occurs in two conformations, as identified by the splitting of the g_z peak. Analysis of the testosterone spectrum again suggests the presence of a thermal equilibrium between the low-spin and high-spin forms as although there is a UV-Visible high-spin component noted for this interaction at room temperature, this is not evident in the EPR data recorded at 10 K.

3.13 Mtb CYP51 magnetic circular dichroism

Magnetic circular dichroism (MCD) is a valuable technique that can precisely report on the oxidation and spin states of metalloproteins, including those binding porphyrins and iron-sulphur clusters. Its use is widespread for the characterization of cytochromes P450, as the position of the obtained spectral bands report upon the ligation and oxidation states of the heme iron, as well as the effects of inhibitors and substrates on the electronic configuration of this chromophore (158,217,218), and here it is utilised to further investigate the ligation of the azole anti-fungal fluconazole to Mtb CYP51. The technique records the circular dichroism (i.e. the differences between the absorption of left- and right-handed circularly polarised light) of a sample that is subjected to the influence of a magnetic field. This magnetic field disturbs the electronic and magnetic states of paramagnetic species, such as heme iron and iron sulphur clusters, altering their ability to absorb circularly polarised light. The spectrum that is derived from the difference in the absorbance of left- and right-handed circularly polarised light thus reports on electronic transitions in the sample that may be hard to detect by other optical methods. As the ligation and oxidation states of molecules such as heme are governed by their electronic configurations, these spectra report accurately on such facets of the macrocycle, whilst data recorded in the presence of substrates and inhibitors can discern small changes in electronic and magnetic properties induced by these compounds. Most pertinently, such ligand studies can confirm whether a molecule that affects the spin-state of a cytochrome P450 ligates directly to the heme iron, displaces the distal water molecule and pushes the heme iron to the high-spin form, or ligates via another molecule such as the distal water molecule (219,220). Here the oxidation state and ligation state of Mtb CYP51 are investigated in order to further confirm the findings of EPR and resonance Raman studies. Additionally, due to the contradictory nature of the UV-Visible and EPR spectroscopy studies of the fluconazole ligation to the CYP51 heme iron, the former indicating direct ligation and the latter demonstrating no perceivable interaction, this anomaly is also investigated by magnetic circular dichroism.

Magnetic circular dichroism spectra were recorded for the ligand-free form of CYP51, as well as for CYP51 in complex with fluconazole, on two circular dichrographs, each covering a different part of the electromagnetic spectrum. A JASCO J-500D was used for UV-Visible wavelengths between 280 to 1000 nm, whilst a

JASCO J-730 recorded near-infrared data between 800 to 2000 nm. Protein samples were prepared at 150 – 200 μM in deuterated 50 mM HEPES, pH 7.5 and mounted on a SM-1, 6 Tesla superconducting solenoid (Oxford Instruments) with an ambient-temperature bore for measurements at room temperature. For the ligand-bound CYP51 MCD spectrum, solid fluconazole was added to the CYP51 sample until no further changes in the UV-visible spectrum were observed. MCD spectra were recorded by Dr. H.E. Seward at the University of East Anglia. The UV-Visible spectrum of fluconazole-bound CYP51 is shown in Figure 31, whilst the near-infrared spectra for the ligand-free and ligand-bound enzyme are shown in Figure 32.

The UV-Visible region of the fluconazole-bound Mtb CYP51 MCD spectrum (Figure 31) demonstrate significant features at 400 – 420 nm and 500 – 600 nm that respectively correspond to the electronic transitions that underlie the Soret and Q-band regions. The shapes and positions of these features are akin to those observed for other cytochromes P450, including Mtb CYP121, and P450 BM3 from *B. megaterium*, indicating that CYP51 is found in the low-spin ferric form (158,217). Furthermore, the absence of any significant features between 600 and 700 nm indicate that this *M. tuberculosis* cytochrome P450 possesses no significant high-spin component, whilst the low intensity of the Soret band feature, which is also observed for the aforementioned P450s, is typical of a thiolate-ligated heme iron, and thus supports the findings of UV-Visible, resonance Raman, and EPR spectroscopy studies of Mtb CYP51 (Chapters 3.4, 3.11, and 3.12).
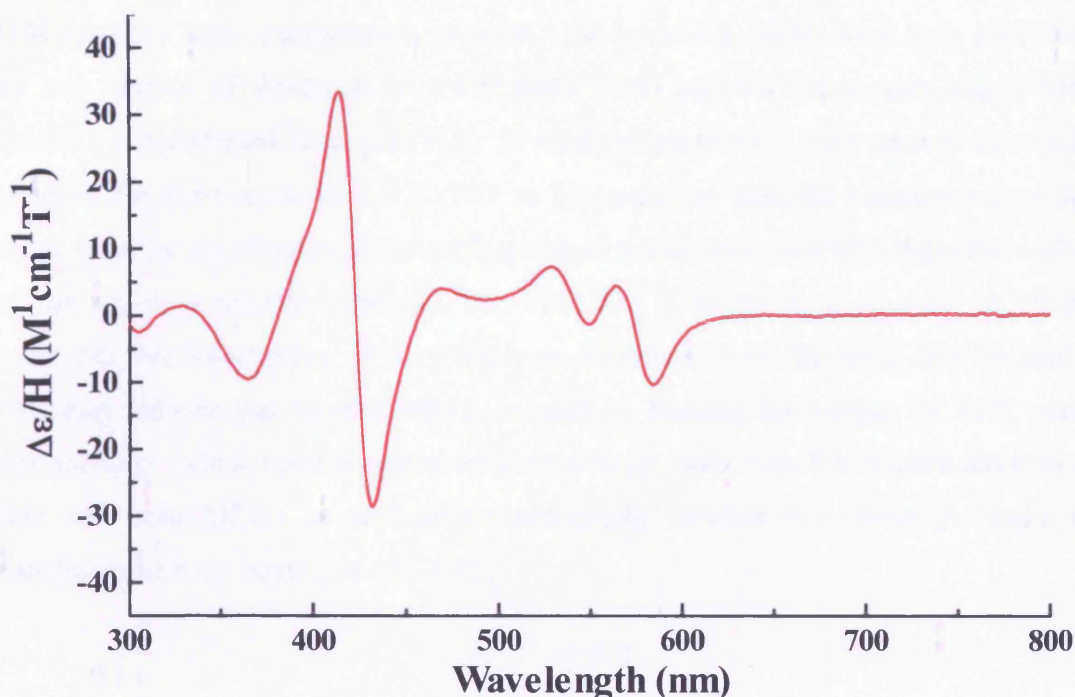
Figure 31 The UV-Visible MCD spectrum of fluconazole-bound Mtb CYP51 recorded at the University of East Anglia by Dr. H.E. Seward. The significant features observed at 400 – 420 nm and 500 – 600 nm correspond to the electronic transitions that underlie the Soret and Q-band features of the Mtb CYP51 UV-Visible absorption spectrum. The positions of these features, which are similarly positioned in other cytochromes P450 (158,217), indicate a thiolate-ligated, ferric, low-spin heme iron, thus confirming findings of UV-Visible, EPR, and resonance Raman studies of this P450. CYP51 was diluted to 150 – 200 μM in deuterated 50 mM HEPES, pH 7.5, and spectra were recorded using a JASCO J-500D circular dichrograph at room temperature and using a magnetic field strength of 6 Tesla.

The near infrared region MCD spectrum (between 800 nm and 1400 nm) for ligand-free CYP51 identifies a low-spin charge transfer band centred at 1110 nm with an intensity of 0.37 $M^{-1}cm^{-1}T^{-1}$. The position of the band is similar to that of other ligand-free, oxidised cytochromes P450 including P450 BM3 from *Bacillus megaterium* (1080 nm, (217)) and the *Mycobacterium tuberculosis* P450 CYP121 (1110 nm, (158)), and indicates that the heme of CYP51 contains a ferric iron molecule that ligates proximally to thiolate and distally to water. The spectrum obtained for fluconazole-bound CYP51 sample identifies a decrease in the intensity of the recorded band to 0.19 $M^{-1}cm^{-1}T^{-1}$ as well as the peak shifting to a longer wavelength of 1165 nm. Peaks at similar wavelengths have been observed for numerous systems including the cysteinate/histidine ligated heme 2 of the thiosulfate oxidation enzyme SoxAX from *Rhodovulum sulfidophilum* at 1150 nm and for the proline/cysteine ligated CooA at

105

1190 nm (221,222). Furthermore, peaks at 1180 nm and 1160 nm have been identified for the ligation of imidazole to P450 BM3 (218) and for fluconazole-bound Mtb CYP121 (unpublished data, Dr. H.E. Seward) respectively. This shows the result obtained for fluconazole-bound CYP51 to be consistent with the replacement of the distal water by the nitrogen of the azole group of fluconazole, and with the preservation of the proximal thiolate ligation. The EPR data (Chapter 3.1), recorded at 10 K, contradict this information, as they imply no coordination of the heme and the azole. This may indicate that thermal effects induced by freezing the sample for EPR cause this anomaly – since room temperature spectroscopy (both from UV-Visible absorption data and from MCD), as well as crystallographic studies (51) show the azole to coordinate with the heme iron of CYP51.
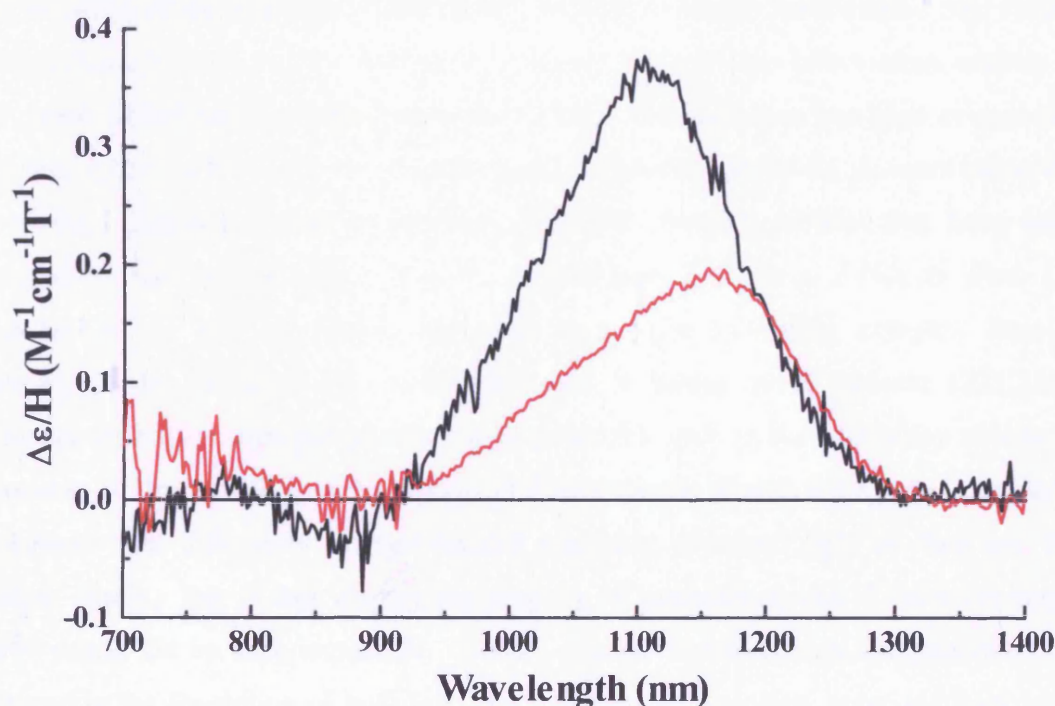
Figure 32 The near-infrared magnetic circular dichroism spectra of ligand-free CYP51 (black) and fluconazole-bound CYP51 (red). The MCD was performed at room temperature and the magnetic field strength was 6 Tesla. Spectra were recorded using a JASCO J-730 circular dichrograph. Enzyme samples were prepared at 150 – 200 μM and for the ligand-bound sample fluconazole was added as a solid until no further spectral changes observed. The data show ligand-free CYP51 to exhibit a broad peak of intensity 0.37 $M^{-1}cm^{-1}T^{-1}$ centred at 1110 nm, whilst the fluconazole-bound spectrum has a peak at 1165 nm with an intensity of 0.19 $M^{-1}cm^{-1}T^{-1}$.

Having made a thorough spectroscopic characterization of the heme of Mtb CYP51, subsequent sections focus on structural aspects of the P450, utilising circular dichroism to assess its secondary and tertiary structure in the presence and absence of a possible physiological redox partner protein. Additionally, the stability of the protein is assessed by UV-Visible and fluorescence spectroscopy in the presence of the chaotropic agent guanidinium chloride.

3.14 Circular dichroism of Mtb CYP51

Circular dichroism (CD) differs from the spectroscopy featured so far as, instead of focusing upon the properties of the heme of CYP51, CD spectroscopy in the far UV (~190 – 260 nm) and near UV (~260 – 320 nm) regions describe the protein environment of the enzyme. Additionally, moving to longer wavelengths (the visible range, typically from ~320 – 600 nm or beyond) also provides information relating to the heme chromophore of the cytochromes P450. The technique has been extensively utilised in the study of enzyme structure and is especially useful for demonstrating the secondary structure content of proteins (223,224). Indeed, proteins that have been studied by this method range from the cytochromes P450 (e.g. P450cam from *Ps. putida*) and *E. coli* flavodoxin reductase to a light harvesting complex from a photosynthetic bacterium (*R. acidophila*) and a human prion protein (223,224). Circular dichroism uses the principle that molecules such as the secondary structural elements of proteins (e.g. alpha helices and beta sheets) absorb left-handed circularly polarised light differently to right-handed circularly polarised light as they are, by nature, chiral – that is they display the property of handedness, and if rotated through 180° would not be superimposable. Hence, circular dichroism data are generated by measuring the absorption of both left- and right-handed circularly polarized light by a protein or any other chiral molecule. A difference spectrum is created from the data and, from the shape and magnitude of the features of a far UV CD spectrum, an assessment of the structural components of the protein can be made (223,224). In this study, spectra were recorded for both the far-UV and near-UV/Visible regions of the electromagnetic spectrum, as the two parts report on different properties of the protein. The far-UV region is more useful in predicting content of α-helices and β-sheets, whilst the near- UV/Visible region identifies features and chirality of incorporated

chromophores, such as the heme cofactor, as well as of the aromatic residues that comprise significant proportions of the protein (223,224).

Spectra were recorded on a Jasco J-715 CD spectrophotometer with the far-UV data recorded between 190 and 260 nm (Figure 33a), and the near-UV/Visible data recorded between 260 and 600 nm (Figure 33b). Temperature was maintained at 25 °C using a Jasco PTC348W1 Peltier system, and prior to recording the protein spectra a baseline was recorded using 50 mM KPi pH 7.4. Far-UV spectra were measured between 190 – 260 nm using protein diluted to 2 μM in a cell of pathlength 0.2 cm and with a scan rate of 10 nm/minute. Near-UV/Visible spectra were recorded between 260 – 600 nm using protein diluted to 10 μM in a cell of pathlength 0.5 cm at a scan rate of 20 nm/minute. In both cases, 5 accumulations of data were made and averaged to give the final results that were baseline corrected.

The far-UV CD data obtained for Mtb CYP51 shown in Figure 33a display a spectrum with a large positive peak at 195 nm as well as two smaller negative troughs at 208 and 224 nm. This spectrum is typical of the cytochrome P450 superfamily of enzymes and is comparable with those obtained for P450 BM3 from *Bacillus megaterium*, P450 BioI from *B. subtilis*, and P450cam from *Pseudomonas putida* (225-227). The features of the spectrum identify that CYP51 is predominantly composed of α-helices with little β-sheet contribution and also adds confidence that the structure is fully folded as no characteristic random coil spectrum is evident. Additionally, the spectrum is consistent with the known atomic structure of CYP51 (35,51) that reports a predominantly alpha helical composition.

The spectrum of Mtb CYP51 collected in the near-UV/Visible region identifies significant positive peaks at 287, 397, and 448 nm, and troughs at 345 and 427 nm. The peak at 287 nm pertains to the presence of several aromatic amino acid residues contained within the primary structure of CYP51, whilst the features between 390 and 450 nm are due to the presence of the heme of CYP51 and correspond to the same transitions that are responsible for the UV-Visible absorption spectra of this cytochrome P450. Furthermore, it is likely that the minor features of this spectrum observed between 500 and 600 nm relate to the transitions that generate the Q-band signals in the UV-Visible absorption spectrum (223-225). The near-UV/Visible spectrum is again typical of that obtained for the cytochromes P450 and compares favourably with those seen for P450cam from *Ps. putida*, and P450 BM3 from *B. megaterium*, whose features are similar in shape and intensity, although some variations exist between the spectra of

108

these proteins and that of Mtb CYP51. For example, the Soret band region features of these two enzymes are observed at approximately 410 nm compared to 427 nm for CYP51, whilst the trough feature at ~345 nm corresponding to the δ-band in UV-Visible absorption spectra (the shoulder between approximately 320 and 380 nm) of the *M. tuberculosis* enzyme is appreciably more pronounced than in the spectra of P450 BM3 and P450cam (225-227). Unfortunately, as the electronic transitions that underlie the spectral features observed in this region of the CD spectra are generally difficult to assign, it serves mainly as a fingerprint of the protein, and is of limited use in structurally interpreting differences in heme conformation or aromatic amino acid environment. Additionally, the near UV-Visible spectrum of Mtb CYP51 differs significantly from the UV/Visible spectrum of another Mtb cytochrome P450, CYP121, whose spectrum shows a positive feature (Cotton effect) in the region that corresponds to the Soret band (~419 nm), although features relating to the aromatic residues (~280 nm) and the δ-band (~350 nm) are found in similar positions (158). The intensity of the Mtb CYP121 feature at 280 nm is considerably smaller than observed for CYP51, most likely because the former is composed of approximately 5 % aromatic residues, whilst the latter possess far more (approximately 9 %) and is particularly replete in the tyrosine and tryptophan residues which have most influence at this wavelength (158).

In summary, the circular dichroism of CYP51 shows the enzyme to be a fully folded protein possessing a number of aromatic residues, a heme cofactor and a largely α-helical spectrum which confirms it to be typical of the cytochromes P450. In subsequent sections the stability of the protein is assessed by denaturation with guanidinium chloride, a chaotropic agent, and the interactions of Mtb CYP51 and a ferredoxin from the same organism are assessed by further circular dichroism studies.

a)

b)
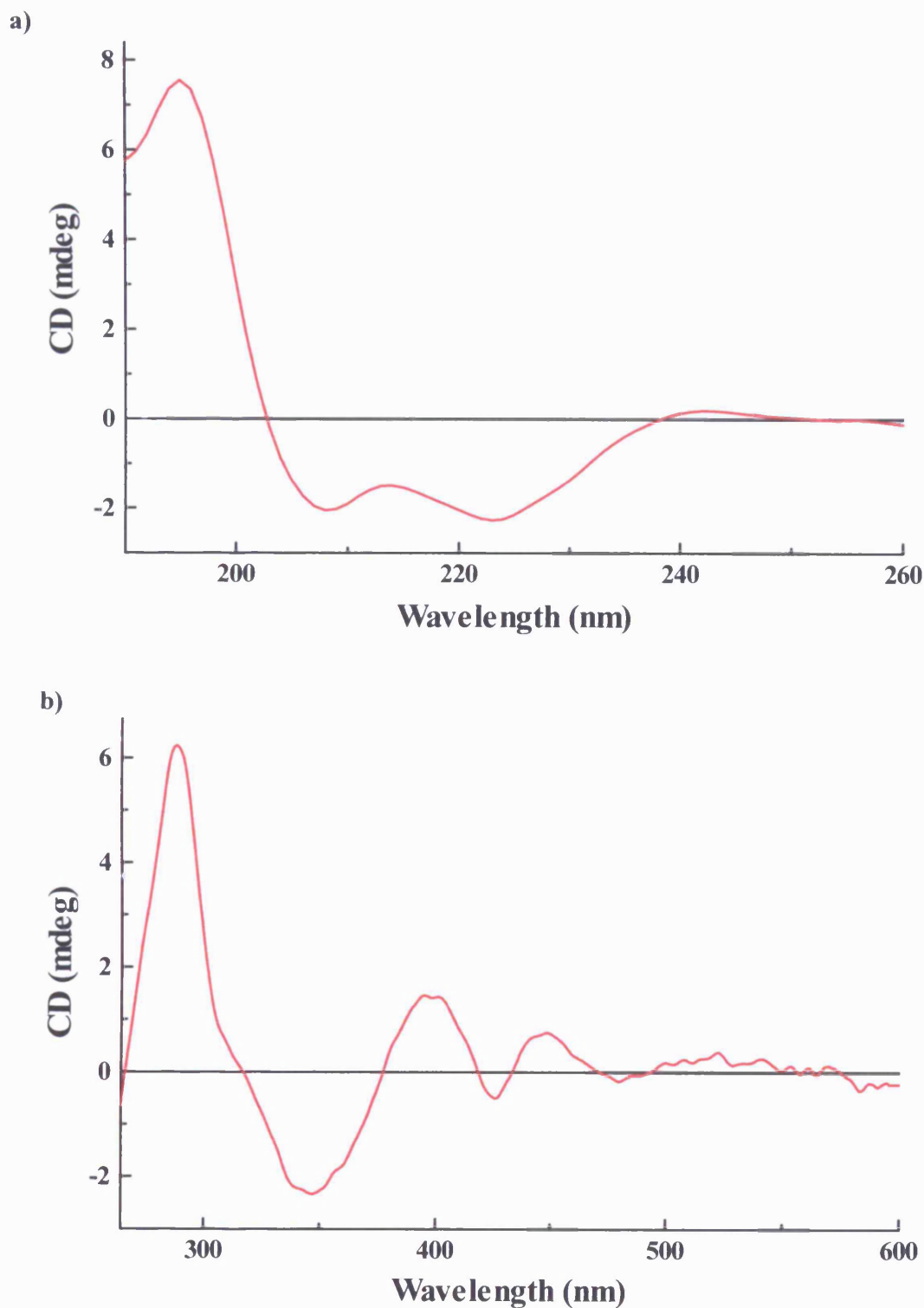
Figure 33 a) The Far-UV and **b)** Near-UV/visible CD spectra collected for CYP51. Spectra were recorded on a Jasco J-715 instrument using 2 μM and 10 μM CYP51, respectively. The far-UV spectrum maxima and minima are located at 195, 208, and 224 nm, and suggest a protein with high α-helical content. For the near-UV/Visible spectrum, maxima and minima are found at 287, 345, 397, 427, and 448 nm, and are indicative of the presence of a heme cofactor and aromatic amino acid residues in particular environments in the structure of CYP51.

3.15 Guanidinium chloride denaturation of Mtb CYP51

The nature and stability of the protein component of CYP51, and all cytochromes P450, is integral to their function as biological catalysts and as such it is important that these aspects are investigated thoroughly in order to define structure and structural stability of the protein. This is of particular importance if the P450 is to be exploited for biotechnological purposes, since loss of structural integrity and of catalytically competent binding to the heme chromophore will destroy enzyme activity. Hence, following the identification of the predominant secondary structural component as α-helical by circular dichroism (Chapter 3.14), an assessment of the stability of both the protein and heme binding was carried out using the chaotrope guanidinium chloride. Such chaotropic agents, which also include urea, cause disruption to the secondary and tertiary structure of proteins. These highly polar molecules are capable of forming multiple hydrogen bonds with appropriately charged or other hydrogen bond donor/acceptor regions of a protein, and as such out-compete other regions of the protein for these bonds. Subsequently, the protein unfolds as it cannot form sufficient hydrogen bonds to retain its secondary and tertiary structure, as these bonds are occupied by the chaotrope (228,229). Hence, by studying the influence of chaotropes on proteins over a range of concentrations, an understanding of the stability of general structure and of cofactor binding can be realised. The study can be performed using UV-Visible absorption spectroscopy, which predominantly provides data relating to the loss of cofactor, or by fluorescence spectroscopy which uses the intrinsic fluorescence of aromatic residues to report on the denaturation of the protein (and hence on the disruption of tertiary structure). These techniques are frequently used in studies of the stability of various proteins ranging from the dihydrofolate reductase of *E. coli* to bovine ribonuclease A, as well as rat CYP2B1 and P450 BM3 from *B. megaterium* (228,230,231). These studies of the cytochromes P450 have demonstrated that the chaotrope-induced heme dissociation and the loss of the protein's structural integrity typically occur over the same chaotrope concentration ranges (0.5 – 2 M), and are thus probably intrinsically interrelated. Subsequently, in this study both UV-Visible spectroscopy and fluorescence methods are utilised in order to best characterize the stability of the Mtb CYP51 and the robustness of its heme binding.

To observe the UV-Visible denaturation of CYP51 by guanidinium chloride (GdmCl), a Cary UV-50 UV-visible spectrophotometer scanning from 250 to 800 nm

was utilised. As for the study of P450 BM3 by Munro *et al.* (231), samples were prepared by mixing the appropriate volumes of buffer A and 8 M GdmCl (also in buffer A) to achieve final GdmCl concentrations over the range 0 to 8.0 M. Aliquots of enzyme were added to a final enzyme concentration of 2.3 μM. The solutions were incubated at room temperature for 10 minutes in order for the system to approach equilibrium, before an absorbance spectrum was recorded for the sample. The experiment was repeated across the same range of GdmCl concentrations on a Cary Eclipse fluorescence spectrophotometer using the same enzyme preparation (2.3 μM final concentration) and GdmCl stock solution. The fluorescence spectra were recorded by excitation of the pre-incubated sample at 290 nm (close to the absorption maximum for the aromatic amino acids), with subsequent emission spectra collected between 300 – 500 nm. All data were recorded at 30 °C to ensure consistency between samples and the two experiments.

The UV-Visible absorbance spectrum for the denaturation of CYP51 (Figure 34) identifies that the 419 nm Soret band of the CYP51 diminishes in intensity and shifts to shorter wavelengths as the concentration of GdmCl increases. These data demonstrate how the heme is affected as the protein disassembles in the presence of a chaotropic agent. Specifically, the absorption changes observed demonstrate the loss of ligation of the heme to the protein, followed by its dissociation from the protein matrix as the latter unfolds. Between 0 and 2 M GdmCl, complete conversion of the heme signal, which is related to its incorporation into the enzyme and its cysteinate ligation to the protein, from a native-like Soret band at 419 nm to a lower intensity feature more typical of unbound heme is observed. This is consistent with observations for rat CYP2B1 and P450 BM3 (230,231). It can also be seen that the alpha and beta band intensities diminish over the same concentration range as the protein structure denatures and the heme is lost. Above 2 M guanidinium chloride there is very little spectral change, which suggests that dissociation of the heme from the protein is completed by 2 M GdmCl. In this experiment, protein aggregation, visualised by a large baseline shift in absorbance spectra, occurs in the presence of 0.4 to 1 M GdmCl. The aggregation, also observed in the fluorescence spectra for CYP51 denaturation, appears to dissipate once the concentration of GdmCl reaches 1 M, and this may be a feature of the way in which the protein unfolds. That is, moderate unfolding leads to exposure of hydrophobic regions that promote aggregation of polypeptides. At higher concentrations of GdmCl,

these aggregates are dissociated and solubilised again by the high concentrations of the chaotrope.

The data from UV-visible spectroscopic analysis indicate that dissociation of the heme is completed in the range of 0 – 2 M GdmCl, which is comparable with previous studies of cytochromes P450 (230,231). In these studies it was indicated that the integrity of the protein structure was also lost over this range, and thus it was of interest to compare the UV-Visible data for CYP51 with those for general protein stability (using fluorescence to monitor structural disruption) in order to establish whether heme dissociation precedes structural loss, *vice versa*, or whether the two phenomena occur over the same GdmCl concentration range.
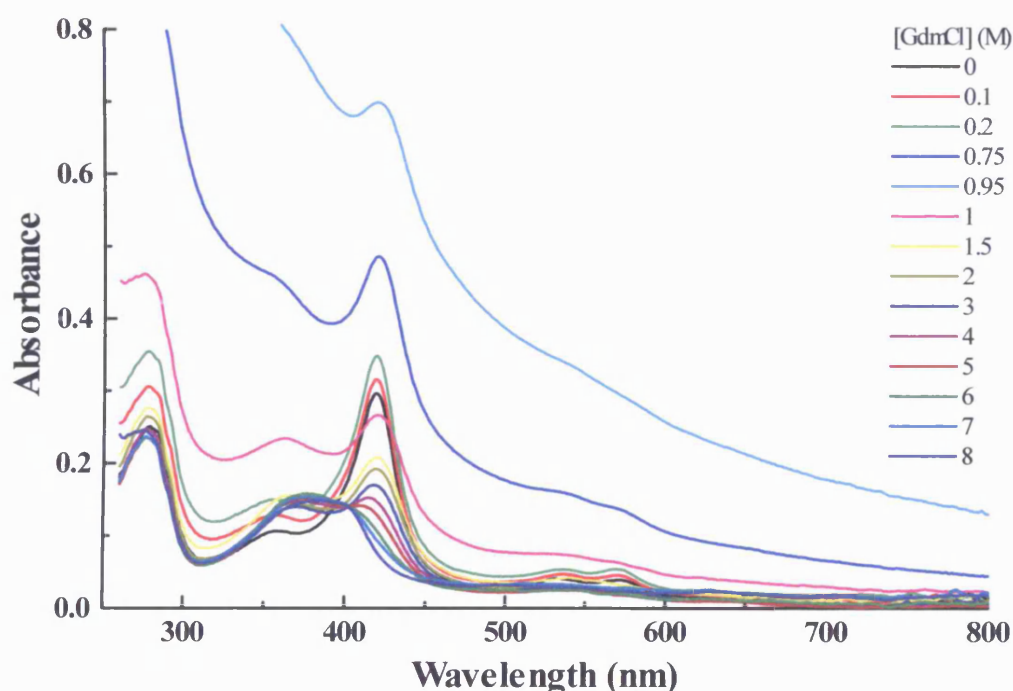
Figure 34 The UV-Visible spectra obtained for the guanidinium denaturation of CYP51 (~2.3 µM). Early spectra (0 – 1 M GdmCl) identify protein aggregation due to the exposure of hydrophobic residues when the protein is partially unfolded. Above 1 M GdmCl the aggregation dissipates as the protein unfolds further causing the Soret band at 419 nm to diminish as the heme ligation is broken. By 8 M GdmCl denaturation is complete and a species reminiscent of a free-heme, with a signal centred at 380 nm, is formed.

The fluorescence spectra recorded for CYP51 denaturation (Figure 35) identify a shift to longer wavelengths and a concomitant sharpening of the peak as the protein denatures in the presence of GdmCl. This change in the protein's fluorescence relates to previously 'quenched' aromatic residues (predominantly tryptophans) becoming more solvent exposed as the protein unfolds. The fluorescence change, which reflects loss of tertiary structure, is rather small between 0 – 1 M GdmCl. There is an increase in intensity (without any significant shift to longer wavelengths) above 0.4 M GdmCl that relates to protein aggregation due to the exposure of hydrophobic regions of the protein to the solvent. Above 1 M guanidinium chloride the aggregates disperse as more of the protein unravels due to the chaotrope. The fluorescence change is more marked at mid-range concentrations of guanidinium chloride (2 – 4 M), with a shift from 338 nm towards longer wavelengths, as well as an increase in intensity of the fluorescence. The spectra finally come to rest with emission maximum at 357 nm, a point where the protein is apparently completely denatured (8 M GdmCl). These data thus suggest that the secondary and tertiary protein structure is quite resilient to significant denaturing conditions (0 – 1 M GdmCl), but as the concentration increases further the protein unfolds more readily - as indicated by the increases in intensity of aromatic residue fluorescence and the shift in fluorescence maximum to longer wavelengths, consistent with more solvent exposure of the aromatic amino acids. When cross-referenced with absorbance spectra for this study, it appears that heme loss occurs quite early on during the denaturation (between 0 and 2 M GdmCl), and before the majority of protein unfolding occurs (i.e. above 2 M). This implies that while the protein itself is fairly stable to lower concentrations of the chaotrope, the coordination and binding of the heme to the CYP51 protein is less tolerant, and that heme quite readily dissociates from the protein matrix. The resilience of protein structure to the chaotrope appears to be greater for Mtb CYP51 than P450 BM3 and CYP2B1, as these proteins lose their secondary and tertiary structure between 0 and 2 M guanidinium chloride (230,231), and perhaps relates to differences in their environments (e.g. effects of detergents for CYP2B1) or the amino acids from which they are composed, and hence the degree of hydrogen bonding that maintains their folding.
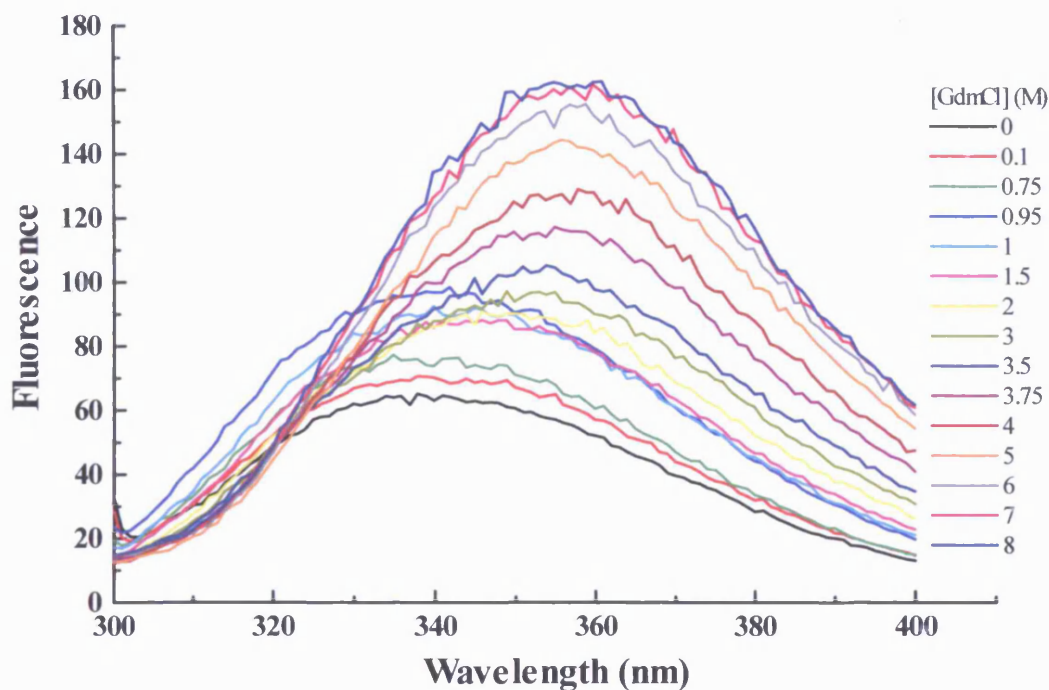
Figure 35 The fluorescence emission spectra obtained from the guanidinium chloride denaturation study of CYP51 (~2.3 μM). The samples were excited at 290 nm with emission spectra collected between 300 and 400 nm. Between 0 and 1 M guanidinium chloride the spectral changes (increase in intensity but no shift to longer wavelengths) may pertain to protein aggregation of the partially unfolded protein. Above 1 M guanidinium chloride the spectra shift from 338 to 357 nm as the protein denatures and the aromatic residues are solvent exposed. At 8 M chaotrope there are no further changes in the spectra, suggesting that denaturation is complete.

In order to quantify the fluorescence and UV-Visible absorption data gathered during the guanidinium chloride denaturation of Mtb CYP51, and verify that heme dissociation occurs prior to major structural disruption, the data were further analysed. This involved plotting the absorbance and fluorescence data at which maximal spectral changes occur (i.e. 419 nm for absorbance data and 357 nm for fluorescence data) *versus* GdmCl concentration. The resultant plots (Figure 36a and b) were fitted with a sigmoidal function (Equation 4) in order to determine the unfolding midpoint – i.e. the concentration of guanidinium chloride denaturant at which the protein unfolding is 50 % complete. Subsequently, the free energy (ΔG) of the unfolding processes was calculated for each set of data using Equation 5. As the UV-Visible absorption data report predominantly on the heme ligation in Mtb CYP51 and the fluorescence data predominantly relate to structural changes of the protein, comparisons of these values

115

will indicate whether heme dissociation and protein unfolding occur concomitantly or that one process precedes the other.

$$y = \left(A1 - A2/\left(1 + e^{((x-x0)/dx)}\right)\right) + A2$$

Equation 4 The sigmoidal function utilised to fit curves of absorbance at 419 nm or fluorescence at 357 nm *versus* concentration of guanidinium chloride (Figure 36a and b). In this equation A1 and A2 are, respectively, the maximal and minimal absorbance/fluorescence values, y is the absorbance or fluorescence at the given wavelength, x is the concentration of guanidinium chloride, x_0 is the concentration at which y is half maximal (i.e. the midpoint of unfolding event or K_u), and dx is the gradient of the slope at x_0.

$$\Delta G = RT \ln K_u$$

Equation 5 The equation utilised for the calculation of the Gibbs free energy (ΔG) of the unfolding of Mtb CYP51 in the presence of the chaotropic agent guanidinium chloride. In this equation R is the universal gas constant (8.3144 $J.K^{-1}.M^{-1}$), T is the temperature (in Kelvin) at which the experiment was performed, and K_u (M) is the dissociation constant determined for the unfolding event, as determined by Equation 4.

The fitting of the plots in Figure 36a and b with the sigmoidal function (Equation 4) determines a midpoint unfolding value (K_u) value of 2.39 ± 0.28 M for the absorbance data, whilst the K_u for the fluorescence data is 3.61 ± 0.12 M. When these stability constants are converted to free energies (ΔG) utilising Equation 5, the fluorescence data yields a value of 3.23 kJ whilst the UV-Visible absorption data value is 2.19 kJ. These values indicate that the energy associated with the heme dissociation is significantly less than for the loss of protein structure. Hence, the lower energy value identified for heme dissociation confirms the findings from the initial spectral data that indicate that heme is lost from Mtb CYP51 prior to large scale structural disruption. Although these data identify that the two events occur independently, there is likely to be some overlap between heme loss and protein unfolding, with minor structural changes occurring before heme dissociation is complete.

In the next section, the structure of Mtb CYP51 is further investigated, this time with respect to its interactions with a ferredoxin protein from *M. tuberculosis* that is postulated to be the physiological redox partner of this cytochrome P450.

a)
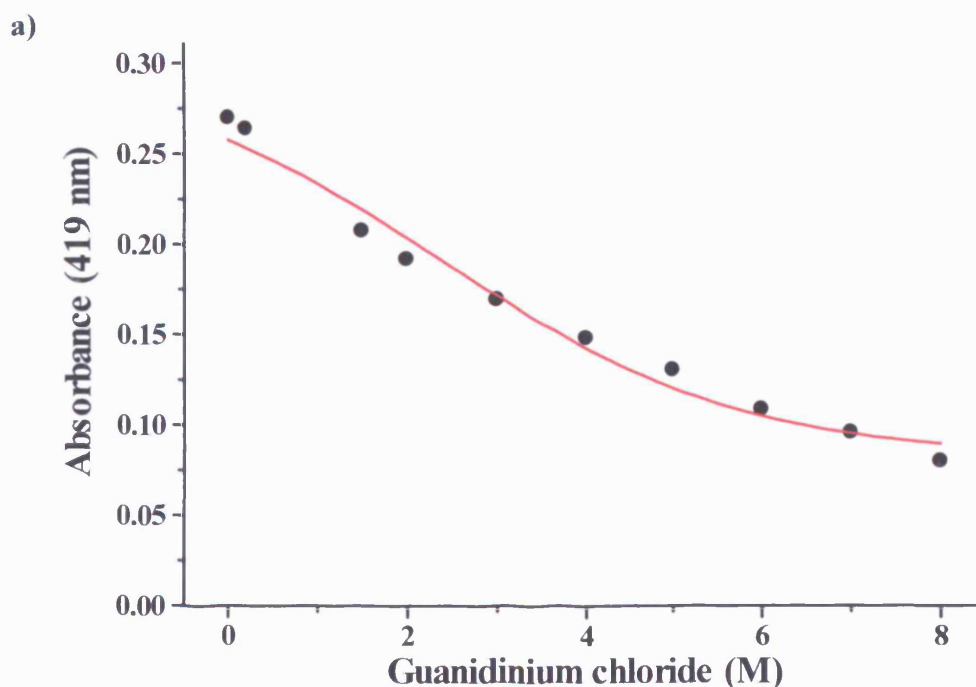
Figure 36 Plots of **a)** the absorbance at 419 nm and **b)** the fluorescence at 357 nm *versus* guanidinium chloride concentration utilised for the determination of the free energies of heme dissociation and protein unfolding of Mtb CYP51. Plots were fitted with a sigmoidal function (Equation 4) in order to determine midpoint unfolding (K_u) values for the two events. Points due to protein aggregation (i.e. between ~0.5 – 1.5 M) were excluded due to perturbation of the fitting process. A K_u of 2.39 ± 0.28 M was calculated from the UV-Visible data, whilst the unfolding (stability) constant for the fluorescence data was determined as 3.61 ± 0.12 M. Absorbance and fluorescence data were generated from the absolute spectra presented in Figure 34 and Figure 35 for the guanidinium chloride denaturation of this *M. tuberculosis* P450.

b)
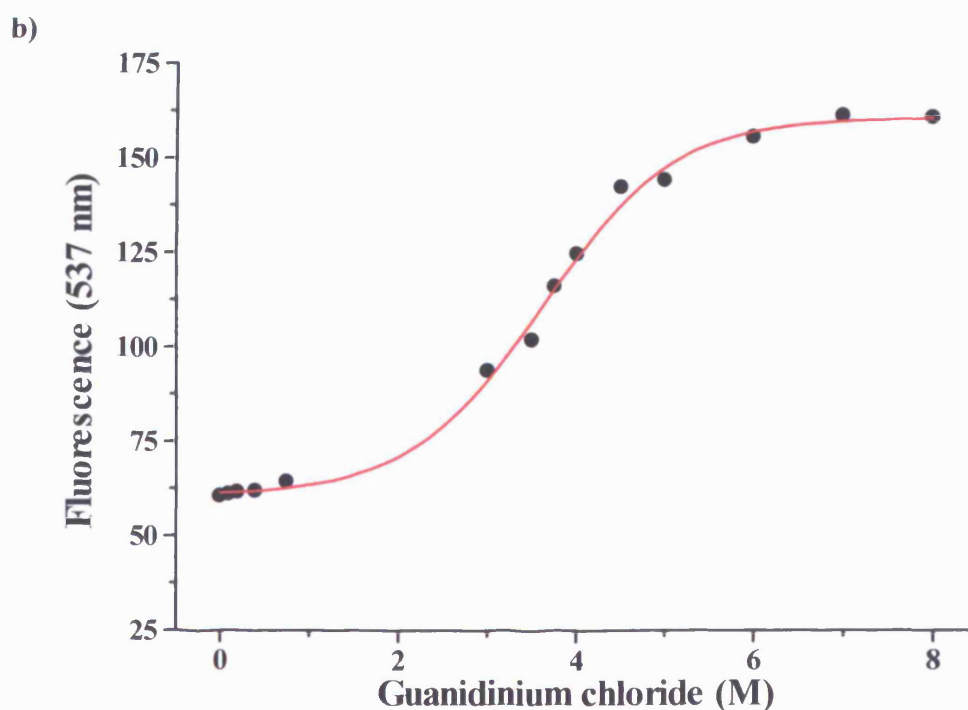
3.16 Circular dichroism of Mtb CYP51/ferredoxin interactions

In Chapter 3.2 the analysis of the region of the *M. tuberculosis* genome surrounding the *Rv0764c* (CYP51) gene identified an adjacent gene as encoding a putative ferredoxin protein (*Rv0763c*). This prediction was confirmed in work by Bellamine *et al.* (169), which characterized the gene product as a 68 amino acid protein with a broad UV-Visible spectrum. The UV-Visible spectral features at 412, 460, and 580 nm for the oxidised protein were consistent with a ferredoxin, whilst EPR and MCD studies confirmed the presence of a redox active 3Fe-4S centre. All cytochromes P450, with the exception of P450 BSβ from *Bacillus subtilis* (and its relatives, which interacts with hydrogen peroxide) and P450nor from *Fusarium oxysporum* (which binds NADH directly) (81-83,109), derive electrons via redox partner proteins (flavoproteins and ferredoxins) (131-133). Thus, as the *Rv0763c* gene-product exhibits the features of a ferredoxin with an iron-sulphur cofactor, it is postulated to be the physiological redox partner for the P450. Furthermore, as they lie besides one another on the genome it seems logical that the ferredoxin should be transcribed at the same time as the P450. Hence, as these two proteins are hypothesized to act as redox partners, the work in this section probes, by circular dichroism, for physical interactions between the ferredoxin and CYP51. As discussed in Chapter 3.14 circular dichroism reports on the secondary and tertiary structural properties of proteins, and previous studies have used this technique to provide evidence of protein:protein interactions (232), including that of a cytochrome P450 and a ferredoxin (233). Hence, it is hoped that structural changes induced by protein interactions can be identified spectrally, thus adding to existing evidence (based on electron transfer) that these proteins are physiological redox partners.

The CD spectra were recorded as in Chapter 3.14 using a Jasco J-715 CD spectrophotometer maintained at 25 °C. Both proteins were diluted in 50 mM KPi pH 7.4 and Near UV/Visible CD spectra were recorded between 260 and 600 nm. Studies in the Far UV region (190 to 260 nm) were not performed as this region reports predominantly upon the secondary structure (α-helices and β-sheets) of the proteins, which was not expected to change significantly during protein:protein interactions. CYP51 was used at 20 μM whilst the ferredoxin (donated by Dr. K.J. McLean, University of Manchester) was used at 285 μM in order to obtain spectra of similar intensity, as well as ensuring that high amounts of complex should be observed (i.e.

118

concentrations likely well in excess of the complex K_d). Initially, independent spectra of CYP51 and the ferredoxin were recorded. Spectra were then recorded for a mixture of the proteins at the same concentrations as had been used to record the initial CYP51 and ferredoxin spectra. A spectrum for the ferredoxin in the protein mixture was created by subtracting the initial CYP51 spectrum from the spectrum of the protein mixture (Figure 37a). The reverse subtraction was also performed (i.e. subtracting the initial ferredoxin spectrum from the mixture spectrum) to obtain the spectrum of the interacting CYP51 (Figure 37b). In both cases, comparison of the initial spectra with those of the corrected mixture spectra would reveal if changes in the spectral properties of the two proteins occurred on complexation. A further spectral comparison was performed by creating a spectrum of the protein mixture mathematically, by adding the initial CYP51 spectrum to the initial ferredoxin spectrum (Figure 37c). As the mathematical spectrum is created from two independently recorded data sets, it represents the spectrum expected if there are no interactions between the two proteins and serves as a comparison for the protein mixture spectrum. Hence, the data presented in this section represent structural studies to determine whether interactions between a P450 from Mtb (CYP51) and the product of an adjacent gene (a ferredoxin) can be measured by CD, and to provide complementary data to those from kinetic studies on these putative physiological redox partners.

The spectra presented in Figure 37 show the results of these circular dichroism studies. It can be seen in Figure 37a that the spectrum of the ferredoxin in the protein mixture shows only very slight differences to the initial ferredoxin spectrum. The positions of major peaks and troughs are the same, as is the overall shape of the spectrum. Equally, the spectra observed for CYP51 before and after mixing with the ferredoxin show very little perturbation of the obtained signals (Figure 37b). Although small spectral differences are observed for the mixture of proteins, it seems most probable that these are related to the slight variations in concentrations of the solutions of protein used. These results imply that any interaction between the ferredoxin and CYP51 does not noticeably affect the CD spectra of these proteins. This is further confirmed by comparing the mathematical protein mixture spectrum with the true spectrum obtained for the protein mixture (Figure 37c), again suggesting that no interaction that alters the CD spectrum is determinable. The most likely implication that can be drawn from these data is that the interaction between the P450 and ferredoxin from *M. tuberculosis* is transient and peripheral, and does not impact

significantly (or detectably) on conformational properties of either protein. However, it is plausible that there is a more stable interaction that is spectrally silent and thus not detected by this technique. In later sections (Chapter 3.23) the results of stopped-flow kinetic assays are discussed which serve to shed further light upon the interaction of the two *Mycobacterium tuberculosis* proteins.
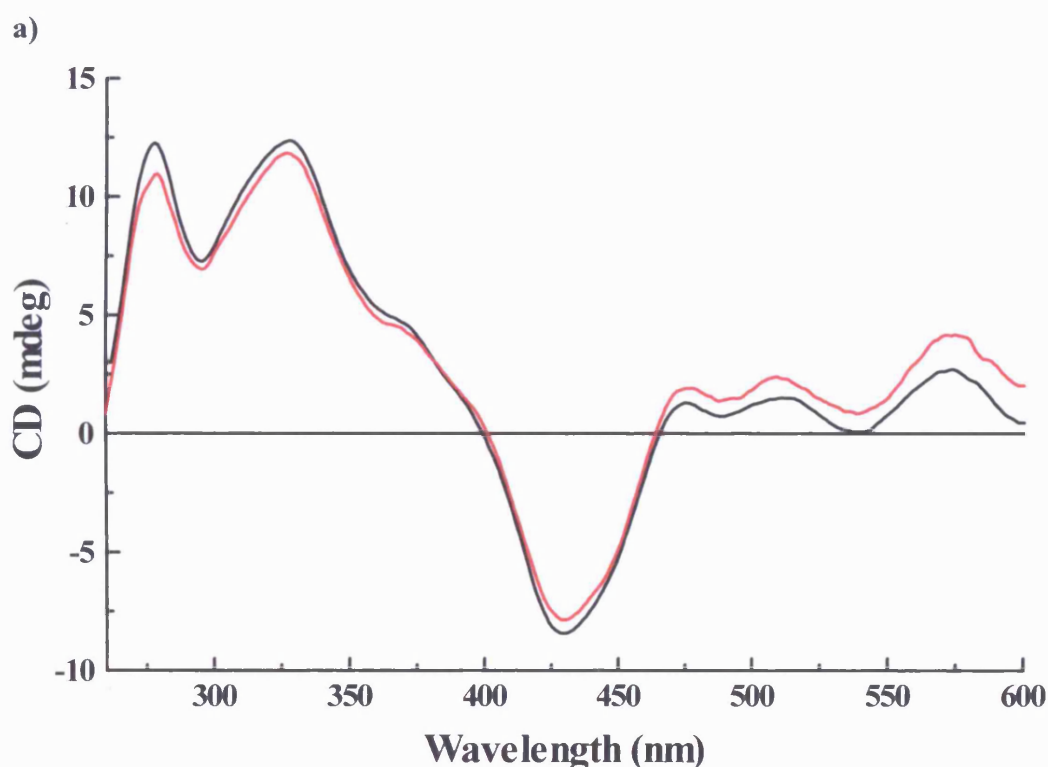
a)

Figure 37 a) The Near UV-visible CD spectra of *M. tuberculosis* ferredoxin in the absence (black) and presence (red) of Mtb CYP51. Spectra were produced under identical conditions using a JASCO J715 spectropolarimeter collecting data between 260 and 600 nm. The concentrations of CYP51 and ferredoxin are 20 and 285 µM respectively prepared in 50 mM KPi pH 7.4. **b)** The CD spectra of CYP51 in the absence (black) and presence (red) of the Mtb ferredoxin. **c)** The CD spectra of the mixture of CYP51 and ferredoxin (black) and the mathematical additive spectrum (red) produced by addition of the individual ferredoxin and CYP51 spectra. In all three sets of spectra, alterations in signal intensity are observed, but there are no major changes in the positions or shapes of the bands observed. It is concluded that the interactions between the ferredoxin and the CYP51 does not give rise to major changes in chirality of the heme chromophore or arrangement of aromatic amino acids (that contribute CD features in the near UV range). Thus, it is likely that transient and peripheral contacts occur between the ferredoxin and CYP51, as is frequently seen for redox partner proteins.

b)

c)
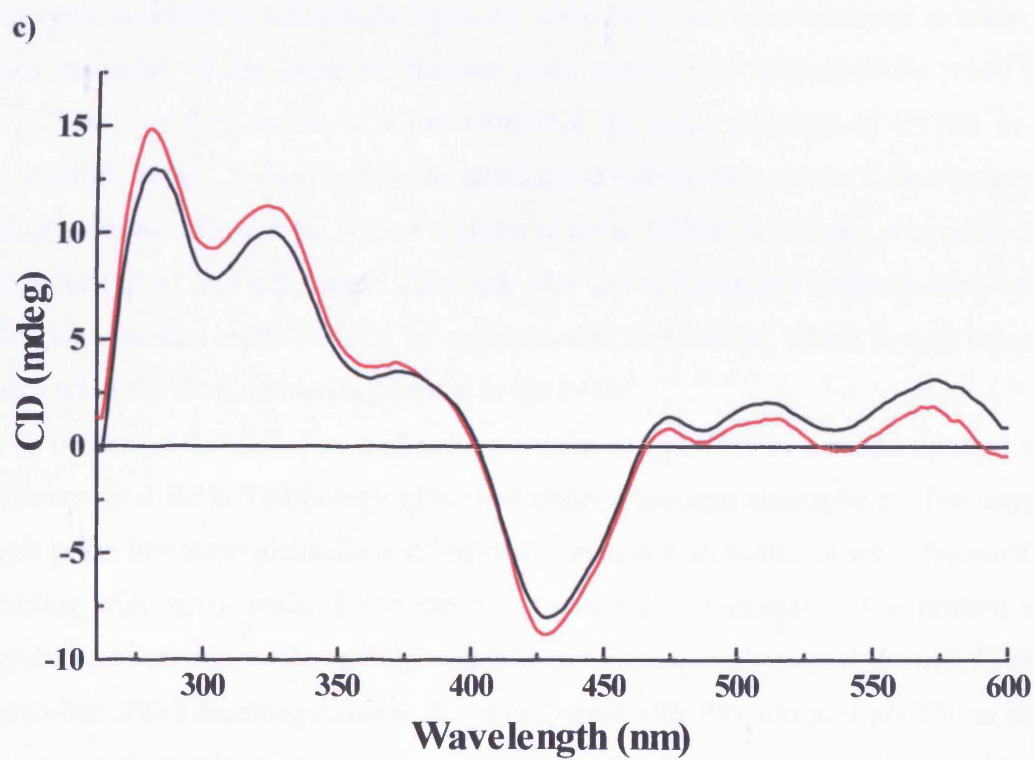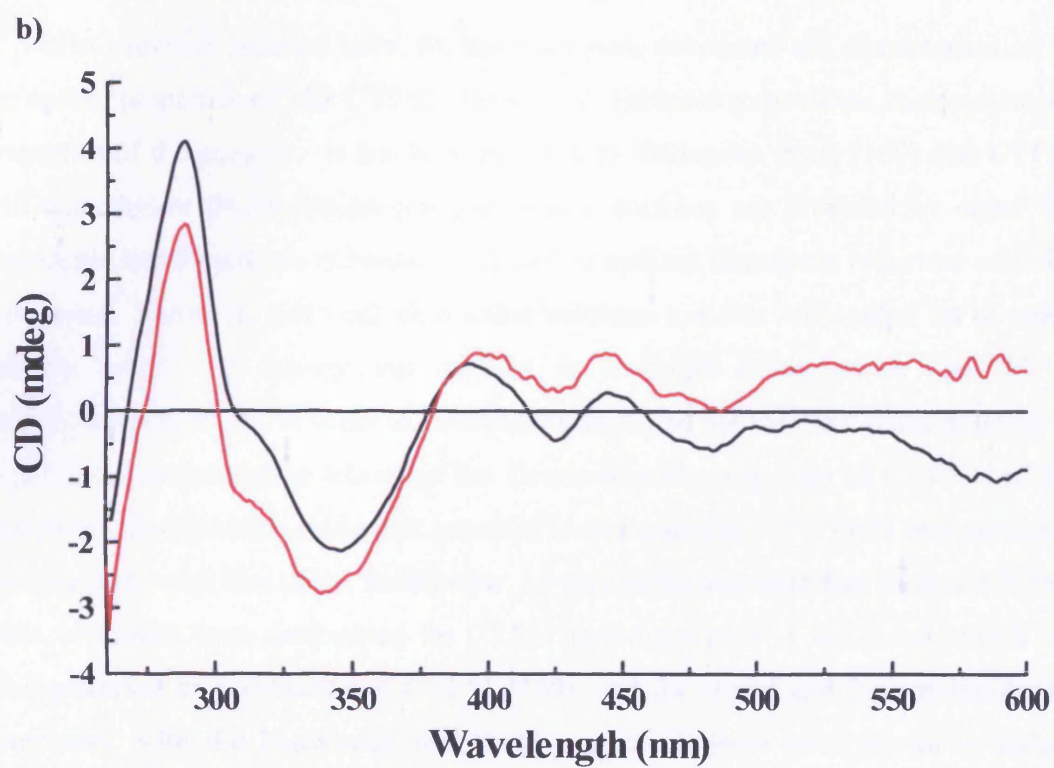
3.17 Determination of Mtb CYP51 mid-point reduction potentials

Whilst previous sections have, for the most part, concerned the characterization of the optical properties of Mtb CYP51, this section discusses some of the thermodynamic properties of the enzyme. It has been reported by Bellamine *et al.* (169) that CYP51 will demethylate 24,25-dihydrolanosterol when electrons are provided by either the flavodoxin and flavodoxin reductase of *E. coli* or spinach ferredoxin reductase and Mtb ferredoxin. However, this work shows that substrate turnover with either set of redox partners occurs very slowly and requires an overnight incubation to yield 20 % demethylated product. In order to determine whether or not the slow demethylation of 24,25-dihydrolanosterol is related to the thermodynamic properties of CYP51 and the ferredoxin, the reduction mid-point potential (redox potential) of CYP51 was measured and compared with that of the ferredoxin. As well as the substrate-free form of CYP51, redox potentials were determined for CYP51 in the presence of lanosterol, which has been proposed as a substrate of CYP51 (169), and for estriol and 2-phenylimidazole complexes, with the knowledge that these compounds have been shown to induce optical shifts indicative of a switch in the equilibrium of the heme iron from low- to high-spin. In previous redox potential studies, compounds which appear to shift the spin-state equilibrium towards the high-spin form have also been observed to cause the redox potential of the heme to become more positive by approximately +140 mV (117,234). For this reason, it is important that the redox potential of CYP51 in the presence of estriol, 2-phenylimidazole and lanosterol is studied, as the values generated will give further affirmation to their abilities to act as CYP51 substrates or to mimic the natural effects of true substrates. They may also add to further the understanding of the reduction potential shifts induced by substrate-like compounds, which in turn enhance electron transfer from the redox partners to the P450.

To determine the reduction mid-point potential of Mtb CYP51 a redox titration was performed in a Belle Technology glove box under a nitrogen atmosphere. The oxygen levels in the box were maintained at less than 2 ppm and all solutions were degassed by bubbling with argon under a vacuum to remove residual oxygen. The protein was introduced to the anaerobic environment and was subsequently passed down a BioRad Econo-Pac 10DG desalting column, pre-equilibrated with 100 mM KPI pH 7.0, in order to purge the sample of any enduring oxygen. Further dilution of the enzyme in degassed 100 mM KPI pH 7.0 (containing 10 % glycerol to aid protein stability during

the experiment) was performed to achieve a concentration of ~10 μM in a final volume of 5 ml. Included in this solution were a number of mediator compounds (i.e. 7 μM 2-hydroxy-1,4-naphthoquinone, 2 μM phenazine methosulfate, 0.3 μM methyl viologen, and 1 μM benzyl viologen) which act to facilitate electronic interactions at the enzyme/electrode interface across a range of potentials from +100 to –480 mV (17). The enzyme titration was performed using the technique of Dutton (235) by adding small volumes (typically 0.2 – 1.0 μl) of a sodium dithionite solution (typically 10 – 50 mM) to the protein solution in order to progressively reduce the enzyme. This was followed by a reverse titration using potassium ferricyanide (also 10 – 50 mM) which returned the sample to the oxidised form. After each addition of reductant (or oxidant) the electrode was allowed to equilibrate for at least 10 minutes before an absorbance spectrum was recorded, using a Cary UV-50 Bio UV-Visible spectrophotometer scanning between 250 and 800 nm. At the same time the electrochemical potential of the solution was recorded using a Pt/Calomel electrode (Thermo Russell Ltd.), calibrated using the Fe^{3+}/Fe^{2+} EDTA couple as a standard (+108 mV), linked to a pH meter (Hanna pH 211) set to read in mV. The data were analysed and corrected by +244 mV to give results relative to a standard hydrogen electrode (17). Plots of data at wavelengths best reflecting the change between oxidised and reduced forms of the enzyme versus the applied potential were created. The data were fitted to a single-electron Nernst function (Equation 6) using Origin software (Microcal) to define the midpoint reduction potential for the Fe^{3+}/Fe^{2+} transition of the CYP51 heme iron. Having performed this study, further redox titrations were then performed using precisely the same method as for the substrate-free CYP51 experiment. Attempts were made to record a redox potential for CYP51 in complex with lanosterol whilst data were also acquired for CYP51 in the presence of near-saturating concentrations of estriol (90 μM) and 2-phenylimidazole (7.5 mM).

$$A = \left(A_{abs} + B_{abs} \times 10^{\left((E^0 - E)RTF\right)}\right) / \left(1 + 10^{\left((E^0 - E)RTF\right)}\right)$$

Equation 6 The single-electron Nernst equation used for fitting absorption *versus* potential curves to determine mid-point reduction potentials of the Mtb CYP51 and ferredoxin proteins. A is the absorption determined at the various midpoint potentials (E, corrected *versus* the hydrogen electrode), A_{abs} and B_{abs} are the maximal and minimal absorbance values (for oxidised and reduced forms, respectively), and E^0 is the midpoint reduction potential of the redox centre under investigation. RTF is a constant derived from the universal gas constant, absolute temperature (in Kelvin), and the Faraday constant.

The UV-visible absorption spectra recorded during the experiment to identify the reduction mid-point potential of substrate-free CYP51 are shown in Figure 38. The initial spectrum of the oxidised form of the enzyme is identical to those shown in previous sections (Chapters 3.4) with a Soret band at 419 nm and alpha and beta bands at 571 and 537 nm respectively. During the redox titration, the Soret band of CYP51 decreases in intensity and shifts to longer wavelengths whilst concomitant increases in the intensities of the alpha and beta bands are identified. When complete reduction of the enzyme has been achieved, the final position of the Soret band is located at 423 nm and isosbestic points are found at approximately 405 and 430 nm which indicate a clean transition from the oxidised to reduced form of the enzyme. In the reduced enzyme, there are also substantial changes in the visible region – with the development of a sharp peak at 558.5 nm that overshadows the smaller band at 530 nm.
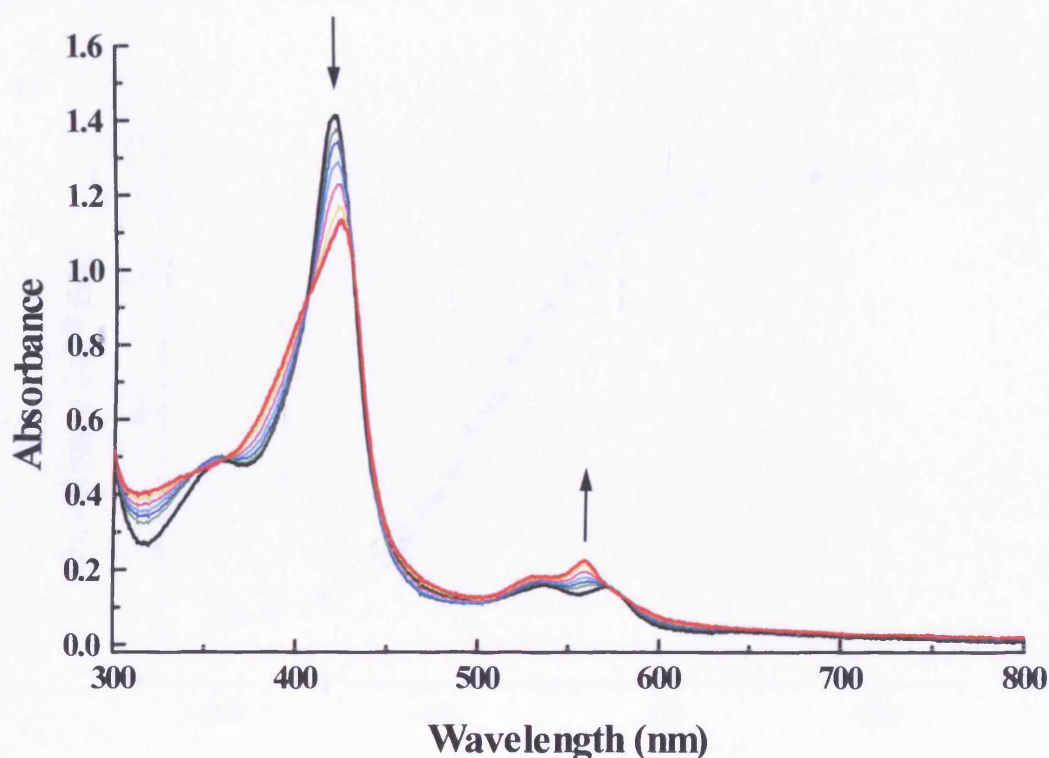
Figure 38 Selected UV-Visible absorption spectra recorded during the redox titration of ligand-free Mtb CYP51 (10.5 μM). The spectrum of oxidised CYP51 (black), prior to the redox titration, identifies the characteristic Soret band at 419 nm and alpha and beta bands at 571 nm and 537 nm respectively. The fully reduced form of CYP51 (red) exhibits a Soret peak of decreased intensity at 423 nm whilst there is development of a band centred at 558.5 nm with increased intensity over the features of the oxidised CYP51. Two isosbestic points, at 405 and 430 nm, identify that there is a clean transition from the oxidised form of the enzyme to the reduced form during the redox titration. The arrows indicate the direction of spectral changes at their respective positions.

The obtained spectral data and associated potentials were analysed by plotting the change in absorbance at each of three independent wavelengths (385, 419, and 558 nm) against the corrected reduction potentials. The resultant sigmoidal curves (Figure 39) were fitted with a single-electron Nernst equation (Equation 6) and the mid-point reduction potentials obtained (Table 9). The first two wavelengths (385 and 419 nm) were selected as they describe spectral changes at (419 nm) and close to (385 nm) the Soret feature of CYP51 whilst the third wavelength (558 nm) was chosen as it monitors the changes in the visible region associated with the heme Fe^{3+}/Fe^{2+} transition. Essentially identical spectral changes were observed in both the oxidative and reductive directions. The results of the three separate redox potential determinations are summarised in Table 9 and are all in agreement, within an acceptable margin of error, that the mid-point reduction potential of the heme iron of *M. tuberculosis* CYP51 is – 375 ± 5 mV (against the standard hydrogen electrode).

a)
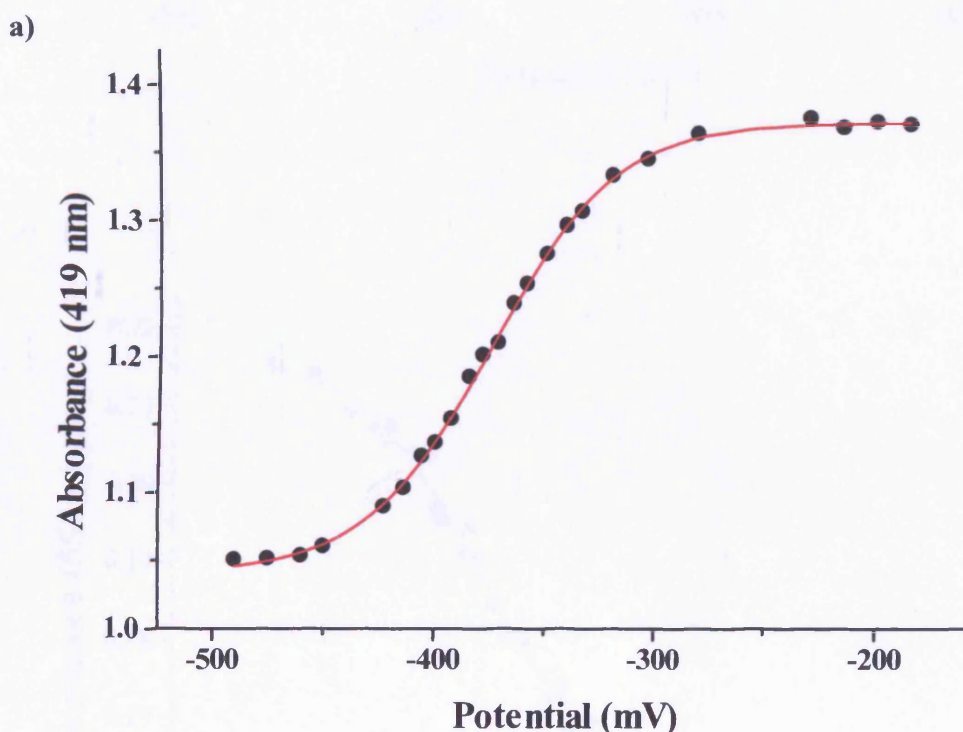
Figure 39 a) The absorption *versus* potential curve representing the spectral changes observed at 419 nm during the redox titration of Mtb CYP51. These data were produced from the recorded UV-Visible absorption spectra and potentials are fitted to the single-electron Nernst equation (Equation 6) that identifies the heme iron redox potential as –375 ± 5 mV. **b)** and **c)** show the Nernst-fitted absorption *versus* potential curves representing the spectral changes observed at 385 and 558 nm, and determine the redox potential of CYP51 as –370 ± 5 mV and –378 ± 7 mV respectively. All potentials are shown in mV and are normalised against a standard hydrogen electrode (SHE).

b)
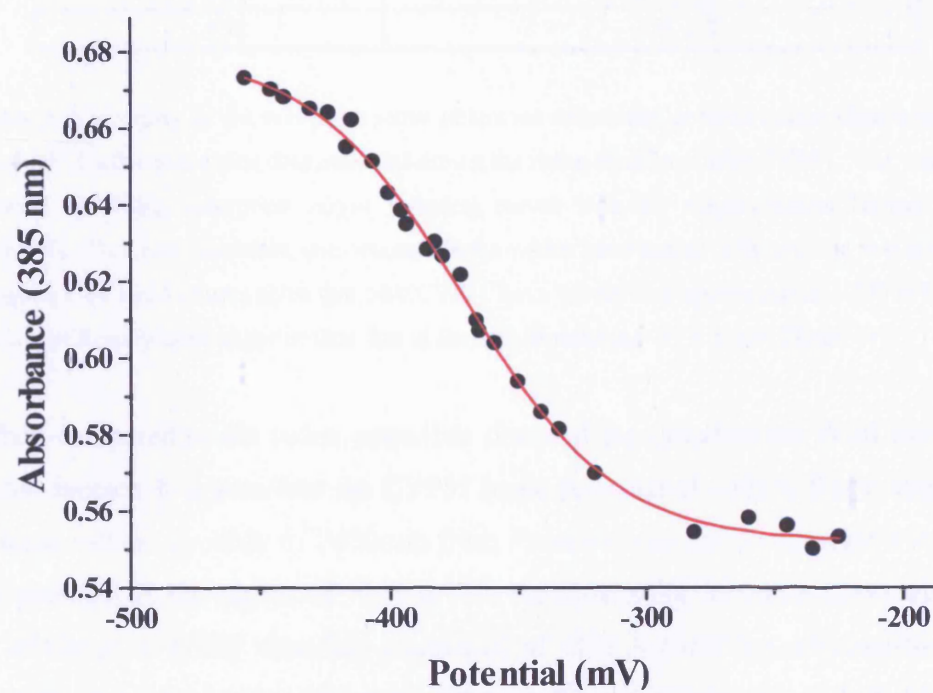
c)
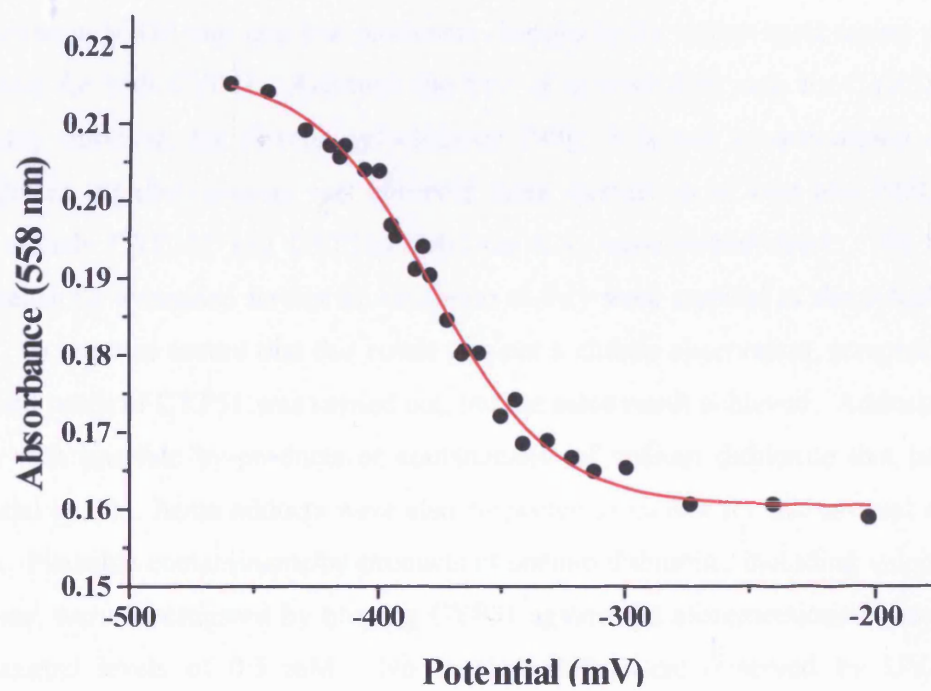
Wavelength (nm)	Mid-point reduction potential (mV)
385	−370 ± 5
419	−375 ± 3
558	−378 ± 7

Table 9 A summary of the mid-point redox potentials determined at three independent wavelengths from the UV-Visible absorption data collected during the redox titration of Mtb CYP51. The values were determined by fitting absorption *versus* potential curves with the single-electron Nernst equation (Equation 6). The three potentials, one obtained in the visible band region (558 nm) and two in the Soret band region (385 and 419 nm) agree that Mtb CYP51 has a potential of approximately −375 mV, a value which is significantly more negative than that of the Mtb ferredoxin (−31 ± 5 mV, Figure 41).

When compared to the redox potentials obtained for cytochromes P450 from other bacterial species, it is seen that the CYP51 heme potential of −375 ± 5 mV aligns well with these values. A study of P450cam from *Pseudomonas putida* revealed it to have a redox potential in the region of −300 mV in the absence of substrate (234) whilst the work of Ost *et al.* (192) identified a potential of −427 ± 4 mV for substrate-free P450 BM3 from *B. megaterium*. However, although the redox potential of Mtb CYP51 is comparable with previously characterized bacterial cytochromes P450, the optical shifts recorded are quite distinct. Reductive titrations for certain other well-characterized P450s (192,194) typically display a shift of the Soret band to shorter wavelengths (approximately 410 nm) and less prominent changes in the visible band region than are observed for Mtb CYP51. Although the type of spectral shift seen for CYP51 is not normally observed for ferrous cytochromes P450, it is not as uncommon as first thought, as the phenomenon was observed more recently in at least two P450s from Mtb, namely CYP121 and CYP144 (McLean K.J., unpublished data). The CYP51 spectral shifts warranted further investigation as they were atypical of the cytochromes P450. In order to ensure that this result was not a chance observation, a repeat with a different batch of CYP51 was carried out, but the same result achieved. Adducts of the heme with possible by-products or contaminants of sodium dithionite that have the potential to form heme adducts were also suspected as causes for the unusual spectral shifts. Plausible contaminants/by-products of sodium dithionite, including sulphite and sulphate, were investigated by titrating CYP51 against the aforementioned compounds at maximal levels of 0.5 mM. No spectral shifts were observed by UV-visible spectrometry suggesting that the unusual shift seen in CYP51 is indeed accreditable to the spectrum of the ferrous P450, and not due to heme adduct formation.

Further research into the spectral phenomena seen for CYP51 identified a very similar feature for a mutant (H93G) of another heme containing protein, sperm whale myoglobin (236). In this study, a thiol-ligated ferrous form of the enzyme was created when sulphur was donated by cyclopentanethiol and tetrahydrothiophene, and gave spectral shifts akin to those witnessed for CYP51. When this work is taken into consideration, it appears feasible that the UV-Visible absorption spectral changes pertain to the protonation of the cysteine residue (Cys 394), which ligates proximally to the heme of CYP51, during the reduction titration. This protonation, which would convert the thiolate ligand to a thiol ligand, may also give rise to the formation of the inactive P420 form of the enzyme. This form of the reduced, CO-complexed enzyme, which derives its name from the position of its Soret maxima, has been seen to rapidly develop following the creation of the P450 species of CYP51, and is further investigated in Chapter 3.18.

As previously mentioned, redox potential studies were also performed in the presence of a number of known Mtb CYP51 substrate and substrate-like molecules in order to determine their effects on the potential of the enzyme. Attempts were made to perform redox titrations of CYP51 in the presence of lanosterol, as studies have suggested that this compound is utilised by the enzyme in its role as a 14α-sterol demethylase (169). However, due to the adverse effects of the solvent in which lanosterol was dissolved on the CYP51 protein solution, and the inclination of lanosterol to precipitate in assay buffer, even at relatively low concentrations, no mid-point reduction potential could be determined for CYP51 in the presence of this compound.

The determination of the mid-point reduction potential for estriol-bound CYP51 was more fruitful, as estriol is significantly more soluble in assay buffer than lanosterol. The UV-Visible spectra and resultant absorption *versus* potential curve for CYP51 in the presence of a near-saturating concentration of estriol (90 µM), determined by binding studies, are shown in Figure 40. The initial spectrum of the estriol-bound form shows the CYP51 Soret band to have a diminished intensity and to be split between two wavelengths (approximately 414 and 395 nm), as is observed in binding studies, which relate to the high- and low-spin components. During the redox titration, the spectral changes in the Soret band region are similar to those observed for the substrate-free CYP51, with a shift to longer wavelength (424 nm), although the intensity of this band remains lower than that of the substrate-free form. The changes in the visible region

bands exhibited by ligand-free CYP51 are echoed when estriol is present, with a sharp peak developing at 558.5 nm, as well as a less intense peak centred at 530 nm. The fitting of the absorption *versus* potential curve with the single-electron Nernst equation (Equation 6) identified the mid-point reduction potential of estriol-bound CYP51 as – 225 ± 10 mV. This value is 150 mV more positive than that of ligand-free CYP51 and is reminiscent of potential shifts observed for P450 BM3 and P450cam when substrate is introduced to the titration (117,159,234). A redox titration was also performed for CYP51 in the presence of a near-saturating concentration of 2-phenylimidazole (7.5 mM). The spectral changes observed for this titration were quite similar to those of the estriol-bound CYP51 titration. Again, the Soret band shifts to longer wavelengths (424 nm) while in the visible region there is development of a strong feature at 558.5 nm, which is of higher intensity than the second band present at 530 nm. Due to the poor affinity of 2-phenylimidazole for CYP51 it was necessary to use a very high concentration of this ligand (7.5 mM). This had detrimental effects on the quality of the optical data collected, and hence these spectra are not presented. Over the time course of the experiment, 2-phenylimidazole was seen to slowly precipitate out of solution, which consequently induced protein aggregation. Despite these difficulties, a mid-point reduction potential was calculated for the 2-phenylimidazole-bound enzyme at –220 ± 20 mV, a change in potential of approximately +150 mV with respect to the ligand-free enzyme. This shift in redox potential is comparable to that of the shift witnessed for estriol-bound CYP51, as well as those observed for P450cam and P450 BM3 (117,234), and further adds to the theory that catalysis is enhanced by a substrate binding event which raises the potential of the heme to a value which is more favourable to electron transfer from the redox partners to the P450. Although estriol and 2-phenylimidazole binding induces such a sizeable shift in the reduction potential of CYP51, it is unlikely that these are physiological substrates for CYP51. The imidazole compound has no known roles in physiology of any organism, whilst as discussed in Chapter 3.9, estriol lacks the methyl group at C_{14} that is removed during the reaction catalysed by CYP51s from other organisms (19,126,165). Any physiological relevance attached to this compound would have to involve oxygenation of the steroid at another position by this Mtb P450. Furthermore, as no sterol/steroid compounds are produced endogenously in *M. tuberculosis*, the only plausible source of this compound is from the host environment (i.e. the infected human). This route for acquirement of substrate is a possibility, and has been observed for other invasive pathogens including *Plasmodium*

falciparum (237). However, the evidence suggests that it is unlikely that estriol is a substrate of Mtb CYP51 and that its substrate-like binding properties are more likely to relate to its structural similarity to 14α-methylated sterols. Mtb CYP51 has ability to demethylate eukaryotic 14α-methylated sterols, but it remains a possibility that this activity is not relevant to a physiological function for CYP51 in *M. tuberculosis*, and instead is relic of an ancient activity in the CYP51 family.
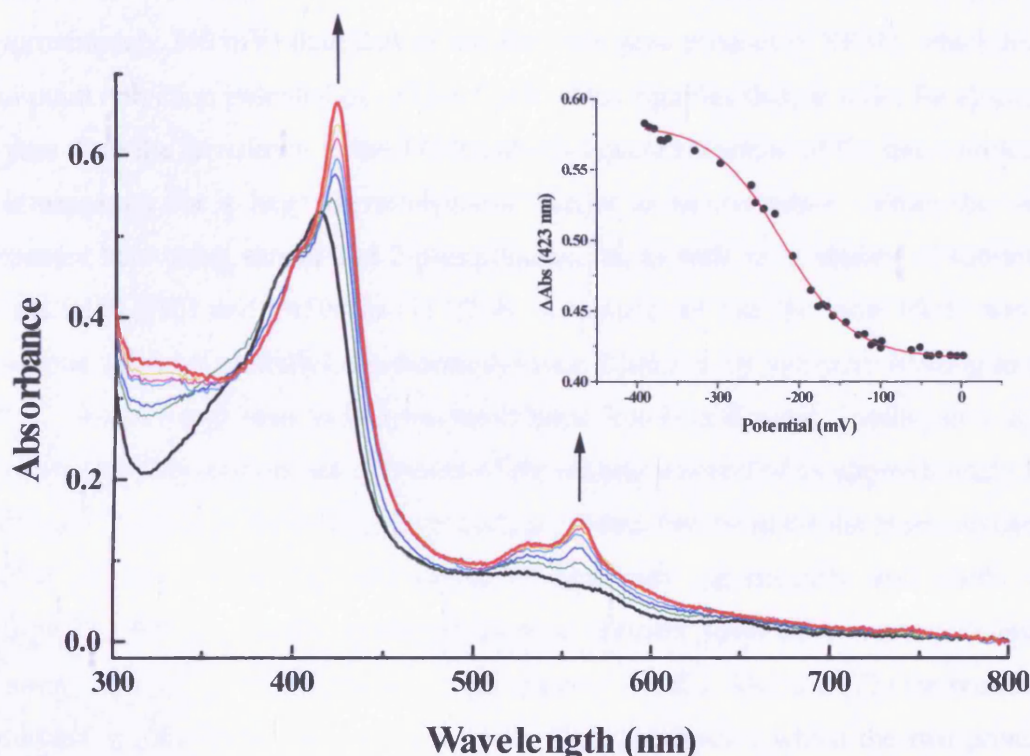
Figure 40 A selection of the UV-Visible absorption spectra recorded during the redox titration of estriol-ligated Mtb CYP51 (5 μM). At the start of the titration the oxidised, estriol-bound enzyme (black) has a mixed-spin Soret band with features at 414 and 395 nm. When the titration is complete the UV-Visible spectrum of the reduced enzyme (red) exhibits a Soret band at 424 nm and a large peak at 558.5 nm in the visible region. The arrows indicate the direction of spectral changes at the Soret band and visible regions during the titration, and identify that at both points there are increases in the intensities of the bands in the reduced enzyme. Isosbestic points at 365 and 412 nm attest to a clean transition from the oxidised to reduced form of the enzyme, although these are less clear than for the ligand-free CYP51 titration due to protein precipitation induced by the presence of estriol and solvent. The inset shows a plot of absorption change at 423 nm *versus* potential (normalised to a standard hydrogen electrode) fitted to the single-electron Nernst equation, and indicates the potential of the estriol-bound CYP51 heme iron as −225 ±10 mV. The value is ~150 mV more positive than the potential of ligand-free CYP51 and shows that estriol is capable of raising the heme potential in a similar manner to substrates of other P450s, such as P450 BM3 (117,234).

The midpoint reduction potential for the purified *M. tuberculosis* ferredoxin (Fdx) was determined in work by Dr. K.J. Mclean (159) as -31 ± 5 mV. The UV-Visible spectra and associated absorption *versus* potential curve are shown in Figure 41 and demonstrate that during the reduction titration the 3Fe-4S signal diminishes in intensity in the region between the two isosbestic points at approximately 385 and 570 nm, with a concomitant increase in absorption focused around 650 nm. The redox potential value obtained for the Mtb ferredoxin (-31 ± 5 mV) is considerably more positive (approximately 340 mV) than that of the *Rv0764c* gene product (CYP51), which has a mid-point reduction potential of -375 ± 5 mV. This signifies that, in order for electrons to pass from the ferredoxin to the P450 and subsequent reduction of the heme to occur, it is necessary for a large thermodynamic barrier to be overcome. From the work presented here using estriol and 2-phenylimidazole, as well as in studies of substrate-bound P450 BM3 and P450cam (117,234), it is apparent that the most likely way to overcome (at least partially) the thermodynamic barrier is by substrate binding to the P450. This event is seen to remove ferric heme iron-bound water, leading to a heme iron spin-state conversion and elevation of the reduction potential by approximately 130 – 150 mV (117,234). By raising the reduction potential of the heme the thermodynamic barrier between P450 and ferredoxin is decreased significantly and shifts the equilibrium that previously restricted electron transfer towards a more permissive situation. In further experimentation performed by Dr. K.J. McLean (75) the reduction potentials of Mtb CYP51 and the ferredoxin were determined whilst the two proteins were in complex. The mid-point reduction potential for CYP51 was determined as – 370 $\pm$ 4 mV whilst the ferredoxin potential was shown to be -33 ± 4 mV. These potentials are not significantly perturbed from the independently determined values and suggest that the thermodynamic barrier is not affected significantly in the complex. Thus, these data reinforce substrate-binding as the most important factor in decreasing the thermodynamic barrier to electron transfer. A caveat to these data is that we conclude that the likely reason for the unusual optical changes seen for Mtb CYP51 on reduction relate to protonation of thiolate. Thus, the midpoint potentials determined are for species in which both redox state (ferric to ferrous) and coordination state (thiolate to thiol) has changed. Notwithstanding this problem, the potential of the Mtb CYP51 heme iron determined (and the effect of substrate-like molecules) are consistent with studies on the well characterized P450cam and P450 BM3 systems, whereas the potential of the ferredoxin is more positive than those of the redox partner systems of

P450 BM3 and P450cam (117,234). These data are also consistent with the CD data reported earlier, that suggested the ferredoxin and CYP51 might have only transient and peripheral interactions. The thermodynamic barrier between Mtb CYP51 and the ferredoxin is a substantial obstacle to overcome and although catalytic turnover experiments show that this can be achieved and potentiometry studies here indicate that substrate binding likely plays an important part in the process, the potential of the ferredoxin is still more positive than that of the substrate-bound heme iron in CYP51. This leads to speculation that the thermodynamic barrier exists in order to limit product formation from CYP51, tuning it to the slow-growing pathogen in which it is found (151). In short, the electron transfer equilibrium is poised in favour of the donor and the acceptor uses oxygen binding to ferrous heme iron to "trap" the electron once it is delivered (and as a means of further perturbing the heme iron potential and enabling the efficient transfer of the second electron). This down-regulation of the enzyme would serve to decrease the catalytic activity of CYP51 and prevent over-accumulation of products, which could be toxic to the organism when in excess. The reduction potential data presented here suggests that electron transfer between the ferredoxin and CYP51 is improbable when the P450 is in the ligand-free, low-spin, form, and in later sections (Chapter 3.23) results from stopped-flow investigations into the electron transfer between Mtb CYP51 and its ferredoxin are discussed.
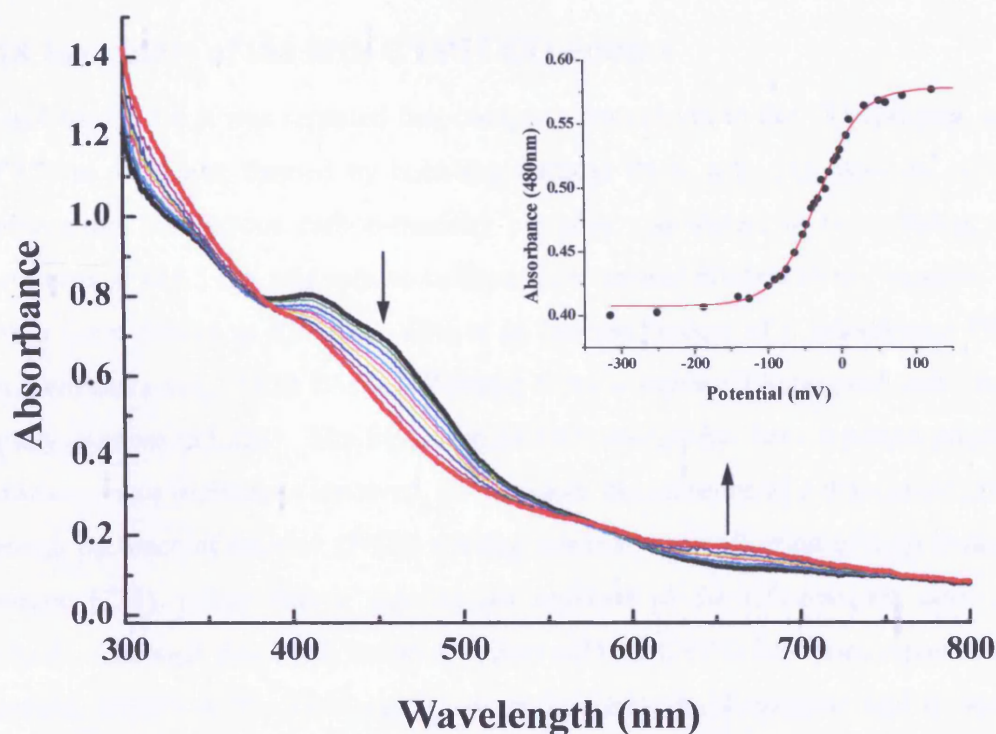
Figure 41 Selected UV-Visible absorption spectra documenting the optical changes observed during determination of the redox midpoint potential of Mtb ferredoxin. Experiment was performed by Dr K.J. McLean (159). The black line identifies the initial spectrum of the oxidised ferredoxin (~71 µM), whilst the fully reduced ferredoxin spectrum is identified in red. As the titration proceeds and the iron-sulphur cluster is reduced, the spectral intensity at 650 nm increases noticeably, whilst simultaneously diminishing most significantly between 400 and 500 nm. Isosbestic points at 385 and 570 nm indicate a smooth transition between the oxidised and reduced forms, and arrows indicate the direction of spectral changes. The inset displays a plot of the absorbance at 480 nm *versus* potential (normalised against a standard hydrogen electrode), fitted with the single-electron Nernst equation (Equation 6). From this fit a midpoint potential of −31 ± 5 mV was determined for the ferredoxin. This value is approximately 340 mV more positive than that of substrate-free CYP51, and identifies a large thermodynamic barrier opposing electron transfer between these two proteins from *Mycobacterium tuberculosis*.

3.18 Instability of the Mtb CYP51 CO-adduct

In Chapter 3.4 it was reported that complete conversion to the CO-complex of Mtb CYP51 at ~450 nm, formed by bubbling reduced P450 with CO, was not achieved. Furthermore, the ferrous carbon-monoxy complex was shown to be unstable, as the Soret peak at 448.5 nm was seen to collapse over several minutes to an "inactive" form with a Soret feature at 420 nm. This is an unusual feature of a cytochrome P450 as most enzymes (e.g. P450 BM3, P450cam) form a stable CO-complex that does not rapidly collapse (37,226). The formation of P420 species has been reported previously. However, these incidences involved, for example, the presence of a denaturant (231), or through presence of inactive (P420) starting material, or application of high hydrostatic pressure (238), rather than a spontaneous collapse of the CO-complex once it had formed. Although this P450 collapse feature of Mtb CYP51 has been reported in, for example, studies of the P450 epoK system by Ortiz de Montellano and co-workers, (169,196), there have been almost no systematic investigations into the reasons for its occurrence. Hence this study, and those in subsequent sections (Chapters 3.19, 3.20, and 3.21,), focuses on investigating a number of variables that may affect the collapse of the CYP51 CO-complex. Furthermore, the Mtb ferredoxin protein has been postulated, due to its genomic location, to be the physiological redox partner of CYP51 (159,169). Although circular dichroism studies into the interactions of the two Mtb proteins (Chapter 3.16) proved inconclusive, work presented here investigates the possibility of ferredoxin-induced structural or thermodynamic, changes that may stabilise the ferrous carbon-monoxy complex in its P450 form.

The collapse of the CYP51 CO-complex from the "active" P450 form to the "inactive" P420 form was studied by monitoring the UV-Visible absorption spectra of Mtb CYP51 over a time period of up to one hour. The P450 was added to a 1 ml aliquot of CO-saturated 100 mM Tris.HCl, pH 7.2, in an airtight cuvette, to a final concentration of approximately 2.1 μM. The buffer had been previously prepared by extensive CO bubbling in a sealed 30 ml Sterilin tube with a vent to allow air to be displaced. Oxygen was excluded throughout the experiment in order that the effects of displacement of heme-bound CO by atmospheric oxygen, for which the heme iron has a high affinity, could be disregarded. The formation of the CO-complex was initiated by the injection of a saturated sodium dithionite solution, which was also prepared in the CO-saturated 100 mM Tris.HCl, pH 7.2 buffer. From this point onwards spectra were

recorded at 30-second intervals using a Cary UV-50 Bio spectrophotometer maintained at 25 °C, until the decay of the complex was complete (typically 50 minutes). The obtained spectra, which demonstrate how the P450 form of the CO-complex decays to the P420 form over time, are shown in Figure 42. This procedure was repeated in the presence of 5-fold and 10-fold excesses of the Mtb ferredoxin (~10 and ~20 μM respectively) and the decay of the P450 complex again recorded. The data obtained from these three CO-complex collapses were plotted as the change in absorption at 448 nm *versus* time (Figure 43), and from these plots rates of P450 decay were determined using an exponential function (Equation 7).
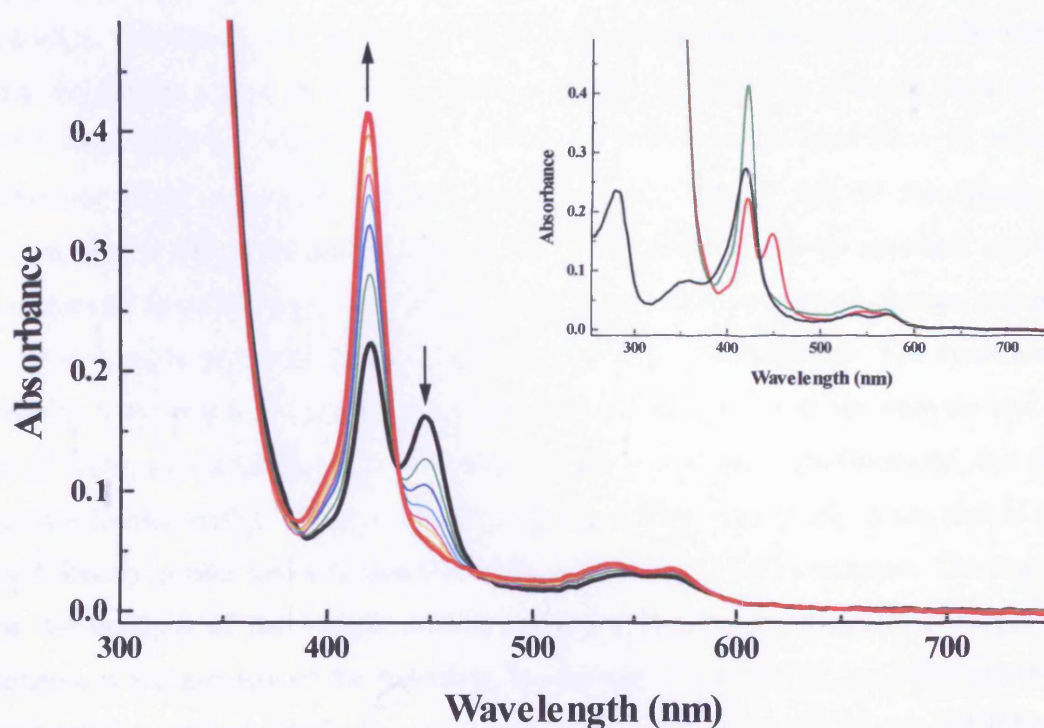
Figure 42 Selected UV-Visible absorption spectra detailing the decay of the ferrous carbon-monoxy complex of Mtb CYP51. Protein was diluted to approximately 2 μM in an airtight cuvette containing CO-saturated 100mM Tris.HCl pH 7.2. P450 CO-complex formation was initiated by the injection of a saturated sodium dithionite solution and spectra captured every 30 seconds for a period of fifty minutes. The initial spectrum (black), recorded immediately after sodium dithionite addition, possesses a Soret band at 448.5 nm and fused visible bands typical of a CO-ligated heme, and identifies the maximal amount of the "active" P450 form obtained. Subsequent spectra demonstrate the manner in which the collapse proceeds until complete conversion to the "inactive" P420 form (red) is achieved after 50 minutes. The arrows indicate the direction of spectral changes during the study. For clarity, the inset shows the spectra displaying maximal P450 and P420 content (red and green respectively) alongside the spectrum of oxidised CYP51 (black), prior to reduction and CO bubbling.

The UV-Visible spectra recorded during the collapse of the P450 CO-complex of CYP51 in the absence of Mtb ferredoxin are shown in Figure 42. Upon reduction with sodium dithionite the Soret band of the P450 is seen to shift to 448.5 nm and the visible bands fuse to form a broad band centred at 554 nm. These two features are indicative of a water molecule bound at the distal face of the heme being displaced by a molecule of CO, and thus the formation of the ferrous carbon-monoxy complex. However, as was reported in Chapter 3.4, full conversion to the P450 CO-complex is not achieved following the addition of a saturated sodium dithionite solution. This is evident from the small Soret feature at approximately 420 nm and suggests that a proportion of the enzyme converts directly to the "inactive" P420 form by the time the first spectrum is recorded. The spectra recorded at 30 second intervals demonstrate that from the instant that the ferrous carbon-monoxy complex is formed it begins to collapse back to the P420 form, with the majority of the collapse occurring in the first 10 – 15 minutes following P450 formation. This is most evident when a plot of the change in absorbance at 448.5 nm against time is created (Figure 43), as the resultant curve is exponential in nature with initial spectra giving the most absorption change and only gradual changes observed at later time points (i.e. 12 – 50 minutes). The spectra also identify that there is a clean transition between the P450 form of the enzyme and the P420 form, as indicated by the isosbestic point at 433 nm. Additionally, the final species formed during the experiment possesses a Soret band at 421.5 nm that is of a significantly greater intensity than that of the oxidised form of the enzyme. The reasons for the collapse of the ferrous carbon-monoxy complex are uncertain, however the collapse is independent of the reductant, i.e. the rate of collapse of the P450 species is unchanged no matter which electron source (sodium dithionite, NADH, or NADPH) is utilised. Furthermore, the system by which these electrons are delivered (i.e. the *E. coli* flavodoxin reductase and flavodoxin system (239), or the Mtb ferredoxin (Fdx) and ferredoxin reductase (FprA) system (134)) does not affect the collapse rate. It has been suggested that formation of the P420 species arises due to the protonation of the thiolate ligand, which coordinates the iron at the proximal face of the heme and hence binds it to the protein (236). It is well understood that the thiolate ligand is integral to the characteristic UV-Visible absorption feature (Soret band at 448.5 nm) of the ferrous carbon-monoxy complex of a cytochrome P450, and this work postulates that the conversion of the thiolate ligand to a thiol causes the loss of this feature and the concomitant formation of the P420 form. Utilising this information it is apparent that

the gradual decay of the CYP51 P450 species observed in this study relates to persistent protonation of the thiolate ligand (for Mtb CYP51 this is Cys 394), and that this continues until complete conversion from the P450 form to the P420 form is achieved.

$$y = a \times \exp\left(- x/t_1\right) + y0$$

Equation 7 The single exponential equation utilised to determine the rates of the ferrous carbon-monoxy complex collapse, and for the formation of the P420 species. In the equation, y represents the observed absorption at the given wavelength, a is value of y when t = 0, x is the rate constant, t_1 is the decay half-life, and y0 is the offset value which accounts for the absorbance not being zero at the end of the reaction.
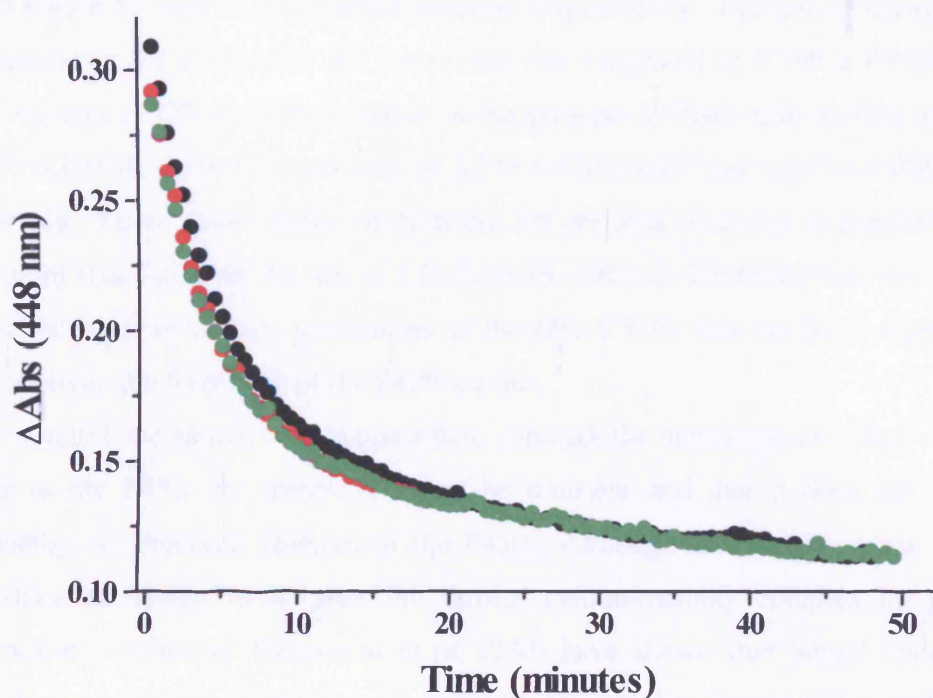
Figure 43 Plots of the decay processes for Mtb CYP51 in the absence (black) and presence of five-fold (red) and ten-fold (green) excesses of Mtb ferredoxin. Fitting of the data with an exponential function (Equation 7) reveals a rate of decay of the P450 species of 0.199 ± 0.003 min^{-1} for the ferredoxin-free sample, whilst the rates in the presence of five-fold and ten-fold excess ferredoxin were calculated as 0.211 ± 0.004 min^{-1} and 0.213 ± 0.006 min^{-1} respectively. These data indicate that the presence of the ferredoxin has no major stabilising influence on the decay of the P450 species to the "inactive" P420 form. Each assay contained CYP51 diluted to a final concentration of ~2.1 µM in 100 mM Tris.HCl pH7.2, as well as the appropriate concentration of ferredoxin protein (i.e. 10 µM for five-fold excess and 20 µM for the ten-fold excess).

The P450 decay processes for the experiments in the presence and absence of Mtb ferredoxin are shown overlaid in Figure 43. The three curves all demonstrate exponential decay with the greatest collapse occurring in the first 15 minutes and complete conversion having been reached after approximately 50 minutes. The curves for the decay of the P450 species in the presence of five- and ten-fold ferredoxin almost exactly overlay the curve of the ferredoxin-free sample and indicate that the rate of P450 collapse/P420 formation is not significantly enhanced or diminished by the presence of the Mtb ferredoxin protein. Indeed, in common with the results for the Circular Dichroism experiments in the presence of ferredoxin (Chapter 3.16), complexation of the P450 and the ferredoxin brings about no significant stabilization of the ferrous carbon-monoxy P450 species. This is further verified by the fitting of the plots in Figure 43 with an exponential function (Equation 7). The rate of decay of the P450 species in the absence of the ferredoxin was calculated as 0.199 ± 0.003 min^{-1}, whilst the rates of CO-complex collapse in the presence of five- and ten-fold excesses of the Mtb ferredoxin were determined as 0.211 ± 0.004 min^{-1} and 0.213 ± 0.006 min^{-1}, respectively. These values hence confirm that the presence of excess ferredoxin elicits no apparent retardation of the rate of CO-complex collapse, indicating that this protein does not prevent, or impair, protonation of the Mtb CYP51 thiolate heme ligand that likely underlies the formation of the P420 species.

The spectral and kinetic data suggest that, although the ferredoxin mediates electron transfer to the P450, the interaction may be transient and that it does not impact significantly on structural features of the P450. Although these experiments do not demonstrate an ability to stabilise the ferrous carbon-monoxy complex by protein complexation, studies by Cheesman et al. (240) have shown that ligand binding to mammalian cytochromes P450 may act to stabilise the thiolate ligated CO-complex. In the next section (Chapter 3.19), further attempts to attain a stable P450 by ligand binding are described, whilst subsequent sections (Chapters 3.21 and 3.22) concern detailed studies of the effects of temperature and pH on the stability of the Mtb CYP51 ferrous carbon-monoxy complex.

3.19 The effects of ligands on Mtb CYP51 CO-complex collapse

In the previous section it was demonstrated that the presence of Mtb ferredoxin had no influence on the rate of collapse of the CO-complex of CYP51 and thus other studies into this phenomenon, as detailed here, were carried out. A recent study (240) identified that the ferrous carbon-monoxy complex of *E. coli*-expressed rabbit CYP1A2 and CYP4B1 was stabilized during purification by binding the ligand α-napthoflavone, and hence it was deemed appropriate that ligand stabilization of the CYP51 CO-complex should be investigated. As α-napthoflavone was a substrate of these enzymes it was most appropriate that the compounds tested against CYP51 should also be substrates of the enzyme, as these would be more likely to stabilise the ferrous carbon-monoxy complex in its P450 state. However, lanosterol and obtusifoliol, which have been shown to be metabolised by Mtb CYP51 (169), are highly insoluble and impractical for use in the required UV-Visible absorption studies. Instead, estriol and 2-phenylimidazole were selected as the most appropriate candidates. These two ligands were chosen on the basis of their effects on the spin-state of the CYP51 heme iron. Both compounds have been shown to induce type I shifts of the CYP51 Soret band towards the high-spin form during UV-Visible spectroscopy (see Chapter 3.9), and were thus adjudged to be substrate-like compounds. Below are described the experiments that were carried out in order to determine whether or not these two compounds would stabilise the ferrous carbon-monoxy complex of CYP51, thus adding to further understanding of the CO-complex collapse process.

In order to study the effects of exogenous ligands on the collapse of the CYP51 CO-complex, an aliquot of the Mtb P450 was diluted to $2 - 4$ μM in 100 mM Tris.HCl pH 7.2. Following equilibration at 25 °C, a UV-Visible absorption spectrum of the oxidized enzyme solution was recorded using a Cary UV-50 Bio spectrophotometer scanning between 250 and 800 nm. The P450 was then reduced with a small amount of solid sodium dithionite before the ferrous carbon-monoxy form of the enzyme was created by gently bubbling the solution with CO. Subsequently spectra were recorded for up to 1 hour at 30 second intervals in order to monitor the collapse of the CO-complex of Mtb CYP51. The effects of the ligands estriol and 2-phenylimidazole on the formation of the P420 form of CYP51 were similarly studied. The ligands were added at near-saturating concentrations, as determined from the binding curves for these two compounds (Chapters 3.9 and 3.10), with estriol added at 87 μM and 2-

phenylimidazole at 7.5 mM. These compounds were added to the enzyme solutions prior to reduction and incubated to ensure equilibrium had been reached before spectra were recorded as for the ligand free sample. The resultant data were plotted as the change in absorbance at 448 *versus* time and analysed with an exponential function (Equation 7) with the purpose of deriving rates for the decay processes of the CYP51 ferrous carbon-monoxy complex in the absence and presence of ligands.

a)
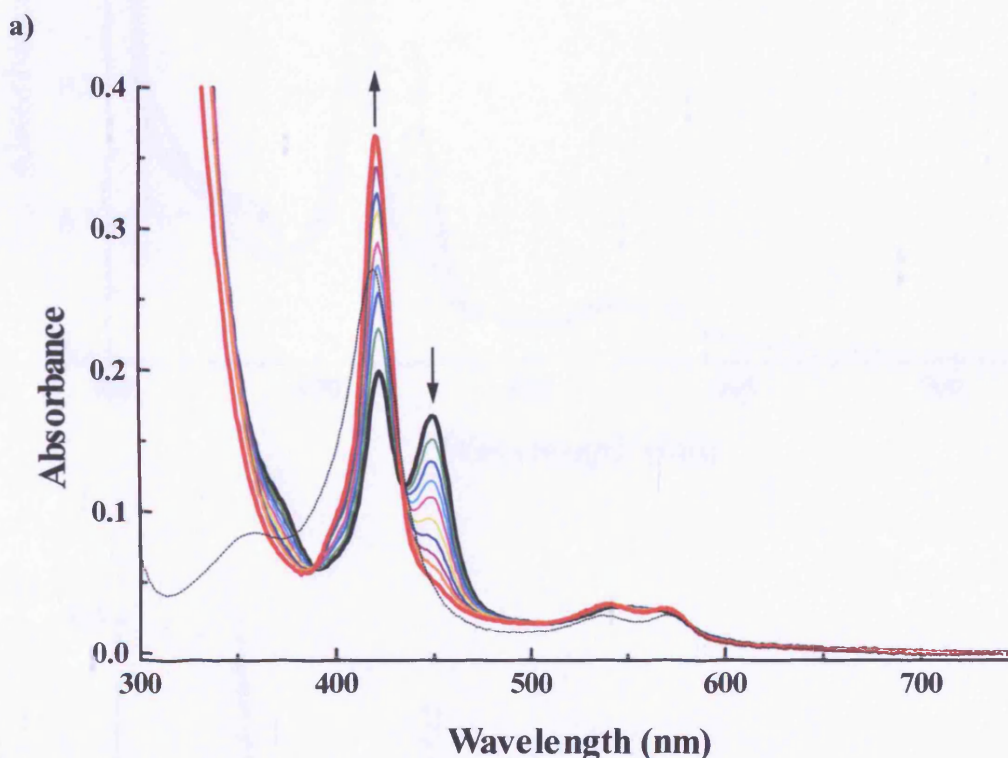
Figure 44 a) Selected UV-Visible absorption spectra collected for the collapse of the ferrous carbon-monoxy complex of ligand-free Mtb CYP51. **b)** and **c)** display selected spectra obtained for the collapse of the CO-complex in the presence of 2-phenylimidazole and estriol respectively. In all cases initial enzyme concentration was 2 – 4 μM prior to ligand addition, and spectra were recorded at thirty second intervals following initiation of the CO-complex. For each plot, the initial spectrum (i.e. prior to complex formation) is identified by a dotted line and spectra containing maximal amounts of "active" P450 are shown as thick black lines. The spectra demonstrating the greatest quantity of "inactive" P420 are shown as thick red lines, whilst arrows indicate the direction of absorbance changes that occur for each sample. In each case the reduction and CO-bubbling results in a shift of the Soret band to 448.5 nm, although significantly more P450 is formed in the presence of estriol. Furthermore, all three samples demonstrate decay of the P450 complex with a peak forming at 421.5 nm. In the case of the ligand-free and 2-phenylimidazole samples, the intensity of the P420 peak at the end of the study was significantly greater than that of the initial spectrum whereas the estriol sample remains predominantly in the "active" P450 form.

b)

c)
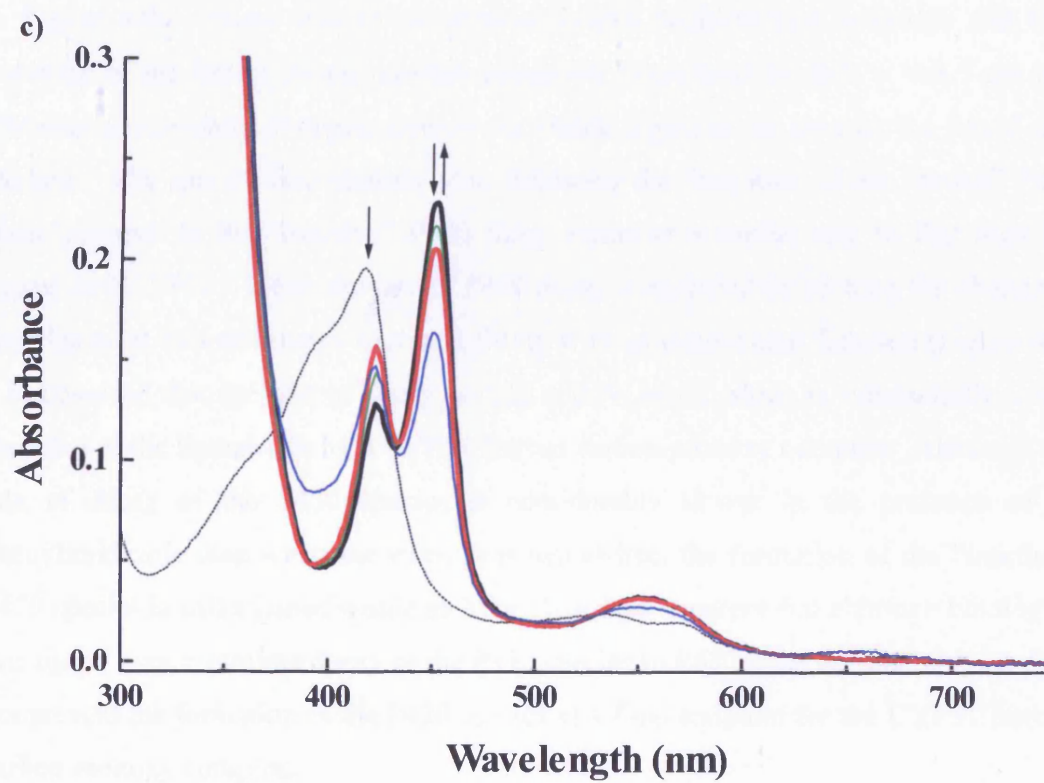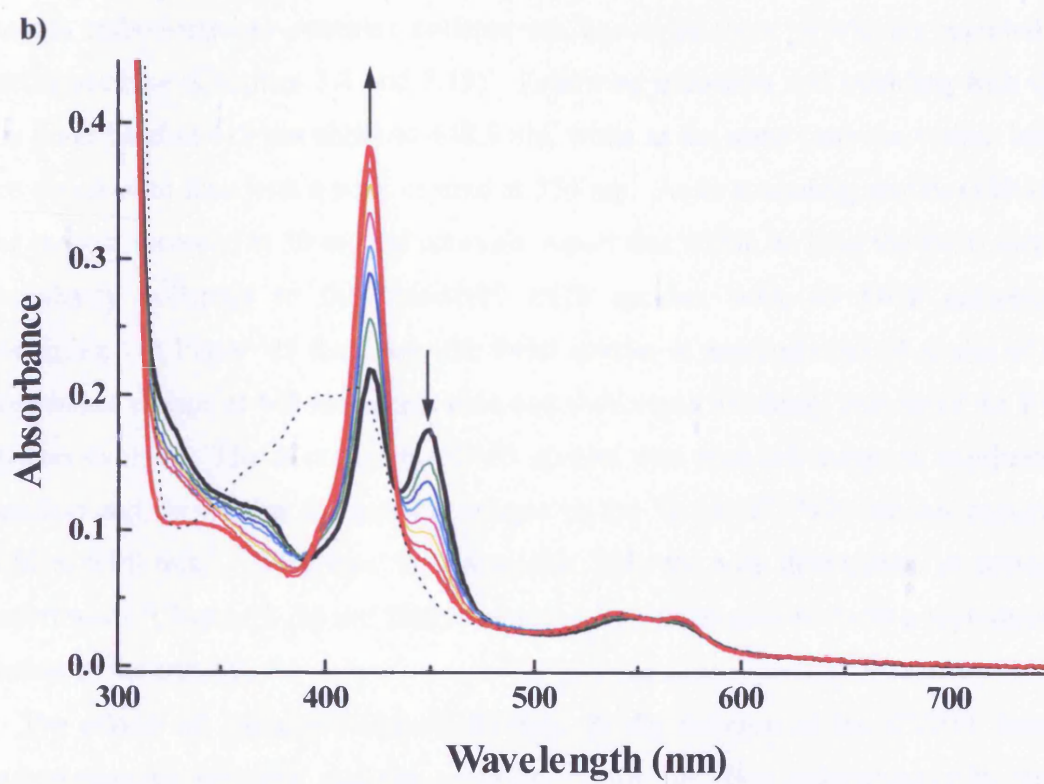
As can be seen in Figure 44a, the UV-Visible spectra of the ligand-free CYP51 ferrous carbon-monoxy complex collapse are typical of those previously reported in earlier sections (Chapters 3.4 and 3.19). Following reduction and bubbling with CO, the Soret band at 419 nm shifts to 448.5 nm, while at the same time the visible bands are observed to fuse with a peak centred at 554 nm. As in preceding studies (169,196) the spectra, recorded at 30 second intervals, report that within an hour the P450 species completely collapses to the "inactive" P420 species, with no P450 component remaining. In Figure 45 the decay the P450 species is demonstrated by a plot of the absorbance change at 448 nm *versus* time and shows how the decay process of the P450 species evolves. The decay of the P450 species was analysed using an exponential function and shows that the rate of collapse to the "inactive" P420 species occurs at 0.30 ± 0.01 min^{-1}. This rate is comparable with the rate determined in previous experiments (Chapter 3.18) and further confirms this decay process to be a reproducible feature of the enzyme.

The effects of 2-phenylimidazole binding on the collapse of the CYP51 ferrous carbon-monoxy complex enzyme solution, which are also concurrent with those observed for the CYP51 P450 decay process in previous studies (169,196), can be seen in Figure 44b. These selected absorption spectra establish that reduction and CO-bubbling of the ligand bound solution causes the Soret band to shift to 448.5 nm and that similar associated changes occur in the visible region as are seen for the ligand-free enzyme. The spectra also identify that, following the formation of the "active" P450 form, collapse to the "inactive" P420 form occurs at a similar rate to that seen for ligand-free CYP51. When the rate of P450 decay is analyzed by plotting the change in absorbance at 448 nm *versus* time and fitting with an exponential function (Figure 45), it is observed that the rate of decay is 0.22 ± 0.01 min^{-1}, which is substantially lower than that of the ligand-free Mtb CYP51 ferrous carbon-monoxy complex. Although the rate of decay of the P450 species is considerably slower in the presence of 2-phenylimidazole than when the enzyme is ligand-free, the formation of the "inactive" P420 species is still attained within an hour. It is thus apparent that although binding of this ligand does retard the decay of the P450 species to P420 quite considerably, it does not prevent the formation of the P420 species as a final endpoint for the CYP51 ferrous carbon-monoxy complex.
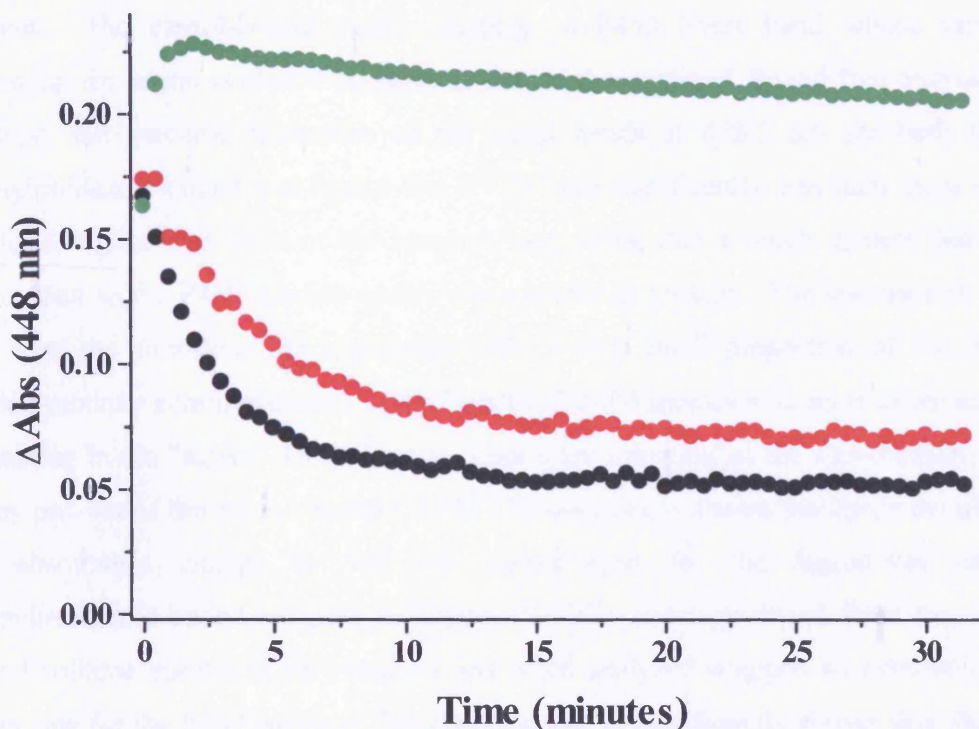
Figure 45 The changes in absorbance at 448 nm *versus* time for the collapse of the ferrous carbon-monoxy species of ligand-free (black), 2-phenylimidazole-bound (red), and estriol-bound (green) Mtb CYP51. The plots demonstrate that the decay of the "active" P450 species' differs significantly between the three samples and data were fitted to an exponential function in order to determine rates of the decay processes. The decay of the ligand-free sample proceeds exponentially, as was reported in Chapter 3.18, occurring at a rate of 0.30 ± 0.01 min^{-1}. The 2-phenylimidazole-ligated sample shows a similar decay process, but the rate (0.22 ± 0.01 min^{-1}) is substantially slower than the ligand-free form and suggests that the presence of the ligand may hinder P450 decay/thiolate to a small extent. Most significantly, the decay process of the estriol-bound form is described by a very shallow curve that shows the rate of decay of the P450 species to be much slower than the previous two samples. The collapse of the estriol-ligated ferrous carbon-monoxy complex was shown to progress extremely slowly and indicates that the presence of this compound in the active site of CYP51 substantially retards the formation of the P420 species, possibly by stabilization of the thiolate ligand. For all three curves, collapse rates were determined using the exponential decay function shown in Equation 7.

Contrastingly, the spectral data presented for the CO-complex collapse in the presence of the ligand estriol (Figure 44c) shows that enhanced stability of the CO-complex can be achieved. The UV-Visible absorption spectra demonstrate that in the presence of estriol the Soret band of CYP51 shifts to 448.5 nm after sodium dithionite reduction and bubbling with CO, similar to the shifts observed for the ligand-free and 2-phenylimidazole samples. However, the spectra identify that an appreciably greater amount of ferrous carbon-monoxy complex at 448.5 nm is created when estriol is

143

present. The estriol-bound sample displays a P450 Soret band whose intensity following formation is almost as great as that of the oxidized, ligand-free enzyme. In contrast, the maximal intensities of the Soret bands at 448.5 nm for both the 2-phenylimidazole-bound and ligand-free CYP51 are significantly less than those of the oxidized, ligand-free form of the enzyme, suggesting that a much greater degree of conversion to the P450 species occurs when estriol is present. The spectra also show that over the course of the experiment only a very small proportion of the ferrous carbon-monoxy complex decays to the "inactive" P420 species with most of the enzyme remaining in the "active" P450 form an hour after initiation of the CO-complex. The decay process of the estriol-bound CYP51 CO-complex is shown alongside the plots of the absorbance change at 448 nm *versus* time for the ligand-free and 2-phenylimidazole-bound samples in Figure 45. The curve produced from the estriol-bound collapse spectra is very shallow and when analyzed suggests an extremely slow decay rate for the P450 species. The rate of decay is significantly slower than those of the 2-phenylimidazole and ligand-free samples and demonstrates that the presence of estriol dramatically decreases formation of the P420 species. These data thus show that binding of the Mtb CYP51 substrate-like compound estriol effects a stabilization of the ferrous carbon-monoxy complex which retards the decay to the "inactive" species. This result compares to that of the study by Cheesman *et al.* (240) in which binding of α-napthoflavone to rabbit CYP1A2 and CYP4B1 prevents conversion to the P420 forms of these enzymes and suggests that binding of a true substrate of Mtb CYP51, if one were known, might act to inhibit completely the conversion to the P420 species. This result, which shows that the rapid decay of the ferrous carbon-monoxy complex can be averted by ligand binding, is a significant step in the understanding of the P450 decay process. From the results it can be assumed that binding of the ligand causes a stabilization of the thiolate ligand, whose conversion to thiol is thought to be the basis of the collapse. Although it is still unclear how the thiolate ligand is stabilized it seems likely that the presence of the substrate-like molecule induces an electronic reconfiguration (i.e. spin-state change) of the heme iron and probably a protein structural reorganization. These may act to shift the P450/P420 equilibrium such that thiolate remains favoured over the thiol as the proximal ligand. However, as decay still occurs, albeit very slowly, this equilibrium still favours the thiol ligand even in the estriol-bound form. Having determined that the collapse of the P450 species of Mtb CYP51 can be significantly impaired on ligand binding, the next section (Chapter 3.20)

investigates whether the process is reversible. Recent work by Ortiz de Montellano and co-workers (43) reports upon the re-conversion of the P420 form to the P450 form of a cytochrome P450 by binding of a substrate compound. Replication of such an effect would add further to understanding the thiolate/thiol equilibrium in the CYP51 system.

3.20 Ligand-binding rescue of the Mtb CYP51 CO-complex

The rapid decay of the ferrous carbon-monoxy species of *Mycobacterium tuberculosis* CYP51 is an unusual feature of the enzyme and various investigations into its nature have been performed (169,196). It is understood that conversion to the "inactive" P420 species may be related to the switching of the thiolate ligand to a thiol ligand by protonation (236), and it is apparent that binding of substrate or substrate-like molecules may retard the transition from the P450 form to the P420 form (Chapter 3.19, (240)). In this section the possibility of a reversal of the "deactivated" enzyme is investigated, based upon a study by Ortiz de Montellano and co-workers (43). In this study of the *Sorgangium cellulosum* cytochrome P450 epoK, which is required for the synthesis of epothilones (prospective anti-cancer agents), it was observed that binding of the enzyme's true substrate epothilone D effected the conversion of the P420 form to the P450 form at low temperatures (15 °C). Here the epoK/epothilone D experiment is replicated using Mtb CYP51, with estriol as the substrate, in order to observe the possibility of reforming the CO-complex at 450 nm by ligand addition.

The experiment to investigate ligand-induced reformation of the P450 species of CYP51 was carried out as per Ogura *et al.* (43). An aliquot of CYP51 was placed in a quartz cuvette and diluted to 2 – 4 μM in 100 mM Tris.HCl pH 7.2 containing 10 % glycerol. The cuvette was then incubated at 15 °C in a Cary UV-50 UV-Visible spectrophotometer (Varian) fitted with a Peltier arrangement, until equilibration had been attained. Absorption spectra were recorded between 250 and 800 nm before the sample was dithionite-reduced and bubbled with carbon monoxide to incite formation of the ferrous carbon-monoxy complex of CYP51. The P450 form of the enzyme was next allowed to collapse fully to the P420 form with UV-Visible spectra recorded at 5 minute intervals. A saturating concentration of estriol (87 μM) was added to the enzyme solution and spectra recorded for several hours in order to observe the effects of ligand addition. As well as performing the experiment using 2-phenylimidazole, at room temperature, and in the absence of 10 % glycerol to further investigate this

phenomenon, studies were also made to investigate whether the P450 form could be reformed by repeating the reduction and CO-bubbling steps following complete reoxidation of the enzyme (i.e. after dissociation of CO and the reoxidation of the enzyme to the ferric form). The P420 solution was prepared as described above, at 25 °C, and allowed to reoxidise until the spectrum returned to that of the ferric, ligand-free form. The sample was then re-reduced with sodium dithionite and bubbled with carbon monoxide, following which spectra were recorded to monitor the effects of this treatment.

The work of Ortiz de Montellano's group describes the reformation of the P450 form of epoK when its substrate, epothilone D, was added to the P420 form of the enzyme (43). In our study, the addition of estriol to a solution of CYP51 in the P420 form was not seen to cause any notable re-conversion to the P450 form. Duplicates of the study in the absence of glycerol, at higher temperature (25 °C), as well as attempts using the substrate-like compound 2-phenylimidazole were also unsuccessful in raising a peak at 448 nm which would demonstrate re-conversion of the P420 form to the P450 form. However, the study of repeating the reduction and CO-bubbling of a sample of the enzyme (which had been allowed to fully reoxidise following the creation of the ferrous carbon-monoxy species) was more successful. The obtained UV-Visible spectra from this study are presented in Figure 46 and demonstrate that a proportion of the P450 species is reformed, as identified by the reappearance of a peak at 448.5 nm. The reformed P450 peak exhibits no unusual features, although the intensity of this band identifies that only approximately 40 % of the original P450 peak is recovered. This species behaves similarly to that created by the initial reduction and CO-bubbling process. It decays, at a comparable rate to that previously determined, from the "active" P450 form to the "inactive" P420 form. This shows that the P420 form is not a terminal product of P450 collapse. That is, protonation of the thiolate can be reversed in the reoxidised enzyme, allowing a thiolate-coordinate P450 species to be reformed. These results are in agreement with the reversibility of the redox titrations shown earlier (Chapter 3.17) and suggest that there may be a "natural" equilibrium, in absence of substrate at least, that favours the thiol-coordinated (P420) form of CYP51 in the reduced state and the thiolate coordinated (P450) form in the oxidised state.
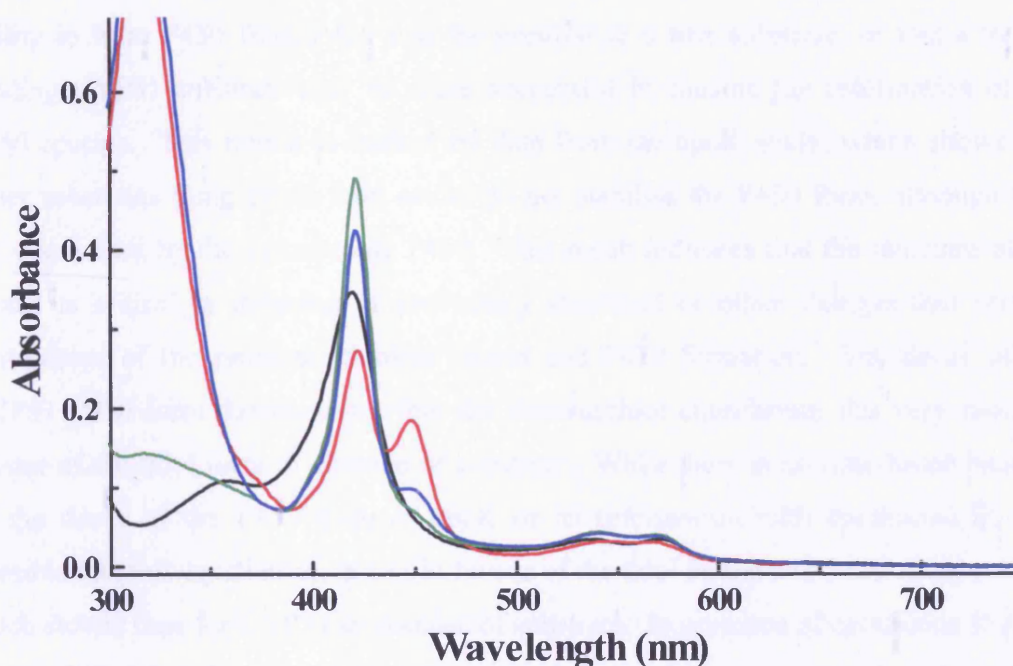
Figure 46 Selected UV-Visible absorption spectra from a study to determine whether the carbon monoxy-ferrous form of Mtb CYP51 can be reformed following collapse to the P420 species. Oxidised Mtb CYP51 (~2.6 μM, black) was reduced with a minimal amount of sodium dithionite and bubbled with carbon monoxide to generate the P450 species (red), before being allowed to fully collapse to the P420 form (green). This was then allowed to reoxidise completely. Repeat reduction and CO bubbling of the sample resulted in the reformation of the P450 species (blue), although only ~40 % of the original amount of P450 was recovered. These data thus demonstrate that formation of the P420 species is not terminal and is reversible, although in the substrate-free form the thiol-ligated (P420) form is appreciably favoured over the thiolate-ligated form (P450).

The results of the ligand-induced P450 reformation investigations identify that, unlike the epoK/epothilone study, the addition of a substrate-like molecule (estriol) does not result in the reformation of the P450 form of the enzyme from the P420. The fact that estriol addition does not produce a reversal of the decay of the P450 form may be due to a number of factors, including the nature of the ligand. Epothilone D is known to be the true substrate of epoK, with catalysis by the *Sorgangium cellulosum* cytochrome P450 resulting in the epoxidised compound epothilone B. This contrasts with estriol which, although having been shown to induce substrate-like binding spectra, is not the true substrate of *M. tuberculosis* CYP51 and binds only moderately tightly (K_d = 21.7 μM, Chapter 3.9) to the active site of the P450. Indeed epothilone D binds with a K_m of 1.6 μM (43) which suggests much tighter than the binding of estriol to CYP51 (although it should be remembered that a K_m is only an "apparent" K_d) and thus suggests that the

ability to form P450 from P420 may be peculiar to a true substrate, or that a tighter binding CYP51 substrate may be more successful in causing the reformation of the P450 species. This notion is backed by data from the epoK study, which shows that other substrates (long chain fatty acids) do not stabilise the P450 form, although they are epoxidised by the cytochrome P450. This result indicates that the structure of the ligand is critical in inducing or preventing structural or other changes that prevent protonation of the proximal thiolate ligand and P420 formation. The decay of the CYP51 P450 form demonstrates that the thiolate/thiol equilibrium lies very much in favour of the thiol form in absence of substrate. While there is no time-based analysis of the decay of the P450 form of epoK or its reformation with epothilone D, it is possible that this equilibrium is less in favour of the thiol ligand and P450 decay may be much slower than for CYP51 in absence of substrate. In presence of epothilone D it can be concluded that the rate of thiolate protonation now becomes lower than that of it's deprotonation, leading to P450 reformation. The fact that estriol appears to have a lesser effect in CYP51 than epothilone D does in P450 epoK must relate finally to the balance of rate constants for the protonation and deprotonation of the thiolate/thiol. The weaker binding of estriol (compared with epothilone D) may also be a factor that accelerates the rate of P420 formation in the CYP51 system, although estriol should be predominantly bound to oxidised CYP51 under the conditions used.

Although the ligand addition studies show that estriol is unable to induce re-conversion to the P450 form, the data from the repeat-reduction and CO-bubbling experiment demonstrates that the P420 form of CYP51 can be recovered to the P450 form, albeit to a slightly lesser extent than for the starting form used. The result proves that the protonation of the thiolate ligand associated with P450 decay is a reversible process, and that the protonation of Cys 394 of Mtb CYP51, the residue which ligates the heme to the protein, does not necessarily signify the irreversible inactivation of the enzyme. Furthermore, it is plausible that the two forms (P450 and P420, which I take here to represent the thiolate- and thiol-coordinated forms of the heme iron, and not the CO complexes thereof) are in a state of equilibrium, and are present in varying ratios in all cytochromes P450. Substrate binding could then act to suppress the thiol-ligated P420 form via enhancement of the stability of the thiolate-ligated P450 form. The amount of P420 may vary between the P450s due to structural and thermodynamic influences, and in the next sections (Chapters 3.21 and 3.22) the impact of pH and temperature are investigated. A working model is that the P420 (thiol) form of CYP51

is favoured for the ferrous enzyme form, but that this conversion can be inhibited or stopped altogether if the correct substrate is bound. The ferric form of the enzyme then reverts to the thiolate-coordinated species, thus explaining the ability of the enzyme to be converted back, partially, to P450 in CYP51. Thus, this model also requires that the CO-ligated species known as P450 and P420 reflect a difference in protonation state of the cysteine ligand, and that CO binding simply provides a convenient spectral assay for a process that involves thiolate protonation, and which occurs (for CYP51 at least) in the reduced, ligand-free enzyme.

3.21 The effect of pH on the collapse of the Mtb CYP51 CO-complex

The discovery that ligand-binding can stabilise the ferrous carbon-monoxy complex of Mtb CYP51 (Chapter 3.19) and that it is possible to reform this P450 species following collapse to the P420 form (Chapter 3.20) suggests that the two forms exist in a state of equilibrium whose balance is dependent upon the thermodynamic and structural properties of the enzyme. In previous studies, this equilibrium, which governs the formation of the "inactive" P420 form of cytochromes P450, was identified as the consequence of protonation of the proximal thiolate ligand (236). Having previously identified external influences that perturb the equilibrium (Chapters 3.19 and 3.22), this section attempts to further investigate factors more closely related to the mechanism of P420 formation through studies of the influences of buffer pH on the decay of the CYP51 ferrous carbon-monoxy species. The study utilises UV-Visible spectroscopy to monitor the transition of the P450 form to the P420 form when enzyme is resuspended in buffers of differing pH, and reports both the nature of the P450 decay and the rates at which the shift in equilibrium occurs.

The experiments to determine pH influence on the Mtb CYP51 ferrous carbon-monoxy complex were performed using similar methods to those employed for the studies of CO-complex collapse of ligand-free CYP51 in Chapter 3.18. An aliquot of ligand-free Mtb CYP51 was diluted in 50 mM Tris.HCl pH 7.0 to a final concentration of 2 – 4 μM, and a spectrum was recorded using a Cary UV-50 Bio spectrophotometer scanning between 250 and 800 nm. The enzyme was then reduced with a small quantity of solid sodium dithionite, before being gently bubbled with CO to induce formation of the ferrous carbon-monoxy species. Subsequently, absorption spectra were collected at 1 minute intervals until the collapse of the P450 species was complete, typically over 1

hour. This experiment was repeated at 0.5 pH unit increments across a pH range from 6.0 to 9.0, and the collated spectra analysed in order to determine the rates of formation of the P420 form of the enzyme. Plotting the absorption changes at 421 nm *versus* time created the curves presented in Figure 48, from which the P420 formation rates were calculated by fitting with an exponential function (Equation 7).

The experiment to study the effects of pH on the decay of the Mtb CYP51 ferrous carbon-monoxy complex was carried out in buffer at a number of pH values from pH 6.0 to 9.0. However, the most significant variation in CO-complex collapse was noted between spectra recorded at pH 7.0 and 6.0, and hence the data presented in Figure 47 show the absorption spectra recorded in buffers at these pH values. The spectra recorded at pH 7.0 are typical of those previously reported for ligand-free CYP51 (Chapters 3.18 and 3.19), showing incomplete conversion to the P450 following dithionite reduction and CO bubbling, and subsequent rapid decay of the ferrous carbon-monoxy species to the P420 form. The spectra display an isosbestic point at 433 nm, indicative of a clean transition between the two species and, characteristically, the intensity of the P420 species is greater than the intensity of the Soret band of the enzyme sample prior to formation of the CO-complex. Following reduction and CO-bubbling, the CYP51 sample diluted in buffer at pH 6.0 also displays a shift of the Soret band to 448 nm, symptomatic of formation of the ferrous carbon-monoxy complex. As with the pH 7.0 CYP51 sample, the CO-complex decays rapidly to the P420 with an isosbestic point at approximately 433 nm. However, unlike the pH 7.0 sample, the absorption (Soret) band associated with the P450 species at pH 6.0 (from the spectrum collected immediately after induction of the CO-complex), is less intense than the band corresponding to the P420 species. Furthermore, when the collapse of the ferrous carbon-monoxy species at pH 6.0 is complete, after approximately 25 minutes, the intensity of the band at 421 nm exceeds the intensity of the oxidised, ligand-free enzyme by a considerably greater amount than is seen for enzyme studied at pH 7.0.

a)

b)
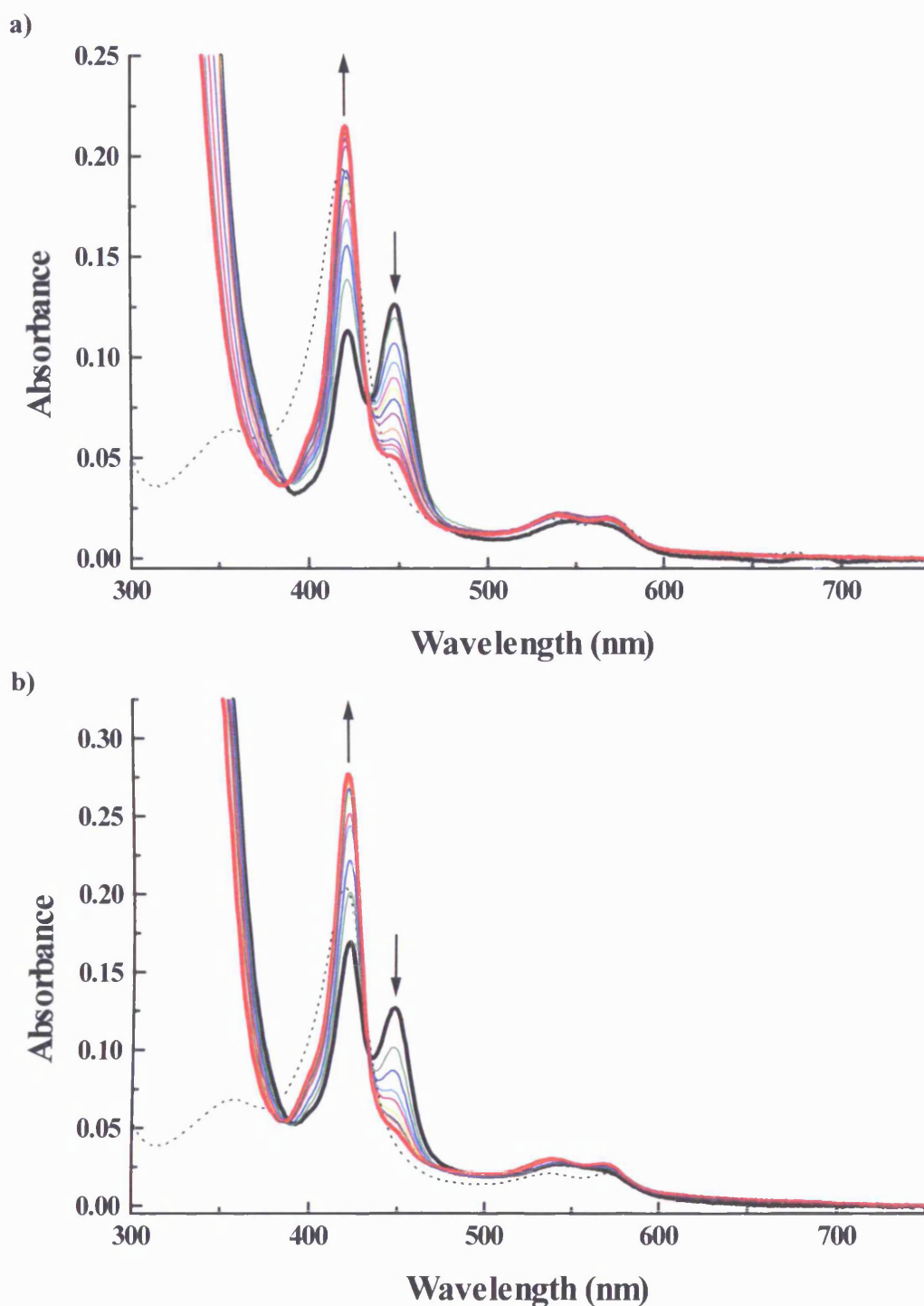
Figure 47 a) and **b)** Selected UV-Visible absorption spectra reporting the collapse of the Mtb CYP51 ferrous carbon-monoxy complex recorded in 50mM Tris.HCl at pH 7.0 and pH 6.0 respectively. For both sets of data, the thick black line represents the spectrum captured immediately after induction of the CO-complex (which displays maximal P450 content), whilst the final spectrum (exhibiting maximal P420 content), is identified by a thick red line. In each case, the initial concentration of oxidised CYP51 was approximately 1.5 µM and is shown as a black dotted line for comparison. The spectra, which demonstrate how the P450 decay proceeds, both show isosbestic points at approximately 433 nm, and the direction of spectral changes as time passes are denoted by arrows.

The differences between the rates of P420 formation at pH 7.0 and pH 6.0 are highlighted by the plots of the change in absorbance at 421 nm *versus* time displayed in Figure 48. The curves show that maximal P420 content was achieved more quickly when the study was performed in the more acidic pH 6.0 buffer, and that the final magnitude of the absorption corresponding to the P420 species is greatest for the sample diluted in the lower pH buffer. Analysis of both sets of data was achieved by the application of a mono-exponential function (Equation 7, Chapter 3.18) to the plots in Figure 48. Subsequently, it was revealed that P420 formation proceeds at a rate of 0.246 ± 0.007 min^{-1} for enzyme diluted in pH 7.0 buffer, and that at pH 6.0 the P420 formation rate is accelerated significantly to 0.298 ± 0.019 min^{-1}.
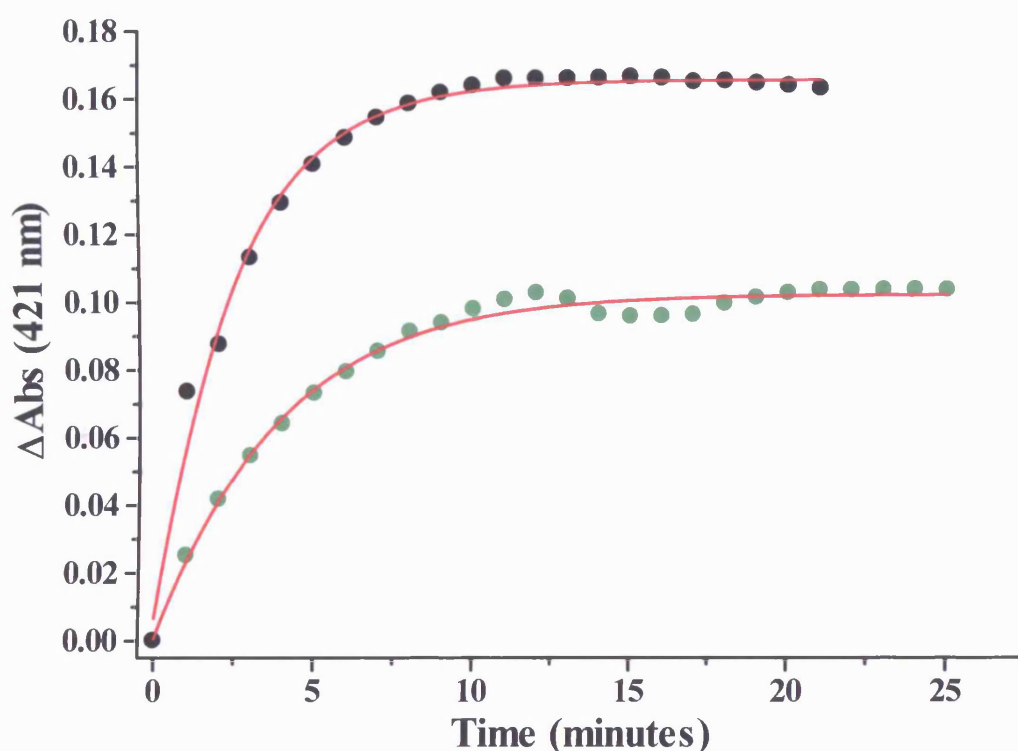
Figure 48 Plots of the change in absorbance at 421 nm *versus* time for Mtb CYP51 diluted in buffer at pH 6.0 (black circles) and pH 7.0 (green circles). The data, which were created by subtracting the first spectrum recorded post-P450 complex induction from all subsequent spectra, were fitted with a mono-exponential function (Equation 7) to determine the rate of formation of the P420 species. The curve-fitting analysis determined the P420 formation rate at pH 7.0 to be 0.246 ± 0.007 min^{-1}, whilst the rate at pH 6.0 was 0.298 ± 0.019 min^{-1}, indicating that the P420 species is formed more rapidly under the more acidic conditions.

The collapse of the CYP51 ferrous carbon-monoxy species has been described and investigated in previous studies (169,196), as well as Chapters 3.18, 3.19, and 3.22, and the data presented in this section further expand on the understanding of this phenomenon. An important initial finding of this study is that it was possible to record spectra of the CO-complex across a wide range of pH values (at least from 6.0 to 9.0) with little change in the nature of the spectra recorded. This suggests that the protein structure of Mtb CYP51 is quite tolerant of fluctuations in pH within this range, and that exposure to these conditions do not significantly impinge on heme binding or cysteinate/cysteine coordination. The spectra documenting the decay of the CYP51 CO-complex, gathered at pH 6.0 and 7.0, illustrate distinct variations in the amounts of the P450 and P420 species formed following dithionite reduction and CO binding. It appears that a greater amount of P420 is ultimately attained in more acidic conditions, where protons are more abundant, which is consistent with previous studies that identified conversion of P450 to P420 to be the result of protonation of the thiolate ligand (236). The rate of formation of P420 is also accelerated at pH 6.0. Thus, the data suggest that pH perturbs the P450/P420 equilibrium, as buffers of lower pH induce a greater degree of protonation of Cys 394 of Mtb CYP51 than buffers of neutral or basic pH, and stimulate the rate of P420 formation. The fact that at lower buffer pH (i.e. at pH 6.0 compared to 7.0) less P450 is formed (as measure immediately after inducing complex formation) further backs this theory, as do the rates of P420 formation obtained from the data shown in Figure 48. These data show that the rate of formation of the P420 species is appreciably enhanced at pH 6.0, thus indicating that rate of protonation is increased by decreasing pH, and that the equilibrium between the P450 and P420 forms is shifted in favour of the latter. This again supports the findings of Perera et al. (236) that the P420 form of cytochromes P450 arises because of a modification of the proximal ligand of the heme, and shows, as is described in previous sections (Chapters 3.18, 3.19, and 3.22), that the stability of the CO-complex of Mtb CYP51 is dependent on both thermodynamic and structural factors.

This series of studies of the ferrous carbon-monoxy complex of Mtb CYP51 has helped to expose important thermodynamic and structural facets that influence its stability and decay. However, until a true substrate for this monooxygenase is defined it is unlikely that the mechanism (structural or otherwise) that underlies stabilization of "active" P450 species of CYP51 (and thus extends enzyme catalysis) will be fully understood.

3.22 The temperature dependence of the Mtb CYP51 spin-state

The optical spectra of estriol- and 2-phenylimidazole-bound CYP51 display blue shifted Soret bands (from 419 nm to 392 and 395 nm, respectively) indicative of type I spectral changes induced by substrate-like compounds (Chapters 3.9 and 3.10). For the estriol-ligated enzyme, this binding mode is confirmed by EPR studies through the demonstration of the presence of high-spin heme iron (Chapter 3.12). However, the CYP51 EPR spectra recorded in the presence of 2-phenylimidazole are typical of a low-spin heme iron and show no evidence for the high-spin component. As these data contradict both the optical spectra recorded prior to, and following, the recording of the EPR spectra, as well as room temperature Resonance Raman spectroscopy by Matsuura et al. (202) this phenomenon required further investigation. Thermal influences on the spin-state of the heme iron of cytochromes P450 have been recognised for a number of years (69,241,242). In a seminal study of phenomenon in P450cam by Sligar (69), it was observed that increased high-spin heme content could be achieved for both substrate-free and substrate-bound enzyme by elevating the incubation temperature of the sample. As the EPR data obtained for the binding of 2-phenylimidazole to CYP51 were non-standard it was thus decided that the influence of temperature on the CYP51 heme spin-state should be studied and compared to the P450cam study by Sligar (69). This may identify any features of the interaction between CYP51 and 2-phenylimidazole underlying the apparent EPR anomaly. Accordingly, this section describes the temperature-induced spectral changes pertaining to the heme iron spin-state of CYP51. The study was carried out at a range of temperatures between 5 and 50 °C in the absence of ligand, as well as in the presence of the substrate-like compounds estriol and 2-phenylimidazole. The results of these studies are described below.

The effects of temperature on the spin-state of the heme iron of Mtb CYP51 were investigated by recording the UV-Visible absorption spectra of the protein at a range of temperatures. Spectra were collected between 250 and 800 nm using a Cary UV-50 Bio spectrophotometer, which was fitted with a Peltier accessory that enabled the temperature of the sample to be varied between 5 and 50 °C. Ligand-free CYP51 was diluted to ~2 μM in 50 mM Tris.HCl pH 7.2 to a final volume of 1 ml, and allowed to equilibrate at 30 °C before an initial spectrum was recorded. Subsequently, as the temperature of the sample was progressively decreased in 2 °C intervals, spectra were recorded. Having reached the minimal possible temperature attainable for the apparatus

(approximately 5 °C) spectra of the sample were recorded at this temperature and as the temperature was elevated in intervals of 2 °C up to 50 °C. Following each temperature decrease, and increase, a respite of two minutes was allowed in order that the enzyme should fully equilibrate to the new temperature before recording absorption spectra. Spectra above 50 °C were rarely recorded due to precipitation and aggregation of the protein above this temperature, preventing the enzyme equilibrating and effectively terminating the individual experiment. In order to observe the influences of ligands on thermally induced spin-state changes, the study was also performed in the presence of estriol and 2-phenylimidazole (87 μM and 7.5 mM respectively) which were levels approaching saturation, but did not cause excessive turbidity of the samples. Data analysis involved firstly creating difference spectra by subtracting the spectrum recorded at the lowest temperature from all other spectra. Subsequently, the troughs (absorbance minima at approximately 389 nm) were subtracted from the peaks (absorbance maxima at approximately 423 nm) for each difference spectrum, and the resultant absorption changes were plotted versus temperature. These plots are presented in Figure 49, and reveal how the presence or absence of ligand compounds impact upon the overall spin-state equilibrium of the heme iron and the temperature dependence of the equilibrium.
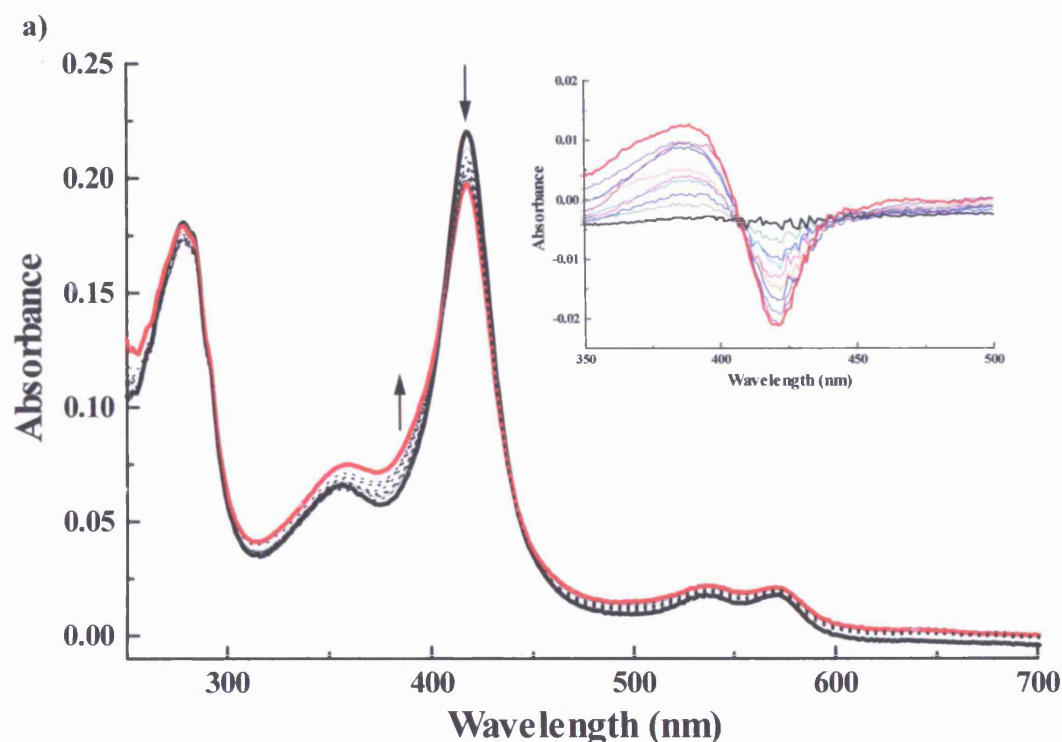
Figure 49 a) Selected UV-Visible absorption spectra recorded for ligand-free Mtb CYP51 during experiments to observe thermally-induced heme iron spin-state changes. **b)** and **c)** (next page) display selected spectra collected in the presence of 87 μM estriol and 7.5 mM 2-phenylimidazole, respectively. For each set of spectra, arrows denote the direction of spectral changes as temperature is increased and insets show difference spectra, created by subtracting the initial (lowest temperature) spectrum from all subsequent spectra. The difference spectra demonstrate that increases in temperature cause the proportion of ligand-free and estriol-bound low-spin heme iron to decrease and high-spin heme iron proportion to increase, whilst the reverse is true for 2-phenylimidazole-bound enzyme. Solutions of CYP51 were prepared at ~2 μM, prior to ligand addition (where applicable), and spectra were recorded between 278 and 323 K. The lowest temperature spectrum (at 5 °C) is shown as a thick black line in each case, and the highest temperature spectrum (typically recorded at 50 °C) is shown as a thick red line.

b)

c)
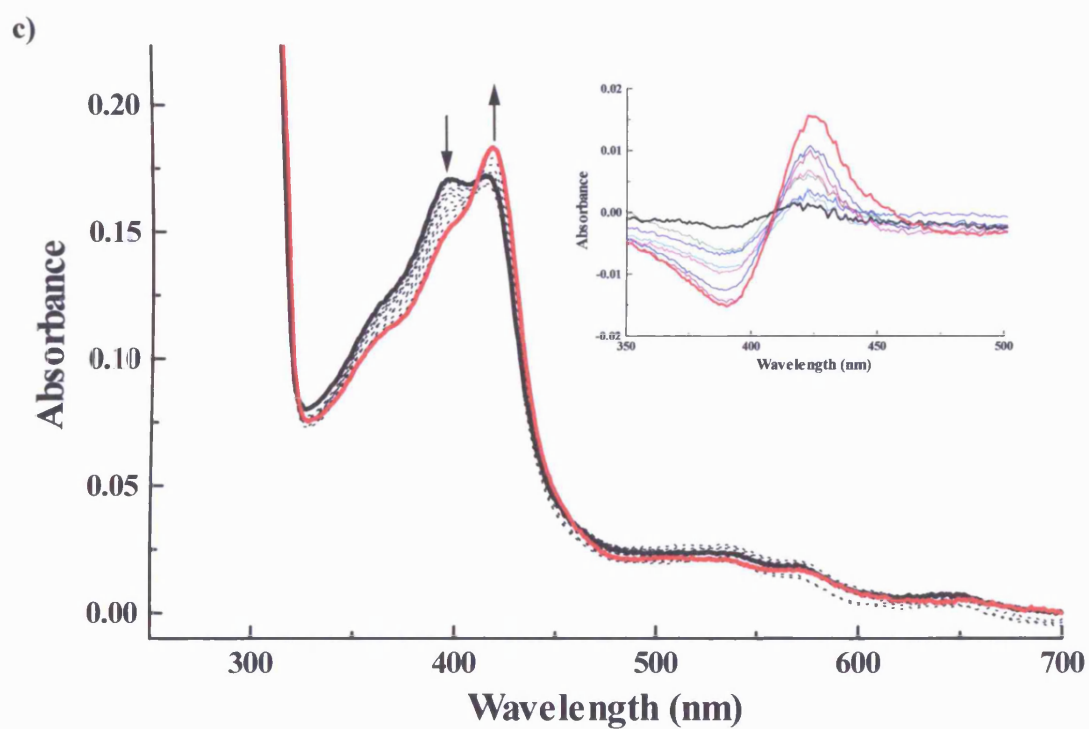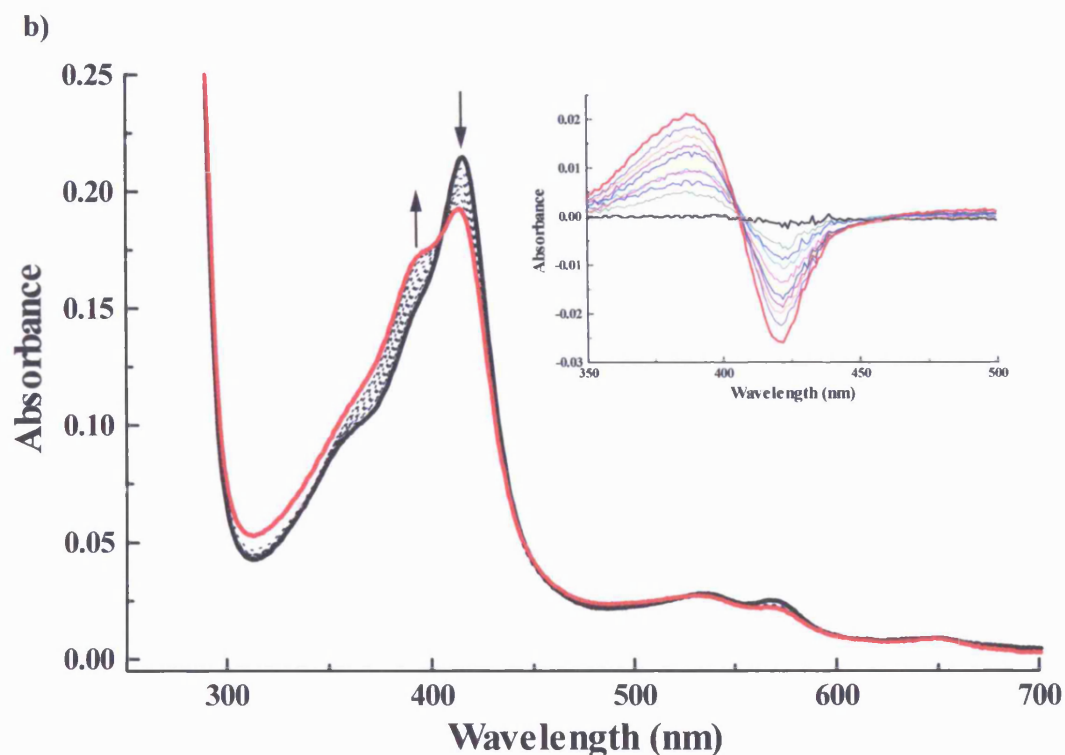
Spectra identifying how the spin-state of ligand-free Mtb CYP51 alters due to induced temperature changes are shown in Figure 49. These spectra illustrate that as the temperature of the sample increases the intensity of the Soret band at 419 nm decreases with a concomitant increase in intensity at ~390 nm. Within the constraints of the

157

experiment, the maximal low-spin contribution at 419 nm is achieved at approximately 8 °C whilst maximal amounts of high-spin enzyme occur at approximately 37 °C. Above this temperature, further increases in the intensity of the Soret band at ~390 nm may occur, but due to turbidity of the protein solution these changes are difficult to distinguish from protein precipitation and aggregation. An isosbestic point is found at approximately 406 nm and suggests a clean transition between the high- and low-spin states of the enzyme. The absorption spectra obtained for estriol-ligated CYP51 show a similar trend with elevated high-spin contributions at 390 nm achieved at high temperatures whereas low temperatures result in a greater intensity of the low-spin form at 419 nm, although the amplitude of the thermally induced changes are greater for the estriol-bound form than for substrate-free CYP51. Furthermore, similar to the substrate-free CYP51, the estriol-ligated form demonstrates an isosbestic point at 405 nm, again indicating that the high- and low-spin states are intrinsically related and that they are inter-converting as temperature is varied.

The absorption spectra for the 2-phenylimidazole-bound CYP51 study display intriguingly different thermally induced spectral changes. From the spectra, it is observed that, as temperature increases, the 2-phenylimidazole-induced high-spin peak at ~390 nm is diminished, whilst the absorbance at the low-spin Soret band peak (approximately 419 nm) increases. Although these spectral changes occur in the opposite direction to those seen for the substrate-free and estriol bound enzymes, the 2-phenylimidazole spectra otherwise display comparable features. Indeed, the data demonstrate a clean transition between the high-spin and low-spin forms of CYP51 that is further confirmed by the presence of an isosbestic point at ~409 nm. Furthermore, in spite of the thermally-induced spectral changes occurring in opposite directions, the overall changes in Soret region absorption intensity of the 2-phenylimidazole- and estriol-ligated samples are seen to be roughly equivalent in amplitude.

The dissimilarities between the spin-state changes of ligand-free and estriol-bound enzyme compared to the 2-phenylimidazole-ligated CYP51 are clearly demonstrated by the difference spectra insets in Figure 49. These were created by subtracting the spectra recorded at the lowest achieved temperature from all other spectra, and show that the estriol-bound and substrate-free samples exhibit difference spectra akin to those seen for compounds displaying type I binding in other P450 systems, whilst the 2-phenylimidazole difference spectra is analogous to that of a compound demonstrating type II binding. Further distinction between the thermally induced spin-state changes

for the three samples is shown in Figure 50, which plots the difference between absorbance at 390 and 423 nm, determined from the difference spectra in Figure 49, against temperature. This figure shows how the amplitudes of the absorbance changes observed for estriol- and substrate-free enzyme differ, as well as making differing temperature dependence of the spin-state changes of the three samples more apparent. The plots clearly present the inverse relationship between the high-spin component of the 2-phenylimidazole-bound CYP51 and temperature contrasted with the substrate-free and estriol-bound data, where the high-spin component increases in conjunction with temperature elevations.
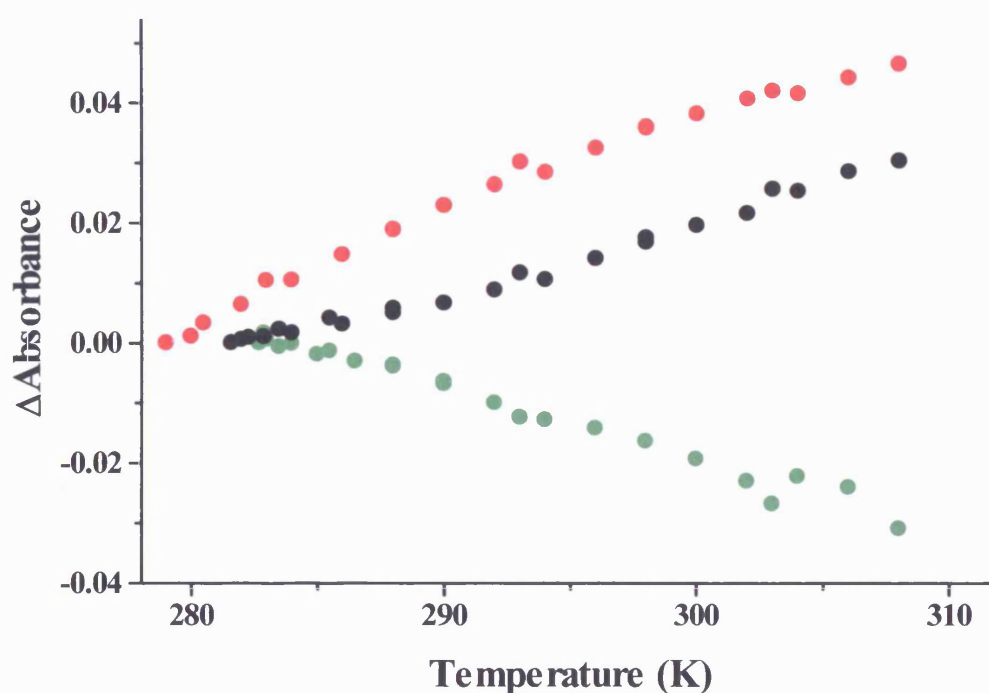
Figure 50 The thermally-induced absorption changes recorded for ligand-free (black), estriol-bound (red), and 2-phenylimidazole-bound (green) Mtb CYP51 (~2 μM). The data represent the maximal absorbance changes induced on temperature modulation, calculated by subtracting absorbance at 388, 389, and 390 nm from absorbance at 422, 423, and 425 nm, for the ligand-free, estriol-bound, and 2-phenylimidazole-bound samples, respectively. Due to protein aggregation and precipitation caused by elevated temperatures and high ligand concentrations, data are shown between 280 and 310 K. Replicates of the 2-phenylimidazole-bound data using phosphate buffer rather than Tris buffer also reported a decrease in absorbance at 390 nm as sample temperature was increased, suggesting the phenomenon to be a genuine feature of this ligand-enzyme complex.

159

The results of the thermally induced spin-state changes for substrate-free and estriol-bound Mtb CYP51 display a positive correlation between temperature and the proportion of high-spin heme iron present. For these samples, temperature increases lead to a depletion of the low-spin component and a concomitant increase in the high-spin form. These data are typical of the cytochromes P450 and are in agreement with the temperature-dependent optical changes observed by Sligar for the well-documented monooxygenase P450cam in both the presence and absence of substrate (69). The approximately linear dependency of the spin-state changes upon increasing temperature, as seen in Figure 50, as well as the clean transitions between the low- and high-spin forms displayed in the optical spectra (Figure 49), indicates that a thermal equilibrium exists between the two spin-states. In this equilibrium, the low-spin form is favoured by low temperatures, whilst higher temperatures promote a shift in the equilibrium towards greater amounts of high-spin heme iron. However, the result of increasing sample temperature on the spin-state of 2-phenylimidazole-bound CYP51 is that decreased quantities of high-spin enzyme form. This is a non-standard change for those cytochromes P450 studied to date, conflicting with other data from this study and from previous work (69). The isosbestic point at approximately 409 nm implies that the high- and low spin-states are in equilibrium, although in this case the thermal equilibrium influencing the ratio of high and low spin heme iron is reversed with respect to the above-mentioned samples. The EPR spectra for this enzyme-ligand complex were recorded at 10 K and show no evidence of a high-spin signal. However, the optical spectra, recorded at room temperature, attest to 2-phenylimidazole inducing formation of the high-spin form of the enzyme (at the expense of the low-spin form). According to these data, at 10 K the equilibrium between high- and low-spin heme iron lies very much against the high-spin form and for this reason it may not be observed under the conditions of the EPR experiment. Moreover, further evidence for the thermal equilibrium is demonstrated by absorption spectra of the thawed EPR sample, which also identify the presence of the high-spin form of 2-phenylimidazole-bound CYP51.

Thermal influences on the dissociation of 2-phenylimidazole were not expected to be of significance in this experiment, due to the ligand being present at a near-saturating concentration. However, to further ensure the validity of these results, control experiments were carried out to exclude the influences of temperature upon buffer pH. The experiment was replicated utilising potassium phosphate buffer and the same

160

phenomenon was again observed, suggesting that the inverted dependence of spin-state change on temperature, as seen for 2-phenyimidazole-bound CYP51, were not in any way related to thermally-induced changes in buffer pH.

An explanation for the unusual spin-state changes observed for 2-phenylimidazole-ligated CYP51 could originate from the effects of temperature on the ligand-binding mode or protein structure. Structural data for the CYP51 protein from a study by Podust *et al.* (35) identifies that substantial conformational changes are induced by ligand binding, particularly in the C helix and BC loop regions, and play important roles in permitting ligand access to the active site and ligand binding. Hence, with the knowledge that Mtb CYP51 demonstrates structural flexibility, the atypical thermally induced spin-state changes seen for the 2-phenylimidazole-bound CYP51 could be due to ligand-induced alterations in the protein's structure, or the adoption of alternative binding modes brought about by temperature-dependent conformational changes. These factors could in turn explain the lack of a high-spin EPR signal for the 2-phenylimidazole-bound enzyme, as the low temperature at which the spectra were recorded may promote a particular binding mode or structural conformation that favours the low-spin state. It is possible that, at ambient temperatures, thermally induced structural changes alter the mode of binding of 2-phenylimidazole between states in which the axial water is either removed (favouring high-spin) or maintained (favouring low-spin). At low temperature, temperature-dependent effects on the spin-state equilibrium (favouring low-spin at low temperature) along with any structural and binding effects result in the absence of detectable high-spin heme iron content. Clearly structural studies of the CYP51:2-phenylimidazole complex might shed further light on the phenomenon.

3.23 Stopped-flow studies of ferredoxin/Mtb CYP51 electron transfer

In addition to identifying the location of the CYP51-encoding gene *Rv0764c*, analysis of the *Mycobacterium tuberculosis* genome in Chapter 3.2 identified a number of noteworthy proteins in the immediate vicinity, including a ferredoxin (*Rv0763c*) and a putative oxidoreductase (*Rv0765c*). Early studies by Gunsalus and co-workers (243) on P450cam from *Pseudomonas putida* identified that cytochromes P450 require a series of redox partner proteins in order to derive electrons from the coenzymes NADH and NADPH. With some notable exceptions, e.g. P450 BM3 from *B. megaterium* (129) and P450nor from *F. oxysporum* (82,83), the redox partners of prokaryotic cytochromes P450 (Class I) are typified by the ferredoxin and ferredoxin reductase type system observed for e.g. P450cin from *Citrobacter braakii* (200). Genomic analysis of the pathogen *M. tuberculosis* does not indicate that the P450 systems here should be anything other than Class I in nature. Hence, based upon the requirement of Mtb CYP51 for a ferredoxin, and by analogy to a similar genomic arrangement of cytochrome P450 and ferredoxin in *Pseudomonas putida* (244), the Mtb ferredoxin protein is postulated to be the natural redox partner of CYP51 , and the fact that this ferredoxin supports sterol demethylation is also consistent with this conclusion (169). In this study, an attempt to recreate part of the proposed physiological redox system that delivers electrons to CYP51 (in order to drive catalysis of substrate oxygenation) is investigated by rapid mixing kinetic studies. The experiments, based on those reported by Munro *et al.* (26), involve mixing reduced Mtb ferredoxin with CYP51 in a saturated CO buffer system. This will allow determination of the rate of electron transfer from the ferredoxin to the P450, with the signal followed (reflecting the formation of the ferrous carbon-monoxy complex of CYP51) occurring on electron transfer from the ferredoxin to the P450. The employment of stopped-flow absorption techniques should permit determination of the limiting rate (k_{red}) for the single-electron transfer from the ferredoxin to the P450, as well as allowing the collapse of the ferrous carbon-monoxy complex (in an oxygen-free environment) from P450 to P420 to be studied over a longer timescale. Furthermore, the potentiometry presented in Chapter 3.17, and by McLean *et al.* (159), identifies redox midpoint potentials of -375 ± 5 mV for substrate-free Mtb CYP51, and -31 ± 5 mV for the ferredoxin protein. Hence, in order for reduction of the P450 to occur, this large thermodynamic barrier must be overcome, with electrons having to be transferred against a gradient of approximately 340 mV.

Electron transfer against a redox potential gradient has been reported previously for physiological systems (129), and it is clearly the case that electronic equilibration between two centres will occur according to their respective potentials. In addition, if kinetics of the forward reaction are faster than those of the reverse reaction (for structural or other reasons), then equilibrium position can be altered. Moreover, if the product of the forward (thermodynamically disfavoured) reaction is rapidly converted to another species, then a redox potential barrier could be a mechanism to control overall reaction rate in the system. This is a potential explanation in the CYP51/ferredoxin system, where dioxygen binding likely traps the ferrous P450 in a state that favours a subsequent electron transfer from the ferredoxin and the progression of the overall reaction cycle. In the stopped-flow system used the "capture" of electrons transferred to the P450 is achieved by the rapid binding of CO and the formation of a relatively stable CYP51 CO complex, or physiologically in the form of an oxy complex. In some ways this mimics the physiologically relevant reaction with the formation of an oxy complex that likely pulls the reaction towards completion. This stopped-flow study will thus reveal the kinetics of electron transfer from the redox partner to CYP51 and will demonstrate that electron transfer from the ferredoxin is still feasible even for the substrate-free P450 – where electron transfer must occur over a much larger potential gradient than for the substrate bound form.

The experiments to determine the rate of single electron transfer from the Mtb ferredoxin to CYP51 were performed under a nitrogen atmosphere in an anaerobic glove box (Belle Technology), in which oxygen levels were maintained at less than 2ppm. Data collection was achieved via an Applied Photophysics SX18MV UV-visible stopped-flow instrument coupled to a photodiode array UV/visible detector scanning between 250 and 750 nm, and maintained at 30 °C. The P450 was equilibrated in anaerobic 50 mM KPi pH 7.5, previously bubbled extensively with carbon monoxide in order to produce a saturated solution. Equilibration was done using a Bio-Rad 10DG desalting column, before dilution of CYP51 to a final concentration of 2 – 5 μM. The ferredoxin was prepared immediately prior to use, initially being reduced using a minimal amount of solid sodium dithionite. The protein was then passed down a Bio-Rad 10DG desalting column (equilibrated with CO-saturated 50 mM KPi pH 7.5) to remove superfluous dithionite, and the spectrum of the protein checked to ensure complete reduction of the protein was achieved. The ferredoxin (~20 μM) and CYP51 proteins were mixed rapidly using the stopped-flow apparatus, and spectra recorded at

time intervals of between 0.5 seconds and 1 minute until the collapse of the ferrous carbon-monoxy complex was deemed to have finished. Control experiments were performed with CYP51 or ferredoxin in CO-saturated buffer in the absence of reductant, in order to eliminate the possibility of photoreduction of the samples, which has been reported previously for other systems, including P450cam from *Pseudomonas putida* (245). In order to calculate both the rate of electron transfer to CYP51, and the collapse of the P450 species to the P420 form of the enzyme, a two-step model (A→B→C) was applied to the ligand-free time resolved spectra (Figure 51) using ProKin global analysis software (Applied Photophysics). This software was utilised to perform analysis across the entire spectra, rather than only considering the absorbance at 448 and 421 nm, and the rates calculated in this way are reported in Table 10. These values represent the rates of reduction of CYP51 by the ferredoxin and thus electron transfer from the electron donor (reduced ferredoxin) to the CO-saturated CYP51. They also report upon the rate of collapse of the ferrous carbon-monoxy P450 form to the P420 species.
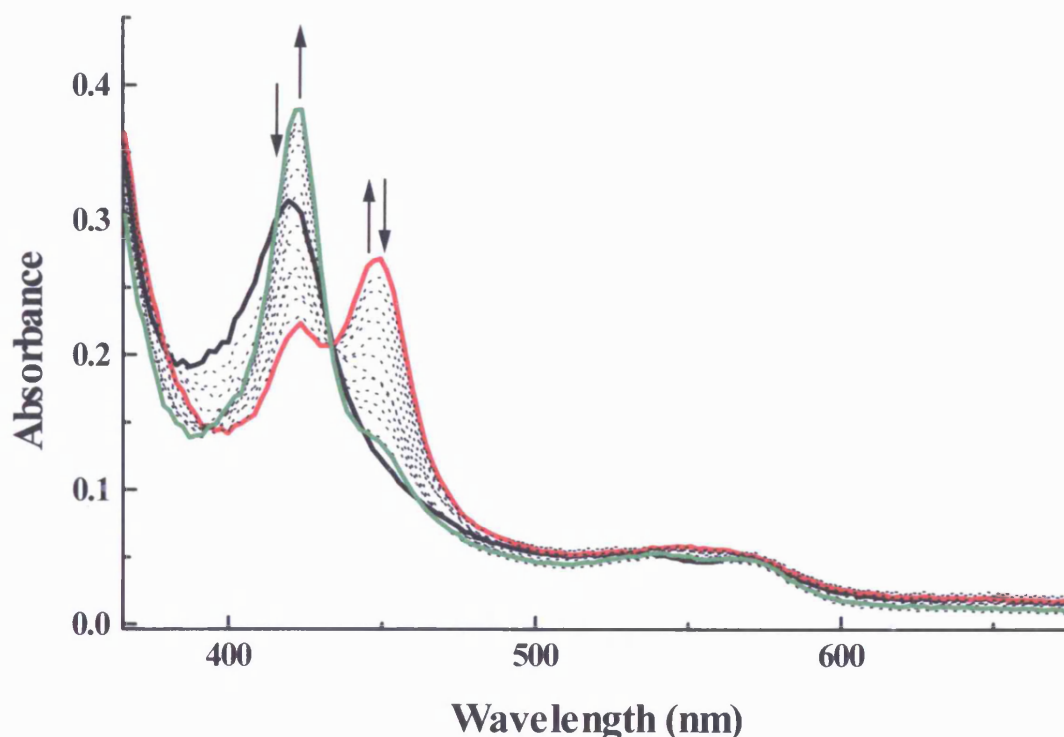
Figure 51 Selected UV-Visible spectra recorded during anaerobic stopped-flow kinetic studies to reconstitute the interaction of CYP51 and the product of its adjacent *M. tuberculosis* gene, *Rv0763c*. The formation and collapse of the Mtb CYP51 ferrous carbon-monoxy complex were monitored, following rapid mixing of CO-saturated CYP51 and pre-reduced ferredoxin, by photodiode array apparatus linked to a SX18MV UV-visible stopped-flow instrument (Applied Photophysics). The initial spectrum of the mixed proteins (black, solid), when compared to spectra of ferredoxin-free CYP51 (Chapter 3.4), exhibits a broadening of the Soret band due to the presence of the ferredoxin protein. The red and green spectra identify the maximal extents of the P450 and P420 species respectively, and indicate that electron transfer between the ferredoxin and CYP51 occurs, despite an apparent thermodynamic barrier. Dotted lines identify intermediate spectra, whilst arrows identify the directions of spectral changes. Rates of ferrous carbon-monoxy species formation and collapse were determined by fitting entire spectra using ProKin global analysis software (Applied Photophysics), and are displayed in Table 10.

The UV-Visible spectra presented in Figure 51 demonstrate that rapid mixing of CO-saturated CYP51 and pre-reduced ferredoxin results in the formation of the ferrous carbon-monoxy complex of the *M. tuberculosis* cytochrome P450. As with the formation of the ferrous carbon-monoxy complex in aerobic conditions (Chapters 3.18), the Soret band of the P450 species is red-shifted to 448.5 nm. However, under the anaerobic conditions of this experiment the initial intensity of this peak predominates over the peak at 421 nm. This likely reflects the ability to record spectral details at an earlier time point than is feasible using a standard UV-visible spectrophotometer. The spectra also report that, in concurrence with the aerobic data, the P450 complex decays

rapidly, typically within 30 minutes, to the "inactive" P420 form. The rates of the formation and collapse of the CYP51 P450 species, determined by the use of global analysis software, are shown in Table 10 alongside those reported by McLean *et al* (159) for identical experiments performed in the presence of 50 μM estriol and 3 mM 2-phenylimidazole. These data identify that the rate of the Mtb CYP51 P450-complex formation, in the presence of 20 μM ferredoxin, occurred at 3.0 ± 0.1 min^{-1}. In the presence of 2-phenylimidazole the rate of formation of the ferrous carbon-monoxy complex (3.0 ± 0.1 min^{-1}) is unchanged from the ligand-free enzyme. However, in the presence of estriol the rate is increased to 4.3 ± 0.1 min^{-1}. The rate of the ligand-free CYP51 P450-complex collapse was determined as 0.294 ± 0.008 min^{-1}, a value that is approximately 10-fold slower than the rate of formation of the ferrous carbon-monoxy complex. This rate was observed to decrease to 0.174 ± 0.009 min^{-1} in the presence of 2-phenylimidazole, and to 0.018 ± 0.001 min^{-1} when estriol was present.

Mtb CYP51 ligand	Rate of complex formation (A→B) (min^{-1})	Rate of complex collapse (B→C) (min^{-1})
Ligand-free	3.0 ± 0.1	0.294 ± 0.008
2-phenylimidazole	3.0 ± 0.1	0.174 ± 0.009
Estriol	4.3 ± 0.1	0.018 ± 0.001

Table 10 The rates of the formation and collapse of the Mtb CYP51 ferrous carbon-monoxy complex, determined by stopped-flow studies in the absence of an additional ligand, as well as in the presence of 3mM 2-phenylimidazole and 50 μM estriol. The data describe both the conversion of oxidised CYP51 (2 − 5 μM) to the ferrous carbon-monoxy species, induced by reduction by electrons delivered via the ferredoxin (~20 μM), and the spontaneous decay of the P450 form to the P420 form. The estriol- and 2-phenylimidazole-bound CYP51 data were obtained by Dr. K.J. McLean (159), and all data were calculated by analysis of entire spectra (e.g. Figure 51) using ProKin global analysis software (Applied Photophysics).

The results of the Mtb CYP51/ferredoxin stopped-flow kinetic studies reveal a number of interesting features of this physiologically relevant system, the most notable of which is that there is a productive redox interaction between CYP51 and the ferredoxin. The formation of the CYP51 ferrous carbon-monoxy species indicates that electrons are indeed transferred from the pre-reduced ferredoxin protein to CYP51, inducing enzyme reduction and facilitating CO-ligation at the heme. In turn, this shows the prediction that the gene products of *Rv0763c* and *Rv0764c* would form part of a redox-active physiologically relevant system to be correct. The rate of electron transfer

to the P450 (3.00 ± 0.1 min^{-1}) is significantly slower than rates determined for other prokaryotic systems, such as those from *Bacillus megaterium* (~14000 min^{-1}) and *Pseudomonas putida* (~6000 min^{-1}) (26,246). This indicates that the equilibrium governing the transfer of electrons from the Mtb ferredoxin is finely poised at a point where electrons will only "trickle" across to CYP51. However, it does signify that, although there is a considerable thermodynamic barrier between the two proteins, as determined by redox potentiometry (Chapter 3.17), electrons can be successfully passed across this barrier. Another interesting feature of the recorded spectra is that the amount of P450 complex achieved immediately after mixing is significantly greater than that obtained under aerobic conditions by standard UV-Visible spectroscopic measurements (Chapter 3.4). This may be due to absence of oxygen during the experiment, thus preventing spontaneous oxidation, or due to the stopped-flow technique capturing spectra much sooner after P450 complex induction than is possible in aerobic "steady-state" studies.

Although estriol and 2-phenylimidazole have both been shown to bring the redox potential of Mtb CYP51 closer to that of the Mtb ferredoxin by approximately 150 mV (Chapter 3.17, (159)), the rate of ferrous carbon-monoxy complex formation was shown to only increase in the presence of estriol. This increase does not raise the rate of electron transfer to levels as great as those observed for other systems, e.g. P450 BM3 from *B. megaterium* (26), but suggests that the presence of a "true" substrate may instigate a much larger increase in rate of ferredoxin-mediated P450 reduction. These data also add to the evidence that the true substrate of Mtb CYP51 is likely to be more structurally similar to that of estriol than 2-phenylimidazole, as this substituted-imidazole compound fails to enhance the rate of electron transfer to the P450 to any significant extent.

The spectra show that, as was reported by Aoyama *et al.* (196), the P450 complex of the ligand-free enzyme is unstable, collapsing at a rate that is approximately 10-fold slower than the formation rate of this species (i.e. the apparent electron transfer rate from the ferredoxin) (Table 10). As with the studies in Chapter 3.16 and 3.18, these data show that the presence of excess Mtb ferredoxin does not stabilise the ferrous carbon-monoxy P450 species, which still collapses to P420. As above, this has been shown to be the result of protonation of the thiolate ligand of the heme iron (Chapter 3.22, (236)). However, the data for the collapse to the P420 species in the presence of estriol and 2-phenylimidazole concurs with data in Chapter 3.19, as these two

compounds appear to stabilise the P450 complex (retarding decay to P420). The extent of the stabilization of the thiolate ligand is most obvious for the estriol-bound enzyme, as the P450 decay rate is decreased by approximately 16-fold compared to ligand-free CYP51, whereas stabilization due to 2-phenylimidazole is much less and has a much smaller influence on the decay rate. Although both ligands effect high-spin Soret band shifts (Chapters 3.9 and 3.10), the fact that estriol appears to stabilise the ferrous carbon-monoxy complex to a greater extent, allied with the enhanced rate of electron transfer reported in the presence of estriol, implies that this bulky sterol compound emulates the true substrate of CYP51 much more successfully than does 2-phenylimidazole. Previous studies have shown Mtb CYP51 to be capable of sterol demethylation at a very slow rate (169), which, when considered with these data, implies that the sterol used (lanosterol) is unlikely to have induced significant shifts in the redox potential of the P450. Hence, this further supports the theory that although CYP51 from *Mycobacterium tuberculosis* may have common ancestors in all kingdoms of life (36,197), the Mtb P450 may have evolved to catalyse a different reaction from eukaryotic CYP51 enzymes, although it still retains some ability to demethylate sterols.

In Chapter 3.17 it was proposed that the thermodynamic barrier imposed upon the CYP51/ferredoxin system of *M. tuberculosis* might be a control mechanism to down-regulate CYP51 activity. These data supports this theory as it demonstrates that the midpoint potentials of the two proteins are quite unfavourable for P450 reduction. This control would limit the amount of catalysis performed by CYP51 to a rate appropriate to *M. tuberculosis*, a very slow-growing organism that spends long periods in a dormant state (151). A requirement for this model might be that the oxy complex of the P450 is quite stable under cellular conditions, avoiding non-productive collapse until delivery of the second electron for catalytic turnover. Alternatively, the second electron delivery could be substantially faster than that of the first electron. The stopped-flow data show that partial stabilization is achieved by binding of the substrate-like compound estriol, and hence the binding of the true substrate of Mtb CYP51 may elicit similar (or greater) stabilization of the oxy complex. An alternative explanation is that the product of the CYP51 reaction is toxic to the host organism at high levels and thus its rate of production is restricted to non-toxic (or physiologically relevant) levels by imposing the thermodynamic barrier on the system. However, until the physiological CYP51-catalysed reaction is elucidated, and until a true substrate for this enzyme is found, these theories are unlikely to be confirmed by direct study of the Mtb CYP51.

Chapter 4

Characterization of CYP116B1; a novel cytochrome P450

from *Ralstonia metallidurans*

4.1 General information

The study of *M. tuberculosis* CYP51 in Chapter 3 was performed in order to comprehensively characterize a cytochrome P450 whose physiological function could be significant to this organism's pathogenicity in humans, thus potentially identifying new targets for which anti-tuberculosis drugs could be developed. These studies introduced numerous methods by which to characterize cytochromes P450, and in this chapter these techniques are employed similarly in order to study a monooxygenase from the soil bacterium *Ralstonia metallidurans*. The initial aim of the CYP51 study was to perform a detailed biochemical study of this cytochrome P450. However, due to unusual findings made as the CYP51 investigation evolved, the study came to incorporate a number of studies more closely related to the thermodynamic and mechanistic properties of this system and its interactions with redox partners. Unlike CYP51, the cytochrome P450 studied in this section (CYP116B1) is not medically significant. However, like Mtb CYP51, this P450 from *R. metallidurans* is also of mechanistic interest, due to its novel fused protein arrangement (Chapters 1.7 and 4.2). Furthermore, CYP116B1 is of potential biotechnological interest, as homology to cytochromes P450 from other organisms suggests it may degrade thiocarbamate herbicides (124,125). Such a function means that this P450 could be employed in soil decontamination procedures. Hence, this chapter presents the first characterization of *R. metallidurans* CYP116B1, encompassing spectroscopic, kinetic, and thermodynamic investigations, using a combination of techniques including those utilised in Chapter 3.

As detailed in Chapter 1.10, *R. metallidurans* CYP116B1 was initially identified during speculative Blast searching for cytochromes P450 homologous to ThcB, a previously characterized monooxygenase from *Rhodococcus erythropolis* (125). It was proposed that this cytochrome P450, along with a homologue from the soil bacterium *Rhodococcus sp.* NCIMB 9784, would possess an amino terminal monooxygenase fused to a carboxyl terminal 2Fe-2S ferredoxin via a FMN-containing domain (125). These protein configurations, which are fusions of typical prokaryotic redox systems, have led to the expansion of cytochrome P450 classification, producing a fourth class of the enzyme, and demonstrate that the diversity of P450 systems is far wider than was initially envisaged. Sequence alignment studies for these two putative Class IV cytochromes P450 revealed that the monooxygenase terminal demonstrated highest homology with the CYP116 (ThcB) from *Rhodococcus erythropolis* (125), a protein

identified as having the capability of oxygenating thiocarbamate herbicide compounds (182). Hence, these studies identify two putative cytochromes P450 that are of interest in terms of both the reactions that they catalyse, and as a consequence of their fusion to novel redox partners. Such fusions likely evolve to enhance electron transfer and catalytic activity of the systems, and are also of significant interest for further understanding of P450/redox partner interactions. Initial confirmation that a Class IV cytochrome P450 could be expressed to generate a viable fusion protein was reported in an investigation of the *Rhodococcus sp.* NCIMB 9784 gene by Roberts *et al.* (124). This study aims to provide more detailed characterization of a class IV P450 system by the characterization of the *R. metallidurans* redox-partner fused cytochrome P450.

4.2 The genomics of *Ralstonia metallidurans* CYP116B1

The 6.9 megabase pair genome of *Ralstonia metallidurans* encodes approximately 6300 candidate genes, including the gene for the monooxygenase CYP116B1. This gene, first identified by speculative Blast searches for homologues of a herbicide degrading cytochrome P450 (125), is found between 54212 and 51870 base pairs, and is assigned as gene 1832 in the *R. metallidurans* genome database (http://genome.ornl.gov/microbial/rmet/). The nucleotide sequence of gene 1832 is 2343 bp in length, has a GC content of 63.5 %, and is proposed to encode a protein of 780 amino acid residues. The region of the genome in which the CYP116B1 is found contains various genes including transcriptional regulator proteins (1831 and 1834) and transmembrane proteins (1830 and 1836), and more notably a glutathione S-transferase (1835) and a heme biosynthesis protein (1828). The proximity of the protein involved in heme production may be of relevance in the context of the heme-binding properties of P450s, whilst it is plausible that the role of the glutathione S-transferase is to enhance the solubility and excretion of the products of CYP116B1 catabolism, as is seen in mammalian drug detoxification systems (247).

```
MPQTNAPASSGSCPIDHSALRAPNGCPISHQAAAFDPFEDGYQQDPPEYVRWSRA
QEPVFYSPKLGYWVVTRYDDIKAIFRDNITFSPSIALEKITPTGEAANAVLASYG
YAMNRTLVNEDEPAHMPRRRALMEPFTPAELAHHEPMVRKLTREYVDRFIDTGRA
DLVDEMLWEVPLTVALHFLGVPEEDMDLLRQYSIAHTVNTWGRPKPEEQVAVAHA
VGNFWQLAGRILDKMREDPSGPGWMQYGLRKQRELPEVVTDSYLHSMMMAGIVAA
HETTANASANAIKLLLQHPDVWREICEDPALIPNAVEECLRHNGSVAAWRRLVTR
DTEVGGMSLAAGSKLLIVTSSANHDEHHFADADLFDIHRDNASDQLTFGYGSHQC
MGKNLARMEMQIFLEELTSRLPHMRLAGQRFTYVPNTSFRGPEHLWVEWDPARNP
ERTDPTVLAPRDAVRIGEPTGGTTGRTLIVERVETAAQGVSRIRLVSPDGRALPR
WSPGSHIDIECGHTGISRQYSLCGDPADTSAFEIAVLREPESRGGSAWIHASLRA
GDKLKVRGPRNHFRLDETCRRAIFIAGGIGVTPVSAMARRAKELGVDYTFHYCGR
SRASMAMIDELRALHGDRVRIHAADEGQRADLAQVLGAPDANTQIYACGPARMIE
ALEALCATWPEDSLRVEHFSSKLGTLDPSREQPFAVELKDSGLTLEVPPDQTLLA
TLRAANIDVQSD            EVRVLAGEIDHRDVVLTRGERDANNRMMACCSRA
AKGGKIVLGL
```

Figure 52 The 780 amino acid residues encoded by *Ralstonia metallidurans* gene 1832 (CYP116B1). This sequence contains motifs, highlighted in red, green, blue, and orange respectively, for *b*-type heme binding, FMN phosphate group binding, an NADH binding site, and a 2Fe-2S cluster. The incorporation of these four motifs, which are typical of those found in cytochromes P450 and their redox partner proteins, implies that this polypeptide is multi-redox centre enzyme, derived from a fusion of genes encoding individual P450 and FMN/2Fe-2S-cluster-containing redox partner domains. The presence of the motifs were determined using the web-based ScanProsite program (www.expasy.org), which compares the amino acid sequence inputted to a library of consensus motifs (see Table 11) in order to identify potential features of the encoded protein.

The bioinformatic analysis of the amino acid sequence encoded by the CYP116B1 gene (Figure 52), using the web-based Protparam program (www.expasy.org), predicts a protein with a molecular weight of 86.356 kDa and a pI of 5.72. This analysis also reveals that 16 of the 780 amino acids encoded by this gene are cysteine residues. This is an unusually high number when compared to other cytochromes P450, including CYP51 from *M. tuberculosis* (4 Cys residues, Chapter 3.2), P450cam from *Ps. putida* (8 Cys), and the heme domain of P450 BM3 from *B. megaterium* (3 Cys). However, analysis using the ScanProsite program (www.expasy.org) reveals that a number of these cysteine residues are found in regions of the amino acid sequence that exhibit motifs typical of monooxygenases and their redox partners. For example, the region of the amino acid sequence highlighted in Figure 52, between residues 378 and 387 (FGYGSHQCMG), is shown to fit the criterion of the heme-binding consensus motif (Chapter 3.2), hence identifying Cys 385 as the cysteinate ligand that binds the heme macrocycle to the protein structure via a Fe-S bond. Three further cysteine residues are identified in a region of the sequence between amino acids 728 and 736 (CEEGLCGSC)

that exhibits a 2Fe-2S binding motif (Table 11), thus suggesting the gene to encode a ferredoxin protein, as well as the P450 monooxygenase. The binding of a 2Fe-2S cluster requires the coordination of the two iron atoms with four cysteine residues, and hence accounts for the presence of an additional cysteine, which derives from another part of the protein and is most likely located towards the protein's carboxyl terminal.

Binding site	Consensus motif	Corresponding CYP116B1 sequence
2Fe-2S cluster	C-X-X-[GA]-X-C-X-X-C	C-E-E-G-L-C-G-S-C
NADH	G-X-G-X-X-P	G-I-G-V-T-P
FMN phosphate group	[GS]-R-G-G-S	S-R-G-G-S

Table 11 The consensus motifs employed to identify regions of a protein capable of binding an iron-sulphur complex, the 5'-phosphate groups of NAD(P)H, and the phosphate group of FMN, as utilised by ScanProsite software (www.expasy.org). For each of the three consensus motifs, the corresponding region of the CYP116B1 amino acid sequence is also shown. For each motif, conserved residues are indicated by their single letter amino acid code, whilst an X identifies positions that can be occupied by any amino acid. At positions where the amino acid is restricted but not conserved, candidate residues are contained within square brackets. The consensus motif for heme binding is reported in Chapter 3.2.

As is indicated in Figure 52, the CYP116B1 amino acid sequence also demonstrates the presence of binding sites for the 5'-phosphate groups of NAD(P)H and the phosphate group of FMN, in the regions located between those for the P450 and ferredoxin domains. These two binding sites, found at amino acids 578 – 583 and 537 – 541, respectively, align with the consensus motifs shown in Table 11, and further imply that this sequence encodes an entire redox system (with both a NAD(P)H- and FMN-binding flavoprotein domain and a ferredoxin domain) contained within a single polypeptide. However, the arrangement of the redox centres is unlike those previously observed for fused P450-redox partner fusions, such as P450 BM3 from *B. megaterium* (129). The nature of the fused redox partner is distinct from that of e.g. human and other cytochrome P450 reductases (CPRs) (17), in which the two ancestral flavin-binding domains are fused to form a single membrane-incorporated diflavin protein. These CPR systems are constructed such that electrons pass from NADPH to a FAD cofactor bound to its domain at the carboxyl terminal of the protein, and then via an FMN cofactor (bound to its domain at the amino terminal) and onto the heme-containing P450 (Figure 53). In the case of BM3 (and its homologues), the heme

domain is covalently attached to the CPR, at the amino terminal of the flavocytochrome (129).

From these bioinformatic studies, and by homology to the *Rhodococcus sp.* NCIMB 9784 fused system (CYP116B2) (124), the configuration of the CYP116B1 redox centres differs from P450 BM3 and its CPR-like reductase, as the NADH binding site and ferredoxin reductase domain are found in the centre of the polypeptide. This arrangement requires electrons from NAD(P)H to pass from the FMN to the iron-sulphur cluster at the carboxyl end of the polypeptide, before being passed to the P450 domain, which itself must be positioned close enough to the ferredoxin domain to ensure electron transfer (Figure 53). Thus, as part of this study of CYP116B1, the unusual redox centre arrangement is investigated to examine the CYP116B1 domain interactions and the electron transfer system to the heme iron.
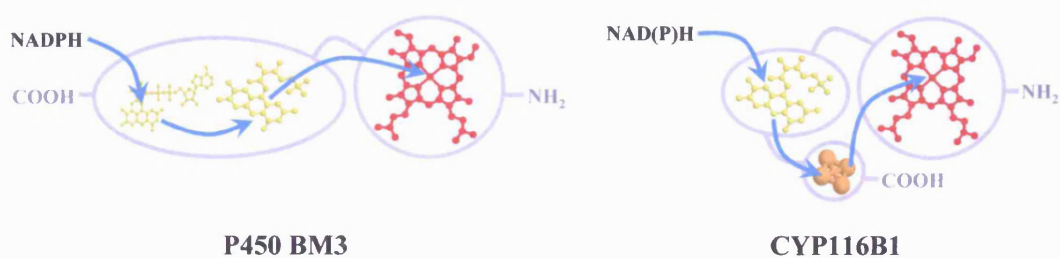
P450 BM3   **CYP116B1**

Figure 53 A schematic representation of the electron transfer routes (light blue arrows) from the pyridine nucleotide reductant to the heme iron in P450 BM3 from *B. megaterium* and CYP116B1 from *R. metallidurans*. In P450 BM3 NADPH-derived electrons follow a linear pathway from the carboxyl terminal FAD cofactor to the amino terminal P450 domain via an FMN molecule. In CYP116B1, the cofactor arrangement dictates that electrons entering the system at the centrally orientated FMN cofactor must pass firstly to the carboxyl terminal 2Fe-2S cluster before skipping across to the amino terminal P450 domain (129). In order to permit heme reduction, this route requires that the CYP116B1 protein folds in a manner that brings the heme- and iron-sulphur-containing regions within an electron transfer-permitting distance of each other (typically <14 Å, (248)).

As previously mentioned, the *R. metallidurans* CYP116B1 protein has similarities in domain architecture to *B. megaterium* P450 BM3 (125), with P450 and redox partner domains covalently joined. Using the CYP116B1 amino acid sequence as a template, Blast searches using the web-based ClustalW software (www.ebi.ac.uk/clustal/) identify numerous putative homologues of the *R. metallidurans* P450, almost all of which are from bacterial species, and a significant number of which are from human pathogens. A

174

summary of the percentage identities (compared to CYP116B1) for these putative redox-partner-fused cytochromes P450 is shown in Table 12, and a multiple alignment of the most closely related proteins is displayed in Figure 54. As well as full-length alignments, CYP116B1 shows significant homology to several smaller proteins. These include the cytochrome P450, ThcB (CYP116A1) from *R. erythropolis* (52 % identity), a phthalate oxygenase reductase from *Burkholderia cepacia* R18194 (40 % identity), and the vanillate monooxygenase reductase subunit from *Rhodococcus sp.* DK17 (48 % identity) (all identities cited are within the respective P450 or redox partner domains). From these similarity studies, it is apparent that the CYP116B1 protein is most likely derived from an ancient fusion of three genes, encoding three separate parts of a redox system. More recently, CYP116B1 almost certainly originated from a fusion of a P450 to a phthalate dioxygenase reductase-like redox partner. However, the reductase clearly should have originated from ancestral fusion of genes encoding smaller FMN- and 2Fe-2S-binding proteins. The evolution of CYP116B1-like fusion proteins clearly enables concerted transcriptional and translational regulation over an entire P450 redox system, and the fusion arrangement likely improves electron transfer rates between the domains, and thus enhances P450 catalytic activity. Furthermore, as this particular fusion is more abundant in nature than was previously thought, it is likely that the CYP116B1-like fusion plays important and widespread roles in various microbes, rather than being peculiar to *R. metallidurans*.

Host organism of homologous gene	% identity to *R. metallidurans* CYP116B1
Ralstonia eutropha JMP134	79
Burkholderia dolosa AU0158	75
Burkholderia thailandensis E264	73
Burkholderia mallei ATCC23344	71
Burkholderia pseudomallei Pasteur	70
Rhodococcus sp. NCIMB 9784 (CYP116B2)	66
Rhodococcus ruber	65
Rhodococcus erythropolis (CYP116A1)	52
Gibberella zeae PH-1	33

Table 12 The percentage identities of the nine putative cytochromes P450 with highest sequence similarity to *R. metallidurans* CYP116B1, as determined from Blast search data using the amino acid sequence of CYP116B1 as a template. Apart from the fungal *G. zeae* protein, all the proteins identified derive from bacterial species, including the human pathogens *B. dolosa*, *B. pseudomallei*, and *R. ruber*. The data show that a significant number of proteins exhibit the same redox partner fusion as CYP116B1, and that many of these are more closely related to the *R. metallidurans* P450 than previously identified members (i.e. CYP116A1 and B2) of the CYP116 family. The soil bacteria *R. metallidurans* and *R. eutropha* are very closely related organisms, and the exceptionally high identity (79 %) of their respective proteins suggests that these fused redox partner enzymes share a close common ancestry. This is further supported by a comparative alignment of the four *Burkholderia* species' proteins, which produce identities of up to 92 %, and hence indicate that these enzymes are almost certainly descended from a single common ancestor. The percentage identity value stated for *R. erythropolis* CYP116A1 corresponds to its alignment with only the heme domain of CYP116B1, as the former possesses no reductase-like domain. Blast searches were performed using web-based software found at www.ncbi.nhm.nih.gov/BLAST/.

a)

```
Ralme  SSANHDEHHFADADLFDIHRDNASDQLTFGYGSHQCMGKNLARMEMQIFLEELTSRLPHM 409
Raleu  SSANHDEAHFADADLFDIRRENAADQLTFGYGSHQCMGKNLARMEMQIFLEELTRRLPHM 412
Burdo  SSANHDEARFADADLFDIRRENASDQLTFGYGSHQCMGKNLARMEMQIFLDEFTRRLPHM 411
Burth  SSANRDERRFADADLFDIHRDDCAEHLTFGYGAHQCMGKHLARMEMQIFIDELTRRLPHM 415
Burma  SSANRDERRFADPDLFDIHRDNPADHLTFGYGSHQCMGKHLARMEMQIFIDELSRRLPHM 416
Burps  SSANRDERRFADPDLFDIHRDNPADHLTFGYGSHQCMGKHLARMEMQIFIDELSRRLPHM 416
Rhosp  ASANHDERHFERPDEFDIRRPNSSDHLTFGYGSHQCMGKNLARMEMQIFLEELTTRLPHM 406
Rhoru  ASANHDERHFDRPDEFDIRRPNSSDHLTFGYGSHQCMGKNLARMEMQIFLEELTTRLPHM 404
Gibze  NSGSRDESKFENPNKLDISRQSKTQHLGFGRGVHACLGAPFARLLLRTELAVLYTRLPNL 385
Rhoer  ASANRDDSMFPEPDDFDIHRGNAQRHLTFGIGSHTCLGATLARLEMKVFLEEVSRRLPHM 399
       *..:**  :*    .:  :**  *  .  :::*  **  *  *  *:*   :**:  ::    :    :    ***::
```

b)

```
Ralme  EIAVLREPESRGGSAWIHASLRAGDKLKVRGPRNHFRLDETCRRAIFIAGGIGVTPVSAM 587
Raleu  EIAVLREPESRGGSAWIHDHVKPGDRLKIRGPRNHFRMDEGCRKAIFIAGGIGITPVSAM 590
Burdo  EIAVLREAQSRGGSAWVHANLRVGDVLKIRGPRNHFRFAADAGKAIFVAGGIGITPIGAM 589
Burth  EIAVLREPASRGGSAWMHERLRPGMRVKIRGPRNHFRLDAHASRAILIAGGIGITPIGAI 593
Burma  EIAVLREPASRGGSAWMHERLRPGMRVKIRGPRNHFRLDGHAARAILIAGGIGITPIGAI 594
Burps  EIAVLREPASRGGSAWLHERLRPGMRVKIRGPRNHFRLDGHAARAILIAGGIGITPIGAI 594
Rhosp  EIAVHLDPESRGGSRYIHEQLEVGSPLRMRGPRNHFALDPGAEHYVFVAGGIGITPVLAM 582
Rhoru  EIAVLLDPESRGGSRYVHEQLRVGGSLRIRGPRNHFALDPDAEHYVFVAGGIGITPVLAM 580
Gibze  KIAVLREDQGTGGSRYLHENLKVGDKISIRGPRNNFKFTPGTRRTFLIAGGIGITPMIPM 561
Rhoer  ------------------------------------------------------------
       :***   :   .  ***  ::*   :.  *   :  :******:*  :      :  .::*******:**:  .:
```

c)

```
Ralme  LEVPPDQTLLATLRAANIDVQSDCEEGLCGSCEVRVLAGEIDHRDVVLTRGERDANNRMM 764
Raleu  VTVPADQTLLTTLRCAGIDIQSDCEEGLCGSCEVRVLSGSVDHRDVVLTRGEREANTKMM 767
Burdo  LTVAANQTVLDALQHANIDVQSDCREGLCGSCEVRVLAGRVDHRDSVLTRAERDAHDRMM 766
Burth  LTVPANRTLLATLRAANVDLQSDCEEGLCGSCEVRVLAGEIDHRDSVLSAGERAANTRMM 768
Burma  LTVPANRTLLATLRAANVDVQSDCEEGLCGSCEVRVLAGEVDHRDSVLSADERALNTRMM 769
Burps  LTVPANRTLLATLRAANVDVQSDCEEGLCGSCEVRVLAGEVDHRDSVLSADERALNTRMM 769
Rhosp  VRVEPTQTVLDALRANNIDVPSDCEEGLCGSCEVAVLDGEVDHRDTVLTKAERAANRQMM 758
Rhoru  VRVEPTQTVLDALRANNIDVPSDCEEGLCGSCEVTVLEGEVDHRDTVLTKAERAANRQMM 756
Gibze  LHVPEDKTVLEVINEAGGNVLSTCNKGLCGTCEVGVLEGTPEHRDVVLTAAERAENSSMM 740
Rhoer  ------------------------------------------------------------
       : *    :*:*  .:.   .  ::  *  *.:****:*** ** *   :*** **;   **   :   **
```

Figure 54 An alignment of significant regions of the amino acid sequences of *Ralstonia metallidurans* CYP116B1 and homologous proteins from various organisms. The aligned amino acid sequences were determined by web-based Blast searches (www.ncbi.nhm.nih.gov/BLAST/) utilising the CYP116B1 sequence as a template. The proteins included in the alignment are from *Ralstonia metallidurans* (Ralme), *Ralstonia eutropha* (Raleu), *Burkholderia dolosa* (Burdo), *Burkholderia thailandensis* (Burth), *Burkholderia mallei* (Burma), *Burkholderia pseudomallei* (Burps), *Rhodococcus sp.* NCIMB 9784 (Rhosp), *Rhodococcus rubber* (Rhoru), *Rhodococcus erythropolis* (Rhoer), and *Gibberella zeae* (Gibze). **a)** displays the region of the sequences containing the heme binding site motif (red), and the conserved cysteine residue (light blue) that ligates the heme iron. Important regions concerned with binding the FMN phosphate group (green) and NADH coenzyme (blue) are shown in **b)**, whilst **c)** highlights the position of residues involved in coordinating the 2Fe-2S cluster motif (orange), with the conserved cysteines (light blue). The identities of the amino acid sequences with CYP116B1 (and its heme domain in the case of *R. erythropolis* CYP116A1), which range between 79 and 33 %, are summarised in Table 12. Alignments were performed using ClustalW software (www.ebi.ac.uk/clustalw).

4.3 Cloning of *R. metallidurans* CYP116B1

Following the identification of gene 1832 from the *R. metallidurans* CH34 genome as a putative cytochrome P450 with a novel redox-partner fusion, a culture of the host organism was obtained in order that cloning of this gene could be performed. In this section the steps involved in cloning *R. metallidurans* CYP116B1, are described, along with the initial attempts at expression of the encoded protein.

The CYP116B1 encoding gene was cloned from genomic DNA prepared from a culture of *Ralstonia metallidurans* CH34 supplied by Professor Nigel Brown, University of Birmingham. A 30 ml Sterilin (Bibby Sterilin Ltd.) containing 5 ml of sterile antibiotic-free LB media (Luria-Bertani Media) was inoculated with a single bacterial colony derived from the donated culture, before incubation overnight at 30 °C in a shaking incubator (New Brunswick Scientific) at 220 rpm. After 14 – 16 hours, a small aliquot of this culture was spread onto an antibiotic-free LB agar plate, and the plate incubated overnight at 30 °C. To generate the DNA template, single colonies picked from this plate were resuspended in 1 ml ddH$_2$O, of which 50 µl was heated at 99 °C for 9 minutes using a PHC-2 thermal cycler (Techne). The PCR reaction to amplify the CYP116B1 sequence was performed using a Techne PHC-2 thermal cycler, and involved 30 cycles of (a) denaturation at 95 °C for 45 seconds, (b) annealing at 59 °C for 1 minute and (c) polymerisation at 72 °C for 5 minutes, followed by a final polymerisation step of 72 °C for 10 min. The forward and reverse primers used for this reaction were based upon the published genome sequence of *R. metallidurans* (http://genome.ornl.gov/microbial/rmet/), and are shown in Table 13. The forward and reverse primers were designed to include the appropriate initiation and termination codons, as well as incorporating, respectively, *Ase*I and *Blp*I restriction sites in order to facilitate future cloning steps. To check that the PCR product was of the correct size, it was run on an ethidium bromide-containing 1 % agarose (Melford Laboratories, Ipswich, UK) gel alongside a 1 kb DNA ladder (New England BioLabs). The resultant DNA bands were visualized by exposure to UV light, although this exposure was as brief as possible to avoid damaging the DNA. Having confirmed that the band present was of the expected size (2453 bp), the DNA fragment was purified using a Qiagen gel purification kit (Qiagen, Hilden, Germany) to remove agarose and other contaminants that may inhibit further cloning steps. The fragment was then A-tailed by incubation of

~50 ng of the isolated fragment with 1 µl 2 mM dATP, 5 units *Taq* polymerase, and 1 µl 10x *Taq* polymerase buffer (all New England BioLabs) at 70°C for 30 minutes in a final reaction volume of 10 µl. This procedure was performed in order to add cohesive ends to the cloned DNA fragment, thus enabling its insertion into the pGEM-T vector (Novagen, Nottingham, UK). This vector was chosen due to its enhanced screening opportunities, as it possesses a gene that confers ampicillin resistance, as well as the *lacZ* gene that incorporates a multiple cloning site. This gene can be utilised for blue/white screening as uninterrupted *lacZ* expresses β-galactosidase, an enzyme which converts 5-bromo-4-chloro-3-indolyl β-D-galactopyranoside (X-gal) to a blue derivative in the presence of isopropyl-β-D-thiogalactoside (IPTG, which is a stable mimic of lactose and induces expression of *lacZ*). However, when insertion at the multiple cloning site occurs, functional β-galactosidase is not expressed and thus no formation of coloured product occurs. White colonies obtained are thus those that should contain plasmid with the desired gene cloned.

CYP116B1 PCR primer	Primer sequence (5'→3')
Forward primer	GGACTAATCTCGCTGGACTGATTAATGCCGC
Reverse primer	CGCTCAGCATCCGTGATGCCGT GCTGAG

Table 13 The nucleic acid sequences of the oligonucleotide primers utilized in the PCR reaction to clone the CYP116B1-encoding gene from *Ralstonia metallidurans*. The forward and reverse primers were designed to incorporate both the initiation and termination codons, as well as the *Ase*I and *Blp*I restriction digest sites (identified in red and green respectively) that would facilitate later sub-cloning steps. The nucleotide triplet encoding the start codon is underlined. The primers were designed against the published *R. metallidurans* amino acid sequence (http://genome.ornl.gov/microbial/rmet/) and synthesised by the Protein and Nucleic ACid Laboratory (PNACL), University of Leicester.

Subsequently, attempts were made to ligate the A-tailed fragment into pGEM-T using the methods of Sambrook *et al.* (186), which involved incubating vector and insert, both at 50 ng, at 4 °C in the presence of T4 DNA ligase and the appropriate T4 DNA ligase buffer. The ligation step to create the plasmid CYP116B1 pGEM-T (Figure 55) produced some setbacks, as a successful ligation was not achieved for some time. Various conditions for the reaction were tried, including variations in ligation temperature and concentrations of the vector insert. Ultimately, the ligation was successful and the ligation mixture was transformed into competent JM109 *E. coli* cells

179

following standard methods (186). The transformations were performed by co-incubating 50 µl JM109 competent cells (New England BioLabs) and 10 ng plasmid DNA on ice for ten minutes, before heat shocking the sample at 42 °C for 45 seconds. Following a further incubation on ice for 2 minutes, 450 µl of LB media, pre-warmed at 37 °C, was added to the cells, which were then incubated in a shaking incubator at 220 rpm for one hour. Aliquots of the cells, typically 100 – 200 µl, were then spread onto agar plates containing ampicillin (50 µg/ml), 20 µl of 0.125 M X-gal, and 100 µl of 0.1 M IPTG, and the plates incubated overnight at 30 °C. The addition of X-gal and IPTG allowed for blue/white screening of the colonies to be carried out, as only plasmids containing the CYP116B1 gene should result in white colonies, as they are incapable of utilizing X-gal to yield a blue product. Hence, white colonies isolated were cultured in ampicillin-enriched LB media overnight, and plasmid was extracted from the cultures by Miniprep (Qiagen).
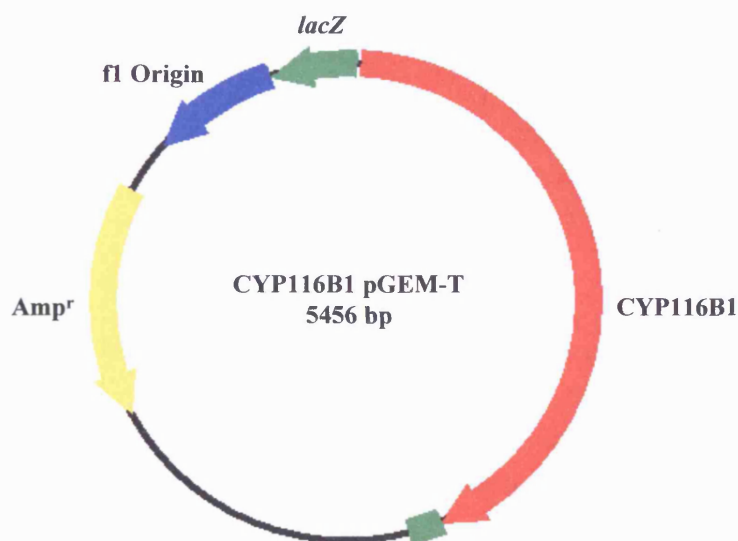
Figure 55 A plasmid map of the CYP116B1 pGEM-T construct, formed by the ligation of the CYP116B1 PCR product and the pGEM-T vector (Novagen). As identified by the map of the plasmid, the main features are the beta-lactamase gene conveying ampicillin resistance (Amp^r), the f1 origin, and the *lacZ* gene, which encodes the alpha peptide segment of the enzyme β-galactosidase. Interruption of the *lacZ* gene by inserted DNA, as is demonstrated here, prevents production of an active β-galactosidase protein in *E. coli*, and thus results in white colonies rather than blue colonies, due to inactivation of *lacZ*-catalysed reaction with 5-bromo-4-chloro-3-indolyl β-D-galactopyranoside (X-gal) when the gene is interrupted. The plasmid map was created using Plasmid software (www.biovisualtech.com).

A diagnostic restriction digest using *Xho*I (New England BioLabs), resulting in a single band of 5456 bp when visualised on an agarose gel, was performed on the plasmid to confirm the clone had been correctly created (Figure 56). This digest was selected as the CYP116B1 insert possesses a *Xho*I restriction site not present in the pGEM-T vector. Thus, unsuccessful cloning results only in bands for intact, circular plasmid vector on an agarose gel, whilst successful cloning of the P450 gene into the pGEM-T vector yields a band of the correct size when digested with the restriction enzyme.
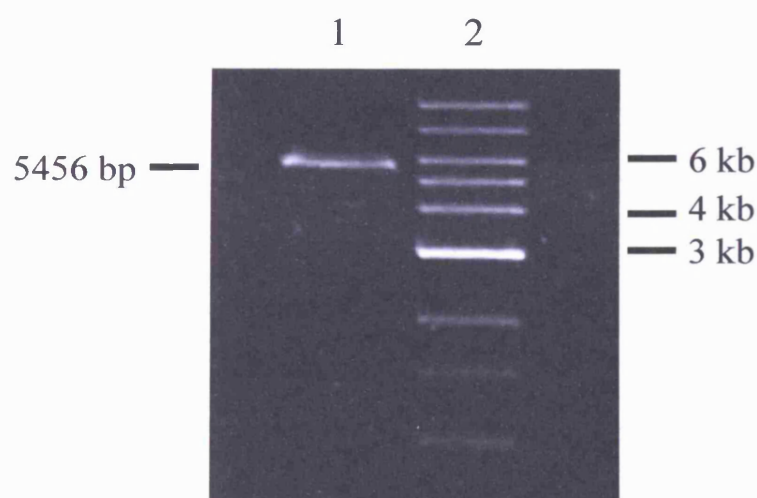
Figure 56 The diagnostic *Xho*I restriction enzyme digest of the CYP116B1 pGEM-T construct (lane 1) run alongside 1 kb DNA Ladder (lane 2). The resultant digest pattern, a single band at 5456 bp, identifies the successful creation of the plasmid, and completion of the first cloning step. The digest was run on a 1 % agarose gel containing ethidium bromide (0.25 µg/ml) and visualised by exposure to ultra-violet light (UV). The positions of relevant 1 kb ladder bands are indicated.

In order to check the cloned gene for errors, the plasmid was subsequently sequenced by the Protein and Nucleic ACid Laboratory (PNACL) (University of Leicester) using seven primers designed against the published CYP116B1 sequence. These oligonucleotides, designed to provide sequencing coverage of the entire 2346 bp gene sequence, are displayed in Table 14 and were synthesised by PNACL. The automated DNA sequencing revealed that the clone of CYP116B1 was free from errors, and that the gene could now be transferred to plasmids suited to expression of the encoded protein.

CYP116B1 sequencing primer	Primer sequence (5'→3')
M13 reverse	CAGGAAACAGCTATGACC (-126 - -109)
CYP116B1a	CTGGTCCGGAGGAACTTCAA (211 - 230)
CYP116B1b	GGTGTAGTCGACGCCCAGTT (547 - 566)
CYP116B1c	GTCTCGACGCGCTCGACAAT (920 - 939)
CYP116B1d	CGACGACGTGACGATCAGCAAT (1291 - 1312)
CYP116B1e	CTTCGCGCATCTTGTCGAGAATG (1632 - 1654)
CYP116B1f	GATTCATCGCGTAGCCGTACGAG (2001 - 2023)

Table 14 The oligonucleotide primers used for sequencing of the CYP116B1-encoding gene that was successfully cloned into the pGEM-T vector. The primers were designed to bind at intervals along the inserted DNA in order that the entire *R. metallidurans* gene may be checked for frameshift, silent and other mutations, which could affect expression of a *bona fide* CYP116B1 protein. Primer synthesis and sequencing was carried out by PNACL, University of Leicester. Primer M13 reverse is a universal primer for pGEM-T vectors supplied by PNACL that binds upstream of the incorporated gene to allow complete insert sequencing. The position at which each primer binds to the non-coding strand of the CYP116B1 gene is indicated in parenthesis.

4.4 Sub-cloning of CYP116B1 pET-11a

In order to express the CYP116/redox partner fusion protein, the cloned gene was excised from the CYP116B1 pGEM-T plasmid using the restriction sites (*Ase*I and *Blp*I) that were introduced during initial cloning (Chapter 4.3). The digest was analysed by visualisation on a 1 % agarose gel and the gene fragment gel purified (Qiagen), with the resultant 2423 bp fragment thus isolated further confirming the correct cloning of the gene and the introduction of the two restriction sites. A digest of pET-11a (Novagen) was performed with *Blp*I and *Nde*I (the latter enzyme producing ends cohesive with *Ase*I) to generate a vector fragment of 5586 bp. The pET-11a vector was selected for protein production as expression is under the tight control of the T7 *lac* promoter, which allows transcription only when IPTG is present. The vector also possesses an ampicillin resistance gene that enables screening for plasmid-containing cells, and helps to prevent contamination of the cell cultures.
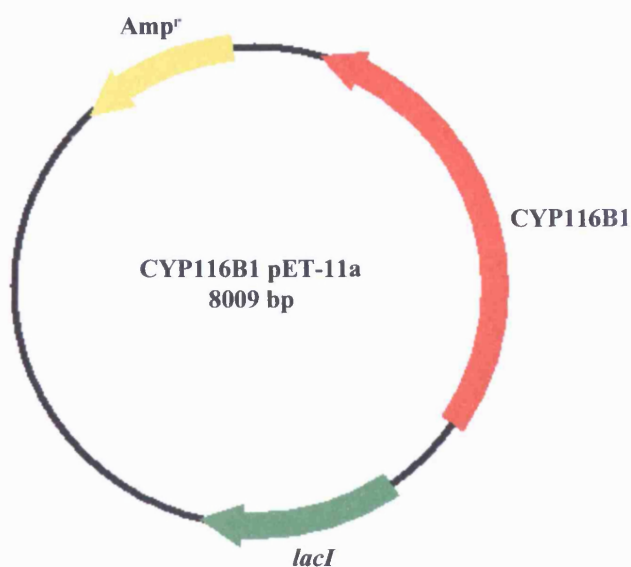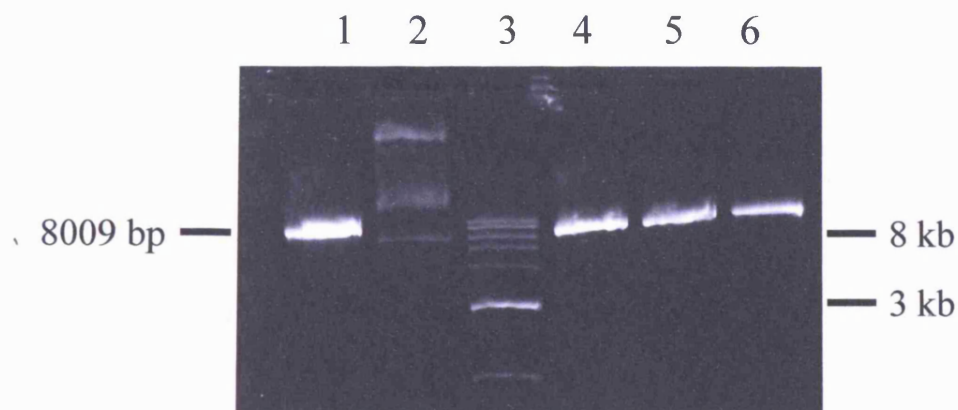
Figure 57 A plasmid map of CYP116B1 pET-11a identifying the most significant features of the plasmid, created using Plasmid software. Again, this plasmid possesses the ampicillin resistance gene (Amp^r) that enables screening for the construct. Instead of the *lacZ* gene that is present in pGEM-T, this plasmid contains the *lacI* gene. This gene is responsible for suppressing gene transcription from the T7 promoter, a 16 bp sequence found immediately upstream of the target gene, in the absence of an inducing agent such as IPTG. Repression is achieved by preventing binding of host RNA polymerase to the plasmid at the site required for production of the T7 RNA polymerase. IPTG displaces the lac repressor (product of *lacI*) and enables T7 polymerase production, which then efficiently transcribes the P450 gene. The construct was formed by the incorporation of the *Ase*I/*Blp*I-excised fragment from CYP116B1 pGEM-T (Figure 55) into *Nde*I/*Blp*I-digested pET-11a (Novagen).

The vector and insert were ligated, as described in Chapter 4.3, to create the 8009 bp CYP116B1 pET-11a plasmid (Figure 57) that was then transformed into JM109 competent cells by heat shock-induced plasmid uptake (Chapter 2.9). Viable colonies from the transformation were cultured in ampicillin-enriched LB media and the plasmid extracted by Miniprep (Qiagen). In order to confirm the success of the cloning step, restriction enzyme digests were performed and visualised on 1 % agarose gels. A *Sma*I digest (Figure 58a), cutting once in the CYP116B1 insert, produces a single band of 8009 bp and verified the correct clone. These data were backed up using a *Sal*I digest (Figure 58b), which cut the plasmid twice in the insert region to give 1320 and 6689 bp fragments. The plasmid was also digested with *Sca*I (Figure 58b), which cut the plasmid once in the insert and once in the vector region to give bands on an agarose gel of 2617 and 5392 bp. The digests all confirmed the successful production of

CYP116B1 pET-11a, which was then used in attempts to express the P450 fusion enzyme.
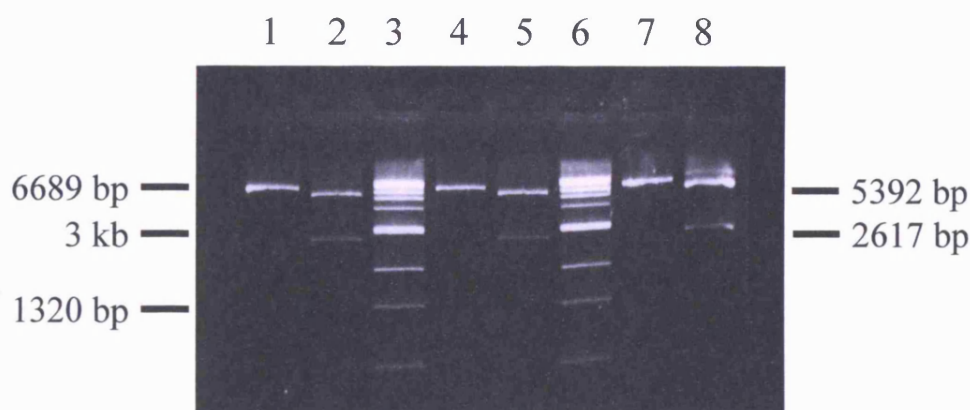
a)

b)

Figure 58 a) The *Sma*I restriction digests of five potential clones of CYP116B1 pET-11a run alongside 1kb DNA Ladder (lane 3). Single bands at 8009 bp for the clones in lanes 1, 4, 5, and 6 identify the correctly cloned construct. The plasmid in lane 2 has not been linearised by the *Sma*I digest, indicating it is not a successful CYP116B1 clone. The position of the 3 and 8 kb markers of the DNA ladder (New England BioLabs) are indicated to the right of the gel. **b)** The *Sal*I and *Sca*I restriction digests of three clones of CYP116B1 pET-11a. Lanes 1, 4, and 7 display the *Sal*I digests of the clones, whilst the *Sca*I digests are shown in lanes 2, 5, and 8. Lanes 3 and 6 contain 1 kb DNA ladder and the position of the 3 kb marker is identified at the left of the gel. Bands at 1320 and 6689 bp for the *Sal*I digests, and 2617 and 5392 bp for the *Sca*I digests, further verify the construction of the plasmid CYP116B1 pET-11a. All digests were visualized by exposure to UV light following electrophoresis on 1 % agarose gels containing 0.25 µg/ml ethidium bromide (Sigma-Aldrich).

4.5 Sub-cloning of CYP116B1 pET-40b

The cloned CYP116B1 gene was also excised from the pGEM-T vector and ligated into pET-40b, using the same procedures as described above for the creation of the pET-11a clone (Chapter 4.4). As with pET-11a, the pET-40b vector incorporates the β-lactamase gene that confers ampicillin resistance, but has the additional benefit of integrating a Dsb protein at the C-terminal end of the cloned gene. The addition of this protein should facilitate export of the recombinant gene product to the periplasm of the host cell, as well as enhancing the formation of disulphide bonds. Hence, as this fusion can improve the solubility of the expressed protein, this vector was selected for expression studies alongside the pET-11a clone.
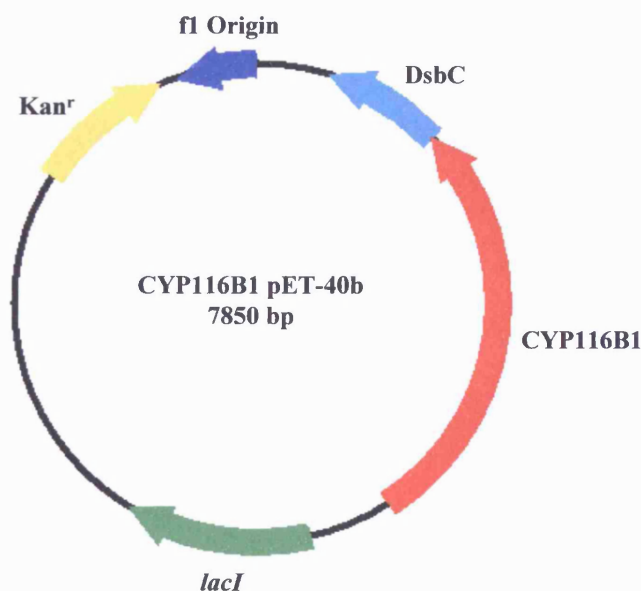
Figure 59 The map of the 7850 bp CYP116B1 pET-40b plasmid constructed by the ligation of *NdeI*/*BlpI*-cut pET-40b vector (Novagen) and the *AseI*/*BlpI* fragment excised from CYP116B1 pGEM-T (Figure 55). This plasmid has the same *lacI* gene to control protein expression and f1 origin as the pET-11a construct but differs in the respect that it has a gene for kanamycin resistance (Kan^r) rather than ampicillin resistance. Furthermore, by cloning the CYP116B1 gene into the multiple cloning site of this vector a Dsb tag is incorporated at the carboxyl terminal of the transcribed protein. This protein tag acts to enhance the formation of disulphide bonds, which aids correct protein folding, possibly increases protein solubility, and promotes export of the polypeptide to the cell periplasm. The map was created using Plasmid software (www.biovisualtech.com).

As previously described, the 2423 bp *Ase*I/*Blp*I fragment from CYP116B1 pGEM-T was ligated to the 5427 bp *Nde*I/*Blp*I-cut pET-40b vector fragment to create the 7850 bp CYP116B1 pET-40b plasmid (Figure 59). To confirm the correct production of the plasmid, an initial restriction digest using *Xho*I was performed as described in Chapter 4.3, and visualised on a 1 % agarose gel. This enzyme, which cut the plasmid once in the CYP116B1 gene region, gave a single band at 7850 bp, as expected, and is shown in Figure 60a. Further confirmation was obtained by digestion of the plasmid with *Sma*I to give bands of 4732 and 2848 bp, and *Sal*I to give bands of 6260 and 1320 bp (Figure 60b). Each of these digests of CYP116B1 pET-40b were seen to yield bands of the correct size by gel electrophoresis, meaning that expression trials could begin with these plasmid expression constructs.

a)
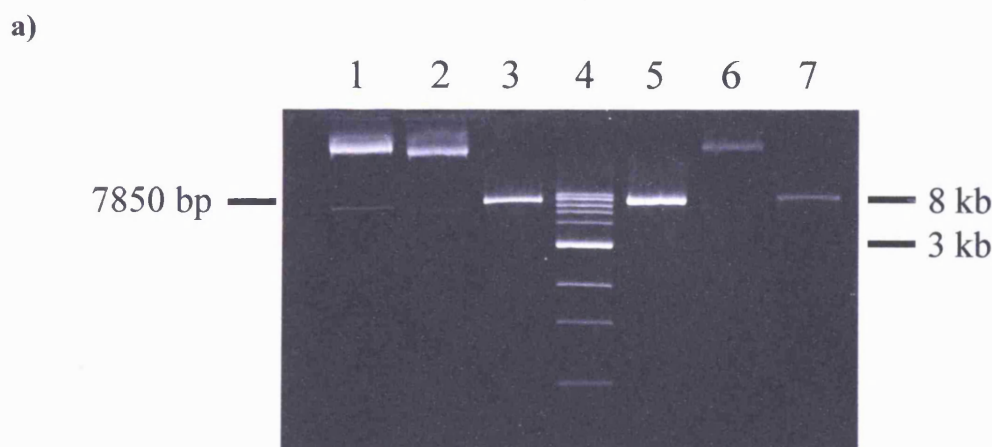
Figure 60 a) The *Xho*I restriction digests of six CYP116B1 pET-40b clones run alongside a 1 kb DNA ladder (lane 4). The digested constructs in lanes 3, 4, and 7 produced the expected pattern for correctly ligated plasmid, a single band of 7850 bp. However, clones in lanes 1, 2, and 6 did not show the correct pattern and were not used for expression studies. The positions of the 3 and 8 kb markers of the DNA ladder are indicated to the right of the gel. **b)** *Sma*I and *Sal*I restriction digests of the three successful CYP116B1 pET-40b clones, as identified by *Xho*I digestion. The DNA bands at 6260 and 1320 bp for the *Sal*I restriction digests in Lanes 1, 4, and 7 confirm the correct construction of the plasmids, as do the bands at 4732 and 2848 bp for the *Sma*I digests in lanes 2, 5, and 8. Both sets of digests were run on ethidium bromide-containing 1 % agarose gels and visualised by exposure to UV light.

b)
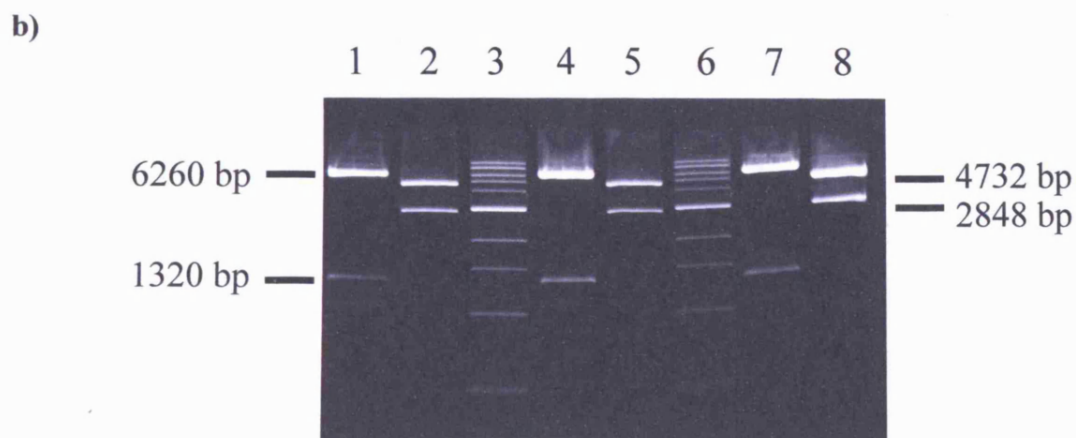
4.6 Protein expression from CYP116B1 pET-40b

The successfully cloned CYP116B1 pET-40b plasmid was transformed into HMS174 (DE3) and Rosetta (DE3) competent cells using the heat-shock method described in Chapter 4.3. The HMS174 (DE3) *E. coli* cell strain was selected for these studies, as it is a general expression host with IPTG-induced control of protein production. The Rosetta (DE3) strain was also selected for this reason. However, this cell strain has the added benefit of providing rare codon tRNAs, including AUA, AGG, AGA, CUA, CCC, and GGA, which can enhance protein translation if the expressed gene contains these less common codons, thus improving the yield of protein.

Small-scale expression trials were then performed using these two *E. coli* transformant cell strains in an effort to produce the CYP116B1 protein. The cultures, typically 50 ml, were grown aerobically in an orbital shaker (New Brunswick Scientific), initially at 37 °C, until $O.D._{600} = 0.6$. The shaker temperature was then reduced to 18 °C, and the cells induced with IPTG at low (100 μM), and high (1 mM), levels when the $O.D._{600} = 0.8$. The incubation temperature was reduced to 18 °C as the expression of genes from GC-rich genomes, which include those of *R. metallidurans* and *M. tuberculosis*, may be benefited by such a temperature drop. Whilst IPTG levels were also varied, as this can be critical to define conditions for optimal protein expression (40,159).

To assess the degree of protein expression in the cells strains that grew successfully (HMS174 (DE3) transformants), SDS-PAGE analysis was performed on the cultures at approximately 16 hours post-induction, using the techniques detailed by Sambrook *et al* (186). This analysis involved taking two aliquots of the culture and centrifuging them

at 13000 g for 1 minute using a benchtop centrifuge. Supernatant was discarded. One cell pellet was resuspended in 50 mM Tris.HCl pH 7.2 and became the total protein sample, whilst the other pellet was resuspended in Bugbuster solution (Novagen) in order to lyse the cells. This sample was shaken at room temperature for 20 minutes before centrifugation. The resultant supernatant and pellet were separated and used as the soluble and insoluble protein fractions, respectively. Each sample was incubated at 95 °C for 5 minutes in the presence of dithiothreitol (DTT) and a loading dye (New England BioLabs) before being loaded onto a 10 % acrylamide gel and run against a broad range protein weight marker (NEB). The gel, full details of preparation for which can be found in Chapter 2.20, consisted of a stacking gel (containing 2% SDS) layered on top of a running gel (1% SDS) and was run at constant 150 V voltage. Upon completion of the electrophoresis, the gel was visualised using Coomassie blue stain, which binds selectively to the proteins resolved in the gel. The resultant gel for the analysis of CYP116B1 expression from pET-40b is shown in Figure 61.
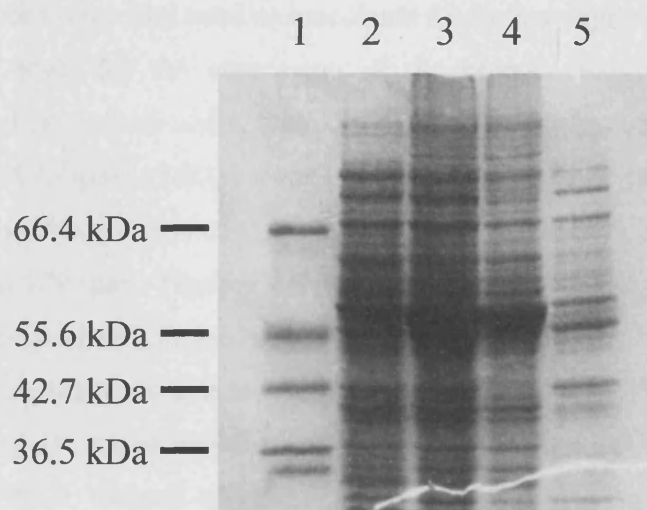

Figure 61 An SDS-PAGE analysis of CYP116B1 pET-40b expression from HMS174 (DE3) *E. coli* cells. Cells were grown at 37 °C until $O.D._{600}$ = 0.6, after which the temperature was reduced to 18 °C. At $O.D._{600}$ = 0.8 the cells were induced with 100 μM IPTG and harvested 14 – 16 hours later. The total, insoluble, and soluble protein samples are shown in lanes 3, 4, and 5, alongside broad range protein marker and untransformed HMS174 (DE3) cells (lanes 1 and 2 respectively). The gel shows that no significant over-expression of a protein of the correct size (86.4 kDa) is observed in these cell extracts, and thus expression from other *E. coli* cell strains was investigated. The analysis was performed using an SDS-containing 10 % acrylamide gel, which was visualised with Coomassie blue stain following electrophoresis. Sizes of significant bands of the protein marker are identified at the left of the gel.

From the SDS-PAGE gel, the degree of protein expression was assessed and it was seen that there was no significant over-expression of a protein of predicted mass (86.356 kDa) for the fusion protein (Figure 61). The trials were repeated using fresh competent cell strains, but the results were unchanged. Thus, it was decided that protein expression from another vector system should be attempted.

4.7   Protein expression from CYP116B1 pET-11a

The plasmid CYP116B1 pET-11a was transformed into Origami (DE3) and Rosetta (DE3) competent *E. coli* cell strains (Novagen). Colonies of transformed cells were picked and cultured at 37°C in 5 ml LB media enriched with the appropriate antibiotics. For growth, the transformed Rosetta (DE3) cells required 50 µg/ml ampicillin and 34 µg/ml chloramphenicol whilst the Origami (DE3) cells required 12.5 µg/ml tetracycline and 15 µg/ml kanamycin. From these cultures, glycerol stocks were prepared by addition of 100 µl glycerol to a 500 µl aliquot of the cells and frozen rapidly at -80 °C. These stocks were later used as inoculants for further expression cell cultures.

Initial trials for the expression of the protein from CYP116B1 pET-11a were performed on a small scale, typically 5 ml. The glycerol stocks (transformed Rosetta (DE3) and Origami (DE3)) were utilised to inoculate 5 ml LB media (containing the required antibiotics) and cultures were incubated overnight at 37 °C in an orbital shaker shaking at 220 rpm. These overnight cultures were used to inoculate 50 ml volumes of antibiotic-enriched LB media that were grown until $O.D._{600}$ = 0.6 at 37 °C. The temperature was then reduced to 26 °C, or maintained at 37 °C, and growth continued until $O.D._{600}$ = 0.8, at which point low level induction was initiated by the addition of 100 µM IPTG. Growth was continued overnight at the respective temperatures and the samples subjected to SDS-PAGE analysis, as described in Chapter 2.21, at the end of the growth period. Transformants of the two cell strains, Rosetta (DE3) and Origami (DE3), were analysed at 37 °C and 26 °C to assess the levels of expression of the protein encoded by the CYP116B1 gene. The SDS-PAGE gels (Figure 62) did not identify the over-expression of any protein compared to the normally expressed cellular proteins in the Rosetta (DE3) cells. This implied that little to no expression of the CYP116B1 gene occurred. In the Origami (DE3) transformant cells grown at 37 °C there appeared to be some evidence of an over-expressed protein at 86.4 kDa in the total and insoluble fractions, suggesting that expression of the soluble protein may be

possible by alteration of the growth conditions. The conditions of the trials were later replicated, using HMS174 (DE3) *E. coli* cells transformed with the CYP116B1 pET-11a plasmid, but these showed that no significant amount of protein was expressed from this transformant cell strain (Figure 62).
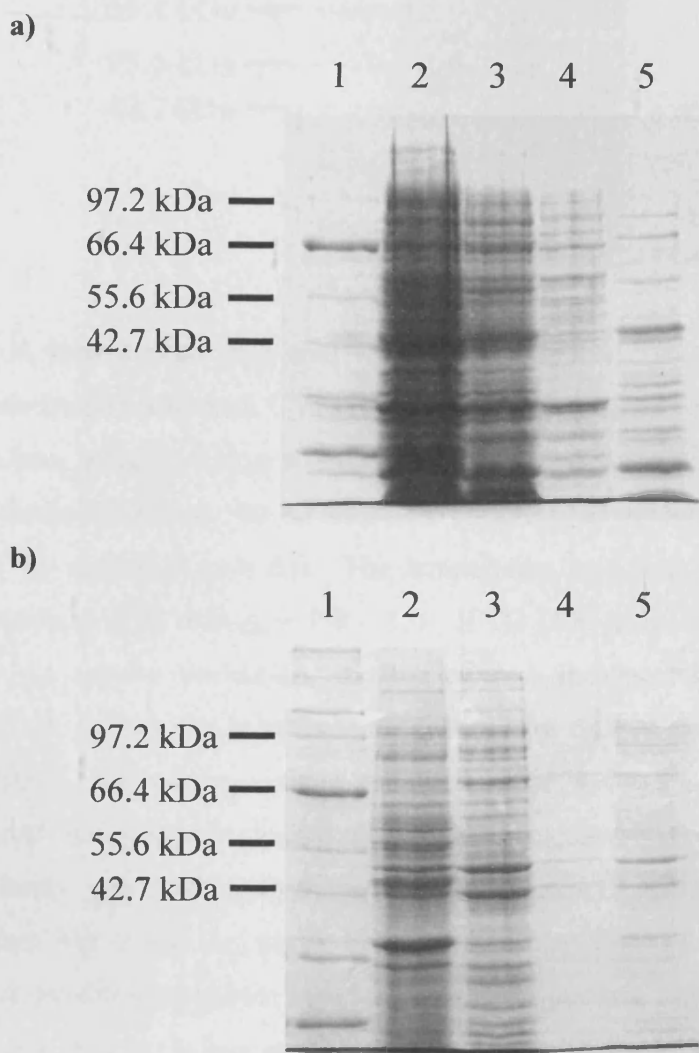
a)

b)

Figure 62 SDS-PAGE analysis of CYP116B1 pET11a expression in **a)** Rosetta (DE3), **b)** HMS174 (DE3), and **c)** Origami (DE3) *E. coli* cell strains. In each 10 % polyacrylamide gel, lane 1 contains broad range protein marker, lane 2 contains a sample of the respective untransformed *E. coli* strains, and lanes 3, 4, and 5 contain the total, insoluble, and soluble protein samples. No overexpressed protein was visible in extracts from the Rosetta (DE3) or HMS174 (DE3) transformant cells, although a small quantity of insoluble protein was visible in the CYP116B1-transformed Origami (DE3) cells at approximately 86.4 kDa. This band confirmed that expression of the CYP116B1 gene-encoded protein was possible, and determined that future studies to optimise protein expression would involve only the Origami (DE3) strain. The significant marker band masses are indicated at the left of the gels.

c)
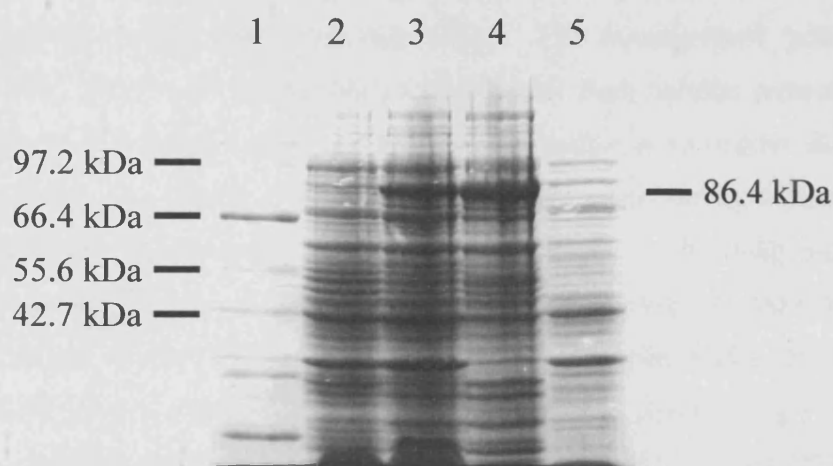
A second expression trial was carried out using Origami (DE3) and Rosetta (DE3) cells transformed with CYP116B1 pET-11a plasmid. For each cell strain an overnight culture, inoculated from a glycerol stock, was grown at 37 °C for use as an inoculant for 2 flasks containing 500 ml antibiotic-enriched LB media. The flasks were incubated at 37 °C until O.D.$_{600}$ = 0.6. The temperature was then reduced to 18 °C and growth continued until O.D.$_{600}$ = 0.8 – 1.0. IPTG (100 μM) was then added to each flask to induce protein production, and the cultures incubated overnight. At the end of the growth period, the cultures were pelleted by centrifugation at 6000 rpm for 20 – 30 minutes and the supernatant removed. The pelleted cells from the Origami (DE3) transformant cultures were seen to be considerably redder than the Rosetta (DE3) cultures, potentially indicating a greater presence of cytochrome P450, and thus this cell strain was chosen for use in larger scale preparations of the protein. The reduction of cell growth temperature appeared to have a positive effect on expression of the P450 fusion protein, as has previously been observed for P450 and redox partner enzymes from *Mycobacterium tuberculosis* (40,159).

Before large-scale preparation of transformant cells was carried out, protein from the cell pellet from two flasks (1 litre) of Origami (DE3) cells was purified to determine whether the red colour of the pellet actually corresponded to the presence of cytochrome P450. The purification involved the pellet being resuspended in 50 mM Tris.HCl, 1 mM EDTA (pH7.2) (buffer A), before being broken using a French press (Thermo Electron Corp.), operating at 1500-2000 psi, and a sonication step utilising a Bandelin Sonoplus GM2600 set to administer 6 x 20 second bursts at 45 % full power, with 5 minutes rest periods between each pulse. These methods were employed as they disrupt

the cell wall and membranes and free any loosely bound protein, and thus improve the yield of soluble protein from the cell pellet. The homogenised pellet was then centrifuged at 18000 rpm to separate cellular debris from soluble proteins, the pellet was disposed of, and the supernatant dialysed into buffer A to remove dissolved salts and impurities such as metal ions. The dialysis was performed by constantly stirring supernatant-filled dialysis tubing in 2 litres of buffer A at 4 °C, with buffer replaced three times over the course of several hours. The supernatant was then loaded onto a DEAE-Sephacel column (Pharmacia) pre-equilibrated with buffer A, and washed thoroughly to remove unbound proteins. The protein was eluted using a 500 ml linear gradient consisting of buffer A and buffer B (50 mM Tris.HCl, 1 mM EDTA, 500 mM KCl pH 7.2). Fractions were collected and those displaying red colouration were assessed across UV-visible wavelengths (200 – 800 nm) using a Cary UV-50 UV-Visible spectrophotometer (Varian) for the presence of a Soret peak in the region of 418 nm. Those fractions demonstrating the greatest peak at 418 nm, in relation to general protein absorption at 280 nm, were retained and concentrated by ultrafiltration (Millipore). In order to determine if the protein was a cytochrome P450, the sample was assayed using a widely used method (50) that employs the Soret band shift from 418 to ~450 nm, associated with the formation of the ferrous carbon-monoxy species of the cytochrome P450. The result of this assay, which is described more fully in Chapter 4.8, confirmed the presence of the monooxygenase in the sample and indicated that large-scale cultures and further studies of the enzyme could begin.

A large-scale preparation of the Origami (DE3) transformed cells was performed under the same conditions as the successful small-scale preparations. The culture was carried out in 12 flasks containing 500 ml LB media containing 50 μg/ml ampicillin. Following inoculation, the flasks were incubated at 37 °C until $O.D._{600}$ = 0.6, at which point the temperature was reduced to 18 °C. Induction of the cultures with 100 μM IPTG was executed when $O.D._{600}$ = 0.8. Following growth, the cells were harvested by centrifugation, and broken by French press and sonication techniques. The enzyme was purified by two anionic exchange steps, firstly using a DEAE column (Pharmacia), and secondly with a Q-Sepharose column (Pharmacia). Both steps utilised buffer A for loading and washing the protein, and buffer B for the elution gradient, whilst dialysis was performed before and after the use of the Q-Sepharose resin to ensure the removal of salts and contaminants. The semi-purified protein was subjected to a number of

spectroscopic studies in order to make an initial characterization of the CYP116/redox partner fusion protein.

The preparation of the CYP116/redox partner fusion was also assessed by SDS-PAGE to ensure that the protein being produced was of the correct size and was being sufficiently over-expressed. The gels in Figure 63 show the presence of an 86.4 kDa protein that is in agreement with the predicted size of CYP116B1. However, as can be seen on the gels, there were at least two other bands of smaller over-expressed polypeptides visible at approximately 39.6 kDa and 52 kDa. Examination of fractions collected from the columns showed that some of the fractions preceding those with the greatest intensity Soret peaks were yellow, and when viewed on a spectrophotometer demonstrated flavin-like spectra, i.e. exhibited two broad absorption bands with maxima close to 450 nm and 390 nm. These bands were thus likely to be proteolysed CYP116B1 (i.e. reflective of the reductase and heme domains of the enzyme) and suggested that the protein was susceptible to degradation either during cell growth or during the purification process. Inter-domain linker regions are often hydrophilic and protease-sensitive (as seen with the P450 BM3 system (140)), and a likely scenario is that the fusion protein is cleaved in this region to produce individual heme- and flavin/iron sulphur-containing polypeptides.

In an attempt to determine whether the proteolysis could be avoided or minimised, preparations were carried out to study the effects of induction strength and the time course of protein production during culture growth. The results of these trials showed that there was greatest production of the CYP116/redox partner fusion when the cells were induced at a low level (100 μM), rather than without induction or with induction at high levels (1 mM IPTG). The results also showed that protein production occurred consistently over the course of the cultures, and apparently without production of breakdown bands in the intact cells. Thus, it appears likely that proteolysis occurs predominantly during purification.
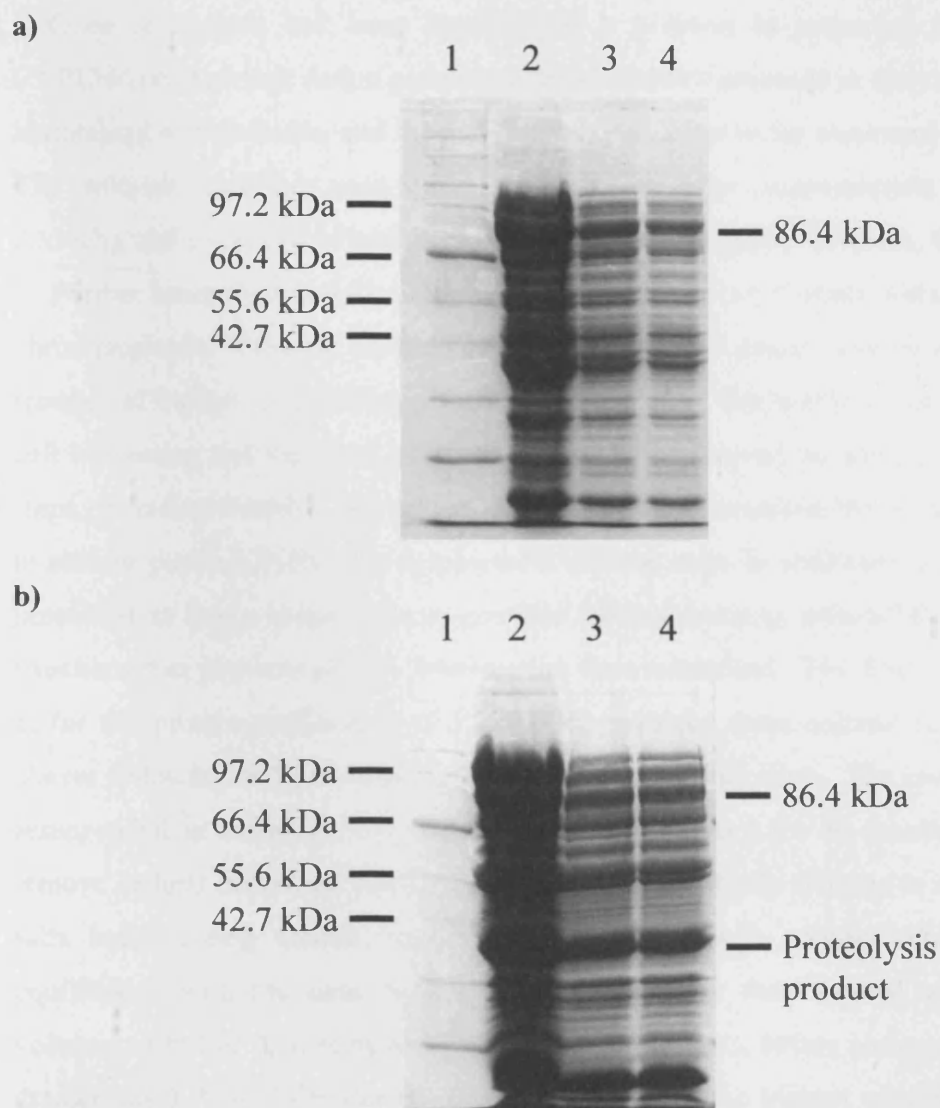
a)

b)

Figure 63 a) The SDS-PAGE analysis of fractions of Origami (DE3)-expressed, partially purified CYP116B1 containing the intact 86.4 kDa protein. In these fractions there is a high proportion of the intact protein, with some degradation product seen between 36.5 and 42.7 kDa. **b)** The SDS-PAGE analysis of fractions preceding those in a) which exhibit strong flavin-like absorption features. A much higher degree of degradation is seen, with a large proportion of proteolysis product and little intact protein. Both samples were collected post-Q-Sepharose column and in both gels lane 1 contains broad range protein marker, whilst lanes 2, 3, and 4 display the total, insoluble and soluble protein samples, prepared as described in Chapter 2.21. Relevant marker sizes are indicated, where appropriate, on the left side of each gel.

Once proteolysis had been identified as a problem in preparing the full-length CYP116/redox partner fusion protein, protease inhibitor presence in dialysis buffers was maintained at high levels, and the purification carried out in the minimum time possible. The protease inhibitors used were PMSF, benzamidine hydrochloride (both Sigma-Aldrich), and a cocktail of inhibitors in tablet form (Complete™, Roche, Welwyn, UK).

Further attempts to reduce proteolysis of CYP116B1 were made utilising a range of chromatography columns, such as cation exchange and phenyl Sepharose resins, in a number of buffers of differing pH and ionic strength. Furthermore, the time between cell harvesting and the breaking of the cells was minimised, as were chromatography steps, including washing and protein dialysis, in order to reduce the overall time taken to achieve purified P450. The employment of these steps, in addition to maintaining the protein at as low a temperature as possible without freezing, ensured that exposure to situations that promote protein deterioration were minimised. The final scheme arrived at for the protein purification of CYP116B1 involved three column chromatography phases following cell disruption by French press and sonication. The crude cell lysate, resuspended in buffer A, was centrifuged twice (18000 g for 40 minutes at 4 °C) to remove cellular debris, the resultant supernatant being briefly dialysed to remove excess salts before being loaded to a DEAE anion exchange column (Pharmacia) pre-equilibrated with the same buffer. The column was then washed with 2 column volumes of buffer A to remove unbound cellular proteins, before elution using a linear gradient of 0 – 100 % buffer B. Fractions displaying the highest quantities of protein with a Soret feature at approximately 418 nm were retained and concentrated by centrifugation using Centriprep tubes (Millipore). The protein was diluted with a small volume of buffer A containing 0.75 M ammonium sulphate and loaded to a phenyl Sepharose column (Pharmacia) equilibrated in identical buffer. Following the application of a linear gradient of buffer A plus 0.75M ammonium sulphate – buffer A to elute the protein, cytochrome P450-containing fractions were concentrated and dialysed into buffer A in readiness for the final column chromatography step. This step utilised a Q-Sepharose column pre-equilibrated with buffer A for the final purification step, and used the same wash and elution steps as the DEAE column. However, due to the differing binding properties of the two resins, the DEAE binds proteins via a diethylaminoethyl group whilst the Q-Sepharose interacts with proteins through a quaternary ammonium group, the two columns remove different protein contaminants. The fractions of highest purity collected from the Q-Sepharose, as determined by the

ratio of the 280 and 418 nm peaks of the UV-Visible spectra, were pooled, dialysed, concentrated, and stored at −80 °C until required. Typically, purification of CYP116B1 from 12 L of cell culture yielded approximately 20 mg of protein with an R_z value ($A_{418/280}$) of ~0.8, indicating that essentially homogenous protein was obtained. SDS-PAGE analysis of purified CYP116B1 (Figure 64) identifies that the majority of contaminant cellular proteins are removed using DEAE, phenyl-Sepharose, and Q-Sepharose chromatography columns. Furthermore, the gel exhibits that bands at 36.5 and 42.7 kDa have been distinctly diminished, in comparison to those seen in Figure 63b, demonstrating that the aforementioned purification steps have averted much of the proteolysis. Having determined a method of purification for *R. metallidurans* CYP116B1, the following sections describe the initial spectral and biophysical characterization of this redox partner-fused P450, contrasting this novel enzyme with the characterization described in Chapter 3 for the ancestral cytochrome P450, CYP51.
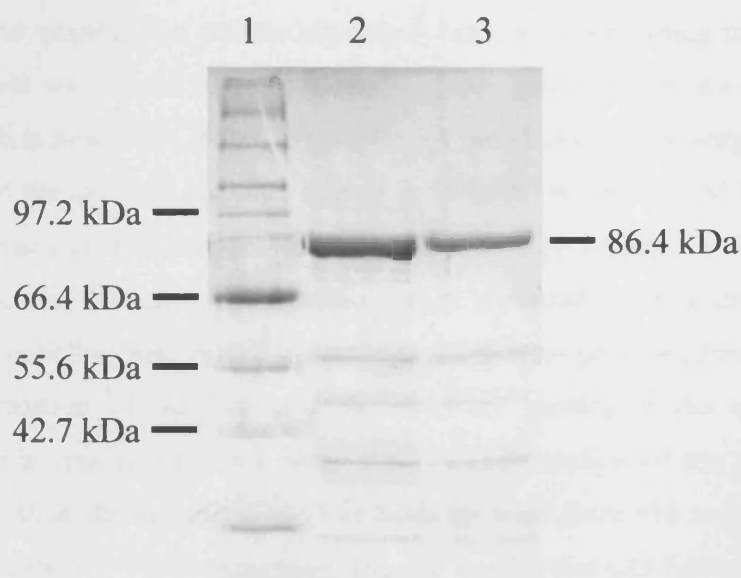

Figure 64 The SDS-PAGE analysis of purified *R. metallidurans* CYP116B1 run alongside broad range protein marker (lane 1). The samples in lanes 2 and 3 are 1-in-5 and 1-in-10 dilutions of the pooled protein collected following purification using DEAE, phenyl-Sepharose, and Q-Sepharose chromatography columns, and show a considerable improvement with respect to the partially purified enzyme shown in Figure 63a. Furthermore, bands representing the products of proteolysis between 36.5 and 42.7 kDa are distinctly less prominent than those observed in Figure 63b, implying that much of the degradation of the enzyme has been prevented by the addition of protease inhibitors and by decreasing the time taken from breaking the cells to obtaining purified protein. This analysis was performed on an SDS-containing 10 % acrylamide gel, with proteins visualised by staining with Coomassie blue. Relevant protein marker band sizes are identified to the left of the gel, whilst the band corresponding to the CYP116B1 protein is indicated at the right of the gel.

4.8   UV-visible spectroscopy of *R. metallidurans* CYP116B1

This section details the basic UV-visible absorption spectroscopic characterization performed on the protein product of the *R. metallidurans* CYP116B1 gene; the cloning, expression, and purification of which was described in the preceding section (Chapter 4.7). These studies were performed to (i) confirm that, as postulated, the gene product contained cytochrome P450 and flavin components, and (ii) to produce basic UV-Visible data that can be used to compare this protein with the *M. tuberculosis* CYP51, which was studied in Chapter 3, and with other P450 and P450 fusion systems. Hence, this section reports upon the results of the classic P450-identifying study involving reduction by sodium dithionite and binding of carbon monoxide, as well as the interactions of the protein with the ligands nitric oxide, (sodium) cyanide, and imidazole, and the coenzymes β-Nicotinamide-Adenine-Dinucleotide (NADH) and β-Nicotinamide-Adenine-Dinucleotide-Phosphate (NADPH).

To determine whether the protein expressed from cells containing the CYP116B1 pET-11a plasmid was indeed a cytochrome P450, the method of Omura and Sato (50), which was used to assay for CYP51 in Chapter 3.4, was used. The absorption spectrum of an aliquot of the oxidised enzyme, diluted in 50 mM Tris.HCl, 1mM EDTA pH 7.2 to 2 – 4 μM, was recorded between 250 and 800 nm using a Cary UV-50 UV-Visible spectrophotometer (Varian).   Spectra were then recorded after sodium dithionite reduction, and bubbling with carbon monoxide, which were performed in an attempt to induce the formation of the ferrous carbon-monoxy species of the enzyme.   The formation of this species has long been used as confirmation of the presence of a cytochrome P450, as the associated shift of the Soret band from 418 nm to ~450 nm is easily detectable by UV-Visible spectroscopy, and verifies that CO-ligation to enzyme's heme iron, with concomitant displacement of a distally bound water molecule, has occurred (50).   The Soret band shift to ~450 nm is a hallmark of the cysteinate-coordinated heme iron found in P450 enzymes.
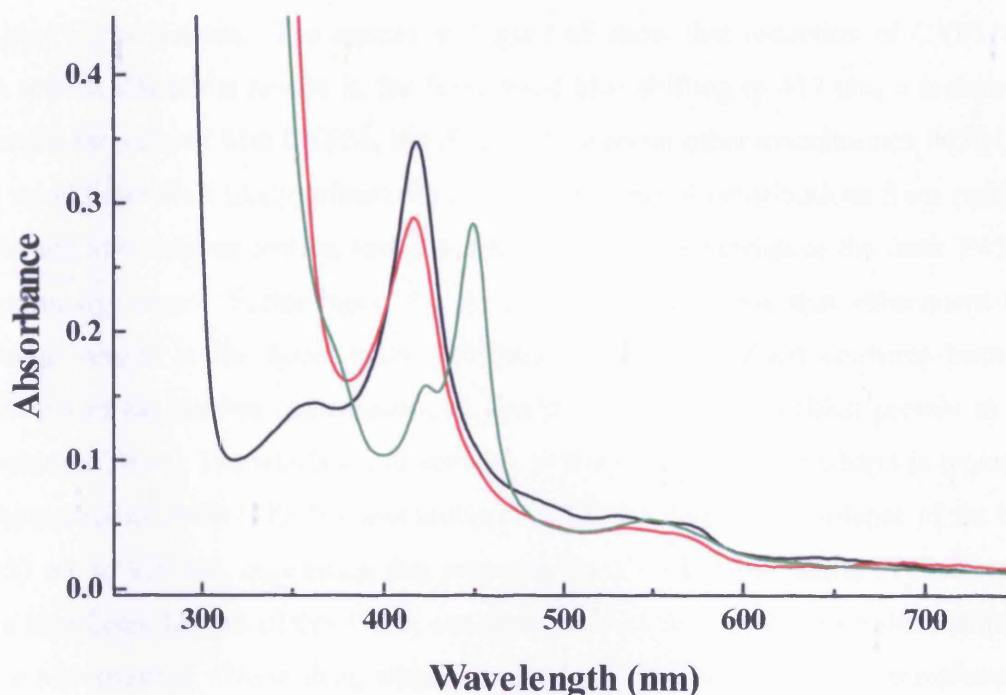
Figure 65 The UV-Visible absorption spectrum of the oxidised form of the CYP116/redox partner fusion (black), recorded between 250 and 750 nm at room temperature. Traces were recorded following the addition of solid sodium dithionite (red) and following bubbling of the solution with CO (green). The oxidised enzyme possesses a Soret peak at 418 nm and a shoulder between 450 – 500 nm relating to presence of flavin. The addition of dithionite causes the major absorbance feature to shift to shorter wavelengths (~417 nm), whilst CO-bubbling produces a shift in the Soret peak to 449 nm, identifying the protein as a cytochrome P450. Bleaching of the absorption feature between 450 and 500 nm occurs following addition of the reductant, indicating the presence of a flavin cofactor and resulting from reduction of the flavin (to predominantly the hydroquinone form). However, detection of the weakly-absorbing iron-sulphur cluster is not possible by this type of study, since its features are buried by the flavin and heme absorption. Enzyme used for this spectroscopic study was diluted in 50 mM Tris.HCl, 1 mM EDTA pH 7.2 to a final concentration of approximately 2.5 µM and spectra were recorded using a Cary UV-50 UV-Visible spectrophotometer (Varian).

The CYP116B1 absorption data in Figure 65 identify that this enzyme displays a spectrum typical of a cytochrome P450, with a Soret band at 418 nm and alpha and beta bands at 568 nm and 531 nm respectively. These Q band values, although slightly different to those of *M. tuberculosis* CYP51 (571 nm and 537 nm, Chapter 3.4), are within the range observed for other well characterized cytochromes P450, such as P450 BM3 and P450cam, whose alpha and beta bands are recorded at 569 nm and 536 nm, and 570 nm and 535 nm, respectively (192,199). In addition, the absorption features may be slightly skewed by the presence of the other redox centres (flavin and iron-

sulphur) in the protein. The spectra in Figure 65 show that reduction of CYP116B1 with sodium dithionite results in the Soret band blue-shifting to 417 nm, a feature not observed for reduced Mtb CYP51, but frequently seen for other cytochromes P450 (37). The small Soret shift likely reflects the removal of spectral contributions from oxidised flavin and iron-sulphur centres, and possibly the partial conversion of the ferric P450 to a ferrous-oxy state. Furthermore, the spectra also demonstrate that subsequent CO-bubbling results in the Soret feature shifting to 449 nm, which confirms both the formation of the ferrous carbon-monoxy species, and that the purified protein to is a cytochrome P450. The position and stability of this red-shifted Soret band is typical of the cytochromes P450 (37,159), and unlike Mtb CYP51 there is no collapse of the band at 450 nm to 420 nm, suggesting that protonation of the thiolate ligand of the heme is not a significant feature of this P450, and does not warrant the extensive study afforded to the Mtb enzyme. These data, which confirm that the electrons can be transferred to the protein's redox centre from the reductant, and that CO-binding to the heme iron is feasible, thus confirm that the CYP116B1/redox partner fusion has been correctly cloned from the *R. metallidurans* genome, and that the encoded protein is correctly folded and successfully incorporates the cysteinate-ligated heme macrocycle.

The absorption data also indicate the incorporation of flavin into the CYP116B1 protein. Comparing the CYP116B1 spectrum with that of oxidised Mtb CYP51 reveals the *R. metallidurans* P450 to posses a shoulder between 450 and 500 nm. Flavin cofactors typically demonstrate major UV-Visible absorption features between 300 and 550 nm, and in the case of human cytochrome P450 reductase the FMN domain maxima are found at 453 and 373 nm (17). Thus, the shoulder exhibited by CYP116B1 between 450 and 500 nm is in the correct wavelength range to suggest that it is due to the presence of a flavin redox centre. Further evidence of this is provided by the sodium dithionite-reduced spectra, which shows that the shoulder diminishes significantly upon reduction, as do the absorption spectra of flavin adenine dinucleotide (FAD) and flavin mononucleotide (FMN) when subjected to the same treatment and they are reduced from the quinone to the 2-electron reduced hydroquinone form (17). In addition, these spectral data are similar to those reported by Roberts *et al.* for RhF, the homologous protein from *Rhodococcus sp.* NCIMB 9784 (130). This P450 also exhibits an absorbance shoulder between 450 and 500 nm that is bleached upon sodium dithionite reduction. Spectral differences arise however, in the positions of the Soret and Q-bands, as these appear at longer wavelengths for the CYP116B1 homologue. The Soret

feature of the oxidised form of this enzyme is found at 424 nm, 6 nm longer than CYP116B1 and 5 nm longer than P450 BM3 (37), whilst the alpha and beta bands are similarly shifted to 574 and 539 nm. One possible explanation for these differences may be the buffer environment in which the enzymes were studied, as CYP116B1 was diluted in Tris.HCl at pH 7.2, whereas RhF was studied in potassium phosphate buffer at pH 7.8. However, red shifted Soret bands (to ~424 nm) are also typically observed in P450s for which the distal site is occupied by a ligand such as imidazole. RhF was purified by nickel affinity and imidazole elution, and thus the unusual Soret position likely reflects the purification of an inactivated hexacoordinated complex with imidazole.

Although these data corroborate the speculation that the CYP116B1 incorporates a flavin redox centre, they do not establish the nature of this centre (i.e. FAD or FMN) due to the masking of its spectrum by the more dominant absorption of the heme. Furthermore, the data cannot determine whether an iron-sulphur cluster is present as these generally have fairly broad and unfeatured spectra of much lower intensity than flavins and hemes (see Chapter 3.17). These contributions may be virtually undetectable under the absorption of the heme (159). Hence, in later sections (Chapters 4.15 and 4.17) investigations to determine both the nature of the integrated flavin, and the postulated iron-sulphur cluster, are performed using fluorescence spectroscopy and electron paramagnetic resonance (EPR) techniques.

From amino acid sequence similarity, the *R. metallidurans* protein CYP116B1 was postulated to incorporate a flavin redox centre, as well as the heme macrocycle and iron sulphur complex (125). Although this was supported by the aforementioned absorption bleaching in the flavin region, further studies were required to confirm the presence of flavin and to establish its reduction by pyridine nucleotide coenzyme. Hence, the following two experiments were performed in order to determine whether, like other redox partner fused P450s such as P450 BM3 (26), the protein could utilise electrons supplied from the coenzymes NADH and NADPH.

The initial study involved repeating the previously described experiment (used to determine that the expressed protein was a cytochrome P450), substituting sodium dithionite for NADPH. This would indicate the ability of the protein to interact productively with the coenzyme, as well as further substantiating the presence of flavin, as sodium dithionite indiscriminately reduces most redox centres in cofactor-containing proteins, whilst NAD(P)H should bind specifically to, and reduce the CYP116B1

flavocytochrome. CYP116B1 should contain a defined binding site for the coenzyme in the phthalate dioxygenase reductase-like domain. Indeed, NAD(P)H will not directly reduce any P450 enzyme (at least at any significant rate), with the exception of the nitric oxide reductase P450nor from *Fusarium oxysporum* (81-83,109). The experiment was performed under identical conditions to the preceding study, recording spectra of the oxidised, NADPH-reduced, and CO-bubbled sample between 250 and 800 nm. The resultant spectra are displayed in Figure 66, and indicate that when NADPH is added to the sample there is a bleaching of the absorption intensity between 450 and 500 nm, as is observed for numerous NAD(P)H-binding flavoproteins, such as P450 BM3 from *B. megaterium* and the CYP116B1 homologue studied by Roberts *et al.* (26,130). This further indicates that flavin is incorporated into CYP116B1, and that NADPH binds to the protein, eliciting reduction of this cofactor by hydride transfer from the coenzyme. This provides further evidence for a flavoprotein redox partner fused cytochrome P450. The spectrum recorded after bubbling with CO reveals that electrons delivered by NADPH are able to reduce the heme iron of the P450, as formation of the ferrous carbon-monoxy complex, with its characteristic peak at 449 nm, was observed. These spectral shifts in the heme Soret band act as further confirmation that the enzyme is a cytochrome P450, but also suggest that the sample contains intact, full-length protein as the reductase domain is clearly capable of passing electrons from the NADPH to the P450 domain. The direct reduction of cytochromes P450 by NADPH is not generally possible, other than in P450nor and its family, and thus these data are consistent with CYP116B1 containing the three cofactors (FAD, FeS and heme), and with an efficient electron transfer conduit from NADPH to the P450, resulting in heme reduction and subsequent CO-complex formation. This occurs, apparently, even in the absence of a CYP116B1 substrate bound to the heme, although the rate of electron transfer to the heme may be rather slow. In later sections (Chapters 4.18 and 4.19), stopped-flow and steady-state kinetics are performed in order to allow measurement of electron transfer rates from the coenzymes NADH and NADPH to the reductase of CYP116B1, and hence to better understand how the P450 receives the electrons required for reduction in a physiological situation. That is, which coenzyme is favoured, what is the rate of electron transfer to the enzyme from these coenzymes, and what are the relative affinities for NADH and NADPH.
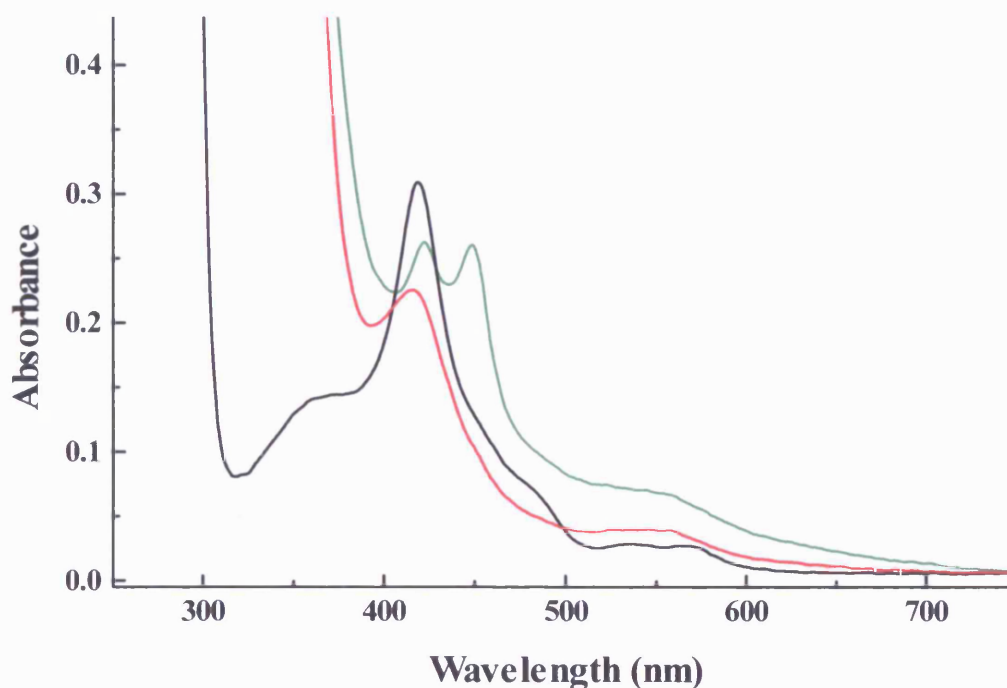
Figure 66 Absorbance spectra of oxidised (black), NADPH-reduced (red), and CO bubbled (green) *R. metallidurans* CYP116B1. The spectra identify bleaching of the flavin shoulder signal between 450 and 500 nm when NADPH is added to the oxidised enzyme, and a shift in the Soret peak to 450 nm following CO bubbling. This further confirms that the protein is a cytochrome P450, as well as demonstrating that electron transfer from NADPH to the P450 heme is possible, facilitating CO-ligation to the ferrous heme, producing the Fe(II)CO complex. Furthermore, the data suggest that purified CYP116B1 is intact and comprises all of the proposed redox centres, as degraded protein or CYP116B1 devoid of components of the redox chain is unlikely to allow electron transfer from the coenzyme to the heme (225). It should be noted that a proportion of the complex appears to be in the P420 form (as well as the P450 component). Oxidised enzyme was prepared to a final concentration of approximately 2.3 μM in 50 mM Tris.HCl, 1 mM EDTA pH 7.2, whilst excess NADPH was introduced to the assay from a stock solution (~20 mM) prepared in the same buffer to a final concentration of ~100 μM.

Reduction of the enzyme preparation was performed with both NADH and NADPH, in order to establish whether the enzyme has a preference for one or other of these pyridine nucleotide coenzymes. Previous studies have determined distinct preference for either NADPH or NADH in several flavoproteins and cytochrome P450 redox partner proteins, e.g. for NADPH in the flavoprotein reductase FprA from *M. tuberculosis* (134). The effects of these two compounds on the flavin signal were observed by UV-Visible spectroscopy. Following the recording of the absorption spectrum of oxidised CYP116B1 (~2.2 μM) between 250 and 800 nm, a 5 μl aliquot of NADH was added to the enzyme sample from a 20 mM stock solution (final

concentration ~100 μM), and the UV-Visible spectrum re-recorded. This procedure was repeated with NADPH (at the same final concentration), and the resultant spectra for the two reducing agents analysed to determine any difference in the final reduction state achieved and hence any perceivable preference of coenzyme by CYP116B1.

The spectra (Figure 67) demonstrated that when NADPH was added to the enzyme, the absorption intensity of the flavin-associated shoulder between 450 and 500 nm diminished considerably. However, the bleaching of the flavin shoulder was virtually non-existent when NADH was added to CYP116B1 at the same final concentration. This suggests that the reductase domain of the *R. metallidurans* enzyme shows a greater preference for NADPH than NADH, possibly indicating that the affinity for NADPH is much greater than for NADH, and that under physiological conditions electrons are preferentially derived from NADPH in order to reduce the flavin of this cytochrome P450-redox partner fusion. However, this does not rule out NADH as a viable electron donor for CYP116B1, although the affinity and rate of reduction may be less than for NADPH. If the rate of CYP116B1 reduction by NADH (under these conditions) was sufficiently slow, then reoxidation rate of the flavin may be similar and explain the relatively low level of NADH-dependent flavin reduction observed. Many redox systems, including those of P450 BM3 from *B. megaterium* and the P450cam-supporting system from *Ps. putida*, can be driven by both coenzymes, albeit not with comparable efficiencies (249).

These data aid the early characterization of the flavin domain, in so much as suggesting the reducing agent of preference for the protein, and demonstrating that the flavin domain is biochemically active, correctly folded, and incorporates a flavin molecule. Given the fact that NADPH and NADH have almost identical reduction potentials (~ -320 mV) it is unusual that NADPH facilitates flavin reduction of CYP116B1 at equilibrium, whereas NADH achieves little or no flavin reduction. Future work will be directed towards establishing the identity of the flavin as FMN, and examining its redox characteristics. A more detailed analysis of the pyridine nucleotide coenzyme preference will also be undertaken using steady-state kinetics (Chapter 4.19).
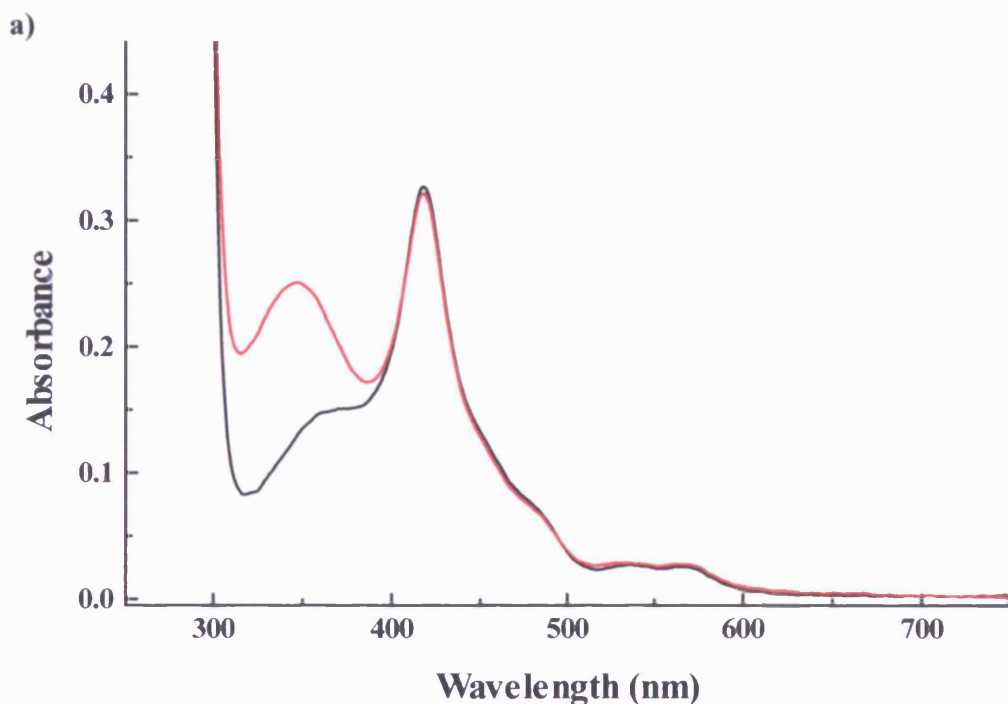
203

a)

Figure 67 The absorbance spectra of oxidised (black) and **a)** NADH-reduced and **b)** NADPH-reduced (both red) CYP116B1. The results show that the flavin signal component of the CYP116B1 absorbance spectra is bleached far more significantly in the presence of NADPH than when NADH is added, suggesting the reductase domain preferentially accepts electrons from NADPH. Protein samples (~2.2 μM) and NAD(P)H stock solutions (20 mM) were both prepared in 50 mM Tris.HCl, 1 mM EDTA (pH7.2), and all spectra were recorded at room temperature using a Cary UV-50 UV-Visible spectrophotometer (Varian).

b)
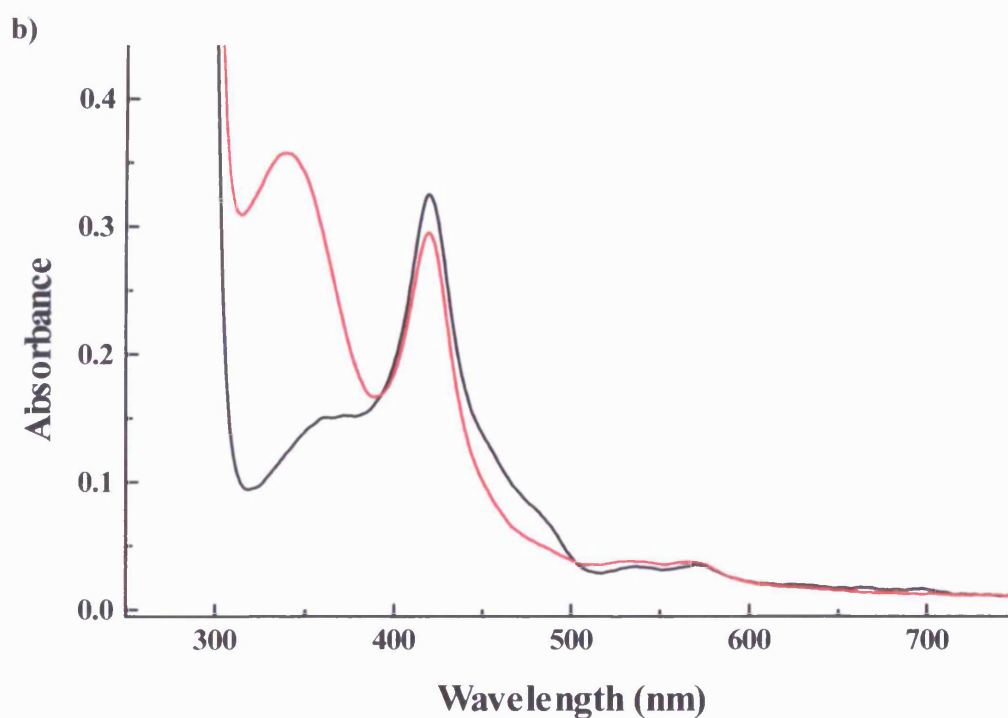
4.9 Further spectroscopic studies of *R. metallidurans* CYP116B1

The previous section described the results of widely used optical assays that determine whether a protein is a cytochrome P450. The small molecule-binding studies utilised in this section are also commonly used in this capacity (159,199). They are particularly useful in confirming the presence of a displaceable distal ligand on the heme macrocycle, and for comparisons of the spectroscopic behaviour and ligand affinities with other cytochromes P450. The following studies describe CYP116B1's binding to three chemically distinct compounds, nitric oxide, imidazole, and sodium cyanide. Each of these molecules coordinates P450 heme iron to produce distinctive spectral features. The spectral data collected further characterize the heme-binding site of this redox partner-fused cytochrome P450, and allow comparisons with both Mtb CYP51 and other well-documented P450s.

The binding of nitric oxide, imidazole, and sodium cyanide to CYP116B1 were performed as for Mtb CYP51 (Chapter 3.5) using oxidised enzyme diluted to 2 – 4 μM in 50 mM Tris.HCl, 1 mM EDTA pH 7.2. In each case, an absorption spectrum between 250 and 800 nm was recorded prior to the addition of ligand using a Cary UV-50 UV-Visible spectrophotometer (Varian). To obtain a nitric oxide-bound CYP116B1 spectrum, 5 – 6 bubbles of NO gas were gently introduced to the sample to avoid excessive agitation of the protein and turbidity associated with excessive acidification, and a further spectrum recorded. The imidazole- and sodium cyanide-bound spectra were recorded following the progressive addition of 0.2 – 0.5 μl aliquots of concentrated stock solutions of the respective compounds until spectral changes were complete. All assays were performed at room temperature and stock solutions were prepared in the same buffer as the enzyme sample to minimise alterations in pH and ionic strength during the experiments.

The spectra recorded following the addition of nitric oxide, imidazole, and sodium cyanide are shown in Figure 68 and demonstrate that each compound elicits a different spectral change in the Soret band of CYP116B1. The binding of nitric oxide causes the Soret band to shift from 418 nm to 434 nm and decrease in intensity, as is observed for Mtb CYP51 and P450cam from *Ps. putida* (Chapter 3.5, (159,199)). Furthermore, similar to the results observed for the CYP51, nitric oxide binding causes a noticeable increase in intensity in the Q band region, with development of features at 574 nm and 545 nm. The binding of imidazole to CYP116B1 causes the Soret band to decrease in

intensity and shift to 424 nm, as well as inducing a partial spectral fusion of bands in the visible region. Similarly, sodium cyanide binding elicits a Soret band shift of 14 nm to 432 nm and produces a single peak in the visible region centred at approximately 550 nm. For both compounds, the spectral changes are akin to those of Mtb CYP51 (Chapter 3.5, (159)), although the decreases in intensity of the Soret bands for CYP116B1 are slightly greater.
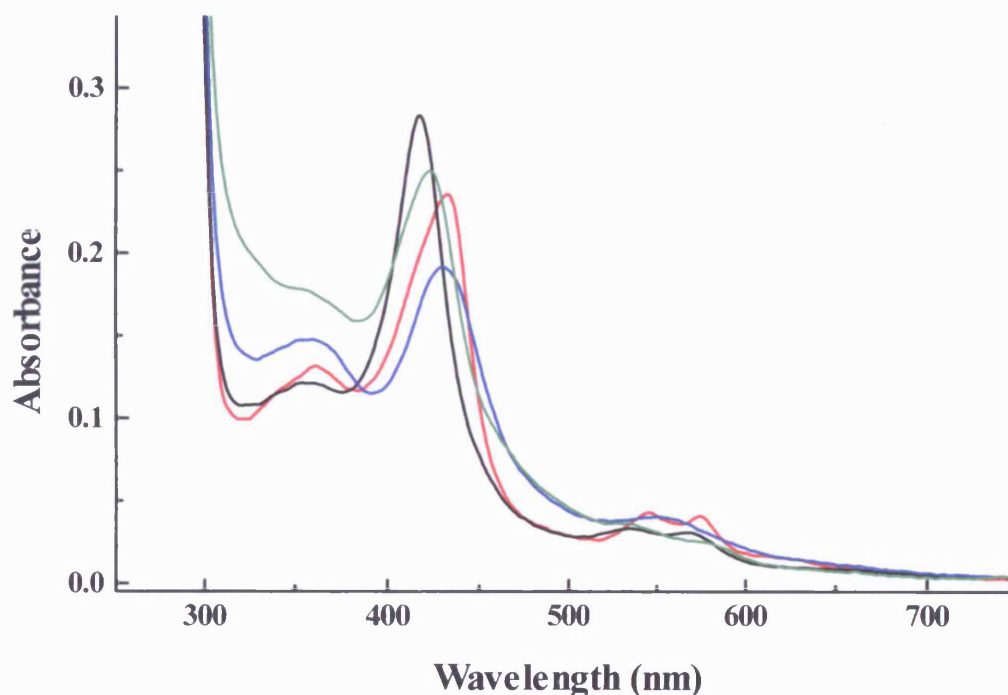

Figure 68 The absorption spectrum of oxidised *R. metallidurans* CYP116B1 (black), shown alongside spectra of nitric oxide-, imidazole-, and sodium cyanide-bound enzyme (red, green, and blue respectively). Each of the three compounds induces an inhibitor-like type II shift in the Soret band to 434 nm (nitric oxide), 424 nm (imidazole), and 432 nm (sodium cyanide). These shifts indicate that the compounds displace the water molecule bound on the distal face of the heme, and ligate, via a nitrogen or carbon atom, to the heme iron. The spectral shifts are typical of those seen in other P450 enzymes and thus further confirm the enzyme to be a cytochrome P450. All assays were performed using approximately 3 μM enzyme diluted in 50 mM Tris.HCl, 1 mM EDTA pH 7.2, and maintained at 25 °C using the Peltier attachment of a Cary UV-50 UV-Visible spectrophotometer (Varian). Imidazole and sodium cyanide were added to final concentrations of approximately 2 and 10 mM, respectively, whilst nitric oxide saturation was achieved by the introduction of 6 – 8 bubbles of this gaseous ligand.

The absorption spectra presented here for CYP116B1 are typical of this class of enzyme. The data confirm that small ligands compounds of differing size and hydrophobicity can access the active site of *R. metallidurans* CYP116B1, where they approach the distal face of the heme and displace the iron-bound water molecule, resulting in the observed spectral changes as novel hexa-coordinated heme species develop. These optical shifts thus further confirm that the hemoprotein expressed from *R. metallidurans* gene 1832 undergoes spectral changes typical of P450s, and that the heme iron can be coordinated at the distal position by various small ligands that are known to inactivate P450s and other heme enzymes. Having confirmed that this *R. metallidurans* protein contains a P450-type heme molecule, the next section describes the determination of the extinction coefficient of the heme of CYP116B1 by the hemochromagen assay. Following this study, investigations of the ligand specificity of the CYP116B1 active site will be investigated by optical binding titrations. Following these studies, further investigations of the properties of the heme will be investigated by electron paramagnetic resonance and resonance Raman spectroscopy techniques.

4.10 Determination of the CYP116B1 heme extinction coefficient

As was reported in the study of Mtb CYP51 (Chapter 3.6), the concentration of cytochromes P450 are typically determined using an extinction coefficient of 91 mM^{-1}.cm^{-1} for the reduced/CO-bound minus reduced difference spectrum, and using the wavelength pair 450 minus 490 nm (50). However, the ferrous carbon-monoxy complex of CYP51 was not stable in the P450 form due to protonation of the proximal ligand under the conditions of the assay, and collapsed to the P420 state. Thus, this technique was considered inaccurate for the concentration determination of this enzyme. Hence, the pyridine hemochromagen technique was utilised, as this method does not rely on the formation of the CO-complex, but instead uses the formation of a heme-pyridine adduct (extracted from the protein matrix) to determine the extinction coefficient of cytochromes P450 (or other heme proteins). The coefficient determined for Mtb CYP51 by this method was 134 mM^{-1}.cm^{-1} at 418 nm, a value somewhat larger than the 91 mM^{-1}.cm^{-1} utilised in the majority of P450 studies. It should be noted that the Omura and Sato method exploits absorption differences between CO-bound and ferrous species (rather than reflecting absorption at the Soret peak *per se*) and was performed on a rabbit liver microsome extract likely containing a mixture of

cytochrome P450 isoforms. However, even when the value computed from the Omura and Sato coefficient is related back to absorption at the Soret maximum, it still (generally) only predicts a coefficient of ~95 $mM^{-1}.cm^{-1}$ for most P450s. This disparity, together with values reported for other P450s by the hemochromagen method (158,194), suggests that the use of a single extinction coefficient for all cytochromes P450 is not accurate and that a method that reports on a more stable and/or more completely populated heme adduct is preferable to the study of the ferrous carbon-monoxy complex. Also, on consideration, the assumption that all P450s could have identical extinction coefficients appears naïve given the widely differing heme environments in this superfamily of proteins, even though all share cysteinate coordination to heme iron. For this reason, and so that further comparisons with Mtb CYP51 could be made, the hemochromagen assay was performed on R. metallidurans CYP116B1.

The pyridine adduct of CYP116B1 was created in the same manner as the CYP51 adduct (Chapter 3.6), using the method reported by Berry and Trumpower (187). A sample of CYP116B1 was prepared in 50 mM Tris.HCl (pH 7.2) to a final concentration of 2 – 4 µM, and placed in a quartz cuvette. A 500 µl aliquot of a solution containing 200 mM NaOH, 40 % pyridine (by volume), and 0.6 mM $K_3Fe(CN)_6$ was added to the cuvette, agitated thoroughly, and a UV/Visible absorption spectrum recorded between 250 and 800 nm using a Cary UV-50 UV-Visible spectrophotometer (Varian). The cuvette contents were then reduced by the addition of 2 – 5 mg solid sodium dithionite, and a further spectrum recorded. Complete reduction of the sample was confirmed by recording a further spectrum following a second addition of dithionite. The difference in absorbance at 557 and 540 nm was calculated, and from the computed value an extinction coefficient for CYP116B1 was determined.

The results of the assay, which were replicated using separate protein samples, identify that the extinction coefficient (ε_{419}) is 137 $mM^{-1}.cm^{-1}$, which is similar to the value reported Mtb CYP51 (Chapter 3.6, (159)), but considerably greater than the 'standard' cytochrome P450 coefficient of ~95 $mM^{-1}.cm^{-1}$ for the oxidised enzyme at its Soret peak. When the CYP116B1 coefficient is considered with the values determined by this method for Mtb CYP51 and P450cin from Citrobacter braakii, which possesses a ε_{419} of 150 $mM^{-1}.cm^{-1}$ from pyridine hemochromagen assay (200), it is apparent that there is no 'typical' value for the cytochromes P450, and that the use of a single coefficient is inappropriate in most cases. For this reason the coefficient determined for CYP116B1 by the hemochromagen assay will be used to calculate enzyme

concentrations wherever necessary, and should most likely be employed in the characterizations of all cytochromes P450 to further improve the consistency of data.

Having identified an accurate extinction coefficient with which to determine the concentration of CYP116B1, the next section describes the determination of the binding constants for imidazole and sodium cyanide, as well as for a number of other compounds of varying size and chemical nature. These studies will enable further characterization of the active site of the *R. metallidurans* enzyme, as well as helping to define a substrate or substrate class for this monooxygenase.

4.11 *R. metallidurans* CYP116B1 ligand binding studies

Ralstonia metallidurans CYP116B1 has no known substrate and thus in this section possible candidates for this role were assessed with a view to determining the type of compound that this cytochrome P450 may metabolise as a part of the host organism's physiology. Optical binding studies have frequently been utilised in studies of P450s (28,158,199), as they are generally a quick and easy assay that can distinguish between a substrate and an inhibitor on basis of the type of spectral change induced, and indeed, tetradecanoic acid was determined as a substrate of CYP110 from *Anabaena* sp. PCC 7120 by this method (250). The basis of these studies is to follow the optical shift of the Soret band upon binding of a ligand, and to plot the induced absorption change *versus* ligand concentration to obtain the dissociation constants (K_d), which can subsequently be utilised for comparisons of ligand affinity across the cytochromes P450. Typically, substrate-like compounds, which bind in the active site of the enzyme but which do not ligate to the heme directly, induce shifts of the Soret band towards shorter wavelengths (type I shift) due to their influence on the electronic configuration (spin state) of the heme. This is generally caused by displacement of the 6th (water) ligand to the heme iron and the creation of a penta-coordinate heme iron. Most P450 inhibitors, on the other hand, ligate directly to the heme iron via a carbon or nitrogen centre, displacing the bound water molecule, and inducing type II Soret band shifts to longer wavelengths (28,69). In a previous section (Chapter 4.9) imidazole and sodium cyanide were identified as inhibitory compounds by their influence on the absorption spectrum of CYP116B1, and here optical binding titrations with these compounds are performed in order to determine their dissociation constants. In subsequent sections (Chapters 4.11, 4.12, and 4.13) numerous other compounds are investigated, ranging from inhibitory

(heme iron coordinating) azoles and triazoles, through to possible substrate-like molecules such as fatty acids and sterols. These studies were performed to identify structural features associated with enhanced affinity of ligand binding to the CYP116B1 active site, and with the possibility that the nature of its substrate might be identified.

Throughout these investigations binding assays were performed as described in Chapter 3.7, and by McLean *et al.* (157). Aliquots of CYP116B1 were diluted to 2 – 4 μM in 50 mM Tris.HCl, 1 mM EDTA pH 7.2 and incubated at 25 °C prior to an absorption spectrum of the oxidised enzyme being recorded between 250 and 800 nm. A range of putative substrate-like and inhibitor compounds were then added to the enzyme in small aliquots, typically 0.2 – 0.5 μl, and UV-Visible spectra recorded after each addition until no further spectral change could be detected. Stock solutions of each compound were prepared so that minimal volumes of the solvents required to solubilise them were added to the assay mixture, thus avoiding excessive turbidity and solvent effects on the protein sample that may hinder the determination of dissociation constants. In each case, the ligands were classified, as either an inhibitor or substrate-like compound, by the Soret band shift that they induced, and data were analysed as for the Mtb CYP51 data in order to determine the dissociation constant values that are shown in Tables 12, 13, and 14.

Initially, the small compounds imidazole and sodium cyanide, frequently used as standards in the characterization of P450 inhibitor binding (159,199), were added and showed noticeable effects by shifting of the Soret band from 418 nm towards 424 nm (imidazole) and 432 nm (cyanide). These Soret shifts, which are akin to those observed for Mtb CYP51 (Chapter 3.7), imply that imidazole and sodium cyanide bind in the active site of the P450 and ligate to the heme iron via their respective azole nitrogen and carbon atoms. Following this preliminary study, these compounds were accurately titrated against samples of the P450 to produce the binding-titration curves displayed in Figure 69 and Figure 70. Sodium cyanide was titrated using a 500 mM stock solution whilst imidazole was titrated from a 100 mM stock solution; these concentrations having been identified as the optimal ligand concentrations, due to the requirement for small volume additions (to avoid dilution effects) and their relatively low affinity for the P450 heme iron. The data were analysed and difference spectra were produced to show how absorbance changed as a function of the concentration of the two compounds. Maximal absorption changes from these difference spectra were computed by subtracting the absorption value at the trough minimum from that at the peak maximum

in each difference spectrum, and plotting this overall absorption change against the relevant ligand concentration. These data were then fitted to rectangular hyperbolic curves (see Equation 2, Chapter 3.7), and from these K_d values for the two compounds determined (Figure 69, Figure 70, and Table 15).
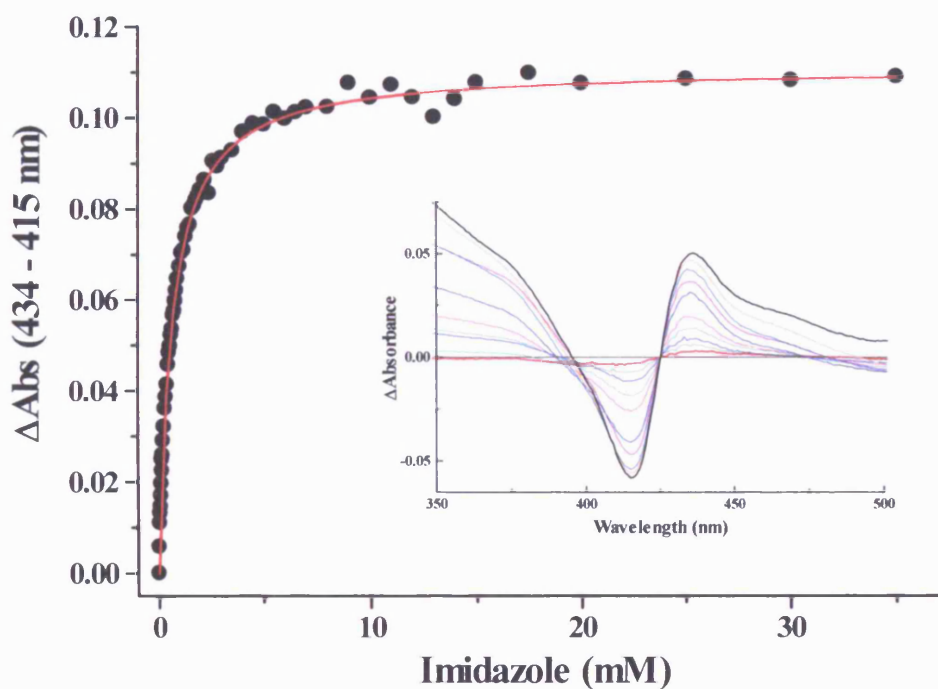

Figure 69 The binding titration curve for the interaction of imidazole with *R. metallidurans* CYP116B1. The titration was performed by sequential additions of imidazole to a sample of CYP116B1 (~2 μM), with UV-Visible absorption spectra between 250 and 800 nm recorded following each incremental addition. As reported in Chapter 3.7, imidazole induces an inhibitory type II shift of the Soret band, with a final position 424 nm. The change in absorbance was established as the difference between the recorded spectra at two distinct wavelengths (434 and 415 nm) where the overall optical change was maximal, as identified by the inset difference spectra. Fitting of the plot to a rectangular hyperbola (Equation 2, Chapter 3.7) determines a K_d value of 646 ± 13 μM, demonstrating a weak affinity of this ligand for *R. metallidurans* CYP116B1.
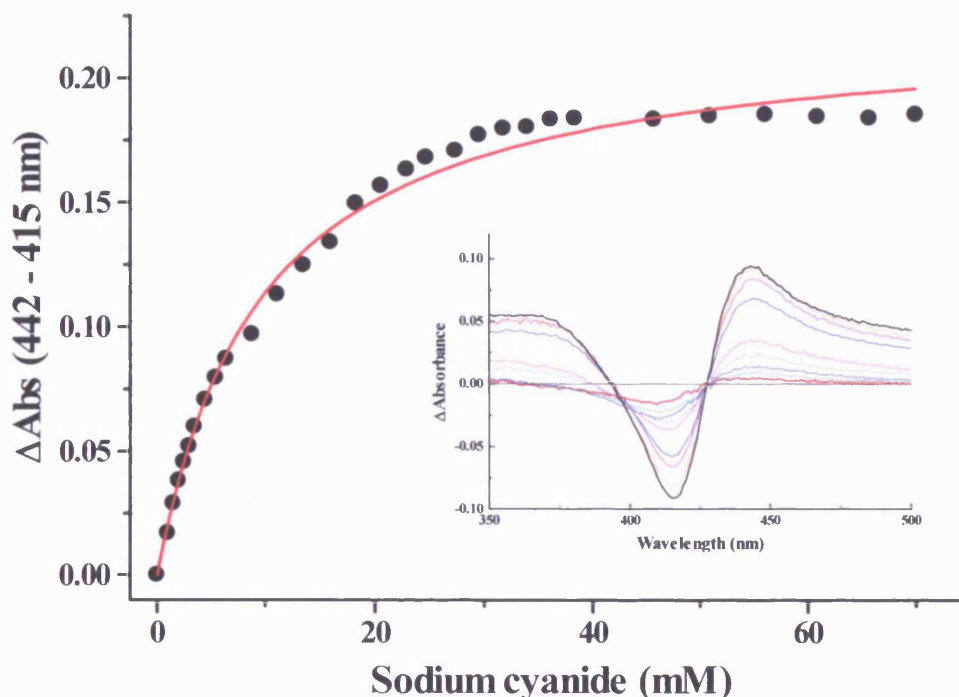
Figure 70 The plot of induced absorbance change *versus* ligand concentration for the binding of sodium cyanide to CYP116B1 (~2 μM) from *R. metallidurans*. The absorbance change was calculated at the wavelengths at which maximal spectral changes were observed (i.e. 442 and 415 nm), as identified by the inset difference spectra. These difference spectra confirm that, as reported in Chapter 3.7 for Mtb CYP51, sodium cyanide induces an inhibitory type II shift of the CYP116B1 Soret band, with a final position of 432 nm. The plot is fitted to a rectangular hyperbola (Equation 2, Chapter 3.7) that determines a K_d of 9.7 ± 0.6 mM for sodium cyanide, thus demonstrating this compound to bind significantly less tightly than imidazole (Figure 69 and Table 15).

Compound	Dissociation constant (K_d)
Imidazole	646 ± 13 μM
(Sodium) cyanide	9.7 ± 0.6 mM

Table 15 Dissociation constants determined for the binding of imidazole and cyanide to *R. metallidurans* CYP116B1. The K_d values were calculated from the plots of absorption change *versus* inhibitor concentration shown in Figure 69 and Figure 70. The absorption changes were themselves calculated from the raw absorption data by subtracting the spectrum of oxidised, ligand-free CYP116B1 from all subsequent spectra recorded during the titration. The values show that these two compounds, which differ in both size and chemical nature, bind to CYP116B1 with significantly different affinities.

212

The results of these binding titrations identify that these small molecules were capable of freely diffusing into the active site of the enzyme and ligating to the iron at the centre of the heme macrocycle. This effects an optical shift in the Soret band of the protein from 418 nm to 424 nm for imidazole, and to 432 nm for sodium cyanide. The resultant curves show that the binding of the compounds describes Michaelis-type behaviour (i.e. saturable, reversible, single-site binding) and that binding is saturable in the mM range. The K_d values indicate that imidazole binds to the enzyme with approximately 15 times greater affinity than sodium cyanide, although both ligands have relatively low affinity for the P450. Alterations in the affinity for the two ligands are likely partially due to differences in charge and size of the ligands, with cyanide being a smaller and negatively charged ligand. Altered affinity likely also has its foundations in the unusual nature of the P450 heme iron, with the cysteinate ligand placing a relatively high electron density on the heme by comparison with many other cytochromes. This phenomenon likely also disfavours cyanide binding and elevates its K_d for the CYP116B1 heme iron.

4.12 *R. metallidurans* CYP116B1 azole binding studies

In addition to imidazole and sodium cyanide, more complex ligands, namely the azoles and triazoles: econazole, fluconazole, miconazole, ketoconazole, clotrimazole, and voriconazole, were individually titrated with CYP116B1 to determine their K_d values and to further characterize the nature of the active site of the enzyme. As reported in Chapter 3.8, these large hydrophobic molecules are potent inhibitors of many cytochromes P450s, including Mtb CYP51, and have been proven as effective treatments for fungal infections such as those caused by *Candida albicans* and 'Athlete's Foot' (*Trichophyton mentagrophytes*) (108). Their role in the treatment of these diseases, and others such as cryptococcal meningitis (201), has been identified as due to inhibition of selected P450s of the pathogen, effectively preventing sterol synthesis, and thus disrupting cellular integrity (108,201). The azoles are frequently used to probe the active sites of cytochromes P450 and generally have high affinity for monooxygenases that bind bulky, apolar substrates (158,159). In this section, the spectral dissociation constants for the aforementioned azoles are determined and contrasted with those of Mtb CYP51 and other cytochromes P450.

The compounds were titrated from 1 mg/ml stock solutions (except clotrimazole, 0.5 mg/ml) and their effects on the P450 spectrum observed between 250 and 800 nm using a Cary UV-50 UV-Visible spectrophotometer (Varian). The data collected were baseline-corrected, difference spectra compiled in the same manner as previously reported (see Chapter 3.7), and from fitting of the resultant plots of absorbance changes *versus* concentration of azole compound (Figure 71), dissociation constants (K_d values) were calculated (Table 16).
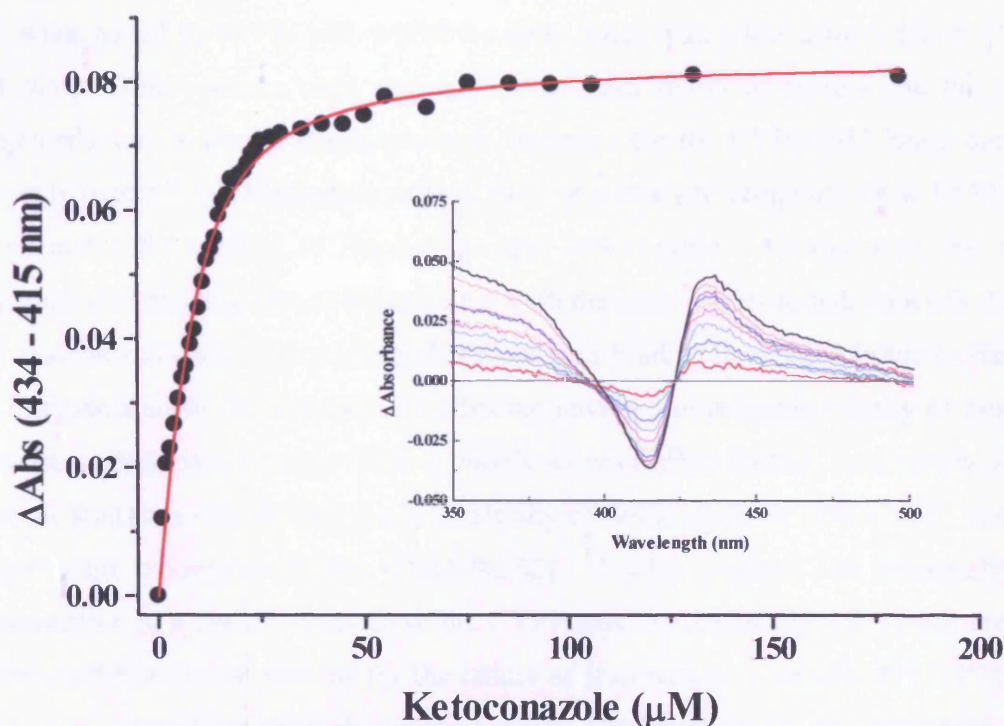

Figure 71 The binding titration curve and selected difference spectra (inset) for the interaction of ketoconazole with *R. metallidurans* CYP116B1. The difference spectra demonstrate a type II shift of the enzyme's Soret band, with a decrease in absorbance at 415 nm and a concomitant increase at 434 nm, confirming ketoconazole as an inhibitor of CYP116B1. Curve fitting using a rectangular hyperbolic function (Equation 2, Chapter 3.7) determined the K_d for ketoconazole as 4.3 ± 0.6 µM, a value which indicates that the azole to bind relatively tightly to the heme iron of CYP116B1, and much more tightly than imidazole. Similar optical changes were observed for all the azole compounds tested, the K_d values for which are displayed in Table 3.7. Absorption spectra were recorded between 250 and 800 nm, and converted into difference spectra by subtracting the spectrum of oxidised, ligand-free CYP116B1 from all spectra recorded after azole additions. Enzyme was present in the assay at approximately 2.5 µM and diluted in 50 mM Tris.HCl, 1 mM EDTA pH 7.2. A stock solution of ketoconazole (1mg/ml) was also prepared in this buffer.

In all cases, binding of the azoles to CYP116B1 caused the Soret band to move, in an inhibitory type II manner, towards longer wavelengths (typically 424 nm); shifts analogous to those observed for CYP51 (Chapter 3.8) and CYP121 from *M. tuberculosis* (158,159). The K_d values calculated for econazole (7.48 µM) and clotrimazole (0.02 µM) show that the azole compounds used bind to the protein with quite different affinities, although a generally similar trend is observed for the binding of these compounds to Mtb CYP51 (Chapter 3.8). However, the results for fluconazole and voriconazole were not in agreement with other azoles, as the former showed no shift when added up to 170 µM, whilst the latter binds with a low affinity (K_d = 4.76 ± 0.71 mM). These results were replicated with fresh stocks of protein and the azole compounds, and a similar phenomenon is observed for the CYP116B1 heme domain protein (Chapter 5.6). These data suggest that the active site geometry of the P450 may be unsuitable for binding of fluconazole and voriconazole. Alternatively, the more polar nature of these compounds compared with the other azoles tested, which is due to their fluorine moieties, may possibly disfavour their binding in a hydrophobic active site and mitigate against fluconazole, in particular, having a measurable affinity of binding based on optical perturbation. This is clearly an interesting finding, particularly given previous studies demonstrating the high affinity of fluconazole for Mtb CYP51 and for several other eukaryotic P450s (159,198,202). Further studies, and ultimately the determination of a crystal structure of the CYP116B1 heme domain, will be required to determine the structural reasons for the failure of fluconazole to coordinate CYP116B1 heme iron. Notwithstanding the unusual results with fluconazole, the remaining data give some important indications of the nature of the active site in terms of the type (volume, hydrophobicity, etc.) of compound that will enter the active site and bind the heme iron. Several large, bulky azoles penetrate the CY116B1 active site and bind tightly to the heme iron, suggesting that the natural substrate may be a hydrophobic, polycyclic molecule. However, the affinities of certain azoles differ markedly from those reported for Mtb CYP51 (e.g. the K_d of miconazole is 7.48 ± 0.72 µM for CYP116B1 c.f. 0.31 ± 0.04 µM for CYP51), whilst voriconazole interacts only weakly with this enzyme and fluconazole shows no evidence of binding within the CYP116B1 active site. Hence, it can be concluded that the active sites of these two P450s are likely to differ in both capacity and hydrophobicity, and thus also in their selectivity of substrate type. In the following section, further studies of ligand binding are reported using a wide range of inhibitor and potential substrate-like molecules in order to

develop a more clearly defined impression of CYP116B1 and its ligand and substrate binding capabilities.

Azole compound	Dissociation constant (K_d)
Clotrimazole	0.02 ± 0.01 μM*
Econazole	7.48 ± 0.72 μM
Fluconazole	Not determined
Ketoconazole	4.3 ± 0.6 μM
Miconazole	0.21 ± 0.06 μM*
Voriconazole	4.76 ± 0.71 mM

Table 16 Dissociation constants for the binding of the azole anti-fungal compounds to CYP116B1, determined from spectral titrations of the six azole anti-fungal compounds with the *R. metallidurans* protein. As previously (Chapter 3.7), K_d values were determined by fitting plots of change in absorbance at appropriate wavelengths *versus* azole concentration with a rectangular hyperbola (Equation 2, Chapter 3.7). Data marked * were fitted to Equation 3 (Chapter 3.8) due to the tight-binding to the enzyme exhibited by these compounds, whilst no K_d could be determined for fluconazole as the recorded spectra displayed no indication of binding (i.e. no shift of the Soret band or other spectral perturbation of the heme).

4.13 Further *R. metallidurans* CYP116B1 binding studies

Following the testing of the azole compounds, a large number of different inhibitor and potential substrate-like compounds, including unsaturated fatty acids, sterols, and imidazole derivatives, were titrated against CYP116B1. This was done in order to determine further inhibitors of this cytochrome P450 and their potency, as well as potentially identifying one or more substrate-like compounds that could induce low-spin to high-spin transitions of the heme iron. The table below (Table 17) lists the compounds tested, their effects on the spin state of the heme, and a K_d value (where obtained). Figure 72 shows the chemical structures of these compounds. The studies were performed using the same techniques as detailed previously for the determination of dissociation constants of imidazole, sodium cyanide, and the azole anti-fungals (Chapters 4.11 and 4.12). For each compound, an initial assessment was performed to determine whether perturbation of Soret band was effected, with a full binding titration being performed for those compounds eliciting either a substrate-like type I, or inhibitory type II shift. All assays were performed in 50 mM Tris.HCl, 1 mM EDTA pH 7.2, with enzyme concentration between 2 and 4 μM and sample temperature maintained at 25 °C.

The data in Table 17 identify that there are a number of compounds that induce a type II inhibitory Soret peak shift from 418 nm towards 430 nm. These compounds are predominantly derivatives of imidazole, including those linked to fatty acids at the ω-carbon (C_{10} – C_{12} imidazoles), and most bind more tightly than imidazole itself (K_d = 296 μM, Chapter 4.11). This suggests that the lipophillic nature of the side chains of the imidazole derivatives may be an important factor in "driving" these compounds from the hydrophilic solution into the more hydrophobic active site of CYP116B1, thus increasing the affinity for these compounds.

Compound	Observed spin state shift			Final Soret poistion (nm)	Dissociation constant (K_d)
	Type I	Type II	No shift		
1-butylimidazole		✓		424	1.01 ± 0.03 mM
4-phenylimidazole		✓		423	0.15 ± 0.01 mM
C_{10} imidazole		✓		423	3.47 ± 0.36 μM
C_{11} imidazole		✓		423	0.59 ± 0.12 μM*
C_{12} imidazole		✓		423	0.52 ± 0.11 μM*
Lauric acid			✓		
Myristic acid			✓		
Palmitic acid			✓		
Pentadecanoic acid			✓		
Myristoleic acid	✓			416	4.80 ± 1.76 μM*
Palmitoleic acid	✓			416	33.45 ± 6.27 μM
Arachidonic acid	✓			416	5.62 ± 1.26 μM*
Oleic acid	✓			417	N.D.
Fluorene			✓		
Acetosyringone			✓		
1-aminobenzotriazole			✓		
Hydrocortisone			✓		
Testosterone			✓		
7-ethoxycoumarin			✓		
N-palmitoyl glycine		✓		422	N.D.

Table 17 The results of a screen of various compounds for their ability to bind to CYP116B1, as determined by their influence on the absorption spectrum of the oxidised enzyme. The Soret band shifts induced by each compound, substrate-like type I or inhibitory type II, are indicated, as are the final Soret band positions and the dissociation constants determined from binding titration data. K_d values for the binding of compounds marked * were determined using the tight-binding equation (Equation 3, Chapter 3.8) rather than the standard (Michaelis) hyperbolic function (Equation 2, Chapter 3.7). Compounds denoted 'no shift' induced no optically detectable perturbation of the CYP116B1 absorbance spectrum, whilst 'N.D' indicates that the K_d could not be determined due to excessive sample turbidity induced by the compound itself, or the solvent in which it was prepared. Figure 72 shows the structures of a selection of these compounds.
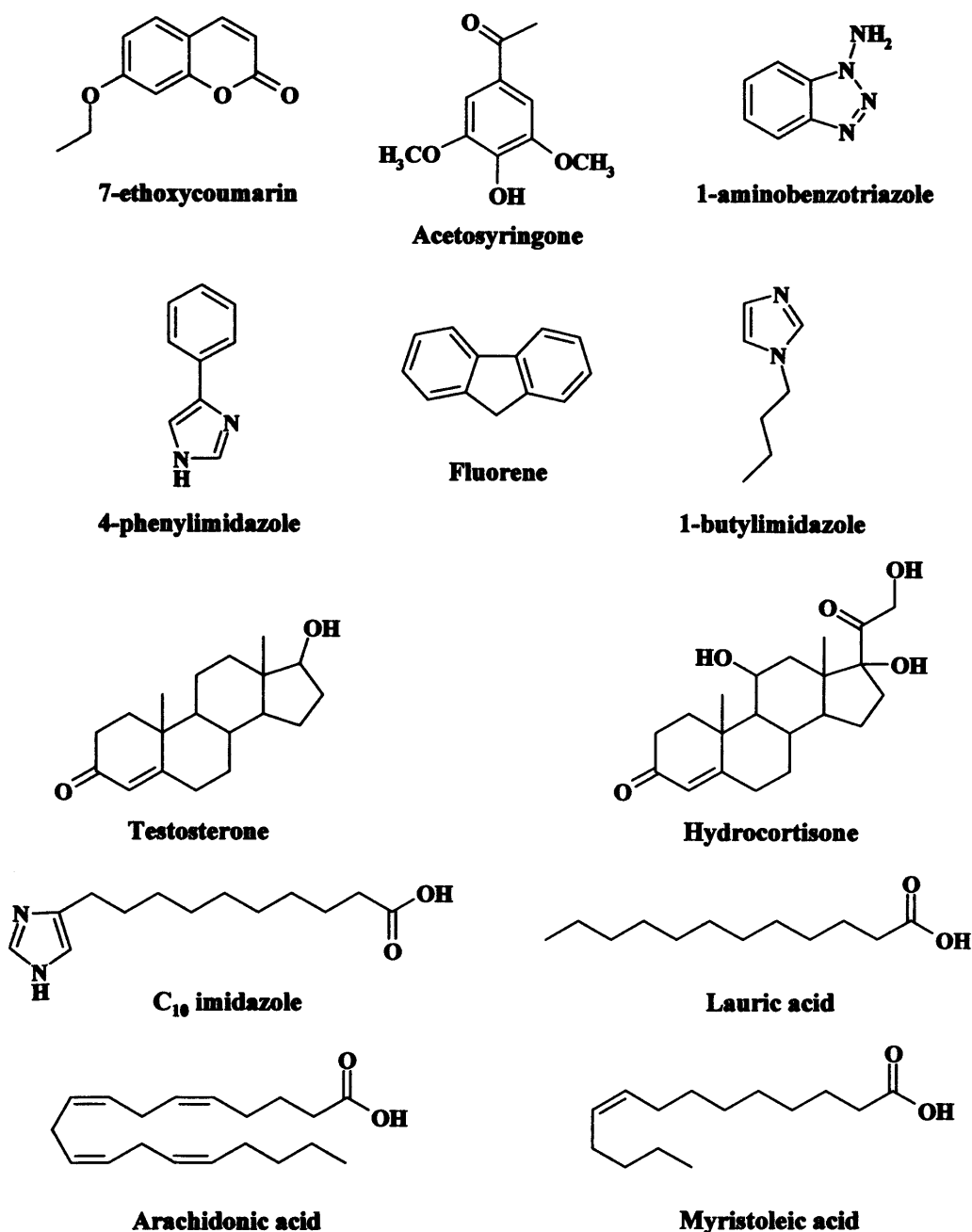
Figure 72 Selected chemical structures corresponding to the compounds listed in Table 17 investigated for their ability to bind to *R. metallidurans* CYP116B1. Many of the bulky, polycyclic compounds, such as hydrocortisone, fluorene, 7-ethoxycoumarin, 1-aminobenzotriazole, and acetosyringone, elicit no appreciable spectral shifts, thus indicating them not to interact with the CYP116B1 heme iron. Conversely, many of the imidazole- and alkyl chain-based compounds, including 4-phenylimidazole, 1-butylimidazole, and C_{10} imidazole, are shown to be inhibitors of this P450, inducing typical type II inhibitor-like Soret band shifts and generating K_d values ranging from ~1 mM (1-butylimidazole) to ~3.5 μM (C_{10} imidazole). Interestingly, substrate-like type I Soret shifts, implying perturbation of the electronic configuration of the CYP116B1 heme iron, are induced by unsaturated fatty acids, including arachidonic acid (K_d = 5.62 μM) and myristoleic acid (K_d = 4.80 μM). However, saturated fatty acids show no evidence for binding to this *R. metallidurans* cytochrome P450.

An example of the binding curve for determination of the K_d for one of these substituted imidazole compounds is shown in Figure 73, and from the calculated values it can be seen that with increasing chain length ($C_{10} - C_{12}$) there is apparent increased tightness of binding. This again implies that the hydrophobicity of the side-chain, which increases with length, plays a role in determining affinity of inhibitor binding. It should be noted, though, that the difference between the binding of C_{11} and C_{12} imidazoles is marginal, with the K_d values being statistically inseparable (Table 7). However, a number of saturated fatty acids (e.g. lauric acid (C_{12}) and pentadecanoic acid (C_{15})), which are also highly lipophillic, do not give any spectral indication of a binding interaction. This may relate to the degree of solubility of these compounds, which do not dissolve easily in the titration buffer. However, in view of the tight binding of the similar imidazole derivatives, it is perhaps more likely that these fatty acids bind CYP116B1 in a mode that does not involve displacement of the distal axial ligand, rather than the imidazole group itself being a critical determinant of ligand binding. Some further assessments of the nature of the CYP116B1 active site can be made by identifying those compounds that do not induce spectral shifts on titration with CYP116B1. It should be noted, however, that lack of spectral perturbation does not necessarily mean lack of P450 binding. Compounds that do not induce spectral changes include the steroids hydrocortisone and testosterone, 1-aminobenzotriazole, and 7-ethoxycoumarin, all of which are bulky, polycyclic compounds (see Figure 72 for structures). Since several such polycyclic azoles clearly do bind to the P450, it is not clear whether those bulky compounds which do not induce a spectral change cannot access the active site, or simply bind in a position distal to the heme-bound water which does not affect heme absorption. Alternatively, the K_d for these compounds may be significantly greater than their solubility limit. However, the fact that none of these compounds induce spectral shifts typical of P450 substrates (i.e. type I shifts) indicates that they are unlikely to be substrates. Distinctive results were obtained for Mtb CYP51, which has been shown to interact with polycyclic substrates, including lanosterol and obtusifoliol (169), although spectral shifts induced by these molecules are very small within their solubility range. More substantial Mtb CYP51 spectral changes are seen with the steroid estriol, although this molecule is not itself a substrate for CYP51 demethylation (159). It appears that the active site of CYP116B1 is significantly structurally different from that of CYP51, and that the substrate of R. metallidurans P450 is unlikely to be a sterol- or steroid-like polycyclic compound.
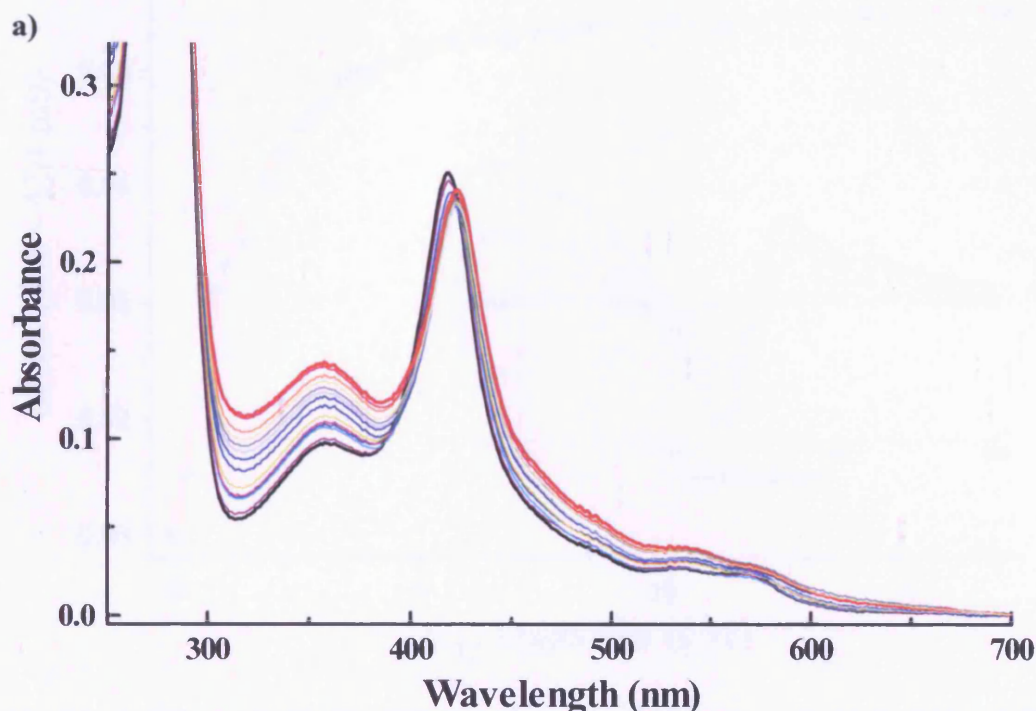
a)

Figure 73 a) Selected UV-Visible absorption spectra recorded during the titration of C_{12} imidazole (0 – 20 µM) with *R. metallidurans* CYP116B1 (~2 µM). The spectra identify that C_{12} imidazole induces a type II shift of the CYP116B1 Soret band from 418 to 423 nm, suggesting that this compound is an inhibitor of CYP116B1. Spectra were recorded between 250 and 800 nm for the ligand-free enzyme, and following each subsequent addition of C_{12} imidazole from a 500 µM stock solution prepared in DMSO. **b)** The binding titration curve for the interaction of C_{12} imidazole with CYP116B. The change in absorbance was established as the difference between the recorded spectra at two distinct wavelengths (435 and 414 nm) where the overall change was maximal, and is plotted against ligand concentration. The inset difference spectra identify that this compound induces an inhibitory type II Soret band shift as absorbance decreases at shorter wavelengths (414 nm) and increases at longer wavelengths (435 nm) as the ligand concentration is progressively increased. This indicates that C_{12} imidazole is able to occupy the CYP116B1 active site, displacing the bound water molecule and ligating, via an azole nitrogen atom, to the heme iron. The data are fitted to the tight-binding function (Equation 3, Chapter 3.8) and determine a K_d value of 0.52 ± 0.11 µM that indicates this ligand to have a high affinity for the *R. metallidurans* P450.

b)
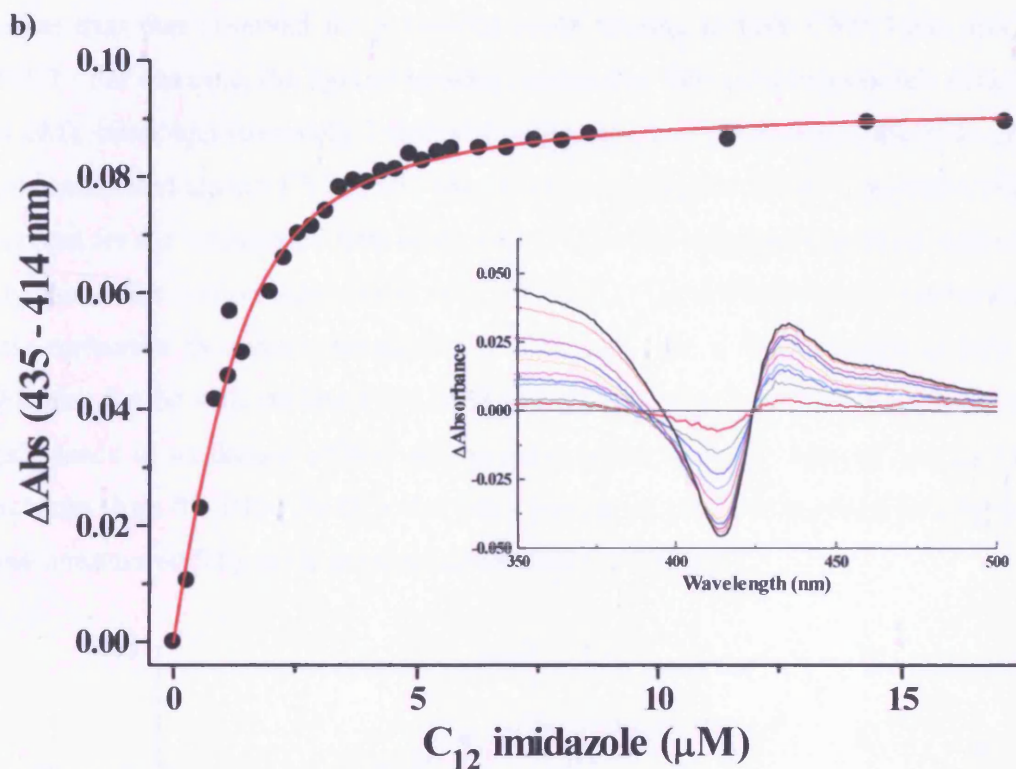
Binding studies with CYP116B1 also determined several compounds that induce a Type I substrate-like Soret shift when titrated with the P450. These compounds, including myristoleic acid and palmitoleic acid, are all unsaturated fatty acids ranging in chain length between C_{14} and C_{20} (see Figure 72 for structures). The shift they induce is not as prominent as is seen with substrate-induced spin-state shifts seen in certain other fatty acid-binding P450s (28), and it is estimated that perhaps only a maximum of 20 % of the P450 in solution is shifted to the high spin form before protein aggregation and development of turbidity occurs. This might be taken to reflect that the affinity for these fatty acids is insufficiently tight to allow their saturation of CYP116B1 within their solubility range in aqueous buffer. However, evidence against this comes from the fact that they produce saturation curves in optical binding assays, thus suggesting that they perturb heme iron spin-state only partially at saturation. Despite some turbidity problems, binding constants for arachidonic, palmitoleic, and myristoleic acid could be determined from the spectral data obtained (Table 17), and in Figure 74 the titration curve for myristoleic acid binding to CYP116B1 is displayed. There is considerable variation between the dissociation constants of these three compounds; the weakest K_d is seen with palmitoleic acid (K_d = 33.45 µM) whilst tightest binding is achieved with myristoleic acid (K_d = 4.8 µM). The dissociation constants determined demonstrate that these compounds bind quite tightly in the active site, although binding is significantly

221

weaker than that observed for polycyclic azole binding to both CYP116B1 and Mtb CYP51. For example, the tightest binding unsaturated fatty acid (myristoleic acid, K_d = 4.8 μM), binds approximately 240-fold less tightly than clotrimazole, the most potent azole compound against CYP116B1 (K_d of 0.02 μM, Chapter 4.12). The type I binding observed for the unsaturated fatty acids with CYP116B1 suggests that these compounds may mimic the natural substrate(s) of CYP116B1. The affinity range determined for these molecules by spectral titrations (~5 – 35 μM) is in a similar range as fatty acid substrates for the well-studied P450 BM3 system (28). The hydroxylation of substrates likely leads to weakened affinity of the more polar products, helping to effect their discharge from the P450 BM3 active site. Further studies are required to establish if these unsaturated fatty acids are true substrates for CYP116B1.
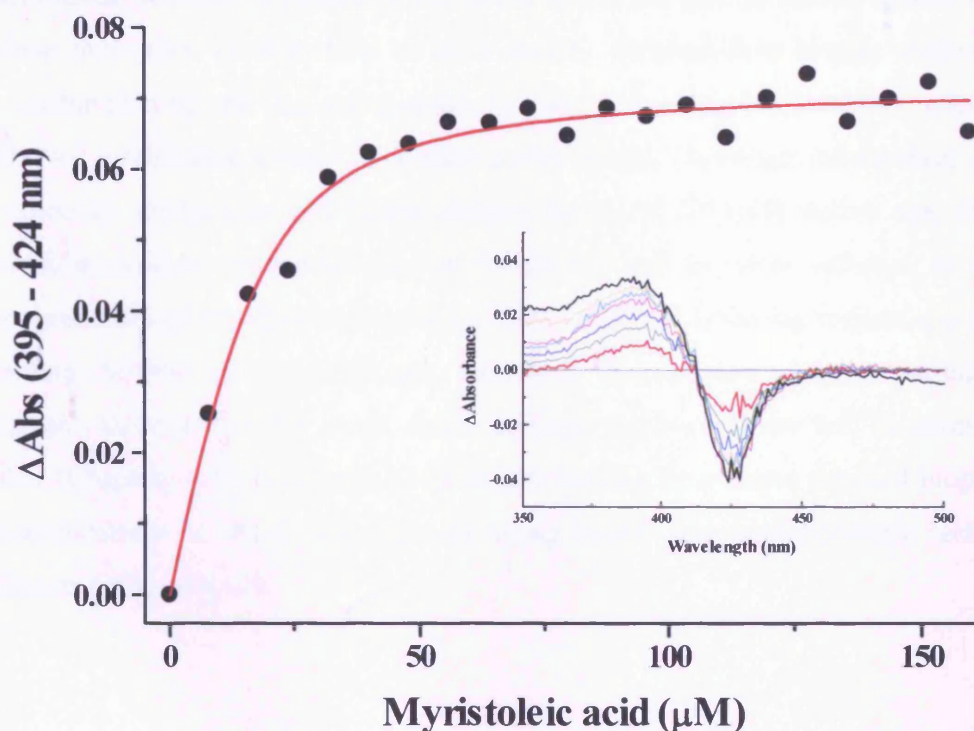

Figure 74 The binding titration curve for the interaction of myristoleic acid with CYP116B1. The binding plot was determined from the inset difference spectra, and was created by plotting the difference between the points of maximal absorbance change, i.e. the peak at 395 nm and trough at 424 nm, *versus* the relevant ligand concentration. The difference spectra exhibit a typical type I Soret band shift, where absorption increases at shorter wavelengths, and decreases at longer wavelengths as the ligand is added. These spectra suggest that myristoleic acid mimics the true substrate(s) of CYP116B1 and binds close to the heme iron to effect removal of the distal water molecule. A K_d of 4.8 ± 1.8 μM for the binding of myristoleic acid was calculated from the binding plot when fitted with Equation 3 (Chapter 3.8). The enzyme was diluted to approximately 6 μM in 50 mM Tris.HCl, 1 mM EDTA pH 7.2, and UV-Visible absorption spectra recorded between 250 and 800 nm.

These data are very interesting as they give some insight into the possible natural substrate for this P450. Although the natural CYP116B1 substrate is unlikely to be one of the unsaturated fatty acid compounds tested, it is possible that such a substrate could be a derivative or closely related chemical, or a more complex molecule containing an unsaturated fatty acid side chain. These data also serve to further distinguish the binding site of CYP116B1 from that of Mtb CYP51, as molecules with long alkyl chains did not induce substrate-like optical changes in the *M. tuberculosis* enzyme. Hence, the active sites of the two monooxygenases are probably quite different in hydrophobicity and capacity. Furthermore, the ability of unsaturated fatty acids to elicit type I Soret band shifts in CYP116B1 could provide the basis for more detailed studies of the interactions of these molecules with the P450. For instance, turnover studies should reveal whether oxygenation can occur across the carbon-carbon double bond(s) in these molecules, or elsewhere on their chains. Stopped-flow kinetic studies could also enable binding rate (k_{on}, and possibly k_{off}) data to be collected for these molecules.

Having established, using UV-Visible spectroscopy, important information relating to molecular recognition and ligand affinity for the CYP116B1 active site, the next sections investigate other properties of the protein and its heme cofactor, as well as those properties of the other redox centres of this enzyme. Utilising various approaches, including fluorescence spectroscopy, resonance Raman, and electron paramagnetic resonance, the nature of the heme, flavin and iron-sulphur clusters will be investigated further (Chapters 4.15, 4.16, and 4.17), before moving on to more detailed biophysical characterizations of the monooxygenase using kinetic and potentiometric techniques (Chapters 4.18 and 4.22).

4.14 Circular dichroism of CYP116B1

Circular dichroism was introduced in Chapter 3.14 as a useful method for the study of the protein structure and heme environment of *M. tuberculosis* CYP51, as well its interactions with the Mtb ferredoxin. This spectroscopic technique has been employed in numerous cytochrome P450 characterizations, including those of the "benchmark" monooxygenases P450cam and P450 BM3 (225-227), and serves as a useful point of comparison across this class of enzyme. In these studies, it was possible to determine the nature of the secondary structure of the proteins, confirming their predominantly α-helical content, as well as identifying features in the near UV-Visible spectra which correlate to maxima of the absorption spectra, such as the Soret band. The method records the interaction of chiral elements of protein structure, such as the peptide linkages in α-helices and β-sheets, with left- and right-handed circularly polarised light. The CD data are presented as a difference spectrum reflecting the differential absorption of left and right handed circularly polarised light at different wavelengths. This provides important information concerning the relevant protein's secondary structure (from data in the far-UV region, typically 190 – 260 nm) and the heme environment in the near-UV/Visible region (~300 – 600 nm). Furthermore, as was demonstrated in the circular dichroism studies of Mtb CYP51 and P450 BM3 (159,225), this technique can be used quantitatively to estimate the percentages of the α-helices and β-sheets that constitute the structure of the protein.

In this study, circular dichroism of CYP116B1 was performed to determine that the secondary structure of the protein was consistent with the predicted high α-helix content typically associated with cytochromes P450 (225,251). It was also expected that the far-UV CD spectrum of this protein should confirm a significant complement of β-sheet, as the homologous reductase protein from *Ps. cepacia* is predominantly β-sheet in secondary structure (6). To this end, the far-UV (190 to 260 nm) and near-UV/Visible (260 to 600 nm) CD spectra were recorded as for CYP51. For the far-UV region, CYP116B1 protein was diluted to a concentration of 2 μM and placed in a quartz cell of pathlength 0.2 cm. For the recording of the near-UV/Visible spectrum, a cell of pathlength 0.5 cm was utilised, whilst the protein concentration was 20 μM. Both sets of spectra were recorded in 50 mM KPi pH 7.4, utilising a Jasco J-715 CD spectrophotometer maintained at 25 °C by a Jasco PTC348W1 Peltier system, and using scan rates of 10 and 20 nm/minute for the far-UV and near-UV/Visible spectra,

respectively. The resultant spectra, as displayed in Figure 75, are the average of 5 accumulations of the data, as this led to improved quality of the final output.
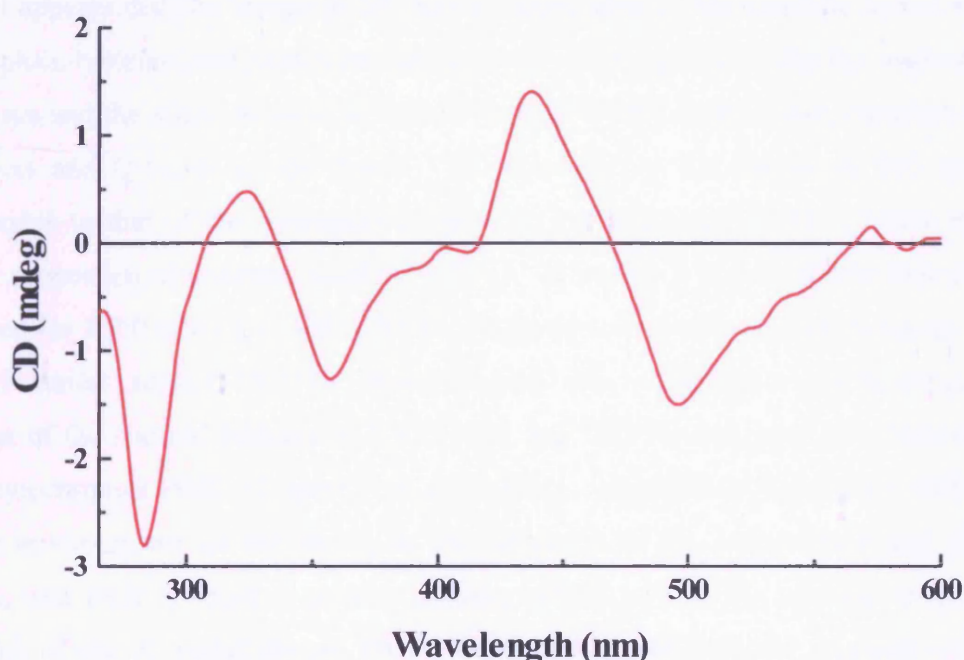

Figure 75 The near-UV/visible circular dichroism spectrum collected for CYP116B1. Spectral maxima occur at 324, 437, and 572 nm, whilst minima are observed at 283 nm, 357 nm, and 496 nm. The region which corresponds to heme optical transitions (~400 – 600 nm) demonstrates a positive CD signal in the Soret region. This is relatively unusual, and a positive Soret CD has been observed previously only in the case of CYP121 from *M. tuberculosis* (158). P450cam, P450 BM3 and other P450s studied in this wavelength range have negative Soret CD signals (159,225,226). The negative CD feature centred at 283 nm corresponds primarily to the optical contributions of aromatic amino acids in the protein (223). The relative intensity of this feature is similar to that of Mtb CYP121 and P450 BM3 (159,225). The spectrum was recorded at 25 °C using a Jasco J-715 instrument, and is the average of five accumulations of the data recorded at 20 nm/minute. CYP116B1 was diluted to 20 μM in 50 mM potassium phosphate buffer (pH 7.4).

The near-UV/Visible CD data collected for CYP116B1 show, as may be expected due to their structural differences, significant dissimilarities to those for Mtb CYP51, as well as those for P450 BM3 from *B. megaterium* and P450cam from *Ps. Putida* (159,225,226). The major difference appears to be that the CD spectrum of CYP116B1 in the Soret region has positive ellipticity, whereas there is a negative Soret CD signal for Mtb CYP51. Also, certain other features which appear as troughs in the CYP51 spectrum are represented by peaks in the CYP116B1 spectrum, and *vice versa*. The major peaks of the CYP116B1 spectrum are found at 324, 437, and 572 nm, with troughs at 283, 357, and 496 nm. This contrasts with peaks at 287, 397, and 448 nm,

225

and troughs at 345 and 427 nm for Mtb CYP51. Assignments for the features of P450 circular dichroism spectra are reported by Kelly *et al.* (223,224), and based upon this work it appears that the trough at 283 nm is largely due to the aromatic amino acids (tryptophan, tyrosine, and phenylalanine) in chiral environments, whilst the major peak at 438 nm and the minor features between 530 and 575 nm, respectively, correlate with the Soret and Q-bands of the heme. The intensity of the feature at 283 nm is comparable to that of the corresponding peak in the spectra of CYP121 which has a similar proportion of aromatic residues (~5 %). However, it is less intense than those observed for P450 BM3 and Mtb CYP51, which are composed of approximately 9 % aromatic amino acids (158,224). It is not clear why differences exist between the position of the spectral features of CYP116B1 and CYP51 and those of a number of other cytochromes P450 (Chapter 3.14, (194,225)). Possibilities include the differing protein environments of the heme, or the influence of the iron-sulphur and flavin centres, and their associated protein domain, which perturb the circular dichroism spectrum of the *R. metallidurans* P450. Additionally, although the inversion of the Soret CD band is relatively unusual for cytochromes P450, it has been previously reported for CYP121 from *M. tuberculosis*. However, this phenomenon is remains largely unexplained as the electronic transitions underlying the spectral features observed in this region of circular dichroism spectra are generally difficult to assign (223,224). Thus, although studies of this region can be utilised for basic comparisons of cytochromes P450, they serve mainly as a fingerprint of the protein and are of limited use in interpreting differences in heme conformation or aromatic amino acid environment (224).

Circular dichroism in the far-UV region is most frequently utilised to report upon the secondary structure of the protein (224). In the case of CYP116B1, the spectrum identifies this protein to be primarily composed of α-helices. The overall shape of the CYP116B1 spectrum (Figure 76) demonstrates a broad feature with negative CD between 200 and 230 nm. This profile is typical of a predominantly α-helical protein (224), confirms that CYP116B1 is correctly folded, and is a similar CD spectrum to those of Mtb CYP51, P450cam, P450 BM3, and *B. subtilis* P450 BioI in this region (Chapter 3.14, (159,194,225,226)). However, the spectrum exhibits a noticeable difference to these P450s in the region between 210 and 220 nm. In the spectrum of CYP51, for example, the trough between 200 and 230 nm is interrupted by a minor peak centred at approximately 212 nm. The CYP116B1 spectrum however, exhibits no such

226

peak. It is known that the typical β-sheet spectrum shows a trough in this region (224), and it is thus speculated that the flattened region between 210 and 220 nm in the CYP116B1 CD spectrum is due to the contribution of the β-sheets of the reductase domain of the protein. The crystal structure of a homologous protein to this domain, phthalate dioxygenase reductase from *Ps. cepacia*, identifies that this oxidoreductase is predominantly composed of β-sheet (6). Thus, with an amino acid identity of 31 % between this protein and the reductase domain of CYP116B1, it is likely that the *R. metallidurans* reductase domain has similar secondary structure. It is concluded that variation in the form of the CYP116B1 far-UV CD spectrum (when compared to those of the other well characterized cytochromes P450) results from the beta sheet-rich reductase domain (159,225,226).
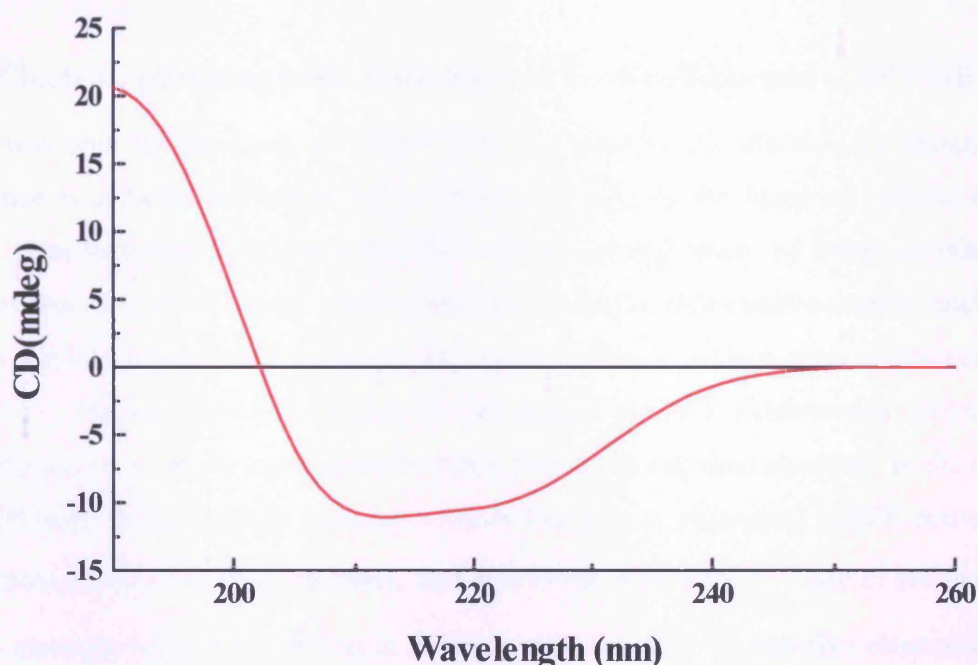

Figure 76 The CYP116B1 circular dichroism spectrum recorded in the far-UV/visible region. The spectrum exhibits a shape indicative of a secondary protein structure composed mainly of α-helices. However, a distinctive feature between 210 and 220 nm, typically observed for many cytochromes P450 (159,225,226), is barely discernible for CYP116B1. An explanation for this is the greater beta sheet content in CYP116B1. Beta sheet structures exhibit a trough in this region, and the reductase domain likely distorts this spectral region with respect to other P450s (224). Aside from this difference, the strong CD spectrum is typical of a well-folded protein, indicating that the *R. metallidurans* protein adopts its correct conformation when expressed in *E. coli* (159,225,226). Data were recorded using a Jasco J-715 instrument maintained at 25 °C and by scanning at 10 nm/minute. Enzyme was at 20 μM, diluted in 50 mM potassium phosphate buffer (pH 7.4), and the spectrum shown is an average of five data accumulations.

In summary, these far-UV and near-UV/Visible circular dichroism studies reveal that the secondary structure of CYP116B1 is composed not only of α-helices (which dominate the structures of known cytochromes P450) (159,225,226,251), but also a large quantity of β-sheets that likely correspond mainly to the reductase domain of the protein. The reductase is homologous to the predominantly β-sheet protein phthalate dioxygenase reductase (6). In addition to confirming that the CYP116B1 protein is correctly folded, the data also identify a positive CD signal in the Soret region – which has been observed previously in P450s only for Mtb CYP121 (158), although the reasons for this phenomenon are uncertain. In the next sections, electron paramagnetic resonance and resonance Raman studies are utilised to further investigate properties of the redox centres of CYP116B1.

4.15 Electron paramagnetic resonance of *R. metallidurans* CYP116B1

As was seen for the study of Mtb CYP51 in Chapter 3.12, electron paramagnetic resonance is a useful technique for the characterization of the heme of cytochromes P450. The technique has not only been utilised for the study of heme-containing proteins, but also numerous enzymes containing a range of redox active centres, such as flavins and iron-sulphur complexes, as well as for studies of various other biomolecules (214,215). The common feature of heme and these other EPR active redox centres is their population of one or more states in which there is an unpaired electron. In the case of P450 heme iron, the ferric enzyme (whether low-spin or high-spin) is EPR active as both states possess unpaired electrons. In the low-spin form (S = $\frac{1}{2}$) one of the five d-orbital electrons is unpaired, whilst in the high-spin state (S = $\frac{5}{2}$) all five electrons are unpaired. Conversely, P450 ferrous heme iron is EPR silent as it possesses no unpaired electrons. As described in Chapter 3.12, EPR spectroscopy detects the unpaired heme iron electrons by recording the microwave absorbance of a sample under the influence of a constantly changing magnetic field. At a particular magnetic field strength the unpaired electrons resonate due to the perturbation of their electronic spin by the applied field, and subsequently absorb microwave energy. From the shape, amplitude, and position of the resultant microwave absorbance spectrum a number of qualities of the studied redox centre can be ascertained. For heme iron, these include important information regarding the oxidation, ligation, and spin-states of the heme iron (214,215).

As EPR is such a powerful tool for the study of redox active centres, including hemes and iron-sulphur clusters, CYP116B1 was subjected to EPR investigation in the oxidised and (sodium dithionite) reduced states. As with studies of Mtb CYP51, P450 BM3 from *B. megaterium*, and P450 BioI from *B. subtilis* (Chapter 3.12, (37,159,213)), the oxidised CYP116B1 EPR spectra was expected to report on the ligation state, spin-state, and oxidation state of the ferric heme iron, and to identify any disparity between these well-characterized monooxygenases and the *R. metallidurans* protein. Furthermore, CYP116B1 is postulated to incorporate a 2Fe-2S cluster (Chapter 4.2), which, as reported earlier in this chapter (Chapter 4.8), is masked by the spectrum of the flavin and heme centres and is not resolved by UV/Visible absorption spectroscopy. However, EPR has been used to good effect in diagnosing the presence of iron-sulphur clusters, e.g. the 3Fe-4S cluster found in the ferredoxin of *M. tuberculosis* (159), and was thus proposed as a technique that could confirm the presence of such a redox centre in CYP116B1.

In the oxidised state, the 2Fe-2S cluster proposed to be present in CYP116B1 possesses two ferric iron moieties and a formal charge of $[2Fe-2S]^{2+}$. In this state the magnetic moments of the unpaired electron of each iron atom are spin-coupled, cancelling each other out (S = 0), and thus no EPR spectrum is observed. When reduced, the formal charge is $[2Fe-2S]^+$ as the cluster contains one ferric iron (Fe^{3+}) and one ferrous (Fe^{2+}) iron. In this state spin-coupling does not occur and the sample generates an EPR signal as S = $\frac{1}{2}$ (252,253). Additionally, unless the incorporated flavin is in a one electron-reduced state (i.e. semiquinone), it will also be EPR silent (214). Thus, in the oxidised state the only signal obtained from a sample of CYP116B1 should be from the ferric heme iron. Conversely, a reduced sample of the enzyme (where the heme and (probably) flavin signals are EPR silent due to a lack of unpaired electrons) should reveal the presence of the EPR active reduced iron-sulphur complex, thus enabling a fuller characterization of CYP116B1.

EPR spectra of oxidised and reduced CYP116B1 were recorded at University of East Anglia by Dr M. Cheesman, using a sample of the enzyme diluted to approximately 250 μM in 50 mM potassium phosphate buffer (pH 7.5). Spectra were recorded at 10 K, with 2 mW microwave power and a modulation amplitude of 10 G, using a Bruker ER-300D series electromagnet and microwave source, interfaced to a Bruker EMX control unit, and fitted with a dual mode microwave cavity from Bruker (ER-4116DM). The

229

temperature was maintained at 10 K by an ESR-9 liquid Helium flow cryostat (Oxford Instruments). Following collection of EPR data for the oxidised enzyme, the sample was carefully thawed and, in order to obtain the reduced spectrum, the minimal required quantity of solid sodium dithionite was added. Conversion of the heme iron to the ferrous state was confirmed by a Soret band shift to shorter wavelength (~417 nm), observed in UV/Visible spectroscopy of CYP116B1. The EPR spectrum of this sample was then recorded using the same parameters as for the oxidised sample. The results were analysed, and from derivations of the microwave absorption data the EPR spectra in Figure 77 and Figure 78 were obtained.

The EPR spectrum of oxidised CYP116B1 shown in Figure 77 serves as further confirmation that the *R. metallidurans* enzyme is a typical cytochrome P450. The rhombic shape of the spectrum and g-values of g_x = 2.42, g_y = 2.25, and g_z = 1.93 lie in the appropriate ranges determined for cytochromes P450 (37,159,194,247) and attest to the presence of a hexa-coordinate, cysteinate-ligated heme. The g-values and spectrum profile are similar to those reported for Mtb CYP51 (Chapter 3.12) and a number of well-characterized cytochromes P450, including P450 BM3 from *B. megaterium* and P450 BioI from *B. subtilis*, whose EPR spectra yield g-values of g_x = 2.42, g_y = 2.26, g_z = 1.92, and g_x = 2.41, g_y = 2.25, and g_z = 1.92 (37,194). This agreement gives greater security of assignment of CYP116B1 as a cytochrome P450. The data also demonstrate that there is no detectable high-spin component in the spectrum, thus confirming that CYP116B1 is purified in the resting, low-spin state. However, it should be noted that the spectrum is recorded at 10 K, and that the spin-state equilibrium is temperature sensitive in P450s. Thus, any minor high-spin species at room temperature may be "frozen out" at much lower temperature. Thus, both UV-visible absorption and EPR data are consistent with CYP116B1 being a *bona fide* P450, with EPR data consistent with cysteinate and water axial ligands to the heme iron.
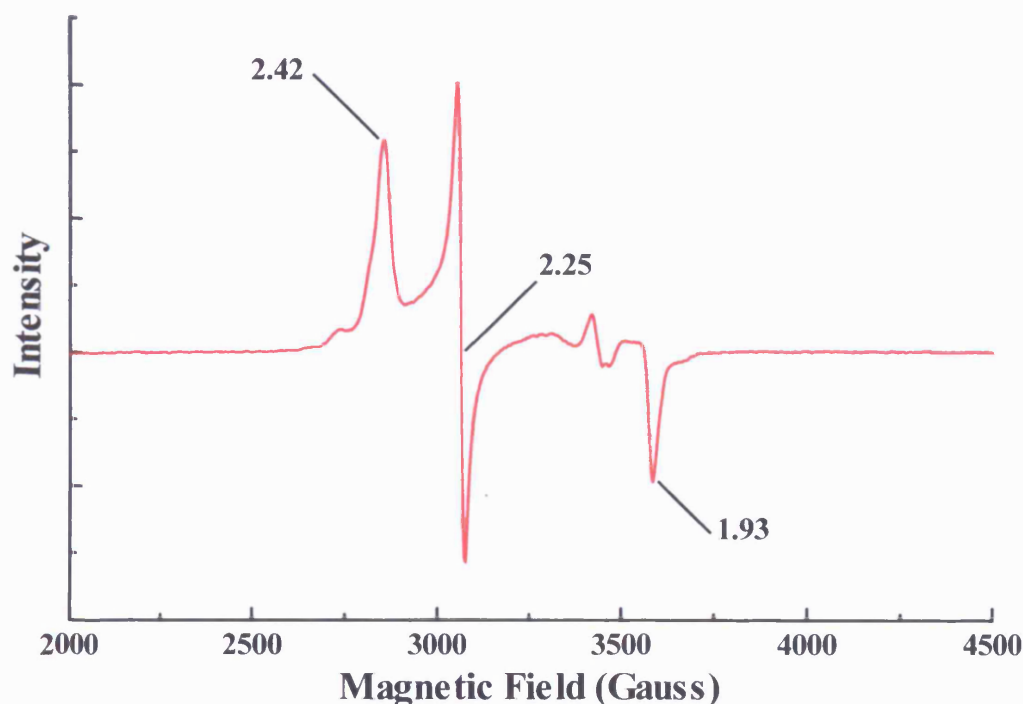
Figure 77 The electron paramagnetic resonance spectrum of oxidised *R. metallidurans* CYP116B1. The rhombic shape of the spectrum is comparable with those reported for Mtb CYP51, P450cam, P450 BM3, and P450 BioI (37,159,194,213), suggesting this enzyme to be typical of the cytochromes P450, whilst the g-values obtained from the spectrum (g_x = 2.42, g_y = 2.25, and g_z = 1.93) confirm CYP116B1 to possess a cysteine-ligated, hexa-coordinated, low-spin ferric iron molecule. The spectrum shows no evidence of contributions from the flavin and iron-sulphur centres of the protein. Data were recorded and analysed by Dr. Myles Cheesman (University of East Anglia) at 10 K with 2 mW microwave power and a modulation amplitude of 1 mT. CYP116B1 was present at 250 μM in 50 mM potassium phosphate buffer (pH 7.4).

The EPR spectrum obtained for dithionite-reduced *R. metallidurans* CYP116B1 (Figure 78) shows very little indication of the heme signal identified in Figure 77, suggesting that essentially complete reduction of the enzyme was achieved. The spectrum is more compact than that of the oxidised enzyme (Figure 77), with the major features appearing between 3250 and 3750 gauss. The reduced CYP116B1 spectrum demonstrates a rhombic shape and has g-values of g_x = 2.06, g_y = 1.97, and g_z = 1.88 that fall within the typical ranges reported by More *et al.* (214), and thus clearly identify the presence of a 2Fe-2S cluster. Furthermore, the reported EPR spectrum of the reduced reductase domain of RhF from *Rhodococcus* sp. NCIMB 9784 is very similar to that of reduced CYP116B1 and produces identical g-values of g_x = 2.06, g_y = 1.97, g_z =1.88 (130). The g-values of both RhF and CYP116B1 are in close agreement with

231

those published for phthalate dioxygenase reductase from *Ps. cepacia* (g_x = 2.04, g_y = 1.95, g_z =1.90, (145)), further confirming these proteins to possess typical 2Fe-2S clusters.
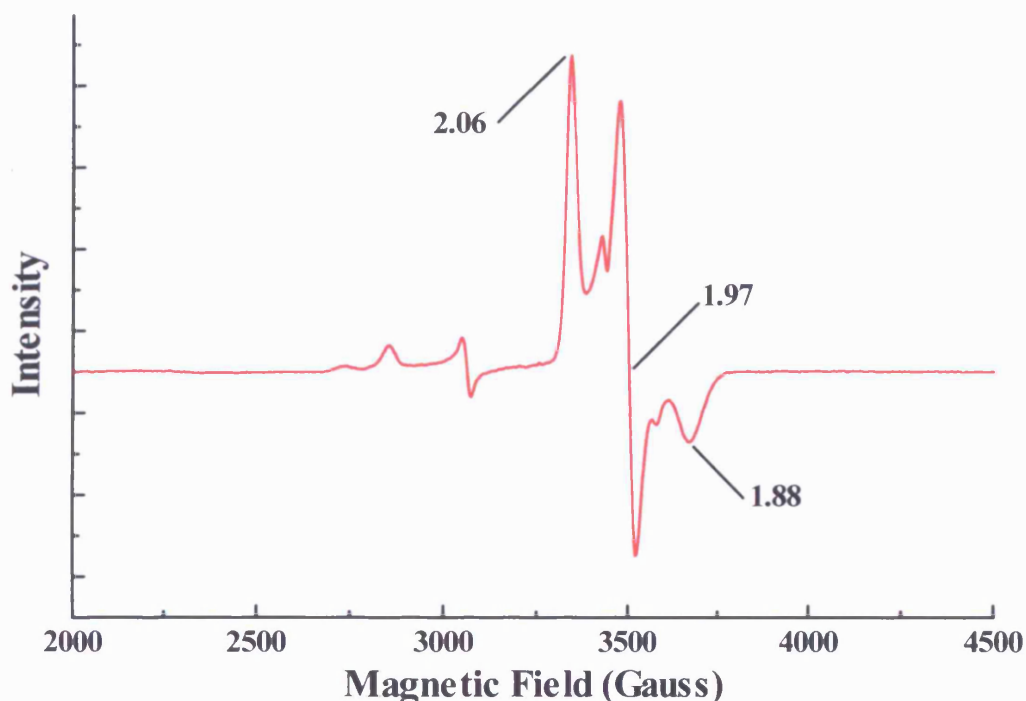

Figure 78 The EPR spectrum of sodium dithionite-reduced CYP116B1, recorded at The University of East Anglia by Dr M Cheesman. The rhombic shape of the spectrum and g-values of g_x = 2.06, g_y = 1.97, and g_z = 1.88, suggest the presence of a typical 2Fe-2S cluster (145,214), and confirm incorporation of the iron-sulphur cluster into CYP116B1 protein structure. In reduced CYP116B1 the heme no longer possesses an unpaired electron and thus loses the signal displayed in Figure 77. In contrast, reduction of the enzyme donates an electron to the previously EPR-silent iron-sulphur cluster, manifesting as a signal of a typical reduced 2Fe-2S cluster. This spectrum was recorded with 250 μM of sodium dithionite reduced-CYP116B1 in 50 mM potassium phosphate (pH 7.4) using the same instruments as reported for the oxidised enzyme (Figure 77).

These data are very encouraging as they imply correct folding of the CYP116B1 protein, which allows incorporation of the cluster, and infers that CYP116B1 is indeed a fusion of a P450 with a 2Fe-2S-containing phthalate dioxygenase reductase-like module. Indeed, the reductase itself is likely a fusion of ancestral genes encoding distinct 2Fe-2S and FMN cofactors. The data are also useful as they increase confidence that the kinetic studies and other data collected for CYP116B1 are a study of the intact system and not an enzyme depleted in some, or all, of its 2Fe-2S cluster

232

complement, as may be the case for the studies of RhF, in which uncertainties of the levels of iron-sulphur cluster incorporation are reported, and in which cofactor content is artificially enhanced by reloading with ferrous iron and inorganic sulphide (185). Comparison of the intensity of the CYP116B1 spectrum with those from other proteins is difficult as the intensity of EPR signals are rarely reported. However, the CYP116B1 signal strength suggests that it possesses a high complement of 2Fe-2S, and thus suggests that the purified *R. metallidurans* protein is replete with the iron sulphur cluster. Additionally, the absence of any radical signal that would correspond to a flavin (FMN) semiquinone is also consistent with expected behaviour of phthalate dioxygenase-like proteins, and indicates that bound flavin is converted between quinone and hydroquinone forms on reduction with dithionite. However, it should be noted that flavin content (at this stage) has not been rigorously characterized for CYP116B1.

In the ensuing sections, further information concerning the heme and other cofactor content of the enzyme are gathered using fluorescence and resonance Raman spectroscopy. Having obtained these data, detailed studies of kinetic and biophysical properties of CYP116B1, utilising potentiometry and both steady-state and stopped-flow kinetic techniques are reported, in order to further characterize the thermodynamic and kinetic features of this multidomain P450 monooxygenase.

4.16 Resonance Raman spectroscopy of *R. metallidurans* CYP116B1

Resonance Raman is a technique which has been frequently utilised in the characterization of cytochromes P450, including P450 BioI from *B. subtilis* and P450 BM3 from *B. megaterium* (194,205,206). It reports on various facets of the incorporated heme macrocycle. As well as providing information on bond vibrations, stretches, and the planarity of the porphyrin ring, the method is a useful means for determining the spin and oxidation states of the central heme iron (207,208). Hence, the remit of resonance Raman overlaps with that of electron paramagnetic resonance and UV/Visible spectroscopy in the study of cytochromes P450, consolidating findings from these methods and also giving further insight into the heme in its protein environment at ambient temperatures.

As reported in Chapter 3.11, resonance Raman details the aforementioned heme features by the detection of photons emitted from a protein sample, following excitation using a laser source finely tuned to the resonant frequency of the chromophore. The

233

consequence of sample excitation is scattered photons, which are detected by a spectrophotometer, and result in a spectrum consisting of numerous, often-overlapping peaks. Interpretation of the positions and intensities of these peaks, based on the work of Hildebrandt *et al.* (209,210), leads to the assignment of a particular structural or electronic feature, denoted by a v value. For example, in the study of *B. megaterium* P450 BM3 by Smith *et al.* (205), the substrate-free enzyme exhibits a split v_3 peak at 1484 and 1500 cm^{-1} that signifies the protein is in a mixed spin form, whilst the v_{11} peak at 1566 cm^{-1} denotes that the heme macrocycle is domed rather than planar. Unfortunately, under the conditions used for the study of CYP116B1, this technique is of little use in determining features of the flavin due to the highly fluorescent nature of this cofactor (254). Furthermore, whilst previous studies have shown that resonance Raman of iron-sulphur clusters can inform upon Fe-S stretching vibrations (255), they are less informative than resonance Raman of heme centres, and require less practical conditions. For example, the recording of spectra of 2Fe-2S cluster-containing proteins, such as reported for the bovine adrenodoxin (256), is impractical as it requires enzyme concentrations of 1 mM (compared to 50 μM protein in this study), and must be performed at very low temperatures (−196 °C or below).

In the previous chapter (Chapter 3.11) resonance Raman spectroscopy of oxidised Mtb CYP51 demonstrated that this monooxygenase contains a non-planar, low-spin, six-coordinate, ferric heme, with asymmetrical vinyl groups. In this study it is hoped to ascertain similar information concerning the electronic and structural nature of the CYP116B1 heme, which can be utilised to both contrast with previously characterized cytochromes P450, and to corroborate complementary data gathered by EPR and UV/Visible spectroscopy.

In order to generate a resonance Raman spectrum for *R. metallidurans* CYP116B1, an aliquot of the enzyme was diluted in 50 mM Tris.HCl, 1 mM EDTA (pH 7.2) to a final concentration of 50 μM. The sample was positioned in the path of a 15 mW Coherent Innova 300 krypton ion laser and subjected to five 15 second bursts of excitation at 406.7 nm, during which time CYP116B1 emission data were collected between 250 and 2000 cm^{-1} by a Renishaw micro-Raman system 1000 spectrophotometer (Renishaw). As in the study of Mtb CYP51, the laser provided excitation at 406.7 nm, a value very close to the wavelength of the CYP116B1 Soret band, and thus predominantly exciting only the heme of the protein. The collated spectral data were subjected to baseline correction and curve-fitting analysis utilising

Grams software (Galactic Industries Corp.) prior to peak assignment, according to the nomenclature of Hildebrandt *et al.* (209,210), and are presented in Figure 79, Figure 80, and Figure 81. In order that the annotation of the major peaks with appropriate v-values can be clearly discerned, the resonance Raman spectrum of *R. metallidurans* CYP116B1 was divided into high (1200 – 1700 cm^{-1}), middle (900 – 1350 cm^{-1}), and low (200 – 850 cm^{-1}) frequency sections.

The high frequency region (Figure 79) of the spectrum identifies a number of key peaks, including the oxidation state marker v_4. This band at 1372 cm^{-1} dominates the spectrum, and has an intensity that is over 4-fold greater than the next largest peak, v_2. This peak, which reports on 'breathing' vibrations of the C-N bonds of the heme, is found in an identical position to those identified for the v_4 peaks of Mtb CYP51 (Chapter 3.11), Mtb CYP121, and P450 BM3 (158,205), thus confirming that the heme iron of CYP116B1 is also purified in the ferric (Fe^{3+}) state. Another significant peak of the high frequency region is the v_3 band at 1500 cm^{-1}. For Mtb CYP51 this band, which has been identified as a spin state marker, was found as a single peak at 1502 cm^{-1}, and showed the monooxygenase to be present in the low-spin state. In the case of P450 BioI the v_3 band was split into two components, with a smaller peak at 1500 cm^{-1} and a dominant feature centred at 1487 cm^{-1} that confirms the enzyme to be purified in a predominantly high-spin state (194). In a parallel study of P450 BM3, the secondary band was present as a smaller component, demonstrating that the enzyme was in a mixed spin state with the low-spin form predominant (205). Unlike these two cytochromes P450, the high frequency spectrum of CYP116B1 shows no evidence of any significant high-spin component and, akin to Mtb CYP51, this enzyme is demonstrated to be purified in an almost completely low-spin state.
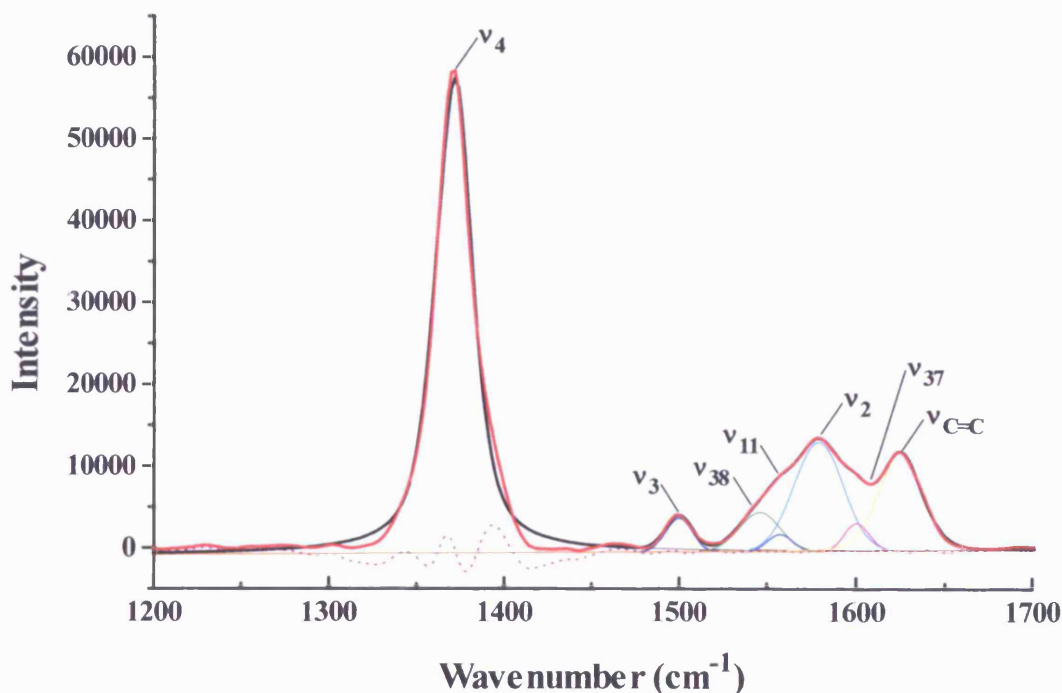
Figure 79 The curve fitting and peak assignment for the high frequency region of the *R. metallidurans* CYP116B1 resonance Raman spectrum. Samples were excited at 406.7 nm, close to the resonant frequency of the heme macrocycle, using a krypton laser. The subsequent emission data were collected using a Renishaw micro-Raman system 1000 spectrophotometer and analysed using Grams software (Galactic Industries Corp.) to produce the above spectrum. The most notable peaks in this region are the v_4 peak at 1372 cm^{-1} and the v_3 peak at 1500 cm^{-1}, which together confirm that the CYP116B1 heme iron is in the ferric, low-spin state. A peak at 1578 cm^{-1} (v_2) further confirms this, whilst the presence of other bands (v_{37} and v_{11}) at 1600 and 1556 cm^{-1} suggest that CYP116B1 contains a *b*-type heme that is domed rather than planar. Enzyme was used at a final concentration of 50 µM, and peak assignments are based on the work of Hildebrandt *et al.* (209,210).

Further confirmation that the *R. metallidurans* protein is found in the low-spin state comes from the presence of a v_2 peak at 1578 cm^{-1}. This band, which is spin state sensitive and corresponds to tetrapyrrole stretches in the heme (211), has been identified for numerous cytochromes P450, including Mtb CYP51 and P450 BM3 (Chapter 3.11, (159,205,212)), and hence as CYP116B1 also demonstrates this band at a similar wavenumber it is confirmed as a predominantly low-spin heme. This region of the resonance Raman spectrum also identifies v_{11} and v_{37} peaks at 1556 cm^{-1} and 1600 cm^{-1}, which report on significant features of the porphyrin ring contained within this enzyme, and are found in similar positions in the spectra of Mtb CYP51 and P450 BM3 (Chapter 3.11, (159,205,212)). Whilst the $v_{c=c}$ band relates to stretches in the vinyl groups of the

heme, the v_{11} band pertains to C_β-C_β stretches within the heme macrocycle and confirms, as with previously characterized proteins, that CYP116B1 contains the b-type heme typical of cytochromes P450. Furthermore, the presence of this band, and that of the v_{37} feature, identify that the heme is domed, rather than planar, and that the protruding vinyl groups are asymmetrical, as was reported for P450 BM3 and Mtb CYP51 (159,205,212).
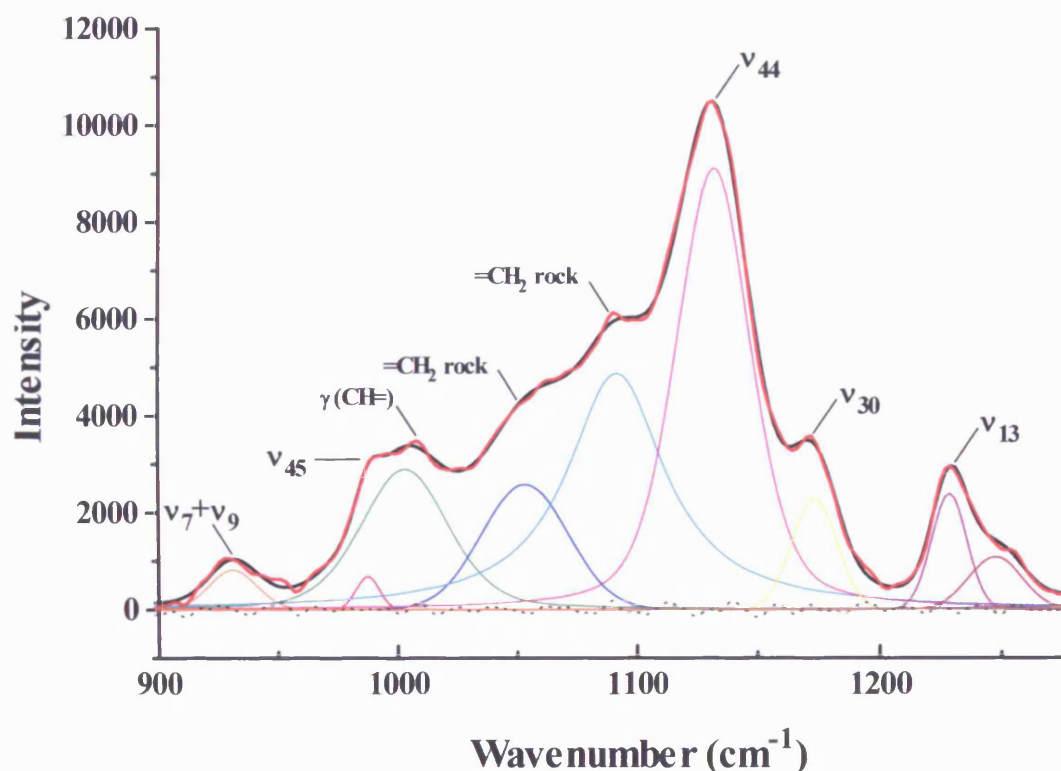

Figure 80 The middle frequency region of the CYP116B1 resonance Raman spectrum, showing peak assignments based on work by Hildebrandt *et al.* (209,210). The predominant feature of this region of the spectrum at 1130 cm^{-1} was identified as v_{44}, and pertains to vibrational modes of the non-planar heme, supporting findings from analysis of the high frequency region (Figure 79). The presence of =CH$_2$ peaks at 1092 and 1051 cm^{-1}, and the γ(CH=) peak at 1007cm^{-1}, denote asymmetry and deformation of the vinyl groups that protrude from the porphyrin ring.

The non-planar nature of the heme is further confirmed in the middle frequency range of the CYP116B1 resonance Raman spectrum (Figure 80) as the ν_{44} peak at 1130 cm^{-1}, which is similarly positioned in the spectrum of Mtb CYP51 (Chapter 3.11, (159)), relates to vibrational modes of a non-planar heme. In spectra of P450 BM3, bands at 1092 and 1051 cm^{-1} relating to vibrations and asymmetry of the vinyl groups attached to the porphyrin ring have been identified (205,212). In the CYP116B1 spectrum these $=CH_2$ rock peaks are also found at 1092 and 1051 cm^{-1}, confirming that the vinyl groups of this enzyme do not lie in the plane of the heme. Further deformation of the vinyl groups is confirmed by the presence of the $\gamma(CH=)$ band at 1007 cm^{-1}. However, as little is understood about the peaks in the region between 1100 and 1250 cm^{-1}, the significance of features in this region is unclear.
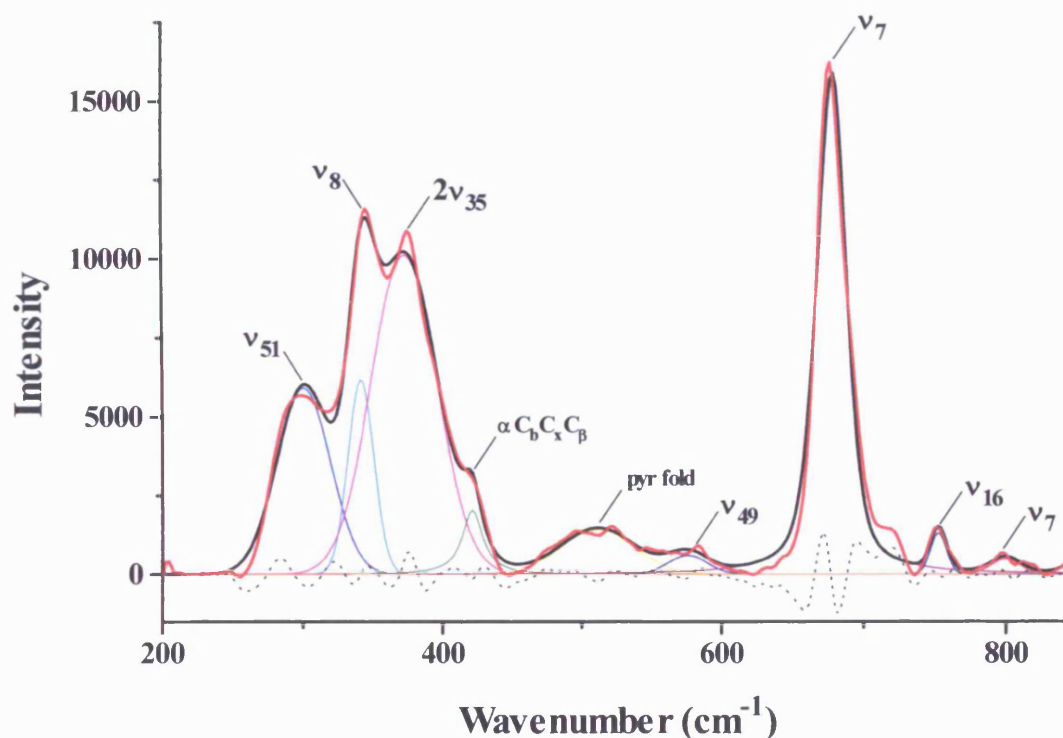

Figure 81 The curve fitting and peak assignment of the low frequency region of the CYP116B1 resonance Raman spectrum. The significant peaks of this region are the ν_7, ν_8, and $2\nu_{35}$ peaks at 677, 241, and 372 cm^{-1} respectively, as well as the $\alpha CbCxC\beta$ band at 422 cm^{-1} and a pyrrole fold peak at 500 cm^{-1}. The ν_7, ν_8, and $2\nu_{35}$ peaks report on in-plane vibrations of the heme, whilst the pyrrole fold band, as with the ν_{37} peak of the high frequency region (Figure 79), denotes a domed heme. The $\alpha CbCxC\beta$ band position is consistent with findings from analysis of the other regions of the spectrum that indicate asymmetry of the heme vinyl groups.

The low frequency resonance Raman spectrum of CYP116B1 (Figure 81) contains the v_7 peak at 677 cm^{-1}. This band, the second largest of the entire spectrum, pertains to vibrations in the plane of the heme macrocycle. These vibrations are also reported on by the v_8 band at 341 cm^{-1} and the $2v_{35}$ band at 372 cm^{-1}, as well as the v_{16} band at 752 cm^{-1}. Other significant peaks in this region of the spectrum include the $\alpha CbCxC\beta$ band at 422 cm^{-1} and a pyrrole fold feature at 500 cm^{-1}. Both of these bands have equivalents at similar wavenumbers in the spectrum of P450 BM3 (205,212), and the former has been identified as pertaining to vibrational and bending modes of the vinyl groups. The latter reports on doming or deformation of the heme macrocycle, possibly induced by heme:protein interactions, and supports the evidence of a non-planar heme indicated by the presence of the v_{37} peak in the high frequency region (Figure 79).

The three regions of the CYP116B1 resonance Raman spectrum possess many peaks that are duplicated at similar wavenumbers in the spectra of well-characterized cytochromes P450, such as P450 BioI, P450 BM3, and Mtb CYP51 (Chapter 3.11, (159,194,205,206)). Although the intensities of some of these features vary between the enzymes due to different heme environments, with such a high degree of agreement these data suggest that the *R. metallidurans* is a relatively typical member of the cytochrome P450 superfamily with respect to coordination, structural and electronic properties of the heme iron. Furthermore, specific peaks in the CYP116B1 spectrum, including the v_4, v_3, v_2, and v_{11} bands, confirm the findings of electron paramagnetic resonance and UV/Visible spectroscopy studies that identify this monooxygenase is purified containing a ferric, low-spin, *b*-type heme. Hence, these data, in association with those from the EPR, fluorescence, and UV/Visible spectroscopy studies (Chapters 4.8, 4.15, and 4.17), indicate that all three of the redox centres of CYP116B1 are present and have spectroscopic properties consistent with correctly bound and coordinated cofactors. Thus, the kinetic and biophysical studies reported in subsequent sections could be performed with confidence in the integrity of the enzyme.

4.17 Identification of the *R. metallidurans* CYP116B1 flavin cofactor

The bioinformatics analysis of the CYP116B1-encoding gene from *Ralstonia metallidurans* revealed that this protein should consist of three domains containing heme, flavin, and iron-sulphur cluster redox centres (Chapter 4.2). Verification of the presence of each of these centres has been reported in previous sections utilising an array of techniques including UV/Visible spectroscopy, EPR, and resonance Raman (Chapters 4.8, 4.15, and 4.16). The presence of heme was identified initially by absorption spectral data, and later confirmed as typical of P450 cysteinate-coordinated heme by resonance Raman and EPR of the oxidised enzyme. EPR of reduced CYP116B1 also confirmed the binding of a 2Fe-2S cluster, something that could not be determined by UV/Visible spectroscopy due to its weak spectral signal being masked by that of the heme. However, although UV/Visible spectroscopy detected the presence of a flavin cofactor, as identified by a distinctive absorption shoulder between 450 and 500 nm, neither this technique, nor any other utilised so far, could identify whether this cofactor is FMN (as postulated) or FAD. This is significant, as the presence of FMN (rather than FAD) would provide further confirmation that the reductase domain of CYP116B1 is highly related to phthalate dioxygenase reductase from *Ps. cepacia* (6,145,146), as well as distinguishing it from typical bacterial Class I P450 system where electrons are directed to the monooxygenase via FAD- and iron-sulphur-containing proteins (3).

The determination of the flavin cofactor of CYP116B1 is based on a fluorescence spectroscopy technique that utilises the fact that that the fluorescence emission of flavin adenine dinucleotide (FAD) between 500 – 600 nm, when excited at 450 nm, increases upon the addition of concentrated acid, whilst the fluorescence of flavin mononucleotide (FMN) decreases under the same conditions (188-191). Under neutral pH conditions the fluorescence of free FAD is naturally quenched by the folding of its structure, in which the adenosine dinucleotide moiety interacts with the isoalloxazine component. However, when concentrated acid is added hydrolysis of pyrophosphoryl bond occurs, resulting in the production of FMN and ADP (189-191). The hydrolysis diminishes the fluorescence quenching effect and thus increases fluorescence emission. The FMN molecule does not possess an adenine dinucleotide component and thus, when treated with acid, no fluorescence emission increase is observed. However, a decrease is seen as FMN has reduced fluorescence at acidic pH values (189-191). This

principle, which can be applied to flavin-containing enzymes by prior denaturation of the protein (to release cofactor from the protein matrix) (188), is accordingly utilised in this study to determine whether FAD or FMN is bound to *R. metallidurans* CYP116B1.

Prior to assaying the flavin of CYP116B1, standard curves for the change in fluorescence of free FMN and FAD (Sigma-Aldrich) were created by recording fluorescence spectra prior to, and following, acid addition. A range of dilutions of each cofactor were prepared between 0 and 10 μM in 100 mM potassium phosphate (pH 7.7) and retained on ice in darkness until required. Utilising a Cary Eclipse fluorescence spectrophotometer (Varian) fitted with a Peltier attachment, samples were excited at 450 nm, after being allowed to equilibrate to 20 °C for several minutes. The resultant emission spectra were recorded between 500 and 600 nm, before 200 μl of 1M perchloric acid was added to each sample, and the spectrum re-recorded. By subtracting the peak fluorescence at 530 nm of the pre-acid treated sample from the peak fluorescence of the post-acid sample (also at 530 nm), the overall fluorescence change was calculated. By measuring the changes at a number of concentrations of each flavin and plotting the calculated differences, standard curves were produced (Figure 82a and b). The experiment was then repeated for samples of CYP116B1 between 0 and 2 μM, also diluted in 100 mM potassium phosphate (pH 7.7). In order to remove the bound cofactor from CYP116B1, samples were heated to 95 °C for three minutes before centrifugation at 14,000 g to remove denatured protein. The supernatant was then submitted to the same procedure as for the FAD and FMN standards. Following analysis of the spectral data obtained from these studies, which included correction for the background fluorescence contribution of the assay buffer, plots of fluorescence change *versus* protein concentration were created and are presented in Figure 82c.
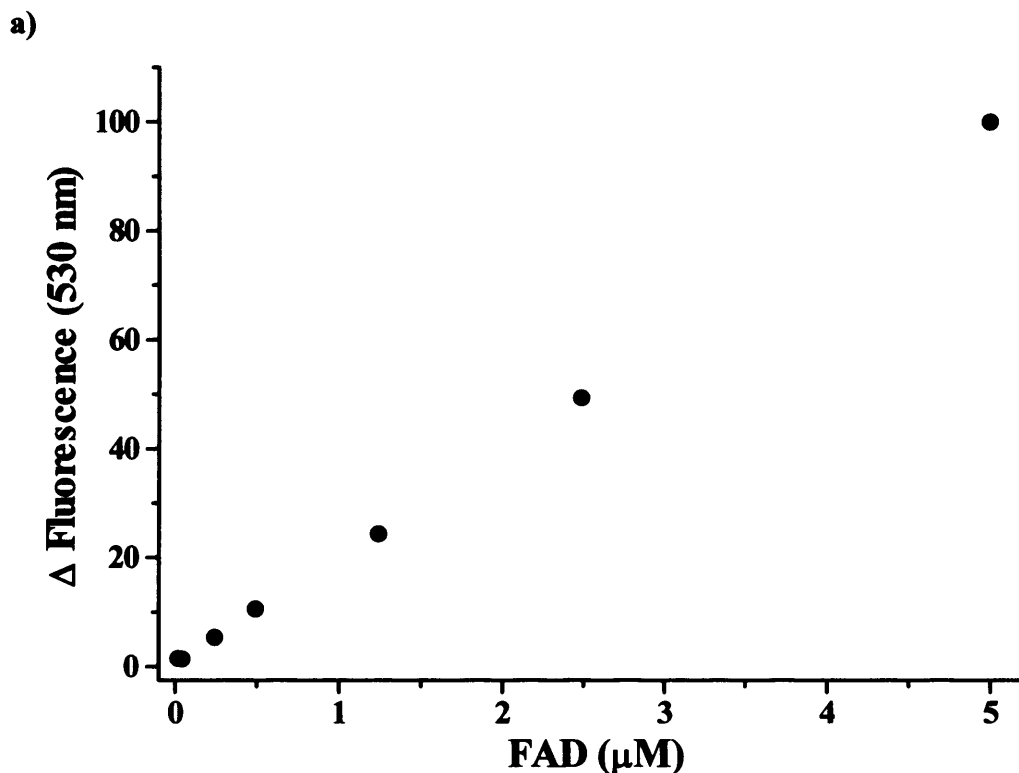
.

a)

Figure 82 The standard curves for the change in fluorescence at 530 nm of a) flavin adenine dinucleotide (FAD), and b) flavin mononucleotide (FMN) upon treatment with 1 M perchloric acid. FAD fluorescence demonstrates a relatively linear increase in intensity upon the addition of acid, whilst FMN intensity diminishes linearly following the same treatment. c) The change in fluorescence for the supernatant extracted from heat denatured CYP116B1 demonstrates a linear decrease in intensity, akin to that of FMN, and thus confirms the presence of FMN as the redox active flavin of this redox partner fused system. Fluorescence emission spectra were recorded between 500 and 600 nm utilising a Cary Eclipse Fluorescence spectrophotometer following excitation at 450 nm. All data points were calculated at the peak fluorescence at 530 nm by subtracting the fluorescence of the pre-acid spectrum from the fluorescence post-acid spectrum at this wavelength, and are reported in arbitrary fluorescence units.

b)

c)
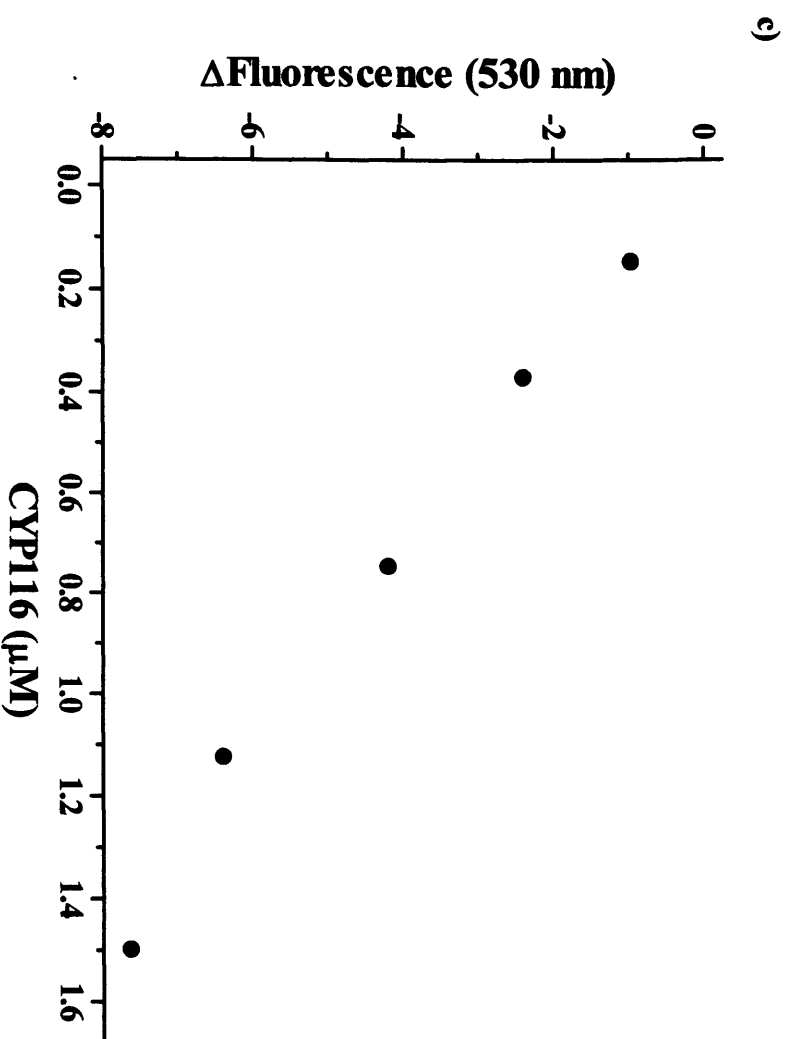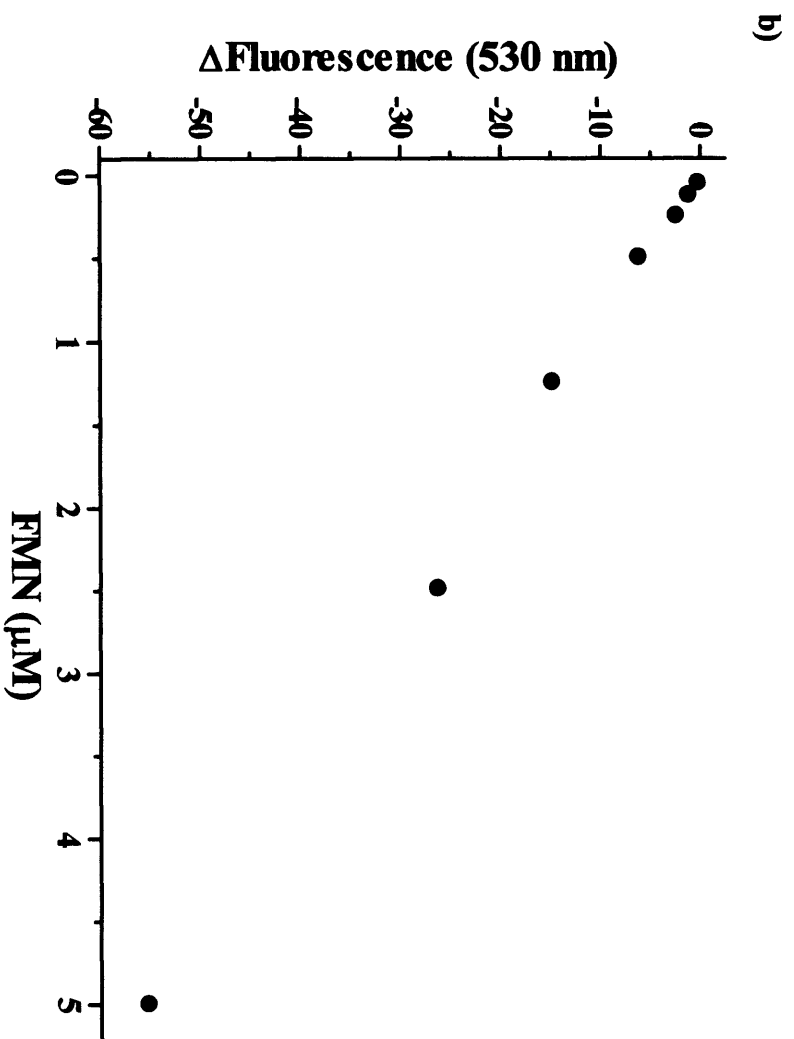
As reported previously by Weber (189), the fluorescence emission of flavin adenine dinucleotide is enhanced upon the addition of acid, whilst the emitted fluorescence of flavin mononucleotide decreases upon acidification. Across the concentration range studied, the acid-induced change in fluorescence of FAD is observed to increase linearly as its concentration in solution rises (Figure 82a). Conversely, across the same concentration range the fluorescence of FMN diminishes upon acid treatment, but also follows a relatively linear dependence upon concentration (Figure 82b), and both sets of data generate standard curves for the respective cofactors. When the CYP116B1 data are compared to the two flavin standard curves, it is seen that the samples show an FMN-like decrease in fluorescence which is linearly related to the concentration of the sample (Figure 82c). Furthermore, as no increase in the intensity of the fluorescence is noted for the CYP116B1 samples the assay confirms that the incorporated cofactor is, as postulated, FMN. When used in conjunction with the EPR data from Chapter 4.15, the reductase component of CYP116B1 is further confirmed to be akin to the phthalate dioxygenase reductase of *Pseudomonas cepacia*, similarly incorporating FMN and 2Fe-2S cofactors (6,145,146). This result is also in agreement with those of Hunter *et al.* who demonstrated that the CYP116B1 homologue, RhF from *Rhodococcus* sp. NCIMB 9784, possessed FMN as a cofactor, albeit by a UV/Visible absorption method (185). The data are limited in that they cannot be used to quantify the amount of flavin present in the sample, as heat denaturation may not free all flavin from the protein, and some may be pelleted with protein during centrifugation. However the data are consistent with the flavin cofactor of CYP116B1 being FMN, as predicted from amino acid sequence alignments and evolutionary relationships with phthalate dioxygenase reductase (Chapter 4.2). Thus, this study confirms the presence of a flavin cofactor in CYP116B1 and provides fluorescence data consistent with it being FMN. With this added confidence that the *R. metallidurans* redox partner fused cytochrome P450 is replete with its redox centres, the characterization of this enzyme continues in subsequent sections, starting with stopped-flow and steady-state kinetic studies, and moving on to redox potentiometry and product analysis studies.

4.18 Stopped-flow kinetic studies of *R. metallidurans* CYP116B1

In Chapter 4.8 it was inferred that *R. metallidurans* CYP116B1 favoured reduction by NADPH over reduction by NADH. This assay utilised UV/Visible spectroscopy to show that this coenzyme was more effective than NADH in bleaching the absorbance between 450 and 500 nm; a spectral region that corresponds to the FMN cofactor incorporated into this protein. Although this assay provided some information on the coenzyme preference of CYP116B1, it did not afford any quantitative information (e.g. K_d values) that could be utilised to compare and contrast this system with that of other well-characterized systems such as P450 BM3 from *B. megaterium* and the CYP116B1 homologue, RhF from *Rhodococcus* sp. NCIMB 9784. During the characterization of numerous proteins, including the reductase domain of P450 BM3, the adrenodoxin reductase FprA of *M. tuberculosis*, as well as the CYP116B1 homologue RhF (26,130,134,257), stopped-flow techniques have been extensively employed in order that the nucleotide preference, and associated electron transfer rates to FMN or FAD cofactors, could be determined for these enzymes. Hence, with the purpose of clarifying the coenzyme specificity of *R. metallidurans* CYP116B1, as well as the rate at which flavin reduction from the NADH and NADPH coenzymes occurs, single-wavelength stopped-flow kinetic studies were performed. These studies were done in the expectation that the coenzyme preference of CYP116B1 would be established and to facilitate comparison with the homologous proteins from *Rhodococcus* sp. NCIMB 9784, and other cytochrome P450 reductase systems.

Stopped-flow studies of the interaction between CYP116B1 and the coenzymes NADH and NADPH were performed similarly to reported methods for the coenzyme preference determination of P450 BM3 by Munro *et al.* (26). Data were recorded in an anaerobic nitrogen environment within a Belle Technology glove box, with oxygen levels maintained at less than 2 ppm. Measurements of the reduction rate of CYP116B1 were carried out over a time course of 0.5 seconds utilising an Applied Photophysics SX18MV UV-visible stopped-flow instrument, and by monitoring absorbance at 465 nm. This wavelength was determined, using UV/Visible spectrophotometry, as being the point of maximal absorbance change during coenzyme reduction, as well as being sufficiently distanced from the Soret band of the enzyme that contributions of the heme are minimised. However, negligible heme reduction is expected in the absence of substrate for the P450. Using the stopped-flow apparatus, the changes in absorbance of

CYP116B1 at 465 nm were recorded, utilising a constant concentration of enzyme (6.6 µM) whilst varying the coenzyme concentration from stoichiometric levels to 500 µM. All samples were prepared in argon-degassed 10 mM potassium phosphate (pH 7.4), whilst the temperature of the samples was maintained at 30 °C by a Peltier attachment. In order to discount the effects of photo-reduction of the samples, which is a known phenomenon that may lead to the reporting of inaccurate reduction rates (245,258), control experiments in which CYP116B1 was mixed rapidly with coenzyme-free buffer were performed. The transients obtained at 465 nm following rapid mixing were fitted with a double exponential decay curve utilising the SX18MV software (Applied Photophysics) in order to determine the NADH- and NADPH-dependent CYP116B1 reduction rates (Table 18 and Table 19). Single exponential fits did not accurately describe the reaction transients obtained (insets, Figures 83 and 84). To facilitate further interpretation of the data, plots of the reduction rate *versus* nucleotide concentration were created and, where appropriate, fitted with a hyperbolic function (Equation 8, Chapter 4.19) to determine K_d values for the nucleotides.

NADH concentration (µM)	Rate 1 (s^{-1})	Amplitude 1	Rate 2 (s^{-1})	Amplitude 2
3	6.38	0.0081	0.95	0.0063
12.5	8.12	0.0140	0.47	0.0035
25	11.43	0.0145	0.48	0.0032
37.5	13.88	0.0147	0.48	0.0035
50	15.29	0.0148	0.45	0.0033
100	18.45	0.0156	0.47	0.0037
175	19.69	0.0151	0.46	0.0045
250	20.11	0.0153	0.45	0.0042
375	20.44	0.0154	0.47	0.0046

Table 18 The rates of NADH-mediated reduction of CYP116B1, as identified by the change in UV-visible absorption of the *R. metallidurans* protein at 465 nm. The transients obtained at this wavelength were fitted to a double exponential function utilising the software of the SX18MV UV-visible stopped-flow instrument (Applied Photophysics), and Rate 1 and Rate 2 correspond, respectively, to the first and second phases of the absorption transients. Accordingly, Amplitude 1 and Amplitude 2 are the respective changes in absorbance at 465 nm from which Rate 1 and Rate 2 are calculated. The data, which were recorded over a time course of 5 seconds, indicate that the first phase rate increases as the NADH concentration increases, whilst the second phase rate, which is associated with appreciably smaller amplitude, is independent of coenzyme concentration under pseudo first order conditions. In Figure 83 the plot of the first phase reduction rate *versus* the concentration of NADH is shown.
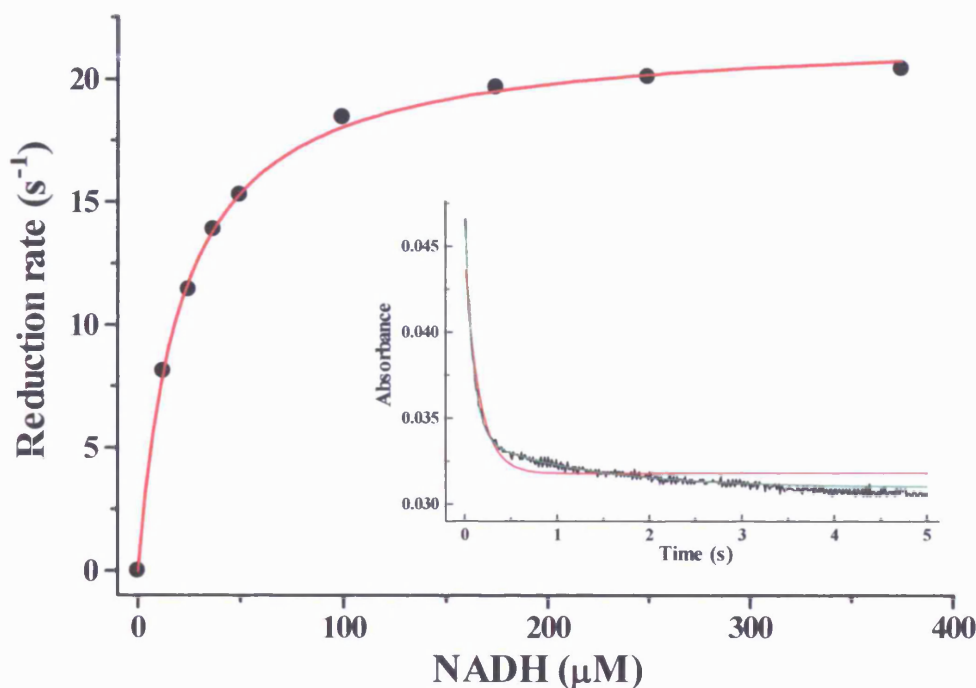
Figure 83 The plot of the rate constants for the first phase (see Table 18) of the biphasic CYP116B1 reduction process at 465 nm *versus* the concentration of NADH. Data were used for the determination of the coenzyme preference and limiting flavin reduction rate in the *R. metallidurans* protein. The data identify that the NADH-mediated reduction rate (1st phase) for CYP116B1 is hyperbolically dependent on coenzyme concentration and, when fitted with a hyperbolic function (Equation 8, Chapter 4.19), determine the K_d of NADH as 21.7 ± 0.8 µM, whilst the maximal reduction rate of CYP116B1 (k_{lim}) is 21.9 ± 0.2 s^{-1}. Data points were calculated from flavin-associated absorbance changes over 5 seconds, determined by single-wavelength stopped-flow kinetic assays. The inset shows a typical reaction transient (black) obtained for NADH-mediated CYP116B1 reduction fitted to single and double exponential fits (red and green, respectively), and demonstrates that the latter is superior for describing this process. In these anaerobic assays CYP116B1 at 6.6 µM was mixed with various concentrations of NADH using an Applied Photophysics SX18MV UV-visible stopped-flow instrument maintained at 30 °C.

The data in Table 18 indicate the rates of reduction of CYP116B1 in the presence of a range of concentrations of NADH, determined by fitting absorbance changes at 465 nm with a double exponential function. Rates for the first phase demonstrate an increase in the rate of CYP116B1 flavin reduction as NADH concentration increases, whilst second phase rates, which are of smaller amplitude, show no dependency on reductant concentration. The plot of the first phase rates of CYP116B1 reduction *versus* NADH concentration in Figure 83 identifies that the rate of CYP116B1 reduction is hyperbolically dependent on the concentration of NADH, and that saturation of the coenzyme binding site of this enzyme is approached above NADH concentrations of

200 µM. The data determine that the maximal reduction rate is 21.9 ± 0.2 s^{-1}, a value which is approximately 5-fold slower than that of the CYP116B1 homologue RhF (111 ± 5 s^{-1}) with the same coenzyme (130). Also, a K_d value of 21.65 ± 0.77 µM determined for the binding of NADH to the *R. metallidurans* protein is approximately 170-fold tighter than that observed for RhF (3.7 ± 0.3 mM). Furthermore, the K_d for NADH binding to phthalate dioxygenase reductase from *Ps. cepacia* has been determined as ~25 µM, which is similar with the value obtained here for CYP116B1. However NADH-mediated reduction of this protein occurs at a maximal rate of ~70 s^{-1} (259,260).

The rates of reduction of *R. metallidurans* CYP116B1 in the presence of NADPH, also determined by the fitting of induced absorbance changes at 465 nm with a double exponential function, are shown in Table 19. From the data it can be seen that the rate of reduction (first phase) of CYP116B1 by this nucleotide is significantly greater than those reported for NADH (Table 18). For example, at 250 µM the NADH reduction rate is 20.11 s^{-1}, whilst at the same concentration the NADPH reduction rate is 74.59 s^{-1}. Interestingly, the NADPH data (i.e. those for the first phase of the biphasic transients) differ from the NADH data, as they show no apparent dependence of the reduction rate upon nucleotide coenzyme concentration. However, as with the second phase rates from the NADH study, the rates for the second phase of the biphasic transients with NADPH (which are again associated with significantly smaller amplitudes than those for the first phase) are also apparently concentration independent.

NADPH concentration (μM)	Rate 1 (s^{-1})	Amplitude 1	Rate 2 (s^{-1})	Amplitude 2
3	68.17	0.0137	4.76	0.0009
6	67.63	0.0130	5.34	0.0011
12.5	73.21	0.0125	4.11	0.0008
25	70.69	0.0121	6.51	0.0014
37.5	83.00	0.0119	6.42	0.0016
50	71.70	0.0121	6.86	0.0012
100	72.88	0.0124	2.37	0.0011
175	77.13	0.0119	9.22	0.0017
250	74.59	0.0136	5.60	0.0015
375	69.74	0.0134	3.80	0.0012
500	69.79	0.0137	5.91	0.0014

Table 19 The rates of NADPH-mediated reduction of CYP116B1, calculated by fitting the absorption spectral changes at 465 nm with a double exponential function. The data indicate that the first phase of reduction occurs at a much greater rate than the second phase (and with a larger amplitude of absorption change), and that rate constants for both phases are independent of coenzyme concentration across the range studied. Rate 1 and Amplitude 1 correspond to the first phase of the double exponential fit, whilst Rate 2 and Amplitude 2 relate to the second phase of CYP116B1 reduction. A plot of Rate 1 *versus* NADPH concentration is shown in Figure 84.

The plot of the first phase reduction rate constants for CYP116B1 *versus* NADPH concentration is shown in Figure 84. Unlike the data recorded for CYP116B1 reduction by NADH, that shows a hyperbolical dependence of reduction rate on the coenzyme concentration, this plot identifies that the NADPH-associated reduction rate is apparently independent (in the range studied) of the amount of titrated coenzyme. As such, these data do not allow determination of a K_d for the interaction of NADPH with CYP116B1, and thus suggest that the binding of NADPH, which is (apparently) saturating even at levels approaching stoichiometry with the enzyme, is much tighter than that of NADH. The plot shows (assuming the first phase of the biphasic transients report predominantly on flavin reduction) that reduction of CYP116B1 by NADPH occurs at a maximal rate of ~72 ± 5 s^{-1}, which is more than three-fold greater than that observed for the respective limiting rate of NADH-dependent reduction of the enzyme (Table 18). However, these data also suggest that the flavin reduction process in slower than that reported for the RhF enzyme by NADPH (~180 s^{-1}, (130)). Data from studies of the interaction of the nucleotides with the CYP116B1 homologue phthalate

dioxygenase reductase from *Ps. cepacia* demonstrate that this protein receives electrons at rates that would support rapid reduction of phthalate dioxygenase that it serves (i.e. reduction by NADH occurs at $\sim$70 s^{-1}, (259,260)). Assuming that the rates determined for CYP116B1 with NADPH as coenzyme accurately reflect flavin reduction in *R. metallidurans* CYP116B1, then the reductase domain here may also be capable of supporting high levels of oxygenase activity (at up to $\sim$72 s^{-1}, corresponding to >4000 min^{-1}). However, such a k_{cat} value is not as high as that observed for P450 BM3 from *B. megaterium*, which hydroxylates substrate at rates of up to $\sim$17000 min^{-1} (192).

As previously mentioned, the NADPH-associated rate of reduction ($\sim$72 s^{-1}) is $\sim$3-fold greater than that seen for NADH-dependent reduction ($\sim$20 s^{-1}). Similarly, studies of the CYP116B1 homologue RhF (CYP116B2) from *Rhodococcus* sp. NCIMB 9784 also demonstrate NADPH-mediated reduction rates appreciably faster than NADH-mediated rates (180 s^{-1} for NADPH cf. 111 s^{-1} for NADH, (130)). However, for this enzyme NADPH-associated reduction follows a hyperbolic dependence on concentration. Although the CYP116B1 data may initially appear unusual (and different from those for RhF), it should be noted that FprA from *Mycobacterium tuberculosis* and human cytochrome P450 reductase have been reported to show an inverse dependence on NADPH concentration, in which reduction rates increase at low concentrations of coenzyme, and are relatively constant at higher concentrations (134,138). A lack of dependence of reduction rate on coenzyme concentration is actually quite frequently observed for NAD(P)H-dependent enzymes, and may be a consequence of tight binding of the coenzyme, or the influence of another rate-limiting step in the reaction. For CYP116B1, the binding of NADPH may be much tighter than that of NADH, and the apparent reduction rate of $\sim$70 s^{-1} may be limited by a process other than the formal hydride transfer reaction (for instance, a protein conformational change on coenzyme binding).
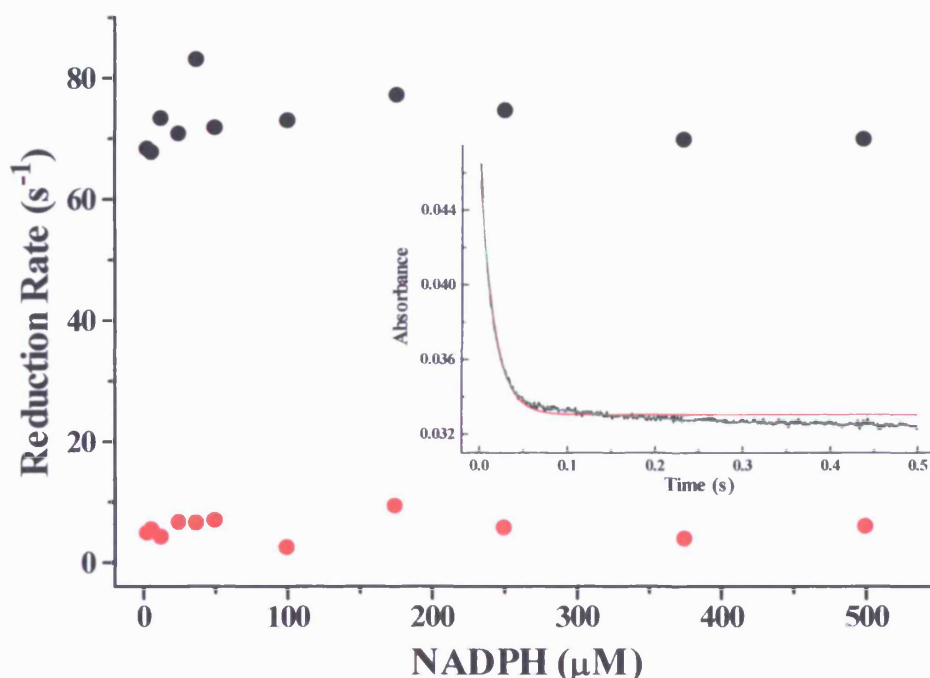
Figure 84 The data obtained by single-wavelength stopped-flow kinetics for CYP116B1 reduction by NADPH. The first phase rates (black) of enzyme reduction (see Table 19) are plotted against the reductant concentration, and identify that the apparent rate of CYP116B1 reduction is independent of the concentration of NADPH. Hence, no K_d value for the binding of NADPH to CYP116B1 could be determined, although a maximal reduction rate of approximately 72 ± 5 s^{-1} was identified. Second phase rates (red) are shown for comparison, and demonstrate that this phase is also independent of NADPH concentration. The inset shows a typical reaction transient (black) for NADPH-dependent reduction of CYP116B1 fitted to single (red) and double (green) exponential fits. As with NADH-mediated reduction (Figure 83), the fits demonstrate that reduction of CYP116B1 is best described by a double exponential function. Reaction conditions replicate those utilised for NADH-mediated CYP116B1 reduction, with enzyme present at 6.6 μM and NADPH concentration varied from stoichiometric levels to 500 μM. All assay components were diluted appropriately in 10 mM potassium phosphate (pH 7.4) and data were recorded using an Applied Photophysics SX18MV UV-visible stopped-flow instrument.

As described by the data in Table 18 and Table 19, and by the insets in Figures 83 and 84, the reaction transients for CYP116B1 reduction at 465 nm by NADH or NADPH are biphasic. The rate constants for the second phases of the process with either coenzyme have no apparent dependence on coenzyme concentration. A possible explanation for the origin of the second phase is that it reports on internal transfer of electrons from the FMN to the iron-sulphur cluster, resulting in bleaching of the absorbance contribution of the latter (as well as further changes in FMN absorption). Although the iron-sulphur cluster is not readily perceivable in UV-Visible absorption spectra (due to FMN/heme contributions), EPR data confirms its presence (Chapter

251

4.15), and the amplitude associated with the second phase of transient absorption change would be consistent with the relatively small absorbance contribution on reduction of the iron-sulphur centre. In addition, the apparent independence of the 2nd phase rate on coenzyme concentration would also be consistent with electron transfer from FMN to the 2Fe-2S cluster as an internal process that is not influenced by events preceding FMN reduction such as binding of the coenzyme. However, further experiments would be required to validate this hypothesis, and the relatively slow rate (~ 5 s^{-1}) would clearly influence the rate of substrate oxygenation by CYP116B1. A further possible explanation for the 2nd phase of absorption change at 465 nm could relate to dissociation of NAD(P)$^+$ coenzyme product. While time did not allow for further studies of the transient kinetics of this system, it would be useful to examine further the reactions of both oxidised CYP116B1 with NAD(P)H and of reduced enzyme with NAD(P)$^+$ using a combination of single wavelength and multi-wavelength analysis (i.e. using photodiode array stopped-flow spectroscopy) in order to resolve further the kinetic processes associated with coenzyme redox chemistry in this system.

Initial UV/Visible spectroscopy studies in Chapter 4.8 indicated that *R. metallidurans* CYP116B1 might favour NADPH as its reductant. The results of these single-wavelength stopped-flow kinetic studies appear to confirm these findings, suggesting that the CYP116B1 reductase has a significant preference for NADPH over NADH, as demonstrated by the faster limiting reduction rate with NADPH. In addition, the apparent lack of reduction rate dependence on NADPH concentration (compared with the hyperbolic dependence observed with NADH) is also suggestive that NADPH is bound tighter to CYP116B1 than is NADH. However, although the data agree with the relative nucleotide coenzyme specificity determined by Roberts *et al.* for the homologous fusion protein (RhF) from *Rhodococcus* sp. NCIMB 9784 (130), homologous phthalate dioxygenase reductase from *Ps. cepacia* actually shows a significant preference for NADH (145). The reasons for this may, in part, relate to structural differences in the region of the coenzyme binding sites of these proteins, which are further discussed following the findings of steady-state kinetic studies in Chapter 4.19. Additionally, the disparity in coenzyme specificity suggests that since these proteins exist in distinctly different organisms, albeit all soil bacteria, the evolution of the coenzyme preference of the reductase domains of the two fused systems may have deviated in order to better suit the environment in which they function and/or the physiology of the host.

4.19 Steady-state kinetic studies of *R. metallidurans* CYP116B1

The stopped-flow kinetic studies reported in Chapter 4.18 confirmed NADPH as the nucleotide of preference of CYP116B1, as well as determining the rates at which this coenzyme, and NADH, reduce the flavin cofactor in the *R. metallidurans* protein. Although this study detailed the rate of electron transfer from the nucleotides to the incorporated FMN centre, it did not inform upon the rate at which electron transfer through the reductase domain of CYP116B1 occurs, which may ultimately influence the rate at which substrate turnover occurs. Thus, in the absence of a substrate for CYP116B1, steady-state studies were performed in which electron transfer from NADH and NADPH, via CYP116B1, to the artificial electron acceptors potassium ferricyanide (FeCN) and cytochrome *c*. As has been reported previously in studies of human cytochrome P450 reductase (CPR) and *E. coli* flavodoxin reductase (239,261), such steady-state kinetic data can identify the rate-limiting steps in the transfer of electrons through a system to the terminal electron acceptor, whether the acceptor may be a relatively large protein (e.g. cytochrome *c*), or a small compound such as potassium ferricyanide. It is the aim of this study to identify rate-limiting catalytic steps, as well as generating further data that can be utilised to contrast the CYP116B1 system with that of homologous proteins, including RhF from *Rhodococcus* sp. NCIMB 9784 and phthalate dioxygenase reductase from *Ps. cepacia* (130,145). Typically, studies of the steady-state turnover rates of flavoproteins by NADPH and NADH are monitored by colorimetric assays utilising artificial electron acceptors, such as potassium ferricyanide (FeCN), cytochrome *c*, and DCPIP (dichlorophenolindophenol). Transfer of electrons from coenzyme-reduced flavoproteins to these artificial electron acceptors is confirmed by the latter's change in UV/Visible absorption at a particular wavelength. This observed absorption change is related to quantity of acceptor reduced through established extinction coefficients, and can thus be utilised to determine rates of electron transfer and apparent binding constants for the interactions of NAD(P)H and the electron acceptor with the flavoprotein. Hence, a series of steady-state kinetic assays were performed in order to determine the reduction rates of two artificial electron acceptors by *R. metallidurans* CYP116B1. From these assays with cytochrome *c* and potassium ferricyanide it was the aim that the K_m values for NAD(P)H binding to the reductase component of CYP116B1 would be calculated, as well as the K_m values for the binding of the protein to the artificial electron acceptors. Additionally, these data

will enable confirmation of the CYP116B1 coenzyme preference, and allow further comparisons with other types of reductase systems (e.g. the CPR module from P450 BM3), as well as with data published by Roberts *et al.* for RhF, the CYP116B1 homologue from *Rhodococcus* sp. NCIMB 9784 (130).

The assays to determine the rates of reduction of cytochrome *c* and FeCN by CYP116B1 were performed in a similar manner to studies of P450 BM3 by Roitel *et al.* (257). Aliquots of CYP116B1 were diluted to a final concentration of 75 – 100 nM in 50 mM Tris.HCl, 1 mM EDTA (pH 7.2), whilst NAD(P)H and the artificial electron acceptors were diluted to appropriate concentrations in the same buffer. Studies were performed on a Jasco V-550 dual beam UV/Visible spectrophotometer (Jasco) in order to negate non-specific reduction of the artificial electron acceptors by the coenzymes NADH and NADPH, which occurs at higher concentrations of these assay components to an extent that affects significantly the rates determined. Thus, in the second sample (blank) cuvette the assay components in the absence of enzyme were mixed to correct for non-specific reduction of acceptors. The rates of change in absorbance of the two artificial electron acceptors were monitored at wavelengths at which the absorbance change is maximal. For potassium ferricyanide and cytochrome *c*, the reduction-associated spectral change maxima occur at 420 and 550 nm respectively, and thus data were recorded at these wavelengths. For the determination of FeCN concentration at 420 nm a difference extinction coefficient ($\Delta\varepsilon$) of 1.02 mM^{-1} cm^{-1} was utilised, whilst measurements for cytochrome *c* used the reduced-minus-oxidised cytochrome *c* extinction coefficient ($\Delta\varepsilon_{550}$) of 22.64 mM^{-1} cm^{-1} (257). The concentrations of NADH and NADPH were calculated spectrophotometrically at 340 nm using the ε_{340} value of 6.21 mM^{-1} cm^{-1} (27,193). Initially, the concentration of NAD(P)H was maintained at near-saturating levels (> 400 μM) whilst the concentrations of the FeCN and cytochrome *c* were varied between 0 and 1.5 mM in order to determine reduction rates dependent upon concentration of the artificial electron acceptors. The collated data from these assays also enabled near-saturating concentrations of FeCN and cytochrome *c* to be determined. In order that coenzyme-dependent reduction rates and apparent affinity for NAD(P)H could be calculated, near-saturating concentrations of the acceptors were then utilised in a second series of assays in which the concentration of NAD(P)H was varied, whilst artificial electron acceptor levels were kept constant. All assays contained 75 – 100 nM CYP116B1, and were maintained at 25 °C using a Peltier attachment to the spectrophotometer. To ensure consistency and reliability of the assay

results, duplicates or triplicates of each of the data points were collected throughout. The recorded changes in absorbance were converted to rates of reduction of the artificial electron acceptor and plotted against the concentration of the varied assay component; FeCN, cytochrome c, or NAD(P)H. The resultant plots were fitted with a rectangular hyperbola (Equation 8), and from these fits the K_m and k_{cat} values, which would report on coenzyme and electron acceptor specificity, were calculated.

$$K_{obs} = k_{cat} \times S/(K_m + S)$$

Equation 8 Rectangular hyperbolic function used for fitting plots of rate *versus* concentration of reductant/acceptor in order to determine K_m and k_{cat} values. k_{obs} is the observed rate for substrate reduction at coenzyme/substrate concentration S. k_{cat} is the maximal rate at coenzyme/substrate saturation, and K_m is the apparent equilibrium binding constant for coenzyme/substrate. This equation was also utilised to determine K_m values for the artificial electron acceptors potassium ferricyanide and cytochrome c in assays where either the reductant was maintained at a single (saturating) concentration whilst the artificial electron acceptor concentration was varied, or vice versa.

Plots created during the determination of the rates of reduction of FeCN, and the calculated K_m and k_{cat} values, are displayed in Figure 85, and Table 20a respectively. The apparent limiting reduction rates of FeCN (k_{cat} values) were determined as 833.1 ± 17.8 min⁻¹ in the presence of NADPH, and 286.8 ± 7.5 min⁻¹ in the presence of NADH. These rates, which are directly related to electron transfer through the reductase of CYP116B1, demonstrate that reduction of FeCN occurs approximately 3 -fold faster for NADPH than for NADH. The K_m determined for NADPH binding to CYP116B1 of 3.0 ± 1.0 μM is also seen to be tighter than the equivalent value for NADH of 102.1 ± 12.2 μM, by approximately 35-fold.

a)

FeCN reductant	K_m NAD(P)H (μM)	k_{cat} NAD(P)H (min^{-1})	K_m FeCN (μM)	k_{cat} FeCN (min^{-1})
NADPH	3.0 ± 1.0	833.1 ± 17.8	103.6 ± 20.5	1109.0 ± 48.1
NADH	102.1 ± 12.2	286.8 ± 7.5	26.2 ± 3.1	246.4 ± 5.6

b)

Cytochrome c reductant	K_m NAD(P)H (μM)	k_{cat} NAD(P)H (min^{-1})	K_m Cyt c (μM)	k_{cat} Cyt c (min^{-1})
NADPH	0.9 ± 0.5	151.1± 8.0	29.9 ± 1.7	196.9 ± 4.0
NADH	399.1 ± 52.1	57.1 ± 2.7	6.5 ± 1.0	71.4 ± 2.5

Table 20 Summaries of the K_m and k_{cat} values determined from steady-state kinetic assays involving the artificial electron acceptors a) potassium ferricyanide (FeCN), and b) cytochrome c (Cyt c), and utilising NADH and NADPH as reductants. The data infer that NADPH is the coenzyme of choice for the reduction of CYP116B1, as demonstrated by faster FeCN and cytochrome c reduction rates, and tighter binding of this coenzyme. All assays performed on a dual-beam spectrophotometer (Jasco) at 25 °C using CYP116B1 at a final concentration of 75 – 100 nM.

As is observed from the data presented in Table 20b and Figure 86, the rate of cytochrome c reduction (k_{cat} value) is 2 – 3-fold greater in the presence of NADPH than for NADH (151.1± 8.0 min^{-1} compared with 57.1 ± 2.7 min^{-1}). The K_m for NADH (399.1 ± 52.1 μM) is also greater than for NADPH (0.9 ± 0.5 μM) and indicates a binding constant approximately 500-fold weaker for NADH. The activity of the CYP116B1 system in cytochrome c reduction is seen to be quite low when compared to that reported for human CPR (~1890 min^{-1}) and the reductase of P450 BM3 from $B.$ $megaterium$ (upwards of ~6000 min^{-1}), whilst both of these reductase systems strongly favour reduction by NADPH (257,261). These data are in agreement with the stopped-flow kinetic data for the reduction of CYP116B1 by the aforementioned coenzymes (Chapter 4.18), although stopped-flow data shows NADPH reduction to be concentration-independent in the range used (i.e. it likely saturates the enzyme at low concentrations, or else the rate is limited by a process such as a protein conformational change preceding reduction). This feature may be obscured in the steady-state kinetics by other processes, such as protein:electron acceptor interaction rates, that occur in the pathway for FeCN/cytochrome c reduction (257). In all the assays the k_{cat} values are seen to decrease when NADH is the reductant. As determined from stopped-flow

analysis (Chapter 4.18), the slower electron transfer from NADH to the CYP116B1 flavin is a likely factor contributing to the lower k_{cat} values when this coenzyme is the electron donor.
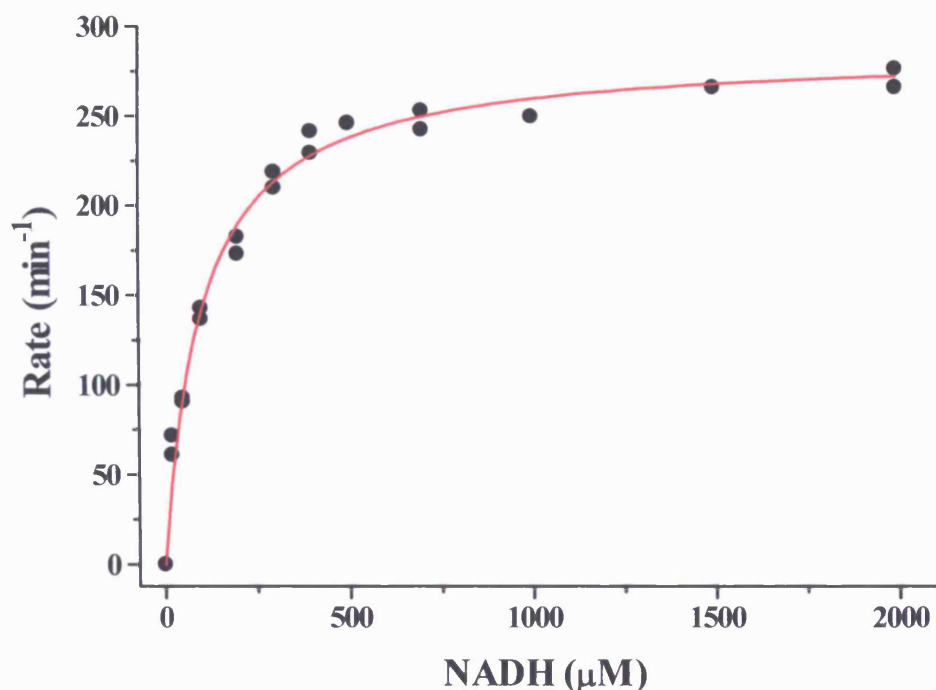

Figure 85 The plot of the rate of potassium ferricyanide reduction *versus* concentration of NADH determined by steady-state kinetic assays. The reduction of FeCN was monitored at 420 nm and resultant data were fitted with a hyperbolic function (Equation 8) to determine the K_m of NADH as 102.1 ± 12.2 μM, and the k_{cat} as 286.8 ± 7.5 min^{-1}. This compares to a K_m of 3.0 ± 1.0 μM for NADPH, and an associated steady-state reduction rate of 833.1 ± 17.8 min^{-1}. These data suggest that the reductase of CYP116B1 is preferentially reduced by NADPH, as both affinity and apparent reduction rate of the flavin are higher than with NADH, and since this coenzyme supports FeCN reduction approximately 3-fold faster than that catalysed with NADH as the electron donor. CYP116B1 and potassium ferricyanide were present in the assay at final concentrations of 75 – 100 nM, and 1 mM respectively. All assay components were diluted in 50 mM Tris.HCl, 1mM EDTA (pH 7.2) and data were recorded on a dual-beam spectrophotometer to allow correction for the effects of non-specific FeCN reduction by the coenzyme in parallel assays in absence of enzyme.

The data identify that the reduction rates of cytochrome c due to both NADPH and NADH are generally 4 – 5-fold less than those observed for FeCN reduction. This phenomenon may be related to some extent to the more positive redox potential of FeCN with respect to cytochrome c (+430 mV and +330 mV, respectively (262,263)), which would provide a greater driving force for electron transfer to ferricyanide.

Electron transfer to FeCN may also occur from either the FMN or iron-sulphur cluster in CYP116B1, whereas it may be the case that cytochrome c must accept electrons via the iron-sulphur cluster. Such a scenario would make cytochrome c reduction dependent upon an additional electron transfer event within the enzyme and on a different interaction site. Another consideration is that cytochrome c is a relatively large protein and its access to the protein and the relevant electron transfer surface may be relatively limited with respect to that for the far smaller FeCN molecule. The apparent limiting rate of reduction of FeCN by NADH (246 min^{-1}, i.e. ~4 s^{-1}) is considerably lower than the apparent limiting rate of flavin reduction by NADH (~22 s^{-1}). Moreover, the delivery of two electrons by NADH means that, if the flavin reduction itself was rate-limiting in steady-state turnover, reduction of FeCN could occur at up to ~44 s^{-1} (i.e. ~11-fold faster than is observed). The limiting rate of FeCN reduction with NADPH is ~1110 min^{-1} (i.e. ~18.5 s^{-1}) compared to electron delivery from NADPH (from stopped-flow) at ~70 s^{-1} (i.e. ~140 electrons s^{-1}) – so there is a similar shortfall of ~7.5-fold here between steady-state turnover and stopped-flow flavin reduction. Clearly, steady-state turnover of the enzyme with both FeCN and cytochrome c is limited by processes other than reduction by coenzyme, and these events could include interactions with redox partners or dissociation of oxidised coenzymes.

In each assay the apparent K_m values determined for FeCN or cytochrome c binding to *R. metallidurans* CYP116B1 are tighter in the presence of NADH than for NADPH. It is postulated that this relates to the rate of electron transfer through the reductase of CYP116B1, which is significantly greater with NADPH. Hence, a greater concentration of artificial electron acceptor may be required before apparent half-saturation with electron acceptor (K_m) occurs, since there is possibly a greater availability of reduced centres for electron transfer in NADPH-reduced enzyme. This could at least partially explain the apparent difference in K_m values for electron acceptors. In both sets of assays (i.e. using either cytochrome c or FeCN as the electron acceptor) coenzyme preference differences are conclusive: 500-fold for cytochrome c and 35-fold for FeCN differences in terms of K_m observed and in favour of NADPH. Other factors that may influence these large differences include the differing natures of interactions between CYP116B1 (in its various redox states) and NAD(P)H and NAD(H). In addition, the mechanisms of electron transfer, i.e. the complexes created between protein, artificial electron acceptor, and coenzyme, may also differ

considerably and be highly dependent on the coenzymes bound and their relative rates of association, dissociation and hydride transfer. Thus, the K_m values determined are in fact complex parameters that may not accurately report on the true K_d values for these molecules. However, given that most NAD(P)H-dependent enzymes discriminate strongly in favour of one or other coenzyme, the data here indicate that NADPH is the favoured coenzyme for CYP116B1. A measure of the catalytic efficiency of CYP116B1 can be obtained by comparing ratios of k_{cat}/K_m values for activities supported by NADH/NADPH. Using the k_{cat} values for NAD(P)H dependent cytochrome c reduction by CYP116B1 and the relevant K_m values for NAD(P)H, these specificity constants are 167.9 μM^{-1} min^{-1} (NADPH) and 0.143 μM^{-1} min^{-1} (NADH). Thus, cytochrome c reduction by CYP116B1 is ~1174-fold more efficient with NADPH than with NADH.
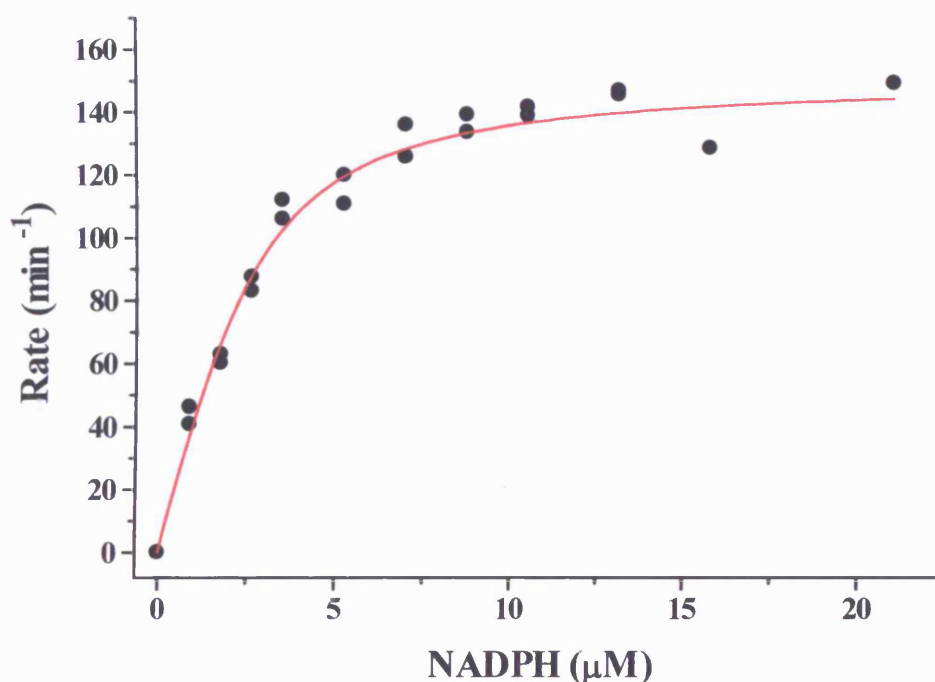

Figure 86 The plot of the reduction rate of cytochrome c *versus* concentration of NADPH in the presence of 75 – 100 nM CYP116B1. Fitting of this data with a hyperbolic function (Equation 8) determines the NADPH K_m as 0.9 ± 0.5 μM, and the k_{cat} as 151.1 ± 8.0 min^{-1}. Similar plots in the presence of NADH were also obtained, with calculated K_m and k_{cat} values of 399.1 ± 52.1 μM and 57.1 ± 2.7 min^{-1}. These data confirm the findings of FeCN steady-state assays (Table 20a and Figure 85), demonstrating that CYP116B1-dependent reduction of cytochrome c occurs more rapidly with NADPH, and that this is the favoured coenzyme in this system, binding approximately 443-fold tighter than NADH. Cytochrome c reduction was monitored at 550 nm using a dual-beam spectrophotometer in order to account for non-specific reduction of electron acceptors by NADH and NADPH. All the components of the assay were diluted in 50 mM Tris.HCl, 1 mM EDTA (pH 7.2), and cytochrome c was present at a final concentration of approximately 150 μM.

The steady-state data gathered for the reduction of FeCN and cytochrome c identify that CYP116B1 is preferentially reduced by NADPH. Similar studies of the homologue RhF from *Rhodococcus* sp. NCIMB 9784 confirm this protein to similarly favour this nucleotide coenzyme as reductant. As with CYP116B1, the RhF-mediated FeCN reduction rate is approximately 3-fold faster with NADPH than NADH, whilst the coenzyme K_m values determined for RhF differ by 27-fold (in favour of NADPH) compared with 35-fold for the *R. metallidurans* protein (130). Although there are small differences in the absolute k_{cat} and K_m values calculated for these two proteins that may derive from structural divergence, their similarity in terms of the extent of their preference for NADPH gives further confirmation that the *R. metallidurans* protein is intact and functional, as well as indicating the common ancestry of CYP116B1 and RhF. The reductase domains of CYP116B1 and RhF are shown by Blast searches (Chapter 4.2, (125)) to possess approximately 34 % identity with the FMN- and 2Fe-2S-containing phthalate dioxygenase reductase of *Burkholderia cepacia*. However, this *B. cepacia* enzyme and its equivalent protein from *Pseudomonas cepacia* have been shown to significantly favour reduction by NADH, with the latter demonstrating rates of cytochrome c and FeCN reduction of 5300 and 4140 min^{-1}, respectively, in the presence of this coenzyme (145). This disparity in coenzyme specificity and steady-state reduction rates no doubt relates to the amino acid environments of the proteins in the region of the nucleotide binding site. Differences in this region likely result in altered specificity and catalytic features, and may indicate a point of divergence between the fused systems and the *Ps. cepacia* phthalate dioxygenase reductase. Indeed, there are precedents in *E. coli* glutathione reductase and human CPR that alanine and arginine residues present in the protein sequence surrounding the nucleotide binding site correspond to a preference for NADPH over NADH (264,265). For example, in a study of *E. coli* glutathione reductase, switching of coenzyme specificity from NADPH to NADH is achieved (as evidenced by decreased binding and subsequent protein reduction by hydride transfer with NADPH) by the mutation of several alanine and arginine residues to non-polar residues (i.e. glycine, leucine, and methionine) (264). In the absence of structural data with which to identify determinants of the coenzyme specificity of *R. metallidurans* CYP116B1 and *Rhodococcus* sp. NCIMB 9784 RhF, a sequence alignment of the NAD(P)H binding regions of these two proteins and *E. coli* glutathione reductase, all of which are preferentially reduced by NADPH, as well as *Ps. cepacia* phthalate dioxygenase reductase, which favours reduction by NADH, was

performed (Figure 87a). In *E. coli* glutathione reductase, Arg 198 and Arg 204 were identified as significant for NADPH specificity, facilitating binding of the 2'-phosphate moiety of the coenzyme. The alignment demonstrates that CYP116B1 and RhF possess arginine residues (Arg 161 and Arg 158, respectively) corresponding to Arg 204 in glutathione reductase, however these proteins do not have arginine residues in positions equivalent to Arg 198. Although the presence of the two arginine residues may be sufficient to confer a preference for NADPH, equivalent residues to Arg 204 and Arg 198 are also present in *Ps. cepacia* phthalate dioxygenase reductase (Arg 143 and Arg 149), suggesting that these residues are not the sole determinants of coenzyme specificity for these enzymes.

a)

```
Psece  VAGGIGITPMLSMARQLRAEGLRSFRLYYLTRDPEGTAFFDELTSDEWRSDVKIHHDHGD 185
Escco  VGAGYIAVELAGVINGLGAKTHLFVRKHAPLRSFDPMISETLVEVMNAEGPQLHTNAIPK 240
Ralme  IAGGIGVTPVSAMARRAKELGVD-YTFHYCGRSRASMAMIDELRALHGDRVRIHAADEGQ 194
Rhosp  VAGGIGITPVLAMADHARARGWS-YELHYCGRNRSGMAYLERVAG-HGDRAALHVSEEGT 190
       :..*    . : .:              :   *.            :    .
```

Figure 87 a) An alignment of the NAD(P)H binding regions of the NADH-favouring *Ps. cepacia* phthalate dioxygenase reductase (Psece), and the NADPH-favouring *E. coli* glutathione reductase (Escco), *R. metallidurans* CYP116B1 (Ralme), and RhF from *Rhodococcus* sp. NCIMB 9784 (Rhosp). For each sequence the NAD(P)H binding motif is identified in blue, whilst the aspartate residue (Asp 173) in phthalate dioxygenase reductase (shown to be important for its NADH specificity ((260,266))), and equivalent residues in the other sequences, are highlighted in orange. The arginine residues (Arg 198 and Arg 204) in glutathione reductase that are significant for its NADPH preference ((264)) are identified in magenta and red, respectively, as are equivalent residues in the CYP116B1, RhF, and phthalate dioxygenase reductase sequences. The alignment shows that although CYP116B1 and RhF have different coenzyme specificity to phthalate dioxygenase reductase, they demonstrate very little sequence divergence at points proposed to influence the NADH preference of the *Ps. cepacia* enzyme. **b)** The structure of *Ps. cepacia* phthalate dioxygenase reductase (PDB no. 2PIA, (6)) identifying the NAD(P)H binding motif (residues 120 – 125, cyan) and Asp 173 (green). The residues that comprise the NAD(P)H binding motif have been shown to be critical for binding the pyridine nucleotide diphosphate moiety of the coenzyme, whilst Asp 173 (found towards the edge of the coenzyme binding cleft), which hydrogen bonds to the 2'-OH group of NADH, has been identified as a significant factor in the preference of NADH over NADPH for this enzyme ((260,266)). The incorporated FMN and 2Fe-2S centres are shown in yellow and orange, respectively, whilst the α-helices and β-sheets of the protein are identified in grey.

b)
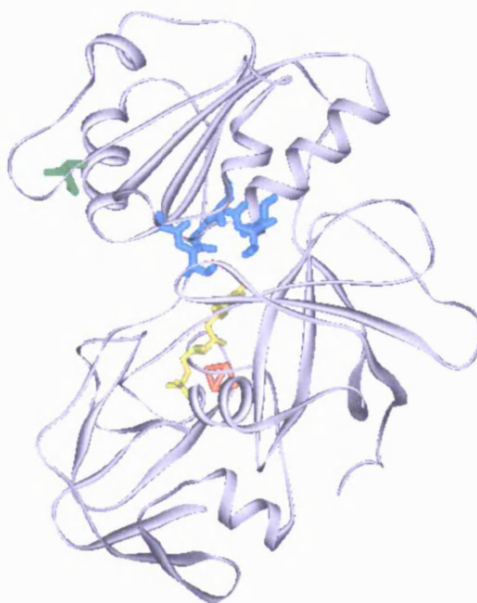
Analysis the region surrounding the pyridine nucleotide diphosphate binding site, which is highly conserved between these enzymes, reveals no obvious points of divergence between the NADH- and NADPH-favouring enzymes that would explain their respective specificities. However, an aspartate residue (Asp 173) found approximately 50 amino acid residues away from the NADH binding site in *Ps. cepacia* phthalate dioxygenase reductase (Figure 87b) has been identified as being significant to the NADH specificity of this enzyme (260,266). This negatively charged residue, which directly hydrogen bonds the 2'-OH group of NADH, is not present in glutathione reductase, being replaced an alanine residue (Ala 239). This switch to a non-polar residue from a negatively aspartate residue (which may repel the negatively charged 2'-phosphate group of NADPH, thus impairing binding of this coenzyme) may hence account for the difference in substrate specificity of these two reductases. However, in the two fusion proteins the equivalent residues to Asp 173 are aspartate (Asp 186, CYP116B1) and glutamate (Glu 182, RhF), both of which are also negatively charged. Hence, although Asp 173 in phthalate dioxygenase reductase has been identified as important for the coenzyme specificity of the *Ps. cepacia* enzyme, as this position is occupied by residues of similar charge and size in CYP116B1 and RhF, this site is unlikely to be significant to their coenzyme preference. Thus, the apparent difference in coenzyme specificity is not easily explained by sequence alignment alone, and may require the resolution of the structures of the two fusion proteins before this phenomenon can be fully understood. However, it should be noted that although

262

CYP116B1 and RhF are similar to phthalate dioxygenase reductase in that they also contain FMN and 2Fe-2S redox centres, they possess only ~34 % identity to the *Ps. cepacia* enzyme. Hence, there is an appreciable degree of structurally dissimilarity between these proteins, and it is probable that this divergence accounts for their differing coenzyme preferences, although as previously mentioned this may not be resolved until structural studies of coenzyme-bound CYP116B1 or RhF are performed.

It should also be noted that the rates of reduction of the artificial electron acceptors by CYP116B1 and RhF are very slow in comparison with those determined for redox-partner fused P450 BM3. For this system, cytochrome c reduction rates in the presence of NADPH of up to 6700 min^{-1} have been reported (257), whilst in fatty oxidation studies utilising arachidonic acid as a substrate, rates of 17000 min^{-1} were obtained (192). As the rates of cytochrome c reduction by CYP116B1 are significantly less than those of P450 BM3, it may imply that this system does not operate as efficient an electron transport chain. Furthermore, although the value of 17000 min^{-1} relates to substrate oxidation rather than the reduction of an artificial electron acceptor, it indicates the rates obtainable by an efficient redox-partner fused P450 system. Thus, it is possible that substrate turnover rates substantially greater than those for cytochrome c reduction may be achieved if a good P450 substrate could be identified for the CYP116B1. This conclusion is supported by the stopped-flow studies, in which electrons are supplied to CYP116B1 at a maximal rate of approximately 70 s^{-1} with NADPH (Chapter 4.18). This rate is considerably faster than the rate of reduction of the electron acceptors, and thus implies that electron flow to these non-physiological acceptors may be substantially slower than to the adjacent oxygenase domain. However, it should also be noted that stopped-flow studies of the P450 BM3 system indicate that reduction of FAD by NADPH occurs at a rate of ~750 s^{-1} (26), and is thus substantially (approximately 10-fold) more rapid than NADPH reduction of FMN in CYP116B1 under similar conditions. This indicates that the *B. megaterium* system is likely better evolved for electron transfer reactions (at least with respect to the hydride transfer reaction from the coenzyme) and that this is a major factor underlying its high rate of oxygenation of substrate to product.

It may be the case, as with Mtb CYP51 and P450 BM3 (Chapter 3.17, (159)), that the binding of substrate increases (makes more positive) the redox potential of the heme iron in P450 domain of CYP116B1, in turn decreasing the thermodynamic barrier that impedes electron transfer through the system to the heme iron when P450 substrate is

absent. This could mean that there is likely negligible NAD(P)H-dependent electron transfer to the heme centre in the absence of P450 substrate (largely consistent with optical studies presented earlier). However, this is unlikely to explain the much lower rate of electron transfer to electron acceptors than might be predicted from the stopped-flow reduction rates. In fact, in the P450 BM3 system the binding of fatty acids to the heme domain is actually considered to enhance steady-state rate of cytochrome c reduction through the reductase domain (267). In a subsequent section, the redox potentials of centres in the enzyme will be investigated further using redox potentiometry (Chapter 4.22).

In summary, the steady-state kinetics studies of CYP116B1-dependent reduction of the artificial electron acceptors cytochrome c and FeCN suggest that NADPH is favoured over NADH as the coenzyme for the reductase component of the $R.$ metallidurans CYP116B1 by a considerable margin. The data also indicate that the limiting rate of electron transfer to the protein acceptor cytochrome c is significantly lower than that to the small, electrophilic FeCN molecule. This could correspond, in part, to the optimal position for electron transfer to cytochrome c being occupied, partially or wholly, by the P450 domain. Thus, the P450 domain might be most suitably positioned to receive electrons from the reductase to which it is fused, and so obstruct binding of the cytochrome c protein to the reductase. Alternatively, docking of the two molecules, or factors such as their differing redox potentials, may explain the reduction rate differences observed. FeCN likely receives electrons from either the flavin or iron-sulphur centres in the system, and this may also give rise to the different rates observed for the two artificial electron acceptors. The data are in accord with the coenzyme preference data produced by stopped-flow methods (Chapter 4.18), and also agree with the findings for RhF from Rhodococcus sp. NCIMB 9784 (130). In this study a weak substrate (7-ethoxycoumarin) for RhF was identified, and whilst this compound was not found to be a meaningful substrate for CYP116B1, the following section (Chapter 4.20) details the discovery of two potential substrates and a number of steady-state kinetic assays performed to confirm that the $R.$ metallidurans enzyme can catalyse reactions with these Soret-shift inducing compounds.

4.20 Further steady-state kinetic studies of CYP116B1

Although the true substrate of CYP116B1 is unidentified, homology to CYP116A1 from *Rhodococcus erythropolis*, which is shown to degrade thiocarbamate herbicides by Nagy *et al.* (182), suggests that the *R. metallidurans* protein may catalyse similar N-dealkylation reactions. Further potential substrates of CYP116B1 were identified in the work of Roberts *et al.* in which a homologue of CYP116A1 and B1, RhF from *Rhodococcus* sp. NCIMB 9784, was demonstrated to generate a fluorescent product by an O-dealkylation reaction (130). In this study, the RhF-catalysed conversion of 7-ethoxycoumarin to 7-hydroxycoumarin was monitored by a dealkylation-associated increase in fluorescence, and identified that this reaction proceeded at a maximal rate of 4.9 ± 0.1 min^{-1}. Having identified another potential substrate for CYP116B1, 7-ethoxycoumarin was obtained and the CYP116B1-mediated conversion to 7-hydroxycoumarin was investigated as described in Roberts *et al.* (130). However, no significant level of catalytic activity was observed by this method through following fluorescence change, nor by steady-state kinetic assays monitoring NAD(P)H consumption, and no perturbation of the UV/Visible spectrum of CYP116B1 was observed on addition of the compound to the P450. Hence, although this compound was identified as a substrate, albeit a poor one, for RhF, it was deemed not to be a substrate of CYP116B1.

In the further pursuit of a substrate for the *R. metallidurans* protein, two thiocarbamate herbicides, S-ethyl dipropylthiocarbamate (EPTC) and S-propyl dipropylthiocarbamate (vernolate), that had been previously identified as substrates of CYP116A1 were obtained. Initial UV/Visible absorption spectroscopy studies of the binding of these compounds, whose structures are shown in Figure 88, identified that they induced minor Soret band shifts of approximately 0.5 − 1 nm towards shorter wavelengths. Such type I Soret band shifts to shorter wavelengths, as are observed for e.g. the interaction of P450 BM3 with arachidonic acid and lauric acid, and for P450cam in the binding of camphor (69,192), indicates that these compounds are binding as substrates within the active site of the P450. These molecules induced optical changes that resulted in perturbation of the equilibrium of the heme iron spin-state towards the high-spin form (69). Although the direction of the Soret band shifts induced by vernolate and EPTC are indicative of substrate-like compounds, the shifts are very small in comparison to those observed for P450 BM3 and P450cam with their

best substrates, where these molecules induce Soret shifts of up to approximately 20 nm (192), and thus further investigation of these compounds was required to validate their apparent substrate-like behaviour in CYP116B1. Following the example of work by Ost *et al.*, in which the addition of substrate stimulates P450 BM3 activity and NADPH oxidation (192), steady-state kinetic assays, described below, were performed in which the rates of NAD(P)H consumption in the presence and absence of vernolate and EPTC were determined.
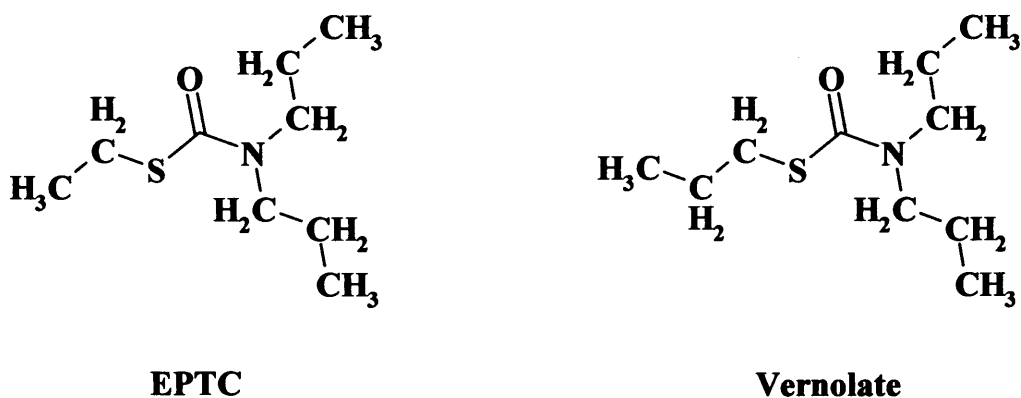

EPTC   Vernolate

Figure 88 The chemical structures of the thiocarbamate herbicides S-ethyl dipropylthiocarbamate (EPTC) and S-propyl dipropylthiocarbamate (vernolate). These compounds have been identified as being N-dealkylated by *Rhodococcus erythropolis* CYP116A1 (182), a homologue of CYP116B1, and were thus speculated to be similarly metabolised by the *R. metallidurans* protein. UV/Visible spectroscopy studies suggested that vernolate and EPTC may be substrates of CYP116B1 as both compounds elicit small type I shifts of the CYP116B1 Soret band. However, as these shifts are very small (shifts of only 0.5 – 1 nm) further confirmation of the substrate-like status of the thiocarbamates was sought utilising the steady-state kinetic assays discussed below.

The steady-state kinetic assays for the determination of vernolate and EPTC as substrates of *R. metallidurans* were performed similarly to those described by Ost *et al.* (192), utilising the change in absorbance of NAD(P)H at 340 nm to monitor enzyme activity. For each data point, an aliquot of enzyme (75 – 100 nM) diluted in 50 mM Tris.HCl, 1 mM EDTA (pH 7.2) was placed in a quartz cuvette and allowed to equilibrate to 30 °C for two minutes. To this, 200 μM of NAD(P)H was added, before the reaction was initiated by the addition of various concentrations of vernolate between 0 and 2 mM. The NAD(P)H was diluted in the same buffer as the protein. However the thiocarbamate compounds were not soluble in this buffer and were diluted in ethanol prior to addition to the assay. The change in absorbance of NAD(P)H at 340 nm, which

corresponds to the oxidation of the pyridine nucleotide coenzyme by CYP116B1, was recorded utilising a Cary UV-50 UV-Visible spectrophotometer (Varian), and converted to a rate of coenzyme oxidation utilising extinction coefficient (ε_{340}) of 6.21 mM^{-1} cm^{-1} for NADH and NADPH (27,193). The experiments were repeated with EPTC to determine the influence of this compound on the oxidation of NAD(P)H, and all data points were duplicated to eliminate the possibility of anomalous results. The subsequent plots of the rate of NAD(P)H consumption *versus* the concentration of vernolate or EPTC present in the assay were fitted using a hyperbolic function (Equation 8, Chapter 4.19) in order to determine maximal reaction rates (k_{cat} values) and K_m values for the thiocarbamate compounds, as presented in Figure 89 and Table 21.
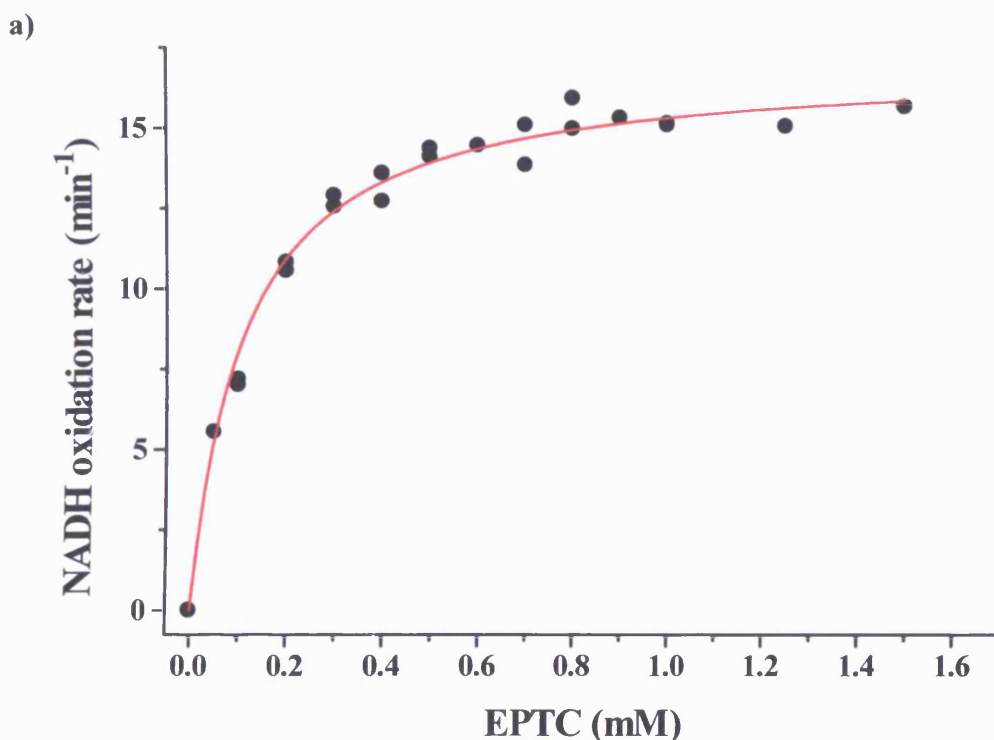
a)

Figure 89 The plots of data recorded for the oxidation rates of **a)** NADH, and **b)** NADPH, by *R. metallidurans* CYP116B1 in the presence of EPTC. The data were collected from steady-state kinetic assays in which the rate of NAD(P)H oxidation was monitored at 340 nm following reaction initiation with varying concentrations of the thiocarbamate herbicide. The k_{cat} values of 17.03 ± 0.38 min^{-1} and 30.74 ± 0.55 min^{-1}, and K_m values of 0.11 ± 0.01 mM and 0.05 ± 0.01 mM were determined for NADH and NADPH, respectively, by fitting of the data with a hyperbolic function (Equation 8, Chapter 4.19). The activity reported confirms EPTC as a substrate of CYP116B1, whilst, as reported in steady-state and stopped flow studies (Chapters 4.18 and 4.19), the data also show that CYP116B1 catalyses faster EPTC/vernolate dependent oxidation of NADPH than of NADH (i.e. NADPH is the preferred coenzyme). The assays were performed in 50 mM Tris.HCl, 1 mM EDTA (pH 7.2) utilising NAD(P)H between 0 and 2.5 mM, and enzyme at a final concentration of 75 – 100 nM.

b)
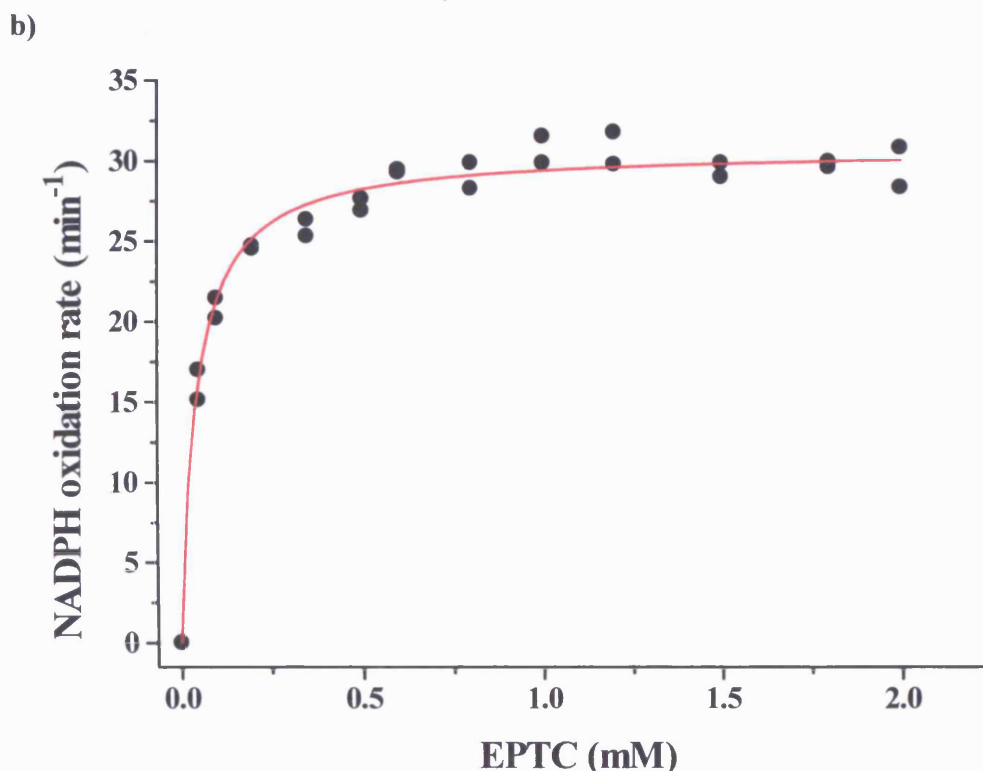
The plots of the rates of NADH and NADPH oxidation *versus* the concentration of EPTC in Figure 89 demonstrate that catalytic activity of the CYP116B1 system is stimulated by the presence of this thiocarbamate herbicide. These studies utilise the fact that in the absence of a suitable substrate for oxygenation (i.e. substrate-free P450) the P450-redox partner system catalyses NAD(P)H oxidation at a basal rate due to reduction of oxygen predominantly through the reductase domain. However, as the concentration of a compound acting as a P450 substrate is increased, there is an accompanying increase in rate of oxidation of the NAD(P)H coenzyme as electrons are passed to the heme domain in order to facilitate oxygen reduction at this centre. The turnover data for NADH and NADPH identify that coenzyme oxidation follows a hyperbolic dependence on the concentration of EPTC, thus suggesting that CYP116B1 is capable of utilising this compound as a substrate. In Table 21 a summary of k_{cat} and K_m values determined by fitting of the EPTC steady-state data with a hyperbolic function (Equation 8, Chapter 4.19) is given. This reveals k_{cat} values for NADH- and NADPH-dependent EPTC oxidation of 17.03 ± 0.38 min^{-1} and 30.74 ± 0.55 min^{-1}, respectively, which suggests, as was implied by stopped-flow and steady-state studies in Chapters 4.18 and 4.19, that the *R. metallidurans* system shows greater reactivity with NADPH over NADH. As reported previously, due to the very small Soret band shifts

induced by EPTC, dissociation constants (K_d values) for this compound could not be determined accurately by UV/Visible absorption spectral data. Hence, the K_m values for EPTC in the presence of NADH (0.11 ± 0.01 mM) and NADPH (0.05 ± 0.01 mM) determined by this study are the first indication of the affinity of this compound for CYP116B1, and show it to bind relatively weakly when compared to many of the compounds assessed in Chapter 4.13. However, values in this range (i.e. ~50 – 110 μM) are fairly typical for substrate binding in other P450s (e.g. lauric acid with P450 BM3). This weak binding will be examined further following discussion of the vernolate data.

Reductant	Vernolate		EPTC	
	K_m (mM)	k_{cat} (min^{-1})	K_m (mM)	k_{cat} (min^{-1})
NADH	0.27 ± 0.06	34.05 ± 2.15	0.11 ± 0.01	17.03 ± 0.38
NADPH	0.21 ± 0.03	57.34 ± 1.93	0.05 ± 0.01	30.74 ± 0.55

Table 21 A summary of the data gathered from the steady-state kinetic assays to determine whether EPTC and vernolate are substrates of *R. metallidurans* CYP116B1. The values, determined by fitting the data from Figure 89 and Figure 90 with a hyperbolic function (Equation 8, Chapter 4.19), identify that both compounds stimulate coenzyme oxidation, suggesting that both are metabolised by CYP116B1. Additionally, the k_{cat} and K_m values identify that, for both vernolate and EPTC, NADPH is the favoured nucleotide coenzyme, whilst also confirming vernolate to induce the greater rates of coenzyme oxidation. K_m data presented indicate affinity for vernolate and EPTC.

The plots for vernolate-induced NAD(P)H oxidation by CYP116B1 reveal that, as was observed for EPTC, the presence of this thiocarbamate herbicide promotes coenzyme oxidation and catalytic activity of the *R. metallidurans* system. The resultant plots in Figure 90 demonstrate that the rates of NADH and NADPH oxidation are hyperbolically dependent on the concentration of the herbicide, with the rates approaching saturation above ~1.5 mM vernolate. The values displayed in Table 21 are the result of fitting of the steady-state data with a hyperbolic function (Equation 8, Chapter 4.19), identifying the k_{cat} for vernolate-dependent NADH oxidation to be 34.05 ± 2.15 min^{-1}, whilst the equivalent value for NADPH is 57.34 ± 1.93 min^{-1}. These values suggest that turnover of vernolate by CYP116B1 occurs more slowly with NADH as the reducing coenzyme and thus, as with the above EPTC results and the stopped-flow and steady-state data from Chapters 4.18 and 4.19, that the *R.*

metallidurans system has preference for NADPH over NADH as coenzyme. The K_m values determined for vernolate in the presence of NADH (0.27 ± 0.06 mM) and NADPH (0.21 ± 0.03 mM) are in close agreement, and suggest that this compound binds relatively weakly to CYP116B1. These values for vernolate binding indicate a similar CYP116B1 affinity as for EPTC, with both compounds producing K_m values in the same sub-millimolar range. The similarity in the binding values for these two compounds is not surprising when their structures (Figure 88) are considered, as they differ by only one methyl group. Thus, similar interactions with a common set of amino acid residues in the active site of the P450 are expected. The very small Soret band shifts observed for the interactions of vernolate and EPTC with CYP116B1 likely arise from binding modes that do not lead to effective displacement of the distal water ligand to the CYP116B1 heme iron. However, the steady-state data indicate that saturation of the CYP116B1 active site with these substrates can be achieved within their aqueous solubility ranges. Potentially, relatively weak substrate binding may be advantageous to the P450, allowing efficient product release. However, whilst these data are useful in providing apparent binding constants describing the interactions of vernolate and EPTC with CYP116B1, these K_m values are indirect measurements of substrate affinity that are made as the enzyme undergoes its complex catalytic cycle. A more accurate estimate of affinity might be obtained by spectral perturbation assay. Nonetheless, when compared to the apparent affinity of binding of 7-ethoxycoumarin to CYP116B2 (K_m = 0.22 mM, (130)), these data suggest that vernolate and EPTC bind with similar avidity (in fact rather tighter) to CYP116B1 as this fluorescent substrate binds to CYP116B2. Moreover, the K_m values for these molecules are rather similar to those for many substrates for mammalian drug-metabolising P450s, as well as for P450 BM3 with short chain fatty acid substrates (84,192). Affinity need not impact on catalytic rate (k_{cat}) and it is also probably the case that vernolate and EPTC are not the natural substrates for CYP116B1, but instead resembles structurally the molecule(s) that the P450 has evolved to oxygenate.
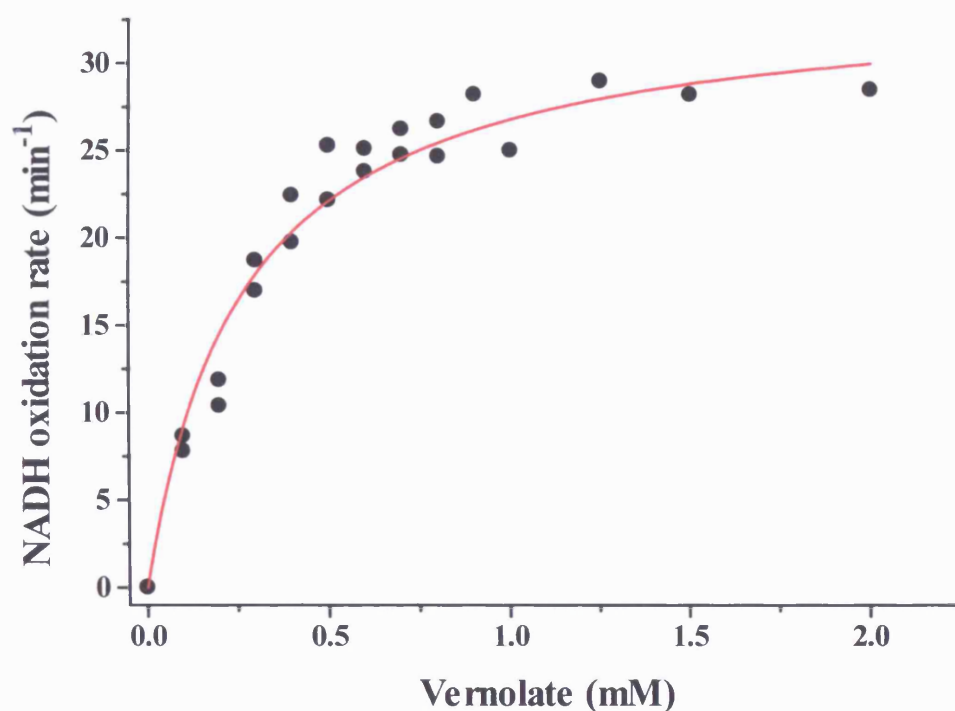
a)

Figure 90 The plots of data recorded for the oxidation rates of **a)** NADH, and **b)** NADPH, by CYP116B1 in the presence of vernolate. The activity of the CYP116B1 system, calculated from steady-state kinetic assays, indicates that vernolate is a substrate for the *R. metallidurans* protein and that CYP116B1 turnover is faster with NADPH as reducing coenzyme. From hyperbolic curve fitting of the data, the k_{cat} in the presence of NADH was determined as 34.05 ± 2.15 min^{-1}, whilst the in the presence of NADPH the $k_{cat} = 57.34 \pm 1.93$ min^{-1}. The corresponding K_m values for vernolate were calculated as 0.27 ± 0.06 mM and 0.21 ± 0.03 mM, respectively. The k_{cat} values identify that vernolate elicits rather higher enzyme activity than EPTC, possibly indicating that vernolate has closer structural similarity to CYP116B1's natural substrate type. These data were recorded under the same assay conditions as the EPTC assays described in the legend to Figure 89, with nucleotide coenzyme oxidation monitored at 340 nm.

b)
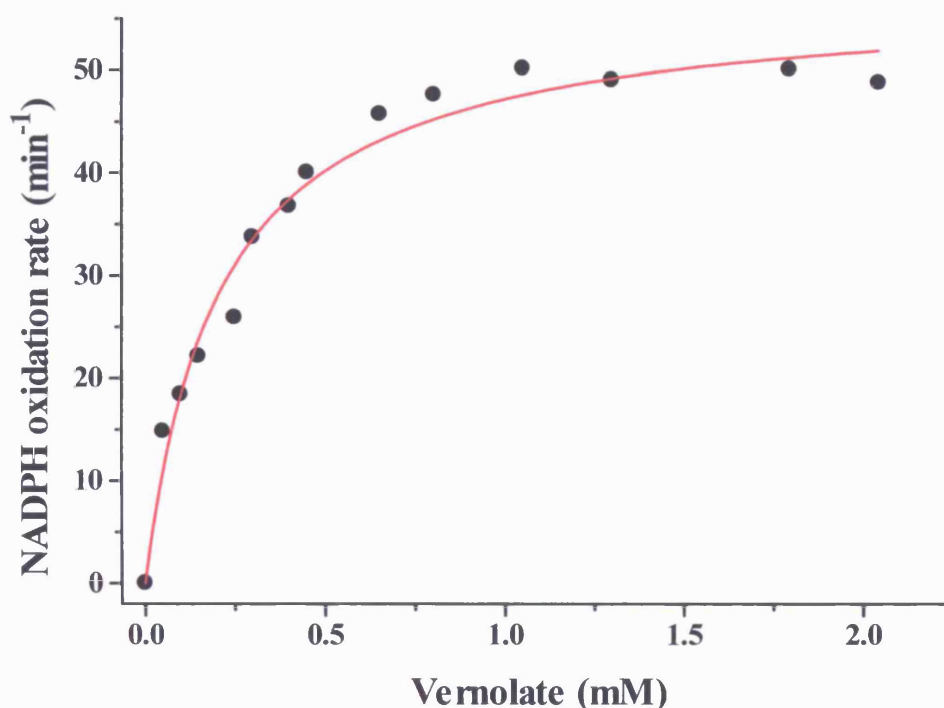
As well as identifying that NADPH is the favoured reductant of *R. metallidurans* CYP116B1, the k_{cat} values detailed in Table 21 show that vernolate is kinetically preferred as a substrate over EPTC. Maximal rates of NADH and NADPH oxidation induced by vernolate are approximately 2-fold faster than when EPTC is used, and thus indicate the larger thiocarbamate may be more suited as the substrate of this cytochrome P450. Although these compounds differ only slightly in structure, the extra bulk attributed to vernolate by an additional methyl group may affect the interactions between the compound and active site amino acid residues, leading to improved positioning of the compound at the distal face of the CYP116B1 heme, and enabling its more rapid oxidation. Additionally, the extra methyl group may enhance the hydrophobicity of vernolate with respect to EPTC, thus driving a greater proportion of the compound from aqueous solution into the hydrophobic active site. However, it is notable that K_m values for vernolate are actually greater than for EPTC (Table 21). As is seen for the binding of fatty acid substrates to P450 BM3, it might be expected that vernolate/EPTC binding would cause a shift in the thermodynamic equilibrium of the heme iron towards a less negative redox potential, through displacement of a weakly bound aqua ligand at the distal face of the heme iron. The subtle optical changes observed on titration of oxidised CYP116B1 with these compounds suggest that this

phenomenon does occur (at least to a small extent). Perturbation of heme iron reduction potential to more positive values would increase the thermodynamic driving force for electron transfer from the reductase components of the system, and hence likely enhance the rate of catalysis (129). In the next section, which details the determination of the reduction midpoint potential properties of *R. metallidurans* CYP116B1, investigations are performed to determine whether the binding of vernolate does, as seen for P450s such as P450 BM3 from *B. megaterium*, influence the CYP116B1 heme iron potential.

In relation to certain other well characterized bacterial cytochromes P450, the rates of vernolate and EPTC catalysis observed for CYP116B1 are comparatively slow. For example, P450 BM3 catalyses the hydroxylation of arachidonic acid at rates of up to 17000 min^{-1}. However, P450 BM3 is the fastest known P450 mono-oxygenase. By comparison the conversion of 5,5-difluorocamphor to 5,5-difluoro-9-hydroxycamphor by *Ps. putida* P450cam (a 3-component redox system) occurs at 50 min^{-1}, a value similar to that observed here for CYP116B1 with the herbicide substrates (192,268). The CYP116B1-mediated catalysis of vernolate occurs at a maximal rate (k_{cat}) of 57 min^{-1}. However, the *R. metallidurans* CYP116B1 k_{cat} values are considerably greater than those obtained by Roberts *et al.* in their study of the homologous protein from *Rhodococcus* sp. NCIMB 9784 (130) with their only substrate. Their work reports the K_m of 7-ethoxycoumarin as 0.22 mM, a value of similar magnitude to the vernolate K_m in this study, and shows that RhF converts this compound to 7-hydroxycoumarin at a maximal rate of 4.9 min^{-1}, a value approximately 11-fold slower than that seen for CYP116B1 with vernolate as substrate. There may be several reasons why the activity of CYP116 family cytochrome P450 enzymes is significantly slower than that of other fused systems such as P450 BM3. As is suggested for the Mtb CYP51 redox pathway (Chapter 3.17) the requirement of the physiological host for the product of CYP116B1 may be very low, or accumulation of this product may be cytotoxic, and thus the system is naturally slow to prevent this occurring. Furthermore, the equilibria of the redox potentials of the heme, FMN, and iron-sulphur cluster contained within CYP116B1 may be poised such that electron transfer to the heme is disfavoured in absence of substrate and not highly driven in its presence. Often, as is reported in studies of P450 BM3, the heme iron spin-state equilibrium is greatly perturbed towards high-spin by the binding of substrate (192), leading to a triggering of electron transfer to the heme iron and rapid catalytic activity. The fact that rates of vernolate and EPTC turnover by CYP116B1 are

273

quite slow even at apparently saturating levels suggests that these compounds may not be the true substrates for this P450, and that a physiologically relevant compound may induce greater heme iron spin-state and concomitant heme iron redox potential shifts that result in much faster electron transfer to the heme iron and overall enzyme activity.

As the studies of CYP116A1 by Nagy *et al.* also confirm activity with EPTC (182), further evidence is provided that the members of this family of P450s are capable of metabolising thiocarbamate herbicides. This is significant for the proposed role of CYP116B1 in the bioremediation of herbicide contaminated soils, as it suggests that it may be possible to introduce this enzyme (perhaps expressed in plants) into contaminated soil and to facilitate breakdown of thiocarbamate herbicides to improve soil quality. However, it appears unlikely that CYP116B1 has naturally evolved to oxygenate thiocarbamate herbicides, which have only been present in the environment for a few decades. Instead, this may be an adventitious (and advantageous) role for the enzyme, and the "true" substrate may be a structurally related molecule such as a polyketide. The CYP116B1-mediated oxygenation of the herbicides is relatively slow by comparison with the well characterized P450 BM3 P450-redox partner fusion enzyme, and it may be the case that CYP116B1 has much faster k_{cat} values with its "natural" substrate(s). However, such "true" substrate(s) of the *R. metallidurans* enzyme remain unknown.

Although these kinetic data verify that vernolate and EPTC are substrates of CYP116B1, they cannot confirm that, like CYP116A1, this cytochrome P450 from *R. metallidurans* mediates dealkylation of these thiocarbamate herbicides. In subsequent sections the influence of herbicides on CYP116B1 heme iron reduction potential and the results of mass spectroscopy studies to identify reaction products from CYP116B1-mediated oxidation of EPTC and vernolate are discussed.

4.21 The identification of CYP116B1-mediated reaction products

The steady-state kinetic assays in Chapter 4.20 identify that the mixture of the thiocarbamate herbicides vernolate and EPTC with nucleotide coenzyme (NAD(P)H) and CYP116B1 results in an increase in the rate of NAD(P)H consumption by the *R. metallidurans* protein. The increased rate of coenzyme oxidation would be consistent with the binding of EPTC and vernolate to the monooxygenase inducing a change in the spin-state of the heme towards high-spin, thus making reduction of the heme iron more

thermodynamically favourable and accelerating electron transfer in the system. The enhanced coenzyme oxidation observed suggests that these compounds are substrates for CYP116B1. As with the steady-state turnover studies of the CYP116B1 homologue from *Rhodococcus* sp. NCIMB 9784 (130), these investigations identify apparent substrates for the enzyme, based on acceleration of coenzyme oxidation. However unlike the RhF studies, in which the reaction catalysed was the slow turnover of an artificial substrate that produces a fluorescent product, the *R. metallidurans* CYP116B1 dependent oxidation of EPTC and vernolate does not produce fluorescent products, or products that are likely to be readily identified on the basis of UV-visible absorption changes. The work of Nagy *et al.* (182) identifies that another CYP116B1 homologue, the unfused P450 ThcB (CYP116A1) from *Rhodococcus erythropolis*, catalyses the N-dealkylation of thiocarbamate herbicides. Thus it is postulated that similar reactions may be performed by CYP116B1, although no such reaction was apparently catalysed by the *Rhodococcus* sp. NCIMB 9784 enzyme (130). Since high amino acid conservation between CYP116A1 and CYP116B1 does not necessarily correlate with a similar substrate selectivity for these P450s, confirmation of the formation of products from the reaction of CYP116B1 with vernolate and EPTC must be sought. Liquid chromatography mass spectroscopy (LCMS) was identified as a powerful tool for the identification of reaction products of cytochrome P450-mediated reactions, following several preceding studies, such as those of Lawson *et al.* and Eble *et al.* (233,268) . These studies successfully demonstrated that P450 BioI from *B. subtilis* converts myristic acid to a monohydroxylated product, and that P450cam catalyses the formation of 5,5-difluoro-9-hydroxycamphor from 5,5-difluorocamphor, respectively. Thus, application of a similar method was considered suitable for the analysis of products from CYP116B1. The cited studies of P450 BioI and P450cam (233,268) involved creating a reaction mixture that incorporated the P450, its substrate, the appropriate redox partner proteins, and sufficient reductant to drive the reaction for an extended period. As CYP116B1 had been shown to possess a reductase domain incorporating an FMN and a 2Fe-2S cluster, the presence of additional redox proteins to transfer electrons from the nucleotide coenzyme to the P450 was not required, thus reducing the number of assay components and simplifying the reaction mixture. Thus, reactions were performed using only CYP116B1, substrate, NAD(P)H and an NAD(P)H regeneration system, as described in the Experimental section.

Following completion of the reactions, dichloromethane extraction was performed to recover solvent-soluble compounds from the reaction mixture, before liquid chromatography was carried out to separate the reactants from any product formed. The liquid chromatography step, which separates compounds according to the degree of their interactions with the column (which are usually hydrophobic in nature) through which they are passed, was directly followed by mass spectroscopy analysis. The absolute mass of product ions identified and fragmentation patterns should then facilitate identification of the transformations performed on these molecules by CYP116B1. The reactions performed for CYP116B1 with the thiocarbamates EPTC and vernolate followed similar protocols to those used in the aforementioned studies of Lawson *et al.* and Eble *et al.* (233,268).

As in the studies of Lawson *et al.* for the study of P450BioI-mediated reactions (233), reactions of CYP116B1 with vernolate and EPTC were performed in 30 ml glass vials that had been cleaned thoroughly with methanol, dichloromethane, and ddH$_2$O to remove potential contaminants. Reactions were performed at room temperature using 50 mM Tris.HCl, 1 mM EDTA (pH 7.2), the same buffer as was used for steady-state assays described in Chapter 4.19. Reaction mixtures were stirred continuously to ensure optimal mixing of assay components. Each reaction (10 ml) contained 1 mM NADPH, as well as 20 mM glucose and 8.25 units of glucose dehydrogenase. This enzyme regenerates NADPH at the expense of glucose, obviating the necessity of addition of high levels of NADPH or any requirement for supplementation of the mixture with NADPH on coenzyme exhaustion. This strategy also prevents the build up of NADP$^+$, a competitor of NADPH, which is inhibitory to reductase systems when present at high concentrations (257). NADH was not utilised in the reactions as kinetic data (Chapter 4.18 and 4.19) inferred that the CYP116B1 system favoured reduction by NADPH. Each of the assays contained CYP116B1 at a final concentration of 6 μM, and either substrate (vernolate or EPTC) at 0.33 mM, and was allowed to proceed for 16 hours before being terminated by the addition of 0.5 ml 1.0 M HCl. Control experiments in the absence of enzyme were performed to ensure that no non-specific conversions occurred in the reaction mixture, whilst substrate-free assays were performed in order to confirm that any products identified were derived solely from the substrates.

Following assay termination, 3 ml of HPLC grade dichloromethane (Sigma-Aldrich) was added to the reaction and mixed thoroughly, before the organic and aqueous layers

were allowed to separate. The organic phase was retained and combined with the solvent layer from a second extraction, performed to ensure maximal product extraction. Residual water was eliminated from the organic phase by the addition of anhydrous magnesium sulphate, and evaporated to dryness before resuspension of the resultant residue in HPLC grade methanol (both Sigma-Aldrich). Samples were maintained at 2 – 6 °C until LCMS was performed.

The LCMS analysis of the CYP116B1 reactions was performed using an Agilent 1100 series HPLC-MSD (Agilent Technologies) at Queen Mary, University of London, by Andrew Lawrence. Resolution of substrate and product was achieved using a Vydac C_8 column (21 x 150 mm) maintained at 30 °C and with a flow rate of 1 ml min^{-1}. The mobile phase was composed of 66 % solvent A (100 % HPLC grade acetonitrile) and 34 % solvent B (0.2 % acetic acid in ddH$_2$O), and an isocratic gradient was run for 28 minutes following sample loading. The concentration of solvent B was then increased to 100 % and the run continued for a further 32 minutes. The resolved samples were analysed for the presence of products using an ion trap mass spectrometer in the positive electrospray mode, and the results are reported below.

The LCMS analyses of the reactions to determine whether *R. metallidurans* CYP116B1 could utilise the thiocarbamate herbicide EPTC as a substrate are shown in Figure 91 and Figure 92. As depicted by the chromatogram of the resolved reaction mixture (Figure 91), no significant peaks are identified in the EPTC-free control, thus confirming that any peaks observed in EPTC-containing reactions derive from the herbicide and not other components of the assays. The chromatogram of the enzyme-free sample identifies a major peak occurs between approximately 46 and 49 minutes post-sample loading. When the associated mass spectrum of this peak (Figure 92a) is analysed, an m/z value of 190, which corresponds to the mass of EPTC, is identified. Further analysis of the m/z 190 peak (Figure 92b), performed by collision-induced disassociation (MS^2), identifies a fragmentation pattern predominated by three peaks with m/z ratios of 162, 128, and 86 respectively. By analysis of the structure of EPTC these m/z values were identified to relate to plausible fractions of this thiocarbamate (Figure 93), including a molecule that lacks the S-ethyl group (m/z 128), and thus confirm the isolation of EPTC from the reaction mixture. Furthermore, these data suggest that non-specific reactions that have been observed in certain previous studies, such as the auto-oxidation of fatty acids (269), do not occur with EPTC under the conditions of these assays.
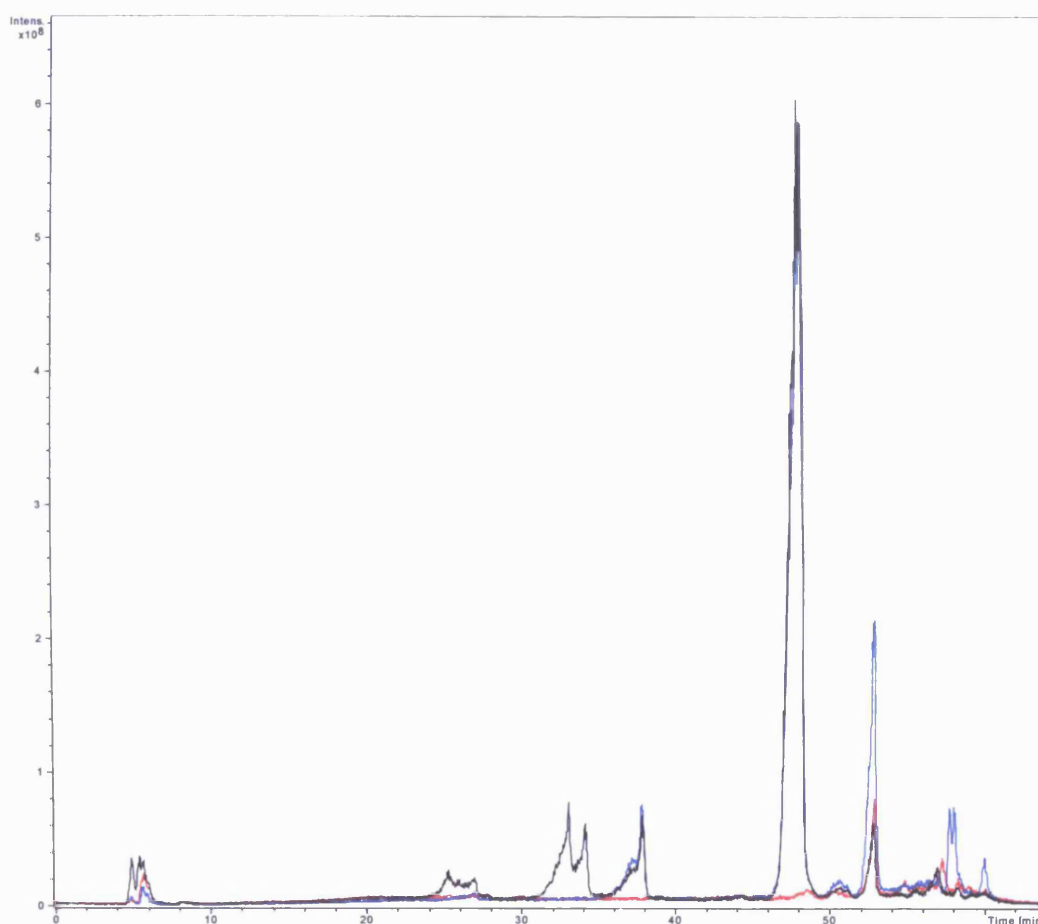
Figure 91 The chromatograms of the eluents of the substrate-free control (red), enzyme-free control (blue), and the substrate- and enzyme-containing reaction (black) performed to determine whether *R. metallidurans* CYP116B1 catalyses oxygenation of the thiocarbamate herbicide EPTC. Samples were resolved by HPLC on an Agilent 1100 series HPLC-MSD utilising a Vydac C_8 column (21 x 150 mm) at Queen Mary, University of London, by Andrew Lawrence. The mobile phase (66 % solvent A (100 % HPLC grade acetonitrile) and 34 % solvent B (0.2 % acetic acid in ddH$_2$O)) was run isocratically for 28 minutes, before increasing the concentration of solvent B to 100 % for the remainder of the elution. The EPTC-free sample identifies no features of significance, suggesting that no assay components are carried-over during the extraction process. The CYP116B1-free sample identifies a major feature at 46 – 49 minutes that, when analysed by mass spectroscopy (Figure 92a and b), confirms the successful extraction of EPTC from the reaction mixture. When both substrate and enzyme are present in the reaction this feature is again observed. However, a second feature between 32 and 34 minutes is also seen. Mass spectroscopy of this feature (Figure 92c, d, and e) identifies that CYP116B1 does indeed facilitate hydroxylation of EPTC.
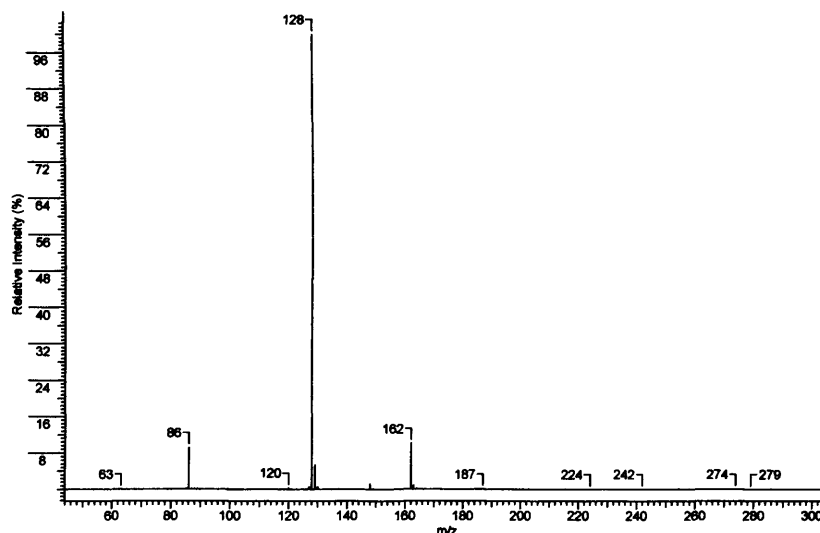
a)
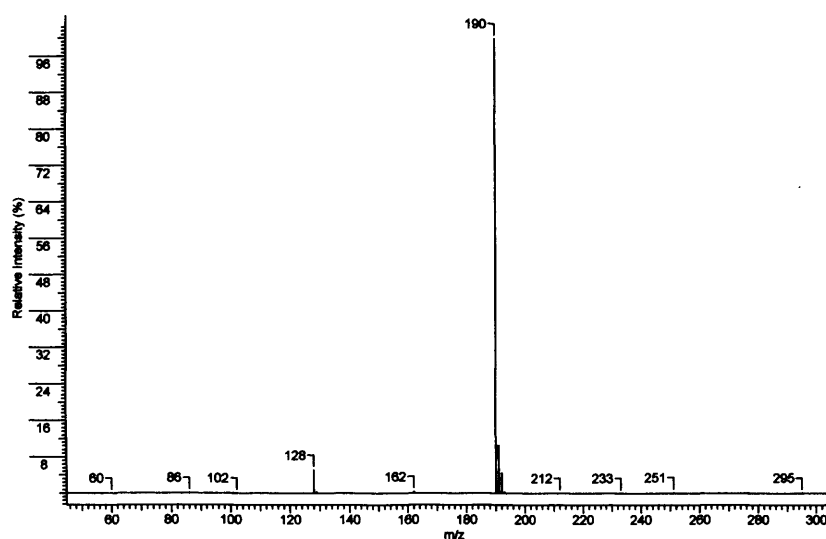
b)

Figure 92 a) The mass spectrum of the chromatogram feature that occurs between 46 and 49 minutes for the enzyme-free control reaction. The peak at m/z 190 identifies the chromatogram feature pertaining to the presence of EPTC, and is further confirmed in panel **b)** by the m/z ratios (m/z 128, m/z 162, and m/z 86) of fragments observed during collision-induced fragmentation studies (MS^2) of this peak. The mass spectra obtained for the same feature of the enzyme- and EPTC-containing reaction were identical to those presented above. Panel **c)** shows the mass spectrum of the feature observed between 32 and 34 minutes in the chromatogram of the complete CYP116B1/EPTC reaction, and identifies peaks with m/z ratios of 206 and 144. The MS^2 analysis of these peaks shown in panels **d)** and **e)** identifies peaks (m/z 144, m/z 116, m/z 100) that confirm that these peaks derive from a hydroxylated EPTC molecule. Hence, these data substantiate kinetic evidence (Chapter 4.20) that suggest CYP116B1 can perform modifications of EPTC, although hydroxylation, rather than the N-dealkylation reaction that was predicted by analogy with a homologous protein from *Rhodococcus erythropolis* (182), is observed. The chemical structures associated with the peaks identified in these mass spectra are shown in Figure 93.
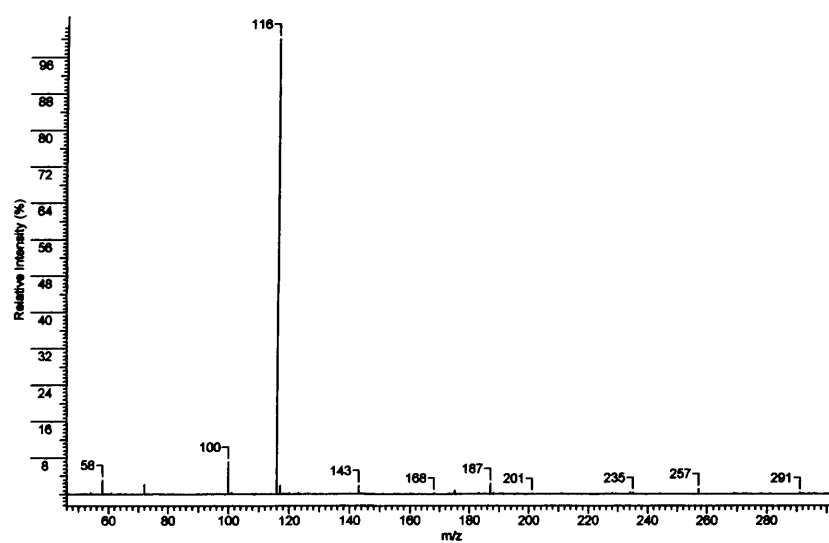
279

c)
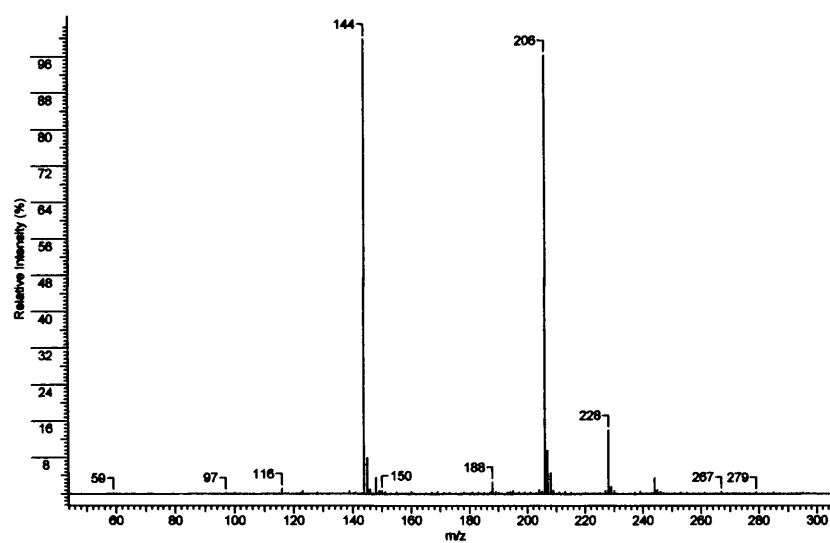
d)

e)
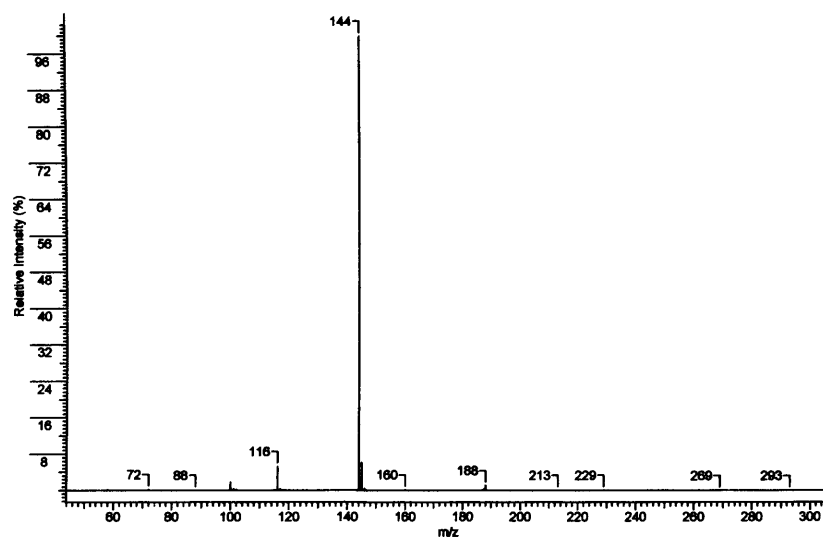
The chromatogram of the reaction in which both enzyme and EPTC were present (Figure 91) also identifies a major peak that elutes between 46 and 49 minutes. Again, the associated mass spectrum identifies an m/z value of 190 which, when further analysed by MS^2, gives an identical fragmentation pattern to that described for EPTC isolated from the enzyme-free reaction. However, as well identifying a peak at 46 – 49 minutes, the chromatogram shows a split peak at 32 – 34 minutes that is not present in the enzyme-free sample. The MS analysis of these peaks reveals the presence of two major species with m/z ratios of 206 and 144 (Figure 92c). The m/z 206 peak is 16 mass units greater than that of EPTC, and thus suggests that hydroxylation of the thiocarbamate is catalysed by CYP116B1. The shorter retention time of this compound, which is indicative of a more polar molecule, is further consistent with the addition of a hydroxyl group to EPTC. However, although this peak identifies a hydroxylated product, it does not reveal the position of this conjugation. Further analysis of the m/z 206 peak by MS^2 (Figure 92d) results in a peak of m/z 144. The structure associated with this m/z ratio is depicted in Figure 93, and relates to the hydroxylation of EPTC on either of the propyl chains that extend from the nitrogen of the molecule. The origin of the m/z 144 peak, found alongside the m/z 206 peak in the mass spectrum of the reaction mixture, was confirmed by MS^2 (Figure 92e), as the major fragment obtained from this peak had an m/z ratio of 116. This value corresponds to the structure shown in Figure 93 that has lost the S-ethyl and carbonyl groups, but which is hydroxylated on either of the propyl chains, and thus confirms that the m/z 144 peak derives from an MS-induced breakdown product of hydroxylated EPTC. Other peaks observed in this fragmentation pattern at m/z 100 and 58 correspond to a loss of the hydroxyl group from the m/z 116 fragment and a non-hydroxylated N-propyl chain respectively, and thus do not aid in the identification of the position of EPTC hydroxylation.

These mass spectroscopy data confirm that hydroxylation of EPTC is mediated by CYP116B1, and further validate the steady-state kinetic data presented in Chapter 4.20 that suggest, by EPTC-induced coenzyme oxidation, that this thiocarbamate herbicide is a substrate of the *R. metallidurans* enzyme. The position of the hydroxylation is confirmed as being on either of the propyl chains of the molecule, although to which carbon it is attached remains unresolved as further fragmentation appears to remove the hydroxyl group in preference to other groups. Unlike the data presented by Nagy *et al.* for ThcB (182), the mass spectroscopy presented here show no evidence for the N-dealkylation of EPTC. This disparity, which is discussed further following the mass

spectroscopy analysis of the vernolate reactions, may derive from structural variations in the active sites of these proteins that cause the positioning of the substrate to differ, thus likely also altering (perhaps subtly) the physiological roles of these homologous enzymes.

EPTC

m/z 190   m/z 162   m/z 128   m/z 86

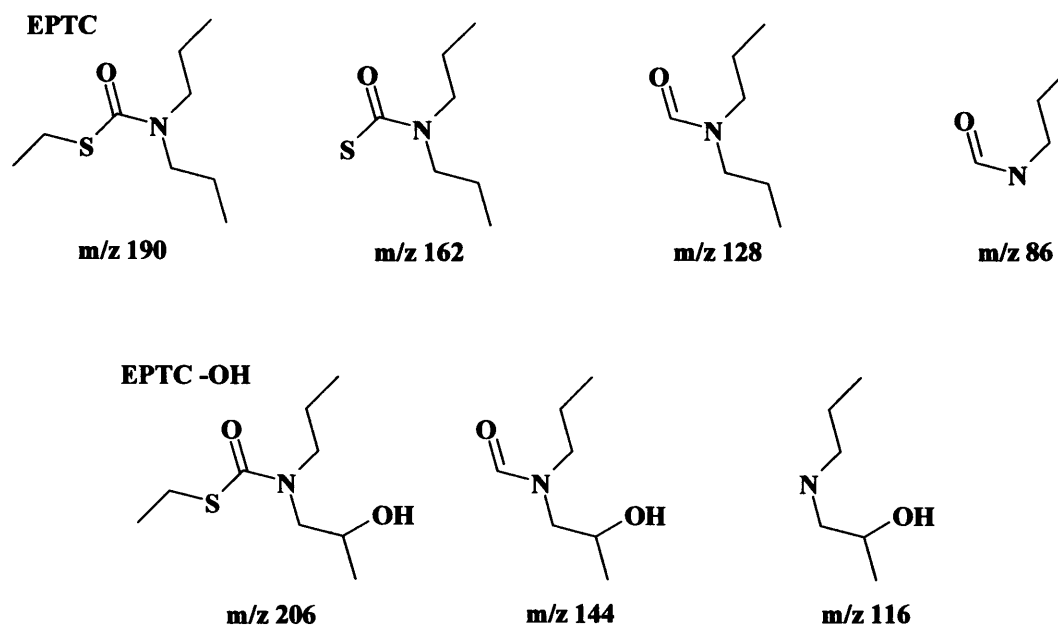**EPTC -OH**

m/z 206   m/z 144   m/z 116

Figure 93 The chemical structures of EPTC, hydroxylated EPTC, and significant collision-induced fragments of these compounds, determined from the m/z ratios of peaks observed in the mass spectra of the reaction samples (Figure 92). Hydroxylations are shown at the ω-1 position which, by analogy to other bacterial cytochrome P450 systems (33,270), is the favoured position for the hydroxylation of alkyl chains, although it is plausible that modification at other points may occur, as mammalian and other eukaryotic fatty acid hydroxylases frequently favour the ω position (271).

The chromatograms obtained for the reaction containing vernolate and the associated substrate-free and enzyme-free control reactions are displayed in Figure 94. As with the herbicide-free reaction performed for the EPTC study, omission of vernolate results in a featureless eluent profile, confirming that the other assay components are not responsible for the peaks observed in the vernolate-containing reactions. The chromatogram of the enzyme-free reaction identifies the appearance of a significant peak between 50 and 52 minutes post-sample loading. The mass spectrum of this chromatogram feature (Figure 95a) displays a peak at a position (m/z 204) that corresponds to the mass of vernolate. Further analysis of the m/z 204 peak by MS^2 results in a fragmentation pattern that consists of three peaks at m/z 176, m/z 128, and m/z 86 (Figure 95b). The peak at m/z 128 is the most prominent, and corresponds to the

loss of the S-propyl group from vernolate, as demonstrated in Figure 96, whilst the peak displaying an m/z ratio of 176 identifies the loss of an ethyl group from the parent compound. Hence, the MS and MS^2 analysis of the enzyme-free sample verifies that vernolate is successfully extracted from the reaction mixture and is not chemically modified by any of the other assay components.
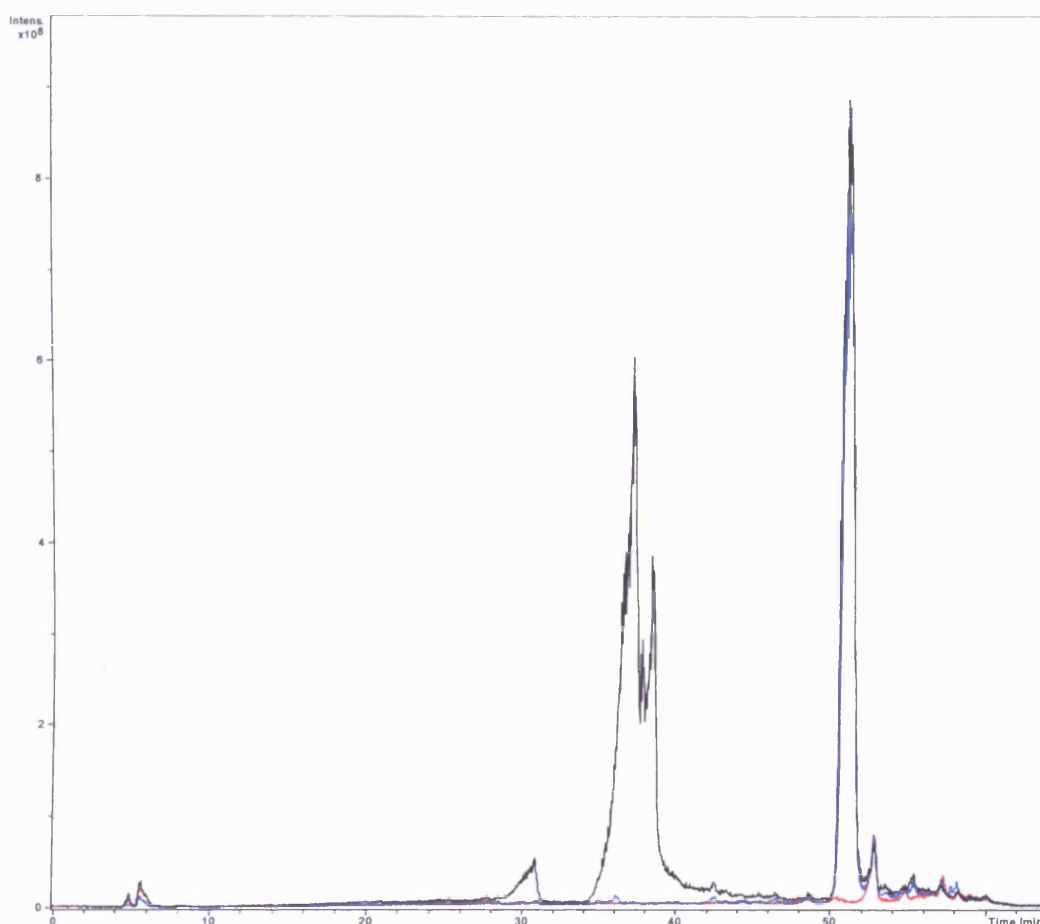

Figure 94 The eluent chromatograms obtained for substrate-free (red), enzyme-free (blue), and substrate- and enzyme-containing (black) reactions during the LCMS investigation of CYP116B1-mediated vernolate turnover. Samples were resolved identically to the EPTC samples described in Figure 91. The featureless vernolate-free sample (red) confirms the solvent extraction process does not retain any of the assay components, whilst the major feature at 50 – 52 minutes in the enzyme-free sample identifies, by the associated mass spectrum (Figure 95), the successful extraction of vernolate. This feature is replicated for the CYP116B1- and vernolate-containing reaction, but an additional feature at 34 – 39 minutes, akin to that seen for EPTC, is also observed. Analysis by mass spectroscopy (Figure 95) indicates that the feature pertains to vernolate that has been hydroxylated, and possibly N-dealkylated, by the *R. metallidurans* monooxygenase.

The chromatograms of vernolate- and CYP116B1-containing reactions are shown in Figure 94 and, as with the enzyme-free control reaction, demonstrate the occurrence of a significant feature that elutes between 50 and 52 minutes. This feature is confirmed to pertain to vernolate, as it possesses an m/z ratio of 204 and MS^2 analysis reveals an identical fragmentation pattern to that observed for the m/z 204 peak from the enzyme-free sample (Figure 95b). Additionally, the chromatogram identifies a significant split feature between 34 and 39 minutes that was not observed for the enzyme-free reaction, and suggests that CYP116B1 catalyses reactions with vernolate, as well as with EPTC. The shorter retention time of these peaks indicates that they derive from compounds that are more polar in nature than vernolate, thus suggesting a CYP116B1-induced modification. This is confirmed by the mass spectra of the two major peaks of this triplet feature, as both demonstrate peaks with m/z ratios of 220 (Figure 95c). This increase of 16 mass units, compared to the mass of vernolate (m/z 204), corresponds to the addition of a hydroxyl group to the thiocarbamate molecule. The fragmentation pattern of the m/z 220 peak is akin to that observed for the MS^2 analysis of the m/z 206 peak of EPTC, and identifies a peak with an m/z ratio of 144 (Figure 95d). Structural analysis reveals that this m/z value relates to a molecule of vernolate lacking the S-propyl group, but hydroxylated on one of the propyl chains that extend from the nitrogen atom (Figure 96). The fact that there are two distinct peaks corresponding to hydroxylated vernolate suggests that the addition of the hydroxyl group may occur at different positions on the propyl chains, however this cannot be resolved from the fragmentation patterns of the m/z 220 peak as the hydroxyl group is seemingly more labile than other parts of the molecule. As with the mass spectrum of hydroxylated EPTC (m/z 206), a large peak at m/z 144 is observed alongside the m/z 220 peak. When analysed by MS^2 (Figure 95e), the fragmentation pattern yields a major peak with an m/z value of 116 that corresponds to the vernolate structure in Figure 96 that lacks the S-propyl and carbonyl groups, as well as minor bands at m/z 100 and m/z 86 that are the products of the loss of the hydroxyl and propyl groups respectively. In addition to confirming that CYP116B1 adds a hydroxyl group to one of the N-propyl chains of vernolate, these data confirm that the peak observed in the EPTC assay is not an anomaly but an MS-induced fragmentation of the hydroxylated substrates.
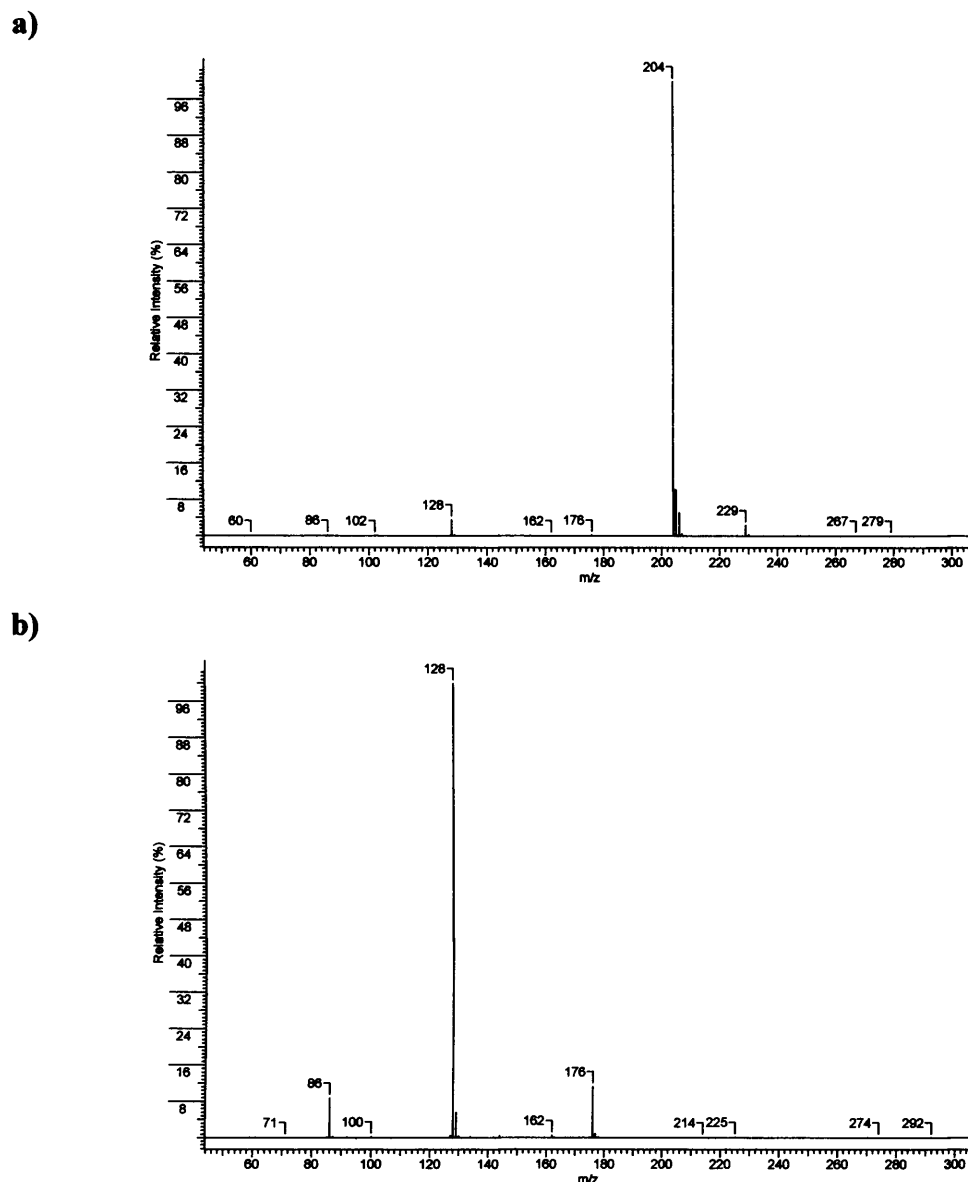
a)

b)

Figure 95 a) The mass spectrum recorded for the feature that occurs at 50 – 52 minutes in the chromatogram of the enzyme-free control reaction. These data, in conjunction with the collision-induced mass spectrum in panel **b)**, confirms the presence of vernolate, as peaks with m/z ratios that correspond to this thiocarbamate (m/z 204), and associated fragments (m/z 176, m/z 128, and m/z 86), are observed. The mass spectra of the equivalent chromatogram feature from the enzyme- and substrate-containing replicate those reported above. **c)** The mass spectrum of the chromatogram feature that occurs between 34 and 39 minutes results in significant peaks with m/z ratios of 220 and 144. Panels **d)** and **e)** show the MS^2 analysis of these peaks and, as for the EPTC samples, identify that peaks with m/z 144, m/z 116, and m/z 100 derive from hydroxylated vernolate, thus confirming that CYP116B1 can metabolise this thiocarbamate compound. The chemical structures of these fragments, and the parent molecules, are shown in Figure 93. **f)** The mass spectrum of the small peak at the centre of the chromatogram feature at 34 – 39 minutes. The predominating peak with an m/z ratio of 162 suggests that CYP116B1, as with its homologue from *Rhodococcus erythropolis* (182), may also catalyse N-dealkylation of vernolate, albeit to a far lesser extent than it catalyses hydroxylation.
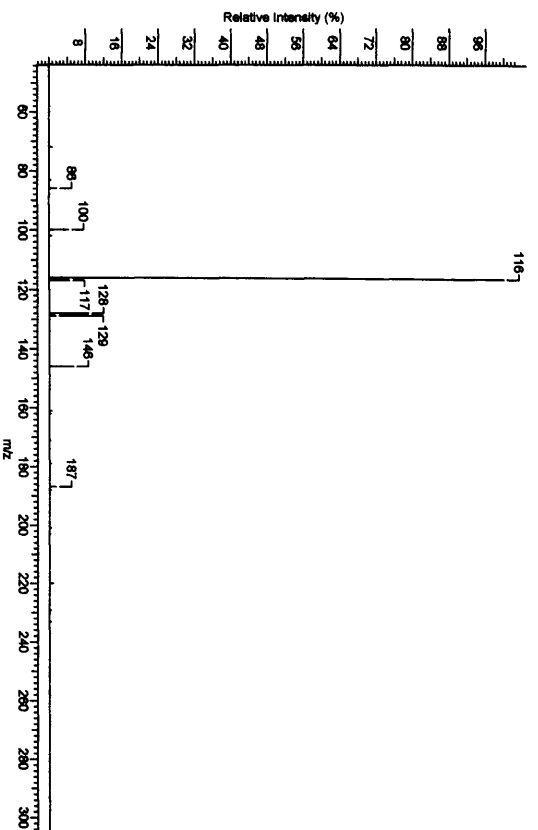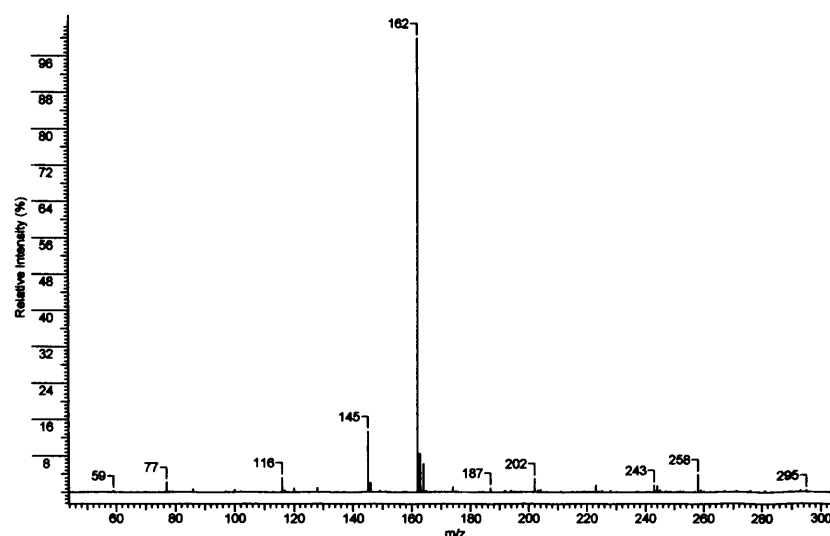
c)
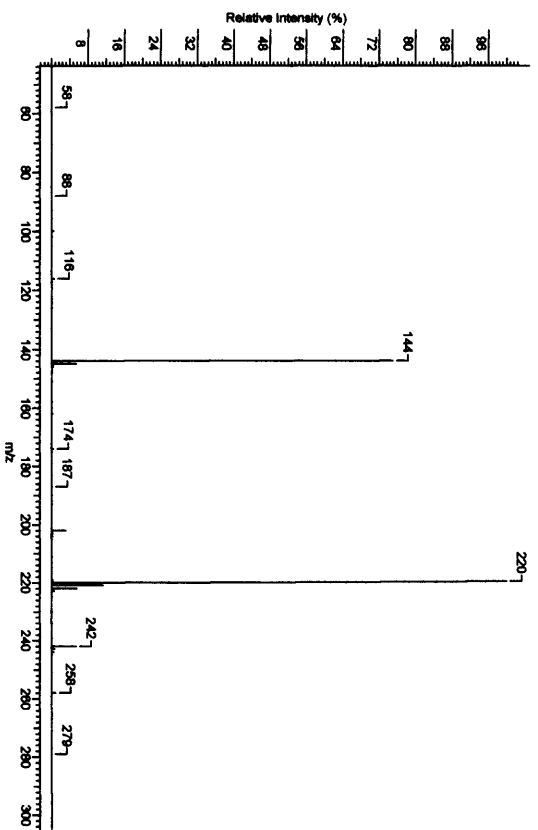
d)
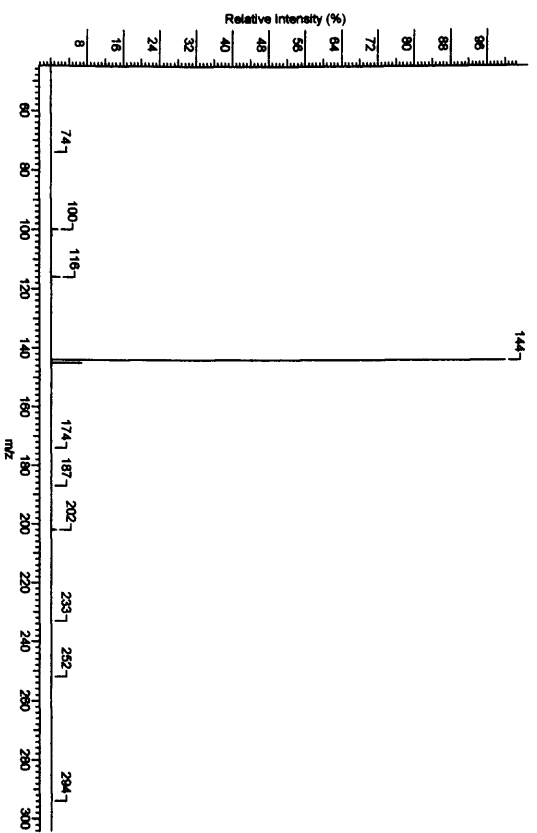
e)

f)

As was previously mentioned, the chromatogram feature that occurs between 34 and 39 minutes possesses a third peak that lies between the two major peaks associated with the hydroxylated products. The major peak of the mass spectrum associated with this feature (Figure 95f) demonstrates an m/z 162, a value that can only correspond to the removal of a propyl group from vernolate (Figure 96). This indicates that CYP116B1, like its homologue ThcB from *Rhodococcus erythropolis* (182), is capable of mediating N-dealkylation of vernolate. However, as identified by the size of the chromatogram feature that relates to the N-dealkylated vernolate, the amount of this product is far outweighed by the hydroxylated compound, thus suggesting that this reaction is significantly favoured by CYP116B1. For human CYP2E1 (271), the chain length of fatty acid substrates influences the position of substrate hydroxylation. By analogy, as no N-dealkylated product is observed in the EPTC reactions, the additional length afforded to vernolate by its extra methyl group may cause it to be positioned differently to EPTC in the CYP116B1 active site, thus increasing the likelihood of N-dealkylation. This theory is further supported when the chromatograms for the two set of reactions are compared, as it is evident that significantly greater quantities of hydroxylated product are achieved with vernolate. This complements the steady-state kinetic data for nucleotide oxidation (Chapter 4.20) that identifies greater rates in the presence of vernolate, and thus implies that the extra length/size of vernolate favours a position in the active site that is more conducive to catalytic activity, and possibly N-dealkylation. Alternatively, as there is far less total product obtained from the EPTC reactions, the amounts of any N-dealkylated EPTC present may be very small, and thus masked by the

287

peaks of the hydroxylated products. The reasons for ThcB appearing to favour N-dealkylation whilst CYP116B1 preferentially hydroxylates the thiocarbamates, can only be speculated, although the divergence likely arises through the influences of different active site residues on the positioning of substrate molecules, and may be resolved by solving crystal structures for these two proteins.
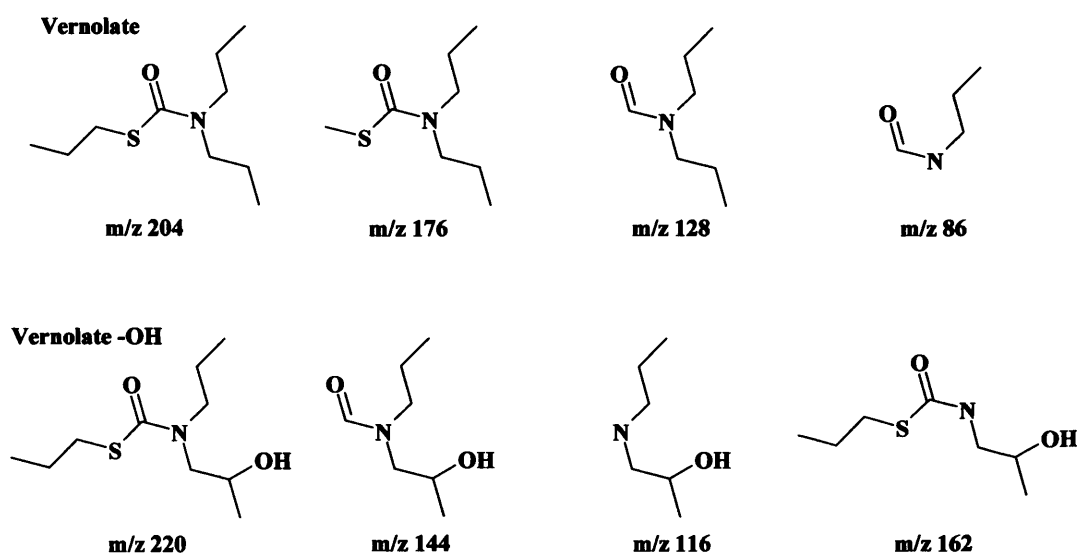

Figure 96 The chemical structures of vernolate and hydroxylated vernolate alongside structures of fragments of these compounds that correspond to the m/z ratios of peaks identified during MS^2 analysis of the reactions (Figure 95). As for the hydroxylated EPTC structures (Figure 93), the position of vernolate modification could occur at alternative points along either of the propyl chains of this compound, but the position indicated is favoured by selected cytochromes P450 (33,270). The fragment that lacks a propyl chain, and has an m/z ratio of 162, represents the structure of N-dealkylated vernolate. Unlike the *Rhodococcus erythropolis* homologue that predominantly performs this reaction with thiocarbamate compounds, the mass spectra of the CYP116B1-mediated reactions in Figure 95 identify this as a minor product, thus suggesting that the *R. metallidurans* monooxygenase preferentially hydroxylates such substrate compounds.

In conclusion, the mass spectroscopy studies presented here indicate that *R. metallidurans* CYP116B1 is capable of performing hydroxylation of thiocarbamate herbicides, and favours, as is implied by kinetic data, vernolate as a substrate. The data also indicate that, akin to a homologous protein from *R. erythropolis*, N-dealkylation may also be catalysed, albeit to a far lesser extent. The data confirm that, in all cases, hydroxylation occurs on either of the N-propyl chains, although it cannot confirm the exact carbon at which this occurs. Studies of other cytochromes P450, such as human

CYP2E1, have revealed that hydroxylation of product usually occurs at the ω to ω-2 positions of alkyl chains (271), whilst bacterial systems, such as P450 BM3, frequently favour the ω-1 position (33,270). Thus it is postulated that CYP116B1 also modifies the thiocarbamates at this position. Further support for CYP116B1-mediated propyl hydroxylation comes from studies of *Rhodococcus* sp. JE1 by Dick *et al.* that identify that the major metabolite of EPTC degradation by this organism is one hydroxylated on the propyl chain of the thiocarbamate (272). Evidence for activity in another *Rhodococcus* strain, which is most likely mediated by a ThcB homologue, thus suggests that hydroxylation of the thiocarbamates by CYP116B1 is a credible route for degradation of these compounds.

Importantly, the data verify the findings of steady-state and optical data presented in this study of the purified *R. metallidurans* protein, confirming that this redox-partner-fused system is replete of its redox centres, and that the reductase facilitates the transfer of electrons from coenzyme to the P450 domain, making the catalytic activity of CYP116B1 possible. The mass spectroscopy data confirm that thiocarbamates are metabolised by CYP116B1, although they are unlikely to be the physiological substrates for this cytochrome P450. It is more conceivable that CYP116B1 has a physiological role unrelated to thiocarbamate degradation, and that this interaction arises from these compounds being structurally similar to the true substrate or substrate class. The fact that CYP116B1 catalyses reactions with these man-made compounds may indicate that this monooxygenase has a role in xenobiotic degradation and clearance, as do the cytochromes P450 of the human liver (271), although this will not be resolved until its true physiological or other role(s) in *R. metallidurans* are determined.

4.22 The redox potentiometry of *R. metallidurans* CYP116B1

The studies of Mtb CYP51 in Chapter 3 introduced various spectroscopic techniques for the characterization of cytochromes P450, including EPR, resonance Raman, and UV/Visible absorption spectroscopy. Whilst these studies were useful in identifying various facets of this monooxygenase, and the heme contained therein, they reported little with regard to the thermodynamic properties of CYP51. Thus, in order to identify the reduction midpoint potentials of this *M. tuberculosis* enzyme in both ligated, and ligand-free forms, the well-characterized technique of anaerobic spectroelectrochemistry, which exploits optical redox titrations, was utilised (117,234). These data indicated a heme iron redox potential of −375 mV for Mtb CYP51, demonstrating that Mtb CYP51 has thermodynamic properties similar to other well characterized cytochromes P450, including P450cam and P450 BM3. Consequently, a parallel study of *R. metallidurans* CYP116B1 was performed with the aim of gathering further data to confirm that this monooxygenase has redox properties and heme iron potential typical of the P450s, and to detail any effects of substrate binding on heme iron potential. Previous work on systems such as *B. megaterium* P450 BM3 (17,117), as well as the CYP51 data in Chapter 3.17, has reported the redox potentials of the various redox components of the P450 reaction pathways; identifying how electron transfer may be more thermodynamically favourable in the presence of substrate due to substrate-induced increases of the heme iron redox potential, and thus how substrate binding can influence electron transfer rates in the system. In this study it was hoped that the reduction potentials of the three redox centres of CYP116B1 may be determined, revealing any thermodynamic barriers to electron transfer through the system and how these may be altered by the binding of the newly-identified substrates of this P450. These data would thus permit comparison of *R. metallidurans* CYP116B1 with Mtb CYP51 and, perhaps more relevantly, with the fused P450 systems of *Rhodococcus* sp. NCIMB 9784 and *B. megaterium*.

The reduction potential titrations for CYP116B1 were performed using the same method as for the CYP51 studies described in Chapter 3.17. Data were recorded at room temperature in the anaerobic conditions of a Belle Technology glove box maintained at less than 2 ppm oxygen. Enzyme was diluted to approximately 8 μM in argon-degassed 100 mM potassium phosphate buffer (pH 7.0) containing 10 % glycerol, following the elimination of residual oxygen from the sample by passing it down a pre-

290

equilibrated BioRad Econo-Pac 10DG desalting column. Following the method of Munro *et al.* (17), 7 µM 2-hydroxy-1,4-naphthoquinone, 2 µM phenazine methosulfate, 0.3 µM methyl viologen, and 1 µM benzyl viologen were added to the CYP116B1 sample prior to the start of data recording in order to enhance the electronic interactions between the electrode and the protein. Small volumes (typically 0.2 – 1 µl) of a concentrated sodium dithionite solution (typically 1 – 10 mM), also prepared in degassed 100 mM KPi buffer, were added to the enzyme sample and the system was allowed to equilibrate for 10 minutes before an absorption spectrum of CYP116B1 was recorded and the applied potential noted. The spectra of CYP116B1 were recorded between 250 and 800 nm using a Cary UV-50 Bio UV-Visible spectrophotometer as the enzyme was gradually reduced by the additions of sodium dithionite. Concomitantly, the potential of the protein solution was recorded using a Pt/Calomel electrode (Thermo Russell Ltd.) linked to a pH meter (Hanna pH 211) reading in mV. When no further reduction could be achieved by dithionite additions, hysteresis was checked for by performing a reverse titration in which the sample is gradually oxidised by the addition of aliquots of a potassium ferricyanide solution. The spectral data collected during the redox titration (Figure 97) were corrected for baseline shift and reduction potentials normalised to a standard hydrogen electrode, by the addition of + 244 mV to each value, prior to analysis. For CYP116B1 it was hoped that deconvolution of the reduction potentials of the heme, FMN, and iron-sulphur centres could be achieved, and thus the data were analysed at wavelengths that would correspond to these centres in different phases of the redox titrations. As detailed below, appropriate wavelengths for determination of reduction potentials centres in the reductase and heme domains transpired to be at ~407 and ~560 nm respectively (Figure 98a and b). By plotting the absorbance changes at each wavelength associated with dithionite-induced reduction *versus* the normalised potentials, curves representing the reduction of the heme iron and the reductase centres were produced. These curves were fitted to the appropriate Nernst equation (Equation 6, Chapter 3.17), thus allowing for the determination of the midpoint reduction potentials of the redox centres of the *R. metallidurans* redox-partner-fused P450 system. Additionally, in order to investigate the influence of the substrate compounds identified in the previous section (Chapter 4.21), a duplicate redox titration was performed in the presence of 2 mM vernolate. This compound was selected over EPTC as it was identified as producing greater optical shifts of the CYP116B1 Soret

291

band, as well as inducing faster rates of coenzyme oxidation in steady-state kinetic assays.
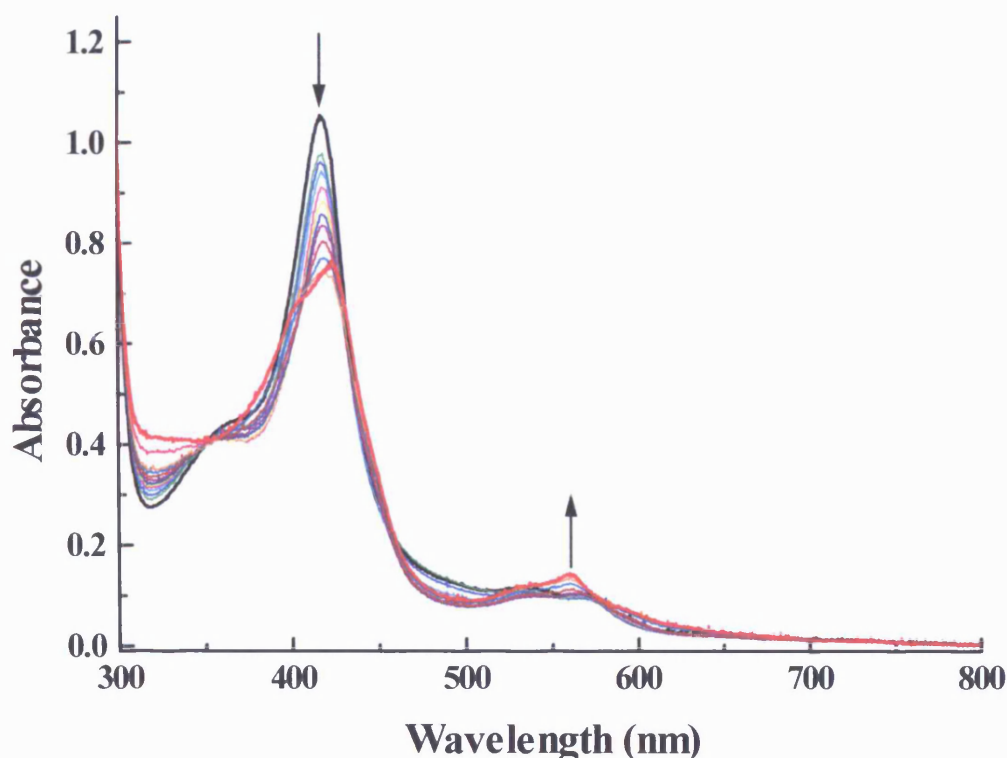

Figure 97 Selected UV/Visible spectra recorded during the reduction potential titration of CYP116B1 (~8 μM) with sodium dithionite and potassium ferricyanide. The spectrum of the fully oxidised enzyme (black) recorded prior to beginning the titration identifies the characteristic signal of a cytochrome P450, with a Soret band at 418 nm and alpha and beta bands at 568 and 531 nm, respectively. During the titration, a Soret band shift to longer wavelengths and the formation of a peak at 559 nm are observed, which are reminiscent of the shifts seen with CYP51 from *M. tuberculosis* (Chapter 3.17, (159)). Isosbestic points at approximately 352, 430, and 459 nm suggest a clean transition from oxidised to reduced CYP116B1 (and perhaps indicate that FMN and iron-sulphur centres have only small absorption changes at these wavelengths in this range), whilst the reduction-induced decrease in absorbance between 450 and 500 nm indicates the presence and reduction of the FMN, and probably the iron-sulphur, redox centres. The arrows denote directions of absorbance change during the reductive titration.

The UV/Visible absorption spectra in Figure 97 show that as CYP116B1 is reduced the Soret band at 418 nm firstly decreases in intensity, and then shifts towards longer wavelengths. These spectral changes are accompanied by the appearance of a peak in between the alpha and beta bands of the oxidised enzyme, centred at approximately 559 nm. This feature is of greater intensity than the original signals for oxidised CYP116B1 in this region. The spectral changes observed for CYP116B1 during the redox titration

are distinct from those seen for certain other cytochromes P450 characterized to date (e.g. P450 BM3 and P450cam, (69,192)), but are very similar to those seen for the Mtb CYP51 redox titration in Chapter 3.17, as well as for CYP144 and CYP121 from *M. tuberculosis* (unpublished data). Thus, it appears that spectral transitions observed here are not confined to the CYP51 and CYP116B1 systems. Data from the Mtb CYP51 study (Chapter 3.17) indicates that these spectral perturbations correspond to protonation of the proximal cysteinate ligand of the heme that occurs over the time course of the titration (i.e. P420 formation). Spectral changes observed are reversible on reoxidation of the enzyme, and there is no hysteretical behaviour. The relative magnitude of the 559 nm peak is greater for CYP51 than CYP116B1, perhaps suggesting that the Mtb enzyme forms a greater amount of thiol-coordinated heme iron at equilibrium than does CYP116B1 (i.e. the thiolate is more susceptible to protonation during reductive titration). However, differences in extinction coefficients for the two enzymes in this region could also explain the perceived difference. The former explanation appears borne out by the fact that the CYP51 CO-adduct collapses rapidly following formation (Chapter 3.4), whilst the corresponding adduct of CYP116B1 is shown to be relatively stable in Figure 65 (Chapter 4.8), which suggests that there is negligible thiolate protonation in the period between reducing the enzyme with dithionite and recording the reduced spectrum. Spectra obtained during the redox titration are collected at equilibrium – typically 10 – 15 minutes after reduction. In this period protonation of the CYP116B1 thiolate appears to occur. The difference in apparent rate of protonation of the CYP51 and CYP116B1 cysteine thiolates likely derives from structural differences between these proteins in the regions of their heme macrocycles.

Plots of the spectral changes at 407 and 560 nm *versus* the normalised potentials, fitted with the Nernst function (Equation 8, Chapter 3.17), are shown in Figure 98. The curve fitting of the 560 nm data, which relates directly to the Fe^{3+}/Fe^{2+} transition, determines the midpoint reduction potential of the heme iron as -396 ± 12 mV. The error range on this value reflects the fact that the potential is sufficiently negative that the heme iron is not completely reduced by dithionite by the end of the titration. This value is slightly more negative than that determined for Mtb CYP51 (–375 mV), and lies within the range of redox potentials previously identified for substrate-free cytochromes P450, which varies from approximately –427 mV for P450 BM3 to –300 mV for P450cam (Chapter 3.17, (69,192)). Furthermore, this potential is similar to the

value of –423 mV reported for CYP116B2 from *Rhodococcus* sp. NCIMB 9784 (130), and suggests that these two proteins, which are 66 % identical in amino acid sequence, are thermodynamically similar with respect to the redox potential of their heme iron. Hence, these data indicate that the substrate-free CYP116B1 heme has thermodynamic properties typical of the cytochromes P450, although the reduced enzyme appears prone to protonation of the heme thiolate. However, in all other respects (e.g. from data collected in Chapters 4.8, 4.15, and 4.16 using such methods as EPR, resonance Raman, and UV/Visible spectroscopy of oxidised enzyme and its ligand-bound forms), the properties of CYP116B1 are entirely consistent with those of an 'archetypal' P450 monooxygenase.

a)
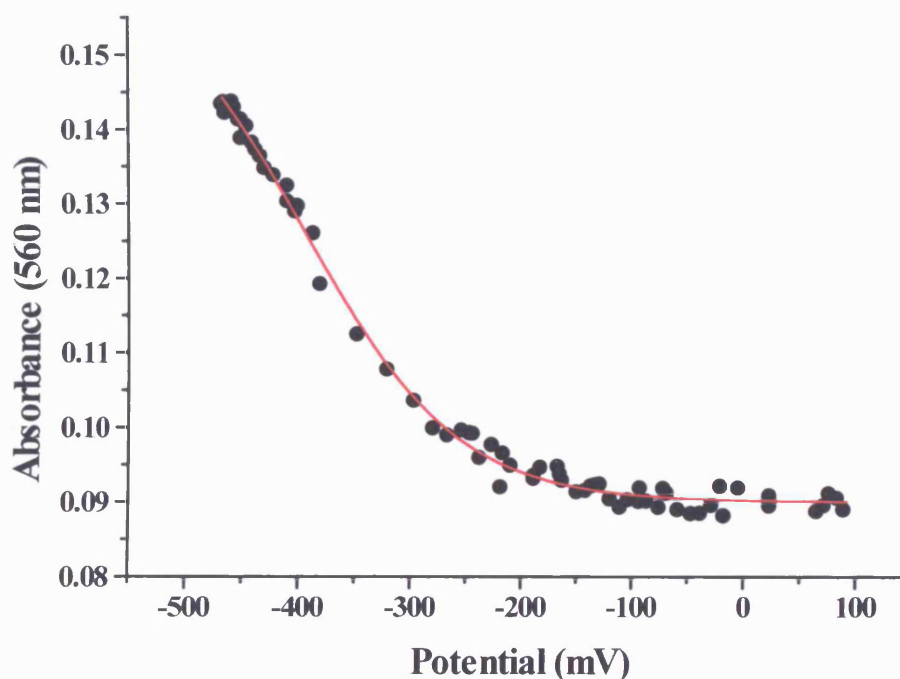
Figure 98 a) The plot of absorbance change at 560 nm *versus* potential (mV) for the determination of the substrate-free CYP116B1 heme mid-point potential. Fitting with a single electron Nernst equation (Equation 8, Chapter 3.17) produce a mid-point potential of –396 ± 12 mV for the Fe^{3+}/Fe^{2+} transition of the heme iron, however this value serves only as a guide to the heme potential of CYP116B1 as the end point of the titration cannot be clearly defined. This value is comparable with the potential reported for CYP116B2 from *Rhodococcus* sp. NCIMB 9784, as well as those for P450 BM3 and P450cam (69,192). **b)** The graph for the estimation of the reductase/FMN mid-point potential utilising the absorbance changes at 407 nm plotted *versus* the measured potentials. The mid-point potential was calculated as – 159 ± 5 mV, a value similar to that reported for the FMN centre of phthalate dioxygenase reductase (–174 mV, (260)), although somewhat different to the midpoint potential reported for the FMN of RhF from *Rhodococcus* sp. NCIMB 9784 (–243 mV, (130)). All potentials are shown in mV and are normalised against a standard hydrogen electrode (SHE).

294

b)
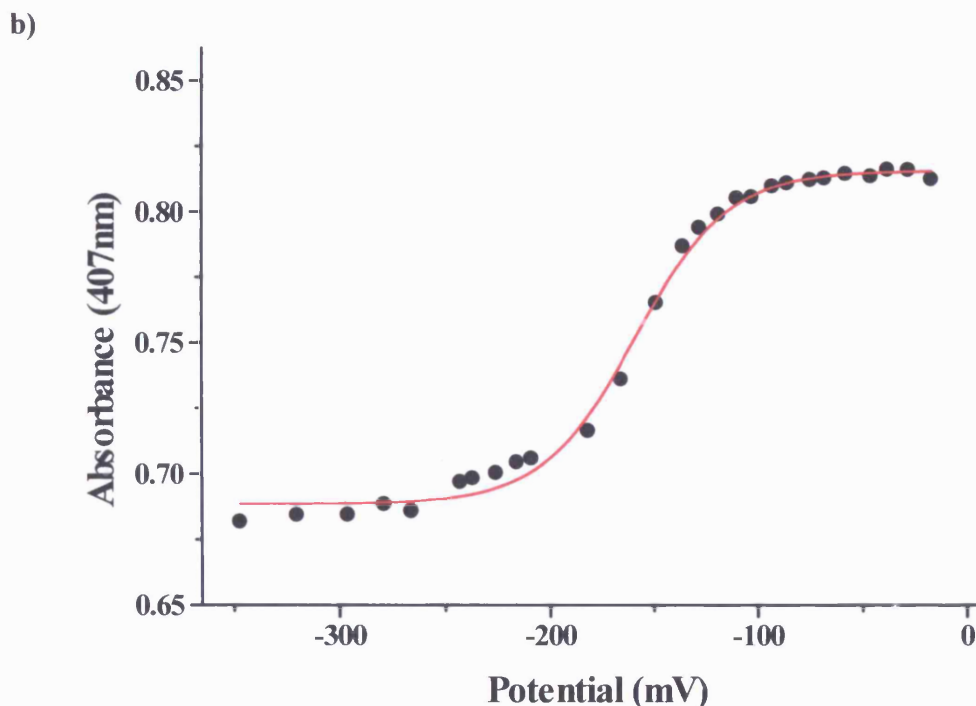
The plot of absorbance change at 407 nm versus potential shown in Figure 98b reports on absorption changes in the region of the Soret band of CYP116B1 that occur during the redox titration. The reason that absorption changes in this region correspond to redox transitions of FMN and iron-sulphur centres (as opposed to heme) is that they occur in a more positive phase of potential change and are apparently complete before any substantial changes in absorption of the heme. Examination of Figure 98b shows the completed A_{407} transition in the range between 0 and $\sim$ –250 mV, and also shows the beginning of absorption changes due to the heme centre that occur at more negative potentials. The apparent midpoint potential from the data presented in Figure 98 is – 159 ± 5 mV, and almost certainly encompasses the absorption changes associated with the reduction of the FMN between quinone (oxidised) and hydroquinone (2-electron reduced) forms, as well as the absorption change associated with the reduction of the iron sulphur cluster. Thus, absorption changes in the Soret region are clearly complex and, across the entire potential range examined, involve optical transitions from all three redox centre. However, reduction of the heme iron occurs at more negative potential than does reduction of the other clusters. The determined heme potential is approximately 230 mV more negative than that estimated as the midpoint for the remaining two centres. The redox transition of the heme iron is more clearly observed at 560 nm, where there is clearly no contribution from any neutral blue semiquinone

295

species and only changes in heme spectrum contribute to the observed absorption change. A fit of the absorption changes at 485 nm, a region that likely relates more closely to flavin absorbance and is less influenced by the heme Soret band, produces a similar redox potential to that determined at 407 nm (−145 ± 5 mV), providing further confidence that the potential determined does relate accurately to that for the FMN (and iron sulphur cluster) of CYP116B1. The incorporation of FMN and an iron-sulphur cluster into CYP116B1 has been confirmed by both UV/Visible and EPR spectroscopy (Chapters 4.8 and 4.15), and as both these redox centres are likely to decrease in absorption intensity between 350 and 500 nm on reduction, the potential (−159 ± 5 mV) reflects contributions from each of these cofactors. The midpoint potential is comparable to those identified for FMN centre in phthalate dioxygenase reductase from *Ps. cepacia* (−174 mV, (260)) and the FMN cofactor of human CPR (−168 mV, (17)). However, it should be noted that the FMN centre in CPR is that which mediates electron transfer to the heme iron (accepting electrons from FAD, which in turn is reduced by NADPH). In CYP116B1, the FMN is the cofactor that accepts electrons from NADPH, prior to mediating electron transfer to heme iron via the iron sulphur cluster. This composite potential is less negative than the potential of −243 mV reported for the reductase component of CYP116B2 from *Rhodococcus* sp. NCIMB 9784 (130), although this disparity may be due to structural differences, as the reductase domains of these homologous proteins display greater amino acid sequence divergence than the heme domains. Also, the detachment of the reductase from its heme domain likely leads to perturbation of the redox potential of the flavin. Further analysis of the redox properties of the CYP116B1 FMN and iron sulphur cofactors is clearly required to resolve the individual potentials of these centres, and (for the iron sulphur cluster), this could be done by repeating the titration at higher protein concentration and freezing samples at various stages for radical measurements by EPR. In this way, the potential of the iron sulphur cluster could be determined from a fit of radical quantity versus applied potential to a single electron Nernst function. What does appear clear from the optical redox transitions is that there is negligible FMN semiquinone development, and thus the midpoint reduction potential for the semiquinone/hydroquinone redox couple of this flavin is probably more positive than that of the oxidised/semiquinone couple. With the assumption that the contribution of the iron sulphur centre to absorption change at 407 nm is much less than that of the FMN (as also appears to be true at 485

nm), the value of −159 mV is thus likely to be an accurate reflection of the midpoint potential of the FMN centre of the *R. metallidurans* protein.

As is the case for the P450 BM3 system (117), there appears to be a large thermodynamic gradient against which electrons must be transferred in order for reduction of the heme by the reductase to occur at a significant rate. An even more daunting barrier is observed for the Mtb CYP51 relative to the potential of its ferredoxin partner (Chapter 3.17, (159)). As has been shown in selected P450 systems, thermodynamic barriers may be overcome if substrate binding raises the heme potential to a level more favourable for electron transfer from the redox partner (i.e. the FMN and iron sulphur centres in CYP116B1). This occurs in the well-studied P450 BM3 system from *B. megaterium* and in *Ps. putida* P450cam (69,117). In such systems, a control mechanism operates whereby non-productive electron transfer is disfavoured in the absence of substrate, thus preventing futile cycling of the heme iron and non-specific reduction of oxygen. Hence it is postulated that the binding of the true substrate of CYP116B1 will induce a change in the potential of the heme that will move the thermodynamic equilibrium of the system to a point that is more favourable to electron transfer from the reductase domain. Redox titrations of CYP116B1 in the presence of vernolate, which increases the rate of CYP116B1-mediated coenzyme oxidation (Chapter 4.20), and which is oxygenated by this *R. metallidurans* protein (Chapter 4.21), were performed to determine whether the CYP116B1 heme potential could be perturbed on binding of this ligand. Unfortunately, over the prolonged duration of the redox titration, the high concentration of this compound required to approach saturation of the P450, as determined from the K_m value in steady-state assays in Chapter 4.20, caused excessive turbidity and protein aggregation that made the determination of the redox potential impracticable. Hence, as the man-made thiocarbamate herbicides are unlikely to be natural substrates, and until a physiological substrate for CYP116B1 is identified, a true picture of substrate-induced heme potential shift in CYP116B1 may not be possible. However, the fact that both vernolate and EPTC induce increased rates of coenzyme oxygenation linked to substrate oxidation suggests that these compounds do induce heme iron spin-state shift and elevation of heme iron potential, although these phenomena may be difficult to follow due to the low aqueous solubility of the molecules. Based on preceding studies of enzymes such as P450 BM3, P450cam, and Mtb CYP51, this positive heme iron potential shift is likely to be of a magnitude of approximately +150 mV (69,117).

This chapter presents the first spectroscopic and biophysical characterization of a novel fusion of a cytochrome P450 and its redox partner proteins from *Ralstonia metallidurans*. The data identify that the P450 domain of this enzyme is typical of the cytochromes P450, demonstrating characteristic features in a range of spectroscopic studies (e.g. UV-Visible absorption spectroscopy, resonance Raman, and EPR), whilst kinetic studies identify that the reductase domain is capable of successfully transferring electrons from a reductant to the heme iron, and has a significant preference for NADPH over NADH. Furthermore, these studies led to the determination of substrates for this P450, although these thiocarbamate herbicides are perhaps unlikely to be the physiological substrate of CYP116B1. In the next chapter, the dissection of CYP116B1 into its constituent domains is described. These studies were performed in order to investigate both regions of the protein in isolation, as well as allowing for the possibilities of structural studies and better resolution of spectral and biophysical properties of each domain.

299

Chapter 5

Characterization of the heme and reductase domains of

Ralstonia metallidurans CYP116B1

.

5.1 General information

The previous chapter (Chapter 4) describes the characterization of the redox-partner-fused CYP116B1 of *R. metallidurans*, from initial cloning, expression, and purification steps through to detailed spectroscopic and kinetic investigations. The studies reveal a number of insights into this unusually fused protein, such as artificial electron acceptor reduction rate and evidence that CYP116B1 may have a role in xenobiotic degradation in its host organism, from its ability to oxygenate herbicide molecules (Chapter 4.19 and 4.21). However, some of the more detailed analyses, including studies of the iron-sulphur cluster and redox potentiometry, are complicated by the presence of multiple domains and cofactors in the protein. Hence, in this chapter the dissection of CYP116B1 into its constituent heme and reductase domains is described, with the aim of confirming the discrete domain construction of the enzyme, and to produce domains that can be kinetically, spectroscopically and structurally characterized in isolation.

There is a strong precedent for this approach in the study of redox-partner-fused cytochromes P450, with the majority originating from the studies of P450 BM3 from *Bacillus megaterium*. Indeed, more than thirty papers have been published on the domains of P450 BM3, ranging in topic from redox properties to structural studies (34,117), whilst other examples come from the dissections of human CPR and CYP116B2 (122,185). These studies have resulted in the clarification of data gathered for the full-length enzymes, as well as generating structural information that may not have been possible without dissection (34). It is hoped that similar results will be obtained in what is a logical progression in the study of the redox-partner-fused CYP116B1. Hence, this chapter firstly describes attempts to clone and express the distinct heme and reductase domains of the *R. metallidurans* protein, followed by spectroscopic and thermodynamic analyses of the resultant proteins that will allow further characterization of this novel cytochrome P450 and further comparison with previously characterized cytochromes P450 and their redox partners.

5.2 Cloning of the CYP116B1 heme and reductase domains

In order to generate the heme and reductase domains of CYP116B1, it was necessary to identify a suitable position for the dissection of the full-length protein. Alignments with the amino acid sequences of *Rhodococcus erythropolis* CYP116A1, which shows a high level of sequence identity with the CYP116B1 heme domain (Chapter 4.2), and a number of oxidoreductases, including those of *B. cepacia* and *Rhodococcus* sp. RHA1, identifies a region of approximately 20 amino acids that appears to form a linker region between the two domains of CYP116B1 (Figure 99). Polypeptide linker regions of similar length have been identified by Roberts *et al.* (124), and Govindaraj and Poulos (273) in respective studies of CYP116B2 and P450 BM3. However, the most appropriate point of dissection could not be determined from direct comparisons between these sequences, as they lack any apparent homology. For this reason it was decided that both the heme and reductase domains of CYP116B1 would be produced to incorporate part of the apparent linker region, in case this was significant to the domains' folding and function.


```
TYVPNTSFRGPEHLWVEWDPARNPERTDPTVLAPRDAVRIGEPTGGTTGRTLIVERVETAAQGVSRIRLVSPDG
SYLPNTSFRGPEHVLVEWDPQQNPVFADRP--------------------LKIASKEKIARDIWSFELTDPQG
:*:**********: ***** :**  :*  .                    *  :   *. *:.:  :.*..*:*
```
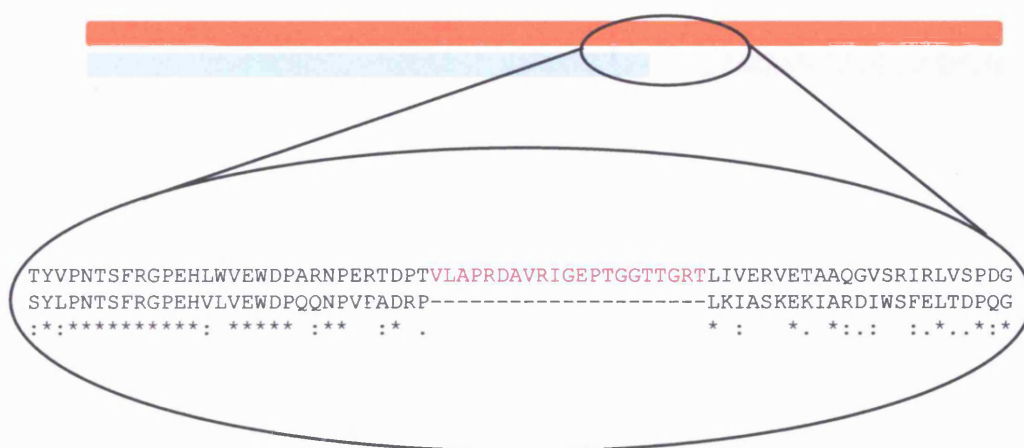
Figure 99 A schematic representation of the alignment of the amino acid sequences of *R. metallidurans* CYP116B1 (orange) with *R. erythropolis* CYP116A1 (light blue) and *B. cepacia* phthalate dioxygenase reductase (grey). The highlighted region of the amino acid sequences corresponds to the point at which there is no homology protein and CYP116B1, thus identifying the likely linker region between the heme and reductase domains of *R. metallidurans* CYP116B1 (red). Consequently these alignments enabled the identification of suitable positions for the incorporation of start and stop codons into the CYP116B1 nucleotide sequence in order to facilitate cloning of the reductase and heme domains of this *R. metallidurans* protein.

Having determined the position of the linker region of CYP116B1, oligonucleotide primers were designed against the relevant sections of the nucleotide sequence of the *R. metallidurans* CYP116B1 in order to both isolate the genes encoding the two domains, and to retain parts of the polypeptide linker in both the P450 and reductase constructs. A mutagenic approach using the CYP116B1 pET-15b plasmid, rather than PCR from genomic DNA, was employed to sub-clone the domains from the full length construct. This pET-15b construct, which incorporates a purification-aiding N-terminal His-Tag onto the expressed gene, was created at the same time as the pET-11a construct (Chapter 4.4), but was not utilised for production of full length CYP116B1 due to successful expression of intact CYP116B1 from the latter construct. The CYP116B1 pET-15b plasmid was generated in exactly the same manner as the pET-11a construct, resulting in an 8068 bp plasmid. Due to the similarity in size of two constructs, the verification of correct CYP116B1 pET-15b formation by *Sma*I, *Sca*I, and *Sal*I restriction digests resulted in almost identical restriction patterns to those obtained for CYP116B1 pET-11a (Chapter 4.4), and are hence not shown.

To create the heme domain, a pair of oligonucleotide primers were designed that would integrate two in-frame stop codons into the linker region of the enzyme (Table 22). Hence, as this mutation (which is incorporated into a section of the linker) ensures that there is no read-through of the CYP116B1 reductase component, there is no requirement for further cloning steps prior to expression trials. The creation of the reductase domain of the *R. metallidurans* enzyme required the set of mutational oligonucleotides that are shown in Table 22. The primers introduce a mutation into the CYP116B1 pET-15b plasmid that integrates a start codon and an *Nde*I site into the polypeptide linker region at the proposed start of the reductase domain. The reductase domain fragment can hence be separated from the heme domain by an *Nde*I/*Blp*I double digest of the mutated CYP116B1pET-15b plasmid. Subsequent ligation of this fragment into *Nde*I/*Blp*I-cut pET-15b results in the creation of the reductase domain-encoding plasmid. Hence, this method requires only one ligation step during the creation of two domains, rather than several more that would be required using a conventional PCR cloning route. Bioinformatic analysis of the resultant amino acid sequences of the heme and reductase domains using the web-based Protparam program (www.expasy.org) identifies the former (heme domain) to be a 450 amino acid protein with a mass of 50.713 kDa and a pI of 5.43, whilst the latter (reductase domain) to be composed of 325 amino acids, with a pI of 6.17, and a mass of 35.080 kDa.

Primer	Primer sequence (5'→3')
HD mutation (Fwd)	GACGGTGCTGGCGCCATGATAGGCGGTCCGCATCGG
HD mutation (Rev)	CCGATGCGGACCGCCTATCATGGCGCCAGCACCGTC
RD mutation (Fwd)	GTGACGCGGTCCATATGGGCGAACCGACTGGCGG
RD mutation (Rev)	CCGCCAGTCGGTTCGCCCATATGGACCGCGTCAC

Table 22 The DNA sequences of the oligonucleotide primer pairs designed for the creation of the heme domain (HD) and reductase domain (RD) of *R. metallidurans* CYP116B1 by mutagenesis of the CYP116B1 pET-15b plasmid. The heme domain primers integrate two different in-frame stop codons (TGA and TAG, identified in red) within the linker region of the full-length gene, thus preventing translation beyond this point. The bases identified in green in the primers for the generation of the reductase domain highlight the *Nde*I restriction site to be introduced into the linker region of the CYP116B1 gene. As the *Nde*I restriction site intrinsically incorporates a start codon (ATG), this mutation serves a second purpose as it also provides the point from which protein translation will begin. This *Nde*I site is utilised, along with the *Blp*I site already present in the gene, to isolate the reductase domain and insert it into *Nde*I/*Blp*I-digested pET-15b, thus creating the CYP116B1 reductase domain-encoding plasmid. The primers were designed against the published *R. metallidurans* amino acid sequence (http://genome.ornl.gov/microbial/rmet/) and synthesised by the Protein and Nucleic ACid Laboratory (PNACL), University of Leicester.

The CYP116B1 heme domain-encoding plasmid (HD pET-15b) was created from the CYP116B1 pET-15b plasmid described above by a PCR-based mutagenesis method previously used by Girvan *et al.* (37). In order to introduce two in-frame stop codons into the CYP116B1-encoding gene, a 50 μl PCR reaction was subjected to 18 cycles of (a) denaturation at 95 °C for 30 seconds, (b) annealing at 60 °C for 1 minute and (c) polymerisation at 68 °C for 18 minutes, in a Techne PHC-2 thermal cycler. The reaction contained 100 ng CYP116B1 pET-15b, 400 μM dNTPs, 3 μl 30 % DMSO, 5 μl PFU 10x buffer, 5 units Pfu Turbo (Stratagene Ltd, Cambridge, UK), ddH$_2$O, and 200 ng of each of the heme domain mutation primers (Table 22). Subsequently, the reaction mixture was incubated for 1 hour at 37 °C with *Dpn*I in order to remove methylated template DNA, and retain only the mutated plasmid. Initial verification of the success of the PCR reaction was performed by running the *Dpn*I-digested reaction against an aliquot of the PCR reaction removed prior to the restriction digest (Figure 100). The presence of a band at 8068 bp in both lanes confirmed that DNA present in the *Dpn*I-digested sample resulted from the PCR reaction rather than the template DNA, and that the reaction was thus successful.
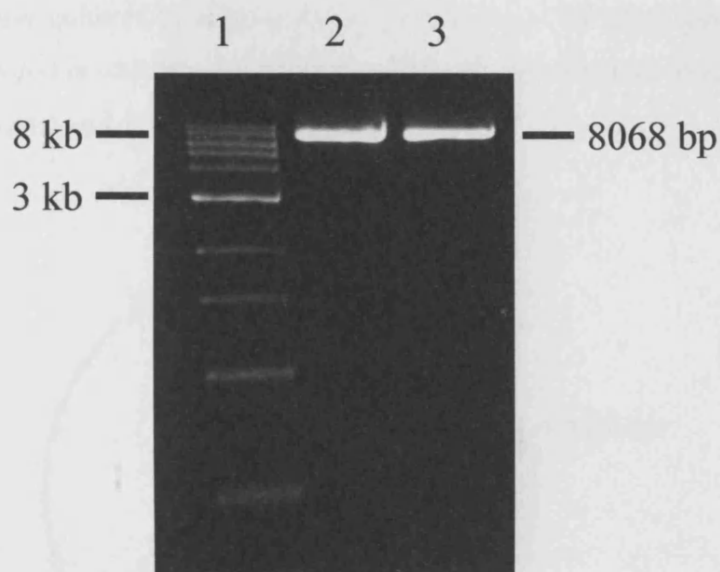
Figure 100 The *Dpn*I restriction digest of the 8068 bp HD pET-15b plasmid, created by mutagenesis of the CYP116B1 pET-15b plasmid, run alongside a 1 kb DNA ladder (Lane 1). The mutation, performed by PCR, introduced two in-frame stop codons into the linker region of the full length gene to allow only heme domain transcription. The bands at 8068 bp in Lanes 2 (Pre-*Dpn*I digestion) and 3 (Post-*Dpn*I digestion) indicate that a plasmid of the correct size has been replicated during the PCR reaction. The band that persists in Lane 3 after the restriction digest confirms that the DNA present is the result of the PCR reaction, and not the methylated template (CYP116B1 pET-15b) DNA that is the target of *Dpn*I. The digests were run on an ethidium bromide-containing 1 % agarose gel and visualised by exposure to UV light.

In order to generate sufficient material for restriction digest confirmations and later work, the newly-created plasmid (HD pET-15b, Figure 101) was transformed into competent NovaBlue cells (Novagen). In Chapter 4.4, JM109 cells were used for this purpose; however NovaBlue competent cells were used from this point onwards due to their increased transformation efficiency and (hence) requirement for less DNA. The transformation involved co-incubating 1 µl of the HD pET-15b plasmid (roughly 10 ng of DNA) and 20 µl cells on ice for 5 minutes, before heat shocking at 42 °C for thirty seconds. The cells were then returned to ice for two minutes prior to the addition of 250 µl SOC medium, and incubation at 37 °C for 1 hour. Aliquots of 100 µl were then plated on ampicillin-enriched agar plates and allowed to grow overnight at 37 °C. Resultant colonies were picked using sterile technique and cultured at 37 °C in 5 ml LB media enriched with ampicillin until O.D.$_{600}$ = 0.4 − 0.6. Glycerol stocks were then

prepared from these cultures by adding 100 µl glycerol to a 500 µl aliquot of the cells, and these were stored at –80 °C. Additionally, plasmid was extracted from the cultures by Miniprep (Qiagen) and stored at –20 °C until required.
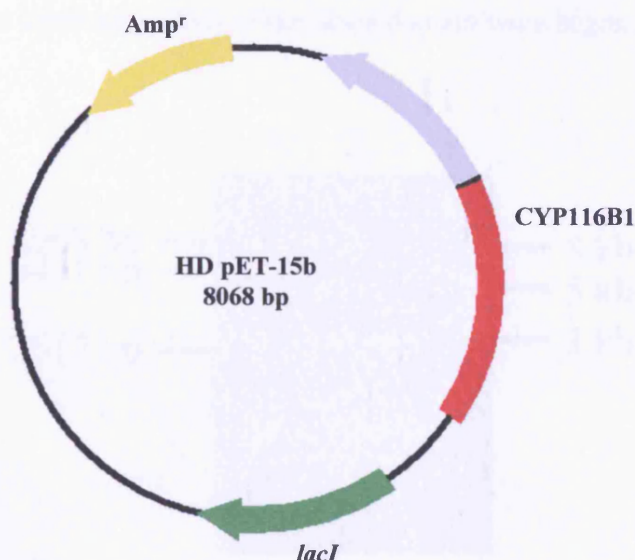

Figure 101 A plasmid map of the 8068 bp HD pET-15b construct that was created by the introduction of two stop codons (TGA and TAG) into the region of the full-length CYP116B1 gene that relates to the linker between the heme and reductase components. The map identifies significant plasmid features, including regions encoding ampicillin resistance (Amp^r), and the *lacI* gene that permits IPTG-inducible gene expression. As the reductase domain-encoding region is present in the plasmid, but is not translated due to the introduced stop codons, this region of the CYP116B1 gene is identified in grey. The purification-aiding His-Tag that is incorporated at the N-terminal of the gene by this plasmid is not shown due to its small size (18 bp). The map was created using Plasmid software (www.biovisualtech.com).

Further confirmation of the creation of the plasmid for heme domain expression was sought by *Nde*I and *Sca*I restriction digests. The *Nde*I digest cuts the plasmid once in the gene-encoding region to produce a band of 8068 bp, whilst the *Sca*I digest cuts the plasmid once in the insert and once in the vector region to give bands of 2617 and 5451 bp. The results of these digests, visualised on an ethidium bromide-containing agarose gel, are shown in Figure 102, and confirm the presence of the HD pET-15b plasmid. As the mutation does not insert a new restriction site into the CYP116B1 gene, nucleotide sequencing was required for verification of the introduction of the stop codons. This was performed by PNACL (University of Leicester) using the appropriate oligonucleotide sequencing primers (primers c, d, e, and f, Table 14, Chapter 4.3),

which were previously used to confirm the correct cloning of the full-length CYP116B1 gene. The results of this sequencing established that the two stop codons had indeed been incorporated into the full-length gene at the correct position, as well as confirming that no other mutations were introduced into the gene during mutagenesis. Following obtaining these data, expression trials of the heme domain were begun.
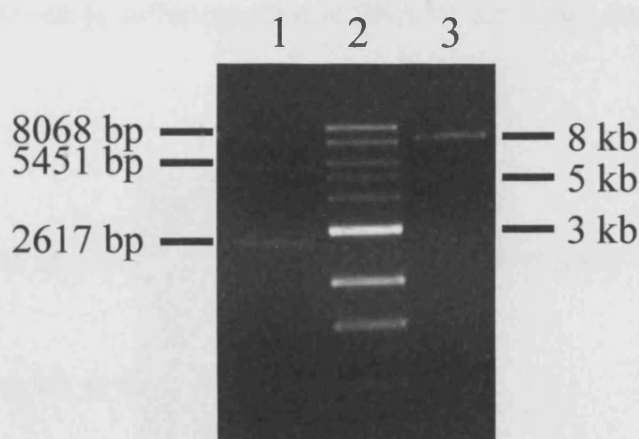

Figure 102 The *Sca*I and *Nde*I restriction digests utilised to further verify that the plasmid obtained from the mutational PCR reaction was HD pET-15b. The *Sca*I digest (Lane 1), which cuts the plasmid once in the inserted gene region and once in the vector region, results in bands at 2617 and 5451 bp, whilst the *Nde*I digest (Lane 3), which only cuts the insert, produces a single band at 8068 bp. These restriction digest patterns were as expected, and thus confirm the correct plasmid to have been replicated by the mutational PCR reaction. The gel was visualized by exposure to UV light following electrophoresis, and for size comparison the 3, 5, and 8 kb bands of the 1 kb DNA ladder (Lane 2) are identified at the right of the gel.

The insertion of an *Nde*I restriction site into the linker region of the CYP116B1 gene that would facilitate isolation of the reductase domain, and thus lead to the generation of the CYP116B1 reductase domain-encoding plasmid, was performed by mutagenic PCR. The reaction mixture utilised was identical in all respects to the reaction reported above for the heme domain mutation, with the exception that the reductase domain mutational primers listed in Table 22 replaced the heme domain primers. As previously, the reaction was subjected to 18 cycles of (a) denaturation at 95 °C for 30 seconds, (b) annealing at 65 °C for 1 minute and (c) polymerisation at 68 °C for 18 minutes, before being digested with *Dpn*I for 1 hour at 37 °C to remove the methylated DNA template.

When an aliquot of this digest was run on an agarose gel alongside a sample of the reaction reserved prior to the *Dpn*I digest, the presence of a band at 8068 bp in both lanes verified that the plasmid has been successfully replicated from the template DNA (Figure 103). Following this positive result, the reaction mixture was, as with the heme domain reaction, transformed into NovaBlue competent cells and cultured in ampicillin-enriched LB media. Glycerol stocks of the culture were taken, and a Miniprep was performed in order to obtain sufficient plasmid DNA for further cloning steps.
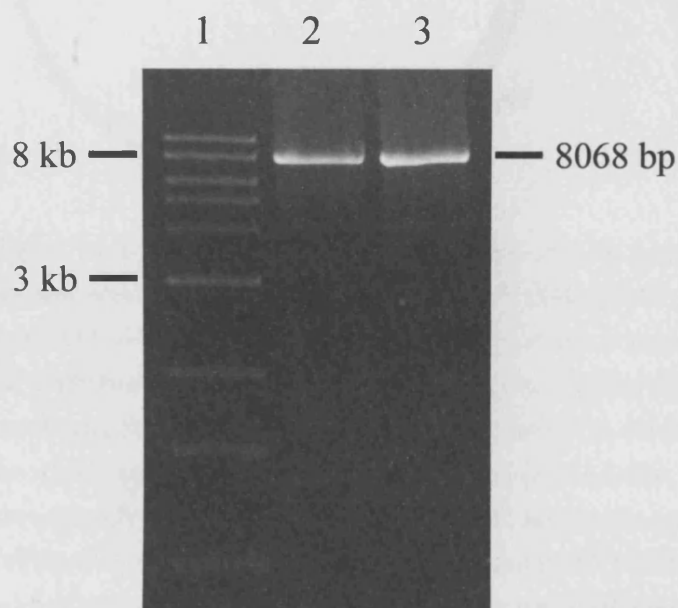
Figure 103 The PCR product from the initial step in the generation of the CYP116B1 reductase domain-encoding plasmid shown before (Lane 2), and after (Lane 3), *Dpn*I treatment, and run alongside a 1 kb DNA marker (Lane 1). The PCR was performed using the primers in Table 22 to introduce an *Nde*I restriction site into the full length gene, in order that the reductase domain could be excised by an *Nde*I/*Blp*I digest and subsequently ligated into pET-15b cut with the same endonucleases. The presence of the band at 8068 bp in Lane 3 following the *Dpn*I digest verifies that the methylated template DNA is not responsible for the observed bands, and hence that the mutagenesis reaction was successful. As previously, electrophoresis of the samples was performed on a 1 % agarose gel containing 0.25 µg/ml ethidium bromide.

Figure 104 The map of the 6701 bp RD pET-15b plasmid constructed by ligating an *Nde*I/*Blp*I-excised CYP116B1 reductase domain-encoding fragment into similarly digested pET-15b. To generate the reductase fragment, an *Nde*I restriction site, and its integral start codon, was introduced into the linker region of the full-length CYP116B1 gene by a mutagenesis reaction that involved primers indicated in Table 22. This m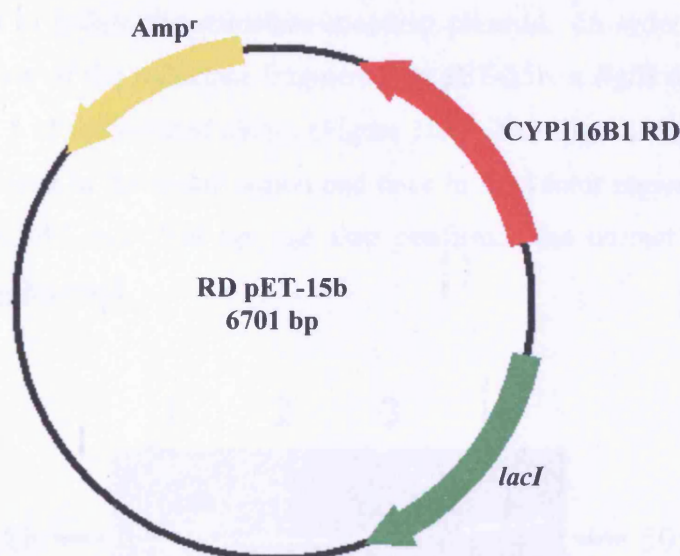utation allowed the reductase-encoding region of the gene to be isolated from the heme-encoding section by the aforementioned restriction digest. The map also identifies the region of the plasmid that encodes the expression-regulating *lacI* gene, and the gene that confers ampicillin resistance (Amp^r). This plasmid differs from the pET-11a plasmid previously used for CYP116B1 expression as it incorporates a His-Tag (6 histidine residues) at the N-terminal of the translated protein in order to aid purification. In this map, created using Plasmid software, the region pertaining to the His-Tag is not shown because of its small size.

In order to create the expression vector for the reductase domain (RD pET-15b, Figure 104), the mutated CYP116B1 pET-15b plasmid and the pET-15b vector were digested with *Nde*I and *Blp*I. The resultant 1056 bp reductase fragment and 5645 bp *Nde*I/*Blp*I-digested pET-15b fragment were purified using a Qiagen gel purification kit (Qiagen) to remove agarose and other contaminants, before a ligation reaction was carried out. The reaction, which was incubated at 4 °C overnight, consisted of 50 ng of the digested pET-15b vector, 50 ng of the reductase domain insert, 400 units of T4 DNA ligase, 10x T4 DNA ligase buffer, and ddH$_2$O. The success of the ligation was confirmed by visualisation on a 1 % agarose gel, after which the resultant reductase domain pET-15b plasmid was transformed into NovaBlue competent cells using the method described for the heme domain ligation product transformation. Resultant

colonies were cultured in ampicillin-enriched LB media before being subjected to Miniprep in order to isolate the reductase-encoding plasmid. In order to confirm the correct incorporation of the reductase fragment into pET-15b, a *Bgl*II restriction digest was performed on 3 of the isolated clones (Figure 105). This digest, which cuts the RD pET-15b plasmid once in the insert region and once in the vector region, generated the expected bands of 747 and 5954 bp, and thus confirmed the correct creation of the reductase encoding-plasmid.
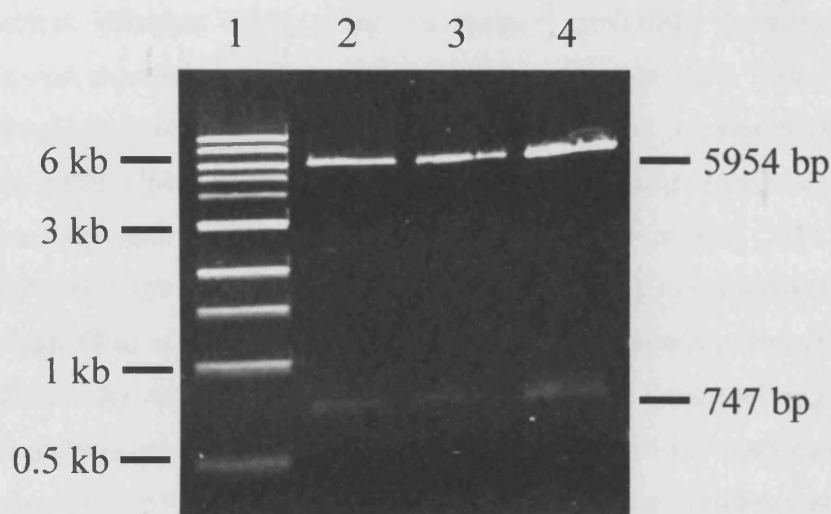
Figure 105 The *Bgl*II restriction digest of three clones of RD pET-15b (Figure 104) (Lanes 2 – 4), run alongside a 1 kb DNA marker (Lane 1). The plasmid was created by ligating the reductase gene, excised from the mutated CYP116B1 pET-15b plasmid using *Nde*I and *Blp*I, with similarly digested pET-15b. Each of the clones in Lanes 2, 3, and 4, demonstrates bands at 5954 and 747 bp that arise due to the endonuclease cutting once within the inserted gene and once in the vector, and thus confirm the correct formation of the *R. metallidurans* reductase domain expression vector. The digests were subjected to electrophoresis on an ethidium bromide-containing 1 % agarose gel, which was subsequently visualised by exposure to UV light.

Having successfully created plasmids for the expression of the separate heme and reductase components of *R. metallidurans* CYP116B1, the following section describes the transformation of these vectors into *E. coli* expression strains, and the subsequent attempts to generate, and purify, the two encoded protein domains.

5.3 Expression and purification of CYP116B1 heme and reductase domains

The completion of the mutagenesis and cloning steps for the generation of the plasmids encoding the CYP116B1 heme and reductase domains allowed for expression trials to be carried out in order identify the most favourable conditions for production of these two proteins. The HD pET-15b and RD pET-15b plasmids were transformed into HMS174 (DE3) and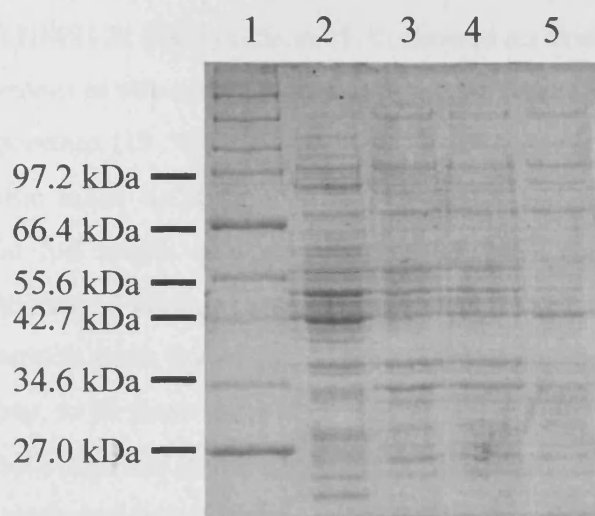 Origami (DE3) *E. coli* cell strains, made competent by calcium chloride treatment (Chapter 2.10), using the method previously described for the transformation and expression of the full length protein (Chapter 4.7). These two cell strains were focused on, as Origami (DE3) was successful for the production of the full-length enzyme, whilst HMS174 (DE3) has been previously utilised to express a number of cytochromes P450 such as Mtb CYP51 (Chapter 3.3), as well as Mtb CYP121 and *S. coelicolor* CYP154C1 (40,274). A 5 µl aliquot (roughly 10 ng) of plasmid DNA was co-incubated with 50 µl of the competent cells on ice for ten minutes prior to being heat shocked at 42 °C for 45 seconds, and returned to ice for a further two minutes. Following the addition of 450 µl of pre-warmed LB media, the cells were incubated in an orbital shaker (New Brunswick Scientific) at 37 °C for 1 hour. Subsequently, 100 – 200 µl aliquots of the cells were spread onto agar plates containing appropriate antibiotics, and were incubated at 37 °C overnight. Resultant colonies were picked and cultured in 5 ml of sterile LB, again containing the appropriate antibiotics, until the O.D.$_{600}$ was 0.4 – 0.6. At this time, the cells were prepared for glycerol stocks or utilised to inoculate larger cultures. For both of the cell strains used in these studies, ampicillin at 50 µg/ml was required for growth. However, Origami (DE3) additionally required tetracycline and kanamycin. The exact concentrations of the antibiotics added to agar plates and liquid culture are detailed in Chapters 2.16 and 2.17.

As for the expression trials for the full-length CYP116B1 gene, the trials for the expression of the heme and reductase domains were carried out on a small scale. Again the influence of varying the growth temperature and the level of IPTG induction on protein expression were investigated in order to optimise growth conditions for future, large-scale cultures. Typically, 30 ml Sterilin tubes (Bibby Sterilin Ltd.) containing 5 ml of sterile LB media and the appropriate antibiotics were inoculated with an aliquot of the glycerol stocks of the transformed *E. coli* cell strains described above. The cultures

were incubated at 37 °C in an orbital shaker shaking at 220 rpm until $O.D._{600} = 0.6$, at which point the temperature was decreased to either 18 or 25 °C, or maintained at 37 °C. Growth was continued until the cultures reached $O.D._{600} = 0.8$, whereupon induction was performed by the addition of IPTG to a final concentration of 100 μM or 1 mM. The cultures were subsequently maintained under the same conditions for a further 14 – 16 hours before samples were removed for protein expression analysis.

The extent of production of the CYP116B1 heme and reductase domains from the two *E. coli* strains was assessed in the same manner as reported in Chapter 4.7, utilising SDS-PAGE to report on protein expression. One aliquot of each culture was pelleted by centrifugation at 13000g and was used as the total protein sample following resuspension in 50 mM Tris.HCl pH 7.2. A second aliquot was also pelleted, but was instead resuspended in a cell lysis solution (Bugbuster, Novagen) and shaken for twenty minutes at room temperature before being centrifuged at 13000 g for a further twenty minutes. The pellet resulting from this treatment was resuspended in 50 mM Tris.HCl pH 7.2 and used as the insoluble protein sample, whilst the supernatant was removed and retained as the soluble protein sample. The samples were loaded onto an SDS-PAGE gel, consisting of a stacking gel (containing 2% SDS) and a running gel (1% SDS), following protein denaturation at 95 °C for 5 minutes in the presence of DTT and loading dye. To facilitate the assessment of protein expression, a broad range protein weight marker (New England BioLabs) and a previously prepared sample from untransformed *E. coli* cells were also loaded onto the acrylamide gel. The gel was subsequently run at 150 V, and, upon completion, was visualized by staining with Coomassie blue stain.

311

a)

b)
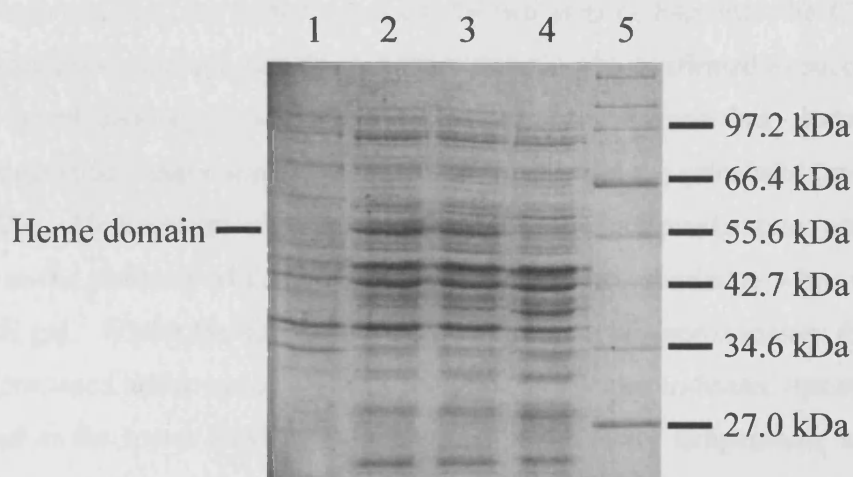
Figure 106 SDS-PAGE analysis of the CYP116B1 heme domain expression from **a)** HMS174 (DE3) and **b)** Origami (DE3) *E. coli* cell strains transformed with the HD pET-15b plasmid. In **a)** lane 1 contains broad range protein marker, lane 2 contains a sample of the respective untransformed HMS174 (DE3) cells, and lanes 3, 4, and 5 contain the total, insoluble, and soluble protein samples. In **b)** lanes 1 – 4 contain untransformed Origami (DE3), total, soluble, and insoluble protein samples, respectively, whilst the protein marker is found in lane 5. The HMS174 (DE3) gel shows no evidence of the expression of the 50.713 kDa heme domain protein. However, the appearance of bands at approximately 55 kDa in the total and soluble samples from the Origami (DE3) trial suggests more success with this cell strain. This was confirmed by UV-Visible spectroscopy (Chapter 5.4), and although this band is approximately 5 kDa larger than the postulated mass of the heme domain, the disparity is most likely caused by gel retardation due to the presence of the N-terminal His tag. Samples for the two gels were taken from cultures of the two transformed cell strains grown overnight at 25 °C following induction with 100 μM IPTG.

The SDS-PAGE gel shown in Figure 106a for the analysis of heme domain protein expression from HMS174 (DE3) cells at 25 °C showed no evidence of the expression of a 50.713 kDa protein in either the soluble or insoluble fractions. The use of a different incubation temperature (18 °C) and variations in the amount of IPTG used to induce protein production made no difference to this result, and thus suggested that, as is observed for the full length enzyme (Chapter 4.7), this cell strain does not favour expression of the heme domain. However, as is shown in Figure 106b, the SDS-PAGE analysis of expression trials involving Origami (DE3) cells proved, as they did with the full length enzyme, to be more successful. In this cell strain, there was evidence of a 55 kDa protein at both high and low IPTG levels, and for cultures grown both at 18 and 25 °C, which thus suggested that expression of the heme domain had been accomplished in this strain. Furthermore, as there is no evidence of an 86 kDa protein corresponding to the full-length enzyme, the introduction of the two stop codons into the CYP116B1 gene to prevent read-through into the reductase domain was confirmed as successful. It should be noted that the protein identified as the heme domain has electrophoretic mobility suggesting a mass approximately 5 kDa larger than the calculated protein mass (50.713 kDa). However this is seen consistently throughout purification, and is most likely due to the presence of the His tag, which may cause retardation when run on an SDS-PAGE gel. Whilst the gels identified that a protein of approximately the correct mass was produced under various growth conditions, they also indicated that expression was optimal at the lower level of induction and at the lower temperature, and hence these conditions were used for subsequent, large-scale growths.

Verification that the protein matching the postulated size of the CYP116B1 heme domain was indeed a cytochrome P450 was achieved following the initial large-scale culture of Origami (DE3) cells transformed with the HD pET-15b plasmid. The culture was performed in twelve 2 L conical flasks, each containing 500 ml of sterile LB and the appropriate antibiotics, and these were inoculated with 5 ml of a 100 ml overnight culture of the transformed Origami (DE3) cells. The cultures were grown at 37 °C until O.D.$_{600}$ = 0.6, whereupon the temperature was reduced to 18 °C. This temperature was selected as SDS-PAGE analysis suggested that more soluble protein was obtained than at 25 °C. When the O.D.$_{600}$ reached 0.8 the cultures were induced with 100 µM IPTG, and were incubated for a further 14 − 16 hours before harvesting at 6000 rpm for 20 − 30 minutes. The resultant pellet was resuspended in cold 50 mM Tris.HCl pH 7.2, and subjected to cell disruption by French press and sonication in the manner described in

Chapter 4.7 for the full-length enzyme. Centrifugation of the homogenised cell pellet at 18000 g for 40 minutes was carried out to separate cellular debris from soluble proteins, before extensive dialysis into 50 mM Tris.HCl, 1 mM EDTA pH7.2 (buffer A). Due to the proteolysis problems encountered for the full-length enzyme (Chapter 4.7), protease inhibitor cocktail tablets (Roche), PMSF and benzamidine hydrochloride (both Sigma-Aldrich) were added to resuspension and dialysis buffers as a preventative measure to avoid a reoccurrence of this problem. The resultant supernatant was loaded onto a DEAE-Sephacel column (Pharmacia) pre-equilibrated with buffer A and washed extensively to remove unbound proteins, prior to elution with buffer B (50 mM Tris.HCl, 1 mM EDTA, 500 mM KCl pH 7.2). Fractions of the eluent were assayed for the presence of cytochrome P450 by UV-Visible spectroscopy using a Cary UV-50 UV-Visible spectrophotometer (Varian) scanning between 200 and 800 nm. Samples displaying a Soret band feature at approximately 418 nm were subsequently subjected to dithionite reduction and CO-bubbling using the technique of Omura and Sato (49,50) described in Chapter 3.4, in order to generate the ferrous carbon-monoxy species, and further confirm the presence of a cytochrome P450. These assays, the details of which are further discussed in Chapter 3.4, positively identified the samples as containing a cytochrome P450, hence indicating the successful generation of the CYP116B1 heme domain.

This result signified that characterization, both spectroscopic and biophysical, of this domain of the *R. metallidurans* protein could begin, following determination of the optimal purification steps. A number of purification techniques were investigated, including anion exchange and affinity chromatography, resulting in a final three-step strategy involving DEAE, Hydroxyapatite, and Q-Sepharose chromatography columns. The initial step, as reported above, involved loading the crude cell extract onto a DEAE-Sephacel column (Pharmacia) pre-equilibrated in buffer A. The bound protein was then washed thoroughly using this buffer, before protein elution was implemented by the application of a 0 – 100 % linear gradient of buffer B. Subsequently, appropriate fractions of the eluent were pooled, concentrated by ultrafiltration (Millipore), and dialysed into buffer C (25 mM KPi pH 6.5) in order to prepare the protein for the next column. The dialysed protein was then loaded onto a Hydroxyapatite column (BioRad) pre-equilibrated with buffer C, washed with 2 column volumes of this buffer to remove unbound contaminants, and eluted using a linear gradient of 0 – 100 % buffer D (500 mM KPi pH 6.5). Fractions of the eluent were assessed for cytochrome P450 content

by UV-Visible spectroscopy, with those containing significant amounts of protein with a Soret feature at 418 nm retained, concentrated, and extensively dialysed into buffer A. Finally, the heme domain protein was loaded onto a Q-Sepharose anion-exchange column (Pharmacia) equilibrated in buffer A and eluted in the same manner as for the DEAE column described above. The degree of purification achieved by this three-step strategy is demonstrated in Figure 107, in which a sample taken from the fractions eluted from the Q-Sepharose column is run alongside a sample of the crude cell extract. The gel demonstrates that the majority of the contaminant proteins have been removed by the three columns, and that, unlike the full-length enzyme, there is no apparent proteolysis of the heme domain protein. Hence, with purification of the CYP116B1 heme domain complete, the characterization of this cytochrome P450 could be carried out. These studies, which were performed in order to compare the spectral and biophysical properties of the heme domain with those of the full-length *R. metallidurans* protein, are described in Chapter 5.4, following discussion of the expression and purification of the reductase domain.
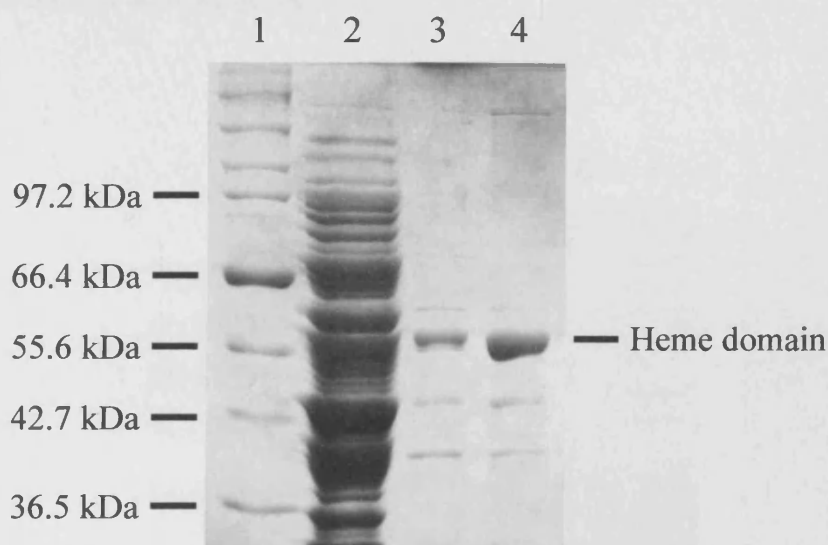
Figure 107 The SDS-PAGE analysis of purified *R. metallidurans* CYP116B1 heme domain run alongside broad range protein marker (lane 1). Lane 2 contains a sample of crude cell extract taken prior to the purification process, whilst lanes 3 and 4 contain 1 in 20 and 1 in 5 dilutions of protein recovered following purification by DEAE, Phenyl-Sepharose, and Q-Sepharose chromatography columns. The gel illustrates that the heme domain has been isolated from the majority of cellular proteins, and that, unlike the full-length CYP116B1 counterpart, there is not any substantial proteolysis of this enzyme. The electrophoresis was performed on an SDS-containing 10 % acrylamide gel, visualised by staining with Coomassie blue. Significant bands from the protein marker are shown at the left of the gel.

The SDS-PAGE gel in Figure 108a shows an example of the results obtained for the expression of the CYP116B1 reductase domain from HMS174 (DE3) cells incubated at 25 °C. This gel, in addition to those for cells cultured at 18 and 37 °C (not shown), does not possess a band corresponding to the proposed mass of the reductase domain. Hence, as with the expression of the full-length protein and the heme domain, this cell strain does not appear to be favourable for the expression of these *R. metallidurans* proteins. As reported above for the heme domain, and in Chapter 4.7 for the full-length enzyme, the Origami (DE3) cell strain was a more suitable host for expressing these enzymes, and resulted in production of proteins of the correct size. As is demonstrated in Figure 108b, this also appears to be the case for the reductase domain, as the gel shows evidence for a band at approximately 35 kDa (the postulated mass of the reductase domain) in the lanes that represent the soluble samples obtained from cultures grown at 18 and 25 °C. These results thus suggest that expression of the CYP116B1 reductase domain is possible, and that the incorporation of the start codon into the linker region of the full length enzyme had been both successful, and correctly positioned to enable production of an intact protein.
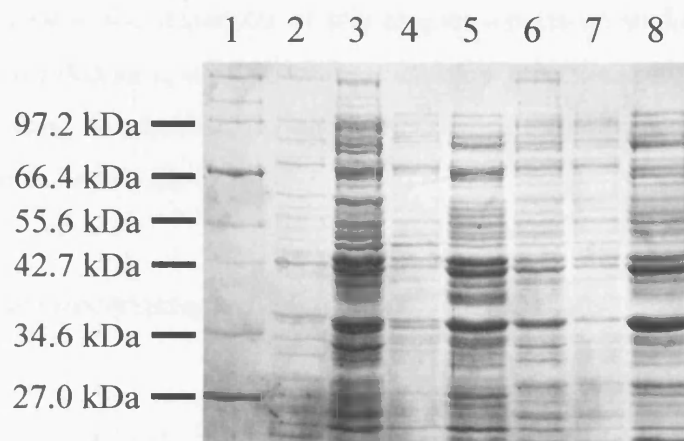
a)

316
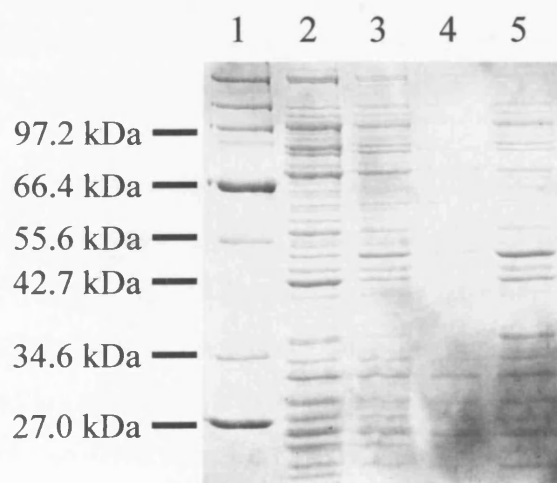
b)

Figure 108 The SDS-PAGE analysis of CYP116B1 reductase domain expression from a) HMS174 (DE3) and b) Origami (DE3) *E. coli* cells. Both cell strains were transformed with the RD pET-15b plasmid, and were cultured overnight following induction with 100 µM IPTG. In a), which demonstrates no evidence for the expression of the reductase domain protein at 25 °C, lane 1 contains broad range protein marker, lane 2 contains an untransformed HMS174 (DE3) sample, and lanes 3 – 5 contain total, insoluble, and soluble protein samples. In b) the first two lanes contain protein marker and untransformed Origami (DE3) *E. coli* cells, whilst lanes 3 – 5 and 6 – 8 contain the total, insoluble, and soluble samples taken from cultures grown at 18 and 25 °C, respectively. The bands at approximately 35 kDa in lanes 3, 5, 6, and 8 are of the correct mass to be the reductase domain, and suggest that expression of the truncated CYP116B1 protein is possible from this cell strain. Further confirmation of the status of this protein as a pyridine nucleotide coenzyme dependent reductase is presented in Chapter 5.4.

To further assess whether this expressed protein was the reductase domain, large-scale culture (6 L) was carried out in order to generate enough protein for preliminary spectroscopic analysis. The culture of the transformed Origami (DE3) cells was carried out in an identical manner to the expression of the heme domain, using low-level IPTG induction (100 µM) and an incubation temperature of 25 °C. Following cell harvesting, the protein was partially purified utilising DEAE-Sephacel and Q-Sepharose columns, and subsequently assayed using UV-Visible spectroscopy. The assays, which are described further in Chapter 5.4, reveal that the protein, which is yellow in colour, displays the spectral characteristics of a flavoprotein (i.e. absorbance maxima at approximately 450 and 370 nm) (17,259), and is thus likely to be the reductase domain of the truncated *R. metallidurans* protein.

Following accomplishment of expression and purification of the heme and reductase domains of CYP116B1, the remainder of this chapter reports on studies carried out to characterize the two domains, starting with preliminary spectroscopic studies (Chapter 5.4), and progressing to electron paramagnetic resonance and redox potentiometry analysis (Chapters 5.7 and 5.8).

5.4 UV-visible spectroscopy of CYP116B1 heme and reductase domains

In order to confirm that the proteins expressed and purified from the HD pET-15b and RD pET-15b plasmids are indeed the *bona fide* heme and reductase domains of *R. metallidurans* CYP116B1 and contain the expected cofactors, a number of UV-visible spectroscopic assays, which include the formation of the ferrous carbon-monoxy complex and reduction with electron donating compounds, were performed. In this section the results of these assays are presented, and data are correlated with those obtained for full length CYP116B1 and Mtb CYP51. In addition to these studies, the interactions between the CYP116B1 heme domain and the heme ligands nitric oxide, sodium cyanide, and imidazole are described so that further comparison between this protein and other well-characterized cytochromes P450 can be drawn.

As is reported in Chapters 3.4 and 4.8, the technique that offers the simplest and most clear-cut verification of the presence of a cytochrome P450 is that of Omura and Sato (49,50). This method utilises UV-Visible spectroscopy to identify the ferrous carbon-monoxy species with a characteristic Soret feature at ~450 nm, indicating coordination of the heme iron by a conserved cysteinate residue. Since the technique requires only minimal amounts of time and equipment, it is hence frequently used in the initial characterization of cytochromes P450 (130,169). Consequently, this method was employed for the verification that the heme domain of CYP116B1 is successfully expressed from the HD pET-15b plasmid. In order to perform the assay, an aliquot of the oxidised protein was diluted to approximately 1.75 μM in 50 mM Tris.HCl, 1mM EDTA pH 7.2. The absorption spectrum of this sample was then recorded between 250 and 800 nm using a Cary UV-50 UV-Visible spectrophotometer (Varian), before the protein was reduced by the addition of a minimal quantity of solid sodium dithionite, and the spectrum re-recorded. Subsequently, several bubbles of carbon monoxide were

introduced to the cuvette containing the protein sample prior to the recording of the final spectrum for this assay.
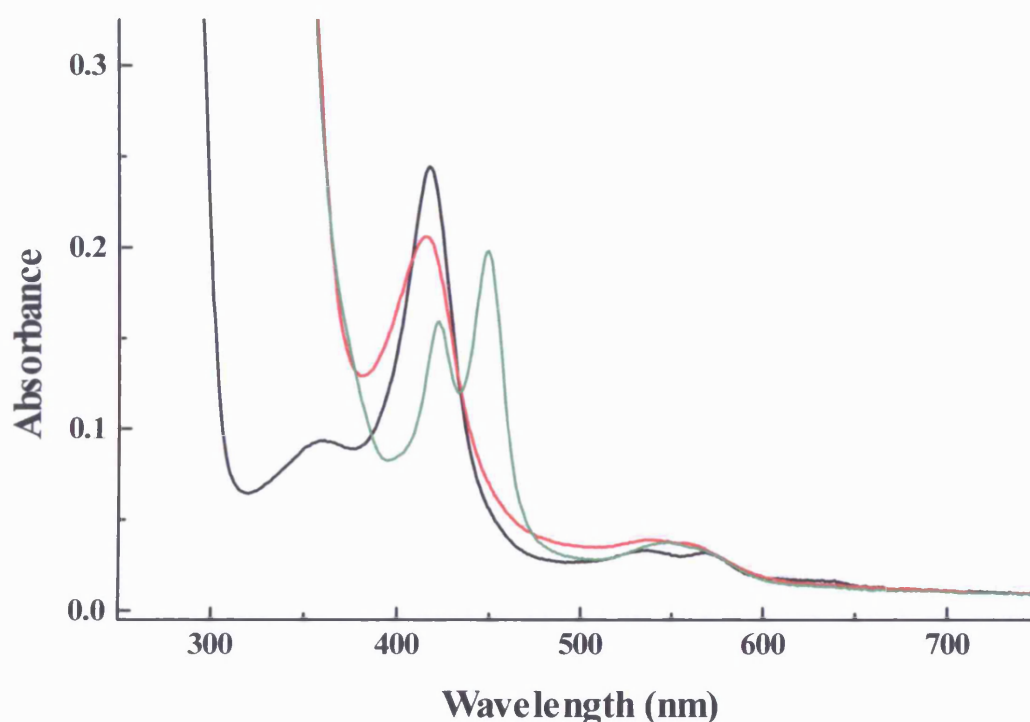
Figure 109 The UV-Visible absorption spectra of the oxidised (black), sodium dithionite-reduced (red), and ferrous carbon-monoxy forms of the CYP116B1 heme domain. The oxidised spectrum, which demonstrates the typical profile of a cytochrome P450, possesses a Soret band at 418 nm and Q-bands at 568 and 534 nm, but does not demonstrate the flavin-associated shoulder between 450 – 500 nm observed for the full-length enzyme (Chapter 4.8). The addition of sodium dithionite to the heme domain results in an optical shift of the Soret band to shorter wavelength (~417 nm), whilst subsequent CO-bubbling induces a Soret band shift to 449 nm that is indicative of the formation of the ferrous carbon-monoxy species, and hence verifies this protein as a cytochrome P450. An amount of P420 species (in which the thiolate ligand is likely protonated to the thiol) is also present. In this assay, the heme domain protein was diluted to a final concentration of approximately 1.75 μM in 50 mM Tris.HCl, 1 mM EDTA pH 7.2. All spectra were recorded at room temperature between 200 and 800 nm using a Cary UV-50 UV-Visible spectrophotometer (Varian).

The absorption spectrum of the oxidised protein, shown in Figure 109, exhibits an intense Soret band centred on 418 nm, whilst the alpha and beta bands are less intense features found at 568 and 534nm, respectively. This profile is typical of the cytochromes P450, and the positions of the major features are comparable with those at 419, 571, and 537 nm identified for CYP51 (Chapter 3.4), and 417, 569, and 536 nm for

319

P450cam (199). Furthermore, the Soret and alpha bands of this protein are in identical positions to those of analogous features of full-length CYP116B1 (Chapter 4.8). However the beta band is red-shifted by approximately 4 nm. Significantly, the heme domain spectrum does not display the absorption shoulder between 450 and 500 nm observed for the full-length CYP116B1 that corresponds to the flavin component of this enzyme, thus further confirming that the construct for the heme domain was correctly generated by PCR (Chapter 5.2). As the influence of the flavin component is absent in the spectrum of the heme domain, the position of the beta band in this spectrum is not skewed by this feature, as is likely to be the case in the full-length enzyme, hence explaining the slight discrepancy between the positions of the beta bands of the two proteins. As for the full-length enzyme (Chapter 4.8), upon reduction the Soret band of the heme domain protein is observed to shift to shorter wavelength (~417 nm) and to diminish in intensity. The sodium dithionite-induced reduction of this protein further confirms the absence of the reductase domain, as this treatment does not result in a bleaching of the spectra between 450 and 500 nm, as is observed for intact CYP116B1. Following bubbling with carbon monoxide, the Soret feature is seen to move to 449 nm, identifying that the ferrous carbon-monoxy species, which defines the cytochromes P450, has been successfully formed. This presence of this feature, which only occurs when carbon monoxide becomes the distal ligand to the ferrous heme iron, hence confirms that the purified protein is indeed a cytochrome P450, and that the heme domain of *R. metallidurans* CYP116B1 has been successfully expressed and purified. As with the full-length enzyme, there is a quantity of P420 species present in the spectrum of the reduced, CO-bubbled heme domain protein. However, unlike Mtb CYP51 (Chapter 3.4), this species does not evolve further over the next 60 minutes. This suggests that the P450 species of the heme domain is stable and far less susceptible to thiolate protonation than CYP51. Hence, further studies into this feature of the *R. metallidurans* protein are not required.

In Chapters 3.5 and 4.9, the verification that the expressed protein was a cytochrome P450 was followed by studies into the interactions of the respective *M. tuberculosis* and *R. metallidurans* proteins with nitric oxide, sodium cyanide and imidazole. The CYP116B1 heme domain was analysed similarly in order to confirm the presence of a displaceable heme ligand (i.e. a water molecule) in the oxidised P450, and to allow further spectroscopic comparison with the full-length enzyme and other well-characterized cytochromes P450.

To assess the interaction of the aforementioned ligands with the CYP116B1 heme domain, the investigations reported in Chapters 3.5 and 4.9 were repeated with this P450. Three discrete aliquots of the protein were prepared to a final concentration of ~2 μM in 50 mM Tris.HCl, 1 mM EDTA pH 7.2, and prior to the addition of each ligand, the absorption spectrum of the enzyme was recorded between 250 and 800 nm using a Cary UV-50 UV-Visible spectrophotometer (Varian). For the sodium cyanide and imidazole binding studies, the compounds were added progressively from concentrated stock solutions, with absorption spectra being recorded after each addition until no further spectral changes were observed. The nitric oxide-bound spectrum was obtained by gently introducing 5 – 6 bubbles of the gas to the cuvette, avoiding excessive (acidifying) additions or agitation of the sample, which result in turbidity of the protein solution. In all cases the assays were carried out at room temperature and the non-gaseous ligands were solubilised in aliquots of the assay buffer so as to minimise changes in pH and ionic strength upon their addition.

A composite of the resultant spectra is shown in Figure 110, and demonstrates the Soret band shifts obtained by the addition of near-saturating amounts of these three cytochrome P450 ligands. The binding of nitric oxide induces a shift of the heme domain Soret band to 434 nm with a concomitant increase in the intensity of the delta band. The binding of this ligand also causes visible features to increase in intensity and shift to 574 and 544 nm, respectively. Since it is likely that the nitric oxide complex is formally ferrous-NO^+, it is inappropriate to refer to these features as alpha/beta bands. The binding of (sodium) cyanide to the heme domain also produces shifts of the Q-bands, resulting in a single feature centred at 550 nm. More significantly, this ligand causes the Soret band to move to 432 nm, and of the three ligands induces the greatest reduction in the intensity of this feature. Conversely, the imidazole binding, which shifts the Soret band to 424 nm, induces the smallest decrease in Soret band intensity and results in only a partial spectral fusion of the Q-bands. The changes in intensity and final positions of the heme domain Soret band induced by these ligands are almost identical to those observed for the full-length enzyme (Chapter 4.9), as well as being similar to those reported for P450cam and Mtb CYP51 (159,199). This indicates that this monooxygenase displays spectral changes typical of the cytochromes P450 on ligand binding, and that the active site of this enzyme is accessible to a range of small ligand compounds of differing chemical character. Furthermore, the data indicate that these small compounds are able to coordinate with heme iron at the P450 distal face and

displace the iron-bound water molecule. Following the discussion of the UV-visible spectroscopy performed with the reductase domain of CYP116B1, further investigation and characterization of the active site of the heme domain is reported, focussing initially on the affinity of binding of these small ligands, before moving on to analysis of interactions with a range of other compounds including the azole anti-fungals and fatty acids.
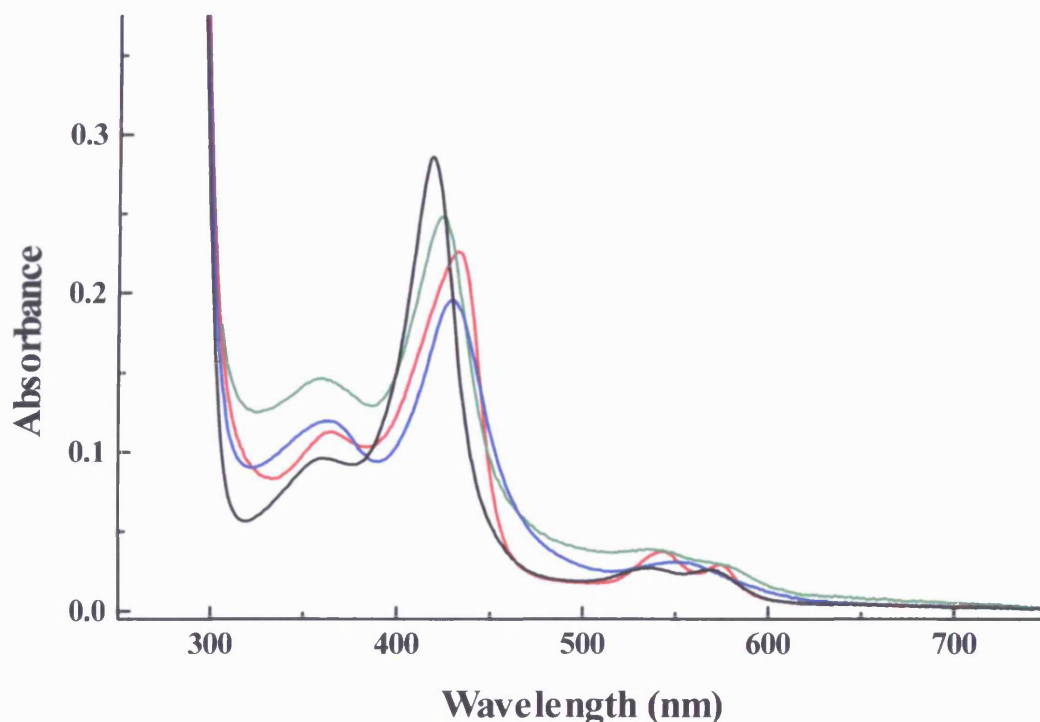
Figure 110 The absorption spectra of the nitric oxide-, imidazole-, and cyanide-bound CYP116B1 heme domain (red, green, and blue respectively) alongside the spectrum of the oxidised enzyme (black). Nitric oxide binding results in a Soret band shift to 434 nm and development of strong features in the visible region, whilst lesser Soret shifts to 432 and 424 nm are induced by the binding of cyanide (~10 mM) and imidazole (~1 mM). These inhibitor-like type II shifts, which are consistent with those observed for the full-length enzyme and for a number of well-characterized cytochromes P450 (Chapter 4.9, (159,199)), indicate that these compounds enter the active site of the enzyme, displacing a distally-bound water molecule and ligating to the heme macrocycle via the central iron atom. Each assay was performed using protein diluted to approximately 2 μM in 50 mM Tris.HCl, 1 mM EDTA pH 7.2, and maintained at 25 °C using a Peltier system.

Absorption spectroscopy was also utilised as a first step in the characterization of the CYP116B1 reductase domain expressed from the RD pET-15b plasmid (Chapter 5.2). The UV-Visible spectrum of the resultant protein (Figure 111) was recorded using a sample of protein diluted to approximately 23 μM in 50 mM Tris.HCl, 1 mM EDTA pH 7.2. The concentration of this CYP116B1 domain was calculated utilising the FMN extinction coefficient (ε_{450}) of 12.2 $mM^{-1}.cm^{-1}$ (190). The reductase domain spectrum displays the typical dual-peaked profile of a flavoprotein, with major peaks at 382 and 451 nm, and a shoulder on the longer wavelength band centred at 477 nm. The shapes and positions of these bands are similar to those observed for the FAD-binding FprA from *M. tuberculosis* (380, 452 and 473 nm) and for the FAD- and FMN-binding human CPR (373, 453 and 483 nm), as well as for the homologous phthalate dioxygenase reductase from *Ps. cepacia* (372, 455, and 485 nm) which contains FMN and 2Fe-2S cofactors (17,134,260), and thus identify the CYP116B1 reductase domain to be a flavin-containing protein. This incorporation of the flavin cofactor hence suggests that protein folding of this *R. metallidurans* CYP116B1 domain was successful. As with the spectrum of the full-length enzyme (Chapter 4.8), the oxidised spectral profile does not reveal the presence of the iron-sulphur cluster of this protein, which is most likely masked by the absorbance of the flavin cofactor. Hence alternative methods, such as EPR, will be necessary to verify the presence of this redox centre.
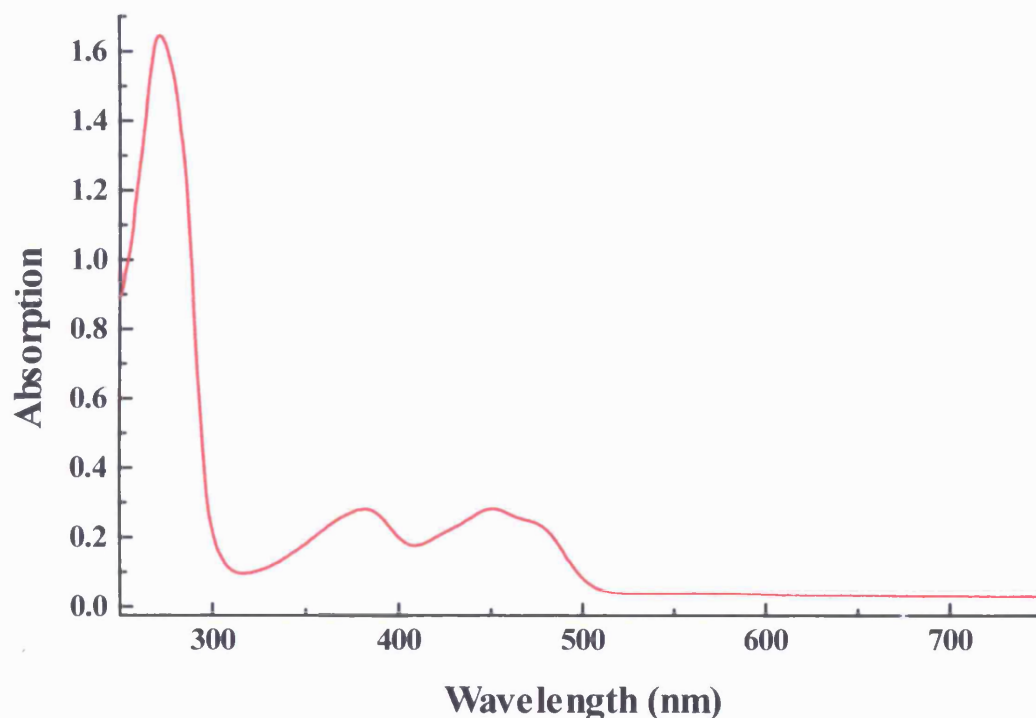
Figure 111 The UV-Visible absorption spectrum of the purified reductase domain of *R. metallidurans* CYP116B1. The profile of this spectrum, with two major peaks at 382 and 451 nm, and a shoulder centred at ~477 nm, is analogous with those observed for a number of well-characterized flavoproteins, including human CPR, *Ps. cepacia* phthalate dioxygenase reductase, and Mtb FprA (17,134,260). Hence, the spectral data confirm the correct cloning and expression of this gene, and indicate that this *E. coli*-expressed protein folds correctly to successfully incorporate a flavin moiety. The spectrum was recorded between 250 and 800 nm on a Cary UV-50 UV-Visible spectrophotometer (Varian) using an aliquot of protein diluted to ~23 μM in 50 mM Tris.HCl, 1 mM EDTA pH 7.2.

To further characterize the reductase domain of CYP116B1, the interactions of this protein with the reductants sodium dithionite, NADH and NADPH were performed. In each case an aliquot of the flavoprotein was diluted to a final concentration of approximately 20 μM in 50 mM Tris.HCl, 1 mM EDTA pH 7.2. The UV-Visible spectrum of the sample was subsequently recorded prior to, and following, reduction by these compounds using a Cary UV-50 UV-Visible spectrophotometer (Varian) scanning between 250 and 800 nm. The resultant spectra are shown in Figure 112, and demonstrate the optical changes induced by these three electron-donating compounds.
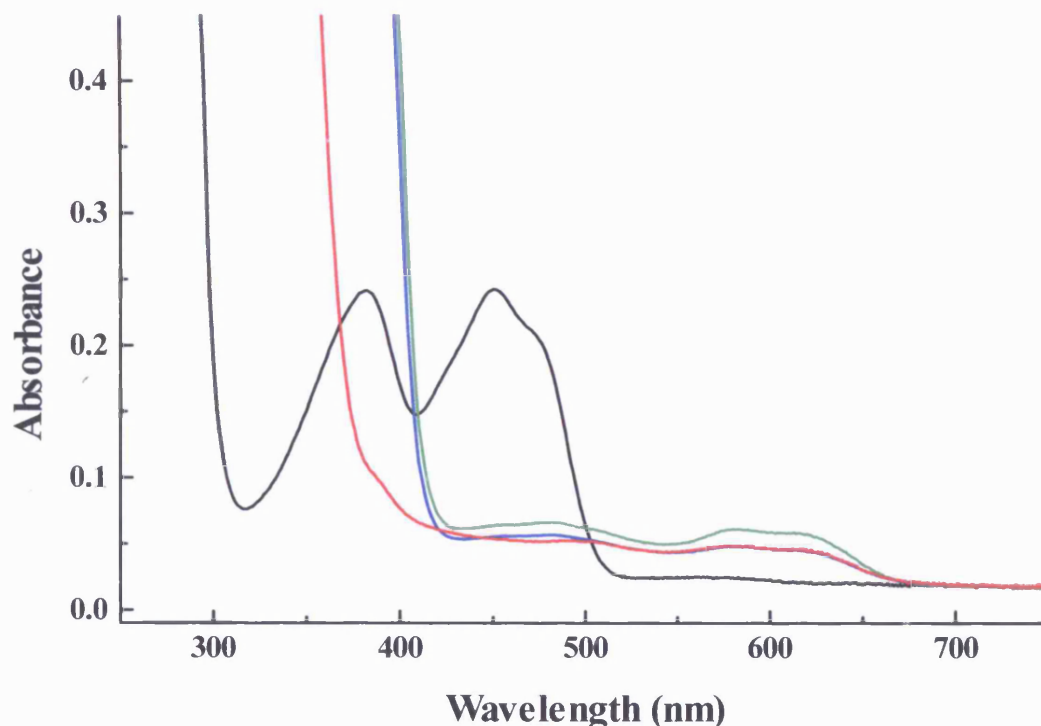
Figure 112 The spectrum of oxidised CYP116B1 reductase domain (black), shown alongside spectra collected following reduction of the protein by excess sodium dithionite (red), NADH (green), and NADPH (blue). The addition of each reductant results in a bleaching of the major absorbance features between 300 and 500 nm, whilst also inducing an increase in absorbance between 500 and 650 nm that likely corresponds to the formation of a neutral flavosemiquinone. The spectral changes, which are similar to those seen for phthalate dioxygenase reductase from *Ps. cepacia* (260), indicate that the enzyme interacts productively with both NADH and NADPH. Also, interestingly, the enzyme is not reduced fully to hydroquinone by the powerful reductant dithionite. In each assay protein was diluted to ~20 μM in 50 mM Tris.HCl, 1 mM EDTA pH 7.2 and reductants added as either a solid (sodium dithionite), or from a concentrated stock (NADH and NADPH) to final concentrations of 250 μM.

Reduction of the CYP116B1 reductase domain by sodium dithionite (Figure 112) results in the bleaching of the intensity of the two major absorbance features of the spectrum, whilst at longer wavelengths (550 – 650 nm) there is a concomitant increase in absorbance. These spectral changes are similarly observed upon reduction by NADH and NADPH, and whilst the spectral changes at longer wavelengths for the sodium dithionite- and NADPH-reduced samples are very similar, NADH-induced absorption changes at these wavelengths produces an absorption band of slightly greater intensity. The reductant-induced spectral changes seen for the CYP116B1 reductase domain are typical of those observed for a number of flavoproteins, including human CPR, phthalate dioxygenase reductase from *Ps. cepacia*, and Mtb FprA (17,134,260), in that

325

the development of absorption in the 550 – 650 nm region likely indicates the development of neutral blue semiquinonone species on the flavin. As NADH and NADPH are obligate two-electron donors (by hydride ion transfer to the flavin), this spectral change may signify that the electrons are distributed between the two redox centres of this reductase, with one electron being shuttled to the iron-sulphur cluster and the other remaining on the flavin to generate the semiquinone form. The fact that less semiquinone is observed for the NADPH-reduced sample (compared to the NADH-reduced sample) at high coenzyme concentrations may reflect e.g. differences in the binding of $NAD(P)^+/H$ to the reduced enzyme and/or electronic comproportionation between various reduced and oxidised species (given that NADPH and NADH have virtually identical redox potentials). It should be noted that NADPH is also preferred over NADH as a reductant from steady-state and stopped-flow kinetic studies of the full-length enzyme in Chapters 4.19 and 4.18. Also of interest is the fact that addition of excess dithionite does not give rise to full reduction of the reductase domain flavin to its hydroquinone form. This may also suggest that the redox couple for the semiquinone/hydroquinone transition of the flavin has a quite negative potential, or else that reduction of the semiquinone form to the hydroquinone by dithionite (a single electron donor) is kinetically very slow, and/or that rapid auto-oxidation of the flavin/iron sulphur centre otherwise prevents full enzyme reduction. As is demonstrated in Figure 113, the spectral changes induced by reduction of the CYP116B1 reductase domain appear fully reversible when the protein is left to reoxidise. This indicates that as well as binding the coenzymes and accepting electrons, this enzyme can also surrender these electrons (albeit to oxygen here, rather than to the heme domain), and that full reoxidation of flavin and iron-sulphur centres occurs efficiently.

In summary, the preliminary spectroscopic studies of the heme and reductase domains of CYP116B1 confirm that their cloning and expression was successful in that the spectral profiles exhibited by both proteins indicate that they have folded appropriately so as to incorporate their respective (at least) heme and flavin redox centres. · Furthermore, the data show that the reductase domain, as expected for the flavoprotein domain of CYP116B1, interacts productively with the coenzymes NADH and NADPH, whilst the heme domain successfully forms a stable ferrous carbon-monoxy species and binds various small ligands to its heme iron. Unfortunately, due to time constraints, further investigation of the CYP116B1 reductase domain protein was not possible. Had time permitted, further kinetic, spectroscopic and biophysical

characterization of the reductase domain would have been undertaken – with particular emphasis on characterising the iron-sulphur centre, and determining the thermodynamic properties of both cofactors. In the following sections, more detailed characterization of the CYP116B1 heme domain is presented. This includes further ligand binding studies, electron paramagnetic resonance and redox potentiometry studies.
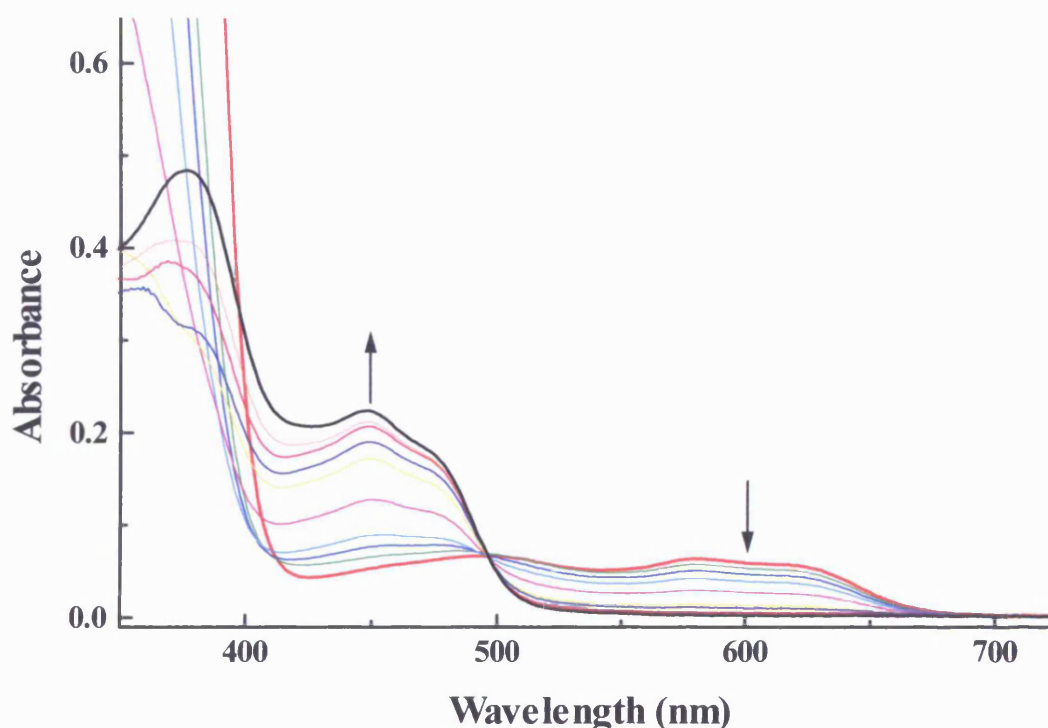
Figure 113 Selected UV-Visible absorption spectra collected for the reoxidation of the CYP116B1 reductase domain following reduction by NADPH (~200 μM). The spectrum recorded immediately after reduction of the protein is shown in red whilst the final spectrum, recorded several hours later, is shown in black. The data identify that, as previously reported (Figure 112), reduction by NADPH results in a bleaching of the flavoprotein absorbance, as well as concomitant semiquinone formation. Over the course of the study, the spectrum of the reductase domain is seen to revert to that of the oxidised enzyme, with the semiquinone feature diminishing and the region between 300 and 500 nm regaining the features typical of a flavin-containing protein. This suggests that the NADPH-induced spectral changes are fully reversible, and that the reoxidation reflects predominantly the conversion between semiquinone and quinone (oxidised) forms, as attested to by the presence of an isosbestic point at 496 nm (presumably a semiquinone/quinone isosbestic point). A repeat of this experiment using NADH resulted in a similar conversion from the reduced to the oxidised form of the enzyme over a similar time-course. Spectra of the protein (18 μM) were recorded every eight minutes using a Cary UV-50 UV-Visible spectrophotometer scanning between 250 and 800 nm.

5.5 The CYP116B1 heme domain hemochromagen assay

Due to the instability of the thiolate-coordinated form of the ferrous carbon-monoxy species of Mtb CYP51, a species that is frequently used for P450 concentration measurements (158,194), an alternative method for protein concentration determination was sought. The hemochromagen method of Berry and Trumpower (187) was deemed to be a suitable alternative for this purpose as it enables the determination of an extinction coefficient for the heme iron at its Soret maximum (~419 nm) through the formation of a highly-stable heme-pyridine adduct of known coefficient. This assay indicated that the coefficient of this monooxygenase was 134 $mM^{-1}.cm^{-1}$ for the oxidised enzyme at its Soret maximum. This value differs considerably from the value of ~95 – 100 $mM^{-1}.cm^{-1}$ that is projected for many low-spin cytochrome P450 enzymes (at the Soret maximum) as a result of use of the Omura and Sato method, and with the assumption that a coefficient of 91 $mM^{-1}.cm^{-1}$ is accurate for difference between the absorption properties of the ferrous and ferrous-CO forms of P450 enzymes (158,194). This result was further supported by the determination of the extinction coefficients of CYP116B1 in Chapter 4.10, and P450cin from *Citrobacter braakii* in a study by Hawkes *et al.* (200), both of which deviate significantly from the more 'standard' value of ~95 – 100 $mM^{-1}.cm^{-1}$. Hence, the use of this generalized extinction coefficient (based on the Omura and Sato difference coefficient) for the calculation of P450 concentration is suggested to be outmoded and likely rather inaccurate for most P450s. For these reasons, the hemochromagen assay was performed on the heme domain protein of CYP116B1 to provide a more accurate estimate of P450 concentration.

As reported in Chapters 3.6 and 4.10, the hemochromagen assay was performed using the method of Berry and Trumpower (187). A 500 µl aliquot of the CYP116B1 heme domain, diluted to 2 – 4 µM in 50 mM Tris.HCl, 1 mM EDTA pH 7.2, was added to a quartz cuvette containing a solution of 200 mM sodium hydroxide, 40 % pyridine (by volume), and 0.6 mM potassium ferricyanide, and mixed thoroughly. A UV/Visible absorption spectrum of the cuvette contents was recorded between 250 and 800 nm using a Cary UV-50 UV-Visible spectrophotometer (Varian). Subsequently, the sample was reduced by the addition of 2 – 5 mg solid sodium dithionite, and the absorption spectrum re-recorded. To ensure complete reduction of the sample had been achieved a second addition of sodium dithionite was made before a third spectrum of the sample was collected. Finally, an extinction coefficient for the CYP116B1 heme domain was

determined using the difference between the absorption at 557 and 540 nm in the difference spectrum generated for the sample.

The hemochromagen assay of the CYP116B1 heme domain determines the extinction coefficient (ε_{419}) of this protein to be 139 $mM^{-1}.cm^{-1}$. This value is almost identical to that identified for the full-length enzyme (137 $mM^{-1}.cm^{-1}$), hence suggesting that this method generates reliable and reproducible data, as well as further confirming that heme incorporation and protein folding in the heme domain is not adversely affected by the gene truncation. Furthermore, as with the oxidised Soret extinction coefficients determined for Mtb CYP51 (134 $mM^{-1}.cm^{-1}$) and P450cin (150 $mM^{-1}.cm^{-1}$), the coefficient for the heme domain deviates significantly from the more 'standard' coefficients of ~95 – 100 $mM^{-1}.cm^{-1}$ (that arise from using the coefficient $\Delta\varepsilon_{(450-490)}$ = 91 $mM^{-1}.cm^{-1}$ for Fe^{2+}-CO minus Fe^{2+} forms). Clearly the extinction coefficient of cytochromes P450 should not be generalised to a single value applicable to all members of this enzyme family, but instead the coefficient for each monooxygenase should be determined independently, hence allowing for more accurate and consistent data comparison. For these reasons the newly determined extinction coefficient for the heme domain of CYP116B1 will be utilised to calculate protein concentration in the subsequent characterizations of this cytochrome P450, which include binding studies, electron paramagnetic resonance, and redox potentiometry (Chapters 5.6, 5.7, and 5.8).

5.6 *R. metallidurans* CYP116B1 heme domain binding studies

In Chapter 5.4 the interactions of the CYP116B1 heme domain with nitric oxide, sodium cyanide, and imidazole were investigated in order to define the spectral features of these complexes, and to allow comparison with other P450 monooxygenases. In this section the binding of cyanide and imidazole is investigated further, utilising UV-Visible spectroscopy-based binding titrations to quantify these enzyme:ligand interactions. During studies of Mtb CYP51 and intact *R. metallidurans* CYP116B1 (Chapters 3.7 and 4.11), this method was used to good effect, producing dissociation constants (K_d) for numerous inhibitory and substrate-like compounds, aiding characterization of the active sites of these enzymes (28,37). For comparative purposes, this method, which reports upon spectral perturbations attributable to the replacement of a heme-bound water molecule by inhibitory ligands, or to alterations of the electronic configuration of the heme iron by substrate-like molecules (low-spin to high-spin shifts)

(69), was used to study the interactions of a range of compounds with the heme domain of CYP116B1. Data generated for the heme domain would be valuable in comparing properties with those of full-length CYP116B1, and would also allow further comparison of ligand-binding properties with other well-characterized cytochromes P450. Furthermore, any disparities identified between ligand affinity and other properties of the heme domain and full-length CYP116B1 data may identify the influence of the reductase domain on the properties of the heme in the full length enzyme. As with the studies of Mtb CYP51 and full-length CYP116B1, this study commences with the determination of K_d values for cyanide and imidazole, before focussing on the interactions of the heme domain with other compounds that exhibited inhibitory (azole anti-fungals) and substrate-like (unsaturated fatty acids) spectral shifts in the studies of full-length CYP116B1 (Chapters 4.12 and 4.13).

The dissociation constants for heme domain:ligand interactions were determined using the method of McLean *et al.* (158) detailed in Chapter 3.7. Following the dilution of an aliquot of heme domain protein to 1.5 µM in 50 mM Tris.HCl, 1 mM EDTA pH 7.2, a UV-Visible absorption spectrum of the oxidised enzyme was recorded between 250 and 800 nm. Subsequently, spectra of the protein, maintained at 25 °C using a Peltier system, were collected following the addition of small aliquots of putative ligands. These were typically 0.2 – 0.5 µl additions from concentrated stock solutions, made until no further spectral changes were observed. The direction of the Soret band shift induced by each ligand was used to distinguish between inhibitory (type II) and substrate-like (type I) compounds, whilst the resultant spectral data were analysed according to the method described in Chapter 3.7. Figures 109, 110, 111, and 112 display examples of the resultant plots of induced absorbance changes *versus* ligand concentration, whilst the associated dissociation constants of the ligands, determined by fitting the plots with a hyperbolic function (Equation 2, Chapter 3.7), are detailed in Tables 20, 21, and 22.

During the titration of sodium cyanide with the heme domain of CYP116B1, the Soret band of this cytochrome P450 is observed to shift to longer wavelengths, coming to rest at 432 nm on cyanide saturation. This type II spectral shift, which is accompanied by a concomitant decrease in intensity of the Soret band and a spectral fusion of the Q-bands, indicates cyanide to be an inhibitor of this cytochrome P450, as seen for Mtb CYP51 and full-length CYP116B1 (Chapters 3.7 and 4.11). Similarly, the titration of imidazole titration identifies this compound as an inhibitor of the heme

domain. Addition of this compound causes a type II Soret band shift to 424 nm. However, there is less alteration in Soret intensity for imidazole than seen on formation of the cyanide complex, and only a partial "fusion" of the alpha and beta bands is observed in the imidazole complex.

Figure 114 and Figure 115 display the plots of maximal induced absorption change *versus* ligand concentration for the titrations of cyanide and imidazole with the CYP116B1 heme domain, as well as the difference spectra from which these plots were created. The data points in these plots represent the difference between the maximal and minimal absorbance (peak and trough) from the difference spectra, which were themselves generated by subtracting the spectrum for the oxidised, ligand-free domain from all subsequent titration spectra. The plots demonstrate that, as is typical of many ligand interactions with cytochrome P450 enzymes (37,158,199), binding of cyanide and imidazole to the CYP116B1 heme domain produce hyperbolic curves of induced absorption change *versus* ligand concentration. The dissociation constants for the two ligands were determined by fitting of the derived plots with a hyperbolic function (Equation 2, Chapter 3.7) and are displayed in Table 23.

These values reveal that imidazole has a greater affinity for the heme domain, with its K_d approximately 13 times lower than that for cyanide. The distinction in ligand affinity identified in these assays is similar to those reported in Chapter 4.11 for the interactions of these compounds with CYP116B1, as well as equivalent data from the study of Mtb CYP51 (Chapter 3.7) (159). However, for both compounds the K_d values determined with the heme domain are seen to be slightly tighter. These studies suggest that the active site of the CYP116B1 heme domain is very similar to that of its full-length counterpart, and thus that the reductase domain has little structural effect on the heme domain active site. The data also suggest that, as for numerous other cytochromes P450 (27,40), the active site of the heme domain (and intact CYP116B1) is hydrophobic in nature, as the K_d values for small, polar ligands indicate weak binding, whereas those for larger, more hydrophobic inhibitor molecules (see below) are much tighter.
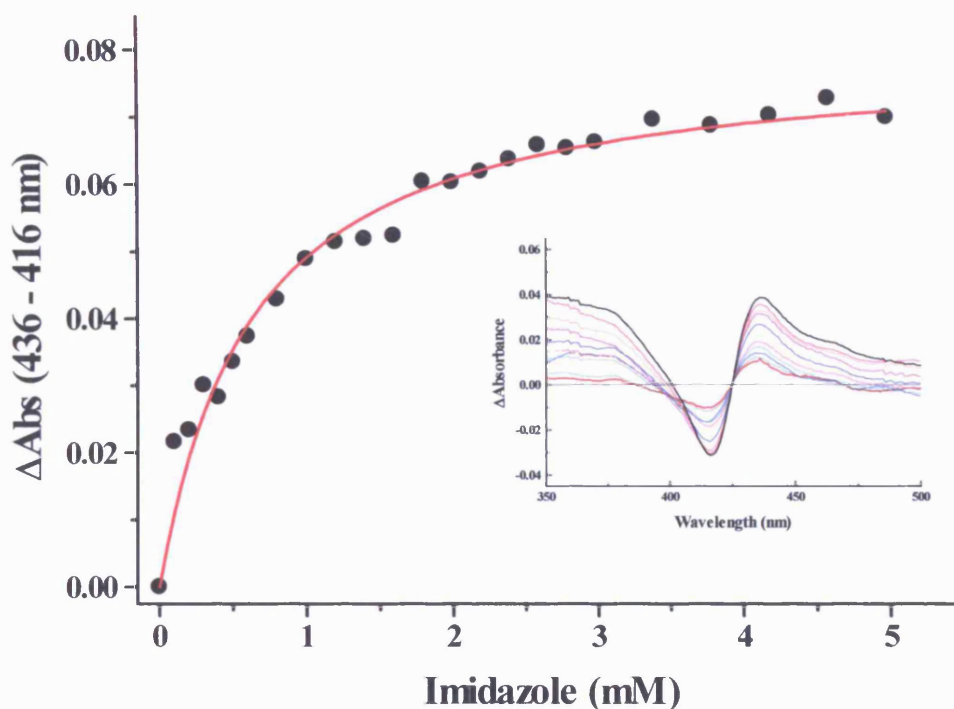
Figure 114 The binding titration plot for the interaction of imidazole with the CYP116B1 heme domain protein. The inset difference spectra, created by subtracting the spectrum of the ligand-free form from all subsequent titration spectra, show that when imidazole binds the protein, a typical type II Soret band shift is produced as imidazole ligates the heme iron of this P450. The titration plot was created by calculating the maximum amplitude of the ligand-induced spectral changes in the difference spectra at two wavelengths (i.e. the peak at 436 and the trough at 416 nm), and plotting these values against the concentration of imidazole at which they occur. This plot demonstrates that the induced optical changes have a hyperbolic dependency on ligand concentration, and when fitted (Equation 2, Chapter 3.7) generate a K_d value of 621.5 ± 57.9 μM for imidazole. The heme domain was diluted to 1.5 μM in 50 mM Tris.HCl, 1 mM EDTA pH 7.2, and the imidazole stock solution was made in the same buffer. The spectra were recorded at room temperature using a Cary UV-50 UV-Visible spectrophotometer (Varian) scanning between 250 and 800 nm.
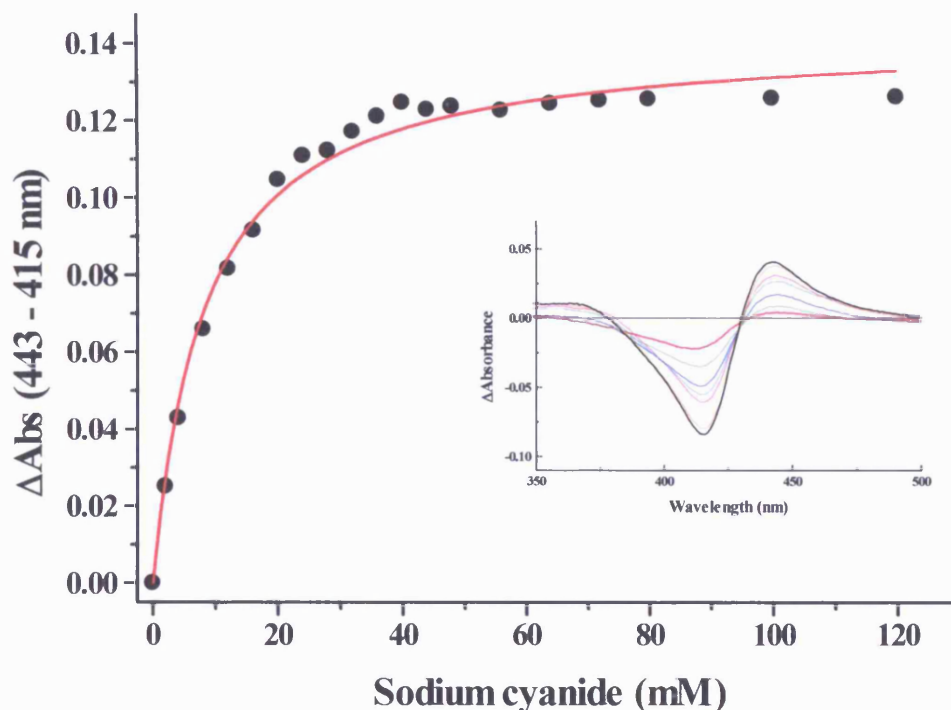
Figure 115 The binding titration plot, and selected difference spectra (inset), for binding of sodium cyanide to the heme domain of *R. metallidurans* CYP116B1. As with imidazole binding (Figure 114), a typical type II difference spectral set is produced, again indicating that this compound binds as an inhibitor. The binding titration plot, calculated as described in Figure 114, shows that the observed absorbance changes are hyperbolically dependent on the concentration of cyanide. Fitting of the plot with a rectangular hyperbola (Equation 2, Chapter 3.7) determines a K_d of 8.15 ± 0.62 mM, indicating that cyanide interacts rather weakly with the heme domain of CYP116B1, most likely caused by unfavourable electrostatic interactions in the hydrophobic active site of the enzyme, and the electron donating effect of the thiolate ligand on the heme iron. The assay was performed at room temperature using an aliquot of CYP116B1 heme domain diluted to ~1.5 μM in 50 mM Tris.HCl, 1 mM EDTA pH 7.2.

Compound	Dissociation constant (K_d)
Imidazole	621.5 ± 57.9 μM
Sodium cyanide	8.15 ± 0.62 mM

Table 23 The dissociation constants for the interactions of imidazole and cyanide with the heme domain of CYP116B1, determined by fitting the plots of induced Soret absorbance change versus ligand concentration (Figures 109 and 110) to a rectangular hyperbola (Equation 2, Chapter 3.7). These K_d values, which are similar to those determined for the full-length enzyme (645.7 ± 12.5 μM for imidazole and 9.67 ± 0.56 mM for cyanide, Chapter 4.11), indicate that the two P450 inhibitors demonstrate relatively low affinity for this *R. metallidurans* monooxygenase.

Having confirmed that the CYP116B1 heme domain binds these small, inhibitory ligands with similar affinity to the intact enzyme, further ligand binding titrations involving larger, more hydrophobic azole and fatty acid molecules were performed. These were done in order to further probe the nature of the active site of this protein and permit further comparisons with full-length CYP116B1. In Chapter 3.8 the binding of azole anti-fungal compounds to Mtb CYP51 was investigated due to their efficacy against sterol-demethylating P450s, a reaction that Mtb CYP51 catalyses *in vitro* (169). Several bulky, hydrophobic azoles were confirmed as potent inhibitors of the *M. tuberculosis* P450, binding extremely tightly to the heme iron of the enzyme. Subsequently azole anti-fungals were utilised in the characterization of intact *R. metallidurans* CYP116B1 (Chapter 4.12), as they gave a good point of comparison between these enzymes, and facilitated assessment of the nature of the active site of this newly-identified monooxygenase. In order to allow for further comparisons of the binding properties of the heme domain and full-length proteins, assays involving the binding of bulky substituted azoles were performed with the CYP116B1 heme domain. In light of the apparent failure of fluconazole to bind to intact CYP116B1, a further reason for a detailed study of the interactions of fluconazole and the other azoles with the CYP116B1 heme domain is to (i) validate that fluconazole does not bind the heme domain and (ii) to have independent assessments of the influence of the reductase on heme domain structure by comparisons of K_d values of these inhibitors for intact CYP116B1 and its heme domain.

a)
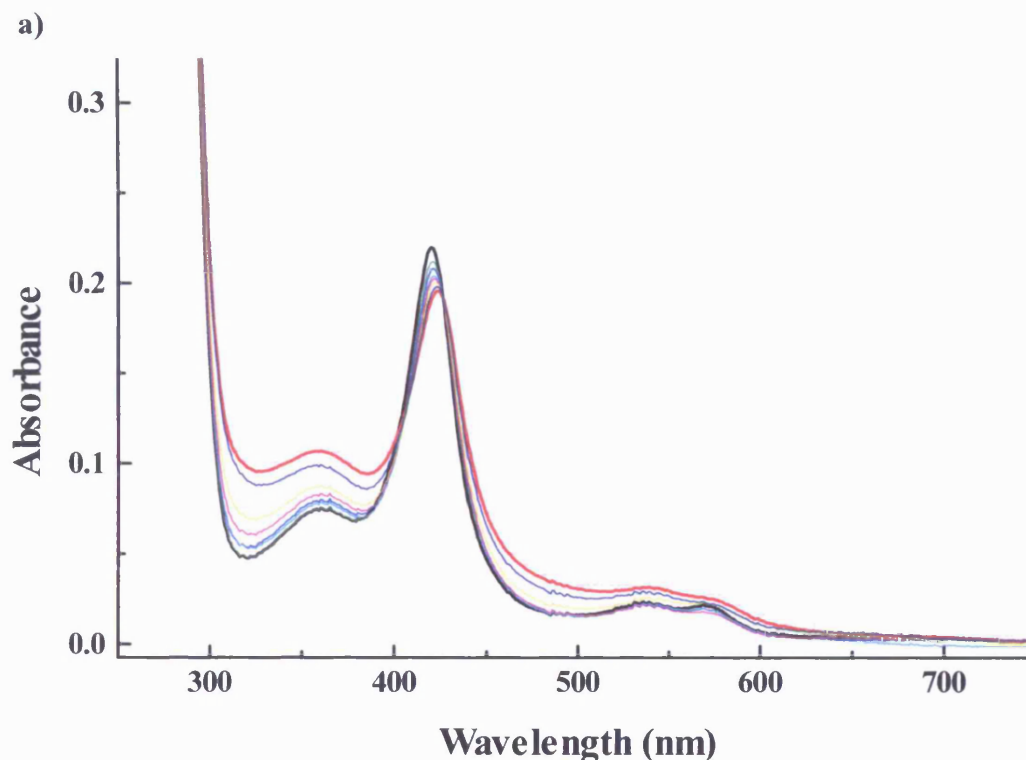
Figure 116 a) Selected UV-Visible absorption spectra collected during the binding titration of econazole with the heme domain of *R. metallidurans* CYP116B1. The spectra describe the shift in the heme domain Soret band from 418 to 424 nm and changes in the Q-band region induced by econazole. These shifts are typical of those observed for all of the azole anti-fungals assayed, with the exception of fluconazole. The assay was performed using an aliquot of heme domain diluted to approximately 1.5 μM in Tris.HCl, 1 mM EDTA pH 7.2 and recorded using a Cary UV-50 UV-Visible spectrophotometer scanning between 250 and 800 nm. For clarity initial and final spectra are shown in black and red, respectively. **b)** The binding plot and selected difference spectra (inset) generated from the UV-Visible absorption spectra recorded during the titration of econazole with the heme domain of CYP116B1. The type II difference spectra indicate that this azole anti-fungal is an inhibitor of this cytochrome P450, ligating to the heme iron. The plot indicates that the spectral changes are hyperbolically dependent on the ligand concentration, whilst the K_d value of 1.08 ± 0.10 μM, determined by fitting the plot with a quadratic function (Equation 3, Chapter 3.8), identifies that this azole binds very tightly to this cytochrome P450.

b)
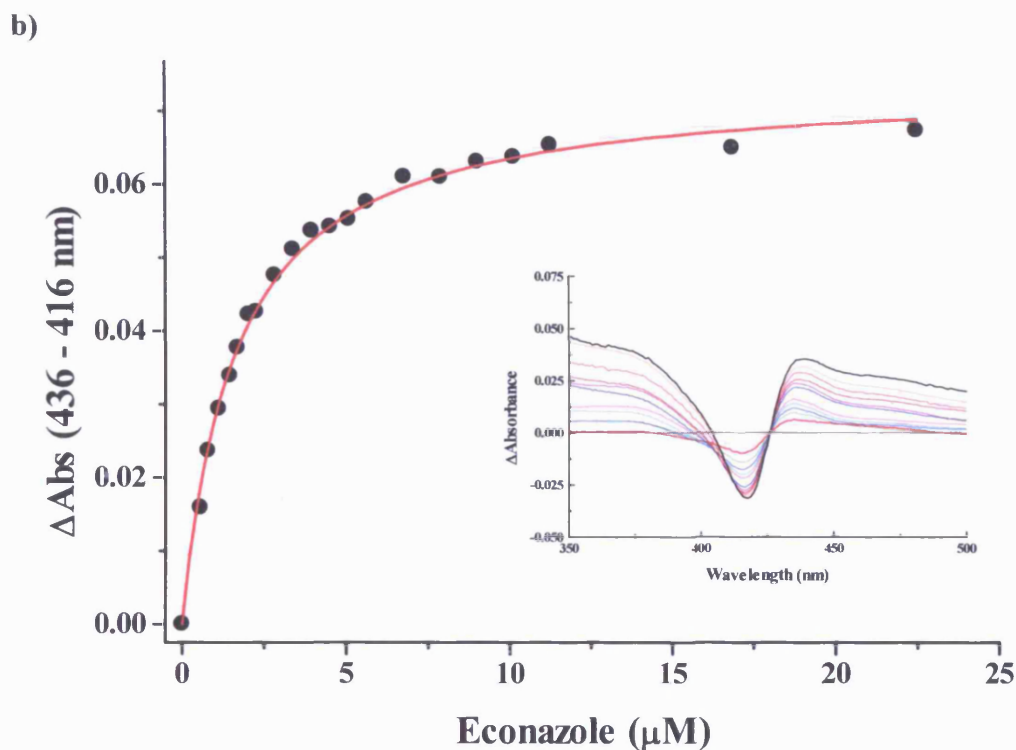
The UV-Visible absorption spectra from the titration of econazole with the CYP116B1 heme domain are shown in Figure 116a, and are typical of those recorded for each of the six azole anti-fungals assayed, with the exception of fluconazole. In each case, the addition of azole induced a type II inhibitory shift of the heme domain Soret band towards longer wavelengths (typically 424 nm), as well as a slight decrease in the intensity of this absorption feature and changes in the visible region apparent as a partial fusion of the alpha and beta bands. These spectral changes are characteristic of the interactions of cytochromes P450 with azole compounds, comparing well with those obtained for Mtb CYP51 and *B. megaterium* P450 BM3 (Chapter 3.8, (28,37,159)) , as well as for the full-length CYP116B1 (Chapter 4.12). As with the studies of Mtb CYP51 and CYP116B1, the dissociation constants were determined by fitting plots of induced absorbance changes *versus* azole concentration with the appropriate functions; either a rectangular hyperbola (Equation 2, Chapter 3.7) or a tight-binding equation (Equation 3, Chapter 3.8) depending on the tightness of binding. An example of these plots is shown in Figure 116b, whilst a summary of the K_d values is given in Table 24. The plot is typical of those obtained during these binding assays and demonstrates that, as reported for CYP51 and intact CYP116B1 (Chapters 3.8 and 4.12), there is a hyperbolic dependence of spectral change with azole concentration. The values in Table 24 are comparable with those obtained for the full-length enzyme, indicating that

the affinity of these compounds ranges between approximately 0.1 and 5 µM (not including voriconazole), and that binding to the heme domain is very tight. As with Mtb CYP51 and intact CYP116B1, the affinity for clotrimazole and miconazole is observed to be significantly tighter than for econazole and ketoconazole. This most likely reflects their differences in size, hydrophobicity, and structure (Figure 13, Chapter 1.9). Interestingly, as with the data obtained for intact CYP116B1 (but in contrast with Mtb CYP51 data), voriconazole is shown to be a relatively weak inhibitor of the heme domain, binding with an affinity of 4.95 ± 0.33 mM. The assays performed to study the interaction of fluconazole with the CYP116B1 heme domain demonstrate that this azole does not perturb the absorption spectrum of the *R. metallidurans* CYP116B1 heme domain. This suggests that fluconazole either does not gain access to the active site, or fails to approach the heme in a manner that permits ligation. The interaction of voriconazole, whose structure is very similar to that of fluconazole (Figure 13, Chapter 1.9), with the CYP116B1 heme domain is significantly weaker than that of the other azoles assayed. However, voriconazole (unlike fluconazole) does ligate the iron and saturates the enzyme, albeit only at millimolar ligand concentrations. The data for these two compounds tally with the data obtained for the full-length enzyme and, as discussed in Chapter 4.12, indicate that the structure of these compounds (and possibly their hydrophilicity – fluconazole and voriconazole are the most water-soluble of the azoles used) influences their ability to ligate to the heme of the *R. metallidurans* CYP116B1 and its heme domain. Possibly, the presence of a fluorine atom in both azoles is also a determinant for their weak/non-measurable binding. However, until the crystal structure of this protein is solved or an accurate molecular model of the protein is developed, the origins of the large differences in affinities of these azoles remains unclear.

Azole compound	Dissociation constant (K_d)
Clotrimazole	0.07 ± 0.02 μM*
Econazole	1.08 ± 0.10 μM*
Fluconazole	No binding detected
Ketoconazole	4.73 ± 0.78 μM
Miconazole	0.045 ± 0.005 μM*
Voriconazole	4.95 ± 0.33 mM

Table 24 The dissociation constants determined for the binding of six azole anti-fungal compounds to the heme domain of CYP116B1. K_d values were determined by fitting plots of absorbance change *versus* ligand concentration with a rectangular hyperbola in most cases (Equation 2, Chapter 3.7). However, those marked * were fitted with an alternative function (Equation 3, Chapter 3.8) due to the extreme tightness of binding of these compounds to the heme domain. As with the full-length enzyme, fluconazole was not seen to bind to this enzyme. However, the K_d values for the other azoles are very similar to those determined for the full-length enzyme (Chapter 4.12), and indicate the compounds (with the exception of voriconazole) to be potent CYP116B1 heme domain inhibitors.

In a further attempt to probe the substrate specificity of *R. metallidurans* CYP116B1, a wide range of compounds, from sterols to fatty acids, were previously tested for binding interactions with this redox partner-fused P450 (Chapter 4.13). The majority of these compounds did not yield a discernable spectral shift of either an inhibitory or substrate-like nature. However, three unsaturated fatty acids (arachidonic acid, myristoleic acid, and palmitoleic acid) produced type I Soret band shifts. Binding titrations determined that these long, hydrophobic molecules bound to CYP116B1 in a manner reminiscent of substrates of other cytochromes P450, including the binding of arachidonate and laurate by P450 BM3 (27,37). Although these compounds were later shown by steady-state kinetics (Chapter 4.20) not to be metabolised by CYP116B1 to any measurable degree, their binding gave a useful insight into the active site of the enzyme, as well as providing further information regarding the type of compound that may be the true substrate of this monooxygenase. Subsequently, in the characterization of the CYP116B1 heme domain, the binding of these unsaturated fatty acids was investigated with a view to further comparison with its full-length equivalent and the influence of the reductase domain on the heme domain structure and ligand-binding properties.

The addition of arachidonic acid, myristoleic acid, and palmitoleic acid to the heme domain induced minor substrate-like type I Soret band shifts, indicating that these

338

compounds are able enter the active site of the protein and approach the heme close enough to perturb binding of the distal water and to influence the electronic configuration of the heme iron. These Soret shifts towards shorter wavelengths, typically by 1 – 2 nm, are similar to those seen for the full-length enzyme and suggest that only a small proportion of the enzyme is shifted to the high-spin form before the onset of turbidity and some protein precipitation induced by the immiscibility of these ligands and aqueous buffer. However, within the concentration range used the saturation of the P450 is apparently achieved. Despite the turbidity induced by arachidonic acid, myristoleic acid, and palmitoleic acid, it was thus possible to determine dissociation constants for these three substrate-like compounds. The plot of induced absorbance change *versus* ligand (myristoleic acid) concentration shown in Figure 117 is typical of the plots obtained for each of these unsaturated fatty acids, and shows that the spectral changes display a hyperbolic dependence on ligand concentration.
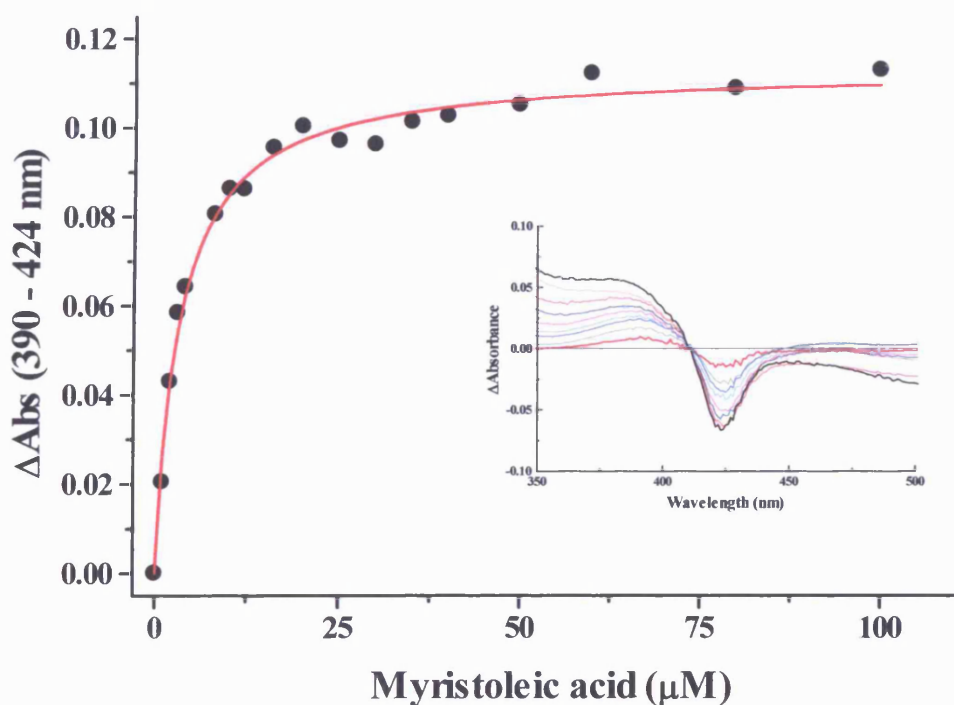
Figure 117 The binding titration plot, and selected difference spectra (inset), for the interaction of myristoleic acid with the CYP116B1 heme domain (3.5 μM). The type I difference spectra induced are typical of binding of substrates to P450s (27,37). The plot indicates that P450 optical change displays a hyperbolic dependence on myristoleic acid concentration, and when fitted with the appropriate function (Equation 2, Chapter 3.7) a K_d of 3.29 ± 0.30 μM is determined. Similar spectral shifts and plots were obtained for palmitoleic acid and arachidonic acid, and the K_d values of these three compounds were comparable with those established for full-length CYP116B1 (Chapter 4.13).

The K_d values for these compounds (Table 25), determined by fitting of the plots with a hyperbolic function (Equation 2, Chapter 3.7), are similar to those determined for the full-length protein (Chapter 4.13), indicating that the three compounds bind to the heme domain in the low micromolar range, although not as tightly as some of the inhibitory azole compounds (e.g. clotrimazole, 0.07 ± 0.02 µM). As with CYP116B1, palmitoleic acid is observed to bind approximately 6 – 8-fold less tightly than arachidonate and myristoleic acid. Hence, these data further verify that this truncated *R. metallidurans* protein displays the same binding characteristics as its full-length counterpart, and that the true substrate(s) of this monooxygenase may have structural features similar to these unsaturated fatty acids in terms of, for example, size and hydrophobicity. Further possibilities are that the true substrate(s) of CYP116B1 has a lipid side chain and/or that fatty acids are able to bind to CYP116B1 via interactions with active site amino acid residues that also interact with true substrate(s). The rather low extent of heme iron spin-state equilibrium shift induced by these fatty acids also possibly reflects that their binding mode places them slightly distant from the heme distal ligand.

Compound	Dissociation constant (K_d)
Myristoleic acid	3.29 ± 0.30 µM
Palmitoleic acid	28.61 ± 1.48 µM
Arachidonic acid	4.24 ± 0.12 µM

Table 25 The dissociation constants determined for the interactions of myristoleic acid, palmitoleic acid and arachidonic acid with the CYP116B1 heme domain. The values were determined by fitting the plots of induced absorbance change *versus* ligand concentration (as exemplified in Figure 117) with a rectangular hyperbola (Equation 2, Chapter 3.7). The data demonstrate that these substrate-like compounds display affinities similar to those determined for full-length CYP116B1 (Chapter 4.13), and indicate that, although all three compounds bind relatively tightly to this P450, palmitoleic acid binding is considerably weaker than for myristoleic acid and arachidonic acid.

In Chapters 4.20 and 4.21, on the basis of a study by Nagy *et al.* (182) that identified a homologous protein from *Rhodococcus erythropolis* as a thiocarbamate herbicide degrading monooxygenase, the ability of *R. metallidurans* CYP116B1 to metabolise such compounds was investigated. Due to the inconclusive nature of UV-Visible spectroscopy assays used to identify EPTC and vernolate as substrates of the P450, detailed studies utilising LCMS and steady-state kinetic techniques were performed,

subsequently confirming enzyme-mediated activity that results in the hydroxylation of these compounds. As with the full-length enzyme, addition of these thiocarbamates to the heme domain protein induced barely detectable blue-shifts of the Soret band before spectra were obscured by ligand-derived solution turbidity, and thus binding titrations with these compounds were not possible. However, the perceived spectral changes are comparable with those of full-length CYP116B1 and thus indicate that EPTC and vernolate may be bound and metabolised by the CYP116B1 heme domain, although turnover would require reconstitution with the CYP116B1 reductase domains (or possibly with another reductase system or with an artificial system such as the peroxide shunt). It should be noted, however, that the isolated domains of the P450 BM3 enzyme have little affinity for each other, and reconstitute only a small level of fatty acid hydroxylase activity (225).

The data assembled here pertain to the binding of a range of ligands, previously shown to interact with full-length CYP116B1, to the heme domain of this *R. metallidurans* protein. Thus, these data report on the interactions between the ligands and the P450 without the influence of the 35 kDa reductase domain. Typically, the K_d values determined for the azole anti-fungals, unsaturated fatty acids, and small polar ligands (imidazole and sodium cyanide) compare well with the data for the full-length enzyme and show the same trends in tightness of binding of these compounds. However, in some cases the dissociation constants obtained for the heme domain are slightly tighter than those for intact CYP116B1. For example, miconazole binds to the heme domain with a K_d of 0.045 ± 0.005 μM compared with 0.21 ± 0.06 μM for the full-length protein, whilst the myristoleic acid dissociation constants determined for the heme domain and full-length protein are 3.29 ± 0.30 μM and 4.8 ± 1.76 μM, respectively. However, while it is noticeable that predicted K_d values are slightly lower for the heme domain in the case of many of the molecules tested, the differences in several instances are within the range of the error reported (e.g. for myristoleic acid above). Thus, the K_d changes do not drastically perturb ligand affinity and are often within the realms of experimental error. Hence, the binding titration data demonstrate that the removal of the reductase domain likely does not affect the configuration of the active site, and subsequently does not markedly influence the ligand/substrate binding properties of the CYP116B1 heme domain. In the full-length enzyme the position of the reductase domain with respect to the heme-containing subunit is unknown. However, the K_d values reported here suggest that the reductase is unlikely to obstruct

entry to the active site of CYP116B1 heme domain. Even if there was some steric hindrance, the minor differences in K_d values from intact CYP116B1 to heme domain suggest that these have no significant overall effect on substrate/inhibitor binding. Understanding of the nature of P450/redox partner interactions is an important issue in the field, and the determination of an atomic structure of intact CYP116B1 thus could provide critical data with ramifications beyond simply the understanding of heme domain/reductase domain reactions in the CYP116B1 system.

This investigation of the ligand binding properties of the CYP116B1 heme domain has confirmed them to be highly comparable with those of intact CYP116B1 across the range of compounds tested. Clearly removal of the reductase does not significantly affect heme domain structure and P450:ligand interactions. In the next section, the study of this *R. metallidurans* P450 progresses to more detailed studies of the properties of the heme, particularly its oxidation, spin and coordination state, using electron paramagnetic resonance spectroscopy.

5.7 Electron paramagnetic resonance of the CYP116B1 heme domain

Initial UV-Visible spectroscopic studies of the heme domain protein in Chapter 5.4 revealed that, when reduced and bubbled with carbon monoxide, the appropriate ferrous carbon-monoxy species was successfully formed, thus confirming this protein to be a cytochrome P450. Subsequently, in Chapter 5.6, the heme domain binding properties, and hence the active site of this protein, were investigated, focussing on the interactions of the P450 with a range of azole anti-fungals, unsaturated fatty acids (and other compounds), and small polar molecules. These spectroscopic studies were useful in characterising ligand-binding properties of the heme domain, and for comparison with the full-length CYP116B1. In order to obtain more detailed information on heme centre of this monooxygenase, electron paramagnetic resonance (EPR) was used. In Chapters 3.12 and 4.15 EPR was successfully employed as a tool to report on the oxidation, coordination, and spin states of the hemes of Mtb CYP51 and intact *R. metallidurans* CYP116B1, confirming the hemes of both of these enzymes to display typical properties of the cytochromes P450, with cysteinate proximal coordination of heme iron. Thus EPR was performed on the CYP116B1 heme domain in order to ensure that the heme of this domain protein has properties similar to those of the full-length protein from which it is derived (and typical of the cytochrome P450 superfamily in general),

and to ascertain whether reductase-dependent effects on the heme are evident by comparison of EPR data for intact CYP116B1 and its heme domain. As previously discussed in Chapter 3.12, EPR reports upon the resonance of unpaired electrons of a redox centre, be it an oxidised (ferric) P450 or a reduced (for the CYP116B1 centre) iron-sulphur cluster. Spectra are detected by sample irradiation with microwaves and in the presence of a varying magnetic field. The resultant spectrum, which is mathematically derived from the recorded microwave absorption data, and associated g-values, which report the size of the magnetic moment of the unpaired electrons acted on by the magnetic field, can subsequently be utilised to report on the oxidation, spin, and ligation states of the heme, as well as (in some cases) the type of heme (e.g. heme *a*, heme *b*, etc.) present in the sample (57,215,275). Hence, this technique has been widely applied to the cytochromes P450, including CYP51 from *M. tuberculosis*, P450cam from *Ps. putida*, and P450 BM3 from *B. megaterium* (159,199,218), thus allowing for uncomplicated comparisons of the properties of the hemes of these monooxygenases.

The EPR spectrum of the heme domain of *R. metallidurans* CYP116B1 was recorded by Dr. H. Seward at the University of East Anglia, using an aliquot of the oxidised enzyme diluted to 200 μM in 50 mM potassium phosphate pH 7.5. Data were recorded using an electromagnet and microwave source (Bruker ER-300D series) fitted with an ESR-9 liquid Helium flow cryostat (Oxford Instruments) and a Bruker ER-4116DM dual mode microwave cavity, and interfaced to a Bruker EMX control unit. In order to gather the EPR data, the protein sample was maintained at 10 K and was subjected to a microwave source with a power of 2.08 mW and modulation amplitude of 10 G. Subsequently, mathematical derivations were performed on the resultant microwave absorption data in order to produce the EPR spectrum shown in Figure 118.
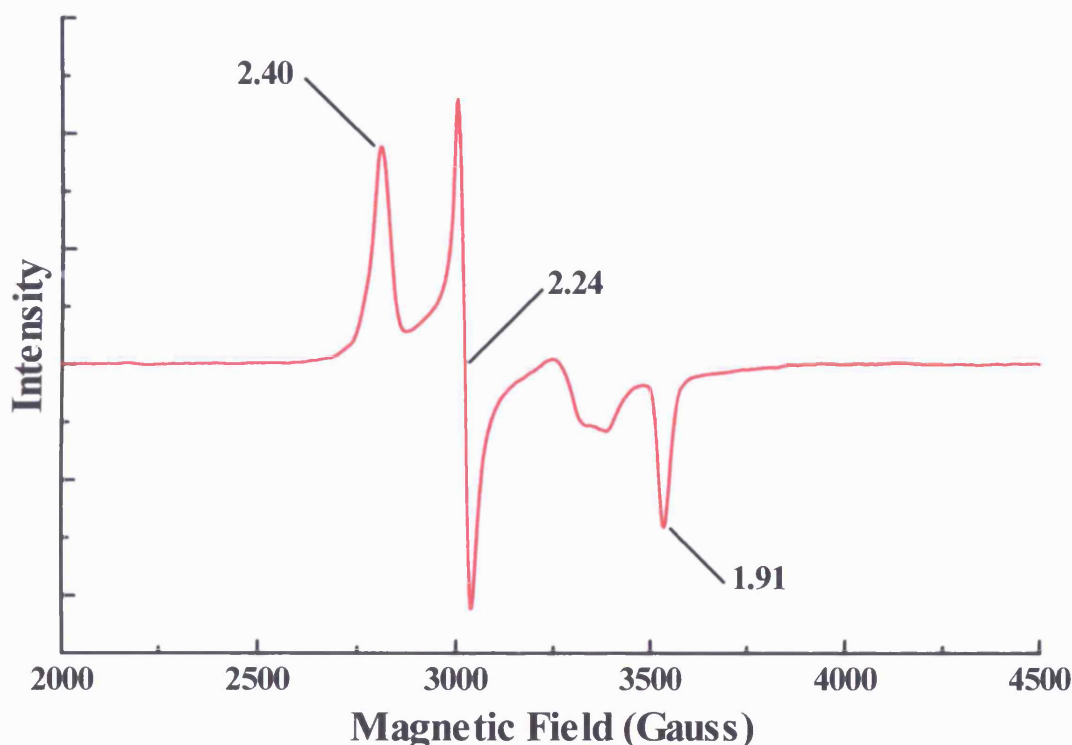
Figure 118 The electron paramagnetic resonance spectrum of oxidised *R. metallidurans* CYP116B1 heme domain. The spectrum profile and g-values ($g_z = 2.41$, $g_y = 2.24$, and $g_x = 1.91$) are similar to those observed for Mtb CYP51, P450 BM3, and CYP116B1, and indicate that the truncated *R. metallidurans* protein is a typical cytochrome P450, possessing a cysteinate-ligated, hexa-coordinated, low-spin ferric iron molecule at the centre of its heme macrocycle. Data were recorded using a Bruker ER-300D series electromagnet and microwave source, interfaced to a Bruker EMX control unit, at 10 K with 2.08 mW microwave power and a modulation amplitude of 10 G. The investigation was performed using an aliquot of protein diluted to 200 µM in 50 mM potassium phosphate pH 7.4.

The EPR spectrum of the heme domain displayed in Figure 118 is similar in profile to that of numerous cytochromes P450, most significantly the intact CYP116B1 from which this protein is derived (Chapter 4.15). Furthermore, the g-values of $g_z = 2.40$, $g_y = 2.24$, and $g_x = 1.91$ are almost identical to those obtained for the full-length enzyme ($g_z = 2.42$, $g_y = 2.25$, and $g_x = 1.93$), and fall within the ranges observed for other well-characterized cytochromes P450 such as *B. subtilis* P450 BioI ($g_x = 2.41$, $g_y = 2.25$, and $g_z = 1.92$), *M. tuberculosis* CYP51 ($g_z = 2.44$, $g_y = 2.25$, and $g_x = 1.91$), and *B. megaterium* P450 BM3 ($g_x = 2.42$, $g_y = 2.26$, $g_z = 1.92$) (159,194,199,218). The similarities to CYP116B1 and these other cytochromes P450 suggest that the heme domain is a typical P450, possessing the hexa-coordinated, cysteinate-ligated heme iron that characterizes enzymes of this class. The g-values obtained for this protein also

confirm that the heme iron is in the ferric, low-spin state (S = $\frac{1}{2}$), in which four of the five d-orbital electrons are paired, rather than the excited, high-spin state (S = $\frac{5}{2}$), where none of the d-orbital electrons are paired, and which subsequently gives rise to a different set of g-values. Furthermore, the shape and associated g-values of this spectrum are consistent with those of a (P450-like) *b*-type heme, as for other heme types (e.g. heme *a*) these features are found at different positions and spectra are broader. For example, horse heart cytochrome *c* and cytochrome aa_3 from *Nitrosomonas europaea*, which respectively contain *c*-type and *a*-type heme macrocycles, demonstrate g-values of g_x = 3.06, g_y = 2.25, and g_z = 1.25 and g_x = 3.04, g_y = 2.26, and g_z = 1.47, respectively (275,276). The CYP116B1 heme domain data also indicate the absence of any significant high-spin component, thus demonstrating that, like its full-length counterpart, the heme domain is purified with the heme in predominantly the low-spin configuration. These confirmations of the spin, oxidation, and ligation states of the heme domain, and the high degree of correlation with the EPR data for *R. metallidurans* CYP116B1, further confirm that folding, and the coordination and environment of the heme centre are highly similar in both intact CYP116B1 and its heme domain. In addition, it is evident that removal of the reductase domain does not perturb these features to any significant degree, at least in the oxidised (heme iron EPR active) forms of these proteins. These data provide evidence for the integrity of the CYP116B1 heme domain, giving further confidence that the redox potentiometry data for CYP116B1 heme domain (reported in the next section) accurately report on the properties of the heme as seen in the intact enzyme.

5.8 Redox potentiometry of the CYP116B1 heme domain

The studies of the CYP116B1 heme domain presented in this chapter have predominantly focussed on the characterization of the oxidation, ligation and spin-states of the heme at the core of this cytochrome P450, and its interactions with various ligands. In this section the redox potential of the heme domain is investigated in order to compare and contrast the thermodynamic properties of this domain with the intact *R. metallidurans* protein (CYP116B1) from which it is derived, as well as to contrast data with those for the *M. tuberculosis* sterol demethylase (CYP51) characterized in Chapter 3.17, and other previously studied cytochromes P450. The precedent for the use of this anaerobic technique in the study of the heme domain comes from its successful

employment in studies of numerous other cytochromes P450 and their associated redox systems. For example, this method has successfully identified the mid-point reduction potentials of the three components of the fused P450 BM3 system from *B. megaterium*, as well as for those of P450 BioI, and its associated flavodoxin and ferredoxin proteins from *B. subtilis* (194,277). Such studies identify the thermodynamic differences between the centres in these enzymes, and report on substrate-dependent effects on heme iron reduction potential. In Chapter 3.17, the technique was used to show that, for Mtb CYP51, heme iron potential is influenced by the binding of a sterol ligand (estriol). The potential of the P450 was elevated to a value closer to that of the ferredoxin, and hence more thermodynamically favourable to electron transfer between these two proteins. Work in Chapter 4.22 also revealed reduction potentials for the heme and reductase (flavin) components of full-length CYP116B1. Hence, comparison of the potential for the isolated heme domain will be of interest in order to provide further data (relating to the consequences of the removal of the reductase domain) on heme iron electronic properties. In addition, removal of the reductase domain will enable collection of absorption *versus* potential data that are not influenced by spectral contributions from flavin or iron sulphur centres. As was described in Chapters 3.17 and 4.22, the central principle of this technique is the change of the equilibrium between the two oxidation states (Fe^{3+} and Fe^{2+}) of the P450 heme iron with respect to an applied potential. Perturbation of the P450 redox equilibrium is achieved by titration with a reductant (sodium dithionite), which reduces the heme iron in increments. The extent of reduction can be followed using UV-Visible spectroscopy to monitor the associated spectral changes at defined potential. On complete reduction, a reverse titration with an oxidant (potassium ferricyanide) is done in the same way to ensure reversibility of the redox titration and absence of hysteretical behaviour in the reductive and oxidative titrations. The absorbance change data are plotted versus applied potential and data fitted to the Nernst equation to determine the mid-point reduction potential of the P450.

The determination of the mid-point reduction potential of the CYP116B1 heme domain was performed in the anaerobic conditions of a Belle Technology glove box, using the technique of Dutton (235) reported previously in Chapter 3.17. Oxygen levels within the nitrogen environment were maintained at less than 2 ppm, whilst all solutions were degassed with argon. A solution of the heme domain protein with a final concentration 5.4 µM was prepared in degassed 50 mM KPi pH 7.0, supplemented with 10 % glycerol for protein stability, subsequent to the enzyme being passed down a pre-

equilibrated BioRad Econo-Pac 10DG desalting column to eliminate residual oxygen. Following the precedent of Munro *at al.* (17) 0.3 µM methyl viologen, 1 µM benzyl viologen, 2 µM phenazine methosulfate, and 7 µM 2-hydroxy-1,4-naphthoquinone were included in the assay, as these compounds assist in the electronic equilibration between the protein and the electrode used to monitor the solution potential. Absorption spectra of the enzyme solution were subsequently recorded using a Cary UV-50 Bio UV-Visible spectrophotometer scanning between 250 and 800 nm following the addition of small aliquots (typically 0.2 – 1 µl) of sodium dithionite stocks diluted in degassed 50 mM KPi pH 7.0. Simultaneously, the potential of the enzyme solution was recorded using a Pt/Calomel electrode (Thermo Russell Ltd.) linked to a pH meter (Hanna pH 211) reading in mV. At the point where no further spectral changes could be achieved with dithionite, the oxidative titration was initiated using potassium ferricyanide from a stock solution (10 – 50 mM), to ensure reversibility of the system (as discussed above). Subsequently, from the collated spectral data (Figure 119), changes in absorbance relating to the reduction of the enzyme were plotted against corresponding potentials of the solution, normalised to a standard hydrogen electrode by the addition of +244 mV. Using Origin software (Microcal), the resultant curves (Figure 120) were fitted to a single electron Nernst function (Equation 6, Chapter 3.17) to define the redox potential associated with the transition from the oxidised to the reduced form of heme iron in the CYP116B1 heme domain.

Spectra demonstrating the optical changes induced by the titration of sodium dithionite with the CYP116B1 heme domain during the determination of the P450's mid-point reduction potential are shown in Figure 119. The initial spectrum of the oxidised heme domain demonstrates the typical features of a cytochrome P450, with a Soret band at 418 nm and Q-bands at 568 and 534nm. Upon reduction, the Soret band is observed to diminish in intensity and shift to towards longer wavelength. Concurrently, in the visible region, an absorbance feature centred at 559 nm is seen to develop. The spectra indicate that (with dithionite as reductant) the Soret band of the heme domain comes to rest at approximately 423 nm, whilst an isosbestic point at 403 nm indicates a clean transition between the oxidised and reduced forms of this cytochrome P450. These spectral changes are very similar to those observed during redox potential determinations for Mtb CYP51 (Chapter 3.17) and intact *R. metallidurans* CYP116B1 (Chapter 4.22), as well as for the *M. tuberculosis* cytochromes P450 CYP144 and CYP121 (unpublished data). However, the optical

changes are unlike those seen for certain other well-characterized P450s, including P450 BM3 and P450cam, in which the visible band for reduced P450 is a single, less intense species, and the Soret band moves to shorter wavelengths (192,234). The most likely origin of the long wavelength Soret shift in CYP116B1 and other P450s is that the cysteine thiolate is protonated to the thiol, as discussed in Chapters 3.17, 3.19, 3.20, and 3.21, and presented in our publication on the properties of Mtb CYP51 (159). As seen for Mtb CYP51, the collapse of the ferrous carbon-monoxy species (from P450 to P420) has its origins in the protonation of the heme thiolate in the ferrous enzyme, and CYP116B1-like spectral shifts are observed for CYP51 on reduction in absence of carbon monoxide.
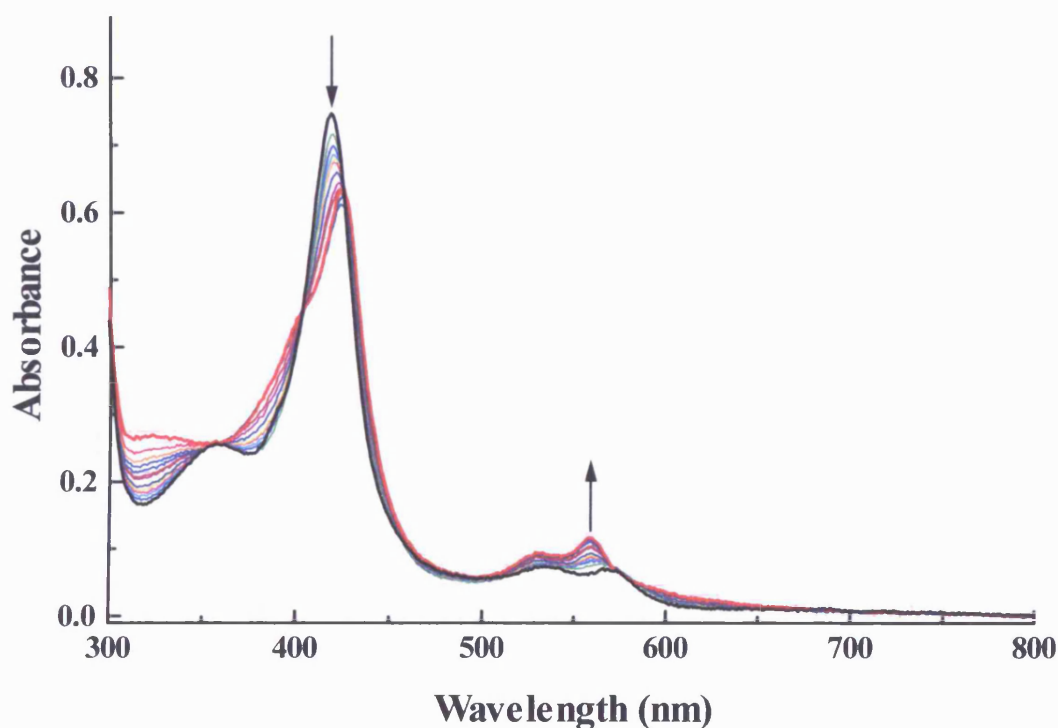
Figure 119 Selected UV-Visible spectra recorded during the determination of the mid-point reduction potential of the CYP116B1 heme domain. The oxidised and fully-reduced spectra of the heme domain protein are shown in black and red, respectively, and identify that, as with the full-length enzyme and CYP51 from *M. tuberculosis* (Chapter 4.22 and 3.17, (159)), titration with sodium dithionite results in a red shift of the Soret band to 423 nm, whilst simultaneously inducing an increase in absorbance at 559 nm. The absence of significant signal bleaching between 450 and 500 nm compared to the equivalent full-length CYP116B1 data (see Figure 97 in Chapter 4.22) indicates that no flavin-containing reductase component is present in this sample. In this investigation, protein was diluted to a final concentration of ~5.4 μM in 50 mM KPi pH 7.0, containing 10 % glycerol to aid protein stability. An isosbestic point at 403 nm signifies a clean transition between the oxidised and reduced forms of the heme iron, and the arrows denote the direction of the spectral changes induced by the addition of the reductant.

348

The spectral data collected for the heme domain compare well with equivalent data for intact CYP116B1 (Chapter 4.22), with both showing similar changes in the position of the Soret and visible region bands. However, the intensity of the full-length enzyme Soret feature decreases to a greater extent than that of the heme domain, and in spectra of the heme domain there is no apparent bleaching between 450 and 500 nm. The cause of these spectral changes in the full-length enzyme were identified as pertaining to reduction of the reductase (flavin- and iron sulphur-containing) component of the protein, and hence confirm that spectral changes observed for the CYP116B1 heme domain relate solely to reduction of the heme iron.
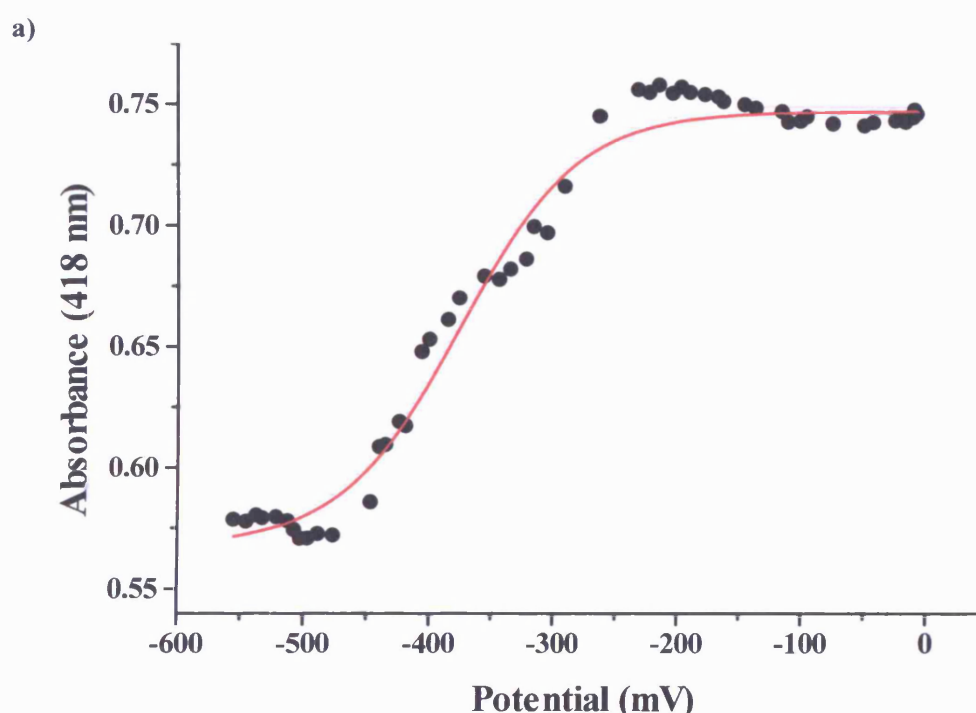
Figure 120 The plots of the changes in absorbance at **a)** 418 nm and **b)** 559 nm *versus* potential (mV) generated from the spectral data recorded during the redox titration of the CYP116B1 heme domain. The plots are fitted with the single-electron Nernst equation (Equation 6, Chapter 3.17) and identify mid-point reduction potentials for the heme iron of –375 ± 8 mV (418 nm) and –386 ± 6 mV (559 nm). These values compare well with the redox potential determined for the full-length *R. metallidurans* protein (Chapter 4.22), indicating that the thermodynamic properties of the CYP116B1 heme iron are not greatly affected by the removal of the reductase component. The potentials are normalised against a standard hydrogen electrode (SHE).

b)
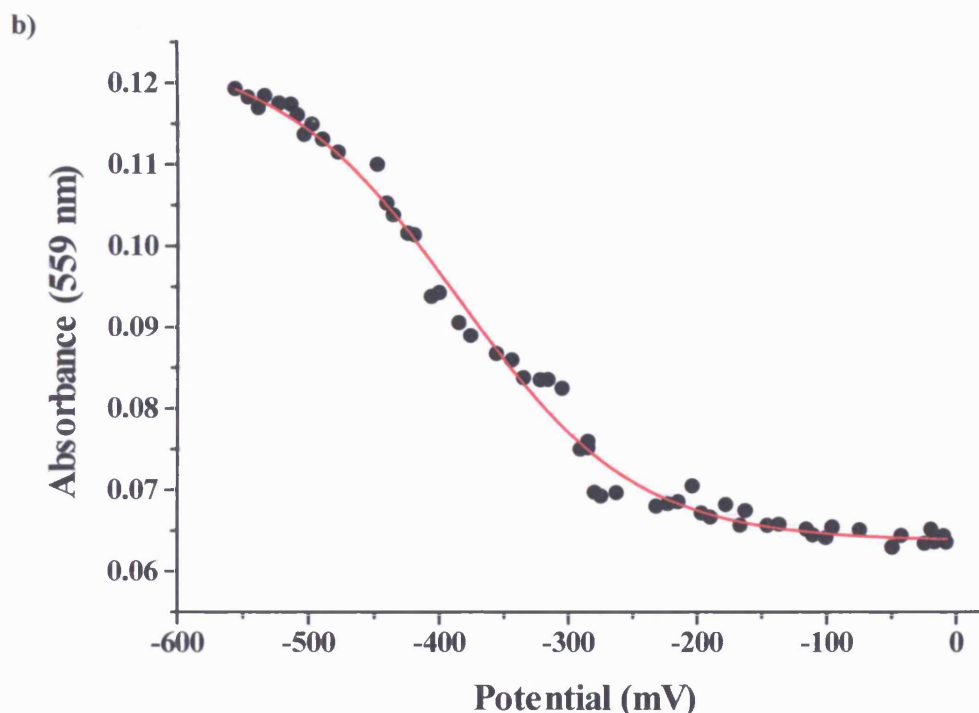
From the spectral data collected during the redox titration of the CYP116B1 heme domain, plots of absorbance changes at two independent wavelengths *versus* normalised potential were created, and are shown in Figure 120. The wavelengths used for these plots were 418 and 559 nm, as the former corresponds to the shift of the Soret band to longer wavelengths, whilst the latter represents the increase in absorbance that occurs in the visible region during the reductive titration. Subsequently, the resultant sigmoidal plots, which relate to the transition from the oxidised Fe^{3+} form to the reduced Fe^{2+} form, were fitted with a single-electron Nernst function (Equation 6, Chapter 3.17) and reveal mid-point redox potentials of -375 ± 8 mV at 418 nm and -386 ± 6 mV at 559 nm. These values are inseparable within error and indicate that the redox potential of this truncated *R. metallidurans* is approximately -381 mV. This value is slightly less negative than that reported for the heme component of full-length CYP116B1 (-396 ± 12 mV, Chapter 4.22). Although this small difference is unlikely to have a major influence on the properties of the heme and its ability to participate in redox reactions, it possibly reflects some structural perturbations on the heme centre mediated by interactions with the reductase component in intact CYP116B1. By analogy to other of multi-domain cytochromes P450, such as P450 BM3 and CYP116B2, these changes were not unexpected, as both previous studies demonstrate that elimination of reductase subunits leads to only minor deviations in the thermodynamic properties of the redox

centres in these heme-containing proteins (185,192). As with the full-length enzyme, the heme domain redox potential falls within the range of -300 mV (P450cam, (234)) to -418 mV (P450 BM3,(117)) identified in previous studies, thus suggesting that this protein is thermodynamically typical of the cytochromes P450. Moreover, as the heme iron reduction potential of the heme domain is barely perturbed from that of full-length CYP116B1, the unfavourable thermodynamic gradient between the heme and reductase sub-units remains intact, thus indicating that substrate-induced shifts in heme potential must account for enhanced electron transfer between these redox centres that facilitates catalytic activity with vernolate and EPTC substrates.

This determination of the mid-point reduction potential of the CYP116B1 heme domain concludes the data gathered for the CYP116B1 enzyme. When EPR and UV/Visible spectroscopy (Chapters 5.7 and 5.4) are considered with these redox potential data, and compared with the studies of intact *R. metallidurans* CYP116B1, Mtb CYP51 and other well-characterized cytochromes P450, several properties of the CYP116B1 heme domain are seen to be typical of other members of the P450 superfamily of monooxygenases. However, there are also important differences – including the tendency of the heme thiolate to be protonated on heme iron reduction. In the following chapter, the significance of the data collected during the characterizations of the two *R. metallidurans* proteins and Mtb CYP51 are further discussed, along with suggestions for further studies of these proteins, in particular for the heme and reductase domains of CYP116B1.

Chapter 6

Discussion and future work

The previous three chapters report the characterizations of CYP51 from *Mycobacterium tuberculosis* and CYP116B1 from *Ralstonia metallidurans*, presenting the data collated and considering their significance with respect to well-characterized cytochromes P450 from other organisms. Furthermore, these chapters attempt to evaluate the data in terms of their impact on the further understanding of the superfamily of monooxygenases to which they both belong. In this chapter an overview of these findings is given; highlighting the most significant points from each study, identifying points that could be expanded on in future investigations and considering the medical and biotechnological implications deriving from these studies. Appropriately, the results from the study of Mtb CYP51, an enzyme considered as one of the ancestral P450s from which all others may derive (195), are presented first before moving on to discussion of data for the redox partner-fused *R. metallidurans* CYP116B1 and its domains.

6.1 *Mycobacterium tuberculosis* CYP51

The studies of CYP51 reported in Chapter 3 were performed in order to provide a comprehensive spectroscopic characterization of this *M. tuberculosis* cytochrome P450, focussing on previously unreported aspects of this protein and its interactions with a physiological redox partner. As discussed in Chapter 3, partial characterization of Mtb CYP51 has previously been reported (36,51,169,170), with many of these studies being directed towards the resolution of the atomic structure of this monooxygenase, often in complex with ligands such as azole anti-fungals and sterols (35,51). Other studies of this P450 indicate, by homology to other P450s, that Mtb CYP51 is a 14α-sterol demethylase (195,196,202), whilst work by Bellamine *et al.* (169) identifies the enzyme as capable of metabolising the plant sterol obtusifoliol, albeit at a very slow rate. A physiologically relevant role for Mtb CYP51 as a sterol demethylase is cast into doubt by the lack of data for a sterol pathway in *M. tuberculosis*. However, this does not prevent the undertaking of detailed biophysical and spectroscopic characterization of a cytochrome P450 that displays great promise as a potential drug target by which to combat this unremitting human disease.

In summary, the study of *M. tuberculosis* CYP51 has provided a thorough spectroscopic and thermodynamic characterization of this sterol demethylase. Many of the techniques employed to study this P450, such as resonance Raman, EPR, circular

dichroism and UV-Visible spectroscopy, have confirmed this monooxygenase to be a typical member of the cytochromes P450, particularly with regards to the spin, ligation, and oxidation states of the heme iron in the resting, ferric form. They also showed that the protein structure (and particularly the heme environment) have apparently normal P450 features, as demonstrated by the fact that binding of azoles and various other ligands within the active site of this protein produce optical and other spectroscopic perturbations consistent with observations made for binding of similar ligands to other P450s (33,158,199). However, Mtb CYP51 also displays non-standard spectral features on reduction and on binding carbon monoxide, as described below. Thus, spectroscopic studies have also advanced the understanding of the nature of the heme thiolate ligand in P450s and its protonation. These studies confirm that the P450 (thiolate-coordinated) and P420 (thiol-coordinated) species of CYP51 are interconvertable, and that the P450 CO-complex is unstable and collapses to the P420 form over a period of minutes. Importantly, this collapse is influenced by external factors (i.e. buffer pH), and that the collapse can be all but arrested by the binding of the substrate analogue estriol. It is likely that binding of a true physiological substrate would completely arrest, or even reverse, the P450-to-P420 collapse. Interestingly, the terms "P450" and "P420" are almost invariably taken to reflect the Fe(II)CO complexes of a particular P450 enzyme, and to describe forms that are "native" and "inactive", respectively. In studies of the reduced, ligand-free species of Mtb CYP51, optical changes indicative of thiol-coordination of heme iron develop, and thus indicate that P420 formation (i.e. heme thiolate protonation) is a phenomenon associated with heme iron reduction, and that the binding of CO (at least for Mtb CYP51) solely serves to provide a spectral signature for an event (heme thiolate protonation) that occurs at the level of heme iron reduction.

One particular aspect of Mtb CYP51 which has not featured strongly in preceding studies of this enzyme is its interactions with a proposed redox partner protein from the same organism. The studies reported in Chapter 3.16 indicate that interactions of the ferredoxin (Fdx, encoded by the gene *Rv0763c* adjacent to CYP51) and the CYP51 are likely to be transient and peripheral, and that these interactions impart little detectable structural change on either protein. Importantly, the reduction potential of the Fdx (−31 mV) is substantially more positive than that of CYP51 in its substrate-free form (−375 mV), as established by spectroelectrochemical titrations of both proteins. The addition of the substrate-like molecule estriol to Mtb CYP51 induces a substantial increase in the midpoint reduction potential of the heme iron (−225 mV), closing the gap partially to

the Fdx. However, a substantial thermodynamic barrier still exists between these proteins (194 mV). Kinetics studies here show that electron transfer can occur across this thermodynamic barrier between reduced Fdx and the estriol-bound CYP51. In the cellular environment, one could consider that the slow-growing pathogen may actually have evolved a thermodynamic "hurdle", put in place in order to tune the enzyme's catalytic activity to the product accumulation required by this slow-growing bacterium. While such a hypothesis clearly remains to be rigorously tested, it is clear that Fdx can support not only electron transfer to the CYP51 heme iron, but also demethylation of sterol substrates (159,169). Thus, there remains further interesting experiments to be done to resolve the unusual interactions between Mtb CYP51 and its adjacent redox partner ferredoxin, and the physiological reasons underlying their peculiar thermodynamic relationship.

With regards to the medical significance of this cytochrome P450, the ligand binding studies provide some of the most important information. The preponderance of cytochromes P450 in the *M. tuberculosis* genome implies that several of these enzymes should have important roles in the pathogenicity or viability of this organism, whilst sequence homology with other P450s indicates Mtb CYP51 should be a sterol demethylase. The data presented here confirm that sterols induce substrate-like Soret band shifts, and go hand-in-hand with previous work in the Waterman group that demonstrated demethylation of obtusifoliol and other sterols by this enzyme (169). In my studies, estriol proved the most effective ligand, inducing by far the greatest shift in heme iron spin state equilibrium (towards high-spin). However, the absence of the C_{14} methyl group in estriol indicates that this is unlikely to be a physiologically relevant substrate for Mtb CYP51. Moreover, since no endogenous sterols were identified in *M. tuberculosis*, it is doubtful that this P450 performs a sterol demethylase role insofar as metabolism of endogenous sterols. However, a role in metabolising host sterols cannot be ruled out at this stage, and in this respect it is pertinent to recall that cholesterol is apparently crucial for Mtb infection of macrophages (172). The extremely tight (i.e. low K_d values) and inhibitory binding (type II spectral shifts induced, indicative of heme iron coordination) of the azole anti-fungals to Mtb CYP51 is significant for the treatment of multi-drug resistant *M. tuberculosis*. In unpublished work (done with Prof. Stewart Cole and colleagues at the Institut Pasteur, Paris), we have shown that azoles of the type used in this study have MIC values comparable (or better) than those for existing leading antituberculars. This indicates that these azole compounds could be

used as a basis from which to design drugs to impair the activity of this (and other) P450s that may be of importance to *M. tuberculosis*. Indeed, if these P450s are identified as being involved in the production of components of the thick waxy envelope of this mycobacterium, then a number of azole-based compounds, whose human toxicity had been established as acceptable and which were systematically tolerated, might well be a suitable treatment for the pathogen. However, this relies on the determination of the identity and cellular function of the target P450s in Mtb. This will require systematic investigation of the role of the various P450s in the physiology, pathogenicity and viability of *M. tuberculosis*.

It is clear that future studies of this enzyme should focus on its cellular role and should be aimed at establishing whether metabolism of host sterols is a *bona fide* function of Mtb CYP51, or if the P450 has been adapted in evolution to perform a distinctive role. Other areas of interest clearly revolve around the unusual spectroscopic features of the P450. For instance, the unusual spectral observations made with 2-phenylimidazole, which appears to behave in a manner typical a substrate rather than an inhibitor in terms of heme optical shifts induced. This phenomenon may result from the binding of 2-phenylimidazole in the vicinity of the CYP51 heme, possibly coupled to an inability of the azole to coordinate the heme iron in this compound due to steric restrictions. Clearly an atomic structure of the CYP51-2-phenylimidazole structure would resolve the binding mode of the ligand and provide an explanation for the unexpected optical shift induced. In addition, the recognition that reduction of CYP51 results in optical changes similar to those observed for thiol-coordinated globins, and that the ferrous-CO complex collapses from P450 to P420 over minutes indicates that protonation of the thiolate bond to the heme iron occurs on reduction. The fact that this process could be arrested by addition of the substrate-like molecule estriol points to the fact that this process is reversible and likely has a regulatory function. It will be of interest to establish whether binding of a "true" physiological substrate could completely prevent P420 formation. In addition, the determination of an atomic structure for the reduced (ferrous) CYP51 would be important to establish if major structural perturbations accompany the P450/P420 transition in this enzyme. Structural studies could be complemented by more detailed spectroscopic analysis of the P420 state and of the P450/P420 transition using spectroscopic techniques such as FTIR, CD and small angle x-ray scattering (SAXS) to further detail any structural changes accompanying the transition. Finally, more detailed analyses of the process of

reconversion of P420 to P450 on enzyme reoxidation clearly requires more detailed analyses, possibly using stopped-flow methods if the formation of thiolate occurs rapidly following oxidation of the heme iron from the ferrous to the ferric form. Clearly this important model enzyme in the CYP51 family (and indeed in the entire P450 superfamily) requires more detailed studies in future, in order to resolve both physiological function, mechanism of inactivation and reactivation, and potential as a *M. tuberculosis* drug target.

6.2 *Ralstonia metallidurans* CYP116B1

The second major P450 system analysed in the work presented in this thesis is the P450-redox partner fusion system CYP116B1, encoded by gene 1832 from *Ralstonia metallidurans*. While the studies on the Mtb CYP51 system relied on substrates and substrate-like molecules identified in preceding work, the work presented here for CYP116B1 led to the identification of substrate molecules and the determination of reaction products from turnover with CYP116B1 (see Chapter 4.21). While the Mtb CYP51 gene was cloned in advance of studies presented in this thesis, the CYP116B1 gene had not been previously cloned or expressed, and hence the first steps in the study of this protein involved cloning gene 1832 (CYP116B1) and optimising the expression and purification of this putative redox partner-fused cytochrome P450. Subsequently, the other studies of *R. metallidurans* CYP116B1 presented in Chapter 4 present the initial characterization of a redox partner-fused cytochrome P450 whose composition is dissimilar to both the previously described P450/CPR fusion class (e.g. P450 BM3), and the more typical multi-component bacterial P450 systems (e.g. P450cam and its associated proteins). Instead, CYP116B1 is a member of a novel class of P450/redox partner fusion enzymes, whose members also include the *Rhodococcus* sp. NCIMB 9784 P450 fusion protein (130). In both cases, it has now been confirmed that the P450 is fused to a reductase system homologous to phthalate dioxygenase reductases (6,145,146). The spectroscopic techniques used to study the *R. metallidurans* protein have generated data that confirm that CYP116B1 is a fully folded protein replete of its three predicted redox centres (i.e. heme in the P450 domain and FMN/2Fe-2S centres in the reductase domain). Furthermore, EPR and resonance Raman studies confirm that the resting P450 heme has spectroscopic properties consistent with a thiolate ligated ferric heme iron in a predominantly low-spin state, and that vibrational signals from the

heme chromophore are indicative of a domed heme conformation with asymmetric positions of the vinyl groups. Spectroscopic studies of the CYP116B1 heme were consistent with those for hemes contained in other structurally characterized P450s (CYP51 and P450 BM3). Analysis of the nature of the CYP116B1 active site by optical binding studies confirms that this *R. metallidurans* P450 interacts with a number of ligands, producing Soret band shifts towards either shorter wavelength (indicating substrate-like binding features) or longer wavelength (indicative of inhibitory coordination of the P450 heme iron). The weak binding of more hydrophilic and/or polar ligands such as imidazole and cyanide is consistent with a hydrophobic CYP116B1 active site pocket in which substrates and inhibitors bind. This, in turn, is typical of the P450 superfamily. By contrast, hydrophobic molecules such as fatty acids and several polycyclic azole antifungals were shown to bind tightly to CYP116B1. Interestingly, a selection of unsaturated fatty acids were shown to induce substrate-like type I Soret band shifts, whereas negligible optical changes were seen for saturated fatty acids of similar chain length. Affinity for unsaturated fatty acids was typically in the low micromolar range, and further evidence for strong affinity of this type of molecule for CYP116B1 was obtained from the tight binding of fatty acid-linked imidazole inhibitors (ω-imidazolyl decanoic, undecanoic and dodecanoic acids). Interestingly, although a number of azole antifungal drugs were shown to coordinate the CYP116B1 heme iron, fluconazole (a leading, systemically tolerated azole) did not induce any significant shift in the heme absorption. Fluconazole is the most water-soluble of the azoles tested, and it is likely that this factor (rather than steric constraints) explains the apparent inability to bind CYP116B1 and ligate its heme iron. In further studies of the heme centre, it was found that the extinction coefficient for the heme iron (by the pyridine hemochromagen method) was 137 mM^{-1} cm^{-1} at the Soret maximum in the oxidised form of CYP116B1. This compared favourably with the value of 134 mM^{-1} cm^{-1} for Mtb CYP51 (187). Both these values are substantially greater than might be predicted by using the method of Omura and Sato relating to the properties of reduced and reduced/CO-bound forms of the enzymes (50). These data are consistent with measurements made for other P450s recently, and cast some doubt on the accuracy of the Omura and Sato method. In parallel studies, EPR (of the reduced enzyme) and fluorescence analyses confirmed that CYP116B1 contains both 2Fe-2S and FMN centres, as predicted on the basis of amino acid sequence similarities of the CYP116B1 reductase with phthalate dioxygenase reductases.

Kinetic studies using steady-state and stopped-flow methods demonstrate that the reductase component of the CYP116B1 enzyme is capable of receiving electrons from the co-enzymes NADPH and NADH, with a preference for the former (i.e. lower K_d and K_m values for NADPH; in the case of stopped-flow data the K_d for NADPH is too low to be determined accurately). Steady-state studies confirm that electrons donated by these co-enzymes can be passed through this domain and onto artificial electron acceptors and to the heme-containing P450 subunit. Furthermore, these studies indicate that electron transfer through the reductase system occurs quite efficiently and at speeds that could allow rapid oxygenase activity (assuming that the heme reduction step is not substantially slower than preceding steps) in this system. The limiting steady-state rate of cytochrome c reduction approaches 200 min^{-1} with NADPH as the electron donor under conditions used. However, it should be noted that this rate is substantially lower (by well over an order of magnitude) than that determined for P450 BM3.

In view of the similarity of CYP116B1 to the "stand alone" P450 CYP116A1 and the fact that CYP116A1 was isolated on the basis of its ability to oxygenate thiocarbamate herbicides, two thiocarbamates were selected for binding studies with CYP116B1: vernolate and EPTC. Optical binding studies indicated minor shifts in spin-state equilibrium towards high-spin, consistent with substrate-like properties for these molecules. Steady-state studies indicated that vernolate k_{cat} values were 57 min^{-1} (with NADPH) and 34 min^{-1} (with NADH); and k_{cat} values for EPTC were 31 min^{-1} (NADPH) and 17 min^{-1} (NADH). Thus, NADPH was apparently the favoured co-enzyme for optimal rate. Turnover studies (using LCMS) confirmed that NAD(P)H oxidation was linked to substrate hydroxylation and that both vernolate and EPTC were hydroxylated on N-alkyl chains, with vernolate being the best substrate (as inferred from steady-state studies). Thus, these data confirm that CYP116B1 is a *bona fide* P450 oxygenase, in which electrons are transferred from NAD(P)H through a phthalate dioxygenase reductase-like redox partner (containing FMN and 2Fe-2S redox centres) and onto the heme iron. Rates of hydroxylation of these substrates are somewhat slower than those for steady-state reduction of cytochrome c (which likely reports on electron transfer from the 2Fe-2S centre, the same cofactor that would deliver electrons to the P450 heme), suggesting that 2Fe-2S-to-heme electron transfer in CYP116B1 may be at least partially rate-limiting in steady-state catalysis of oxygenation of EPTC/vernolate. However, these may not be the optimal substrates for the enzyme, so this conclusion may be slightly premature.

The data presented for CYP116B1 advance our general understanding of the relationship of cytochromes P450 and their redox partner proteins, whilst also demonstrating that what was once considered a rather straightforward format comprised of either a prokaryotic (Class I) or eukaryotic (Class II) electron transfer system, is in fact highly diverse, and specialised for specific physiological roles. The CYP116B1 characterization also indicates that, by the construction of efficient, self-sufficient fusions, this redox system has the potential to be utilised by the biotechnology sector as a mechanism for driving other cytochromes P450, perhaps such as those involved in antibiotic and vitamin synthesis (45,110). Fusions of this type would reduce the number of redox protein components, thus requiring less time and effort in the expression of these individual proteins, and subsequently reducing the costs of generating the desired product from the relevant P450 enzyme. However, the development of this type of system would require careful engineering to establish P450-reductase linkage that is appropriate for efficient electron transfer between the enzymes. The discovery that CYP116B1 can mediate degradation of thiocarbamates signifies that this P450 is likely have descended from a common ancestor to its homologue from *R. erythropolis* (CYP116A1), and hence perform a similar physiological role. The activity of CYP116B1 with these compounds also denotes that, in a time of enhanced ecological awareness, this enzyme could be employed as a non-polluting agent in the bioremediation of contaminated soils, whilst the altered selectivity of the P450 towards particular members of the thiocarbamate herbicides, or similar compounds, may be possible by the mutagenesis of key active site residues. Such progress could be made, for instance, by engineering CYP116B1 into crop or other plants to allow these to survive in the soil and to break down the herbicide contaminants.

The study of *R. metallidurans* CYP116B1 has covered key aspects of the spectroscopic and kinetic characterization of this cytochrome P450. Thermodynamic studies are discussed with relevance to molecular dissection of the domains of CYP116B1 (see Chapter 6.3 below). However, further work on this fascinating system is clearly required. Although substrates for this P450 have been determined, the activity with these compounds is low compared with other fused P450 systems (e.g. P450 BM3, (192)), suggesting these compounds are not the true (or optimal) substrates of this monooxygenase. However, this said, their rates of oxygenation are not substantially lower than the steady-state reduction of cytochrome *c* by the same enzyme. Further investigations to identify a physiological substrate could be done by optical binding

assays to identify compounds from fractions of *R. metallidurans* cellular extracts that induce type I Soret band shifts. In turn, using any further potential substrates identified, this work would allow for further kinetic studies of electron transfer through this multi-redox centre protein, as well as allowing for further product analysis to confirm the reaction that CYP116B1 catalyses with such molecules. As discussed also in Chapter 6.3 below, redox potentiometry studies in the presence of different substrates may also lead to better understanding of mechanisms of control of electron transfer in this system, in which there appears to be a thermodynamic barrier to electron transfer between the iron-sulphur and heme centres. Such barriers are also evident in other cytochromes P450 (117,192,234). Another aspect of this enzyme that has not been investigated in detail as yet is the structural arrangement of the domains that facilitates oxygenase activity. The studies have proven that electron transfer through the system from NAD(P)H to the heme of the P450 is possible. However, the way in which the reductase subunit of the protein positions itself with respect to the heme subunit in order to facilitate this activity is uncertain. The FMN-binding domain (considered to be the point of entry of electrons from NAD(P)H is in the centre of the protein, while the 2Fe-2S- and heme-binding domains are at the ends of the protein. Thus, a "wrapping around" of domains is envisaged to enable catalysis in CYP116B1. Hence, crystallographic studies are necessary in order to identify where the protein subunits make contact, and thus how electrons pass from the FMN to the iron-sulphur cluster, and ultimately to the heme. Although such crystallographic studies would be significant in the further understanding this *R. metallidurans* protein, crystallography of large, multi-domain P450 proteins is difficult and has been unsuccessful, to date, for the P450 BM3 enzyme. For this reason, and in order to deconvolute thermodynamic and spectroscopic properties of the system, as well as further defining its discrete domain nature, studies of the individual heme and reductase domains were reported in Chapter 5.

6.3 *R. metallidurans* CYP116B1 heme and reductase domains

The characterization of the heme and reductase domains of CYP116B1 are still in their relative infancy. However, the initial studies of these proteins have added to our understanding of the thermodynamic and other properties of CYP116B1. The cloning and expression of these domains in Chapter 5.2 have shown that these two protein domains can exist as stable, separate entities, and that their UV-visible spectral properties are consistent with those seen in the full-length enzyme. As with CYP116B1, the formation of the ferrous carbon-monoxy species of the heme domain (comprising the first 450 amino acids of CYP116B1) generates a Soret band shift from 418 to (mainly) 449 nm which, unlike Mtb CYP51 (Chapter 3.4,(159)), remains stable over several hours. This confirms this protein as a cytochrome P450, indicating also that the proximal thiolate ligand of the heme is not prone to protonation to form P420. The heme domain ligand binding studies identify spectral changes that are almost identical to those observed for the full-length protein, whilst many of the dissociation constants calculated for this truncated protein compare favourably with those of intact CYP116B1, indicating that the structure of the heme domain is not significantly altered when expressed in isolation. Additionally, the failure of fluconazole to interact with CYP116B1 (i.e. no spectral changes induced) was replicated for the heme domain (Chapter 5.6), confirming that this observation is not an anomaly, but most likely a consequence of the peculiar properties of this azole anti-fungal, particularly its relatively hydrophilic nature. The pyridine hemochromagen assay indicates an extinction coefficient of 139 mM^{-1} cm^{-1} at the heme domain Soret peak, consistent with the value for the intact CYP116B1.

Further studies of the heme domain by EPR (Chapter 5.7) show that the spectrum for the ferric domain is almost identical to that recorded for its full-length counterpart, indicating that thiolate coordination is maintained and that domain dissection does not cause detectable perturbation of the heme environment. These conclusions are further supported by the redox potentiometry study of the heme domain, which indicates a midpoint potential for the heme iron of approximately –381 mV versus the standard hydrogen electrode. This value is comparable to that of full-length CYP116B1 (estimated at –396 mV against the backdrop of absorption contributions from the FMN and 2Fe-2S clusters), as well as to that for CYP116B2 from *Rhodococcus* sp. NCIMB 9784 (–423 mV) (130), suggesting that the redox properties of the heme iron are not

significantly perturbed by the removal of the reductase domain. For both intact CYP116B1 and its heme domain, long wavelength shifts of the heme Soret band and the development of a visible absorption band at ~559 nm occur on heme iron reduction in equilibrium titrations. This suggests that protonation of the heme thiolate occurs on heme iron reduction, although preceding data from formation of the CO complexes (in which the P450 form dominates over the P420 species) suggest that CO binding may prevent (at least partially) the conversion to a thiol-coordinated species. While the heme iron potentials determined are quite negative (by comparison with those for NAD(P)H at ~−320 mV), it should be remembered that binding of an effective substrate (i.e. one that induces a substantial shift in heme iron spin-state equilibrium towards the high-spin form) is likely to induce an increase in midpoint reduction potential of the heme domain of up to ~150 mV. This is likely to provide the thermodynamic "trigger" for electron transfer from the reductase domain to the heme domain that is essential for catalytic activity in the CYP116B1 enzyme. Thus, substrate binding is likely necessary to bring the heme potential nearer to those of the reductase's other redox centres.

Spectroscopy of the reductase domain (comprising the final 325 amino acids of CYP116B1) confirms the presence of the flavin (FMN) molecule previously identified in intact CYP116B1. While time did not allow for extensive studies of the reductase domain, it was shown that the co-enzymes NADPH and NADH both reduced the reductase domain, with a slightly greater amount of neutral (blue) semiquinone observed on addition of excess NADH than is accumulated with the same amount of NADPH. This appears to suggest that a slightly greater level of cofactor reduction occurs with NADPH (despite the similar potentials of NADPH/NADH). This might reflect small differences in rates of reduction with NAD(P)H and rates of reoxidation of the reductase in presence of NAD(P)$^{+}$, but further studies will be required to provide a complete explanation. Interestingly, dithionite does not cause complete bleaching of the reductase cofactors, which again could be due to rapid reoxidation of FMN/2Fe-2S centres under aerobic conditions. However, further studies (including anaerobic reductive titrations) are clearly required here to provide further details of interactions between co-enzymes/dithionite and the reductase domain.

Whilst spectroscopic studies of the CYP116B1 heme domain confirm that this truncated protein is not significantly dissimilar to the full-length enzyme from which it is derived, there are many more useful studies that could have been performed with this protein had time allowed. Future priorities for characterization of this domain should

363

involve further comparative studies of the coordination and conformation of the heme and its central iron by techniques such as resonance Raman and MCD spectroscopy. These techniques (and EPR) could also be utilised to further analyse the influence of substrates and ligands, such as vernolate, on the spin and coordination states of the heme iron. Reconstitution of the isolated domains of the CYP116B1 system, by bringing the individual heme and reductase domains together in kinetic assays, should be done to establish that the isolated domains are still able to communicate productively in order to facilitate heme iron reduction and substrate oxygenation. In this respect, the fact that vernolate and EPTC are validated substrates for intact CYP116B1 is of benefit, since the oxygenation of these molecules by CYP116B1 domain mixtures would provide evidence that productive domain communication occurs. It should be noted that, for the respective isolated reductase and heme domains of the P450 BM3 system, turnover number is dramatically decreased by comparison with that for intact P450 BM3 (278).

Insights into structural properties of the two domains would clearly be of great use, and would facilitate such aspects as rational mutagenesis to explore structure/function, and modelling of domain interactions. As stated above, the likelihood of successful crystallization of a multidomain enzyme may be rather lower than that for its isolated domains, and this was one of the major factors in mind during construction of the domains. Although time did not allow for any systematic crystallization trials on the CYP116B1 domains, this should clearly be a priority in future work on the system. Knowledge of domain structures would facilitate the *in silico* docking of the domains and the determination of optimal orientations for electron transfer between the redox centres of these proteins. This, in turn, would likely provide close approximations to the structural organization of the full-length CYP116B1. A heme domain structure would also allow rationalization of mode of binding of substrates/inhibitors by modelling, or (preferably) these interactions could be determined at the atomic level by resolution of atomic structures of the relevant P450-ligand complexes. These could be formed either by crystallization of the complexes themselves (co-crystallization) or by soaking of ligands into existing crystals of the ligand-free heme domain (or full length CYP116B1).

As well as the prioritisation of the determination of the crystal structure of the reductase domain, which would identify the arrangement of the FMN and iron-sulphur clusters within this protein, likely demonstrating that they are closely orientated in space

364

and so compatible with efficient inter-cofactor electron transfer, there are many spectroscopic and related studies of the CYP116B1 reductase domain that should be done to better understand the overall properties of CYP116B1. For example, detailed steady-state kinetic assays, similar to those reported in Chapter 4.19, should be done (using e.g. cytochrome *c*, ferricyanide and other artificial electron acceptors). Such assays would also identify rates of electron transfer through the truncated protein, allowing comparison with equivalent data from full-length CYP116B1, and establish coenzyme preference within the reductase and apparent limiting rates of electron transport through the reductase to the acceptors. Establishing the ability of the reductase to function in isolation as an electron transferase to its own isolated heme domain and to other P450s (e.g. CYP51 or the P450 BM3 heme domain) would also be useful information supporting any attempts to fuse the reductase with other cytochromes P450 for biotechnological applications. Determination of the presence of the iron-sulphur cluster in the reductase domain should also be relatively simple by comparison with the full length CYP116B1, due to the absence of the large and broad spectral contribution from the heme cofactor. Thus, spectral redox titrations of the reductase domain should be able to allow deconvolution of the reduction potentials of both FMN and iron-sulphur centres. EPR and/or EPR redox titrations could also be used to determine the presence, concentration and midpoint potential of the 2Fe-2S cofactor in studies of the CYP116B1 reductase domains. EPR may be a particularly useful technique for these experiments, likely superior to UV-Visible spectroscopy, as a result of the small absorption contributions of the 2Fe-2S redox centre, compared to the distinctive and diagnostic EPR spectra available for the iron-sulphur cluster in the reductase domain. The EPR redox titration technique, which has been used by Dunford *et al* (279), is based on the development of an EPR signal from the CYP116B1 reductase domain 2Fe-2S centre upon enzyme reduction. It involves the removal, and rapid freezing in liquid nitrogen, of aliquots of the reductase domain sampled at multiple points throughout the redox titration (i.e. at different, recorded reduction potentials). The aliquots are then analysed by EPR and the proportion of reduced iron-sulphur cluster is related to the relevant potential of the sample by plotting the two parameters. The resultant EPR redox titration curve is then fitted to the Nernst function, enabling the 2Fe-2S potential to be determined. Parallel redox titrations (either by EPR or optical titration) should clearly also be done for the CYP116B1 heme domain in presence of substrate molecules (e.g. EPTC, vernolate).

Further stopped-flow kinetic assays should also be done with the reductase domain. These should involve analysis of the dependence of limiting flavin reduction rate on concentration of NAD(P)H coenzymes, and attempts to define rates of internal electron transfer from FMN to the 2Fe-2S centre (similar to experiments done for intact CYP116B1 in Chapter 4.18). These data would provide important comparisons with those data for full length CYP116B1, and establish that the coenzyme binding site and FMN/2Fe-2S centres are intact and functional in the reductase domain.

In conclusion, studies of CYP116B1 and its component domains have led to a relatively detailed understanding of the cofactor content, thermodynamic, kinetic (steady-state and stopped-flow), ligand- and substrate-binding, and spectroscopic properties of the enzyme. Importantly, its capacity to oxygenate thiocarbamate herbicides was demonstrated, detailing a *bona fide* catalytic function for this oxygenase enzyme. The project came to an end at a point where structural studies on CYP116B1 and its domains had become the next major priority. From the perspective of biotechnological application of this novel enzyme, structural and protein engineering studies will be paramount, and may open up further avenues of study for this *R. metallidurans* cytochrome P450, including those exploring the potential of the reductase domain to support other cytochromes P450 (probably by the creation of other self-sufficient fused systems) and for the application of the full-length enzyme in a bioremediation role (in degrading thiocarbamate herbicides).

Chapter 7

References

1. Goris, J., De Vos, P., Coenye, T., Hoste, B., Janssens, D., Brim, H., Diels, L., Mergeay, M., Kersters, K., and Vandamme, P. (2001) Classification of metal-resistant bacteria from industrial biotopes as *Ralstonia campinensis* sp nov., *Ralstonia metallidurans* sp nov and *Ralstonia basilensis*, *Int. J. Syst. Evol. Microbiol.* **51**, 1773-1782

2. Alberts, B., Bray, D., Lewis, J., Raff, M., Roberts, K., and Watson, J.D. (1994) In *Molecular Biology of The Cell* (3rd ed.), *Garland Publishing Inc., New York and London*, 128-135

3. Munro, A.W., and Lindsay, J.G. (1996) Bacterial cytochromes P450, *Mol. Microbiol.* **20** (6), 1115-1125

4. Lindskog, S. (1997) Structure and mechanism of carbonic anhydrase, *Pharmacol. Ther.* **74** (1), 1-20

5. Hernandez-Romero, D., Solano, F., and Sanchez-Amat, A. (2005) Polyphenol oxidase activity expression in *Ralstonia solanacearum*, *Appl. Environ. Microbiol.* **71** (11), 6808-6815

6. Correll, C.C., Batie, C.J., Ballou, D.P., and Ludwig, M.L. (1992) Phthalate dioxygenase reductase - a modular structure for electron transfer from pyridine nucleotides to 2fe-2s, *Science* **258** (5088), 1604-1610

7. Hames, B.D., Hooper, N.M., and Houghton, J.D. (1997) Instant Notes in Biochemistry, *BIOS Scientific Publishers Ltd*

8. Hubscher, U., Maga, G., and Spadari, S. (2002) Eukaryotic DNA polymerases, *Ann. Rev. Biochem.* **2002** (71), 133-163

9. Tuteja, N., and Tuteja, R. (2004) Unravelling DNA helicases. Motif, structure, mechanism, and function, *Eur. J. Biochem.* **271** (10), 1849-1863

10. Merrick, M.J., and Edwards, R.A. (1995) Nitrogen control in bacteria, *Microbiol. Rev.* **59** (4), 604-622

11. Palmer, S.M., and St John, A.C. (1987) Characterisation of a membrane-associated serine protease in *Escherichia coli*, *J. Bacteriol.* **169** (4), 1474-1479

12. Simpson, E.R., and Davis, S.R. (2001) Minireview: Aromatase and the regulation of estrogen biosynthesis-Some new perspectives, *Endocrinology* **142** (11), 4589-4594

13. Holtwick, R., Keweloh, H., and Meinhardt, F. (1999) Cis/trans isomerase of unsaturated fatty acids of *Pseudomonas putida* P8: evidence for a heme protein of the cytochrome c type, *Appl. Environ. Microbiol.* **65** (6), 2644-2649

14. Roberts, P.J., and Whelan, W.J. (1960) The mechanism of carbohydrase action. 5. Action of human salivary alpha-amylase on amylopectin and glycogen, *Biochem. J.* **76** (8), 246-253

15. Zeng, W., Conibear, P.B., Dickens, J.L., Cowie, R.A., Wakelin, S., Malnasi-Csizmadia, A., and Bagshaw, C.R. (2004) Dynamics of actomyosin interactions in relation to the cross-bridge cycle, *Philos. Trans. R. Soc. Lond. B. Biol. Sci.* **359** (1452), 1843-1855

16. Kedishvili, N.Y., Bosron, W.F., Stone, C.L., Hurley, T.D., Peggs, C.F., Thomasson, H.R., Popov, K.M., Carr, L.G., Edenberg, H.J., and Li, T.K. (1995) Expression and kinetic characterisation of recombinant human stomach alcohol dehydrogenase. Active-site amino acid sequence explains substrate specificity compared with liver isozymes, *J. Biol. Chem.* **270** (8), 3625-3630

17. Munro, A.W., Noble, M.A., Robledo, L., Daff, S.N., and Chapman, S.K. (2001) Determination of the redox properties of human NADPH-cytochrome P450 reductase, *Biochemistry* **40** (7), 1956-1963

18. Youdim, M.B., and Bakhle, Y.S. (2006) Monoamine oxidase: isoforms and inhibitors in Parkinson's disease and depressive illness, *Br. J. Pharmacol.* **147** (Suppl. 1), S287-296

19. Lepesheva, G.I., Nes, W.D., Zhou, W., Hill, G.C., and Waterman, M.R. (2004) CYP51 from *Trypanosoma brucei* is obtusifoliol-specific, *Biochemistry* **43** (33), 10789-10799

20. Andersson, T.B., Bredberg, E., Ericsson, H., and Sjoberg, H. (2004) An evaluation of the *in vitro* metabolism data for predicting the clearance and drug-drug interaction potential of CYP2C9 substrates, *Drug Metab. Disp.* **32** (7), 715-721

21. Poulos, T.L. (2005) Intermediates in P450 catalysis, *Phil. Trans. R. Soc. A* **363**, 793-806

22. Morant, M., Bak, S., Lindberg, B., and Werck-Reichhart, D. (2003) Plant cytochromes P450: tools for pharmacology, plant protection and phytoremediation, *Curr. Op. Biotech.* **14** (3), 355-355

23. Guengerich, F.P., Hosea, N.A., Parikh, A., Bell-Parikh, L.C., Johnson, W.W., Gillam, E.M.J., and Shimada, T. (1998) Twenty years of biochemistry of human P450s. Purification, expression, mechanism, and relevance to drugs, *Drug Metab. Disp.* **26** (12), 1175-1178

24. Nelson, D.R. (1999) Cytochrome P450 and the individuality of species, *Arch. Biochem. Biophys.* **369** (1), 1-10

25. Miles, C.S., Ost, T.W., Noble, M.A., Munro, A.W., and Chapman, S.K. (2000) Protein engineering of cytochromes P450., *Biochim. Biophys. Acta.* **1543** (2), 383-407

26. Munro, A.W., Daff, S.N., Coggins, J.R., Lindsay, J.G., and Chapman, S.K. (1996) Probing electron transfer in flavocytochrome P450 BM3, *Eur. J. Biochem.* **239** (2), 403-409

27. Noble, M.A., Miles, C.S., Chapman, S.K., Lysek, D.A., Mackay, A.C., Reid, G.A., Hanzlik, R.P., and Munro, A.W. (1999) Roles of key active-site residues in flavocytochrome P450 BM3, *Biochem. J.* **339**, 371-379

28. Noble, M.A., Quaroni, L., Chumanov, G.D., Turner, K.L., Chapman, S.K., Hanzlik, R.P., and Munro, A.W. (1998) Imidazolyl carboxylic acids as mechanistic probes of flavocytochrome P450 BM3, *Biochemistry* **37** (45), 15799-15807

29. Joo, H., Lin, Z.L., and Arnold, F.H. (1999) Laboratory evolution of peroxide-mediated cytochrome P450 hydroxylation, *Nature* **399** (6763), 670-673

30. Peters, M.W., Meinhold, P., Glieder, A., and Arnold, F.H. (2003) Regio- and enantioselective alkane hydroxylation with engineered cytochromes P450 BM3, *J. Am. Chem. Soc.* **125** (44), 13442-13450

31. Raag, R., and Poulos, T.L. (1989) Crystal structure of the carbon monoxide-substrate-cytochrome P450cam ternary complex, *Biochemistry* **28** (19), 7586-7592

32. Raag, R., Martinis, S.A., Sligar, S.G., and Poulos, T.L. (1991) Crystal structure of the cytochrome P450cam active site mutant Thr252Ala, *Biochemistry* **30** (48), 11420-11429

33. Ost, T.W.B., Munro, A.W., Mowat, C.G., Taylor, P.R., Pessegueiro, A., Fulco, A.J., Cho, A.K., Cheesman, M.R., Walkinshaw, M.D., and Chapman, S.K. (2001) Structural and spectroscopic analysis of the F393H mutant of flavocytochrome P450 BM3, *Biochemistry* **40** (45), 13430-13438

34. Joyce, M.G., Girvan, H.M., Munro, A.W., and Leys, D. (2004) A single mutation in cytochrome P450 BM3 induces the conformational rearrangement seen upon substrate binding in the wild-type enzyme, *J. Biol. Chem.* **279** (22), 23287-23293

35. Podust, L.M., Yermalitskaya, L.V., Lepesheva, G.I., Podust, V.N., Dalmasso, E.A., and Waterman, M.R. (2004) Estriol bound and ligand-free structures of sterol 14α-demethylase, *Structure* **12** (11), 1937-1945

36. Bellamine, A., Lepesheva, G.I., and Waterman, M.R. (2004) Fluconazole binding and sterol demethylation in three CYP51 isoforms indicate differences in active site topology, *J. Lipid Res.* **45** (11), 2000-2007

37. Girvan, H.M., Marshall, K.R., Lawson, R.J., Leys, D., Joyce, M.G., Clarkson, J., Smith, W.E., Cheesman, M.R., and Munro, A.W. (2004) Flavocytochrome P450 BM3 mutant A264E undergoes substrate- dependent formation of a novel heme iron ligand set, *J. Biol. Chem.* **279** (22), 23274-23286

38. LeBrun, L.A., Xu, F., Kroetz, D.L., and Ortiz de Montellano, P.R. (2002) Covalent attachment of the heme prosthetic group in the CYP4F cytochrome P450 family, *Biochemistry* **41** (18), 5931-5937

39. Zheng, Y.M., Baer, B.R., Kneller, B.M., Henne, K.R., Kunze, K.L., and Rettie, A.E. (2003) Covalent heme binding to CYP4B1 via Glu310 and a carbocation porphyrin intermediate, *Biochemistry* **42** (15), 4601-4606

40. Leys, D., Mowat, C.G., McLean, K.J., Richmond, A., Chapman, S.K., Walkinshaw, M.D., and Munro, A.W. (2003) Atomic structure of *Mycobacterium tuberculosis*

CYP121 to 1.06 Å reveals novel features of cytochromes P450, *J. Biol. Chem.* **278** (7), 5141-5147

41.   Bernhardt, R. (2006) Cytochromes P450 as versatile biocatalysts, *J. Biotech.* **124** (1), 128-145

42.   Gibson, D.T., and Parales, R.E. (2000) Aromatic hydrocarbon dioxygenases in environmental biotechnology, *Curr. Op. Biotech.* **11** (3), 236-243

43.   Ogura, H., Nishida, C.R., Hoch, U.R., Perera, R., Dawson, J.H., and Ortiz de Montellano, P.R. (2004) EpoK, a cytochrome P450 involved in biosynthesis of the anticancer agents epothilones A and B. Substrate-mediated rescue of a P450 enzyme., *Biochemistry* **43** (46), 14712-14721

44.   Parte, P., and Kupfer, D. (2005) Oxidation of tamoxifen by human flavin-containing monooxygenase (FMO) and FMO3 to tamoxifen-N-oxide and its novel reduction back to tamoxifen by human cytochromes P450 and hemoglobin, *Drug Metab. Disp.* **33** (10), 1446-1452

45.   Shafiee, A., and Hutchinson, C.R. (1988) Purification and reconstitution of the electron transport components for 6-deoxyerythronolide b-hydroxylase, a cytochrome-P450 enzyme of macrolide antibiotic (erythromycin) biosynthesis, *J. Bacteriol.* **170** (4), 1548-1553

46.   Crewe, H.K., Notley, L.M., Wunsch, R.M., Lennard, M.S., and Gillam, E.M.J. (2002) Metabolism of tamoxifen by recombinant human cytochrome P450 enzymes: Formation of the 4-hydroxy, 4'-hydroxy and N-desmethyl metabolites and isomerization of *trans*-4-hydroxytamoxifen, *Drug Metab. Disp.* **31** (1), 869-874

47.   Garfinkel, D. (1958) Studies on pig liver microsomes. I. Enzymic and pigment composition of different microsomal fractions., *Arch. Biochem. Biophys.* **77** (2), 493-509

48.   Klingenberg, M. (1958) Pigments of rat liver microsomes., *Arch. Biochem. Biophys.* **75** (2), 376-386

49.   Omura, T., and Sato, R. (1964) The carbon monoxide-binding pigment of liver microsomes. II. Solubilization, purification, and properties., *J. Biol. Chem.* **239**, 2379-2385

50.   Omura, T., and Sato, R. (1964) The carbon monoxide-binding pigment of liver microsomes. I. Evidence for its hemoprotein nature., *J. Biol. Chem.* **239**, 2370-2378

51.   Podust, L.M., Poulos, T.L., and Waterman, M.R. (2001) Crystal structure of cytochrome P450 14 alpha-sterol demethylase (CYP51) from *Mycobacterium tuberculosis* in complex with azole inhibitors, *Proc. Natl. Acad. Sci. U.S.A.* **98** (6), 3068-3073

52.   Pylypenko, O., and Schlichting, I. (2004) Structural aspects of ligand binding to and electron transfer in bacterial and fungal P450s., *Ann. Rev. Biochem.* **73**, 991-1018

53.   Schoch, G.A., Yano, J.K., Wester, M.R., Griffin, K.J., Stout, D., and Johnson, E.F. (2004) Structure of human microsomal cytochrome P450 2C8, *J. Biol. Chem.* **279** (10), 9497-9503

54.   Lee, H.J., Basran, J., and Scrutton, N.S. (1998) Electron transfer from flavin to iron in the *Pseudomonas oleovorans* rubredoxin reductase-rubredoxin electron transfer complex, *Biochemistry* **37** (44), 15513-15522

55.   Wester, M.R., Yano, J.K., Schoch, G.A., Yang, C., Griffin, K.J., Stout, C.D., and Johnson, E.F. (2004) The structure of human cytochrome P450 2C9 with flurbiprofen, *J. Biol. Chem.* **279** (10), 35630-35637

56.   Reedy, C.J., and Gibney, B.R. (2004) Heme protein assemblies, *Chem. Rev.* **104**, 617-649

57.   Daltrop, O., and Ferguson, S.J. (2002) Cytochrome c maturation: The *in vitro* reaction of horse heart apocytochrome c and *Paracoccus denitrificans* apocytochrome c_{550} with heme, *J. Biol. Chem.* **278** (7), 4404-4409

58.   Colas, C., and Ortiz de Montellano, P.R. (2004) Horseradish peroxidase mutants that autocatalytically modify their prosthetic heme group: insights into mammalian peroxidase heme-protein covalent bonds, *J. Biol. Chem.* **279** (23), 24131-24141

59. Mims, M.P., Porras, A.G., Olson, J.S., Noble, R.W., and Peterson, J.A. (1983) Ligand binding to heme proteins, *J. Biol. Chem.* **258** (23), 14219-14232

60. Sono, M., Stuehr, D.J., Ikeda-Saito, M., and Dawson, J.H. (1995) Identification of nitric oxide synthase as a thiolate-ligated heme protein using magnetic circular dichroism spectroscopy. Comparison with cytochrome P450cam and chloroperoxidase, *J. Biol. Chem.* **270** (34), 19943-19948

61. Pilet, E., Jasaitis, A., Liebl, U., and Vos, M.H. (2004) Electron transfer between hemes in mammalian cytochrome *c* oxidase, *Proc. Natl. Acad. Sci. U.S.A.* **101** (46), 16198-161203

62. Das, T.K., Wilson, E.K., Cutruzzola, F., Brunori, M., and Rousseau, D.L. (2001) Binding of NO and CO to the d(1) Heme of cd(1) nitrite reductase from Pseudomonas aeruginosa, *Biochemistry* **40** (36), 10774-10781

63. Schnell, R., Sandalova, T., Hellman, U., Lindqvist, Y., and Schneider, G. (2005) Siroheme- and [Fe4-S4]-dependent NirA from *Mycobacterium tuberculosis* is a sulfite reductase with a covalent Cys-Tyr bond in the active site, *J. Biol. Chem.* **280** (29), 27319-27328

64. Bergmann, D.J., and Hooper, A.B. (2003) Cytochrome P460 of *Nitrosomonas europaea*. Formation of the heme-lysine cross-link in a heterologous host and mutagenic conversion to a non-cross-linked cytochrome *c*, *Eur. J. Biochem.* **270** (9), 1935-1941

65. Matsuura, K., Yoshioka, S., Takahashi, S., Ishimori, K., Mogi, T., Hori, H., and Morishima, I. (2004) Dioxygen reduction by bo-type quinol oxidase from *Escherichia coli* studied by submillisecond-resolved freeze-quench EPR spectroscopy, *Biochemistry* **43** (8), 2288-2296

66. Newmyer, S.L., and Ortiz de Montellano, P.R. (1995) Horseradish peroxidase His42Ala, His42Val, and Phe41Ala mutants - histidine catalysis and control of substrate access to the heme iron, *J. Biol. Chem.* **270** (33), 19430-19438

67. Arciero, D.M., and Hooper, A.B. (1993) Hydroxylamine oxidoreductase from *Nitrosomonas europaea* is a multimer of an octa-heme subunit, *J. Biol. Chem.* **268** (20), 14645-14654

68. Panek, H., and O'Brian, M.R. (2002) A whole genome view of prokaryotic haem biosynthesis, *Microbiology* **148** (8), 2273-2282

69. Sligar, S.G. (1976) Coupling of spin, substrate, and redox equilibria in cytochrome P450, *Biochemistry* **15** (24), 5399-5406

70. Denisov, I.G., Makris, T.M., Sligar, S.G., and Schlichting, I. (2005) Structure and chemistry of cytochrome P450, *Chem. Rev.* **105**, 2253-2277

71. Schenkman, J.B., Cinti, D.L., Orrenius, S., Moldeus, P., and Kraschnitz, R. (1972) The nature of the reverse type I (modified type II) spectral change in liver microsomes, *Biochemistry* **11** (23), 4243-4251

72. Budde, M., Morr, M., Schmid, R.D., and Urlacher, V.B. (2006) Selective hydroxylation of highly branched fatty acids and their derivatives by CYP102A1 from *Bacillus megaterium*, *Chembiochem.* **7** (5), 789-794

73. White, R.E., and Coon, M.J. (1980) Oxygen activation by cytochrome P450., *Annu. Rev. Biochem.* **49**, 315-356

74. Porter, T.D., and Coon, M.J. (1991) Cytochrome P450. Multiplicity of isoforms, substrates, and catalytic and regulatory mechanisms., *J. Biol. Chem.* **266** (21), 13469-13472

75. Guengerich, F.P. (1990) Enzymatic oxidation of xenobiotic chemicals, *Crit. Rev. Biochem. Mol. Biol.* **25** (2), 97-153

76. Schlichting, I., Berendzen, J., Chu, K., Stock, A.M., Maves, S.A., Benson, D.E., Sweet, R.M., Ringe, D., Petsko, G.A., and Sligar, S.G. (2000) The catalytic pathway of cytochrome P450cam at atomic resolution., *Science* **287** (5458), 1615-1622

77. Guengerich, F.P. (1991) Reactions and significance of cytochrome P450 enzymes, *J. Biol. Chem.* **266** (16), 10019-10022

371

78. Matsunaga, I., Ueda, A., Sumimoto, T., Ichihara, K., Ayata, M., and Ogura, H. (2001) Site-directed mutagenesis of the putative distal helix of peroxygenase cytochrome P450, *Arch. Biochem. Biophys.* **394** (1), 45-53

79. Matsunaga, I., Sumimoto, T., Ayata, M., and Ogura, H. (2002) Functional modulation of a peroxygenase cytochrome P450: novel insight into the mechanisms of peroxygenase and peroxidase enzymes, *FEBS Lett.* **528** (1-3), 90-94

80. Matsunaga, I., Yamada, A., Lee, D.S., Obayashi, E., Fujiwara, N., Kobayashi, K., Ogura, H., and Shiro, Y. (2002) Enzymatic reaction of hydrogen peroxide-dependent peroxygenase cytochrome P450s: Kinetic deuterium isotope effects and analyses by resonance Raman spectroscopy, *Biochemistry* **41** (6), 1886-1892

81. Nakahara, K., Tanimoto, T., Hatano, K., Usuda, K., and Shoun, H. (1993) Cytochrome P450 55a1 (P450dnir) acts as nitric oxide reductase employing NADH as the direct electron donor, *J. Biol. Chem.* **268** (11), 8350-8355

82. Shoun, H., Suyama, W., and Yasui, T. (1989) Soluble, nitrate/nitrite-inducible cytochrome P450 of the fungus, *Fusarium oxysporum*, *FEBS Lett.* **244** (1), 11-14

83. Shoun, H., and Tanimoto, T. (1991) Denitrification by the fungus *Fusarium oxysporum* and involvement of cytochrome P450 in the respiratory nitrite reduction, *J. Biol. Chem.* **266** (17), 11078-11082

84. Powell, P.K., Wolf, I., and Lasker, J.M. (1996) Identification of CYP4A11 as the major lauric acid ω-hydroxylase in human liver microsomes, *Arch. Biochem. Biophys.* **335** (1), 219-226

85. Guengerich, F.P. (2003) Cytochrome P450 oxidations in the generation of reactive electrophiles: epoxidation and related reactions, *Arch. Biochem. Biophys.* **409** (1), 59-71

86. Coon, M.J. (2002) Enzyme ingenuity in biological oxidations: A trail leading to cytochrome P450, *J. Biol. Chem.* **277** (32), 28351-28363

87. Celik, A., Sperandio, D., Speight, R.E., and Turner, N.J. (2005) Enantioselective epoxidation of linolenic acid cataylsed by cytochrome P450 BM3 from *Bacillus subtilis*, *Org. Biomol. Chem.* **3**, 2688-2690

88. Helvig, C., Alayrac, C., Mioskowski, C., Koop, D., Poullain, D., Durst, F., and Salaun, J. (1997) Suicide inactivation of cytochrome P450 by midchain and terminal acetylenes, *J. Biol. Chem.* **272** (1), 414-421

89. Kisselev, P., Schwarz, D., Platt, K., Schunk, W., and Roots, I. (2002) Epoxidation of benzo[a]pyrene-7,8-dihydrodiol by human CYP1A1 in reconstituted membranes, *Eur. J. Biochem.* **269** (7), 1799-1805

90. Yu, A., Kneller, B.M., Rettie, A.E., and Haining, R.L. (2002) Expression, purification, biochemical characterisation, and comparative function of human cytochrome P450 2D6.1, 2D6.2, 2D6.10, and 2D6.17 allelic isoforms, *J. Pharmacol. Exp. Ther.* **303** (3), 1291-1300

91. Werner, M., Guo, Z., Birner, G., Dekant, W., and Guengerich, F.P. (1995) The sulfoxidation of the hexachlorobutadiene metabolite N-acetyl-S-(1,2,3,4,4-pentachlorobutadienyl)-L-cysteine is catalyzed by human cytochrome P450 3A enzymes, *Chem. Res. Toxicol.* **8** (7), 917-923

92. Yun, C.H., Kim, K.H., Calcutt, M.W., and Guengerich, F.P. (2005) Kinetic analysis of oxidation of coumarins by human cytochrome P450 2A6, *J. Biol. Chem.* **280** (13), 12279-12291

93. Andersen, M.D., Busk, P.K., Svendsen, I., and Moller, B.L. (2000) Cytochromes P450 from cassava catalyzing the first steps in the biosynthesis of the cyanogenic glucosides linamarin and lotaustralin - Cloning, functional expression in *Pichia pastoris*, and substrate specificity of the isolated recombinant enzymes, *J. Biol. Chem.* **275** (3), 1966-1975

94. Wynalda, M.A., Hutzler, J.M., Koets, M.D., Podoll, T., and Wienkers, L.C. (2003) In vitro metabolism of clindamycin in human liver and intestinal microsomes, *Drug Metab. Disp.* **31** (7), 878-887

95. Obach, R.S., Cox, L.M., and Tremaine, L.M. (2005) Sertraline is metabolized by multiple cytochrome P450 enzymes, monoamine oxidases, and glucuronyl transferases in human: an in vitro study, *Drug Metab. Disp.* **33** (2), 262-270

96. Yanagita, K., Sagami, I., and Shimizu, T. (1997) Distal site and surface mutations of cytochrome P450 1A2 markedly enhance dehalogenation of chlorinated hydrocarbons, *Arch. Biochem. Biophy.* **346** (2), 269-276

97. Watanabe, K., Matsunaga, T., Kimura, T., Funahashi, T., Funae, Y., Ohshima, T., and Yamamoto, I. (2002) Major cytochrome P450 enzymes responsible for microsomal aldehyde oxygenation of 11-oxo-Δ8-tetrahydrocannabinol and 9-anthraldehyde in human liver, *Drug. Metab. Disp.* **17** (6), 516-521

98. Obach, R.S. (2001) Mechanism of cytochrome P4503A4- and 2D6-catalyzed dehydrogenation of ezlopitant as probed with isotope effects using five deuterated analogs, *Drug. Metab. Disp.* **29** (12), 1599-1607

99. Boucher, J.L., Delaforge, M., and Mansuy, D. (1994) Dehydration of alky- and arlyaldoximes as a new cytochrome P450-catalyzed reactio: mechanism and stereochemical characteristics, *Biochemistry* **33** (25), 7811-7818

100. Walsh, M.E., Kyritsis, P., Eady, N.A.J., Hill, A.O., and Wong, L. (2000) Catalytic reductive dehalogenation of hexachloroethane by molecular variants of cytochrome P450cam (CYP101), *Eur. J. Biochem.* **267** (18), 5815-5820

101. Vaz, A.D.N., Roberts, E.S., and Coon, M.J. (1990) Reductive β-scission of the hydroperoxides of fatty acids and xenobiotics: Role of alcohol-inducible cytochrome P450, *Proc. Nat.l Acad. Sci. USA* **87** (14), 5499-5503

102. Lee-Robichaud, P., Akhtar, M.E., and Akhtar, M. (1999) Lysine mutagenesis identifies cationic charges of human CYP17 that interact with cytochrome b_5 to promote male sex-hormone biosynthesis, *Biochem. J.* **342** (2), 309-312

103. Gunsalus, I.C., and Wagner, G.C. (1978) Bacterial P450cam methylene monooxygenase components: cytochrome m, putidaredoxin, and putidaredoxin reductase., *Methods Enzymol.* **52**, 166-188

104. Martinis, S.A., Blanke, S.R., Hager, L.P., Sligar, S.G., Hoa, G.H.B., Rux, J.J., and Dawson, J.H. (1996) Probing the heme iron coordination structure of pressure- induced cytochrome P420(cam), *Biochemistry* **35** (46), 14530-14536

105. Boddupalli, S.S., Hasemann, C.A., Ravichandran, K.G., Lu, J.Y., Goldsmith, E.J., Deisenhofer, J., and Peterson, J.A. (1992) Crystallization and preliminary-X-ray diffraction analysis of P450terp and the hemoprotein domain of P450bm-3, enzymes belonging to two distinct classes of the cytochrome P450 superfamily, *Proc. Natl. Acad. Sci. U.S.A.* **89** (12), 5567-5571

106. Guardiola-Diaz, H.M., Foster, L.A., Mushrush, D., and Vaz, A.D.N. (2001) Azole-antifungal binding to a novel cytochrome P450 from *Mycobacterium tuberculosis*: implications for treatment of tuberculosis, *Biochem. Pharmacol.* **61** (12), 1463-1470

107. Lepesheva, G.I., Podust, L.M., Bellamine, A., and Waterman, M.R. (2001) Folding requirements are different between sterol 14 alpha- demethylase (CYP51) from *Mycobacterium tuberculosis* and human or fungal orthologs, *J. Biol. Chem.* **276** (30), 28413-28420

108. Leveque, D., Nivoix, Y., Jehl, F., and Herbrecht, R. (2006) Clinical pharmacokinetics of voriconazole, *Int. J. Antimicrob. Agents* **27** (4), 274-284

109. Kudo, T., Takaya, N., Park, S.Y., Shiro, Y., and Shoun, H. (2001) A positively charged cluster formed in the heme-distal pocket of cytochrome P450nor is essential for interaction with NADH, *J. Biol. Chem.* **276** (7), 5020-5026

110. Kawauchi, H., Sasaki, J., Adachi, T., Hanada, K., Beppu, T., and Horinouchi, S. (1994) Cloning and nucleotide sequence of a bacterial cytochrome P450 VD25 gene encoding vitamin D3 25-hydroxylase, *Biochem. Biophys. Acta.* **1219** (1), 179-183

111. Sasaki, M., Akahira, A., Oshiman, K., Tsuchido, T., and Matsumura, Y. (2005) Purification of cytochrome P450 and ferredoxin, involved in bisphenol A degradation, from *Sphingomonas* sp. strain AO1, *Appl. Environ. Microbiol.* **71** (12), 8024-8030

112. Chau, M., and Croteau, R. (2004) Molecular cloning and characterization of a cytochrome P450 taxoid 2[alpha]-hydroxylase involved in taxol biosynthesis,, *Arch. Biochem. Biophys.* **427** (1), 48-57

113. Coffman, B.L., King, C.D., Rios, G.R., and Tephly, T.R. (1998) The glucuronidation of opiods, other xenobiotics, and androgens by human UGT2B7Y(268) and UGT2B7H(268), *Drug Metab. Disp.* **26** (1), 73-77

114. Wang, J., Backman, J.T., Taavitsainen, P., Neuvonen, P.J., and Kivisto, K.T. (2000) Involvement of CYP1A2 and CYP3A4 in lidocaine N-deethylation and 3-hydroxylation in humans, *Drug Metab. Disp.* **28** (8), 959-965

115. Spracklin, D.K., Hankins, D.C., Fisher, J.M., Thummel, K.E., and Kharasch, E.D. (1997) Cytochrome P450 2E1 is the principal catalyst of human oxidative halothane metabolism *in vitro*, *J. Pharmacol. Exp. Ther.* **281** (1), 400-411

116. Estabrook, R.W., Cooper, D.Y., and Rosenthal, O. (1963) The light reversible carbon monoxide inhibition of the steroid C21-hydroxylase system of the adrenal cortex, *Biochem. Z.* **338**, 741-755

117. Daff, S.N., Chapman, S.K., Turner, K.L., Holt, R.A., Govindaraj, S., Poulos, T.L., and Munro, A.W. (1997) Redox control of the catalytic cycle of flavocytochrome P450 BM3, *Biochemistry* **36** (45), 13816-13823

118. Nelson, D.R., Kamataki, T., Waxman, D.J., Guengerich, F.P., Estabrook, R.W., Feyereisen, R., Gonzalez, F.J., Coon, M.J., Gunsalus, I.C., Gotoh, O., and al., e. (1993) The P450 superfamily: update on new sequences, gene mapping, accession numbers, early trivial names of enzymes, and nomenclature., *DNA Cell Biol.* **12** (1), 1-51

119. Ost, T.W., Miles, C.S., Murdoch, J., Cheung, Y., Reid, G.A., Chapman, S.K., and Munro, A.W. (2000) Rational re-design of the substrate binding site of flavocytochrome P450 BM3., *FEBS Lett.* **486** (2), 173-177

120. Gotoh, O. (1992) Substrate recognition sites in cytochrome P450 family 2 (CYP2) proteins inferred from comparative analyses of amino acid and coding nucleotide sequences, *J. Biol. Chem.* **267** (1), 83-90

121. Vermilion, J.L., and Coon, M.J. (1974) Highly purified detergent-solubilized NADPH-cytochrome P450 reductase from phenobarbital-induced rat liver microsomes., *Biochem. Biophys. Res. Commun.* **60** (4), 1315-1322

122. Smith, G.C., Tew, D.G., and Wolf, C.R. (1994) Dissection of NADPH-cytochrome P450 oxidoreductase into distinct functional domains, *Proc. Natl. Acad. Sci. U.S.A.* **91** (18), 1870-1874

123. Huang, J.J., and Kimura, T. (1973) Studies on adrenal steroid hydroxylases. Oxidation-reduction properties of adrenal iron-sulfur protein (adrenodoxin). *Biochemistry* **12** (3), 406-409

124. Roberts, G.A., Grogan, G., Greter, A., Flitsch, S.L., and Turner, N.J. (2002) Identification of a new class of cytochrome P450 from a *Rhodococcus* sp., *J. Bacteriol.* **184** (14), 3898-3908

125. De Mot, R., and Parret, A.H.A. (2002) A novel class of self-sufficient cytochrome P450 monooxygenases in prokaryotes, *Trends Microbiol.* **10** (11), 502-508

126. Jackson, C.J., Lamb, D.C., Marczylo, T.H., Warrilow, A.G., Manning, N.J., Lowe, D.J., Kelly, D.E., and Kelly, S.L. (2002) A novel sterol 14alpha-demethylase/ferredoxin fusion protein (MCCYP51FX) from *Methylococcus capsulatus* represents a new class of the cytochrome P450 superfamily., *J. Biol. Chem.* **277** (49), 46959-46965

127. Savenkova, M.I., Newmyer, S.L., and Ortiz de Montellano, P.R. (1996) Rescue of His42Ala horseradish peroxidase by a Phe41His mutation. Engineering of a surrogate catalytic histidine, *J. Biol. Chem.* **271** (40), 24598-24603

128. Matsunaga, I., Ueda, A., Fujiwara, N., Sumimoto, T., and Ichihara, K. (1999) Characterization of the ybdT gene product of *Bacillus subtilis*: novel fatty acid beta-hydroxylating cytochrome P450., *Lipids* **34** (8), 841-846

129. Munro, A.W., Noble, M.A., Miles, C.S., Daff, S.N., Green, A.J., Quaroni, L., Rivers, S., Ost, T.W.B., Reid, G.A., and Chapman, S.K. (1999) Flavocytochrome P450 BM3: a

paradigm for the analysis of electron transfer and its control in the P450s, *Biochem. Soc. Trans.* **27** (2), 190-196

130. Roberts, G.A., Celik, A., Hunter, D.J.B., Ost, T.W.B., White, J.H., Chapman, S.K., Turner, N.J., and Flitsch, S.L. (2003) A self-sufficient cytochrome P450 with a primary structural organization that includes a flavin domain and a 2Fe-2S redox center, *J. Biol. Chem.* **278** (49), 48914-48920

131. Ding, H., and Clark, R.J. (2004) Characterization of iron binding in IscA, an ancient iron–sulphur cluster assembly protein, *Biochem. J.* **379**, 433-440

132. Johnson, M.K. (1998) Iron-sulfur proteins: new roles for old clusters, *Curr. Op. Chem. Biol.* **2** (2), 173-181

133. Sticht, H., and Rosch, P. (1998) The structure of iron-sulfur proteins, *Prog. Biophys. Mol. Biol.* **70** (2), 95-136

134. McLean, K.J., Scrutton, N.S., and Munro, A.W. (2003) Kinetic, spectroscopic and thermodynamic characterization of the *Mycobacterium tuberculosis* adrenodoxin reductase homologue FprA, *Biochem. J.* **372**, 317-327

135. Puchkaev, A.V., Wakagi, T., and Ortiz de Montellano, P.R. (2002) CYP119 plus a *Sultolobus tokodaii* strain 7 ferredoxin and 2- oxoacid : ferredoxin oxidoreductase constitute a high- temperature cytochrome P450 catalytic system, *J. Am. Chem. Soc.* **124** (43), 12682-12683

136. Furdui, C., and Ragsdale, S.W. (2002) The roles of coenzyme A in the Pyruvate : Ferredoxin oxidoreductase reaction mechanism: Rate enhancement of electron transfer from a radical intermediate to an iron-sulfur cluster, *Biochemistry* **41** (31), 9921-9937

137. Zhao, Q., Modi, S., Smith, G., Paine, M.J., McDonagh, P.D., Wolf, C.R., Tew, D.G., Lian, L.Y., Roberts, G.C., and Driessen, H.P. (1999) Crystal structure of the FMN-binding domain of human cytochrome P450 reductase at 1.93 A resolution, *Protein Sci.* **8** (2), 298-306

138. Gutierrez, A., Paine, M.J., Wolf, C.R., Scrutton, N.S., and Roberts, G.C.K. (2002) Relaxation kinetics of cytochrome P450 reductase: internal electron transfer is limited by conformational change and regulated by coenzyme binding, *Biochemistry* **41** (14), 4626-4637

139. Vermilion, J.L., and Coon, M.J. (1978) Identification of the high and low potential flavins of liver microsomal NADPH-cytochrome P450 reductase, *J. Biol. Chem.* **253** (24), 8812-8819

140. Narhi, L.O., and Fulco, A.J. (1987) Identification and characterization of 2 functional domains in cytochrome P450 BM3, a catalytically self-sufficient monooxygenase induced by barbiturates in *Bacillus megaterium*, *J. Biol. Chem.* **262** (14), 6683-6690

141. Hayashi, K., Sakaki, T., Kominami, S., Inouye, K., and Yabusaki, Y. (2000) Coexpression of genetically engineered fused enzyme between yeast NADPH-P450 reductase and human cytochrome P450 3A4 and human cytochrome b5 in yeast, *Arch. Biochem. Biophys.* **381** (1), 164-170

142. Chun, Y.J., Jeong, T.C., Roh, J.K., and Guengerich, F.P. (1997) Characterization of a fusion protein between human cytochrome P450 1A1 and rat NADPH-P450 oxidoreductase in *Escherichia coli*, *Biochem. Biophys. Res. Commun.* **230** (1), 211-214

143. Munro, A.W., Leys, D.G., McLean, K.J., Marshall, K.R., Ost, T.W.B., Daff, S.N., Miles, C.S., Chapman, S.K., Lysek, D.A., Moser, C.C., Page, C.C., and Dutton, P.L. (2002) P450 BM3: the very model of a modern flavocytochrome, *Trends in Biochemical Sciences* **27** (5), 250-257

144. Parikh, A., and Guengerich, F.P. (1997) Expression, purification, and characterization of a catalytically active human cytochrome P450 1A2: Rat NADPH cytochrome P450 reductase fusion protein, *Protein Expr. Pur.* **9** (3), 346-354

145. Batie, C.J., Lahaie, E., and Ballou, D.P. (1987) Purification and characterization of phthalate oxygenase and phthalate oxygenase reductase from *Pseudomonas cepacia*, *J. Biol. Chem.* **262** (4), 1510-1518

146. Correll, C.C., Batie, C.J., Ballou, D.P., and Ludwig, M.L. (1985) Crystallographic characterization of phthalate oxygenase reductase, an iron-sulfur flavoprotein from *Pseudomonas cepacia*, *J. Biol. Chem.* **260** (27), 4633-4635

147. Cline, J.F., Hoffman, B.M., Mims, W.B., Lahaie, E., Ballou, D.P., and Fee, J.A. (1985) Evidence for N coordination to Fe in the 2fe-2s clusters of *Thermus* Rieske protein and phthalate dioxygenase from *Pseudomonas*, *J. Biol. Chem.* **260** (6), 3251-3254

148. Coker, R.J. (2004) Review: Multidrug-resistant tuberculosis: public health challenges, *Trop. Med. Int. Health.* **9** (1), 25-40

149. Smith, I. (2003) *Mycobacterium tuberculosis* pathogenesis and molecular determinants of virulence, *Clin. Microbiol. Rev.* **16** (3), 463-496

150. WHO. Tubeculosis information sheet, www.who.int/health_topics/tuberculosis/en/

151. Cole, S.T., Brosch, R., Parkhill, J., Garnier, T., Churcher, C., Harris, D., Gordon, S.V., Eiglmeier, K., Gas, S., Barry, C.E., Tekaia, F., Badcock, K., Basham, D., Brown, D., *et al.* (1998) Deciphering the biology of *Mycobacterium tuberculosis* from the complete genome sequence, *Nature* **393** (6685), 537-544

152. Crick, D.C., Mahapatra, S., and Brennan, P.J. (2001) Biosynthesis of the arabinogalactan-peptidoglycan complex of *Mycobacterium tuberculosis*, *Glycobiology* **11** (9), 107R-118R

153. Brosch, R., Gordon, S.V., Eiglmeier, K., Garnier, T., and Cole, S.T. (2000) Comparative genomics of the leprosy and tubercle bacilli, *Res. Microbiol.* **151** (2), 135-142

154. Minnikin, D.E., Kremer, L., Dover, L.G., and Besra, G.S. (2002) The methyl-branched fortifications of *Mycobaterium tuberculosis*, *Chem. Biol.* **9** (5), 545-553

155. Lupetti, A., Danesi, R., Campa, M., Del Tacca, M., and Kelly, S. (2002) Molecular basis of resistance to azole antifungals, *Trends Mol. Med.* **8** (2), 76-81

156. Cole, S.T. (1999) Learning from the genome sequence of *Mycobacterium tuberculosis* H37Rv, *FEBS Lett.* **452** (1-2), 7-10

157. McLean, K.J., Marshall, K.R., Richmond, A., Hunter, I.S., Fowler, K., Kieser, T., Gurcha, S.S., Besra, G.S., and Munro, A.W. (2002) Azole antifungals are potent inhibitors of cytochrome P450 mono-oxygenases and bacterial growth in mycobacteria and streptomycetes, *Microbiology* **148**, 2937-2949

158. McLean, K.J., Cheesman, M.R., Rivers, S.L., Richmond, A., Leys, D., Chapman, S.K., Reid, G.A., Price, N.C., Kelly, S.M., Clarkson, J., Smith, W.E., and Munro, A.W. (2002) Expression, purification and spectroscopic characterization of the cytochrome P450CYP121 from *Mycobacterium tuberculosis*, *J. Inorg. Biochem.* **91** (4), 527-541

159. McLean, K.J., Warman, A.J., Seward, H.E., Marshall, K.R., Girvan, H.M., Cheesman, M.R., Waterman, M.R., and Munro, A.W. (2006) Biophysical characterisation of the sterol demethylase P450 from *Mycobacterium tuberculosis*, its cognate ferredoxin, and their interactions, *Biochemistry* **45** (27), 8427-8443

160. Sassetti, C.M., and Rubin, E.J. (2003) Genetic requirements for mycobacterial survival during infection, *Proc. Natl. Acad. Sci. U.S.A.* **100** (22), 12989-12994

161. Sassetti, C.M., Boyd, D.H., and Rubin, E.J. (2001) Comprehensive identification of conditionally essential genes in mycobacteria, *Proc. Natl. Acad. Sci. U.S.A.* **98** (22), 12712-12717

162. Recchi, C., Sclavi, B., Rauzier, J., Gicquel, B., and Reyrat, J.M. (2003) *Mycobacterium tuberculosis* Rv1395 is a class III transcriptional regulator of the AraC family involved in cytochrome P450 regulation, *J. Biol. Chem.* **278** (36), 33763-33773

163. Koshkin, A., Knudsen, G.M., and de Montellano, P.R.O. (2004) Intermolecular interactions in the AhpC/AhpD antioxidant defense system of *Mycobacterium tuberculosis*, *Arch. Biochem. Biophys.* **427** (1), 41-47

164. Sassetti, C.M., Boyd, D.H., and Rubin, E.J. (2003) Genes required for mycobacterial growth defined by high density mutagenesis, *Mol. Microbiol.* **48** (1), 77-84

165. Lamb, D.C., Fowler, K., Kieser, T., Manning, N., Podust, L.M., Waterman, M.R., Kelly, D.E., and Kelly, S.L. (2002) Sterol 14 alpha-demethylase activity in

376

Streptomyces coelicolor A3(2) is associated with an unusual member of the CYP51 gene family, *Biochem. J.* **364**, 555-562

166. Schnappinger, D., Ehrt, S., Voskuil, M.I., Liu, Y., Mangan, J.A., Monahan, I.M., Dolganov, G., Efron, B., Butcher, P.D., Nathan, C., and Schoolnik, G.K. (2003) Transcriptional adaption of *Mycobaterium tuberculosis* within macrophages: Insights into the phagosomal environment, *J. Exp. Med.* **198** (5), 693-704

167. Waddell, S.J., Stabler, R.A., Laing, K., Kremer, L., Reynolds, R.C., and Besra, G.S. (2004) The use of microarray analysis to determine the gene expression profiles of *Mycobacterium tuberculosis* in response to anti-bacterial compounds, *Tuberculosis* **84** (3), 263-274

168. Kendall, S.L., Rison, S.C., Movahedzadeh, F., Frita, R., and Stoker, N.G. (2004) What do microarrays really tell us about *M. tuberculosis*, *Trends Microbiol.* **12** (12), 537-544

169. Bellamine, A., Mangla, A.T., Nes, W.D., and Waterman, M.R. (1999) Characterization and catalytic properties of the sterol 14 alpha-demethylase from *Mycobacterium tuberculosis*, *Proc. Natl. Acad. Sci. U.S.A.* **96** (16), 8937-8942

170. Bellamine, A., Mangla, A.T., Dennis, A.L., Nes, W.D., and Waterman, M.R. (2001) Structural requirements for substrate recognition of *Mycobacterium tuberculosis* 14 alpha-demethylase: implications for sterol biosynthesis, *J. Lipid Res.* **42** (1), 128-136

171. Kannenberg, E.L., Perzl, M., and Hartner, T. (1995) The occurrence of hopanoid lipids in *Bradyrhizobium* bacteria, *FEMS Microbiol. Lett.* **127** (3), 255-261

172. Gatfield, J., and Pieters, J. (2000) Essential role for cholesterol in the entry of mycobacteria into macrophages, *Science* **288** (5471), 1647-1650

173. Podust, L.M., Stojan, J., Poulos, T.L., and Waterman, M.R. (2001) Substrate recognition sites in 14alpha-sterol demethylase from comparative analysis of amino acid sequences and X-ray structure of *Mycobacterium tuberculosis* CYP51., *J. Inorg. Biochem.* **87** (4), 227-235

174. Souter, A., McLean, K.J., Smith, W.E., and Munro, A.W. (2000) The genome sequence of *Mycobacterium tuberculosis* reveals cytochromes P450 as novel anti-TB drug targets, *J. Chem. Technol. Biotechnol.* **75** (10), 933-941

175. Munro, A.W., McLean, K.J., Marshall, K.R., Warman, A.J., Lewis, G., Roitel, O., Sutcliffe, M.J., Kemp, C.A., Modi, S., Scrutton, N.S., and Leys, D. (2003) Cytochromes P450: novel drug targets in the war against multidrug-resistant *Mycobacterium tuberculosis*, *Biochem. Soc. Trans.* **31** (3), 625-630

176. Ji, H.T., Zhang, W.N., Zhang, M., Kudo, M., Aoyama, Y., Yoshida, Y., Sheng, C.Q., Song, Y.L., Yang, S., Zhou, Y.J., Lu, J.G., and Zhu, J. (2003) Structure-based de novo design, synthesis, and biological evaluation of non-azole inhibitors specific for lanosterol 14 alpha-demethylase of fungi, *J. Med. Chem.* **46** (4), 474-485

177. Borremans, B., Hobman, J.L., Provoost, A., Brown, N.L., and Van der Lelie, D. (2001) Cloning and functional analysis of the pbr lead resistance determinant of *Ralstonia metallidurans* CH34, *J. Bacteriol.* **183** (19), 5651-5658

178. Juhnke, S., Peitzsch, N., Hubener, N., Grosse, C., and Nies, D.H. (2002) New genes involved in chromate resistance in *Ralstonia metallidurans* strain CH34., *Arch. Microbiol.* **179** (1), 15-25

179. Mergeay, M., Monchy, S., Vallaeys, T., Auquier, V., Benotmane, A., Bertin, P., Taghavi, S., Dunn, J., van der Lelie, D., and Wattiez, R. (2003) *Ralstonia metallidurans*, a bacterium specifically adapted to toxic metals: towards a catalogue of metal-responsive genes, *Fems Microbiol. Rev.* **27** (2-3), 385-410

180. Nies, D.H. (2003) Efflux-mediated heavy metal resistance in prokaryotes., *FEMS Microbiol. Rev.* **27** (2-3), 313-339

181. Noel-Georis, I., Vallaeys, T., Chauvaux, R., Monchy, S., Falmagne, P., Mergeay, M., and Wattiez, R. (2004) Global analysis of the *Ralstonia metallidurans* proteome: prelude for the large-scale study of heavy metal response., *Proteomics* **4** (1), 151-179

182. Nagy, I., Schoofs, G., Compernolle, F., Proost, P., Vanderleyden, J., and Demot, R. (1995) Degradation of the thiocarbamate herbicide EPTC (S-ethyl dipropylcarbamothioate) and biosafening by *Rhodococcus* sp. strain Ni86/21 involve an

inducible cytochrome P450 system and aldehyde dehydrogenase, *J. Bacteriol.* **177** (3), 676-687

183. Nelson, D.R. Cytochrome P450 homepage,
http//drnelson.utmem.edu/CytochromeP450.html

184. Werck-Reichhart, D., Hehn, A., and Didierjean, L. (2000) Cytochromes P450 for engineering herbicide tolerance, *Trends Plant Sci.* **5** (3), 116-123

185. Hunter, D.J.B., Roberts, G.A., Ost, T.W.B., White, J.H., Muller, S., Turner, N.J., Flitsch, S.L., and Chapman, S.K. (2005) Analysis of the domain properties of the novel cytochrome P450 RhF, *FEBS Lett.* **579** (10), 2215-2220

186. Sambrook, J., Fritsch, E.F., and Maniatis, T. (1989) *Molecular Cloning: a laboratory manual* (2nd ed.), *Cold Spring Harbour Laboratory Press, New York*

187. Berry, E.A., and Trumpower, B.L. (1987) Simultaneous determination of hemes a, b, and c from pyridine hemochrome spectra, *Analyt. Biochem.* **161**, 1-15

188. In Methods in Molecular Biology, vol. 131, Flavoprotein Protocols (Chapman, S.K. and Reid, G.A., eds) (1999), *Humana Press Inc., Totowa, N.J., U.S.A.*, 25-48

189. Weber, G. (1950) Fluorescence of riboflavin and flavin-adenine dinucleotide, *Biochem. J.* **47** (1), 114-121

190. Whitby, L.G. (1953) A new method for preparing flavin-adenine dinucleotide, *Biochem. J.* **54** (3), 437-442

191. Bessey, O.A., Lowry, O.L., and Love, R.H. (1949) The fluorometric measurement of the nucleotides of riboflavin and their concentration in tissues, *J. Biol. Chem.* **180** (2), 755-769

192. Ost, T.W.B., Miles, C.S., Munro, A.W., Murdoch, J., Reid, G.A., and Chapman, S.K. (2001) Phenylalanine 393 exerts thermodynamic control over the heme of flavocytochrome P450 BM3, *Biochemistry* **40** (45), 13421-13429

193. Hintz, M.J., and Peterson, J.A. (1981) The kinetics of reduction of cytochrome P450cam by reduced putidaredoxin, *J. Biol. Chem.* **256** (13), 6721-6728

194. Lawson, R.J., Leys, D., Sutcliffe, M.J., Kemp, C.A., Cheesman, M.R., Smith, S.J., Clarkson, J., Smith, W.E., Haq, I., Perkins, J.B., and Munro, A.W. (2004) Thermodynamic and biophysical characterisation of cytochrome P450 BioI from *Bacillus subtilis*, *Biochemistry* **43**, 12410-12426

195. Aoyama, Y., Noshiro, M., Gotoh, O., Imaoka, S., Funae, Y., Kurosawa, N., Horiuchi, T., and Yoshida, Y. (1996) Sterol 14-demethylase P450 (P45014DM) is one of the most ancient and conserved P450 species, *J. Biochem.* **119** (5), 926-933

196. Aoyama, Y., Horiuchi, T., Gotoh, O., Noshiro, M., and Yoshida, Y. (1998) CYP51-like gene of Mycobacterium tuberculosis actually encodes a P450 similar to eukaryotic CYP51, *J. Biochem.* **124**, 694-696

197. Lamb, D.C., Cannieux, M., Warrilow, A.G., Bak, S., Kahn, R.A., Manning, N.J., Kelly, D.E., and Kelly, S.L. (2001) Plant sterol 14 alpha-demethylase affinity for azole fungicides, *Biochem. Biophys. Res. Commun.* **284** (3), 845-849

198. Lamb, D.C., Kelly, D.E., Schunck, W.H., Shyadehi, A.Z., Akhtar, M., Lowe, D.J., Baldwin, B.C., and Kelly, S.L. (1997) The mutation T315A in *Candida albicans* sterol 14alpha-demethylase causes reduced enzyme activity and fluconazole resistance through reduced affinity, *J. Biol. Chem.* **272** (9), 5682-5688

199. Dawson, J.H., Andersson, L.A., and Sono, M. (1982) Spectroscopic investigations of ferric cytochrome P450cam ligand complexes, *J. Biol. Chem.* **257** (7), 3606-3617

200. Hawkes, D.B., Adams, G.W., Burlingame, A.L., Ortiz de Montellano, P.R., and De Voss, J.J. (2002) Cytochrome P450cin (CYP176A), isolation, expression, and characterization, *J. Biol. Chem.* **277** (31), 27725-27732

201. Venkateswarlu, K., Taylor, M., Manning, N.J., Rinaldi, M.G., and Kelly, S.L. (1997) Fluconazole tolerance in clinical isolates of Cryptococcus neoformans, *Antimicrob. Agents* **41** (4), 748-751

202. Matsuura, K., Yoshioka, S., Tosha, T., Hori, H., Ishimori, K., Kitagawa, T., Morishima, I., Kagawa, N., and Waterman, M.R. (2005) Structural diversities of active site in

clinical azole-bound forms between sterol 14alpha-demethylases (CYP51s) from human and *Mycobacterium tuberculosis, J. Biol. Chem.* **280** (10), 9088-9096

203. Ost, T.W.B., Clark, R.J., Anderson, J.L.R., Yellowlees, L.J., Daff, S., and Chapman, S.K. (2004) 4-cyanopyridine, a versatile spectroscopic probe for cytochrome P450 BM3, *J. Biol. Chem.* **279** (47), 48876-48882

204. Smith, G., Modi, S., Pillai, I., Lian, L., Sutcliffe, M.J., Pritchard, M.P., Friedberg, T., Roberts, G.C.K., and Wolf, C.R. (1998) Determinants of the substrate specificty of human cytochrome P450 CYP2D6: design and construction of a mutant with testosterone hydroxylase activity, *Biochem. J.* **331** (3), 783-792

205. Smith, S.J., Munro, A.W., and Smith, W.E. (2003) Resonance Raman scattering of cytochrome P450 BM3 and effect of imidazole inhibitors, *Biopolymers* **70** (4), 620-627

206. Hudeeek, J., Baumruk, V., Anzenbacher, P., and Munro, A.W. (1998) Catalytically self-sufficient P450 CYP102 (cytochrome P450 BM- 3): Resonance Raman spectral characterization of the heme domain and of the holoenzyme, *Biochem. Biophys. Res. Commun.* **243** (3), 811-815

207. Callahan, P.M., and Babcock, G.T. (1981) Insights into heme structure from soret excitation Raman spectroscopy, *Biochemistry* **20** (4), 952-958

208. Babcock, G.T., Callahan, P.M., Ondrias, M.R., and Salmeen, I. (1981) Coordination geometries and vibrational properties of cytochromes a and a3 in cytochrome oxidase from soret excitation Raman spectroscopy, *Biochemistry* **20** (4), 959-966

209. Hildebrandt, P., Greinert, R., Stier, A., and Taniguchi, H. (1989) Resonance Raman study on the structure of the active sites of microsomal cytochrome P450 isozymes LM2 and LM4, *Eur. J. Biochem.* **186** (1-2), 291-302

210. Hildebrandt, P., Garda, H., Stier, A., Bachmanova, G.I., and Kanaeva, I.P. (1989) Protein-protein interactions in microsomal cytochrome P450 isozyme LM2 and their effect on substrate binding, *Eur. J. Biochem.* **186** (1-2), 383-388

211. Parthasarathi, N., Hansen, C., Yamaguchi, S., and Spiro, T.G. (1987) Metalloporphyrin core size resonance Raman marker bands revisited: implications for the interpretation of hemoglobin photoproduct Raman frequencies, *J. Am. Chem. Soc.* **109** (13), 2865-3871

212. Macdonald, I.D.G., Munro, A.W., and Smith, W.E. (1998) Fatty acid-induced alteration of the porphyrin macrocycle of cytochrome P450 BM3, *Biophysical Journal* **74** (6), 3241-3249

213. Shimida, H., Nagano, S., Ariga, Y., Unno, M., Egawa, T., Hishiki, T., and Ishimura, Y. (1999) Putidaredoxin cytochrome P450cam interaction. Spin state of the heme iron modualtes putidaredoxin structure, *J. Biol. Chem.* **274** (14), 9363-9369

214. More, C., Belle, V., Asso, M., Fournel, A., Roger, G., Guigliarelli, B., and Bertrand, P. (1999) EPR spectroscopy: A powerful technique for the structural and functional investigation of metalloproteins, *Biospectroscopy* **5** (S5), S3-S18

215. Androes, G.M., and Calvin, M. (1962) Electron paramagnetic resonance in biology, *Biophys. J.* **2** (2), 217-258

216. Yoshida, Y., and Aoyama, Y. (1984) Yeast cytochrome P450 catalyzing lanosterol 14 alpha-demethylation. I. Purification and spectral properties, *J. Biol. Chem.* **259** (3), 1655-1660

217. Cheesman, M.R., Greenwood, C., and Thomson, A.J. (1991) Magnetic circular dichroism of hemoproteins, *Adv. Inorg. Chem.* **36** (2), 201-255

218. McKnight, J.E., Cheesman, M.R., Thomson, A.J., Miles, J.S., and Munro, A.W. (1993) Identification of charge-transfer transitions in the optical spectrum of low-spin ferric cytochrome P450 *Bacillus megaterium, Eur. J. Biochem.* **213** (2), 683-687

219. Gadsby, P.M.A., and Thomson, A.J. (1990) Assignment of the axial ligands of ferric ion in low-spin hemoproteins by near-infrared magnetic circular dichroism and electron paramagnetic resonance spectroscopy, *J. Am. Chem. Soc.* **112** (13), 5003-5011

220. Ball, D.W. (2004) Dichroism spectroscopy, *Spectroscopy* **19** (11), 28-30

221. Cheesman, M.R., Little, P.J., and Berks, B.C. (2001) Novel heme ligation in a c-type cytochrome involved in thiosulfate oxidation: EPR and MCD of SoxAX from *Rhodovulum sulphidophilum, Biochemistry* **40**, 10562-10569

222. Dhawan, I.K., Shelver, D., Thorsteinsson, M.V., Roberts, G.P., and Johnson, M.K. (1999) Probing the heme axial ligation in the CO-sensing CooA protein with magnetic circular dichroism spectroscopy, *Biochemistry* **28**, 12805-12813

223. Kelly, S.M., Jess, T.J., and Price, N.C. (2005) How to study proteins by circular dichroism, *Biochim. Biophys. Acta.* **1751** (2), 119-139

224. Kelly, S.M., and Price, N.C. (2000) The use of circular dichroism in the investigation of protein structure and function, *Curr. Protein Pept. Sci.* **1** (4), 349-384

225. Munro, A.W., Lindsay, J.G., Coggins, J.R., Kelly, S.M., and Price, N.C. (1994) Structural and enzymological analysis of the interaction of isolated domains of cytochrome P450 BM3, *FEBS Lett.* **343** (1), 70-74

226. Dawson, J.H., Andersson, L.A., and Sono, M. (1983) The diverse spectroscopic properties of ferrous cytochrome P450cam ligand complexes, *J. Biol. Chem.* **258** (22), 13637-13645

227. Andersson, L.A., and Peterson, J.A. (1995) Active-site analysis of ferric P450 enzymes: Hydrogen-bonding effects on the circular dichroism spectra, *Biochem. Biophys. Res. Commun.* **211** (2), 389-395

228. Dunbar, J., Yennawar, H.P., Banerjee, S., Luo, J., and Farber, G.K. (1997) The effect of denaturants on protein structure, *Protein. Sci.* **6** (8), 1727-1733

229. Mason, P.E., Neilson, G.W., Dempsey, C.E., Barnes, A.C., and Cruickshank, J.M. (2003) The hydration structure of guanidinium and thiocyanate ions: Implications for protein stability in aqueous solution, *Proc Natl Acad Sci U S A.* **100** (8), 4557-4561

230. Yu, X.C., Shen, S., and Strobel, H.W. (1995) Denaturation of cytochrome P450 2B1 by guanidine hydrochloride and urea: evidence for a metastable intermediate state of the active site, *Biochemistry* **34** (16), 5511-5517

231. Munro, A.W., Lindsay, J.G., Coggins, J.R., Kelly, S.M., and Price, N.C. (1996) Analysis of the structural stability of the multidomain enzyme flavocytochrome P450 BM3, *Biochim. Biophys. Acta.* **1296** (2), 127-137

232. Coghlan, V.M., and Vickery, L.E. (1992) Electrostatic interactions stabilizing ferredoxin electron transfer complexes. Disruption by "conservative" mutations, *J. Biol. Chem.* **267** (13), 8932-8935

233. Lawson, R.J., von Wachenfeldt, C., Haq, I., Perkins, J.B., and Munro, A.W. (2004) Expression and characterization of the two flavodoxin proteins of *Bacillus subtilis*, YkuN and YkuP: Biophysical properties and interactions with cytochrome P450 Biol., *Biochemistry* **43** (39), 12390-12409

234. Sligar, S.G., and Gunsalus, I.C. (1976) A thermodynamic model of regulation: Modulation of redox equilibria in camphor monoxygenase., *Proc. Natl. Acad. Sci. U.S.A.* **73** (4), 1078-1082

235. Dutton, P.L. (1978) Redox potentiometry: determination of midpoint potentials of oxidation-reduction components of biological electron transfer systems, *Methods Enzymol.* **54**, 411-435

236. Perera, R., Sono, M., Sigman, J.A., Pfister, T.D., Lu, Y., and Dawson, J.H. (2003) Neutral thiol as a proximal ligand to ferrous heme iron: Implications for heme proteins that lose cysteine thiolate ligation on reduction, *Proc. Natl. Acad. Sci. U.S.A.* **100** (7), 3641-3646

237. Goldberg, D.E., Slater, A.F.G., Cerami, A., and Henderson, G.B. (1990) Hemoglobin degradation in the malaria parasite *Plasmodium falciparum*: An ordered process in a unique organelle, *Proc. Natl. Acad. Sci. U.S.A.* **87** (8), 2931-2935

238. Tschirret-Guth, R.A., Koo, L.S., Hoa, G.H., and Ortiz de Montellano, P.R. (2001) Reversible pressure deformation of a thermophillic cytochrome P450 enzyme (CYP119) and its active-site mutants, *J. Am. Chem. Soc.* **123** (21), 3412-3417

239. McIver, L., Leadbeater, C., Campopiano, D.J., Baxter, R.L., Daff, S.N., Chapman, S.K., and Munro, A.W. (1998) Characterisation of flavodoxin NADP$^+$ oxidoreductase and flavodoxin; key components of electron transfer in *Escherichia coli*, *Eur. J. Biochem.* **257** (3), 577-585

240. Cheesman, M.R., Baer, B.R., Zheng, Y., Gillam, E.M.J., and Rettie, A.E. (2003) Rabbit CYP4B1 engineered for high-level expression in *Escherichia coli*: ligand stabilisation and processing of the N-terminus and heme prosthetic group, *Arch. Biochem. Biophys.* **416** (1), 17-24

241. Ristau, O., Rein, H., Janig, G.R., and Ruckpaul, K. (1978) Quantitative analysis of the spin equilibrium of cytochrome P450 LM2 fraction from rabbit liver microsomes, *Biochem. Biophys. Acta.* **536** (1), 226-234

242. Jovanovic, T., Farid, R., Friesner, R.A., and McDermott, A.E. (2005) Thermal equilibrium of high- and low-spin forms of cytochrome P450 BM3: repositioning of the substrate?, *J. Am. Chem. Soc.* **127** (39), 13548-13552

243. Tyson, C.A., Lipscomb, J.D., and Gunsalus, I.C. (1972) The roles of putidaredoxin and P450cam in methylene hydroxylation, *J. Biol. Chem.* **247** (18), 5777-5784

244. Sevrioukova, I.F., Garcia, C., Li, H., Bhaskar, B., and Poulos, T.L. (2003) Crystal structure of putidaredoxin, the [2Fe-2S] component of the P450cam monooxygenase system from *Pseudomonas putida*, *J. Mol. Biol.* **332** (2), 377-392

245. Pierre, J., Bazin, M., Debey, P., and Santus, R. (1982) One-electron photoreduction of bacterial cytochrome P450 by ultraviolet light. I. Steady-state irradiations, *Eur. J. Biochem.* **124** (3), 533-537

246. Brewer, C.B., and Peterson, J.A. (1988) Single turnover kinetics of the reaction between oxycytochrome P450cam and reduced putidaredoxin, *J. Biol. Chem.* **263** (2), 791-798

247. Shimada, T. (2006) Xenobiotic-metabolizing enzymes involved in activation and detoxification of carcinogenic polycyclic aromatic hydrocarbons, *Drug Metab. Pharmacokinet.* **21** (4), 257-276

248. Page, C.C., Moser, C.C., Chen, X., and Dutton, P.L. (1999) Natural engineering principles of electron tunelling in biological oxidation-reducation, *Nature* **402** (6757), 47-52

249. Neeli, R., Roitel, O., and Munro, A.W. (2005) Switching pyridine nucleotide specificity in P450 BM3: mechanistic analysis of the W1046H and W1046A enzymes, *J. Biol. Chem.* **280** (18), 17634-17644

250. Torres, S., Fjetland, C.R., and Lammers, P.J. (2005) Alkane-induced expression, substrate binding profile, and immunolocalization of a cytochrome P450 encoded on the nifD excision element of *Anabaena* 7120., *BMC Microbiol.* **5** (16), 1-12

251. Tretiakov, V.E., Degtyarenko, K.N., Uvarov, V.Y., and Archakov, A.I. (1989) Secondary structure and membrane topology of cytochrome P450s, *Arch. Biochem. Biophys.* **275** (2), 429-439

252. Evans, E.H., Rush, J.D., Johnson, C.E., and Evans, M.C.W. (1979) Mossbauer spectra of Photosystem-I reaction centres from the blue-gree alga *Chlorogloea fritschii*, *Biochem. J.* **182** (3), 861-865

253. Sellers, V.M., Wang, K., Johnson, M.K., and Dailey, H.A. (1998) Evidence that the fourth ligand to the [2Fe-2S] cluster in animal ferrochelatase is a cysteine, *J. Biol. Chem.* **273** (35), 22311-22316

254. Dutta, P.K., Nestor, J.R., and Spiro, T.G. (1977) Resonance coherent anti-Stokes Raman scattering spectra of fluorescent biological chrompohores:Vibrational evidence for hydrogen bonding of flavin to glucose oxidase and for rapid solvent exchange, *Proc. Natl. Acad. Sci. U.S.A.* **74** (10), 4146-4149

255. Conover, R.C., Kowal, A.T., Fu, W., Park, J., Aono, S., Adams, M.W.W., and Johnson, M.K. (1990) Spectroscopic characterisation of the novel iron-sulphur cluster in *Pyrococcus furiosus* ferredoxin, *J. Biol. Chem.* **265** (15), 8533-8541

256. Han, S., Czernuszewicz, R.S., Kimura, T., Adams, M.W.W., and Spiro, T.G. (1989) Fe_2S_2 protein resonance Raman spectra revisited: Structural variations among adrenodoxin, ferredoxin, and red paramagnetic protein, *J. Am. Chem. Soc.* **111** (10), 3505-3511

257. Roitel, O., Scrutton, N.S., and Munro, A.W. (2003) Electron transfer in flavocytochrome P450 BM3: Kinetics of flavin reduction and oxidation, the role of

cysteine 999, and relationships with mammalian cytochrome P450 reductase, *Biochemistry* **42** (36), 10809-10821

258. Bazin, M., Pierre, J., Debey, P., and Santus, R. (1982) One-electron photoreduction of bacterial cytochrome P450 by ultraviolet light. II. A study using laser flash photolysis of the dynamics of the reduction of bacterial cytochrome P450 in the resence of carbon monoxide. The role of the protein conformation, *Eur. J. Biochem.* **124** (3), 539-544

259. Gassner, G.T., and Ballou, D.P. (1995) Preparation and characterisation of a trunctated form of phthalate dioxygenase reductase that lacks an iron-sulphur domain, *Biochemistry* **34** (41), 13460-13471

260. Gassner, G.T., Ludwig, M.L., Gatti, D.L., Correll, C.C., and Ballou, D.P. (1995) Structure and mechanism of the iron-sulphur flavoprotein phthalate dioxygenase reductase, *FASEB J.* **9**, 1411-1418

261. Dohr, O., Paine, M.J., Friedberg, T., Roberts, G.C., and Wolf, C.R. (2001) Engineering of a functional human NADH-dependent cytochrome P450 system, *Proc. Natl. Acad. Sci. U.S.A.* **98** (1), 81-86

262. Straub, K.L., Benz, M., and Schink, B. (2001) Iron metabolism in anoxic environments at near neutral pH, *FEMS Microbiol. Ecol.* **34** (3), 181-186

263. Wallace, C.J., and Proudfoot, A.E. (1987) On the relationship between oxidation-reduction potential and biological activity in cytochrome *c* analogues. Results from four novel two-fragment complexes, *Biochem. J.* **245** (3), 773-779

264. Scrutton, N.S., Berry, A., and Perham, R.N. (1990) Redesign of the coenzyme specificty of a dehydrogenase by protein engineering, *Nature* **343** (6253), 38-43

265. Sem, D.S., and Kasper, C.B. (1993) Interaction with arginine 597 of NADPH-cytochrome P450 oxidoreductase ias a primary source of the uniform binding energy used to disriminate between NADPH and NADH, *Biochemistry* **32** (43), 11548-11558

266. Correll, C.C., Ludwig, M.L., Bruns, C.M., and Karplus, P.A. (1993) Structural prototypes for an extended family of flavoprotein reductases: Comaprison of phthalate dioxygenase reductase with ferredoxin reductase and ferredoxin, *Protein Sci.* **2** (12), 2112-2133

267. Murataliev, M.B., and Feyereisen, R. (1996) Functional interactions in cytochrome P450 BM3. Fatty acid substrate binding alters electron-transfer properties of the flavoprotein domain, *Biochemistry* **35** (47), 15029-15037

268. Eble, K.S., and Dawson, J.H. (1984) Novel reactivity of cytochrome P450cam. Methyl hydroxylation of 5,5-difluorocamphor, *J. Biol. Chem.* **259** (23), 14389-14393

269. Serhan, C.N., and Ernst, O. (2001) Unorthodox routes to prostanoid formation: new twists in cyclooxygenase-initiated pathways, *J. Clin. Invest.* **107** (12), 1481-1489

270. Capdevila, J.H., Falck, J.R., and Estabrook, R.W. (1992) Cytochrome P450 and the arachidonate cascade, *FASEB J.* **6** (2), 731-736

271. Bellec, G., Dreano, Y., Bail, J., Menez, J., and Berthou, F. (1997) Cytochrome P450 hydroxylation of carbon atoms of the alkyl chains of symmetrical N-nitrosodialkylamines by human liver microsomes, *Mutat. Res.* **377** (2), 199-209

272. Dick, W.A., Ankumah, R.O., McClung, G., and Abou-Assaf, N. (1990) Enhanced degradation of S-ethyl N,N-dipropylthiocarbamate in soil and by an isolated soil microrganism, *In K.D. Racke and J.R. Coats (ed.), Enhanced biodegradation of pedticides in the environment. ACS Chemical Symposium Series no. 426. American Chemical Society, Washington, D.C.*

273. Govindaraj, S., and Poulos, T.L. (1997) The domain architecture of cytochrome P450 BM3, *J. Biol. Chem.* **272** (12), 7915-7921

274. Podust, L.M., Kim, Y., Arase, M., Neely, B.A., Beck, B.J., Bach, H., Sherman, D.H., Lamb, D.C., Kelly, S.L., and Waterman, M.R. (2003) The 1.92-Å Structure of *Streptomyces coelicolor* A3(2) CYP154C1. A new monooxygenase that functionalizes macrolide ring systems, *J. Biol. Chem.* **278** (14), 12214-12221

275. Dispirito, A.A., Lipscomb, J.D., and Hooper, A.B. (1986) Cytochrome aa_3 from *Nitrosomonas europaea*, *J. Biol. Chem.* **261** (36), 17048-17056

276. Brautigan, D.L., Feinberg, B.A., Hoffman, B.M., Margoliash, E., Peisach, J., and Blumberg, W.E. (1977) Multiple low spin forms of the cytochrome *c* ferrihemochrome, *J. Biol. Chem.* **252** (2), 574-582

277. Green, A.J., Munro, A.W., Cheesman, M.R., Reid, G.A., von Wachenfeldt, C., and Chapman, S.K. (2003) Expression, purification and characterisation of a *Bacillus subtilis* ferredoxin: a potential electron transfer donor to cytochrome P450 BioI, *J. Inorg. Biochem.* **93** (1-2), 92-99

278. Miles, J.S., Munro, A.W., Rospendowski, B.N., Smith, W.E., McKnight, J.E., and Thomson, A.J. (1992) Domains of the catalytically self-sufficient cytochrome P450 BM3. Genetic construction, overexpression, purification and spectroscopic characterization, *Biochem. J.* **288** (2), 503-509

279. Dunford, A.J., Marshall, K.R., Munro, A.W., and Scrutton, N.S. (2004) Thermodynamic and kinetic analysis of the isolated FAD domain of rat neuronal nitric oxide synthase altered in the region of the FAD shielding residue Phe1395, *Eur. J. Biochem.* **271** (12), 2548-2560